

PB94-186590

# **CINCINNATI INFRASTRUCTURE INSTITUTE**

**University of Cincinnati  
College of Engineering**

**Cincinnati, Ohio 45221-0071**

Available from  
U.S. Department of Commerce  
National Technical Information Service  
Springfield, Virginia 22161

**NONDESTRUCTIVE AND DESTRUCTIVE TESTING  
OF A REINFORCED CONCRETE SLAB BRIDGE  
AND ASSOCIATED ANALYTICAL STUDIES**

by

**A. E. Aktan, R. Miller, B. Shahrooz, M. Zwick  
M. Heckenmueller, I. Ho, W. Hrinko, and T. Toksoy**

**Report No. UC-CII 92/02**

**December 1992**

**A Report to Sponsors:  
Federal Highway Administration  
and  
Ohio Department of Transportation  
Contract No. 14482 (0)**

**and**

**National Science Foundation  
Grant No. MSM-9002820**

**Cincinnati Infrastructure Institute  
University of Cincinnati  
College of Engineering  
Cincinnati, Ohio 45221-0071**

**The contents of this report reflect the view(s) of the author(s) who are responsible for the facts and the accuracy of the data presented herein. The contents do not necessarily reflect the official views or policies of the Federal Highway Administration, the Ohio Department of Transportation, or the National Science Foundation. This report does not constitute a standard, specification, or regulation.**

1. Report No. <b>FHWA/OH-93/017</b>	2.  PB94-186590	3. Recipient's Catalog No.	
4. Title and Subtitle		5. Report Date December, 1992	
		6. Performing Organization Code	
7. Author(s) Ahmet Emin Aktan, R. Miller, B. Shahrooz, M. Zwick, M. Heckenmueller, I. Ho, W. Hrinko and T. Toksoy		6. Performing Organization Report No. UC-CII 92/02	
		10. Work Unit No. (TRANS)	
8. Performing Organization Name and Address The University of Cincinnati College of Engineering Cincinnati, OH 45221-0071		11. Contract or Grant No. State Job No. 14483(0)	
		13. Type of Report and Period Covered Final Report	
12. Sponsoring Agency Name and Address Ohio Department of Transportation 25 S. Front St. Columbus, OH 43215		14. Sponsoring Agency Code	
		15. Supplementary Notes Prepared in cooperation with the U.S. Department of Transportation, Federal Highway Administration	
16. Abstract <p>Recently, many bridges have failed to perform under service loads, scour, floods or earthquakes. Meanwhile, evidence suggests that a large number of bridges may be deemed structurally deficient without justification by present inspection and rating procedures. Many RC (Reinforced Concrete) slab bridges, which are still useable, are now being replaced before full utilization of their inherent capacity because of a lack of understanding and knowledge of the effects of deterioration and aging on these bridges. To establish procedures that allow for the full utilization of RC slab bridge capacity, a 38-year old sample was loaded to failure. The bridge, which was decommissioned due to its age and deteriorated state, endured the equivalent loading of 22 rating trucks before failure.</p> <p>The research was designed to study and determine the abilities of different NDE (Nondestructive Evaluation) techniques to detect damage and to examine processes for improving the condition evaluation and rating of concrete slab bridges. Accurate condition evaluation and rating of bridges is key for improving the present rating and decommissioning practice. Through this research a better understanding of the complex behavior of slab bridges at all their limit states has been achieved. Improvements in NDE (Nondestructive Evaluation) and NLFEA (Nonlinear Finite Element Analysis) have been accomplished.</p>			
17. Key Words Slab Bridge, Destructive Testing, Nondestructive Testing, Modal Testing, Deterioration, Rating, Nonlinear Finite Elements, Punching Shear.		18. Distribution Statement No Restrictions. This document is available to the public through the National Technical Information Service, Springfield, Virginia 22161	
19. Security Classif. (of this report) Unclassified	20. Security Classif. (of this page) Unclassified	21. No. of Pages	22. Price

## I. ABSTRACT

Recently, many bridges have failed to perform under service loads, scour, floods or earthquakes. Meanwhile, evidence suggests that a large number of bridges may be deemed structurally deficient without justification by present inspection and rating procedures. Many RC (Reinforced Concrete) slab bridges, which are still useable, are now being replaced before full utilization of their inherent capacity because of a lack of understanding and knowledge of the effects of deterioration and aging on these bridges. To establish procedures that allow for the full utilization of RC slab bridge capacity, a 38-year old sample was loaded to failure. The bridge, which was decommissioned due to its age and deteriorated state, endured the equivalent loading of 22 rating trucks before failure.

The research was designed to study and determine the abilities of different NDE (Nondestructive Evaluation) techniques to detect damage and to examine processes for improving the condition evaluation and rating of concrete slab bridges. Accurate condition evaluation and rating of bridges is key for improving the present rating and decommissioning practice. Through this research a better understanding of the complex behavior of slab bridges at all their limit states has been achieved. Improvements in NDE (Nondestructive Evaluation) and NLFEA (Nonlinear Finite Element Analysis) have been accomplished.

## II. ACKNOWLEDGEMENTS

The authors wish to acknowledge the project sponsors; FHWA/ODOT (Contract No. 14482 (0)) and NSF (Grant No. MSM-9002820). Specifically, we would like to acknowledge Dr. K. Chong, NSF Program Director; and from ODOT, Messrs W. Edwards, Engineer of Research and Development; V. Dalal, Research and Development Bureau; D. Hanhilammi, Engineer of Bridges; R. Eltzroth, District 8 Bridge Engineer; and W. Fair, District 8 Chief of Operations as well as numerous other ODOT personnel who provided invaluable support and advice throughout the research.

The following personnel at the University of Cincinnati are also acknowledged: graduate students H. Somaprasad and Chuan Chuntavan; research engineer Charles Young, technician Don Strunk, and Research Associate Dr. Lee who all provided valuable support to the project. Thanks go to the team of Anand Chakravarty, Laurie Aktan, and Chris Edelenbos, who edited the document and prepared it for publication. Professor Elizabeth McCord, Department of English, is also thanked for her edits and advice. In addition we would like to thank the numerous undergraduate students who provided their assistance throughout the project.

Special thanks goes to Mike Carlier of the Manta Corporation who designed and operated the electro-hydraulic servo-controlled loading system, Larry Rayburn of Goettle Corporation who provided invaluable support by installing the rock anchors, and the Sheffer Corporation which provided the loading actuators at a subsidized cost.

Invaluable consultation and collaboration was provided by Drs. R. Iding and D. Meinheit and D. Heidbrink from Wiss, Janney, Elstner, Assoc. of Chicago. Further recognition goes to the Delft Technological University of the Netherlands who collaborated on the NLFEA (Nonlinear Finite Element Analysis).

### III. TABLE OF CONTENTS

	<u>PAGE</u>
<b>I. ABSTRACT</b> .....	i
<b>II. ACKNOWLEDGEMENTS</b> .....	ii
<b>IV. LIST OF TABLES</b> .....	vii
<b>V. LIST OF FIGURES</b> .....	viii
<b>EXECUTIVE SUMMARY</b> .....	1
<b>INTRODUCTION</b> .....	1
<b>TEST SPECIMEN AND CONDITION</b> .....	2
<b>DESIGN OF LOADING AND DATA ACQUISITION</b> .....	3
<b>NONDESTRUCTIVE EVALUATION</b> .....	6
<b>PREDICTIVE ANALYSES</b> .....	8
<b>CORRELATION ANALYSES</b> .....	9
<b>CONCLUSIONS</b> .....	10
<b>CHAPTER 1:INTRODUCTION</b> .....	1-1
<b>1.1 BASIS OF RESEARCH</b> .....	1-1
<b>1.2 GOALS OF RESEARCH</b> .....	1-2
1.2.1 Bridge Inspection and Evaluation .....	1-2
1.2.2 Bridge Rating and Decommissioning .....	1-3
1.2.3 Limit States of Bridge Behavior .....	1-3
1.2.4 Field Destructive Testing .....	1-4
1.2.5 Nonlinear Finite Element Analysis .....	1-4
<b>1.3 PROJECT COORDINATION AND SCHEDULING</b> .....	1-4
<b>CHAPTER 2: TEST SPECIMEN AND MATERIAL PROPERTIES</b> .....	2-1
<b>2.1 DESCRIPTION OF TEST SPECIMEN</b> .....	2-1
<b>2.2 MATERIAL PROPERTIES</b> .....	2-1
2.2.1 Concrete Material Properties .....	2-2
2.2.2 Reinforcing Steel Properties .....	2-4
<b>CHAPTER 3: CONDITION OF TEST SPECIMEN</b> .....	3-1
<b>3.1 CONDITION SURVEYS</b> .....	3-1
3.1.1 Bridge Damage Survey .....	3-1
3.1.2 Damage of Bridge Deck as Indicated by the Cores .....	3-2
3.1.3 Deterioration and Structural Integrity .....	3-3
<b>3.2 MECHANISMS OF MATERIAL DETERIORATION</b> .....	3-3
3.2.1 Petrographic Analysis .....	3-3
3.2.2 Aggregate "D" Cracking and Alkali-Silica Reaction (ASR) .....	3-5
3.2.3 Porosity .....	3-6
3.2.4 Absorption Testing .....	3-7
3.2.5 Chloride Ions .....	3-7

	<u>PAGE</u>
3.2.6 Rusting of the Reinforcing Steel .....	3-10
3.2.7 Alkali and Calcium Ion Testing .....	3-12
3.3 SUGGESTED IMPROVEMENTS .....	3-13
<b>APPENDIX TO CHAPTER 3: PETROGRAPHIC ANALYSES</b>	
<b>CHAPTER 4: DESIGN OF DESTRUCTIVE TESTING .....</b>	<b>4-1</b>
<b>AND INSTRUMENTATION</b>	
4.1 DESIGN OF LOADING SYSTEM .....	4-1
4.1.1 Development of Loading System .....	4-1
4.1.2 Design of Loading System .....	4-2
4.1.3 Design of the Servo-Controlled System .....	4-3
4.2 INSTRUMENTATION .....	4-3
4.2.1 Instrument Selection Criteria .....	4-3
4.2.2 Calibration .....	4-5
4.2.3 Error Types and Description (Figures 4.12 - 4.14) .....	4-6
4.2.4 Final Selection of Instruments and Instrumentation Layout .....	4-10
4.3 TEST PROCEDURE AND CONDUCT .....	4-11
<b>CHAPTER 5: RESULTS OF DESTRUCTIVE TESTING .....</b>	<b>5-1</b>
5.1 BACKGROUND INTO BEHAVIOR OF SKEWED .....	5-1
SLAB BRIDGES	
5.2 RESULTS OF DESTRUCTIVE TESTING .....	5-1
5.2.1 Test Monitoring and Data Reduction .....	5-2
5.2.2 Low-Level Testing .....	5-3
5.2.3 Destructive Testing .....	5-3
5.3 LIMIT-STATES OF BRIDGE RESPONSE .....	5-4
5.4 MECHANICS OF FAILURE .....	5-7
5.4.1 Initiation of Failure .....	5-7
5.4.2 Propagation of Failure .....	5-8
5.4.3 Analysis of Failure .....	5-9
<b>CHAPTER 6: NONDESTRUCTIVE EVALUATION STUDIES .....</b>	<b>6-1</b>
6.1 INTRODUCTION .....	6-1
6.1.1 Nondestructive Evaluation .....	6-1
6.1.2 Objectives and Scope .....	6-1
6.2 METHODS AVAILABLE FOR BRIDGE NDE .....	6-2
6.2.1 Features Desired in a Bridge NDE Method .....	6-2
6.2.2 Classification of Existing Bridge NDE Methods .....	6-2
6.2.3 Proposed NDE Procedure .....	6-4
6.3 APPLICATION OF NDE TO THE BATAVIA BRIDGE .....	6-4
6.3.1 Overview of the Nondestructive Test Program .....	6-4
6.3.2 Design of the Modal Tests .....	6-4

	<u>PAGE</u>
6.3.3 Data Acquisition .....	6-6
6.3.4 Data Post-Processing .....	6-7
6.3.5 Results of the Modal Tests .....	6-10
6.3.6 Derivation of the Flexibility Coefficients from the Modal Test Results .....	6-12
6.3.7 Verification of the Modal Flexibility by Truck Load Testing .....	6-14
6.3.8 Finite Element Modeling .....	6-16
6.3.9 Damage Identification .....	6-19
6.3.10 Comparison of Frequencies, Damping and Mode Shapes .....	6-20
6.3.11 Comparison of Flexibility Profiles .....	6-22
<b>CHAPTER 7: BRIDGE RATING</b> .....	<b>7-1</b>
7.1 INTRODUCTION .....	7-1
7.1.1 Specifications and Trucks .....	7-1
7.1.2 Problems in Bridge Rating .....	7-2
7.1.3 Analysis of Bridge for Rating .....	7-2
7.2 RATING BASED ON AASHTO 1983 AND HS TRUCKS .....	7-3
7.3 RATING BASED ON AASHTO 1983 AND TYPE 3 RATING TRUCKS .....	7-4
7.4 RATING BASED ON AASHTO 1989 .....	7-6
7.5 RATING BASED ON THE CALIBRATED FINITE ELEMENT MODEL .....	7-8
7.6 RATING BASED ON DESTRUCTIVE TEST LOADING POSITION .....	7-9
7.7 COMPARISON OF RATING PROCEDURES .....	7-11
<b>CHAPTER 8: LINEAR AND NONLINEAR FINITE ELEMENT ANALYSES</b> .....	<b>8-1</b>
8.1 INTRODUCTION .....	8-1
8.2 PRELIMINARY ANALYSES .....	8-1
8.2.1 Yield Line Analysis .....	8-2
8.2.2 Linear Finite Element Analysis .....	8-2
8.2.3 Nonlinear Finite Element Analysis .....	8-4
8.3 PARAMETRIC STUDIES .....	8-8
8.3.1 Concrete Material Characteristics .....	8-8
8.3.2 Support Stiffness at Abutments .....	8-9
8.3.3 Geometric Modeling of Slab-Pier Cap Connection .....	8-10
8.3.4 Summary .....	8-10
8.4 POST-TEST CORRELATION STUDIES .....	8-11
8.4.1 Simulation of Results from Truck Load Tests .....	8-11
8.4.2 Correlation of Results from Destructive Test .....	8-12

	<b>PAGE</b>
<b>CHAPTER 9: CONCLUSIONS</b> -----	9-1
9.1 GENERAL CONCLUSIONS -----	9-1
9.2 SPECIFIC CONCLUSIONS FROM EACH CHAPTER -----	9-3
9.2.1 Chapter 1 Conclusions -----	9-3
9.2.2 Chapter 2 Conclusions -----	9-3
9.2.3 Chapter 3 Conclusions -----	9-3
9.2.4 Chapter 4 Conclusions -----	9-5
9.2.5 Chapter 5 Conclusions -----	9-5
9.2.6 Chapter 6 Conclusions -----	9-6
9.2.6.1 Regarding the Modal Test Procedure -----	9-6
9.2.6.2 Regarding the Use of Modal Testing as a Nondestructive Evaluation Tool -----	9-8
9.2.7 Chapter 7 Conclusions -----	9-9
9.2.8 Chapter 8 Conclusions -----	9-9
<b>REFERENCES</b>	

#### IV. LIST OF TABLES

<u>TABLE</u>	<u>PAGE</u>
2.1 Concrete Core Strength Results -----	2-2
2.2 ASTM C642 Test Results for Unit Weights -----	2-3
2.3 Split Cylinder Tests -----	2-3
2.4 Tension Specimen Results -----	2-4
3.1 Rebar Loss of Area and Effect on Internal Strength -----	3-11
3.2 Percentage Loss of Area -----	3-12
4.1 Error Results -----	4-9
4.2 DCDT Specifications -----	4-9
4.3 Slide Wire Potentiometer Specification -----	4-10
5.1 Holds in Loading -----	5-2
6.1 Geometric System Identification Based NDE Procedure -----	6-5
6.2 Data Acquisition Settings -----	6-8
6.3 Typical Time and Labor Requirements for an Impact Test ----- on a Highway Bridge	6-9
6.4 Frequency and Damping Values for the Four Modal Tests -----	6-11
6.5 Comparison of Truck Load Test Deflections with ----- Modal Test Flexibility	6-15
6.7 Comparison of Frequencies and Damping Values for ----- Tests 2, 3, and 4	6-21
7.1 Rating Based on the 1989 AASHTO Specifications: ----- Using the AASHTO H and HS Trucks	7-5
7.2 Rating Based on the 1983 AASHTO Specifications: ----- Using the AASHTO Type 3 Rating Trucks	7-6
7.3 Rating Based on the 1989 AASHTO Guidelines -----	7-7
7.4 Rating Based on the 1989 AASHTO Guidelines: ----- Using Calibrated Finite Element Model	7-9
7.5 Rating Factors Based on Destructive Test Loading -----	7-10

## V. LIST OF FIGURES

### **FIGURE**

- 1(a) Photo of Test Bridge
- 1(b) Deteriorated Shoulder of Test Bridge
- 2 Design Concept of Loading System
- 3 Load-Displacement Response at Point C3
- 4 Response of Key Instruments
- 5(a) Top View of Failure Plane
- 5(b) Appearance of Bottom and Top Failure Planes
- 6 Calibrated Model Parameters
- 7 Bridge Deflection Profiles from 1st Modal Tests and Nominal Analytical Model
- 8 Bridge Deflection Profiles from 2nd and 3rd Modal Tests Corresponding to Uniform Loading
- 9(a) NLFEA Model
- 9(b) Results of NLFEA Analyses
- 10 Refined Analytical Model of Slab-Abutment Connection
- 11 Comparison of Computed Load-Deflection and Load-Rotation Curves with Experimental Results
- 12(a) Comparison of Deflection Profiles from Refined Model
- 12(b) Comparison of Deflection Profiles from Refined Model
- 13 Comparison of Rebar Yield Locations
- 1.1 Project Personnel and Organization Chart
- 2.1 Map Location and Photo of Bridge
- 2.2 Site Plan and Elevation
- 2.3 Slab Reinforcement Details
- 2.4 Additional Slab Reinforcement Details
- 2.5 Reinforcement Details: Top of Slab
- 2.6 Reinforcement Details: Bottom of Slab
- 2.7 Pier Design
- 2.8 Pier Details
- 2.9 Abutment Design
- 2.10 Abutment Reinforcement Details
- 2.11 Bridge Damage - Bottom View
- 2.12 Typical Modulus of Elasticity Graph for Concrete Cylinders
- 2.13 Typical Stress-Strain Curve for the Tension Specimens
- 3.1 Bridge Damage-Top View
- 3.2 Bridge Damage-Bottom View
- 3.3 Top View of the East Shoulder of the Deck

## **FIGURE**

- 3.4 Side View of Damage to East Side of Bridge Deck
- 3.5 Approximate Damage to the Deck, Cross-Sectional View
- 3.6 Layout of Bridge for Condition Survey
- 3.7 Aggregate D-Cracking
- 3.8 Results of Uranyl Acetate Test
- 3.9 Incremental Intruded Volume, Hg Porosimeter Specimens
- 3.10 Cumulative Intruded Volume, Hg Porosimeter Specimens
- 3.11 Chloride Levels, Shoulder vs. Roadway Concrete (\*PPM of Concrete)
- 3.12 Chloride Levels, Roadway Concrete and Core L (\*PPM of Concrete)
- 3.13 Absorption of Water vs. Chloride Concentration ASTM C642 Specimens (\* PPM of Concrete)
- 3.14 Bulk Specific Gravity vs. Chloride Concentration Hg Porosimeter Specimens (\*PPM of Concrete)
- 3.15 Bulk Specific Gravity vs. Chloride Concentration (\*PPM of Concrete)
- 4.1 Design Concept of Loading System
- 4.2 Original Concept for Loading Frame
- 4.3 Original Loading Concept
- 4.4 Materials List for Original Loading Concept
- 4.5 Location of Loading Blocks
- 4.6 Elevation View of Loading System
- 4.7 Details of Load Transfer Blocks
- 4.8 Reinforcement Details for Loading Blocks
- 4.9 Details and Photo of Loading Blocks
- 4.10 Schematic of Hydraulic System
- 4.11 Clip Gage
- 4.12 Illustration of Errors in Instruments
- 4.13 DCDT Calibration Curve
- 4.14 Slide Wire Potentiometer Calibration Curve
- 4.15 Truck Load Test Instrumentation Plan
- 4.16 Destructive Test Instrumentation Plan
- 4.17 Destructive Test Pier Instrumentation
- 4.18 Destructive Test Instrumentation Details
- 4.19 DCDT and Weight Apparatus
- 4.20 Strain Gage Positions on Top Bars
- 4.21 Strain Gage Positions on Bottom Bars
- 4.22 Concrete Distortion Gage Positions
- 5.1 Moment Contours Due to Dead Load

## **FIGURE**

- 5.2 Typical Load Paths for Skewed Bridges
- 5.3 Deflection Profiles Showing Plateaus at the Hold
- 5.4 Creep in Load-Deflection Responed from Holds, and Limit States
- 5.5 Rotational Response at Abutment
- 5.6 Deflections Near Abutment
- 5.7 Rotational Response at Pier
- 5.8 Measured Strain in Top Bars at Pier
- 5.9 Load Deflection Response in Closed Corner
- 5.10 Deflection Profiles Along Lines C & F
- 5.11 Incremental Cracking Marked at 12 and 16 Truck Loads
- 5.12 Incremental Cracking Marked at 20 Trucks
- 5.13 Initiation of Diagonal Tension Failure Following Yielding at Critical Region
- 5.14 Failure Plane
- 5.15 Typical Cross-Sections of Failure
- 5.16 Failure Plane at Side and Bottom
- 5.17 Failure Plane vs. ACI Shear Strength Provisions
- 6.1 Classification of NDE Methods Applicable to Bridges
- 6.2 Loading History and Stages at which Modal Tests Were Conducted
- 6.3(a) First Modal Test Grid
- 6.3(b) Second, Third and Fourth Modal Test Grids
- 6.4 Mode Shapes from Test 1
- 6.5 Mode Shapes from Test 2
- 6.6 Mode Shapes from Test 3
- 6.7 Mode Shapes from Test 4
- 6.8 Demonstration of the Use of Flexibility Matrix
- 6.9 The Effect of the Number of Modes on the Convergence of the Flexibility Coefficients
- 6.10(a) Comparison of Truck Load Test, Modal Test and F.E.M. for One Truck
- 6.10(b) Comparison of Truck Load Test, Modal Test and F.E.M. Results for Three Trucks
- 6.11 Finite Element Mesh for 1st Modal Test
- 6.12 Details of the Finite Element Model for First Modal Test
- 6.13 Calibrated Finite Element Model for First Modal Test
- 6.14(a) Results of Calibration of Test #1, Modes 1 to 5
- 6.14(b) Results of Calibration of Test #1, Modes 6 to 10

## **FIGURE**

- 6.14(c) Results of Calibration of Test #1, Modes 11 to 15
- 6.14(d) Results of Calibration of Test #1, Modes 16 to 20
- 6.15 Finite Element Mesh for 2nd Modal Test
- 6.16(a) Abutment Modeling for 2nd Modal Test
- 6.16(b) Model Parameters for 2nd Modal Test
- 6.17(a) Results of Calibration of Test #2, Modes 1 to 5
- 6.17(b) Results of Calibration of Test #2, Modes 6 to 10
- 6.17(c) Results of Calibration of Test #2, Modes 11 to 15
- 6.17(d) Results of Calibration of Test #2, Modes 16 to 19
- 6.18 1st Test Modal vs. Analytical Flexibility Profiles - Uniform Loading
- 6.19 Flexibility Comparison Modal Test 2 vs. Test 3 - Uniform Loading
- 6.20 Flexibility Comparison of Modal Test 2 vs. Test 3 - Line C Loaded
- 6.21 Flexibility Comparison of Modal Test 2 vs. Test 3 - Line D Loaded
- 6.22 Flexibility Comparison of Modal Test 2 vs. Test 3 - Line E Loaded
- 6.23 Flexibility Comparison of Modal Test 2 vs. Test 3 - Line F Loaded
- 6.24 Flexibility Comparison of Modal Test 2 vs. Test 3 - Line I Loaded
- 6.25 Flexibility Comparison of Modal Test 2 vs. Test 3 - Line M Loaded
- 6.26 Flexibility Comparison Patch Loading in the Damaged Area, Modal Test 2 vs. Test 3
- 7.1 Simple Frame Concept & Analytical Model
- 7.2 H and HS Loading Truck
- 7.3 Response Under H & HS Trucks
- 7.4 Loading Patterns of Type 3 Rating Truck
- 7.5 Response Under Type 3 Rating Vehicles
- 7.6 Response Under Type 3 Rating Vehicle
- 7.7 Placement of Rating Trucks
- 7.8 Moment Contours Due to Dead Load
- 7.9 Maximum Moment Contours Due to Loading in End Span
- 7.10 Maximum Moment Contours Due to Loading Over Pier
- 7.11 Maximum Moment Contours Due to Loading in Middle Span
- 7.12 Loading Scheme Used in Destructive Testing
- 7.13 Response of Simple Frame Model to Destructive Test Loading
- 7.14(a) Dead Load Moment Contours for 2nd Test Model
- 7.14(b) Live Load Moment Contours for Destructive Test Loading
- 7.15 Comparison of Rating Factors
- 8.1 Yield Line Patterns
- 8.2 Elastic Finite Element Model
- 8.3 Truck Load Test Configurations
- 8.4(a) Comparison of Deflection Profiles Along Instrumentation Line 2

**FIGURE**

- 8.4(b) Comparison of Deflection Profiles Along Instrumentation Line 3
- 8.4(c) Comparison of Deflection Profiles Along Instrumentation Line 4
- 8.4(d) Comparison of Deflection Profiles Along Instrumentation Line 5
- 8.4(e) Comparison of Deflection Profiles Along Instrumentation Line C
- 8.4(f) Comparison of Deflection Profiles Along Instrumentation Line D
- 8.4(g) Comparison of Deflection Profiles Along Instrumentation Line E
- 8.5 Analytical Model for a Single Skewed Panel
- 8.6 Deformed Shape For a Single Skewed Panel
- 8.7 Analytical Model for a 2-Span Skewed Panel
- 8.8 Deformed Shape for a 2-Span Skewed Panel
- 8.9 Illustration of Slab Behavior by Beam Strips
- 8.10 Nonlinear Finite Element Model (3DSCAS)
- 8.11 Material Models
- 8.12 Biaxial Failure Envelope (Kupfer & Gerstle)
- 8.13 Deflection Profiles
- 8.14 Moment Contours from SAP90
- 8.15 Moment Contours from 3DSCAS
- 8.16 Stress Resultants
- 8.17 Twist Moment Contours (SAP90)
- 8.18 Finite Element Model of Cantilevered Beam
- 8.19 Moment-Contour Response
- 8.20 Comparison of Load-Deflection Curves
- 8.21 Comparison of Poisson's Ratio ( $\nu$ ) and Shear Retention Factor ( $\beta$ )
- 8.22 Tension Stiffening Models
- 8.23 Stress-Strain Relationship from Different Tension Stiffening Models
- 8.24 Effects of Using Different Tension Stiffening Models
- 8.25 Effects of Tensile Characteristics of Concrete
- 8.26 Sensitivity of Load-Deflection Response to Horizontal Boundary Conditions
- 8.27 Membrane Force Contours
- 8.28 Analytical Model of Slab-Pier Cap Connection
- 8.29 Deflection Profiles for Different Slab-Pier Cap Models
- 8.30 Observed Behavior of Bridge Deck at Abutment
- 8.31 Analytical Model of Slab-Abutment Connection
- 8.32 Simulation of Damage
- 8.33(a) Correlation of Deflection Profiles Under Truck Load Tests (Line 2)
- 8.33(b) Correlation of Deflection Profiles Under Truck Load Tests (Line 3)

**FIGURE**

- 8.33(c) Correlation of Deflection Profiles Under Truck Load Tests (Line 4)
- 8.33(d) Correlation of Deflection Profiles Under Truck Load Tests (Line 5)
- 8.33(e) Correlation of Deflection Profiles Under Truck Load Tests (Line C)
- 8.33(f) Correlation of Deflection Profiles Under Truck Load Tests (Line D)
- 8.34 Failure Surface Proposed by Hsein, Ting and Chen
- 8.35 Final Finite Element Mesh For Nonlinear Analyses
- 8.36 Comparison of Computed Load-Deflection Curves with Experimental Results
- 8.37 Correlation of Computed Load-Deflection Curves with Experimental Results
- 8.38 Measured and Computed Load-Rotation Response at South Abutment
- 8.39 Refined Analytical Model of Slab-Abutment Connection
- 8.40 Illustration of the Technique to Determine the Slopes and Break Points of Trilinear Horizontal Springs
- 8.41 Characteristics of Horizontal Springs
- 8.42 Comparison of Computed Load-Deflection and Load-Rotation Curves with Experimental Results
- 8.43(a) Comparison of Deflection Profiles from Refined Model
- 8.43(b) Comparison of Deflection Profiles from Refined Model
- 8.44 Comparison of Rebar Yield Locations
- 8.45 Out-of-Plane Shear Force Contours in the Loading Span

# **NONDESTRUCTIVE AND DESTRUCTIVE TESTING OF A REINFORCED CONCRETE SLAB BRIDGE AND ASSOCIATED ANALYTICAL STUDIES**

## **EXECUTIVE SUMMARY**

### **INTRODUCTION**

#### **Basis Of Research**

Despite a legislatively mandated program to inventory, inspect and improve the nation's bridges following the collapse of the Silver Bridge over the Ohio River at Point Pleasant, West Virginia in 1977, bridge collapses and failures have not been totally eliminated. In fact, over a five-year period 14 cases of bridge collapse and an additional 19 cases of bridge failure short of collapse were cited (Hadipriono, 1985). However, while present practices have not eliminated collapses, they are still used to decommission and replace many bridges before full utilization of their inherent capacity.

In addition, it has been noted that highly redundant bridge types, such as RC slab bridges with sound piers and abutments, are inherently less likely to collapse due to service loads and natural hazards. An NCHRP review of field tests has also indicated that redundant bridges may have far greater strength than may be anticipated by current rating methods (Burdette and Goodpasture, 1988). Many of these highly redundant bridges have been, or are being, decommissioned without full utilization of the available capacities. The financial implications can be staggering if one considers that the national bridge inventory as of 1987 listed 98,777 RC slab and T-beam bridges, of which 15,519 had a  $SR < 50$ , and 57,331 had  $50 < SR < 80$ . By recognizing and utilizing the inherent capacity of bridges, highway planners can program and utilize highway funds more effectively in the future.

#### **Goals of Research**

The primary goal for this research is to study and advance the technical aspects of inspection, rating and decommissioning of RC slab bridges. In addition, this test is designed to serve as a benchmark for future research involving destructive testing of bridges in the field.

The research is specifically oriented around calibration of Nondestructive Evaluation (NDE) procedures. The NDE procedures studied include visual inspection, truck load testing, and modal testing. Calibration of the modal-test based, quantitative NDE technique, developed by the UC researchers for ODOT/FHWA (Aktan and Raghavendrchar, 1990), is one of the primary objectives of this research and another objective is the determination of the usefulness of this technique to future bridge evaluation.

Another goal of the research is learning about RC slab bridge behavior at different limit states, particularly at failure. This is a particularly vital aspect of the research, since without gaining an experimental understanding of the behavior of concrete slab bridges, it will be impossible to improve the methods for rating similar bridges.

A final goal of the research is to explore analytical tools, including linearized identification of 3-D finite element models for bridge rating and 3-D nonlinear finite element

analysis (NLFEA) of complete, aged bridges which may have properties affected by damage and deterioration. These were studied through extensive efforts in predictive analysis and post destructive test correlation studies.

## **TEST SPECIMEN AND CONDITION**

### **Description of Test Specimen**

The test specimen (Figure 1(a)) is a 3-span, reinforced concrete (RC) skewed slab bridge which was constructed in 1954. The piers are set on footings placed on the bedrock, whereas the abutments are placed on steel piles driven to the bedrock. The piers and abutments are all skewed at a 30 degree angle.

### **Material Properties and Bridge Condition**

Design drawings indicate "class C" concrete while no reference was made to the reinforcing steel grade. Four-inch diameter core samples through the asphalt overlay and the concrete deck were taken to study the material properties and their variations.

Concrete coring revealed that concrete in the shoulder regions was severely deteriorated. It was not possible to obtain sound cores from the shoulders since the concrete under the asphalt would crumble during coring and would then jam the bit. Throughout the driving lanes, full-depth, solid cores could be obtained.

An asphalt overlay prevented the researchers from studying the top surface of the deck for their initial damage surveys. Since overlays are common, especially over older bridge decks, the researchers decided to extensively search for damage underneath the overlay by using NDE techniques.

While the bottom of the bridge did not exhibit any signs of extensive deterioration, the exposed sides of the bridge slab were heavily deteriorated (Figure 1(b)). This was attributed to run-off mixed with salt used in deicing the bridge during winter months. Other than the heavily deteriorated sides, the survey revealed little other damage, mostly limited to some light spalling and cracking on the bottom of the slab.

When the asphalt overlay was removed the shoulder regions were found to be in an extremely deteriorated state, having completely lost the cover over a large number of bars. The concrete in the traffic lanes appeared reasonably solid. Extensive study and petrographic analyses of the concrete samples indicated that the primary agent in the deterioration was "D" cracking of the porous coarse aggregate, which may have begun during the freeze thaw cycles of the first winter. The "D" cracking left pathways through which water and salt could pass through the concrete. This led to the secondary means of deterioration of alkali-silica reaction between some of the aggregates and the cement paste. The overlay further facilitated the deterioration by trapping water between the overlay and concrete deck for long periods. After the cover concrete had deteriorated, some of the reinforcing bars rusted while others in the vicinity were observed to be in excellent shape.

## **DESIGN OF LOADING AND DATA ACQUISITION**

### **Loading Position**

A decision was made to simulate a one-lane, one-trailer loading during the test although a multi-lane loading of the bridge would have been more critical for rating. One-lane loading permitted observing more complex modes of the slab-bridge behavior, and it would be possible to extend the findings to estimate bridge capacity under multi-lane loading with reasonable reliability. Figure 2 shows the position and manner of the loading applied to the bridge during the tests, along with the truck it is simulating. The load simulated the front tandem of a trailer as it enters the bridge in the northbound lane. NDE indicated that the southbound lane of the loaded end-span was stiffer than the northbound lane. Therefore, the decision was made for loading the SE quadrant of the bridge to reveal the extent of the influence of damage and deterioration on bridge behavior.

### **Design of the Loading and Loading Control Systems**

Predictive analyses indicated that the upper bound of the bridge load capacity may be as high as 1400 Kips (about 40 rating trucks) for the loading position which was selected. The loading system was designed for this upper bound. It is not feasible to apply this level of load without hydraulic cylinders. Moreover, application of load to the bridge while simulating tire loads and without creating local crushing was a challenge. An even greater challenge was the manner in which reaction could be developed in applying this type of load.

Based on lengthy research and feasibility analyses, it was decided to use rock-anchors to develop the reaction and to pour two concrete blocks directly on the bridge to simulate the footprints of a tandem trailer (Figure 2). The blocks were designed to accommodate the four hydraulic cylinders (actuators), each with 350 Kips capacity and 12" stroke. The double-acting actuators were acquired with a 4" diameter hole through their length to accommodate 8-strand rock anchor cables.

A state-of-the-art, servo-controlled, electro-hydraulic loading system comprised of a pump, the four actuators, two servo-valves, a two-channel digital servo-controller, pressure feedbacks for load control, and stroke feedbacks for displacement control was developed for loading. Together with the servo-control system, real-time digital plotting was used for instantaneous feedback of actuator loads, strokes and critical specimen responses. This real time system provided the information needed to make decisions for commanding the servo-control system. The test control and data-acquisition systems were located and controlled at a field-office adjacent to the bridge.

### **Instrumentation and Data Acquisition Systems**

A principal objective of the experiment was to evaluate the state-of-the-art in NLFEA. Therefore, extensive global and local instrumentation was required that would permit comprehensive correlations between the analytically predicted (and subsequently simulated) and the measured responses of the bridge. Such instrumentation was designed based on the results of preliminary analyses. In all, more than 160 transducers were placed on the bridge. These electronic transducers measured the forces and strokes of the four actuators, vertical and lateral

displacements of the slab, slab rotations at the abutment and pier, concrete distortions and steel strains through the critical regions of the slab.

Global instrumentation consisted of wire potentiometers used to measure some of the vertical displacements of the bridge deck, and DC-LVDT's used to measure other vertical displacements and the horizontal movements of the bridge deck. For the local instrumentation, DC-LVDT's and clip-gages were used to measure concrete distortions, and pier and abutment rotations. Foil strain-gages were placed on several rebars. All the wire-potentiometers, DC-LVDT's and clip-gages were calibrated in the laboratory through their expected operating spans. The transducer readings were recorded by data acquisition systems supplied by the University of Cincinnati and Wiss, Janney, Elstner Associates.

#### **Design of Loading Program**

Design of the loading program was aided by the upper-bound load-displacement response predicted by the NLFEA, and adjustments were made as the actual responses of the bridge were observed. However, as will be seen, very little reliance could be given to any one computer model; as a result the test had to be conducted in a careful manner to assure the desired results were obtained. Throughout the test, loading was applied in increments of "rating trucks" where one rating truck corresponded to a total of 32 Kips (one-tandem weight) on the two loading blocks. Throughout the test several instruments were monitored closely so the research team could determine what was occurring internally to the bridge while the test was being run.

The first stage of the test was comprised of numerous loading and unloading cycles which corresponded to shakedown at the serviceability limit state. These cycles also permitted debugging the test control, loading and data acquisition systems. The service level load cycles were followed by a large inelastic excursion which revealed the characteristics of the damageability limit state of the bridge and left a permanent vertical deformation of about 0.5 inches after unloading. The final leg of loading led to the failure of the bridge and left a permanent deformation exceeding 4 inches (Figure 3).

#### **Results of Destructive Testing**

The load-displacement responses have been extensively studied to determine the limit states of the response. The definition of limit states used in the examination of the results is any change in the characteristics of a response curve that can be directly attributed to a change in the overall behavior of the bridge. Most of these limit states are not what would typically be expected, such as first cracking and yield; instead they generally refer to changes in boundary condition or load path. The behavior of the skewed bridge is not typical; therefore many limit states found were related to the skew. Also, the bridge was extensively damaged; therefore the point of first cracking cannot be determined.

Five limit states have been found at equivalent truck loads of 7, 9, 12, 17, and 22. Most of the limit states appear in a very localized region of the bridge. For instance, the 7 truck limit state is noted for the sudden drop in rotational stiffness in the slab at the center of the abutment (Figure 4). The 9 truck limit state was noted by a sudden drop in rotational stiffness on the west

side of the pier (Figure 4). It is felt that both of these limit states and the 12 truck limit state are related.

Due to wear and damage, the bridge initially maintained a large amount of rotational stiffness at the center of the abutment. As a result, the bridge tended to carry its load through a longitudinal path from the abutment to the pier. After the rotational stiffness was released, the bridge began to reorient its load-path to carry the load along the skew, which is more typical of this type of bridge. The 9 truck limit state is believed to be the result of the west side of the pier being incorporated in the load path. The 12 truck limit state is believed to mark the point where any rotational restraint provided by the abutment has disappeared.

#### **Mechanics of Failure**

Figure 5 shows the resultant failure plane of the bridge. The failure originated near the pier in the damaged region of the east shoulder and progressed from that point. It appears the failure was, in part, triggered by a change in the load path that was occurring between 17 and 21 trucks. Originally, the bridge carried load perpendicular to the traffic lanes until, at the 7 truck limit state, the rotational restraints at the abutment were released and the bridge began to carry the load parallel to the slab skew.

However, at about 17 trucks the load path again began shift. The changing load path is revealed by the strain gage SG12 located on a top rebar over the pier in the damaged shoulder. As shown in Figure 4, at about 17 trucks this rebar began to see a rapid increase in stress; in fact, by 20 equivalent truck loads it had yielded. Strain gages placed on other bars reveal that bars near the loading blocks began to yield at 20 trucks. It is very possible that yielding began earlier than this at places and bars which were not instrumented. The onset of yielding seems to be the impetus for the shift of load path back to the direction perpendicular to the traffic lanes. This makes sense for two reasons: 1) The analysis which showed that skew bridges carry load parallel to the skew was linear. Yielding of the bars introduces a nonlinearity so it is expected that the linear solution is no longer valid; 2) Once the bars yield, they become dominant in defining the behavior. Since the bars are aligned with the traffic lanes, it is reasonable that the load path would shift parallel to the traffic lanes and the reinforcing bars.

Once the load path shifted back to parallel to the traffic lanes, the shoulder which had been excluded from the load path since the 7 truck limit state now came back into the load path and had to carry load. The damaged shoulder concrete possessed very little shear strength and this triggered the failure since the damaged shoulder could not take the additional load.

Based on an extensive study of the failure surface, it appears that the point of origin of the failure occurred approximately 6 feet from the edge of the bridge, which would be consistent with placing the point of failure at the edge of the shoulder area. At this point it must be recalled that the bridge was tested in load control and that when failure began, the hydraulic actuators continued to apply a constant load. Once the shoulder failed, the sound areas of the bridge had to support the total load, thus increasing the stress in the sound areas. The failure quickly and easily ripped through the damaged shoulder and propagated into the sound areas. The combination of the dynamic propagation of the failure surface and the increasing stress in the

unfailed areas was ultimately fatal to the bridge deck and a punching shear failure resulted.

The failure plane followed the pier up until it reached line 7 of the instrumentation grid, shown in Figure 5. At this point, the cantilevering action of the slab produced a condition where it was more favorable for the failure to progress back towards the abutment. The failure plane then progressed longitudinally along line 7 from the pier back towards the abutment. The failure presents two distinctly different appearances on the top and bottom due to the influence of the top reinforcement over the pier. The bottom slab reinforcement near the pier is relatively light consisting of #9 bars at 15" on center; as a result, the dynamic impact of the shear failure had little trouble propagating through the bottom half of the slab. However, the #9 bars at 6" on center in the top of the slab were sufficient to suppress the propagation of the failure plane through the top layer of the reinforcement. As a result, the failure plane effectively sheared through the bottom half of the slab, and then followed the bottom of the top reinforcement until the cutoffs were reached, where the top failure surface appears. Along the longitudinal line, a normal shear plane is clearly visible as the transverse reinforcement was very light at the top and bottom. It is probable that, if similar reinforcement existed in the bottom mat as in the top mat, the failure may have been temporarily suppressed and this would have given the bridge a chance to redistribute the load.

## **NONDESTRUCTIVE EVALUATION**

### **Modal Testing**

A specific goal of the research project is the evaluation of the multi-reference modal testing procedure which directly reveals bridge flexibility without any assumptions. This test constitutes the basis of a Nondestructive Evaluation (NDE) technique developed by UC researchers (Aktan & Raghavendrachar, 1990). The NDE procedure reveals and quantifies bridge damage, and utilizes truck load testing to validate results obtained from modal testing.

The modal test was performed 4 different times during the research. The first test was about 5 months before the destructive testing, while the asphalt overlay was still in place. The second test was performed after the asphalt overlay was removed, and the loading equipment (hydraulic cylinder, load transfer blocks, etc.) was placed on the bridge. This test served as a baseline for the next two tests. The third test was performed after the bridge was loaded to the equivalent of 20 trucks. The fourth test was performed after the failure of the bridge.

The truck load tests were performed approximately 2 months before the destructive testing and prior to the removal of the asphalt overlay. The truck load test results verified the first modal test. Subsequent modal tests could be verified from the intermediate stepwise linear ranges of the destructive testing.

Three different techniques were explored for evaluating damage based on the modal tests. The first technique deals with identifying damaged regions above the asphalt overlay and without a baseline modal model of the bridge. Baseline here refers to the results of a similar modal test done previously. Having a baseline, and therefore knowing the history and previous condition of the bridge via the results of an earlier modal test, can be a tremendous asset. If such a baseline exists, correlation studies between the results of the previous test and of the present test

can be used to evaluate any damage the bridge might have incurred. However, in general, prior information on the bridge in the form of a modal model is not available. Therefore, in order to replace this missing information, researchers at UC have used a finite element model of the bridge which is globally calibrated with the results of the modal test. Correlating the flexibility coefficients from the modal test with the ones obtained from the "globally" calibrated finite element model, the researchers were able to identify localized damage.

The second technique for evaluating damage is based on a "local" calibration of the finite element model through a system-identification process, by which simulated responses are correlated with the measured responses. The deviations between nominal "expected" and calibrated local properties revealed damage.

The third method of diagnosing damage directly compared the third modal test to the second to detect damage that resulted from the first day of destructive testing. This situation corresponds to having information about the previous state of the bridge from a modal test conducted in the past. An example of this could be intermittently conducting numerous tests during a long-term program to monitor bridge health and comparing/observing the changes in the parameters obtained from tests conducted at different times.

One popular way of testing and rating bridges is by truck load testing. However, the researchers have found that the truck load tests are too cumbersome and cannot serve as a highly competent damage evaluation tool. Nevertheless, they do serve as a proof-testing and as a good means to verify the results from modal testing.

#### **Results of Modal Test**

The modal test data is reduced to produce the natural frequencies and mode shapes for the bridge. This information is then further processed to produce the flexibility matrix of the bridge directly from the results of the modal test. This "dynamically" measured flexibility closely approximates the actual flexibility of the bridge under truck loads and provides an excellent diagnostic tool.

#### **Damage Identification Using Modal Test**

In order to establish the damage indicated by the modal test, and the approximate degree of such damage, the results of the second modal test were used to calibrate a finite element model. In this procedure, the model will be fully calibrated, so that any damage existing in the bridge will be directly incorporated in the finite element model. Thus, when the calibration is complete, all of the damage should be locally represented in the analytical model.

The modal test provides the fundamental frequencies and unit-mass scaled modal vectors of the bridge. These are then used to establish the parameters used in the calibration of the model. The concept behind this calibration is to develop a model that correctly represents the frequencies and mode shapes found by testing as closely as possible.

The calibrated model from the second modal test is given in Figure 6. The basis of this procedure to identify damage is to model the damage in the bridge in the analytical model. Therefore, the model has to be extensively calibrated and has to include all major damage found

in the modal test. The calibration indicated that the most significant problem in the bridge was loss of some continuity in the north span. Specifically, lost continuity occurred in the east shoulder over the north pier. The calibrated model also provided effective thickness values for each span of the deck.

By expanding on the calibration procedures, it appears that it may be possible to reveal even more damage to the bridge. However, the amount of damage which is revealed seems to have some limitations. First, the damage must affect the vertical flexibility since the test was performed only in the vertical sense. As a result, accurately calibrating parameters related to rotations, such as the rotational stiffness of the abutment, is difficult, if not impossible. The test does produce accurate values for the vertical stiffness of the piers and abutments and the flexibility of the slab.

The badly deteriorated shoulder regions did not show any loss of section in the calibrated model. At first glance, it appeared to be a problem in the test procedure since almost 20% of the depth of the concrete throughout the shoulders was lost. However, it has been noted that when comparing the experimental results with the analytical model, up to about 5 equivalent truck loads, the displacement in the shoulder region parallels that predicted by the analytical model. Above 5 or 6 equivalent trucks, the shoulder begins to show signs of weakening. Therefore, the research team concluded that the shoulder, while being badly deteriorated, maintained a great deal of its original structural function in the service limit state.

Using the flexibility obtained from the modal test conducted over the asphalt layer and from the calibrated finite element model proved to be a promising technique for identifying damage. Figure 7 shows a 3-D comparison of the deflection profiles due to uniform loading of the modal test and the finite element model flexibility. The difference between the modal test and the analytical model, which simulates baseline, indicate the regions of damage.

As for the damage identification studies using the results of the second (before the 20 truck loads) and third (after loading) modal tests, Figure 8 shows the deflection profiles due to unit loading of the modal test based on flexibility matrices obtained from these two tests. Striking discrepancies in the deflection profiles are observed, especially in the loaded region, indicating a drastic loss of stiffness in this region. This figure not only points out the presence of damage, but also the location of it. The frequencies and damping factors obtained from these two tests also indicate up to a 5.6 % decrease in the frequencies and up to a 17.7 % increase in the damping factors. It is concluded that the technique of comparing 3-D flexibility profiles is an excellent tool for detecting damage, especially if a baseline model is available.

## **RATING OF THE BRIDGE**

The bridge was rated using the following rating schemes:

- 1) Using the AASHTO 1983 "Manual for Maintenance Inspection of Bridges." This method divides the slab bridge into effective strips according to the provisions of the applicable AASHTO "Standard Specifications for Highway Bridges". Each strip is then assumed

to be a beam which carries half the axle loads plus impact of an H or HS type truck;

- 2) The rating in part 1) was repeated using AASHTO Type 3 trucks;
- 3) The rating in part 2) was repeated using the AASHTO 1989 "Guide Specifications for Strength Evaluation of Existing Steel and Concrete Bridges." This specification still uses the effective strip method, but requires the use of Type 3 vehicles. The specification also modifies the understrength factor,  $\phi$ , used in the rating equation to account for redundancy, deterioration, maintenance and inspection.
- 4) The rating in part 3) was repeated, but a linear finite element program was used to determine the distribution of load as permitted in the 1989 Guidelines.
- 5) The ratings in parts 3) and 4) were repeated, but with a single truck positioned at the load points used for the destructive test.

In all five cases, the effective strip or finite element models were modified to reflect damage in the structure. This was done by removing 1" of concrete from the top of the slab in the damaged shoulder regions.

One of the most significant findings was the extent to which assumed material properties affected the rating of the bridge. For the bridge under consideration, AASHTO recommends using 3000 psi for the concrete strength and 33000 psi for the steel yield stress. However, actual material testing established reasonable lower bound properties of 5000 psi for the concrete and 43500 psi for the steel yield stress. It was found that the change in the assumed material properties increased the rating factors by 50% to 100%. Unfortunately, neither the 1983 Manual or the 1989 Guidelines have specific provisions for using experimentally determined properties for rating.

Methods 1 through 4 above are comparable since they consider critical placement of truck loads to achieve maximum response. The most conservative rating (lowest rating factors) was using the 1989 AASHTO Guidelines. Here, the critical response was the maximum moment over the piers. The rating factors were 0.70 using the code specified material properties and 1.24 using the measured material properties. One reason for the low rating factors was the simplistic model which is used. The bridge is assumed to be a simple frame or beam of a given effective width. This model ignores the actual geometry of the bridge and additional load carrying mechanisms such as interaction between adjacent effective frames or beam strips. The conservative nature of the capacity reduction factors used in the 1989 AASHTO Guidelines also lowered the rating.

The highest rating was obtained from the finite element model. The critical rating point now shifted to maximum positive moment in the middle span and the rating factors were 1.55 (code specified material properties) and 2.45 (actual material properties). Since the load and resistance factors were as given in the 1989 AASHTO Guidelines, the increase in the rating was

totally due to the finite element model being able to consider additional load carrying mechanism and the actual bridge geometry. This provided more accurate load distributions.

Finally, the bridge was rated using the actual loading for the destructive test. The simple frame analysis provided a rating of 2.30 and the linear finite model provided a rating of 4.85. By removing the load and resistance factors from the equation, it is possible to use these ratings to estimate the number of "trucks" needed for failure. The frame analysis predicts failure at 5 trucks and the finite element method predicts 10 trucks. The bridge actually failed at 20 trucks. The difference is due to the fact that both models are linear. Nonlinear analysis would provide more accurate predictions.

### **PREDICTIVE ANALYSES**

Predictive analyses were performed to design the loading setup and to establish the loading program. Another objective was to evaluate the state of the art in nonlinear finite element analysis (NLFEA) for predicting behavior of reinforced concrete bridges. Linear finite element analyses and yield line analyses were also performed to support NLFEA.

Researchers from the DELFT Technological University (The Netherlands) collaborated with UC researchers at this step of the research. The analyses performed by DELFT were helpful in assessing the state of the art, since the software (DIANA) developed by the DELFT group, as well as the NLFEA expertise represented by this group, are considered part of the best in the world.

Figure 9(a) shows the geometric characteristics of the analytical model used by UC for the NLFEA. The initial boundary stiffness at the abutments of this model was established through structural identification, incorporating the dynamic characteristics of the bridge measured by modal testing. Although concrete cracking, concrete plasticity, and yielding of reinforcing bars were accounted for during the NLFEA, the boundary conditions were not. However, after the tests, it became apparent that the boundary conditions at the abutment were the most critical parameter.

Figure 9(b) shows some of the predicted global responses of the bridge computed by UC compared with the corresponding measured response during the test. Analytical responses demonstrate the significance of parameters which define the boundary conditions at the abutment and the stress-strain response of concrete under uniaxial tension. These parameters are associated with the greatest uncertainty in analyzing the bridge, although modal test results and standard material test responses were available.

The sensitivity of analytical responses to the described boundary and material parameters indicates that it is not yet possible to rely on NLFEA to predict available capacities and failure modes of slab bridges. This analytical tool may be used to understand the critical parameters for the optimized designs of new bridges or to upgrade existing bridges.

### **CORRELATION ANALYSES**

Through a series of linear and nonlinear finite element parametric analyses, the importance of the tensile behavior of concrete and more significantly membrane force in the slab

became clear. Other parameters such as Poisson's ratio, shear retention factor, or modeling of slab-pier cap are not apparently important.

The slab-abutment connection was modeled as shown in Figure 10. Using the illustrated geometric model, it was possible to allow for "rocking" of the slab while restraining horizontal movement at the shear keys. The trilinear stiffness characteristics of the horizontal springs allowed to "regulate" the level of membrane force that could be developed in the slab. The observed damage was simulated by reducing slab thickness along the shoulder. The slab-pier cap was modeled similar to the predictive analyses (Figure 9).

After calibration of the stiffness and break points of the horizontal springs at the abutments, the measured load-deflection was correlated rather closely, as seen from Figure 11. The computed slab rotations at two locations along the south abutment also match the experimental results reasonably (Figure 11). A close match of the deflection profiles is clear from Figure 12. Using the calibrated model, it was possible to replicate very reasonably the locations at which the first yielding in the reinforcing bars were detected. The first yield was computed to be at locations shown in Figure 13 corresponding to a total load equal to 640 kips. The experimental results suggest that the bars at locations 4, 8, and 13 (Refer to Figure 14) yielded when the total load on the bridge was approximately 650 kips. Therefore, with the final calibrated model, the global, regional, and local responses could be matched very closely.

## CONCLUSIONS

The modal test procedure for NDE proved its ability to reveal damage in a real structure. However, with present techniques for calibrating the finite element model, it may take longer than a month to fully calibrate a model with a high degree of confidence. Also, at present there are no baseline tests in NDE that can be used to detect damage. The lack of baseline tests in NDE that can detect damage greatly limits the application of NDE until the development of expedited manners of finite element model calibration.

If model calibration can be expedited, the NDE process could be an excellent means for improving bridge ratings. When the bridge was rated using the calibrated finite element model, the bridge capacity was typically found to be twice that of other models using the effective width of the slab, in spite of the deterioration which was incorporated in the finite element model. As a result, a typically higher and more accurate rating factor can be developed from a calibrated finite element model. What is needed is the development of software and procedures that will simplify the calibration of these models so the work can be done in a matter of days instead of weeks.

The bridge appeared to have most probably lost a considerable amount of its strength throughout the shoulders. However, during the destructive testing, it was noted that the damage in the shoulders did not become readily apparent until the load was increased above 5 equivalent trucks into the nonlinear range of the bridge response. This effectively verifies the results of the NDE that, although the appearance of the shoulder was very poor, actually it maintained a considerable amount of its structural function. However, the failure was triggered by the weakness of the region in shear, but this point was not reached until a considerable load of 22

equivalent trucks was placed on the bridge.

The life of the bridge could have been effectively extended by removing all of the loose concrete and topping the bridge with a concrete overlay. However, some questions remain about the shear strength of concrete exposed to this type of damage, so more research needs to be done to establish parameters by which an effective shear strength for damaged concrete can be determined for the purposes of rating.

Bridge engineers should start recognizing the inherent capacities in RC slab bridges which have sound abutments and piers. Even with the extensive deterioration of shoulder concrete, the test bridge safely carried over 20 rating trucks, a load exceeding four times the bridge rating based on a calibrated FE model. It follows that bridge rating and decommissioning based on only visual inspection may greatly underestimate the actual capacity of slab bridges. Considering that the average replacement cost of a two-lane three-span, approximately 100-foot long slab bridge is in the order of \$250,000, the financial savings of using these bridges over longer life spans with needed maintenance can be significant.

Obviously, predicting bridge capacity by NLFEA within a narrow band is not possible since response is very sensitive to a considerable number of parameters which cannot be established with confidence even if the boundary conditions of the bridge are established at the service limit-states and the materials are sampled and tested. The sensitivity of RC slab bridges to parameters such as the tension response of concrete is unlike RC beams or bare frames, the strength of which are less sensitive to similar parameters.

#### **SIGNIFICANT PUBLICATIONS IN REVIEWED JOURNALS FROM THIS WORK**

"Destructive Testing of a Decommissioned Concrete Slab Bridge," R. Miller, A. Aktan, B. Shahrooz, accepted for publication, Journal of Structural Engineering, ASCE, July, 1993.

"Bridge Condition Assessment by Modal Flexibility," T. Toksoy and A. E. Aktan, accepted for publication, Experimental Mechanics, July, 1993.

"Nonlinear Finite Element Analysis of a Deteriorated Slab Bridge," B. M. Shahrooz, I. K. Ho, A. E. Aktan, R. DeBorst, J. Blaauwendraad, C. Veen, R. H. Iding and R. A. Miller, to appear in the Journal of Structural Engineering, ASCE, February, 1994.

"Nondestructive and Destructive Testing of a Decommissioned RC Slab Highway Bridge and Associated Analytical Studies," by A. Aktan, M. Zwick, R. Miller and B. Shahrooz, Transportation Research Record, 1371, May, 1992.

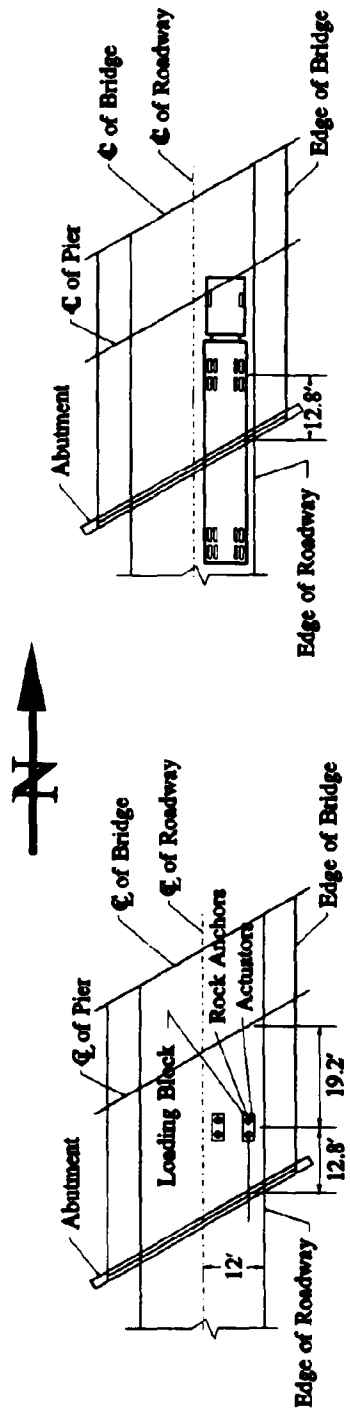
"Understanding Errors and Accuracies in DCDTs and wire Potentiometers for Field Testing," W. Hrinko, R. Miller, C. Young, B. Shahrooz and A. Aktan, accepted for publication to Experimental Techniques, April, 1993.



**FIGURE 1(a): PHOTO OF TEST BRIDGE**

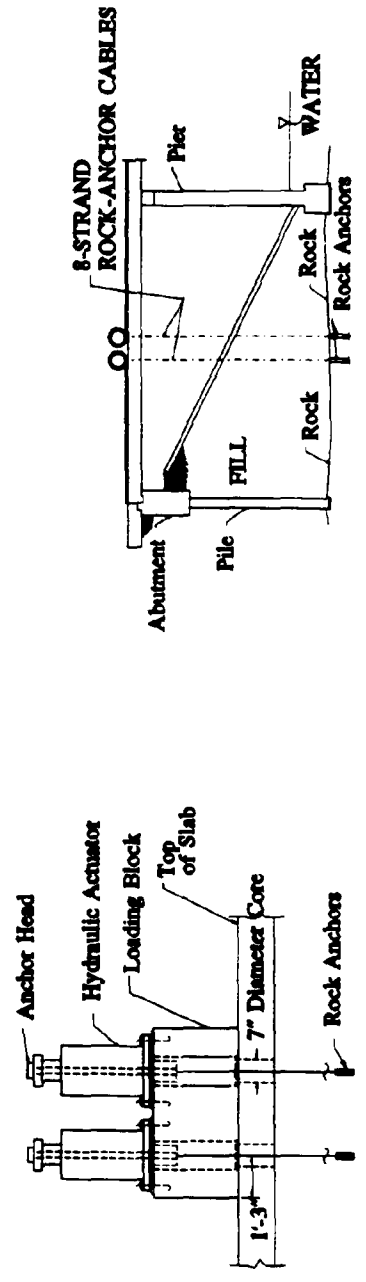


**FIGURE 1(b): DETERIORATED SHOULDER  
OF TEST BRIDGE**



**PLAN VIEW OF LOADING SYSTEM**

**PLAN VIEW OF SIMULATED LOADING**



**ELEVATION VIEW OF LOADING BLOCK**

**ELEVATION VIEW OF SIMULATED LOADING**

**FIGURE 2: DESIGN CONCEPT OF LOADING SYSTEM**

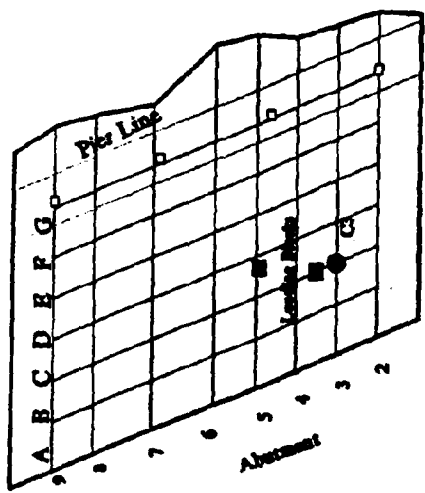
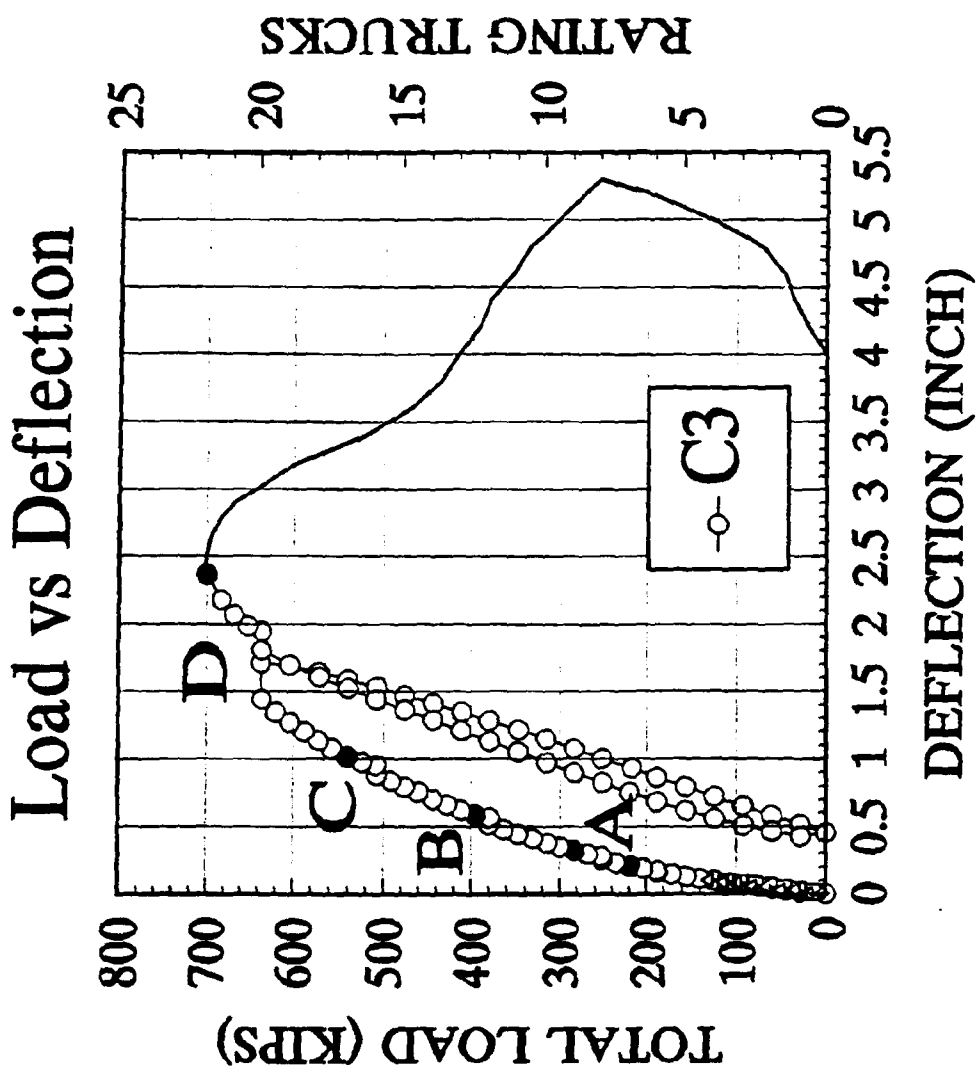
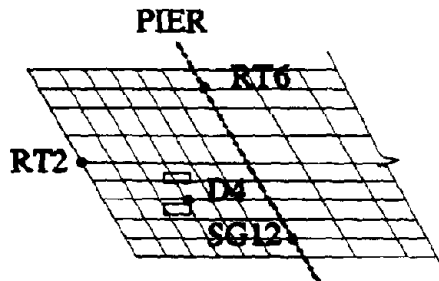
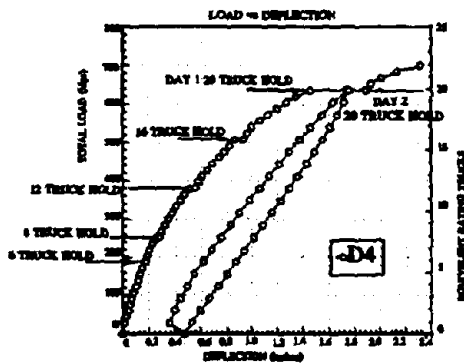


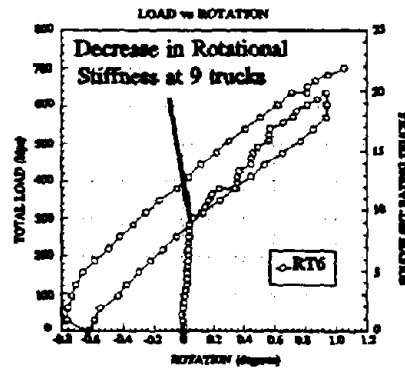
FIGURE 3: LOAD-DISPLACEMENT RESPONSE AT POINT C3



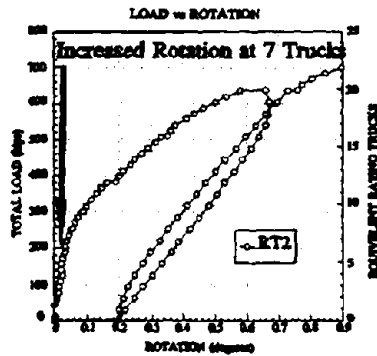
Location of Instruments



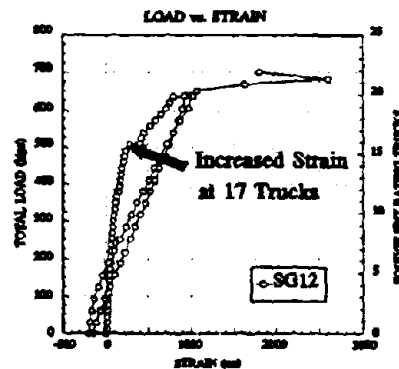
Typical Load Deflection Response



Rotational Response of Slab At East Edge of Pier



Rotational Response of Slab at Center of Abutment



Strain Measured in Top Mat Over East Side of Pier

Figure 4: Response of Key Instruments

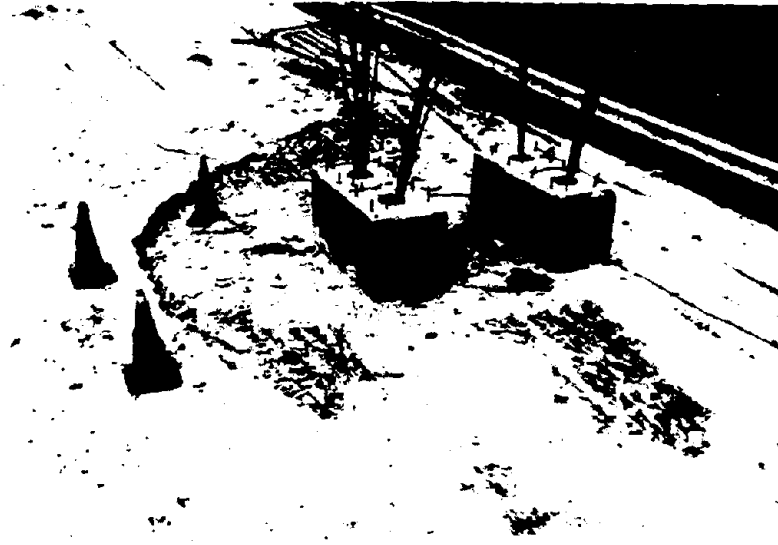


**FIGURE 5(a): TOP VIEW OF FAILURE PLANE**

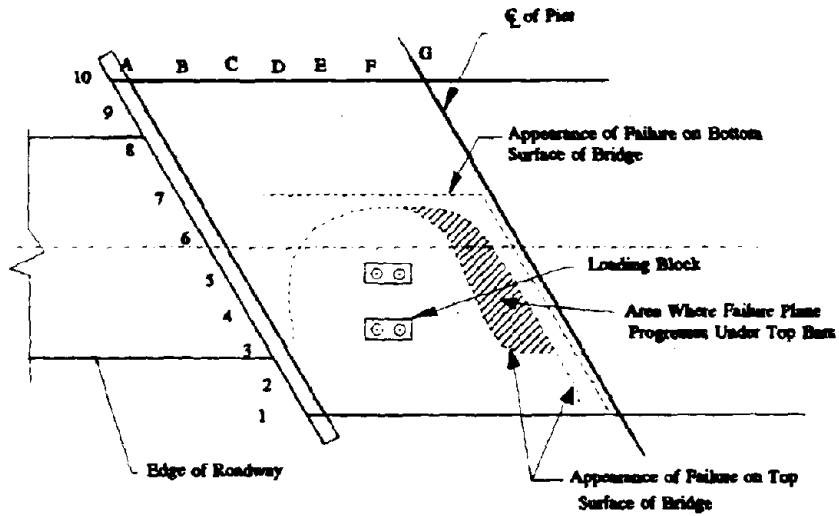
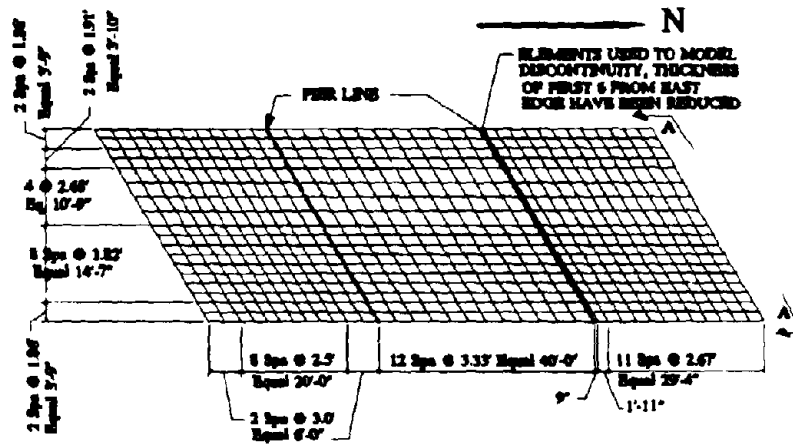
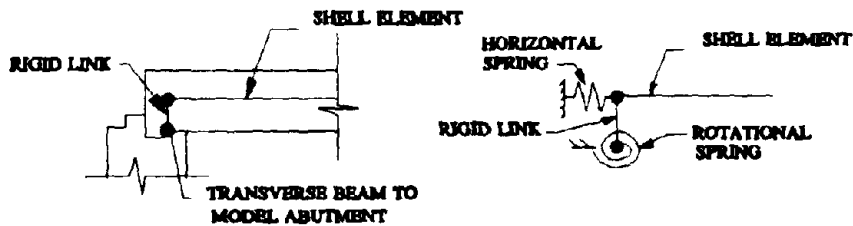
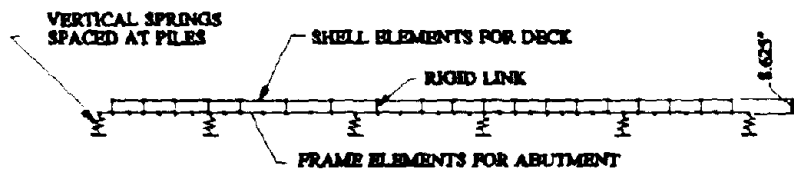


**FIGURE 5(b): APPEARANCE OF BOTTOM AND TOP FAILURE PLANES**

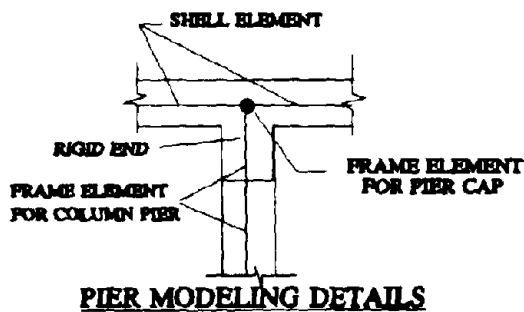
**FIGURE 5: FAILURE PLANE**



**FINITE ELEMENT MESH**



**SECTION A-A ABUTMENT MODELING DETAILS**



**PIER MODELING DETAILS**

**FIGURE 6: CALIBRATED MODEL PARAMETERS**

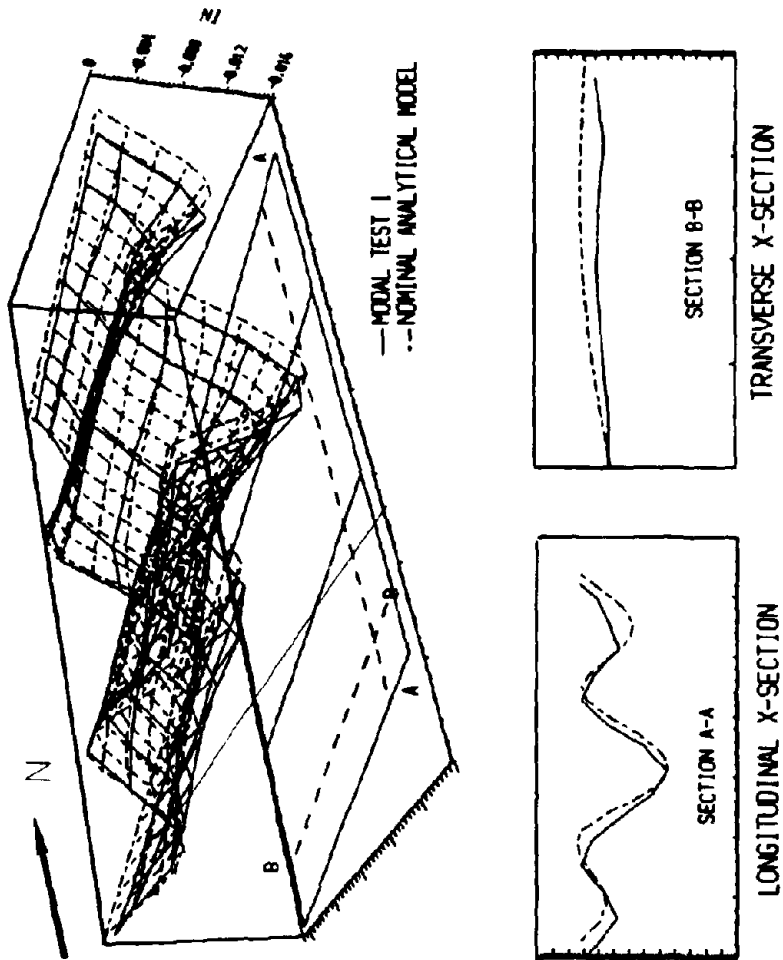
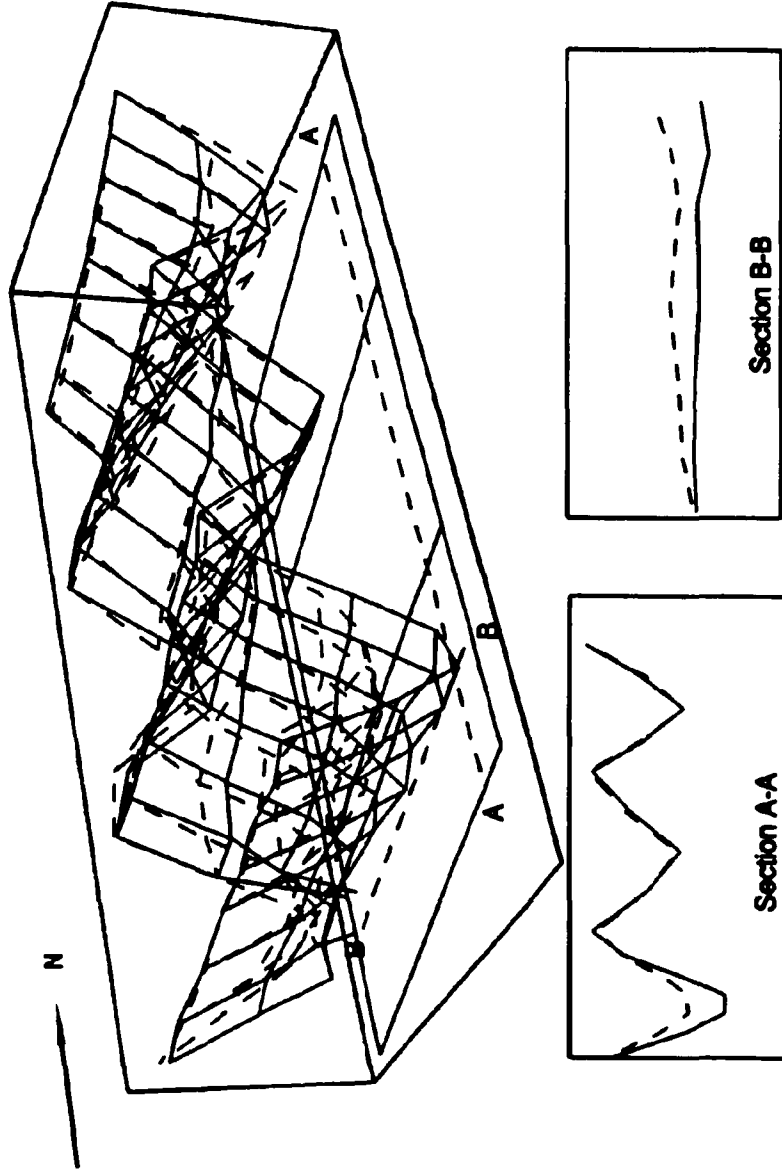


**FIGURE 7: BRIDGE DEFLECTION PROFILES FROM 1ST MODAL TESTS AND NOMINAL ANALYTICAL MODEL**

- TEST 2 --> BASELINE TEST PRIOR TO DESTRUCTIVE TESTING
- TEST 3 --> AFTER 20 EQUIVALENT TRUCKS



LONGITUDINAL CROSS-SECTION      TRANSVERSE CROSS-SECTION

**FIGURE 8 : BRIDGE DEFLECTION PROFILES FROM 2ND AND 3RD MODAL TESTS  
CORRESPONDING TO UNIFORM LOADING**

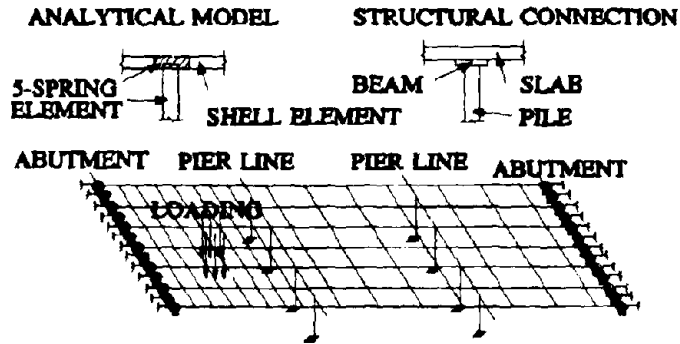


**FIGURE 9(a): NLFEA MODEL**

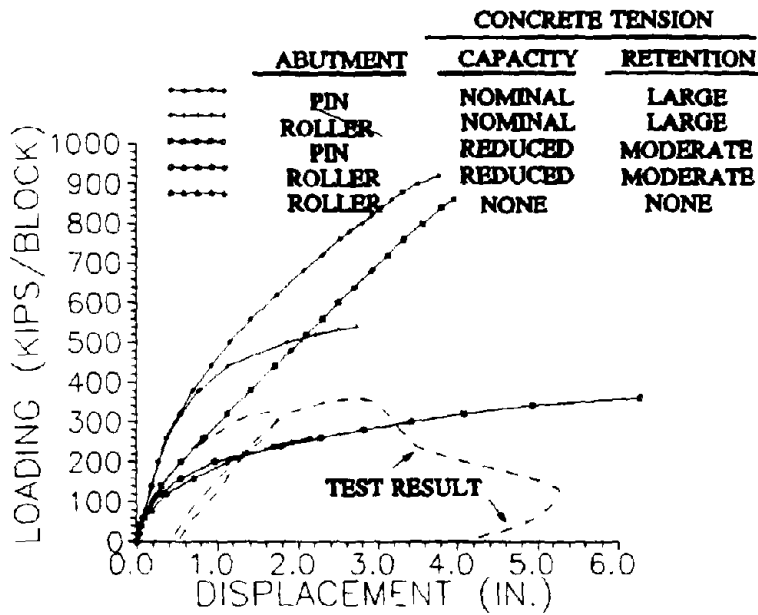
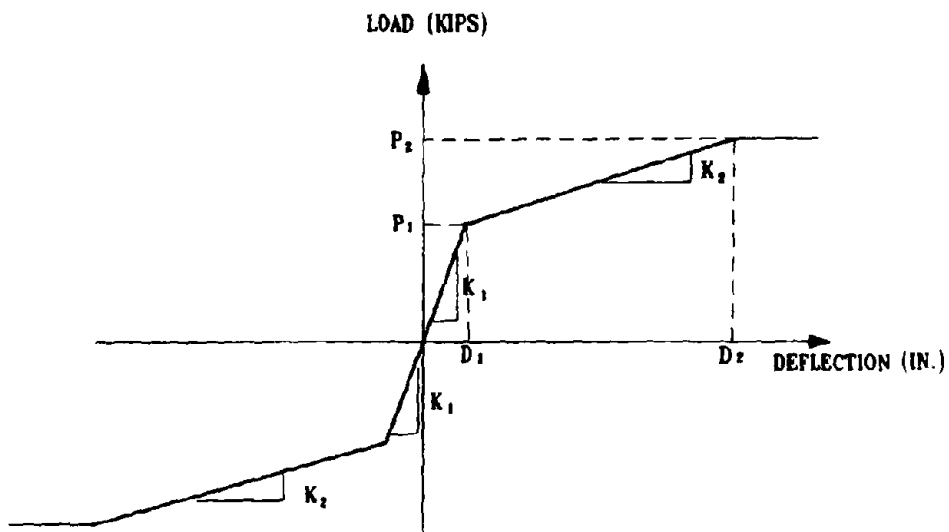
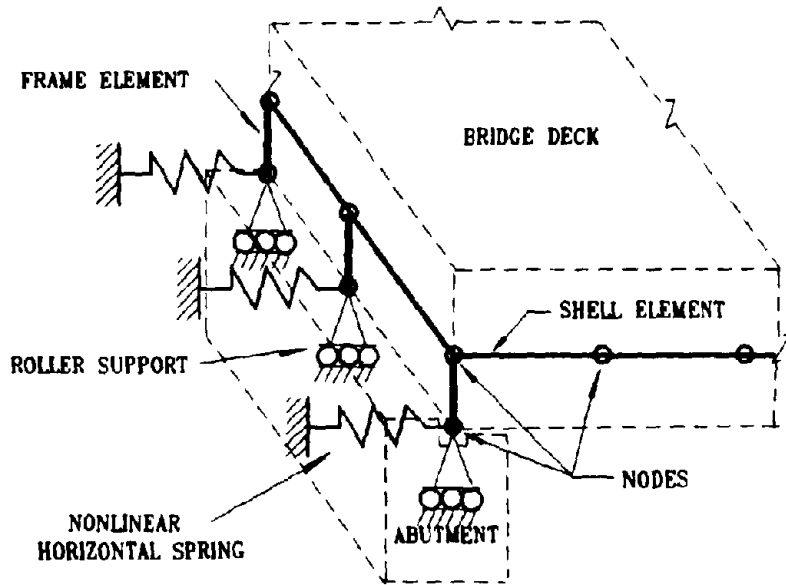


**FIGURE 9(b): RESULTS OF NLFEA ANALYSES**

**FIGURE 9: NLFEA MODEL AND RESULTS**



MATERIAL MODEL FOR NONLINEAR SPRING

**FIGURE 10: REFINED ANALYTICAL MODEL OF  
SLAB-ABUTMENT CONNECTION**

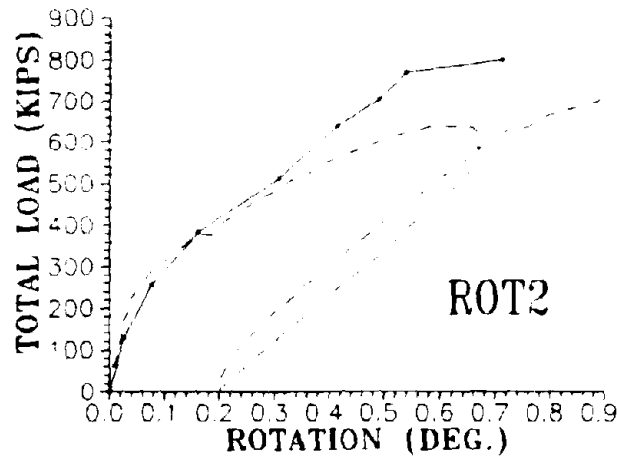
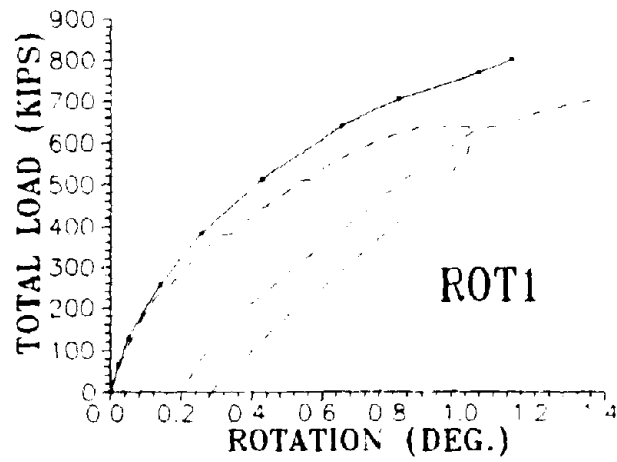
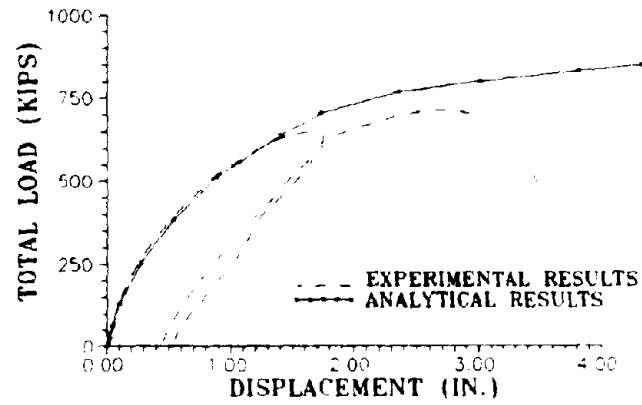


**FIGURE 11: COMPARISON OF COMPUTED LOAD-DEFLECTION AND LOAD-ROTATION CURVES WITH EXPERIMENTAL RESULTS**

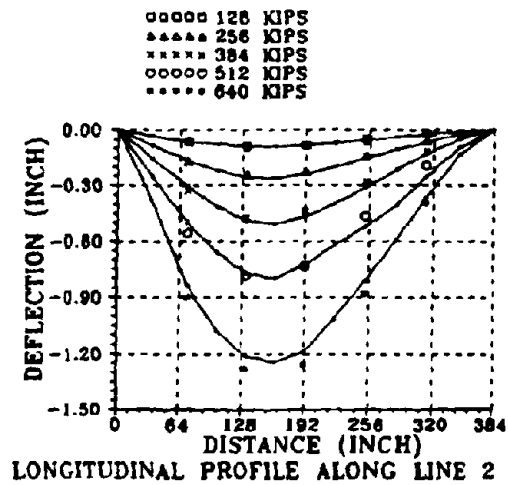
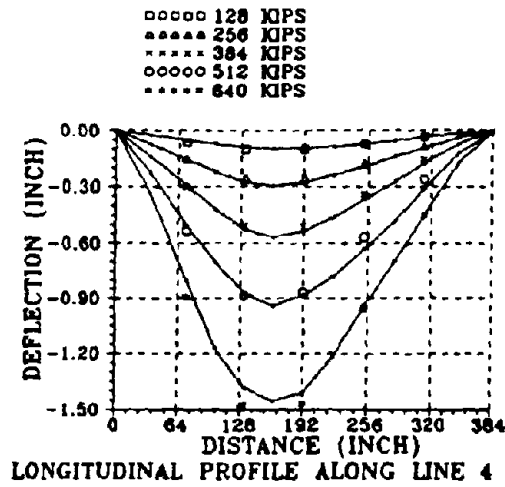
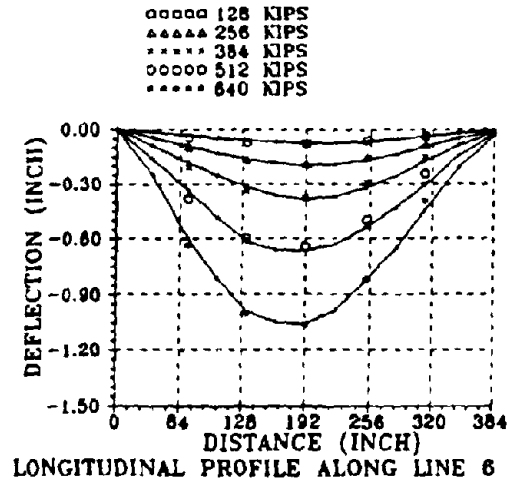


**FIGURE 12(a): COMPARISON OF DEFLECTION PROFILES FROM REFINED MODEL**

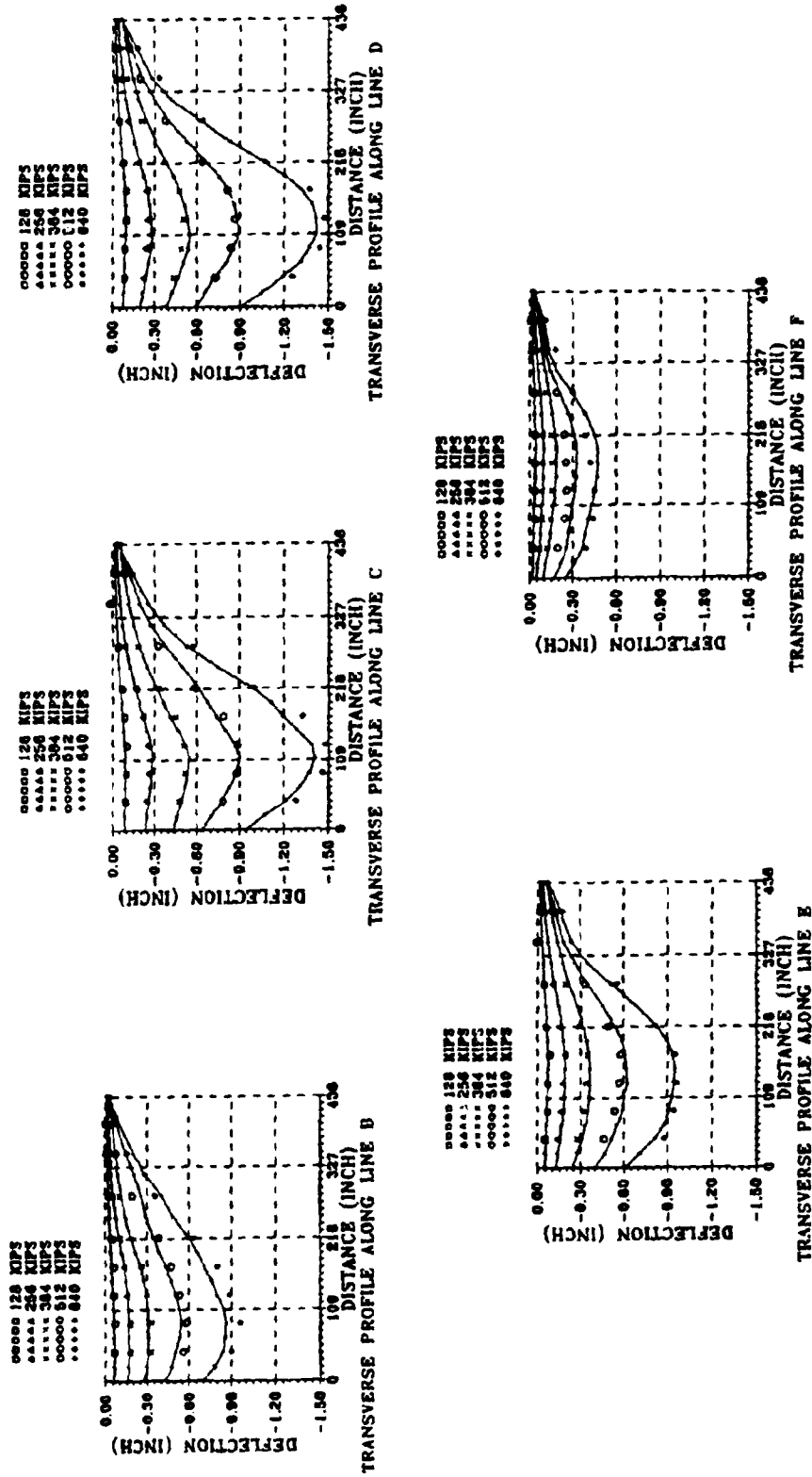


**FIGURE 12(b): COMPARISON OF DEFLECTION PROFILES FROM REFINED MODEL**

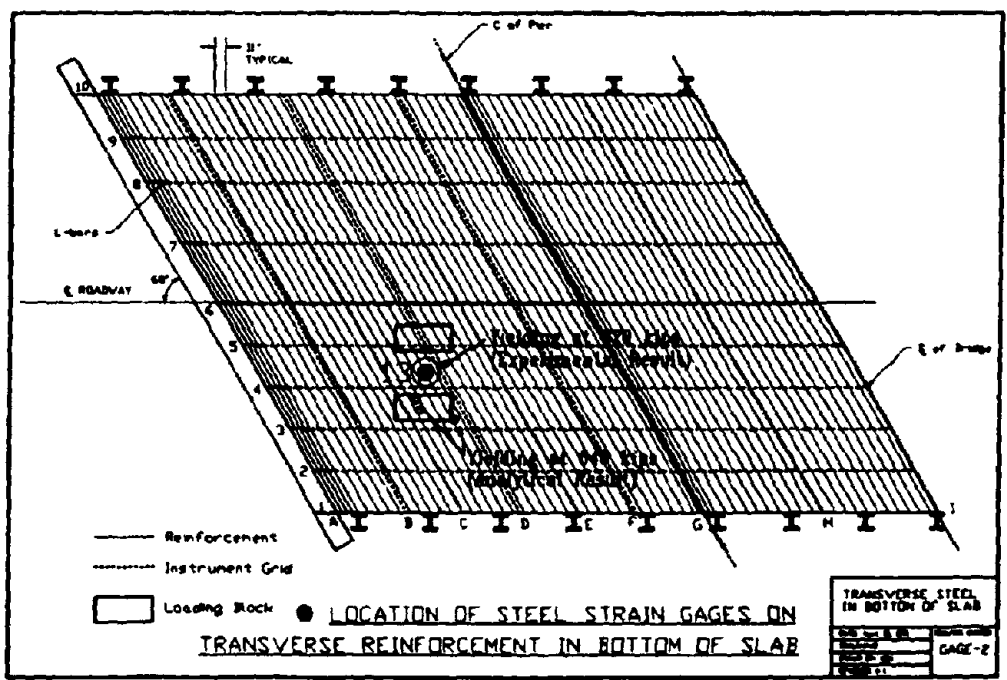
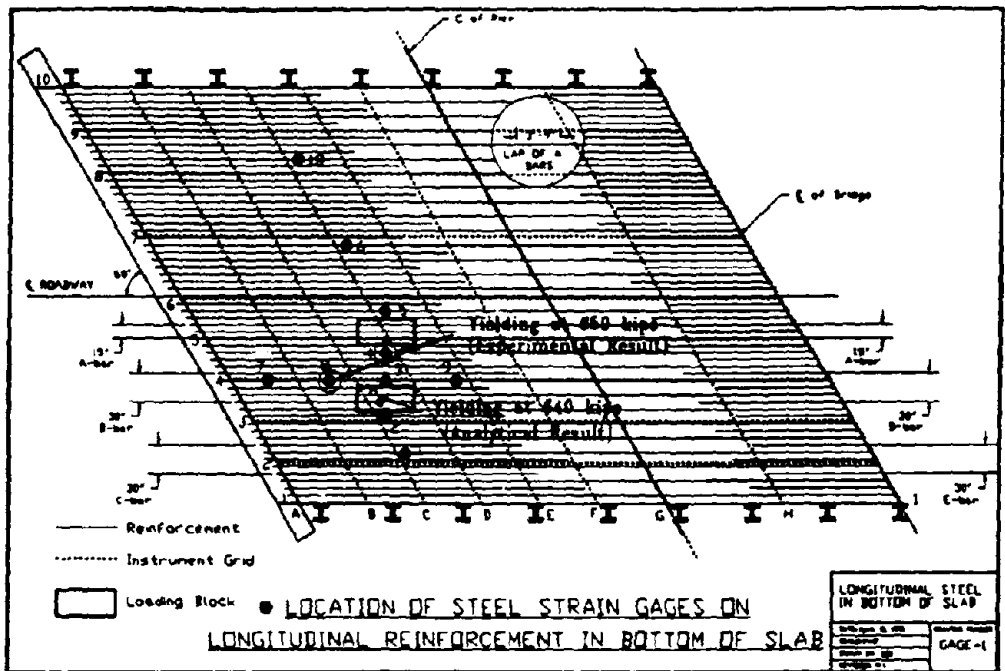


FIGURE 13: COMPARISON OF REBAR YIELD LOCATIONS

## CHAPTER 1: INTRODUCTION

### 1.1 BASIS OF RESEARCH

Following the collapse of the Silver Bridge over the Ohio River at Point Pleasant, WV. (Imbsen et al., 1987) in 1977, a legislatively mandated program to inventory, inspect, and improve the nation's bridges was initiated. Despite this program, bridge collapses and failures have not been eliminated. Over a five year period from 1977-1981, 14 cases of bridge collapse and an additional 19 cases of bridge failure short of collapse were documented (Hadipriono, 1985). More recently, the vulnerability of bridges against natural hazards has been realized in the well-publicized collapse of the Schoharie Creek bridge in New York, 1989, due to scour (Huber, 1991), and the collapse of segments of the Nimitz freeway and the Bay Bridge in 1989 due to the Loma Prieta earthquake. Meanwhile, many bridges are being decommissioned and replaced without full utilization of their inherent capacity. A more effective means of inspection and diagnosis of bridges is needed to reveal the bridges that are highly vulnerable to collapse, and to extend the life of those bridges that possess a higher degree of resistance to collapse due to both traffic and natural hazards.

Certain highly redundant bridge types, such as RC slab bridges with sound piers and abutments, are inherently more immune to collapse due to service loads and natural hazards. In fact, not a single RC slab bridge collapse was reported among the 33 cases studied by Hadipriono (1985). An NCHRP review of field tests has also indicated that redundant bridges may have far greater strength than may be anticipated by current rating methods (Burdette and Goodpasture, 1988). Other studies have supported this view (Bahkt and Jaeger, 1990). Many of these highly redundant bridges have been or are being decommissioned without full utilization of their available capacities. The financial implications can be staggering, if one considers that the national bridge inventory, as of 1987, listed 98,777 RC slab and T-beam bridges, of which 15,519 had a  $SR < 50$ , and 57,331 had  $50 < SR < 80$ . If the capacity of these bridges are under-estimated, as the studies suggest, recognizing and utilizing the inherent capacity of these bridges will allow highway funds to be used more effectively in the future.

Present rating and inspection procedures are based almost entirely on the results of annual visual inspections. Since the effects of age and deterioration on concrete slab bridges are not fully understood, the task of associating visual defects with structural damage is difficult. In addition, in cases such as that of the test bridge, the effects of skew play a major role in the overall behavior of the bridge. Also, severe damage may be hidden inside the slabs, within the piers, or under asphalt overlays. As a result, present procedures for bridge rating tend to be overly conservative. However, this conservatism is born out of ignorance rather than sound scientific foundation, as insufficient research has been conducted to substantiate the rating procedures.

The primary basis for conducting this research is to establish a baseline from which more scientific procedures can be introduced into bridge rating. Whereas one isolated research project can not serve to substantially affect procedures and policies, it is hoped that

what is done here will serve as a benchmark for similar research in the future on concrete slab bridges as well as other types of construction. Through a continuing research program better understanding of the capacities, problem areas, and failure mechanisms of bridges can be realized. This increased knowledge base can then be used to improve the design codes, inspection procedures, and decommissioning processes to improve bridge maintenance and service life.

In addition it must be realized that the organizational aspects of the decommissioning process must be improved in order for any of the findings from this research or any future research to be properly implemented. The most comprehensive structural evaluations of bridges may be successful only if the system can accommodate these findings.

## **1.2 GOALS OF RESEARCH**

Throughout the research, three general goals have been established. The first general goal is a rigorous study of the technical aspects of RC slab bridge maintenance; including inspection, condition evaluation, rating, and decommissioning. This also includes evaluating all the limit states of structural behavior. The second general goal is to study the technical aspects of field destructive testing; including improving and advancing the state-of-the-art in instrumentation, loading system design, and test control procedures in the field. The third general goal is to conduct a rigorous study of the application of NLFEA to real structures.

### **1.2.1 Bridge Inspection and Evaluation**

Under the study of inspection, condition evaluation, rating, and decommissioning several NDE procedures will be evaluated. The NDE procedures studied include visual inspection, truck load testing, and modal testing. Calibrating the modal-test based quantitative NDE technique, developed by the UC researchers for ODOT/FHWA (Aktan and Raghavendrachar, 1990), is one of the primary objectives of this research. Included in this study will be an evaluation of the performance of the modal test in determining damage when an asphalt overlay is present. It is hoped that modal testing can ultimately be implemented as a future bridge condition evaluation procedure, in conjunction with regular visual inspection. This test offers many advantages, especially the relatively simple field testing requirements when compared to other NDE options. However, a great deal of post-processing in the lab is presently required to determine and detect damage.

Truck-load tests, which are often used for proof loading of bridges, will be explored as to their effectiveness as a NDE procedure. The results of the truck load test will be used in an attempt to isolate damage in the bridge. It is felt that the ability of truck load tests to provide "super-loadings" to the bridge may make them very desirable as a bridge evaluation tool.

The present procedure for evaluating bridges relies on annual visual inspections.

This procedure allows for the bridge engineers to track the progress of deterioration and damage, and note any developing problems that may effect the safe operation of the bridge. However, since the effects of deterioration visible in concrete slab bridges are not fully understood and critical damage may be hidden, the visual inspections are not very effective as a tool to predict bridge capacity. Through an extensive study of the materials and causes of deterioration, it is hoped that an improved understanding of the mechanics of the material deterioration can be developed. Also the influence of the visible damage on the behavior of the bridge will be closely studied to determine the effects of the damage on the performance of the bridge. Through this work, a better understanding of the relationship of visible damage to bridge performance can be developed.

### **1.2.2 Bridge Rating and Decommissioning**

Bridge rating is based on the evaluation of the capacity of the bridge compared with the demands. The demands as the result of loads induced by passing trucks are quite well-understood. The calculation of the capacity is less understood and simplifying procedures are often used in its calculation. During this research, bridge ratings were performed using several different techniques. The techniques used include the use of finite element analysis as well as some of the simplified analysis procedures from the AASHTO codes. This allowed the researchers to study the pros and cons of the most common simplifying assumptions used in design and rating.

Some of the performed bridge ratings will use the results of all the NDE techniques. This will allow a better correlation between the bridge evaluation process and the rating process. Also, since rating of a bridge is ultimately linked to its decommissioning, a study of bridge rating can prove quite useful in improving this phase of the decommissioning process. If ratings can be justifiably improved, the service life of the bridges can be extended.

### **1.2.3 Limit States of Bridge Behavior**

Another specific goal of the research was learning about RC slab bridge behavior at different limit states, particularly at failure. This is an especially vital aspect of the research, as without gaining a strong understanding of the behavior of concrete slab bridges, it would be unjustified to extend the findings to the bridge rating and evaluation processes. The goal also included the study of the slab reinforcement detailing as well as abutment and pier design details. Also, the research looked into the different options available for rehabilitating deteriorated bridges.

The geometry of this bridge presented the researchers with an additional opportunity to study the effects of skew on the concrete slab bridge. Since most design and rating concepts rely on simplifications which model the skew bridge as straight it is important to study the problems associated with this assumption.

#### **1.2.4 Field Destructive Testing**

This test marked the first time a bridge would be tested to destruction in a structural identification framework. Not only did the research team want to determine the capacity of the bridge, but to accumulate enough information from measured responses to effectively calibrate NLFEA, calibrate NDE procedures, study the behavior of concrete slab bridges, and study the failure mechanism. For these reasons, extensive time and effort was used to develop a state-of-the-art field test.

Valuable lessons were learned throughout the research project on how to most effectively conduct research of this magnitude. Therefore, throughout this report on the destructive test design, the design decisions leading to the final testing system will be amply considered. Also, where it is practical, suggestions will be made as how to improve future research of this nature.

#### **1.2.5 Nonlinear Finite Element Analysis (NLFEA)**

Severe shortcomings have been observed when NLFEA has been applied to structures of significant nonlinear behavior, such as the 3-span concrete slab bridge which was studied. As part of this research, the state-of-the-art in NLFEA will be used and then evaluated to judge the correlation between the predicted results and the destructive test results.

NLFEA promises to be an invaluable tool for engineers in the future in accurately predicting the complete load cycle response of structures. Ultimately, it could prove very valuable in improving and upgrading our infrastructure. This phase of the research will determine the applicability of present analysis codes to a slab bridge, and evaluate the readiness of NLFEA as an infrastructure preservation tool. Ultimately, the shortcomings and problems of using NLFEA will be discussed.

### **1.3 PROJECT COORDINATION AND SCHEDULING**

In order to better understand the nature of the entire research project, as well as to discuss some of the aspects of conducting such a project it will be very helpful to first review the manner in which the project was coordinated and scheduled.

Throughout the research three separate teams, each lead by one of the co-principal investigators worked on different areas of the project. The first team led by Dr. Shahrooz concerned itself with the NLFEA and predictive analyses. The second team led by Dr. Miller was concerned with the instrumentation and material properties. The third team led by Dr. Aktan dealt with the design of the destructive test and the Nondestructive Evaluation. In addition Dr. Aktan's team globally coordinated the overall project and the collaboration between DOT personnel, academic personnel, research support personnel, consultants, and subcontractors. In this manner, oversights and confusion between the separate teams could be avoided (Figure 1.1).

This arrangement worked extremely well; since, each team was able to focus their

time and energy toward the solution of problems specific to their task. Also, all of the teams would meet periodically to discuss their progress and exchange any needed information. The project coordination and scheduling aspects were key in achieving the high level of cooperation.

In order to complete the project within the allotted time, the coordination and scheduling of individual teams involved in the project was vital. To assure as little disruption to the public as possible, the bridge closure time was kept to a minimum. Therefore, it was vital that a proper schedule was developed so that all parties would be ready as soon as the window to perform the destructive testing opened.

To maintain control of the project critical path scheduling was attempted. Critical path scheduling takes the project and breaks it down into specific tasks. The scheduling is then based on the required time and the priority of each task. The schedule is then used to plan the manpower and material needs. However, to perform such scheduling it has to be possible to lay down a very rigid schedule for the project.

While there is a definite need for extensive scheduling in this type of research project, critical path scheduling does not seem to lend itself well. In research there is no hard blueprint because major tasks can completely change within a week. For instance, based on the suggestions of the consultants, the entire loading system was changed in little more than a week. As a result of similar changes, usually less drastic, the schedule was constantly changing. The critical path from the previous week served as little more than a reminder of the major tasks that needed to be performed. Since most critical path scheduling programs are not designed to be quickly and easily edited, they are probably not appropriate for research work.

A more simple scheduling method is recommended for the future. For instance, as the actual destructive testing approached, the critical path schedule could be replaced by a weekly schedule. By looking only a few weeks ahead it would be much simpler to predict the needs of the research team. However, a long term project schedule must always be maintained in order to make sure that all major deadlines are met and no task is overlooked. Overall, the most important task in coordination of this type of research is keeping each separate team informed of their responsibilities, and the time frame in which the tasks are to be completed. It is much more practical and far easier to maintain and update weekly schedules than it is to try to provide a critical path schedule of the entire project. Therefore, the most effective means of scheduling would be to establish a one-week or two-week schedule at the beginning of each week. This schedule would be developed from an overall project schedule. In this manner each project team knows their responsibilities for the next week, and the project coordinator can make sure that no task gets overlooked.

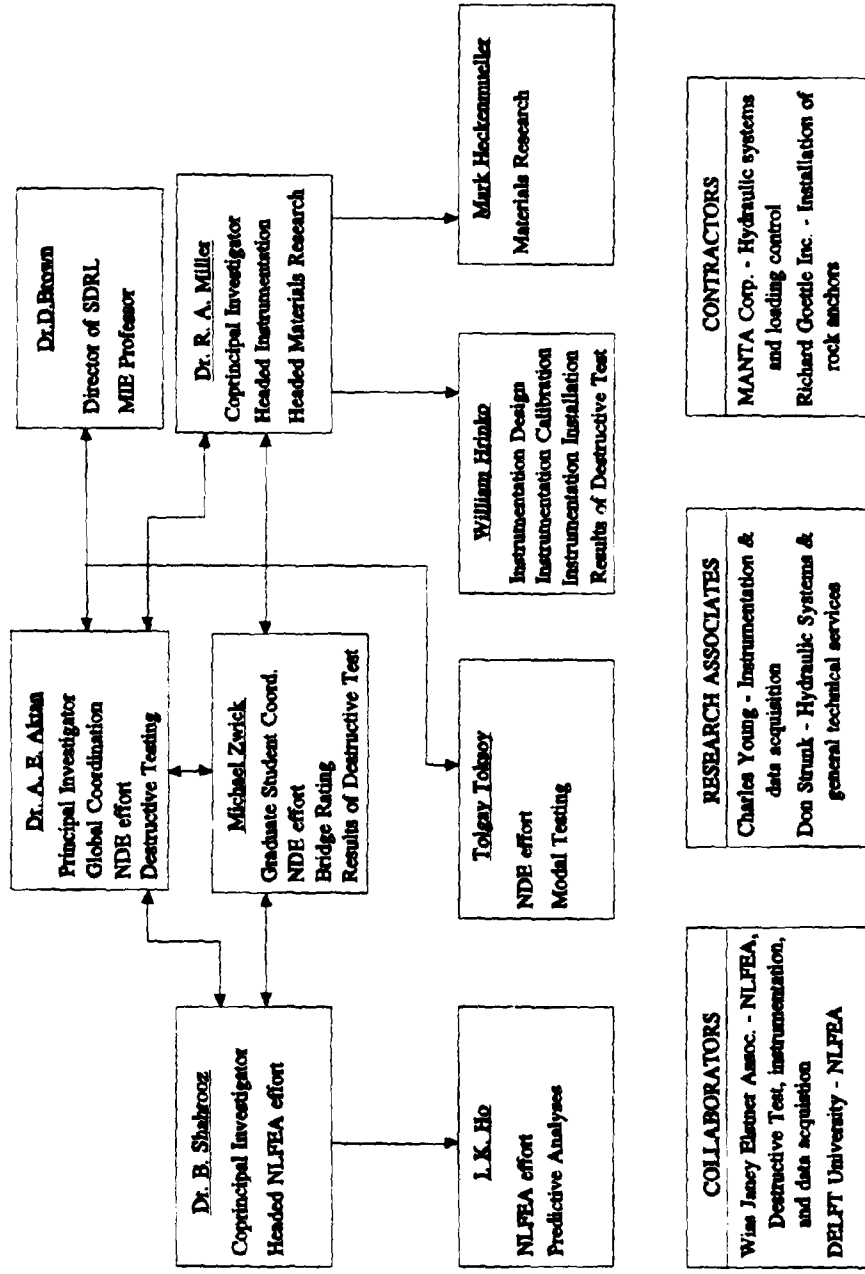


FIGURE 1.1: PROJECT PERSONNEL AND ORGANIZATION CHART

## **CHAPTER 2: TEST SPECIMEN AND MATERIAL PROPERTIES**

### **2.1 DESCRIPTION OF TEST SPECIMEN**

The test specimen (Figures 2.1 and 2.2) is a 3-span, reinforced concrete (RC) skewed slab bridge which was constructed in 1953. Due to the path of the stream, the piers and abutments are skewed at 30 degrees with respect to the roadway. Figure 2.2 also shows the site plan which includes the location of equipment vital to the conduct of the destructive testing.

The reinforcing details of the 17.25 inch thick slab are given in Figure 2.3 through Figure 2.6. Figure 2.3 shows a longitudinal cross section of the deck. The bottom reinforcement has a 1" clear cover, while the top reinforcement has a 1-3/4" clear cover comprised of a 1" cover plus a 3/4" wearing surface. Figure 2.4 gives the bar schedule, construction joint detail, and cutoff locations of the top bars over the piers. Note the manner in which the top bars are cutoff, as this affects the nature of the failure. Figures 2.5 and 2.6 give the plan view of the top and bottom of the slab respectively.

The piers consist of a column bent of four columns (Figures 2.7 and 2.8). The columns are 18" x 30" with the strong axis along the skew. An 18" wide by 32" deep beam cast integrally with the slab, spans across the top of the columns. The base of the columns are set on 4' x 4' footings cast directly on the bedrock.

The abutment was constructed on piles driven to the bedrock (Figures 2.9 and 2.10) and consists of three different sections along its length. The first section being the wing walls on either side of the bridge. The rest of the abutment is designed for the bridge slab to seat into; however, in the roadway portion of the abutment a somewhat different detail is used as opposed to the shoulder portion of the abutment. Section b-b of Figure 2.10 shows the details of the abutment design in the shoulders. This detail provides a key for the slab to tie into, and the top of the abutment is even with the top of the bridge slab. In the roadway portion a similar key is left for the slab to tie into, however the rest of the abutment is designed to provide a seat for the approach slab (See detail a-a Figure 2.10). This is a standard detail as there is no need for the presence of the approach slab outside the roadway, and in general should have no effect on the performance of the bridge. The abutment detailing is emphasized here due to its influence on the behavior of the bridge during destructive testing.

### **2.2 MATERIAL PROPERTIES**

Due to the scope of the overall research project, which includes extensive use of linear and nonlinear finite element analysis, significant effort was given toward the study of the material properties.

The original design drawings indicate "class C" concrete, while no reference could be found as to the reinforcing steel. With little available information on the properties, it became necessary to test the material properties of both the reinforcing steel and the concrete prior to testing. The information gathered from material testing is especially vital

to the predictive analysis effort needed for the design of the destructive test.

### 2.2.1 Concrete Material Properties

**Compressive Strength:** Six 4"-diameter cores from the roadway area of the bridge deck were tested for compressive strength and stiffness. The ultimate compressive strengths of Cores C1, C2, F, N1, N2, and K1 ranged from 7180 psi to 8180 psi, with an average of 7660 psi. The location of these cores can be seen in Figure 2.11, and the results can be seen in Table 2.1. No cores could be tested from the shoulders of the bridge deck because the cores fragmented during coring.

**Modulus of Elasticity:** The values obtained using a compressometer conforming to ASTM C469 ranged from  $4.378 \times 10^6$  psi to  $5.045 \times 10^6$  psi and the results can also be seen in Table 2.1. The modulus was found by using a best-fit straight line through the stress-strain data.

Using the general ACI formula:

$$E = 33w^{1.5}\sqrt{f'_c} \quad \text{EQN. 1}$$

values from  $4.981 \times 10^6$  psi to  $5.316 \times 10^6$  psi were obtained using the corresponding values of  $f'_c$ . The actual and estimated E values compared very favorably. A sample concrete stress-strain curve is shown in Figure 2.12.

**Table 2.1 - Concrete Core Strength Results**

	Length (in.)	Ult. Str. (psi)	Elasticity (psi)	$33w^{1.5}f'_c$ (psi)
Core C1	5-7/8	7843	N/A	$5.204 \times 10^6$
Core C2	7-3/16	8184	N/A	$5.316 \times 10^6$
Core F	8	7184	N/A	$4.981 \times 10^6$
Core N1	6-1/4	7254	$5.045 \times 10^6$	$5.005 \times 10^6$
Core N2	6-1/4	7865	$4.995 \times 10^6$	$5.211 \times 10^6$
Core K1	6-3/4	7637	$4.378 \times 10^6$	$5.135 \times 10^6$
Mean Values		7661	$4.806 \times 10^6$	$5.142 \times 10^6$

**Notes:**

1. A unit weight of 146.91 lb/ft<sup>3</sup> was used for 'w'.
2. The 'elasticity' results for Cores C and F were not found.

**Unit Weights:** ASTM C642 Absorption Tests were run, and the unit weights of the concrete were found through these tests. The results for the roadway and east side concrete specimens are shown in Table 2.2. The mean values were 146.91 lb/ft<sup>3</sup> and 141.61 lb/ft<sup>3</sup> respectively.

**Table 2.2 - ASTM C642 Test Results for Unit Weights**

Roadway Specimen	Stock Unit Wt (lb/ft <sup>3</sup> )	Side Specimen	Stock Unit Wt (lb/ft <sup>3</sup> )
2-C642	147.32	1-C642	141.40
4-C642	146.37	3-C642	142.50
5-C642	156.74	8-C642	140.62
6-C642	144.37	9-C642	141.92
10-C642	145.31	Mean Value	141.61
11-C642	140.64		
7-C642	147.64		
MEAN	146.91		

**Tensile Strength:** The tensile strength was obtained by the split cylinder method (ASTM C496). Note that the tensile strength of the roadway cylinders all fell around 10% of the mean  $f_c$  of 7661 psi, a reasonable value of  $f_t$ . During the coring process, the cores often cracked or a rebar was hit. As a result, core lengths varied. The actual lengths are shown along with the results in Table 2.3.

**Table 2.3 - Split Cylinder Tests**

Specimen	Core Length (in.)	Dia. (in.)	Load (lbs)	Tensile Stress (psi)	% $f_c$ (%7661)
Core C	2.16	3.9375	10120	757.41	9.89
Core E	1.584	3.9375	6760	689.91	9.01
Core F	2.186	3.9375	8600	635.99	8.30
Core F	4.618	3.9375	22940	803.05	10.48
Core H	3.943	3.9375	21210	869.60	11.35

### 2.2.2 Reinforcing Steel Properties

Tension specimens meeting the ASTM A370 Standard for 0.500-inch-round tension test specimens were made from rebar specimens removed from the deteriorated shoulders of the bridge prior to destructive testing. They were tested in a 60-kip capacity Tinius-Olsen machine. A Strawberry Tree data acquisition system, an extensometer, and a strain indicator were used to collect data. The results are seen in Table 2.4.

The properties of the reinforcing steel used on the bridge deck resembled Grade 40 steel, which has specified yield and ultimate stresses of 40 and 70 ksi respectively. The mean strengths found for the tension specimens were 48,900 and 92,200 ksi respectively, indicating that the minimum specified strength of a grade 40 steel was met (Figure 2.13).

A discussion of the effects that rusting had on the yield and ultimate strengths can be found in section 3.2.6.

**Table 2.4 - Tension Specimen Results**

Specimen	F <sub>y</sub> (psi)	F <sub>u</sub> (psi)	E (x10 <sup>6</sup> psi)
KTS	50129	92970	29.37
LTS	38454	72471	30.93
M1TS	49726	94565	28.22
M2TS	50391	94008	31.10
M3TS	48226	94908	N/A <sup>1</sup>
NTS	45809	87062	27.34
PTS	48962	89756	30.43
Mean Values	47400	89400	29.57 <sup>2</sup>

Notes:

1. The initial response for M3TS was not accurate.
2. The average elasticity values do not include that of M3TS.

F<sub>y</sub> : Yield Stress

F<sub>u</sub> : Ultimate Stress

E : Young's Modulus of Elasticity

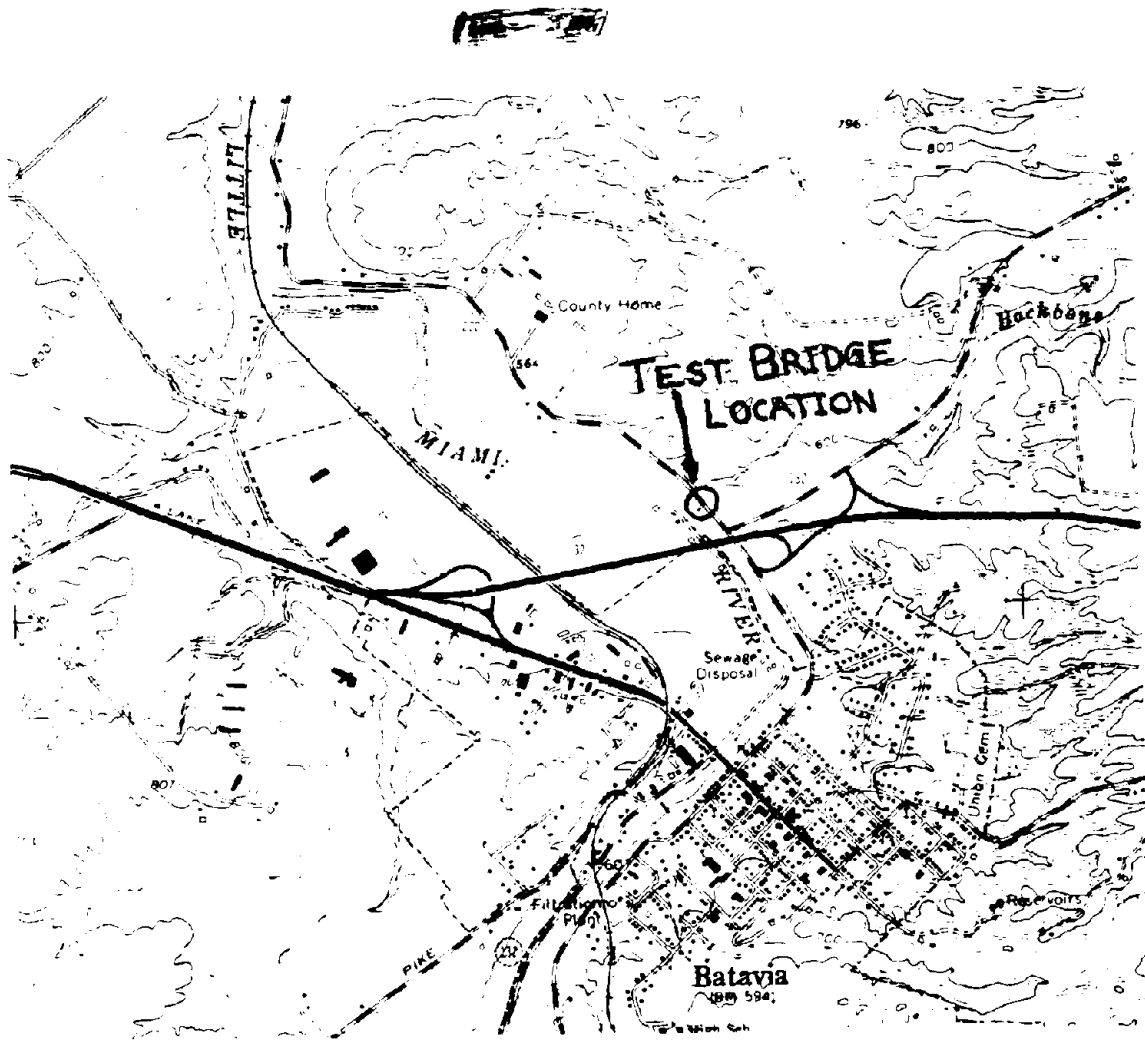
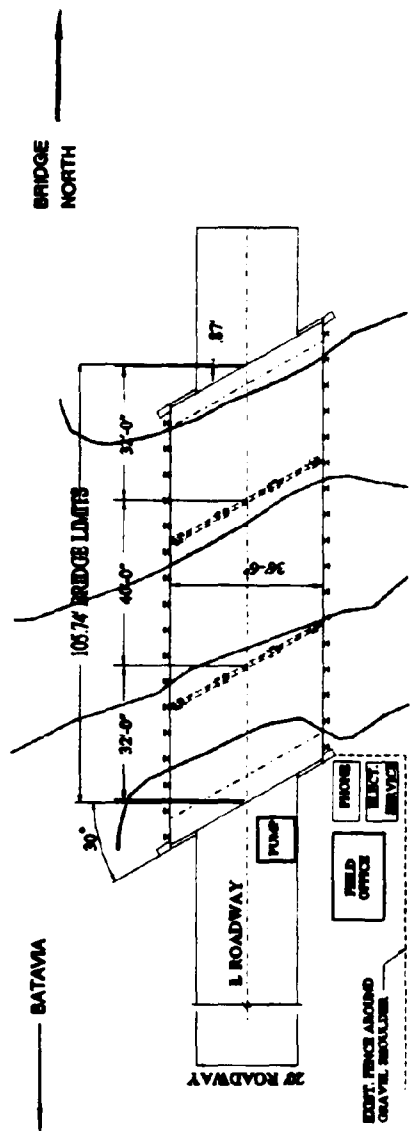
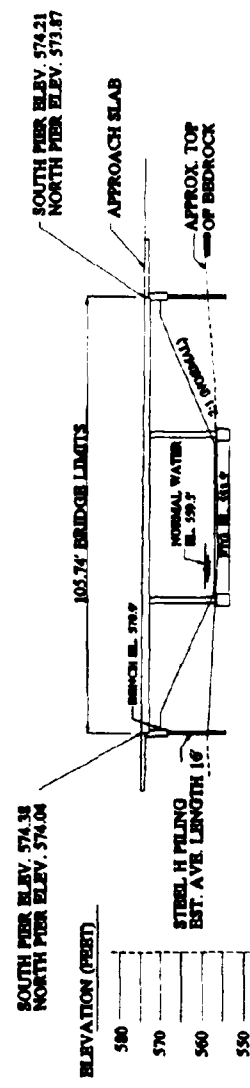


**FIGURE 2.1: MAP LOCATION AND PHOTO OF BRIDGE**



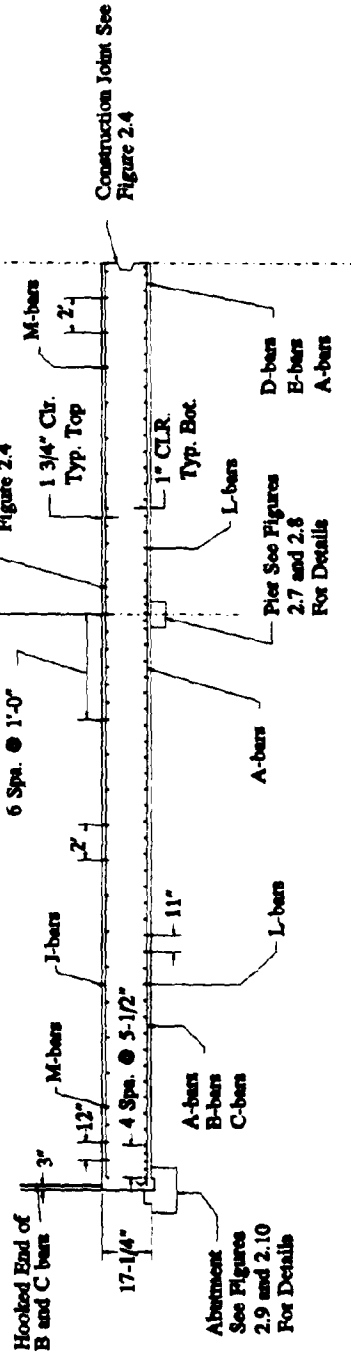
**SITE PLAN**



**SITE ELEVATION**

**FIGURE 2.2: SITE PLAN AND ELEVATION**

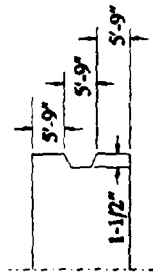
NOTE: - Concrete + 2-1/2" Asphaltic Overlay  
 - See Figure 2.4 For Reinforcing Steel Schedule



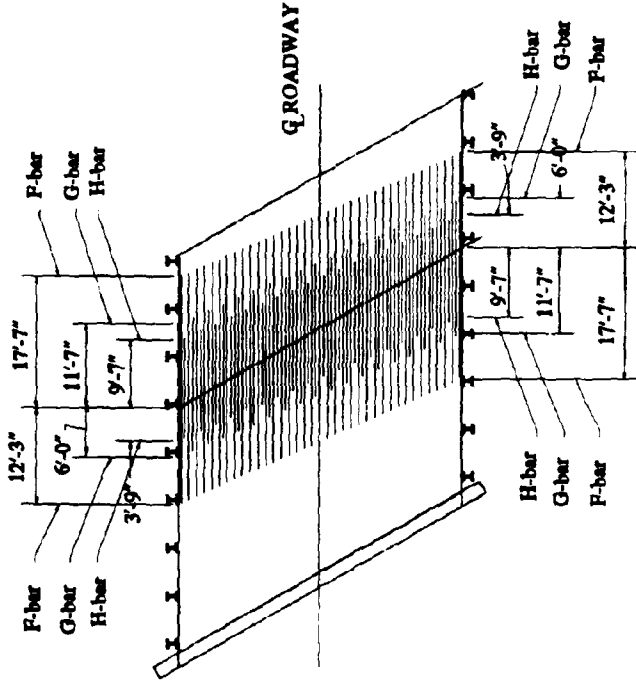
LONGITUDINAL SECTION OF CONTINUOUS SLAB

FIGURE 2.3: SLAB REINFORCEMENT DETAILS

REINFORCING SCHEDULE			
BAR TYPE	SIZE Ø	LENGTH	SPACING
A	1-1/8"	37'-6"	15"
B	1-1/8"	27'-6"	30"
C	1-1/8"	24'-3"	30"
D	1-1/8"	24'-0"	30"
E	1-1/8"	19'-3"	30"
F	1-1/8"	29'-10"	12"
G	1-1/8"	17'-7"	24"
H	1-1/8"	13'-4"	24"
I	3/4"	23'-0"	24"
K	3/4"	20'-3"	24"
L	3/4"	41'-7"	VARIES
M	3/4"	41'-7"	VARIES

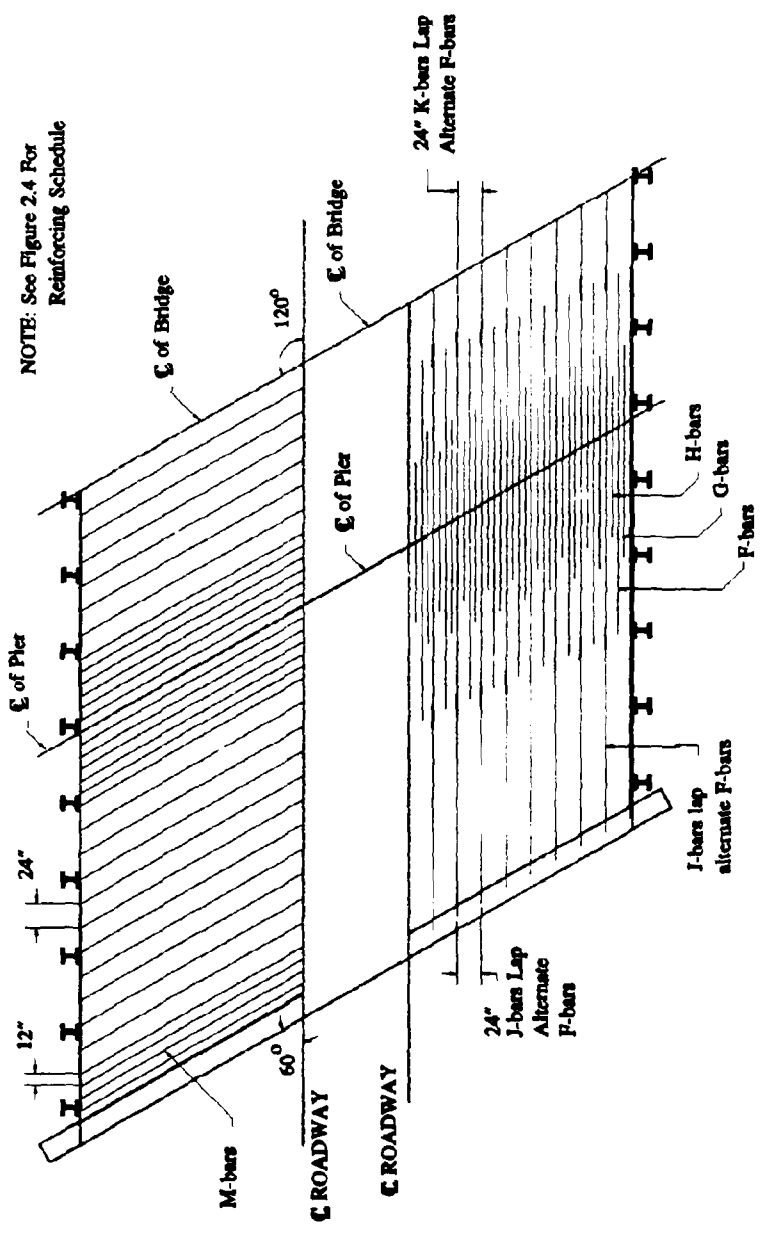


**DETAIL OF CONSTRUCTION JOINT**



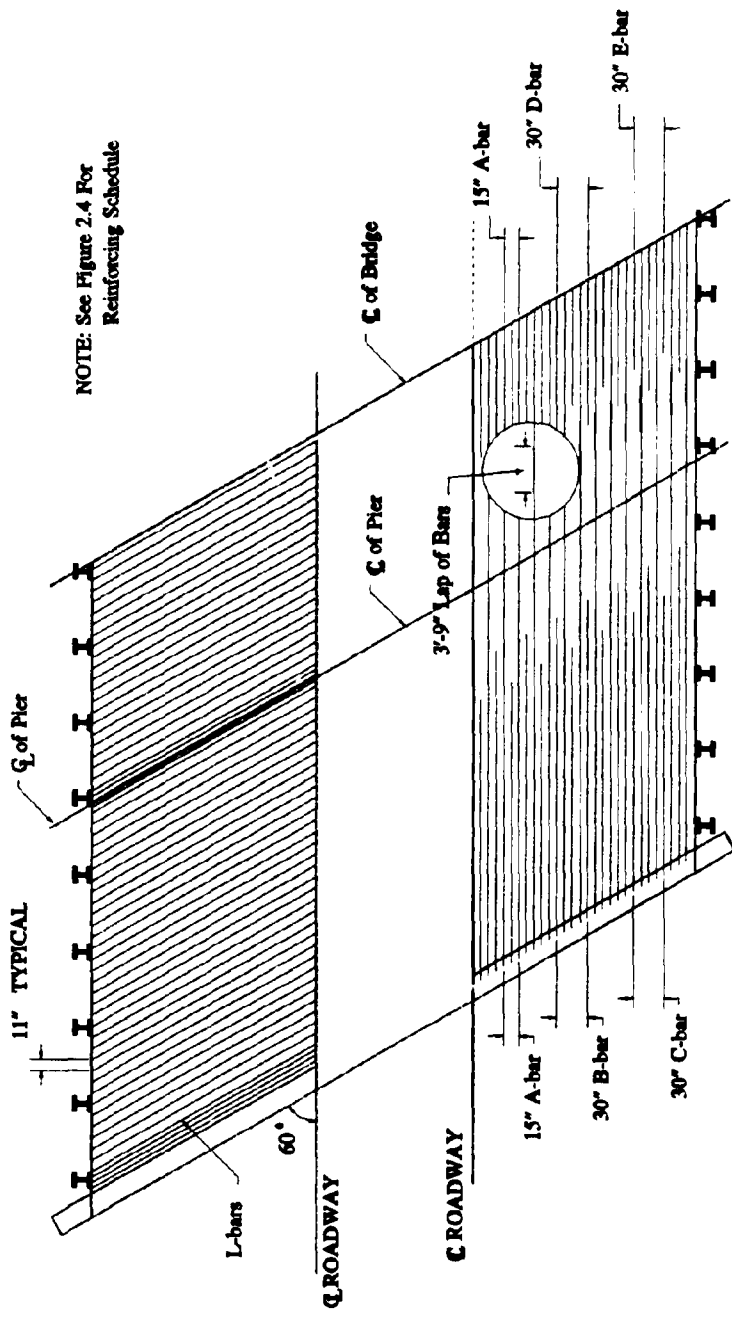
**LOCATIONS OF F, G, AND H BAR CUTOFFS**

**FIGURE 2.4: ADDITIONAL SLAB REINFORCEMENT DETAILS**



REINFORCEMENT IN TOP OF SLAB

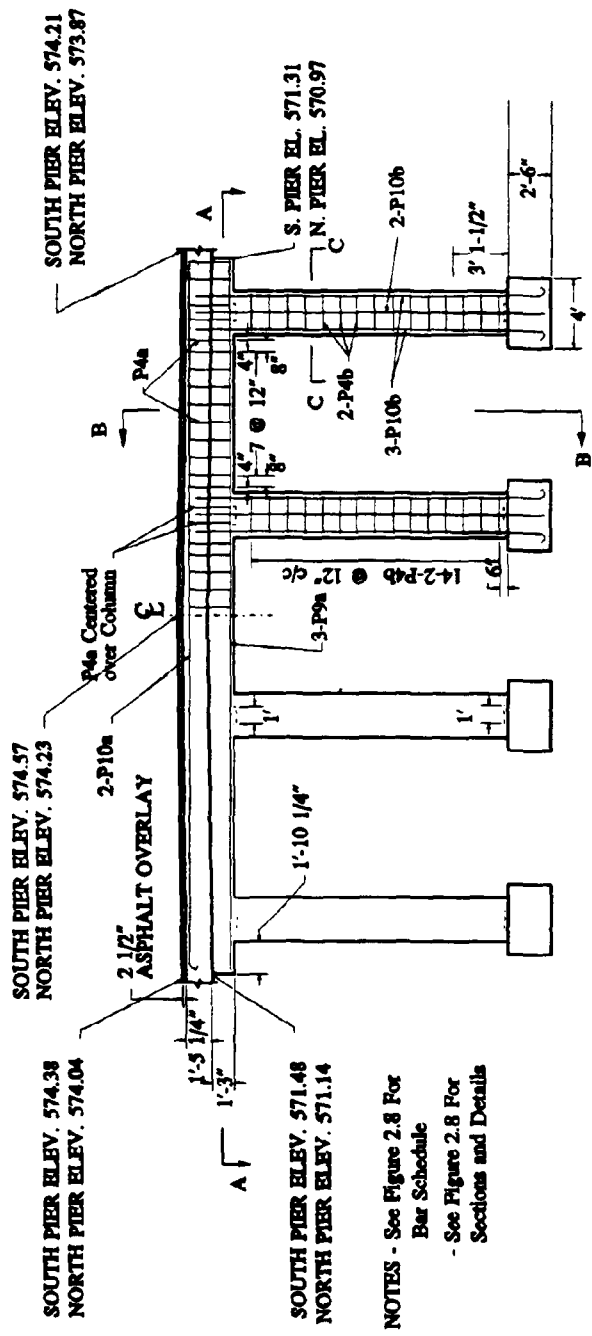
**FIGURE 2.5: REINFORCEMENT DETAILS : TOP OF SLAB**



NOTE: See Figure 2.4 For Reinforcing Schedule

REINFORCEMENT IN BOTTOM OF SLAB

**FIGURE 2.6: REINFORCEMENT DETAILS : BOTTOM OF SLAB**



PIER ELEVATION

**FIGURE 2.7: PIER DESIGN**

NOTES - See Figure 2.8 For Bar Schedule  
 - See Figure 2.8 For Sections and Details

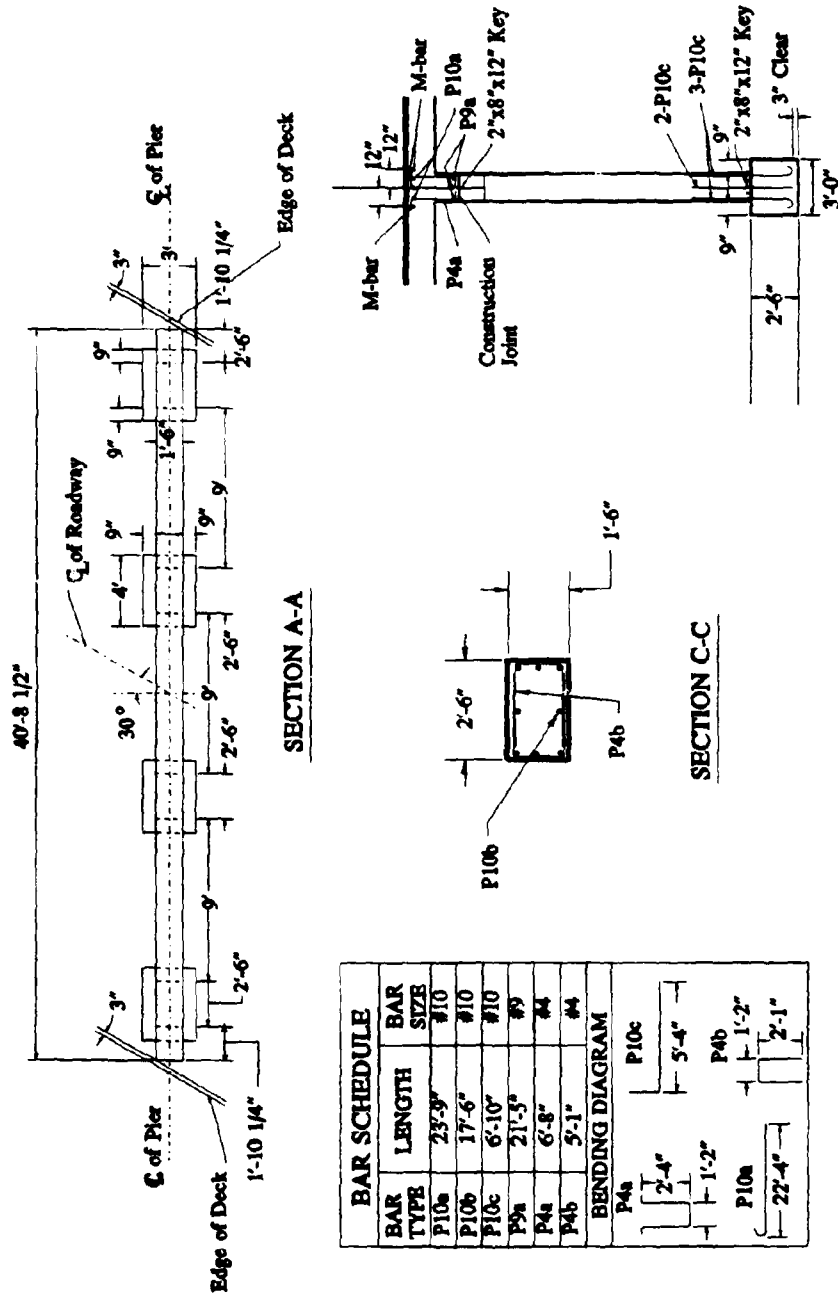
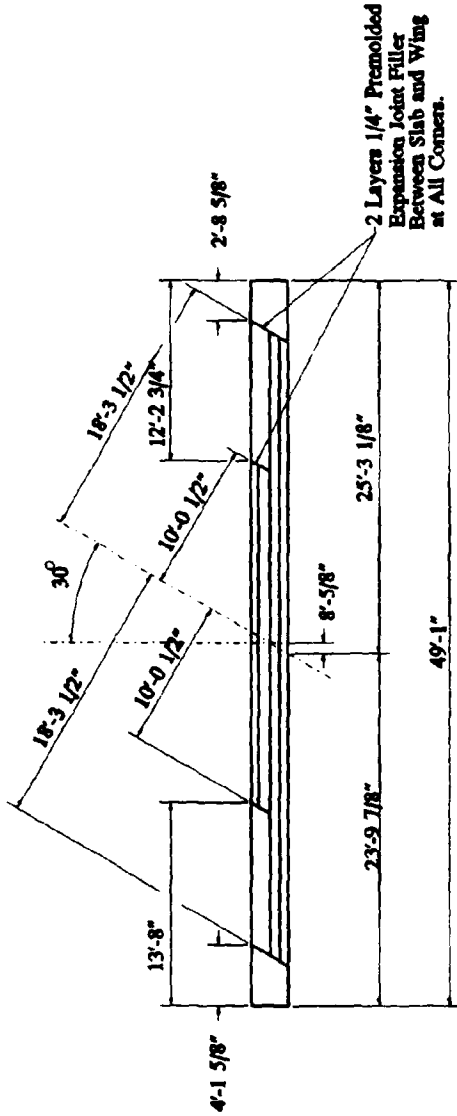
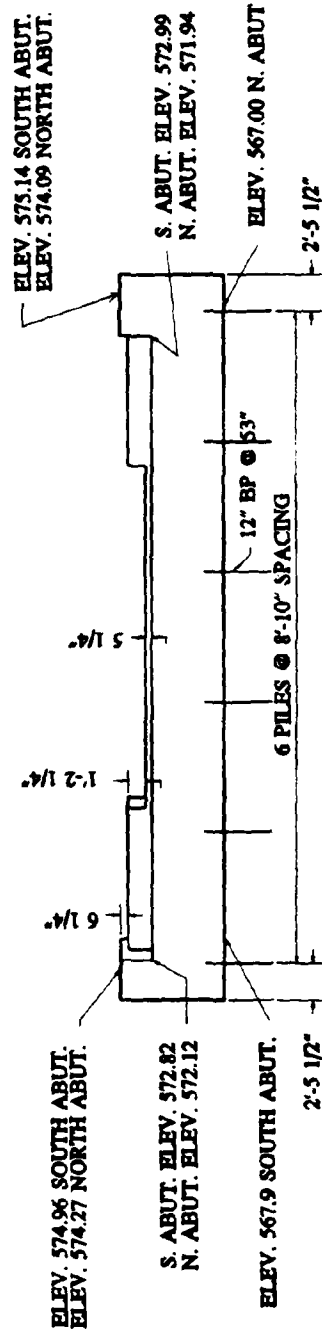


**FIGURE 2.8: PIER DETAILS**

BAR SCHEDULE		LENGTH
BAR TYPE	BAR SIZE	
A7a	1"	26'-3 3/8"
A4a	5/8"	8'-5"
A4b	5/8"	3'-0"
A2a	1/2"	3'-3"
A2b	1/2"	6'-3"
A2c	1/2"	8'-0"
A2d	1/2"	3'-6"
A2e	1/2"	10'-4 3/4"



**ABUTMENT PLAN**



**ABUTMENT ELEVATION**

**FIGURE 2.9: ABUTMENT DESIGN**

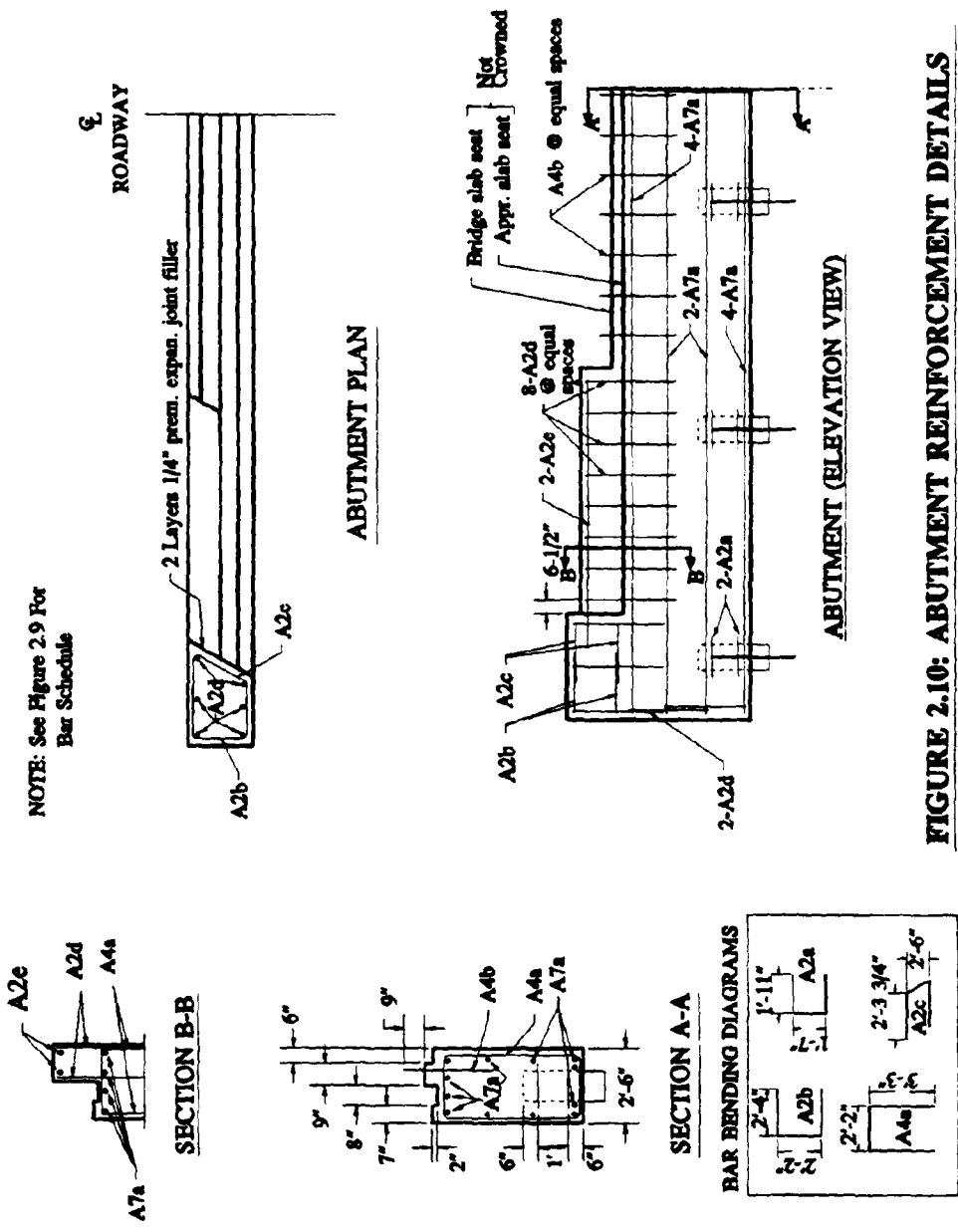


**FIGURE 2.10: ABUTMENT REINFORCEMENT DETAILS**

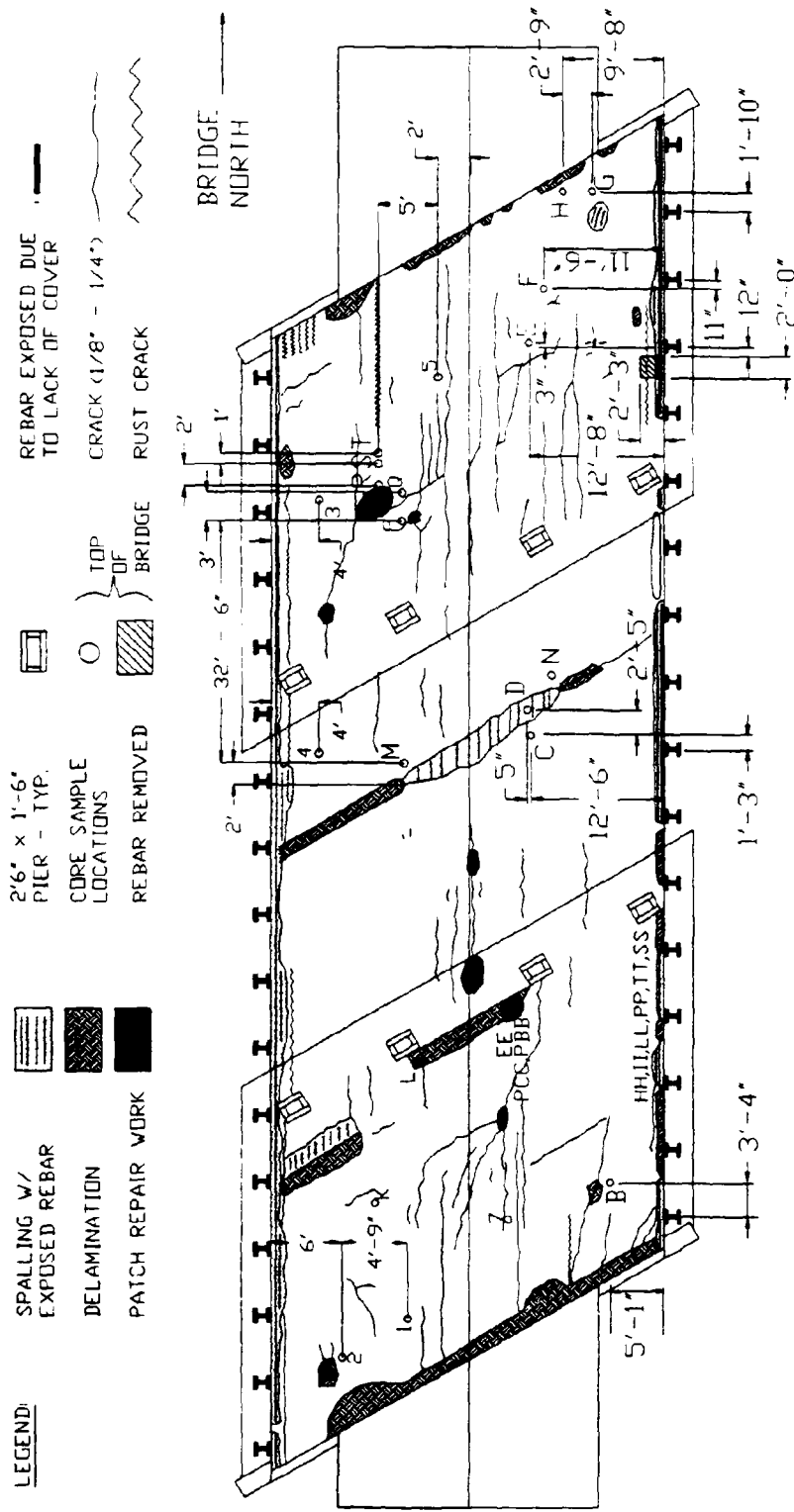


**FIGURE 2.11: BRIDGE DAMAGE - BOTTOM VIEW**

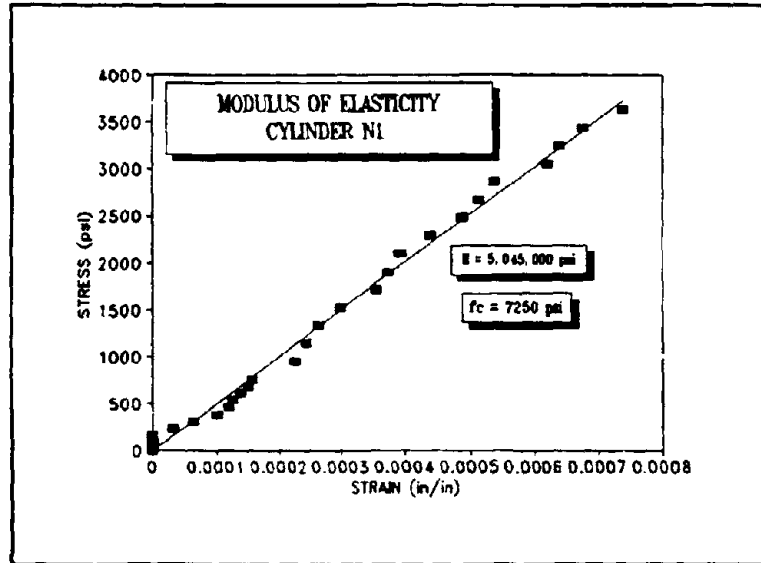


**FIGURE 2.12: TYPICAL MODULUS OF ELASTICITY GRAPH FOR CONCRETE CYLINDERS**

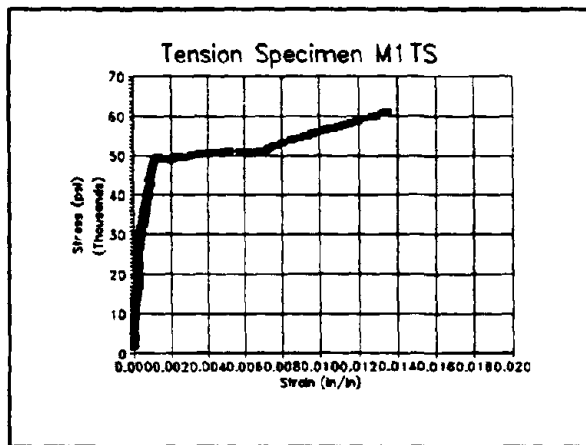


**FIGURE 2.13: TYPICAL STRESS-STRAIN CURVE FOR THE TENSION SPECIMENS**

## CHAPTER 3: CONDITION OF TEST SPECIMEN

### 3.1 CONDITION SURVEYS

#### 3.1.1 Bridge Damage Survey

A damage survey of the bridge slab was performed. The top was surveyed after the 2.5" asphalt overlay was removed. Figures 3.1 and 3.2 show the deterioration of the top and bottom of the bridge deck with both figures drawn as though the viewer is looking down from the top of the bridge (i.e. damage to the bottom of the deck is drawn as though the slab is transparent). These figures only show the damage to the concrete.

In this report, the term 'edge' refers to the vertical side surfaces of the slab. The term 'shoulder' refers to the area on the top of the slab from the slab edge to a distance of 5'-6" from either edge. The remaining top surface area will be called 'roadway' since this area corresponds to the actual traffic lanes.

The major damage to the top of the bridge occurred in the shoulder and the edge regions. There was a complete deterioration of the top layer of concrete on both shoulders and reinforcing bars were exposed (Figure 3.3). There was a difference in the level of rust in the exposed bars. On the west shoulder of the deck, the bars appeared to be in excellent condition, while the bars on the east shoulder were badly rusted. The bars on the east shoulder could sometimes be seen to separate from the concrete when the surrounding concrete was struck with a hammer. The reinforcing bar condition is discussed in Section 3.2.6.

Some of the rusted bars were larger than the nominal diameter. This is not surprising since an apparent expansion due to scaling occurs. As the time the concrete deteriorated is not known, it is not known whether the rebars rusted before or after the concrete spalled. Since the bars on the west shoulder were not rusted, it is doubtful that rusting of the reinforcing bar contributed to the concrete deterioration and the rusting on the east shoulder probably occurred after the concrete was already damaged. Cracking due to cyclic freezing and alkali-silica reaction is believed to be the principal agent in inducing the spalling (Section 3.2.2).

Unfortunately, the top of the bridge deck was covered by an asphalt layer which needed to be removed before a damage survey or any structural testing could be done. The asphalt layer was removed by grinding, and as a result, the top the deck was pitted and grooved. Due to the grooved deck and the deteriorated shoulders, it was impossible to find or map the small hairline cracks which were easily seen in the bottom of the slab.

The damage could best be seen at the edges of the bridge. The concrete was deteriorated to a depth of about 4" to 6" below the original surface of the concrete (Figure 3.4). Rebars along the edges of the bridge were badly rusted. On the east and west edges of deck, the concrete damage was dominated by horizontal cracking.

Using the amount of deterioration shown in the cross sectional view, Figure 3.5, it can be estimated that the cross section had lost between 6% and 9% of the original area at the areas where the concrete was in the best condition. The majority of the loss of concrete was

from the shoulders and edges of the deck. There was more damage at the construction joint in the mid-span and at the south abutment. The loss of cross section in these areas was estimated at about 20%. Loss of cross section at the north abutment was estimated at about 15%. However, loss of cross section is a minor problem compared to the fact that the concrete was deteriorated to a level below the reinforcing bars, which may severely reduce the negative moment capacity of the deck at the piers.

The bottom of the slab was still in a fair condition with the major damage being a few areas of local spalling and a large number of hairline cracks. There were major areas of spalling concentrated at the center of the middle span where there was a construction joint, and near the two abutments. This damage seemed to be caused by the leakage of water and chlorides through the joints at these locations. There was some local spalling in the south span, and the reinforcing bars were rusted in these areas.

### **3.1.2 Damage of Bridge Deck as Indicated by the Cores**

The first indication of the conditions of the bridge came from a study of the concrete cores taken to determine the material properties. These cores provided insight regarding not only the concrete strength, but also the regional variation in the concrete.

The bridge will be divided into three parts for the following discussion as can be seen in Figure 3.6. The three divisions are made at the pier lines : the south span, the middle span and the north span. Figure 3.2 shows the core locations. The usable cores were used for compression and tensile strength tests (Chapter 2) or for material property tests (Section 3.2).

**South Span:** Cores B, K, L, 1, 2 and 7 were taken from this area. Core B was taken from the shoulder in the south span, and the concrete was badly deteriorated; resembling loose gravel. Core K was taken at the center of the west lane. A full depth core was not taken due to a rebar at the bottom of the core, but a usable core was removed. Core L was taken near the South pier line, but it was fragmented due to the presence of a rebar in the core. The top of the rebar was rusted. Although the core appeared sound, later tests showed this core to have a high chloride content (this is discussed in more detail in Section 3.2.5). Cores 1, 2, and 7 were taken from the roadway area in the south span and they all appeared to be in excellent shape.

**Middle Span:** Cores C, D, M, N, and 4 were taken from this area. Cores C and N were taken from the roadway concrete and were sound. Core D was taken at the construction joint where there was a high amount of seepage of water and salts, but it was still in very good condition although it split along the cold joint. Core M was taken near the construction joint in the roadway concrete and was fragmented due to a cut through a rebar, but was otherwise sound. These findings signify that the roadway concrete between the pier lines was sound.

Core 4 was drilled about 4 feet from the west edge of the deck, and had horizontal cracking through the core. This cracking was thought to be a result of cyclic freezing (Section 3.2.1), and it was that believed the cracking extended from the edge of the slab over a distance of 5 to 6 feet into the shoulder area. A view of the east edge of the bridge (Figure 3.4) shows that horizontal cracking dominated both edges of the bridge deck.

**North Span:** Cores E, F, G, and H were taken from the east roadway lane. All of the cores were in good condition, with the exception of Core G, which was taken near the shoulder. Core E was not completed due to the interception of a rebar; however, the concrete appeared to be in good condition. This core came apart at the rebar and the bond between the concrete and rebar was good. The rebars in this area were not rusted, showing that salt and water had not penetrated to the rebars.

Cores P, Q, R, S, T, 3 and 5 were taken from the west lane. They were all in poor condition. Cores P, Q, and R all hit some heavy reinforcement, but the concrete above the reinforcement was fragmented. No bars were hit drilling cores S, T and 3 but the cores were fragmented. Judging by the very poor condition of the concrete here, this portion of the slab may not have been effective in carrying loads. Core 5 came from the center of the roadway was in excellent condition indicating the damage did not extend to this point.

### **3.1.3 Deterioration and Structural Integrity**

The shoulders of the deck were highly deteriorated, and no concrete cores could be tested for compression because of their fractured state. The deterioration appears to have had a profound effect on the structural integrity of the shoulder and edge concrete. However, these areas of concrete did have some stiffness and strength acting as a unit (see Chapters 5 and 6). The mechanical interlock between layers of concrete, and the bond between the reinforcing bars and concrete provided stiffness at the service limit state.

During the destructive test loading for loads up to 4 or 5 trucks, the shoulders had the same effective stiffness as the roadway area. Over 4 or 5 truck loads, the stiffness of the shoulders was reduced as will be further discussed in Chapter 5.

The reduction in reinforcing bar areas may have had an effect on the strength of the deck at critical areas, such as the area where failure began. Most of the reinforcing bars that were tested from the east side concrete had lost 5%-21% of their original area (Section 3.2.6), so that the force capacity of these bars would have to be reduced accordingly. However, the steel had sufficient strength and all tests showed yield and ultimate strengths above nominal. The more probable contribution to the initiation of failure would be the loss of cover over the top reinforcement.

## **3.2 MECHANISMS OF MATERIAL DETERIORATION**

### **3.2.1 Petrographic Analysis**

A petrographic analysis (ASTM C856-83, 1988; ASTM C295-85, 1988) was performed

on various samples of the concrete from the bridge deck by Erlin, Hime Associates in Chicago, Illinois (Refer to Chapter 3 Appendix for Petrographic Analysis Report). Three concrete specimens from the side concrete were studied: HH, PP, and TT (Figure 3.2) From the roadway concrete, two 4" diameter, 9" long concrete cores (Cores 1 and 5 - Figure 3.2) were studied.

**Description of Concrete:** The fine aggregate was a natural and crushed sand consisting of limestone, dolomite, quartz, granite, and feldspar. The coarse aggregate of the specimens was gravel having a maximum nominal size 1" to 1-1/2". This aggregate consisted of limestone, dolomite, granite, quartz, basalt, gabbro, chert, and clay-ironstone. The coarse aggregate was not well graded or uniformly distributed. Intermediate-sized particles were insufficient in number or entirely missing, which gave the concrete a low density. Neither the coarse nor the fine aggregate were chemically stable during the service life of the deck. Alkali-silica gel was present as aggregate rims, as secondary deposits on fracture surfaces and in air voids. The presence of the gel indicated that an alkali-aggregate reaction had occurred.

Physical damage to the individual coarse aggregate particles and to the concrete had occurred due to "D" cracking. This usually indicates freeze/thaw damage to the concrete. The coarse aggregate was very porous and probably susceptible to freeze/thaw damage.

The cement paste was medium to dark gray, and in the non-deteriorated areas was hard, dense, and well bonded to the aggregate particles. It contained a significant amount of residual cement particles. Hydration appeared normal and advanced. The composition and textural characteristics of the paste were indicative of a moderate cement content (estimated to be 5 to 5-1/2 bags/yd<sup>3</sup> or 450 to 500 pounds/yd<sup>3</sup>) and a moderate water/cement ratio (estimated to be .48 to .52). Secondary white deposits of calcium carbonate were present on many fracture surfaces and in voids of the concrete fragments. These deposits indicated that the cement paste had been leached of soluble compounds by water moving through the concrete system.

Air in the concrete occurred as a few large spherical and non-spherical voids characteristic of entrapped air and as a few more small, spherical, discrete voids characteristic of entrained air. The concrete was classed as air entrained; however, it is not known if it was intentional air entrainment, because air entrainment was just beginning to be used in 1954, the year that the bridge was constructed. The entrained air may have resulted from the accidental addition of lubricant oils, detergents or a primitive air entraining agent. The system of air voids was poorly developed, the voids were not well distributed and the estimated air content was only 3 to 3-1/2%. Most of the entrained voids tended to accumulate in clusters around coarse aggregates. The air void system was marginal and was incapable of providing sufficient freeze-thaw protection to the concrete.

After careful examination of the petrographic evidence, a probable sequence of damage was constructed. The concrete shoulders probably absorbed water from snow pushed to the

shoulders by plows. The melting snow was absorbed by the shoulder concrete and as the melting snow ran over the edge of the slab (no drainage was provided) it was absorbed by the edge concrete. The absorbed water froze and cracked the larger porous aggregates and, due to poor air entrainment, the concrete matrix. Freeze/thaw cracking opened passages for more water to seep into the shoulder and side concrete. The aggregates were susceptible to alkali silica (aggregate) reaction (ASR) which requires water. Once the water was provided through the freeze/thaw cracks the reaction began. ASR is expansive and contributed to the cracking of the concrete. The combined forces of freeze/thaw and ASR continued until the concrete was severely deteriorated. The cracking in the shoulder and edge concrete also provided paths for chloride intrusion which may attack the rebars. However, since the west shoulder rebars were not rusted, it is doubtful that rebar corrosion was a major factor in the deterioration, but it may have contributed to the east shoulder deterioration in some small manner. The follow analysis provides evidence to support this possible deterioration sequence and information on how the damage may have affected the concrete and rebar behavior.

### **3.2.2 Aggregate "D" Cracking and Alkali-Silica Reaction (ASR)**

As noted in the previous section, the coarse aggregates were very porous and larger aggregate particles showed signs of "D" cracking (Figure 3.7). This is usually caused by freeze/thaw cycles early in the life of the concrete. Petrographic evidence suggests that since the freeze/thaw damage is expansive, the damaged aggregate would have expanded and damaged the surrounding paste, perhaps by micro and macrocracking. Since this type of damage can occur quickly, it probably occurred first. The coarse aggregate also showed signs of alkali-silica reaction (ASR).

ASR is a major cause of the deterioration of highway structures and pavements in the United States. ASR requires a source of alkali, silica, and water in order to develop. Even high quality concrete can develop ASR, because of the alkalies,  $Ca^{++}$  and the reactive silica aggregates inherent in a concrete mix. The reaction is not expansive in itself, but when the gel absorbs water, it is very expansive and significant pressures result.

ASR could be found where chalcedonic, opaline cherts were present because of a high silica content in chalcedony. As long as some moisture could reach the concrete, ASR probably occurred. The sources of alkalies and calcium were originally the cement paste and aggregates themselves, and later form the NaCl and  $CaCl_2$  from the deicing salts.

**Uranyl Acetate Tests:** Freshly broken pieces of concrete were treated with liquid uranyl acetate for alkali-silica reaction detection. The uranyl ion substitutes for the alkalies in the gel and produces a yellowish-green glow when viewed in the dark using an ultraviolet light. ASR gel fluoresces much more brightly than cement paste due to the greater concentration of alkalies (Stark, 1991).

Core 5 was tested from the roadway, and Specimen PP was tested from the east edge

of the bridge deck. After viewing Core 5 under a UV light, ASR was found in air voids and around a few aggregates. ASR had formed in the roadway concrete but the amount of ASR was not great. The ASR was not expansive enough to cause damage in the roadway concrete because the extent of ASR was low. The surrounding concrete and reinforcing bars may have also restrained cracking in the roadway area.

The edges of the deck were more severely damaged by ASR expansion because of an abundance of water and salt supplied for the reaction to occur. The lack of restraint and the existing freeze/thaw cracking allowed the expansion to occur easily. Specimen PP (Figure 3.8), from the east edge of the bridge deck, showed a path of ASR leading to the edge of the bridge which curved around and lined the edge of the bridge. This indicates that a considerable amount of leaching of alkalis was taking place in the shoulder concrete. The shoulder concrete had a great deal of "D" cracking and was more porous than the roadway concrete (Section 3.2.3). This opened pathways for the leaching of alkalis. In the shoulder concrete, ASR had formed around reactive aggregates, in voids, and at fractures, such as "D" cracks.

### 3.2.3 Porosity

Porosity plays a significant role in the protection of concrete and the rate at which liquids flow through the depth of a concrete slab. A porous concrete allows the aggressive agents to penetrate and attack both the concrete and rebars. Furthermore, porosity affects the frost resistance and strength of the concrete. The freezable water content in the concrete increases and the concrete strength decreases with increased porosity. Porosity may also be an indication of damage as a damaged concrete will be more porous.

Absorption is affected by porosity in that the more porous concrete will absorb more water. Absorption measures the volume of the open pores accessible to water. Higher absorption of water translates to higher absorption of all other liquids, such as melted salts and other aggressive agents. Water which penetrates the upper gel layers can then be absorbed by the absorptive aggregates which may freeze and crack ("D" crack) when the winter months arrive.

**Porosity Test Procedures:** Six concrete gel specimens, approximately 2 grams in weight, were oven-dried at 110°C for 1 week. The shoulder concrete specimens were PSS1, PSS2 and PSS3. The roadway concrete specimens were PCC top (Top of slab) and PCC 2.5" (2.5" below the surface), and PBB 3.5" (3.5" below the surface).

To measure the pore size distributions within various roadway and shoulder concrete gel specimens, a mercury intrusion porosimeter was used. It generated pressures up to 25,000 psi to detect pore diameters between 200 and 0.0073  $\mu\text{m}$ , which are in the capillary pore size range. Positive pressure rather than suction is used to force the Hg into the pores. The size of the pore is a function of the applied pressure. Using the volume of mercury forced into the specimen under a given pressure, the total volume of different pore sizes and pore

size distributions can be calculated.

The Incremental Intruded Volume graph, Figure 3.9, shows that the threshold diameters for the side concrete specimens (PSS), were all approximately 3.36  $\mu\text{m}$ , while the roadway specimens threshold diameters were not as well defined and were between 1.74-3.34  $\mu\text{m}$ . This shows that the threshold diameters were larger for the shoulder specimens. Figure 3.9 shows that there were more pores at all of the capillary pore sizes of the PSS1 and PSS2 side specimens. This shows the overall higher porosity of the shoulder concrete. This is also seen in figure 3.10, the total intruded volume. There was a marked increase in the total amount of mercury intruded in the PSS shoulder specimens.

#### **3.2.4 Absorption Testing**

Tests for the absorption of the concrete were performed according to ASTM C642-82 (1988). In this test, oven dried concrete specimens are submerged in cold water for 48 hours. After the cold water absorption test, the specimens are boiled for 5 hours to drive the water into smaller pores. Absorption is measured by weight gain. The absorption results can then be used to calculate the density of the concrete.

The most important finding was that the east shoulder specimens gained 2% more weight after 48 hour submersion than the roadway concrete did. The mean weight gain was 7.82% for the east shoulder and 6.03% for the roadway concrete. After boiling, the shoulder concrete showed a weight gain of 8.46% (from oven dry) and the weight gain of the roadway concrete was 6.61%. The bulk specific gravity was lower for the shoulder specimens than the roadway specimens. The east shoulder mean values of unit weight and bulk specific gravities were 141.61  $\#/\text{ft}^3$  and 2.27 respectively, and the roadway values were 146.91  $\#/\text{ft}^3$  and 2.35. The higher absorption in the shoulder concrete is an indication of the higher porosity of the shoulder concrete. The absorption tests confirmed the mercury porosimetry tests.

Clearly, the shoulder concrete was more porous than the roadway concrete. Most probably, this higher porosity was caused by microcracking from the freeze/thaw cracking and the ASR. This higher porosity had two undesirable effects on the concrete: 1) Higher porosity will weaken the concrete, 2) Higher porosity provided paths for water and chloride ions, which would continue to damage the deck.

#### **3.2.5 Chloride Ions**

Rusting of reinforcing bars due to chloride intrusion is a major problem with concrete bridges. Although rebar corrosion is not considered to be a major concrete deterioration mechanism in this bridge, the corrosion did reduce the rebar area and affect the structural integrity of the bridge. Because of the importance of corrosion in the deterioration of both the steel and concrete, a careful study was made of the penetration of the chlorides which often cause corrosion.

The chloride ions can destroy the protective passive film of rebars even at high

alkalinity (Slater, 1983; Mindess and Young, 1981). It is believed that the chloride ions and the carbonation through the cracks simultaneously destroyed the protective oxide layer on the rebars. After the protective oxide layer on the rebars is destroyed, the amount of corrosion of rebars depends also on the availability of water and oxygen. The shoulder concrete, which had spalling, cracking, and high porosity, provided pathways for water and oxygen to attack the rebars.

The deicing salts and snow were believed to have been brushed to the shoulder of the bridge by the plows and traffic. Much of the salt penetrated into the pores and cracks of the concrete and slowly diffused down to the reinforcement. Little chloride is lost once it enters the concrete (Mindess and Young, 1981), so that areas with frequent applications of salt will build up chlorides up to critical values.

The corrosion threshold chloride level is the level at which a breakdown of the passive oxide film of the rebar occurs. The threshold levels have been found to be 250-510 ppm chlorides by weight of concrete (Slater, 1983; Mindess and Young, 1981; Kress, 1991; Wilkins and Sharp, 1990). The Federal Highway Administration set 3000 ppm of chlorides by weight of cement (600 ppm by weight of concrete) as the chloride level at which a bridge deck must either be completely replaced (Locke, 1986), or the concrete must be replaced to a level below the rebar level. There is no danger of corrosion at levels less than or equal to 1500 ppm by weight of cement (300 ppm by weight of concrete), and the bridge can be left intact. AASHTO recommends the bridge deck be investigated closely at chloride levels between 300-600 ppm by weight of concrete.

The deicing salt used by the Ohio Department of Transportation (Ohio DOT) consisted of a 50:50 mix of NaCl and sand and gravel. CaCl<sub>2</sub> is frequently sprayed on the NaCl in the trucks before it is laid on top of the snow and ice. The CaCl<sub>2</sub> is used because it is already in a liquid state, so it works better and faster than NaCl in lower temperatures.

The bridge deck had a rebar cover for the top rebars of only 1-3/4", so that the chlorides had a short path to the reinforcing bars. The water/cement ratio was estimated at 0.49 from the mix design of the concrete, which left large capillary pores behind after hydration of the cement, thus providing paths for the chlorides to penetrate the concrete.

To achieve a life of 50 years based on non-activation of the reinforcement, a water/cement ratio of 0.40 and a concrete cover of 2" are needed (Browne and Damone, 1975). ACI also recommends a 2" cover on bridge decks. This is a minimum value however, and a variability of concrete cover is likely in the field, so that a specified cover of 2.5" should be used (ACI Committee 201). The Batavia, Ohio bridge deck would not have been able to achieve a life of 50 years based on the above statistics.

**Chloride Ion Test Procedures:** Various samples of concrete and concrete cores were tested for chloride ion concentrations. The samples were chipped away by a hammer and chisel, and then crushed to a powder by the use of a rock pulverizing device. The powder samples were dissolved according to ASTM C114 (1988), which involved the extraction of chlorides

by nitric acid.

Testing of the samples was performed according to Standard Methods, 17th edition, Section 4500-Cl Chloride, D. Potentiometric Method (1989) in which chloride content is determined by potentiometric titration with silver nitrate solution with a glass and silver-silver chloride electrode system.

**Chloride Test Specimens:** The east shoulder concrete specimens tested were II, LL, and PSS1 (Figure 3.2). The specimens were from various depths of the deck. Specimen LL was dominated by horizontal "D" cracking, and came from the very east edge of the deck.

The roadway lane specimens were EE, PCC, and Cores 5, 7, and L. There was no rusting of the reinforcing bars visible in the roadway concrete (except Core L) and the concrete was in good condition in this area. However, Core L did show some rusting on the top side of an embedded reinforcing bar. The core also showed signs of ASR.

**Chloride Test Results:** Figure 3.11 shows that all the east shoulder chloride ion levels were well above the corrosion threshold level of 250 ppm (mg/kg) of concrete. The mean value was 790 ppm, which is well above the chloride ion corrosion level.

Specimen LL showed a very inconsistent chloride ion profile. The chloride ion level at the top was high, which was expected, and the chloride level dropped to a minimum value of 557.56 ppm at a 3" depth. Below 3", it was expected that the plot would remain fairly consistent, because high levels of salts are not expected to penetrate to depths greater than 3" (Miller et al., 1992, Coggins and French, 1990). However, the chloride ion levels were very inconsistent, and peaked at a 12" depth. This is due to the severe "D" cracking prevalent in specimen LL and the fact that the specimen came from the edge of the bridge slab. Salt was washed over the edge of the bridge and allowed to penetrate the concrete through the horizontal "D" cracking. The "D" cracking was present throughout the depth of the specimen and opened up the concrete at different levels to different amounts of de-icing salts.

Figure 3.11 also shows that the plots for all the roadway specimens (except core L) were very similar. The chlorides were highest at the top level, and then dipped dramatically at 3" to below the chloride ion corrosion threshold level of 250 ppm. The levels remained below 250 ppm at depths greater than 3". Similar results have been obtained in other studies of the chloride penetration in sound concrete in real structures (Miller et al., 1992; French and Coggins, 1990)

It is probable that the roadway concrete was not penetrated by the salt because the salt was brushed to the shoulders of the bridge by the traffic and also, there were no cracks in the vicinity of these roadway concrete specimens that would allow the ingress of salts. Figure 3.12 shows that the chloride levels in Core L were very high even though it was taken from the roadway lane concrete. There was an embedded reinforcing bar that was rusted on its top side, and ASR was also seen in this core. Figure 3.2 shows that Core L was taken

over the south pier line where traffic caused the largest tensile stresses in the top of the bridge deck. It is believed that cracking at this area had allowed the ingress of water and salt. The concrete at the bottom of the bridge deck at this location had been delaminated showing that chlorides and water had penetrated the full depth of the deck at this location. Again, this is consistent with other studies (Miller et al., 1992; French and Coggins, 1990) which show high chloride penetration in cracked areas.

The porosity of the concrete figured prominently in the chloride penetration. Figure 3.13 shows directly that the specimens with higher water absorptions had higher chloride contents.

### **3.2.6 Rusting of the Reinforcing Steel**

The bridge deck showed a considerable amount of rusting of the reinforcing bar. The corrosion of the bars resulted in a considerable loss of cross-sectional area and pitting of the rebars. Corrosion of rebars can occur in a widespread manner or in very localized areas. The general widespread corrosion will more likely result in concrete spalling, while localized corrosion, or pitting, will result in a loss of area of the steel rebars without any significant damage to the concrete cover. Pitting most often occurs under poor quality concrete or at cracked regions of concrete. Most localized corrosion has been detected by the appearance of rust staining or cracks (Wilkins and Sharp, 1990) although this may not occur until severe corrosion.

A study was conducted to analyze the effect that pitting and loss of area due to corrosion of the reinforcing steel had on the yield, ultimate strengths, and modulus of elasticity. In a recent report by Maslehuddin et al. (1990), corrosion of reinforcing steel did not have any effect on the strength parameters. The rebars with increasing periods of exposure to the atmosphere reported a slight increase or no change in their yield and ultimate tensile stresses. Furthermore, the reinforcing bars showed a slight increase or no change in the bond strength with longer exposure to the atmosphere and rusting.

Samples of rusted bars were cleaned of loose material and the bar diameter carefully measured at many points along the length. The measured bar diameters were used to calculate areas which were compared to unrusted bars. The loss of area is the difference between the areas of rusted and unrusted bars.

After the bars were measured, standard tensile ASTM tensile specimens were machined from part of the bars and tested for yield and ultimate strength. The test results are shown in Table 3.1. Note that specimen N showed a slight increase in area probably due to expansion normally associated with corrosion. Table 3.1 shows that  $F_y$ ,  $F_u$ , and  $E$  are within the normal range for Grade 40 steel. The conclusion is that rusting and pitting of the rebars did not affect the internal integrity of the steel.

It is important to note that the tensile specimens were "cleaned" of corrosion during the machining process and only sound metal was tested. The actual bars had both sound and corroded areas. Since the corroded bar would be required to carry load during the

destructive test, it was desirable to determine the cross sectional area of the bar which was effective in carrying the load. The tensile specimens summarized in Table 3.1 were made from one end of the bar sample. The remaining bar sample was tested in tension. An extensometer was attached to the bar during the test, but since it was not possible to predict the position of yield before the test, the extensometer did not produce useful data and yield could not be detected.

After the bar fractured, the position of the fracture along the length of the bar was determined. Since the bar had been measured at several places along the length, it was possible to determine the original area of the fracture point. The effective area was found by dividing the load at fracture by  $F_u$  found from the tensile test of the specimen from the same bar. With the exception of specimen N (Table 3.2), the bars were better than 95% effective in carrying load. However, when the effective area is calculated as a percentage of the original, unruled area, it is seen that losses of area as high as 35% are found and that the average loss was over 20%. Obviously, such large reductions in area will significantly affect the structural integrity.

**Table 3.1 - Rebar Loss of Area and Effect on Internal Strength**

Specimen	Avg Area (in <sup>2</sup> )	Avg % Loss of Area <sup>4</sup>	$F_y$ (psi)	$F_u$ (psi)	E (x10 <sup>6</sup> psi)
K (NL) <sup>1</sup>	1.174	0	50129	92970	29.37
L (NL)	1.168	0	38454	72471	30.93
M1	0.891	23.889	49726	94565	28.22
M2	1.111	5.099	50391	94008	31.10
M3	1.100	6.047	48226	94908	N/A <sup>2</sup>
N	1.180	-0.806	45809	87062	27.34
P	1.136	3.001	48962	89756	30.43
Mean Values	N/A	N/A	47400	89400	29.57 <sup>3</sup>

Notes:

1. (NL): There was No Loss of area for the rebar.
2. The elastic curve for M3 was not accurate.
3. The average elasticity values do not include that of M3.
4. The average % loss of area is based on the average areas of the K and L measurements, which was 1.171 in<sup>2</sup>.

$F_y$ : Yield Stress  
 $F_u$ : Ultimate Stress  
 E: Modulus of Elasticity

**Table 3.2 - Percentage Loss of Area**

Specimen	Measured Ave Area of Rebar (in <sup>2</sup> )	Effective Area as % of Measured	Effective Area (in <sup>2</sup> )	% of Non-corroded #9 Rebar Area (1.171 in <sup>2</sup> )
M1	0.855	95.90	0.820	69.99
M2	0.776	98.51	0.764	65.28
M3	0.998	97.93	0.977	83.46
N	1.174	83.49	0.980	83.70
P	1.086	99.74	1.083	92.50
Average	0.978	95.10	0.925	78.99

**Carbonation of Concrete:** Concrete has a high alkalinity with a pH of about 12 which creates a passive ferric oxide film  $Fe_2O_3$  on the surface of the rebar and prevents corrosion (Slater 1983; Mindess and Young, 1981). The passive iron oxide layer is destroyed when the concrete pH is reduced to 11 or below (Mindess and Young, 1981), and the reinforcing bars lose their corrosion protection. The pH can be lowered by carbonation of the concrete, in which  $Ca(OH)_2$  is converted to  $CaCO_3$  by  $CO_2$  from the atmosphere. Reinforcing steel embedded in sound concrete with an adequate depth of cover to the bars should remain unaffected by carbonation.

**Carbonation Tests:** Phenolphthalein acid base indicator was applied with a dropper on freshly cracked surfaces of concrete. The non-carbonated portions of concrete turn pink, while the carbonated concrete remain clear during this test. The shoulder specimens tested were TT and HH. Core 1 was tested from the roadway concrete.

The tests indicated that carbonation of the concrete did not penetrate the top surface of the concrete except at cracked regions. No carbonation had occurred anywhere in Core 1 or Specimen TT. However, it should be noted that the original top layer of concrete from Specimen TT had spalled off, so that no carbonation testing was possible.

Specimen HH, from the east shoulders of the deck, was broken near a crack, and carbonation had penetrated to the bottom of the crack and ended there. If a rebar had been at the bottom of this crack, carbonation would have set in, and the steel may have lost its protective oxide layer here.

### 3.2.7 Alkali and Calcium Ion Testing

An analysis of the concentration of calcium ( $Ca^{++}$ ), potassium ( $K^+$ ), and sodium ( $Na^+$ ) ions was performed according to Standard Methods, 17th edition (1989), by atomic absorption spectrometry. The specimens tested from the east shoulder of the bridge deck

were II, LL, and HH from various depths of the deck. From the roadway concrete, Cores 5 and 7, and Specimen EE were tested. The locations of these can be seen in Figure 3.2.

This test was conducted to see if the alkalis ( $\text{Na}^+$ ,  $\text{K}^+$ ) from the sodium chloride, and the calcium of the calcium chloride of the deicing salts were detected in the shoulder concrete where they were brushed to by the plows and traffic. Potassium can also be present in road salts. The three metals were all expected to be higher in the shoulder concrete where the deicing salts most abundantly seeped into the concrete.

However, the results of these tests were largely inconclusive. Since calcium is the major component of cement, any calcium from the  $\text{CaCl}_2$  was insignificant and could not be detected. The potassium and sodium tests were also inconclusive since both minerals are easily leached.

### 3.3 SUGGESTED IMPROVEMENTS

**Repair of Existing Bridge Deterioration:** The most commonly used method for chloride ingress prevention on Ohio bridge decks is the micro-silica overlay, while latex-modified and superplasticized-dense concretes are also used. Micro-silica overlays are the most impermeable overlays and have been found to extend the life of bridge decks by 10 to 15 years.

The application of micro-silica overlays first consists of the scarification of the top 1/4" layer of concrete off the deck; this exposes the deteriorated areas of concrete. The pot holes and other pitted concrete areas are filled with micro-silica concrete to the top of the deck. A 1-1/4" micro-silica overlay is then placed on top of the deck, with an adequate seal, while the approaching roadway is pavement planed flush with the top of deck.

Epoxy-type sealers are not used very often by Ohio DOT, because failures in their use have been reported. Very localized pieces of dried surface coatings have been shown to break off, making the layer ineffective at these areas. The application of epoxy-type sealers is the easiest and fastest method for chloride ingress prevention. A 1/4" epoxy waterproof surface coating can be applied in one day. It is simply squeegeed across the deck in one layer and a layer of stone is placed on top of it. A total of four alternating layers of epoxy and stone are used. This is used only on decks in good condition, because the epoxy material cannot be used as a filler material for decks with pitted concrete.

According to Ohio DOT, micro-silica overlays will be used on most Ohio bridge decks in need of maintenance in the near future. These overlays have only been used on bridge decks in need of repair and not on new decks.

If the concrete on a bridge deck is deteriorated through the full depth of the deck in some areas, then its replacement while keeping the rest of the deck intact would be virtually impossible. This is what was found to be true for the Batavia bridge deck. However, if only the top layer(s) of concrete are deteriorated or spalled, and the subsurfaces are intact, then it is possible to replace the bad concrete without interfering with the good concrete. The bad concrete can be drilled away and a microsilica concrete can be placed in its place.

A microsilica concrete is used because it is dense and will keep water and chlorides away from the existing layers of concrete.

Cathodic protection for reinforcing bars have been used recently in 9 bridge decks in Ohio to replace existing rusted reinforcing bars. The use of these is very recent in Ohio's bridge decks and further research is needed in this area.

**Future Research Needed:** Future research is needed in the field of cathodic protection for reinforcing bars. Both their effectiveness in resisting corrosion and the cost to maintain them must be studied. Also, the effectiveness of epoxy-coated bars in resisting corrosion in bridge decks must be further studied as these bridge decks age.

It has been found that the chloride levels were significantly reduced with the use of a waterproof membrane on top of the concrete. The cost and effectiveness of latex-modified concrete, epoxy surface coatings, and micro-silica overlays should be researched.

The behavior of chlorides in concrete bridge decks must be studied in order to better understand the mechanism of deterioration to the concrete caused by chlorides.

The research performed in the study of alkali-silica reaction and "D" cracking is very valuable in the understanding of these mechanisms, and more research should be continued on existing bridge decks.

**Recommendations:** The following recommendations are made in order to prevent the many deterioration mechanisms in future bridge decks that had attacked the 1954 Batavia, Ohio bridge deck. It has been found that some of these recommendations have been utilized in current bridge decks, but they are restated here to reemphasize their importance.

- The use of asphalt overlays is not recommended on bridge decks. Asphalt is very water retentive and it may trap water under it to saturate the concrete.
- Use one of the following overlays on Ohio bridge decks to help prevent the ingress of chlorides:
  - A latex-modified concrete. It has increased the service life of many bridges by 15 years by slowing the ingress of chlorides.
  - An epoxy surface coating has been shown to significantly decrease the concentration of chlorides beneath it.
  - A concrete overlay with a low water/cement ( $\leq 0.32$ ) ratio and adequate air-entrainment. While this does not completely impede the ingress of chlorides, it does slow it down considerably.
  - Micro-silica concrete is currently being used on some of Ohio's bridge decks, because it is dense and will impede the ingress of chlorides.
- Provide adequate drainage for water to flow off the top of the deck so that the concrete does not become saturated.
- 5% to 6% air-entrainment should be used in all Ohio bridge decks to help prevent cyclic freezing damage.

- Sweep the unmelted snow deicing salts off the sides of the bridge decks after the snow/ice has melted and is no longer a threat to drivers. This will remove the water that helped to cause "D" cracking, ASR, and rusting that was seen on the bridge deck.
- Do not spray  $\text{CaCl}_2$  on top of the  $\text{NaCl}$  deicing salt unless it is absolutely necessary. The rate of corrosion in concrete mixed with calcium chloride has been found to be greater than the rate in concrete mixed with sodium chloride and it could be more corrosive to hardened concrete also.
- Use a concrete cover over the reinforcing bars of  $\geq 2.5"$  to retard the ingress of salts to the rebar level. This will also make the top layer of concrete over the rebars less susceptible to spalling. However, wider cracks may develop with larger concrete cover of the top reinforcing bars. This can be critical in areas of high negative moments where cracks may form at the top of the deck. An epoxy coated welded wire fabric should be used above the top rebars to prevent cracks from developing.
- Use as low a water/cement ratio as is feasible. This will prevent excessive capillary pores near the top layer of concrete and slow the ingress of water and melted deicing salts.
- Ensure good consolidation of the concrete.
- Use a low alkali cement.  $\leq 0.6\%$  by weight of  $\text{Na}_2\text{O}$  equivalent.
- Avoid the use of high silica aggregates.
- Do not over-finish the concrete, because this will bring excessive fine pores to the top layer of concrete. If over-finishing or the addition of water to aid in finishing occurs, excessive mortar and water will bleed to the surface, causing a higher water/cement ratio.
- Use a uniformly-graded aggregate. This will improve the durability of the concrete for the prevention of cyclic freezing.
- Use a maximum sized aggregate of  $3/4"$ . The larger the aggregate, the more susceptible it is to "D" cracking.

**LABORATORY STUDIES**  
**OF SEVERAL CONCRETE SPECIMENS**

**FOR**

**THE UNIVERSITY OF CINCINNATI**  
**(Baldwin Hall)**

**WJE No. 918473**  
**October 17, 1991**

**ERLIN, HIME ASSOCIATES DIVISION**  
**WISS, JANNEY, ELSTNER ASSOCIATES, INC.**  
**330 Pfingsten Road**  
**Northbrook, Illinois 60062**

**(708)272-7400**



**Erlin, Hime Associates**  
Construction Materials Consultants

330 Pfingsten Road  
Northbrook, IL 60062-2095  
(708) 272-7730 FAX (708) 291-5189

WJE No. 918473  
October 17, 1991

W. C. HIME  
D. D. CORNOLLY

V. KRNEC  
T. S. PATTY  
J. PETRY  
L. B. SHOTWELL  
C. WEISE

J. A. BACKUS  
B. H. BLUTTE  
R. A. COLEMAN  
P. D. KOSKOFF  
R. H. MARTINEK  
J. J. PHELPS

AFFILIATED CONSULTANT  
J. T. JUGOVIC

**LABORATORY STUDIES  
OF SEVERAL CONCRETE SPECIMENS**

**FOR**

**THE UNIVERSITY OF CINCINNATI  
(Baldwin Hall)**

\*\*\*\*\*

**INTRODUCTION**

Reported herein are the results of laboratory studies of one large concrete segment, several smaller concrete segments, and two concrete cores submitted by Drs. Emin Aktan and Richard Miller, Professors, University of Cincinnati, Cincinnati, Ohio. Requested were studies to determine the cause of deterioration of concrete represented by the segments, and reasons why the concrete in the cores had deteriorated. Reportedly, the segments were taken from the shoulder area roadway of a bridge located on Ohio State Route 132. Accordingly, the concrete was examined using petrographic microscopy methods for evaluation of compositional and textural characteristics of the specimens.

**STUDIES**

**Specimens** - The largest concrete segment was identified as HH and had approximate dimensions of 18 x 12 x 10 inches. All surfaces were broken and the original top surface had scaled. The remaining segments were much smaller; the largest of these had approximate dimension of 10 x 8 x 6 inches and all surfaces were broken. The cores are identified as Nos. 1 and 5. Their diameters are 4 inches and the lengths 9-1/2 inches. The top core surfaces were roughly finished and the ends broken. The concrete from which the cores were taken has subsequently been paved with asphalt. All concrete segments were laced throughout with random fractures. Numerous areas of the segments were coated with deposits of white secondary compounds. Core No. 1 contained a single longitudinal crack that extended the length of the cores. The crack passed around most coarse aggregate particles in the upper portions of the core and around and through the particles in the lower core portion. Core No. 5 was intact and contained two transverse steel reinforcing bars located perpendicular to each other, and 3 inches below the top surface. The steel is noncorroded.

**Petrographic Studies** - Coarse aggregate of all specimens is gravel having a top nominal size of 1 - 1-1/2 inches and consisting of limestone, dolomite, granite, quartz, basalt, gabbro, chert, and clay-ironstone. The fine aggregate is a natural and crushed (manufactured) sand consisting of limestone, dolomite, quartz, granite, and feldspar. The coarse aggregate is not well graded nor uniformly distributed. Intermediate-size particles are insufficient in number or entirely missing. Neither the coarse nor the fine aggregate were chemically stable during service in the concrete of the fragments. Alkali-silica gel is present as aggregate rims and as secondary deposits on fracture surfaces and in air-voids. The presence of the gel indicates that an alkali-aggregate reaction has occurred (Photograph 1). Physical

damage to individual coarse aggregate particles and to the concrete has occurred as a result of "D" cracking (Photograph 2).

The cement paste in all specimens is medium to dark gray, and in nondeteriorated areas is hard, dense, and well bonded to the aggregate particles. It contains a significant amount of residual cement particles. Hydration appears normal and advanced. The compositional and textural characteristics of the paste are indicative of a moderate cement content (estimated to be 5 to 5-1/2 bags/yd<sup>3</sup>) and a low to variable water/cement ratio (estimated to be .48 to .52). Secondary white deposits of calcium carbonate are present on many fracture surfaces and in voids of the concrete fragments. These deposits indicate that the cement paste has been leached of soluble compounds by water moving through the concrete system.

Air in the concrete occurs as a few large spherical and nonspherical voids characteristic of entrapped air and as a few more small, spherical, discrete voids characteristic of entrained air. The concrete is classed as air-entrained; however, the system is not well developed. The estimated air content is only 3 to 3-1/2 percent and the voids are not well distributed. They tend to accumulate in clusters and around coarse aggregate particle surfaces. The air void system is marginal and is not capable of providing sufficient protection to the concrete in a hostile environment. The weathering conditions associated with the bridge location would be considered a hostile environment.

#### SUMMARY AND DISCUSSION

The study results indicate that concrete in both the cores and fragments is air-entrained and made with gravel coarse aggregate, natural and crushed sand fine aggregate, a moderate cement content, and a low to variable water/cement ratio. The estimated air content is 3 to 3-1/2 percent.

Damage to the concrete in the fragments resulted from: (1) an alkali-silica reaction between chalcedonic, opaline chert in the aggregate and alkali in the cement; (2) cyclic freezing of water entrapped in carbonate aggregate particles; (3) cyclic freezing of inadequately air-entrained concrete; (4) extensive leaching of soluble compounds from the cement paste; and, (5) a possible alkali-carbonate reaction between limestone and/or dolomite aggregate particles.

The alkali-silica process forms silica gel as a reaction product. The gel occupies a larger volume than the original reactants and its production builds up internal pressure within the concrete and eventually the pressure surpasses the tensile strength of the concrete and cracking results. A continuation of the reaction eventually causes extensive distress in the concrete structure.

Although the concrete is air-entrained, the air-void system is not well developed. Due to the low air content and an inadequate distribution of the voids, many concrete areas are virtually unprotected from cyclic freezing damage. In addition, much of the coarse aggregate is susceptible to deterioration by "D" cracking and such deterioration has occurred. The process involves the entrapment of water within individual aggregate particles, and deterioration of the particles and the surrounding concrete as cyclic freezing occurs.

Water moving through the concrete can dissolve compounds in the cement paste. These compounds are removed and subsequently deposited in voids, aggregate sockets and on any available surface. The compounds, upon exposure to the atmosphere, are altered to form calcium carbonate. Progressive leaching can seriously reduce the integrity of the concrete.

The possibility of an alkali carbonate reaction also exists. This process causes dedolomitization of carbonate rock types in the aggregate and produces brucite ( $Mg(OH)_2$ ); however, there was no indication that this reaction has yet occurred.

Recent studies have suggested that the use of deicing agents containing sodium and/or potassium salts can promote and even enhance the occurrence of alkali aggregate reaction by increasing the alkali content of the concrete. This situation may also be a cause of the concrete deterioration.

Once the concrete has been subjected to damage from the above conditions, deterioration of the concrete can be anticipated to be progressive and even accelerated.

Erlin, Hime Associates Division (EHA)  
Wiss, Janney, Elstner Associates, Inc.



Virgil Kress  
Consultant

VK:pln

**Storage:** Samples will be discarded after one year unless other disposition is requested. Charges may be made for storage after that period.



**Photograph 1 - Reacted chalcedonic chert particle and associated alkali-silica gel rim. Each increment . represents 1/16 inch.**



**Erlin, Hime Associates**

WJE No. 918473  
Page 5



**Photograph 2 - Fractures in an aggregate particle caused by "D" cracking.  
Each increment represents 1/16 inch.**

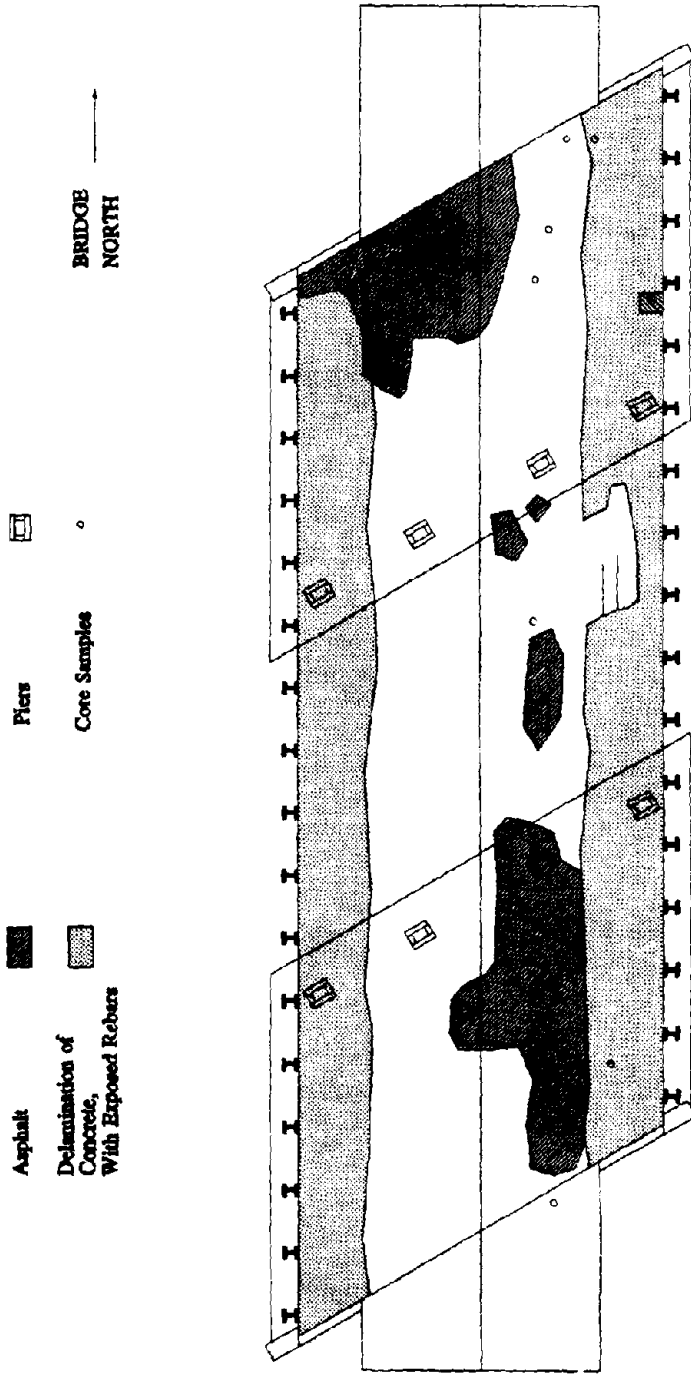


**FIGURE 3.1: BRIDGE DAMAGE-TOP VIEW**



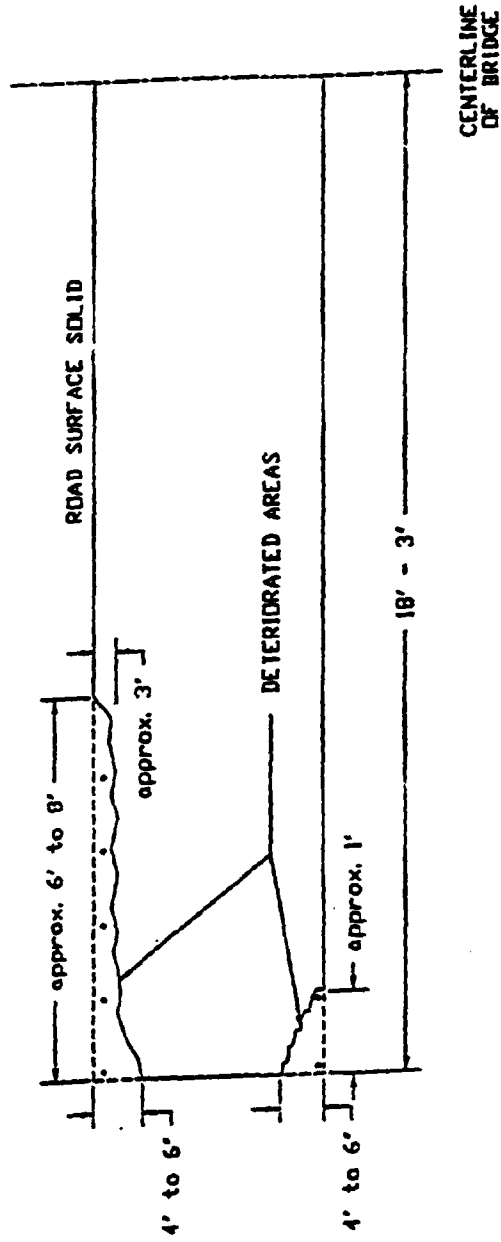


**FIGURE 3.3: TOP VIEW OF THE EAST SHOULDER OF THE DECK**



**FIGURE 3.4: SIDE VIEW OF DAMAGE TO EAST SIDE OF BRIDGE DECK**

NOTE: DETERIORATION IS APPROXIMATELY SYMMETRICAL ON BOTH SIDES OF THE CENTERLINE



CROSS SECTION OF BRIDGE DECK  
CUT PERPENDICULAR TO DIRECTION OF SPAN

FIGURE 3.5: APPROXIMATE DAMAGE TO THE DECK, CROSS-SECTIONAL VIEW

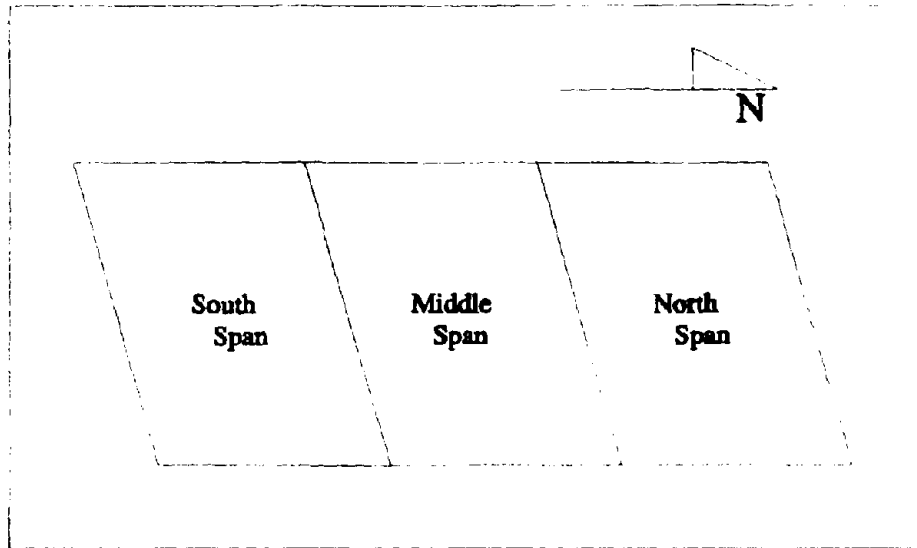


**FIGURE 3.6: LAYOUT OF BRIDGE FOR CONDITION SURVEY**

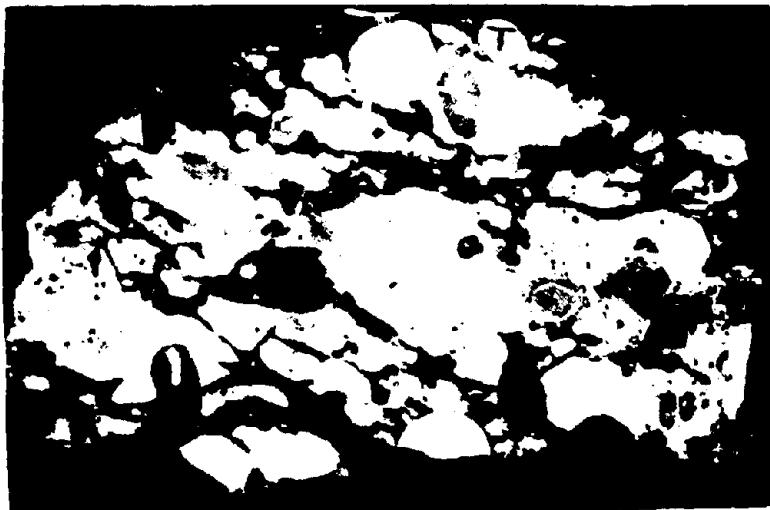


**FIGURE 3.7: AGGREGATE D-CRACKING**

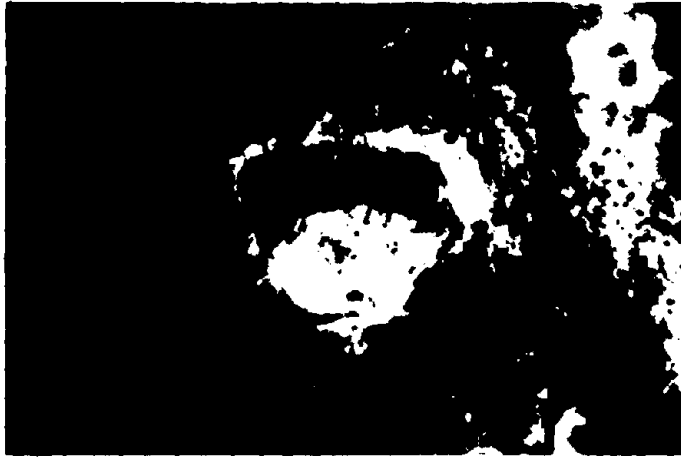


**FIGURE 3.8: RESULTS OF URANYL ACETATE TEST**

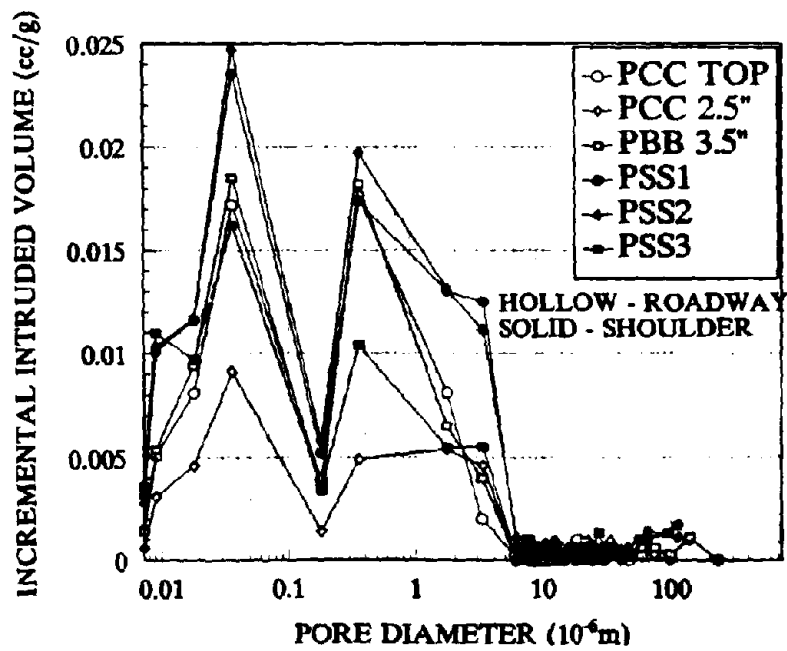


**FIGURE 3.9: INCREMENTAL INTRUDED VOLUME, H<sub>2</sub> POROSIMETER SPECIMENS**

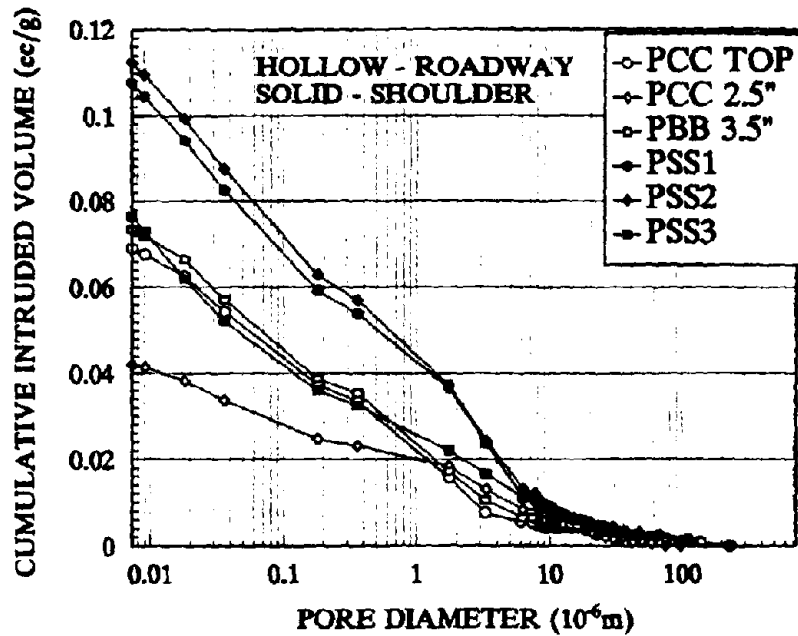


**FIGURE 3.10: CUMULATIVE INTRUDED VOLUME, H<sub>2</sub> POROSIMETER SPECIMENS**

**SHOULDER vs. ROADWAY CONCRETE**

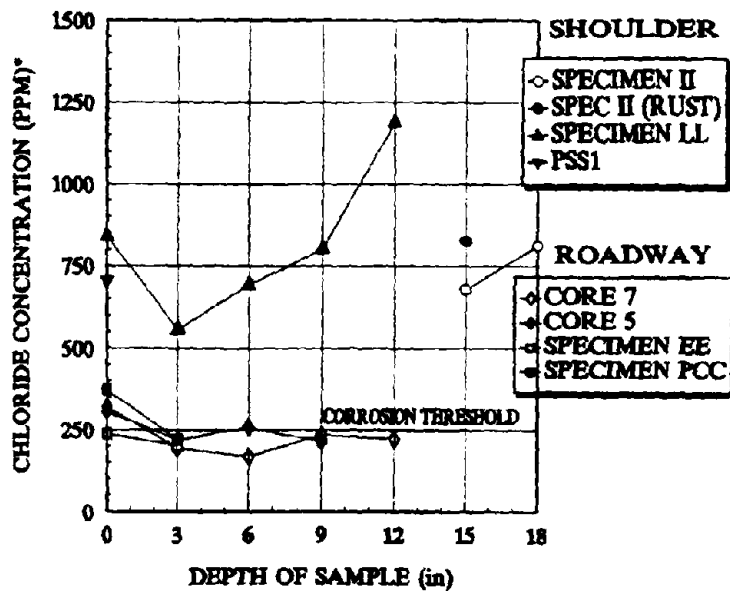


**FIGURE 3.11: CHLORIDE LEVELS, SHOULDER vs ROADWAY CONCRETE (\* PPM OF CONCRETE)**

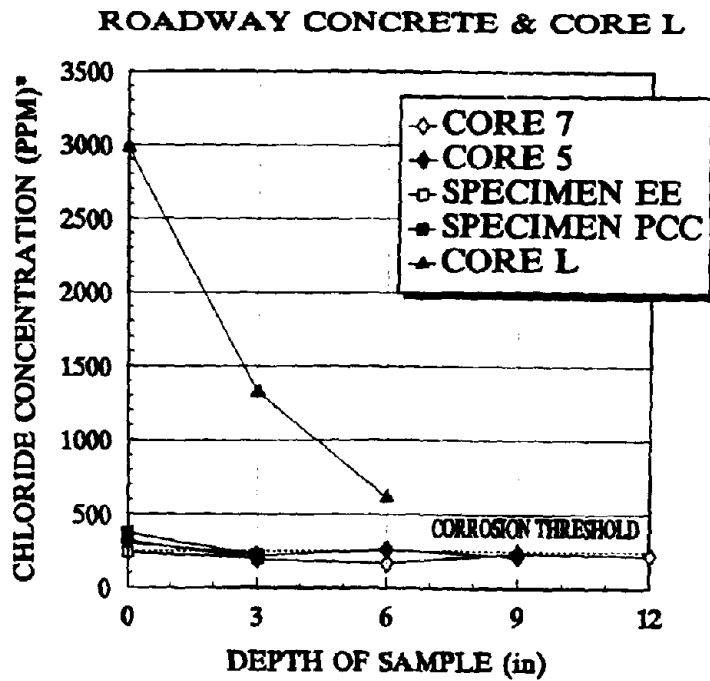


**FIGURE 3.12: CHLORIDE LEVELS, ROADWAY CONCRETE AND CORE L (\* PPM OF CONCRETE)**

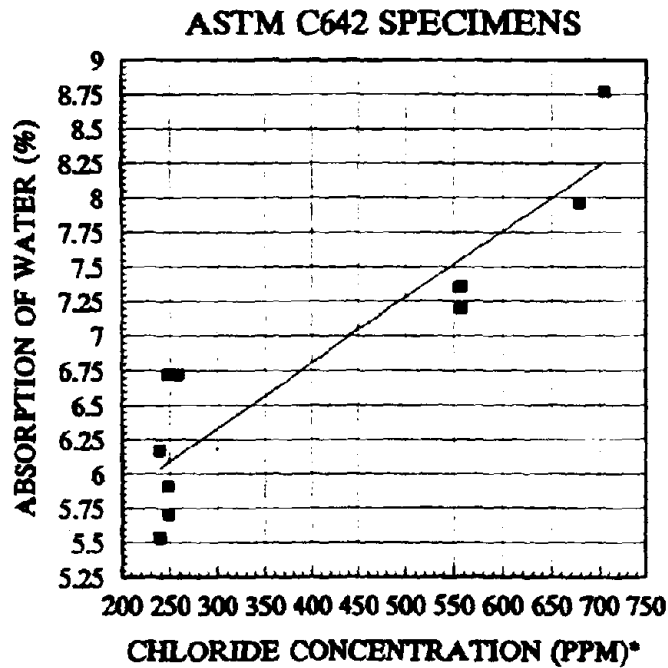


**FIGURE 3.13: ABSORPTION OF WATER vs CHLORIDE CONCENTRATION ASTM C642 SPECIMENS (\* PPM OF CONCRETE)**

**Hg POROSIMETER SPECIMENS  
CONCRETE GEL**

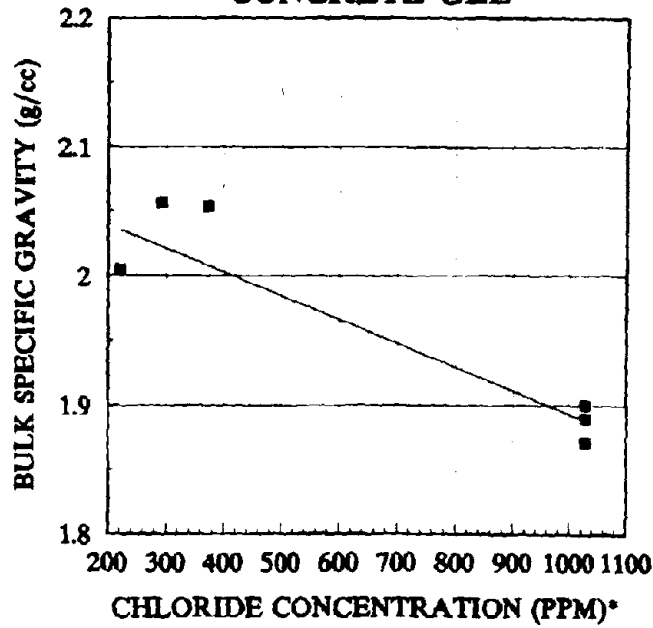


**FIGURE 3.14: BULK SPECIFIC GRAVITY vs CHLORIDE CONCENTRATION  
Hg POROSIMETER SPECIMENS (\* PPM OF CONCRETE)**

**ASTM C642 SPECIMENS**

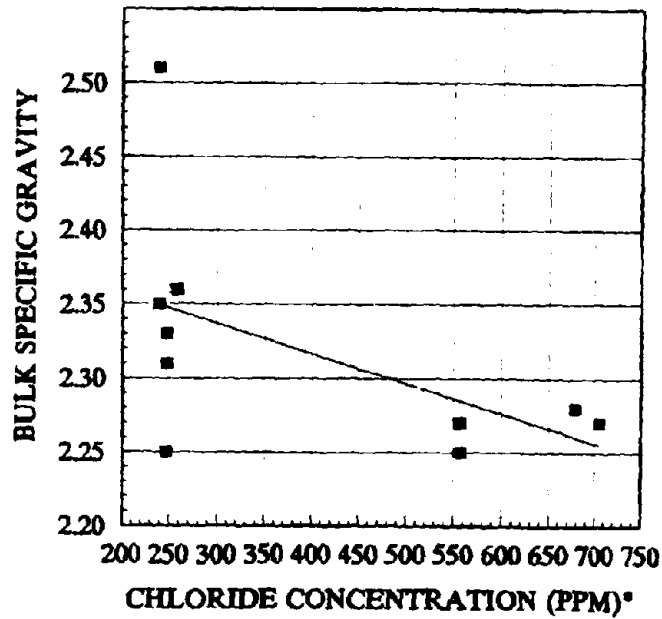


**FIGURE 3.15: BULK SPECIFIC GRAVITY vs CHLORIDE CONCENTRATION  
(\* PPM OF CONCRETE)**

## **CHAPTER 4: DESIGN OF DESTRUCTIVE TESTING AND INSTRUMENTATION**

### **4.1 DESIGN OF LOADING SYSTEM**

Figure 4.1 shows the concept behind the loading system. This system was designed to simulate a single HS20-44 truck entering the bridge in the northbound lane. In form and function the loading system is relatively simple. However, this loading system is very different from the concept envisioned in the proposal and that is presented in Figures 4.2 and 4.3. The original concept envisioned the erection of a frame spanning between the abutment and pier to carry the load. The decision process for the final loading system is presented in the following section.

#### **4.1.1 Development of Loading System**

The original concept for the loading system consisted of two frames designed to transfer the reactions of the applied load from the bridge deck to the abutment and pier. In this manner a self-equilibrating frame would be developed. The result was a closed loop loading system by which only the deck of the bridge would be loaded. The load frame transferred the load away from the columns through the pier and away from piles through the abutment. Originally this concept was desired for several reasons. First, uncertainty of the soil conditions at the bridge site during the development of the concept made it impossible to assume that conditions would be adequate to use tension piles or rock anchors. Second, it was also possible that the bridge would be scheduled for only a deck replacement and the columns and piles would be reused. If this was to be the case, it is doubtful that ODOT would have permitted loading the supports to the levels required for the destructive testing.

Once permission was given for performing the destructive test on the Batavia bridge, the design of the loading system was begun immediately. The first stage in designing the loading system was to determine the level of load the bridge could withstand. Predictive Nonlinear Finite Element Analyses (NLFEA) and Yield Line Analyses (YLA) indicated that the bridge capacity could be as high as 1,400 kips (See Chapter 8). Although deflection could be predicted with considerably less confidence, it was estimated that the maximum deflection could be as high as 10 inches. The level of the load required the use of hydraulic actuators as it would have been very impractical to use other methods, such as stacking concrete blocks or water barrels on the bridge.

Figures 4.2 to 4.4 give the details of the preliminary designs for the loading frame. However, several problems were found to be associated with this concept. The most serious problem was the stability in the loading system. Not only was lateral stability a serious consideration; but also due to the nature of the testing the deflection of the frame had to be limited or the stroke of the actuators would be used up in deflecting the frame rather than the bridge deck. This required a very deep plate girder to transfer the load. A second issue was the necessity to core relatively large holes along both the pier and abutment to accommodate the connection of the frame to the abutment and piers. This could end up substantially affecting those critical regions of the bridge.

An alternative loading system of rock anchors was proposed by D. Meinheit and D. Heidbrink of Wiss Janney Elstner Associates. Richard Goettle Inc. was contacted to evaluate the feasibility of installing rock anchors for providing the reactions loading for the bridge. The rock anchor concept was then found to be a more feasible loading concept. First of all, the concerns over stability no longer presented a problem as the load could now be placed in a straight line through the actuators. The elongations that would be expected in the rock anchors was substantially less than the deflections expected from the loading frame. The rock anchors only required the presence of 4 cores through the deck, half the number required for the loading frame. The cores needed for the rock anchor installation were located in a substantially less critical location and the cores would be reinforced by the load transfer blocks. Finally, the overall simplicity of the rock anchor concept provided obvious advantages for testing in the field, as it is vital to keep designs for field implementation as simple as possible.

Based on cost estimates of the frame and rock anchors it was found that the rock anchors would cost about half the amount of the loading frame. Therefore, in the final assessment it was found that the rock anchors had significant advantages over the loading frame concept.

#### **4.1.2 Design of Loading System**

The loading system has been designed to simulate the front tandem of a HS20-44 truck entering the bridge in the northbound lane as shown in Figure 4.1. Notice that the front axle of the rating truck, when placed in its critical position, is located almost directly above the first pierline, so it was necessary only to simulate the rear wheel load.

Preliminary Nondestructive Evaluation (NDE) and analyses indicated that the most desirable position for the destructive test was the south-east quadrant. This quadrant of the bridge was indicated to have significant damage, while there were no signs of problems that could be detrimental to other aspects of the research. Figure 4.5 shows the exact location of the loading blocks on the bridge. This position of the loading blocks was selected based on the criteria that it represented the most critical loading within the span.

The destructive test simulated bridge loading as envisioned in the rating process, as opposed to the actual manner traffic load is imposed on the bridge. Loading the bridge in this manner permits testing the reliability of the rating process, especially as it applies to computing capacity and demand for RC slab bridges.

The loading system was fabricated by first drilling four 7" diameter cores through the bridge deck after verifying that these holes would not damage the bridge deck (Figures 4.5 and 4.6). The rock anchors were installed by first driving a 6" diameter pipe through the holes in the bridge deck to the bedrock. Holes were then drilled 45 feet into the bedrock. The rock anchor cables were then installed and grouted. The next phase was the installation of the concrete loading blocks (Figures 4.6, 4.7, and 4.8), fabricated directly on the bridge around the rock anchors. Steel pipe sections were fabricated for each block (See Figure 4.9)

which served two purposes. First, they provide a path for the rock anchors to move freely through the load transfer block and bridge deck. Secondly, they allowed room for the cylinder piston to extend down into the load transfer blocks. The blocks were constructed using high strength 9,000 psi concrete (See Figure 4.9) and reinforced to assure that they would not crack since any weakness in the loading blocks could affect the test.

#### **4.1.3 Design of the Servo-Control System**

Several options for controlling the loading system were explored. The system ultimately selected is a servo-controlled electro-hydraulic loading system which is comprised of a pump, the four actuators, two servo-valves, a two-channel digital servo-controller, pressure feedbacks for load control and stroke feedbacks for displacement control. Real-time digital plotting software was used for instantaneous feedback of actuator loads, strokes and critical specimen responses. This real time system provided the information needed to make decisions for controlling the test. All of the test control equipment was located in a field office adjacent to the bridge.

The hydraulic system was designed to control the cylinders in pairs, with both cylinders on the same load block sharing a common pressure feed from one of the two servo-valves (See Figure 4.10). By plumbing the cylinders so that both actuators on a load transfer block shared the same hydraulic pressure feeds, a master slave relationships between the cylinders was created to ensure the same load.

The load applied by each individual cylinders was monitored through a pair of pressure transducers. The difference in the pressure readings between the supply line and return line at each actuator was calibrated against the actuator force in the lab against a load-cell. During the test, the actuator loads obtained from the pressure transducers served as the load control feedbacks to the servo-controller. One load reading from a cylinder at each block was used for control. Wire potentiometers were also attached to the cylinders to measure stroke and their output were used as actuator stroke feedback.

## **4.2 INSTRUMENTATION**

Instrumentation is the vital link between the researcher and the experiment. Selection of the instrumentation and data acquisition system and design of the instrumentation layout is of critical importance if the complete response of the structure is to be captured. The final instrumentation plan was not arbitrary, but was the result of a careful planning in which many factors were considered.

### **4.2.1 Instrument Selection Criteria**

The first task was to consider the response quantities to be measured and then select possible instruments which may be used. It is best to select several possible instruments for a given measurement and then make a final selection based on application, experimental conditions (i.e. lab vs. field), range and accuracy. In this test, it was desirable to measure

both global and local responses of the bridge. The selected quantities to be measured were vertical deflections of the slab, slab rotations at the abutments and piers, horizontal movement of the slab at the abutment, strains in the reinforcing steel and distortions of the slab and column concrete.

The next issue was the range and accuracy of the instrument. In general, the accuracy of the instrument is a percentage of the instrument range, so it is necessary to use the smallest possible range to obtain the most accuracy. However, it is also necessary to assure that the instrument has sufficient range to measure the entire response of the structure. Predicting the maximum response of a structure is not an easy task, especially for a highly redundant concrete structure where accurate methods of predicting structural response are not yet available. Once the range of the instrument is determined, the next task is to select an instrument with the maximum accuracy for the given range. Field measurements of slab deflection under normal traffic loading indicated that vertical slab displacements would exceed 0.01" during the test. Nonlinear finite element models indicated that 10" would be an upper bound for slab deflection. For rotations and slab movement at the abutment, upper and lower bounds were less certain. The best available theoretical predictions indicated that an accuracy of 0.001" was needed and that the total movement would not exceed 0.5". For concrete strains, an accuracy of at least 0.0001 in/in was desired.

Another consideration was experimental conditions, which have a great influence on the selection of instruments. In this project, most of the tests were done in the field which introduced a completely separate set of conditions on the instrument selection process. The points considered were:

**Weather Resistance:** Since field weather conditions are unpredictable, the instruments either had to be weatherproof or capable of being protected from the weather. Instruments which could also be installed in inclement weather were advantageous.

**Dust and Dirt Resistance:** Instruments which require "clean" conditions (e.g. bondable strain gages) are difficult to use in the field.

**Physical Mounting Requirements:** Instruments which require extensive surface preparation or special mounting hardware are not well suited to field use.

**Wind and Vibration:** Wind and vibration are usually present in the field so instruments or instrument mounting devices which are sensitive to wind forces or vibrations can lose accuracy. For example, if long poles are used to mount instruments, the poles tend to move in the wind and this spurious motion is recorded by the instrument.

**Cable Length:** Usually in the field there is large distance between the instrument and the data acquisition system so long cables are used. Long cables introduce noise and resistance into the system. Also, long cables in the field can sometimes act as antennas and be affected by atmospheric electromagnetic waves. Thus, the final selection of an instrument was based not only on the instrument measuring characteristics, but also on the suitability for field use.

After considering all the issues stated, it was decided that four types of instruments

would be used: linear voltage direct current displacement transducers (LVDCDT or usually DCDT) with a  $\pm 1.0''$  range, slide wire potentiometers (slide pots) with a  $10''$  range, bondable strain gages and clip gages.

#### 4.2.2 Calibration

When a transducer is purchased, manufacturer provides specifications on performance of the instruments such as linearity, sensitivity, temperature effects, resolution, etc. In field experiment it is important to verify these specifications and test the transducers under field conditions. Often, the stated values are minimum standards. Careful calibration can uncover better accuracy and/or allow for error compensation. Another factor which affects instrument performance is the data acquisition system. Even though a manufacturer may state the instruments have infinite resolution, the data acquisition system will impose its own limitations on the instrument. Also the noise and electrical resistance of the cables must be considered. When calibrating the instruments, the calibrations were performed using the actual cables and data acquisition system which would be used in the field. Because of this, the stated accuracies and errors are for the entire system, not just the individual instrument. If the instruments were used with a different data acquisition system or different cables, the stated accuracies may no longer be valid. The data acquisition system imposes an accuracy of  $0.0003''$  on all instruments due to the fact that it is a 16-bit system.

Calibration was done using a micrometer which reads directly in ten-thousandths of an inch with a resolution of  $\pm 0.00005$  inch, established by the manufacturer using laser interferometry. Because the range of the instruments exceeded the range of the calibrator, multiple runs were made to accurately calibrate one DCDT and one slide pot. For the rest of the instruments, except strain gauges, only a  $1.0''$  range was calibrated.

The DCDTs were calibrated over the  $1''$  range to one side of the null or 0 point. One problem associated with the DCDT linearity is the phase change of the output when the core passes the null point. It is possible to compensate for this by working to either side of the null point if possible. In using the DCDTs in the field, each DCDT was placed so that at the approximated maximum displacement the instrument would not pass through the null point. This limited the range of the instrument to only half the total movement, but increased the effectiveness of the instrument since the null point was not passed and the linearity error was minimized. Because the movement of the DCDTs in some areas was expected to be  $< 0.5''$ , the DCDTs were also calibrated over a  $0.5''$  range. As will be shown later, this also minimizes the linearity error.

In the field application, the slide pots were extended to an initial reading of  $9''$ , moving back toward 0 as the bridge deflected. For this reason, the slide pots were calibrated over the range between  $8''$  and  $9''$  of extension. Movements over  $1''$  (which were beyond the range of calibrating device) were checked in a machinist's lathe and found to be sufficiently accurate (error  $< 1\%$ )

The clip gage consisted of a thin piece of strain gaged brass attached to two thick

aluminum columns (Figure 4.11). The pinned base of the columns was attached to concrete and as the concrete distorted, the brass flexed and the flexure was measured by the strain gages. Through calibration, the relationship between the strain gage reading and the movement of the base was established. In order not to overstrain the brass piece, the clip gage was calibrated over a 0.5" range with the distance between the base pins being 4.625" to 5.125" (note that to work properly the brass piece must be slightly flexed and remain flexed during measurement).

Calibration was performed by three extensions and three retractions over the range on each instrument, except for the clip gage where time constraints permitted only one trial in each direction. Data was recorded at 0.01" intervals. All errors were treated as random errors with a Gaussian distribution. The sample standard deviation was used in defining the confidence intervals and the error limits. A confidence interval of 95% (two standard deviations) was used. Error types are shown in Figure 4.12 and sample calibration curves are shown in Figures 4.13 and 4.14.

#### **4.2.3 Error Types and Description (Figures 4.12 - 4.14)**

**Linearity:** Linearity is the measure of how far the data deviates from a best fit straight line. There were three trials in each direction (extension and retraction) or 6 trials overall. For each trial the best fit straight line is determined and the deviation from the best fit straight line is calculated. The deviations are then averaged to give the total linearity error for the instrument. Linearity is a bias error and can be eliminated or at least reduced by two methods. One method would be to use a higher order polynomial equation to model the instrument, but this was not found to be necessary or practical. The other method involves calibrating the instrument over a fraction of its normal range. By doing this, a linear equation can be derived which substantially reduces the magnitude of the error. Figure 4.12 illustrates this concept.

For a calibration of 1.0" to one side of the null point on a DCDT, the linearity error was  $\pm 0.0026$ ". For the same DCDT using only a range of 1/2", the calculated error band was  $\pm 0.0003$ ".

A linearity error of  $\pm 0.0027$  in was found for the slide pots. Note that because it was anticipated that the slide pot would need to operate over a large range of displacement, it was not practical to improve the linearity by restricting the range of movement as it was done with the DCDT. For the clip gage a linearity error of  $\pm 0.0043$ " was determined.

**Repeatability:** Repeatability is the ability of the device to output the same value for the same displacement over a number of trials. The data is divided into sets corresponding to a particular calibrator value always approached from the same direction (Figure 4.12). There are then three trials in each direction (extension or retraction). The range of values (spread) at each point is then determined. These range values are then used to obtain a sample standard deviation for the repeatability error. This is a random error for which no

compensation is possible.

For the DCDT, the repeatability error was about 0.006" for all ranges. The 10" slide pot had a repeatability error of  $\pm 0.0046$ ".

**Hysteresis and Backlash:** Hysteresis is the difference in a reading, at the same displacement, depending upon whether the displacement was obtained by an extension or a retraction of the device (Figure 4.12). The three extension trials were averaged and the three retraction trials were averaged. Hysteresis was the difference at a given point between the average curves.

Backlash is related to hysteresis (Figure 4.12). It is a measure of the displacement needed to actually change the instrument reading going from an extension to a retraction. The data is examined at the points where the direction of movement is reversed to see how much movement occurs before the transducer registers the movement. This is a random error for which there is no compensation.

The DCDT had a hysteresis error of  $\pm 0.0005$ " for all ranges. The 10" slide pot had a hysteresis error of  $\pm 0.004$ ". It was noted that a backlash error of 0.0037" was found to occur in the 10" slide pots so the slide pot hysteresis is all backlash. The backlash in the DCDT was below the resolution of the data system. Since backlash was included in hysteresis, it was not considered separately.

**Thermal Drift:** Even if an instrument is not displaced, there will be a change in the output reading called drift. The most common cause of drift is thermal effects, both internal and external. Since the instruments are electrical devices, some internal heat is generated. External changes in temperature also affect the instrument. These temperature changes affect both the electrical and mechanical components causing slight changes in the output. Drift can also be caused by flexibility in the physical instrument support and/or connections, wind and external vibrations.

Instrument drift was checked by using dummy instruments which were placed under the bridge but not displaced. DCDT drift was checked during the truckload test and the slide wire pots were checked during the destructive test. In both cases, the drift was  $< 0.001$ ". Since the drift was an order of magnitude below the instrument accuracy, it was deemed not important.

**Accuracy:** In this context, the accuracy will be taken to represent the combination of all errors, except drift. To determine the accuracy of the data statistical techniques were used to obtain the error within the desired confidence interval. For both the Truck Load Test and the Destructive Load Tests, the interest centers on the overall error. For this test, linearity, repeatability, and hysteresis errors were combined to determine an error band for the instruments. As stated there are ways to reduce the linearity errors but the other errors are random and cannot be reduced. The accuracy assumes linearity errors are minimized.

The total error is determined by using the Root Mean Sum Square method (RMSS) (EQN 4.1).

$$E_c = (E_l^2 + E_r^2 + E_h^2)^{1/2} \quad \text{EQN. 4.1}$$

where

- $E_c$  = Total error
- $E_l$  = Linearity error
- $E_r$  = Repeatability error
- $E_h$  = Hysteresis error

Tables 4.1 - 4.3 summarize the calibration results and the manufacturer's specification. For the DCDT calibrated over a 1.0" range, an total error of  $\pm 0.0028$  inches was established (Table 4.1). From the manufacture's specification (Table 4.2) the error band is expressed as a percent of full scale over the working range of the instrument and is  $\pm 0.005$  inches, two times greater than error established by calibration. Comparing the linearity error of  $\pm 0.0026$  to the total error of  $\pm 0.0028$  it is obvious that the greatest source of error for the DCDT is linearity. As can be seen a careful calibration has reduced the error band and increased the effectiveness of the instrument.

For the second calibration done over a 0.5" range an error band of  $\pm 0.0008$  inches was found. This is increased the effectiveness of the instrument three times over the 1.0" calibration, and over six times that stated by the manufacturer.

For a typical 10" slide pot an error band of  $\pm 0.0065$  inches was established (Table 4.1). The manufacturer states an error band of  $\pm 0.015$  inches. As with the DCDT an increase in effectiveness of the instrument was gained over the manufactures specifications by performing additional calibrations. Unlike the DCDT the largest contribution of error comes from repeatability and backlash, rather than linearity.

The total error for the clip gage is based solely on the transducers linearity,  $\pm 0.0043$ ". The reason for this is because not enough calibration trials were run to give acceptable answers for repeatability and hysteresis.

**Sensitivity:** This was expressed in mv of output/volt of input/inch of displacement and is simply a scaling factor to convert the transducer output to engineering units. For example, the DCDT had a sensitivity of 800 mv/v/inch. Thus, if a 10 volt current were used to excite the DCDT and there was a 1/2" displacement, the output would read 4000 mv (Equal to 800 mv/v/in sensitivity \* 10 v input \* 0.5" displacement). This value is typically derived from

the slope of the best fit line over the full range of the transducer, but for the instruments used in this test, the sensitivity is found for the working range. As previously noted, for the DCDT using the 1" range on one side of the null point, the sensitivity is 800 mv/v/in. The 10" slide pots had a sensitivity of 93.5 mv/v/inch over the 1" range of careful calibration, but this value was found to be acceptable for the entire range of instrument. For the clip gages, the sensitivity was 2.2 mv/v/inch.

**Table 4.1 - Error Results**  
(all units are ±inch)

	Sensitivity mv/v/in	Linearity Error	Repeatability Error	Hysteresis Error	Total Error
DCDT (1")	800	0.0027	0.00055	0.0005	0.0028
DCDT (1/2")	800	0.0003	0.00061	0.0005	0.0008
Slide Pot	93.5	0.0027	0.00460	0.0037	0.0064
Clip Gage	2.2	0.0043	---	---	0.0043

**Table 4.2 - DCDT Specifications**

MODEL NUMBER	0244-0000
RANGE, (working)	±1.00
MAXIMUM, (usable)	±1.50
INPUT, VOLTS DC	6.0 to 30.0
INPUT CURRENT	8.3 ma @ 6V. INPUT TO 52 ma @ 30V. INPUT
LINEARITY % FULL SCALE OVER TOTAL WORKING RANGE	±0.5
OVER MAXIMUM USABLE RANGE	±1.0FFF
INTERNAL CARRIER FREQUENCY (Hz) NOMINAL GREATER THAN	3200
% RIPPLE (RMS) NOM.	0.8
OUTPUT IMPEDANCE (OHMS)	5600
FREQUENCY RESPONSE 3 db DOWN Hz	100
TEMPERATURE RANGE	-65F to +250F
RESOLUTION	INFINITE

**Table 4.3 - Slide Wire Potentiometer Specification**

<b>RANGE</b>	<b>10 INCH</b>
<b>EXCITATION VOLTAGE</b>	<b>25V MAX. AC or DC</b>
<b>ACCURACY</b> (Repeatability and best fit straight line errors combined)	<b>±0.15% F.S.</b>
<b>RESOLUTION</b>	<b>0.008% F.S. MAXIMUM</b>
<b>THERMAL COEFFICIENT OF SENSING ELEMENT: ZERO AND SPAN</b> (Over temperature range from 0F to 200F)	<b>88 P.P.M./F</b>
<b>SENSITIVITY (MV/V/INCH)</b>	<b>94.75</b>
<b>TEMPERATURE RANGE</b>	<b>0F to 200F</b>
<b>HUMIDITY</b>	<b>TO 90% RH</b>
<b>VIBRATION</b>	<b>10 G's to 2000 Hz</b>

**4.2.4 Final Selection of Instruments and Instrumentation Layout**

As was noted in other parts of this report, two types of load tests were conducted; a service truck load test and the destructive test. Complete instrumentation plans are shown in Figures 4.15 through 4.18. For the truck load tests, DCDTs were used for deflection measurement. Since the anticipated deflections were small the more accurate and shorter range DCDT was suitable. The deflections were measured using a "weight and wire" technique suggested by Wiss Janney Elstner Associates. In this method a 2 pound weight is hung from the bottom of the bridge deck by a wire. The weight is attached to the core of the DCDT and the DCDT shell is firmly mounted to the ground (Figure 4.19). As the bridge deflects, the weight moves the core. During the truck load test, a slide pot was installed next to a DCDT to verify the slide pot performance. Also, two dial gages were installed to verify DCDT performance. The dial gages confirmed the DCDT accuracy and the DCDTs confirmed the slide pot accuracy.

For the destructive test, slide pots were in the loaded span and the middle span where large deflections were expected. Deflections in the far end span were expected to be small and were measured with DCDTs using the previously described "weight and wire" mount. Note that no instruments are shown at grid points C8 and E8. Slide pots were present at these points but were attached to wooden frames which kept the extension constant. These

instruments were used to measure drift and thermal effects.

Rotations at the abutment and pier lines were measured with DCDTs installed as shown in Figure 4.17. At the abutments, the DCDTs were placed in a frame and the rotation was the difference in the DCDT readings divided by the distance between them. On the pier caps, rigid body motion (it was assumed the pier caps moved as rigid bodies) and rotation were measured by placing one DCDT on each side of the pier but at different heights (Figure 4.17). It can be shown mathematically that this placement can be used to measure the rigid body rotation and motion.

Steel strains were measured with bondable strain gages (Figures 4.20 and 4.21). Except for exposed bars, holes were jackhammered into the concrete to expose the bar. A flat space was ground onto the bar and the strain gage applied.

Concrete distortions were measured with DCDTs and clip gages. Concrete strain gages were considered, but rejected because of the great difficulty in field installation. Such strain gages need to be long (3 times aggregate length or 4.5" in this case) and surface preparation and bonding become difficult under field conditions. Figure 4.22 shows the location of the DCDTs used to measure concrete strains (Note: DCDTs are on both the top and bottom of the slab). The DCDTs were installed between two angle brackets 6" apart. Using the stated DCDT accuracy and a 6" gage length, the accuracy was about 400 microstrain. This is one order of magnitude above the accuracy of strain gages, but still acceptable.

### 4.3 TEST PROCEDURE AND CONDUCT

The testing procedure in the case of the concrete slab bridge is greatly complicated by the limited information available as to the expected results. Even greater complexity in controlling the experiment is created when it is considered that the bridge is already extensively cracked, which makes it impossible to determine limit states such as first cracking. As a result, the load must be applied carefully, using all the information available from the instrumentation, to set a course of action. During the tests, the load deflection curves are plotted so that any sudden changes in response that could make a limit state or impending failure can be realized as soon as possible.

Based on this, a test procedure was developed by which the response at certain critical points was observed by real-time digital plots as well as others plotted by hand at every load step, while at given intervals the load was held long enough to examine the collected data from instrumentation and mark any new cracks that may have developed.

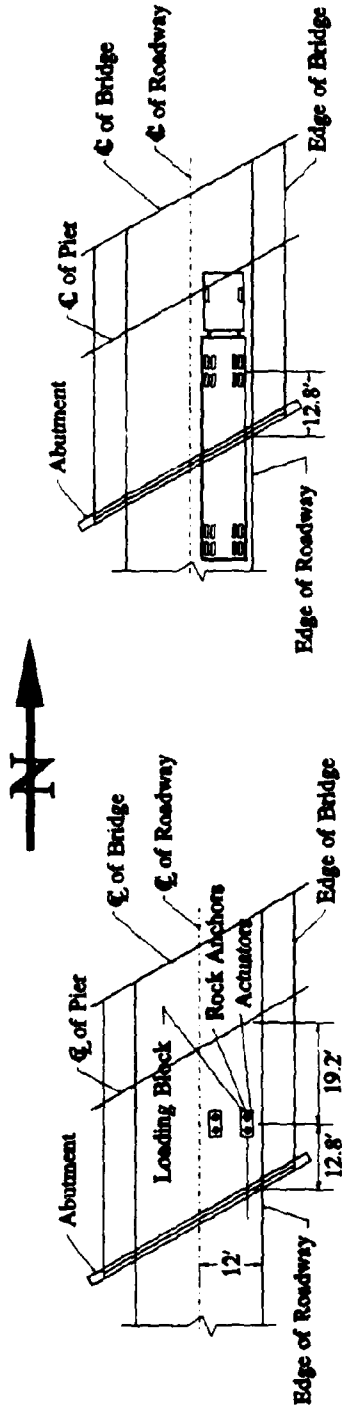
The loading program was designed based on the load-displacement response predicted by the NLFEA. Numerous loading and unloading cycles were incorporated for shake-down at the serviceability limit state. These cycles also permitted debugging the test control, loading and data acquisition systems operation. The service level load cycles were followed by a large inelastic excursion which revealed the damageability limit state characteristics of the bridge and leaving a permanent vertical deformation of about 0.5 inches after unloading. The final leg of loading led to the failure of the bridge and left a permanent deformation

exceeding 4 inches. Throughout all tests, loading was applied in increments of "rating trucks". One rating truck corresponded to a total of 32 Kips (one-tandem axle) on the two loading blocks.

The destructive test lasted for three days after low-level diagnostic loading cycles were completed in about a week. The following procedure was followed during a typical test day.

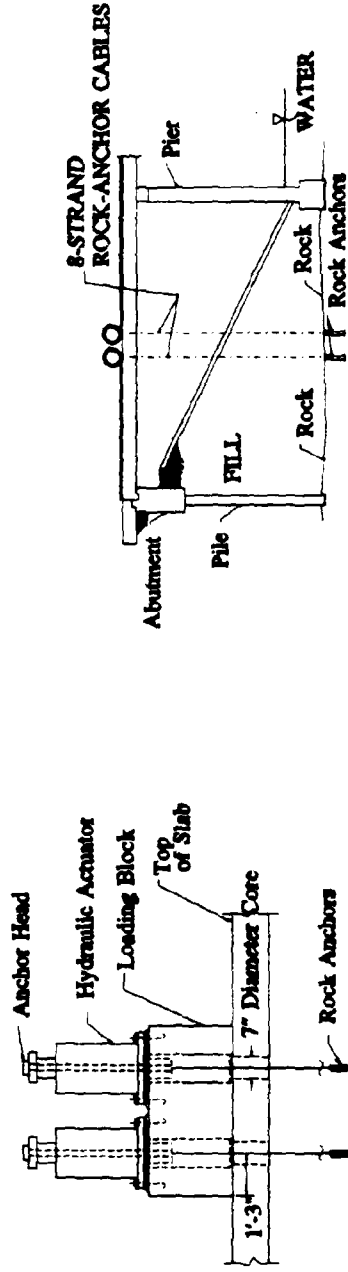
- (a) A check of all test-control electronics and instrumentation, warm-up of the hydraulic pump and oil.
- (b) Begin applying identical loads by all the four actuators in multiples of one-half rating truck-load increments.
- (c) Acquire and record the data from all the instruments after the loads reach the defined increment and while they were held steady by the servo-control system .
- (d) While observing real-time responses of the actuators and the load vs load-point deflection of the bridge, plot additional critical responses of the bridge by hand since the responses were displayed continuously by the high-speed data-acquisition system.
- (e) Every time a pre-determined load level which was deemed critical was reached, data acquired until that point was transferred to a micro-computer and the global displacement profiles of the bridge were plotted to check the instruments and bridge behavior. During this operation the load on the bridge was maintained.
- (f) As the operation described in Step (e) took place, underside and topside of the bridge were visually checked for additional damage. The additional cracking and other were recorded by both sketching and photography.
- (g) A reading is taken before resuming the loading following the completion of steps (e) and (f).
- (h) Reach a decision to continue the test, or how far to continue until next data dump.
- (i) Upon reaching the loading goal for the day, perform Data dump and unload in 1 truck increments back to zero. Duplicate all data for safe-keeping and perform post-processing overnight.
- (j) At the end of testing and removal of all load, the NDE team conducted their tests on the bridge.

The bridge was loaded 7 different times during the destructive testing. The first test was conducted on May 13, 1991 and the bridge was loaded up to 2 equivalent trucks. Four more tests in the elastic range were conducted in the next week. The last of which was performed on May 20th during which the bridge was loaded to 4 equivalent trucks, the maximum load observed to this point. On May 21 the first of the two destructive tests was performed, this time the bridge was loaded to 20 equivalent rating trucks. The next day the bridge was loaded to 22 trucks at which point the failure occurred.



PLAN VIEW OF LOADING SYSTEM

PLAN VIEW OF SIMULATED LOADING



ELEVATION VIEW OF LOADING BLOCK

ELEVATION VIEW OF SIMULATED LOADING

**FIGURE 4.1: DESIGN CONCEPT OF LOADING SYSTEM**

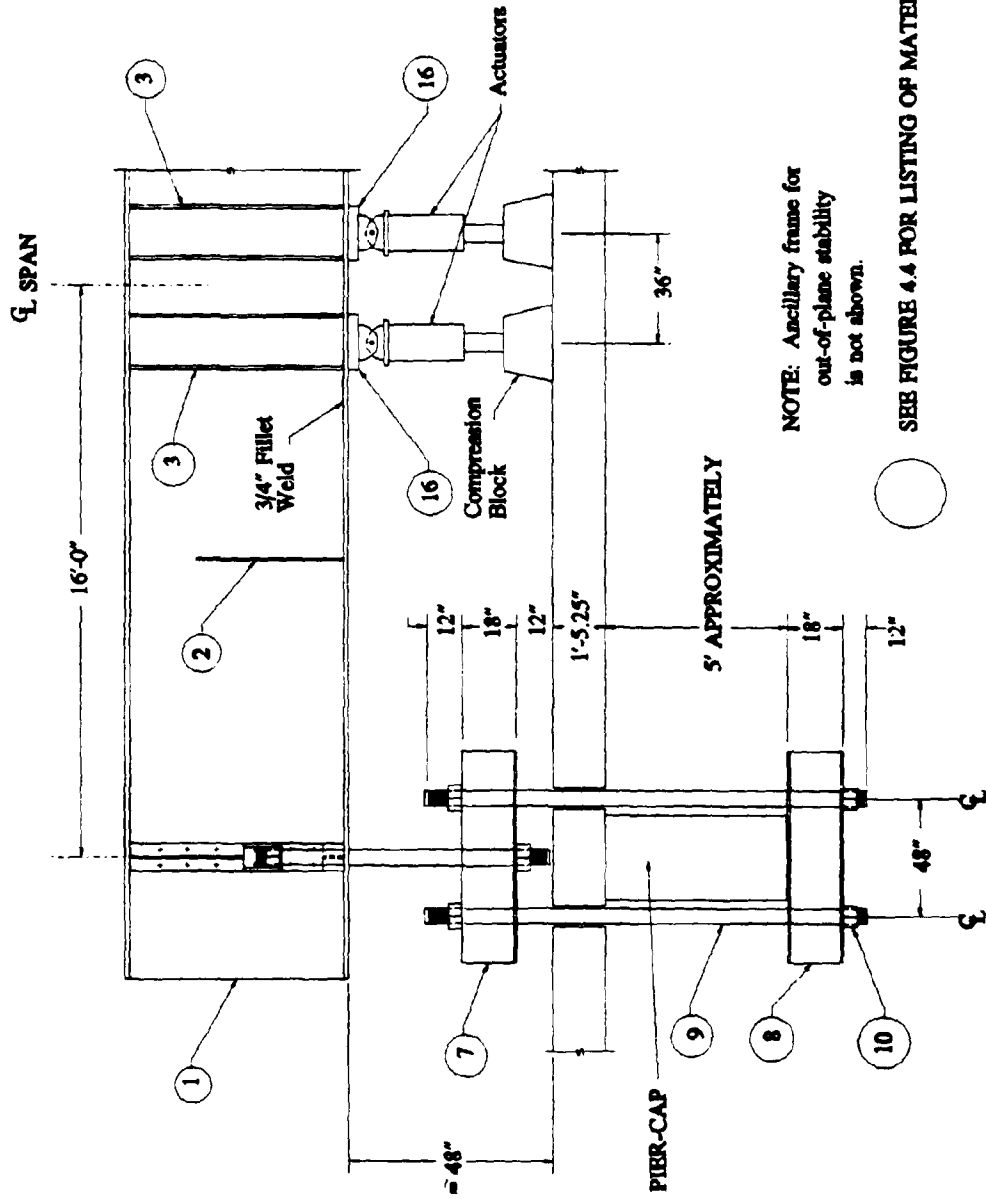


**FIGURE 4.2: ORIGINAL CONCEPT FOR LOADING FRAME**

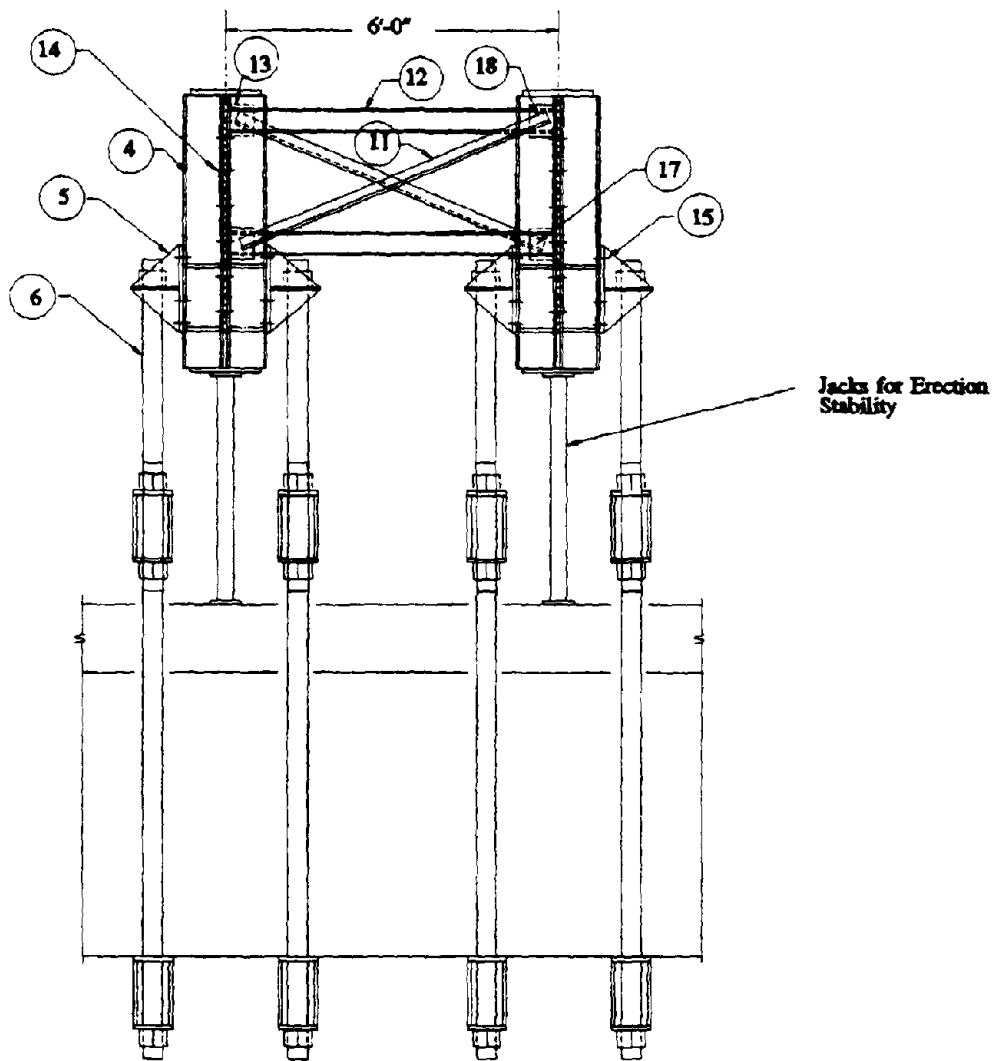


**FIGURE 43: ORIGINAL LOADING CONCEPT**

ITEM	QUANTITY	DESCRIPTION
1	2	Plate Girder 38' long -Web 70" x 3/4" -Flange 18" x 1-1/2"
2	8	Intermediate Stiffener -3/4" x 8-1/2" x 4'-0"
3	16	Center Stiffener -3/4" x 8-1/2" x 5'-10"
4	8	Filler Beams -W10x68 x 5'-10" long
5	8	Gusset Bracket
6	8	Prestressing Rod -5" diameter threaded rod
7	8	Upper Compression Box
8	8	Lower Compression Box
9	16	Clamping Rods -5" Diameter Threaded Rod
10	16	5" Threaded Hex Nut
11	8	Cross Bracing -Angle 6" x 6" x 5/8"
12	4	Lateral Support Beams -W6x25 x 70-3/4" long
13	16	3/4" Connection Plates
14	48	Double Shear Bolts/Washers/Nuts -Astm A490 1-1/2" x 4" long
15	64	Frame Bolts/Washers/Nuts -ASTM A-490 1-1/2" x 4" long
16	4	Load Plate (Upper) -18" x 18" x 3"
17	28	Lateral Support and Cross Bracing Bolts/Washers/Nuts -ASTM A325 3/4" x 3" long
18	8	Support Beam Connection Plate -Angle 4" x 4" x 3/4" x 5" long

**FIGURE 4.4 MATERIALS LIST FOR ORIGINAL LOADING CONCEPT**

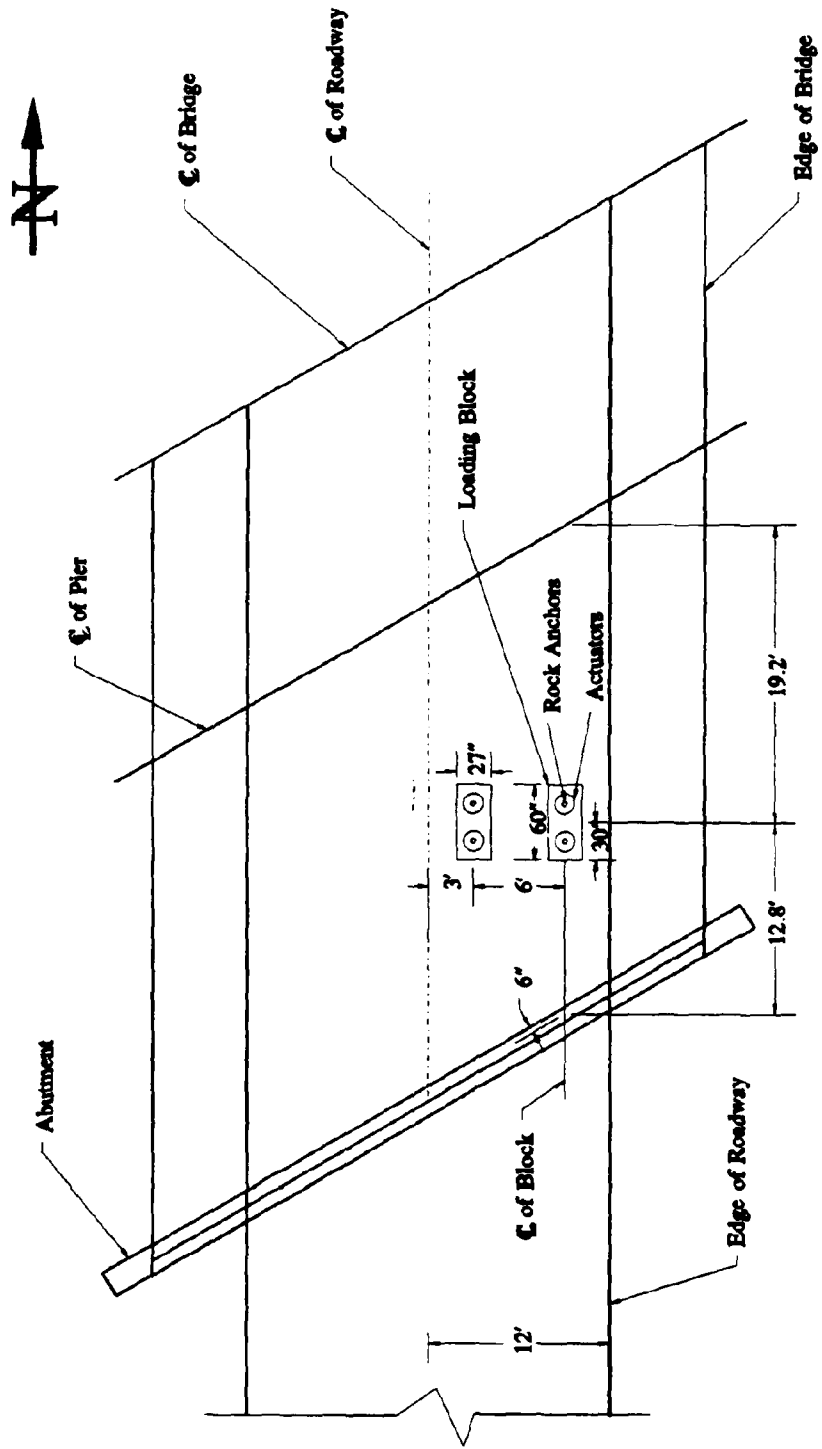


**FIGURE 4.5: LOCATION OF LOADING BLOCKS**



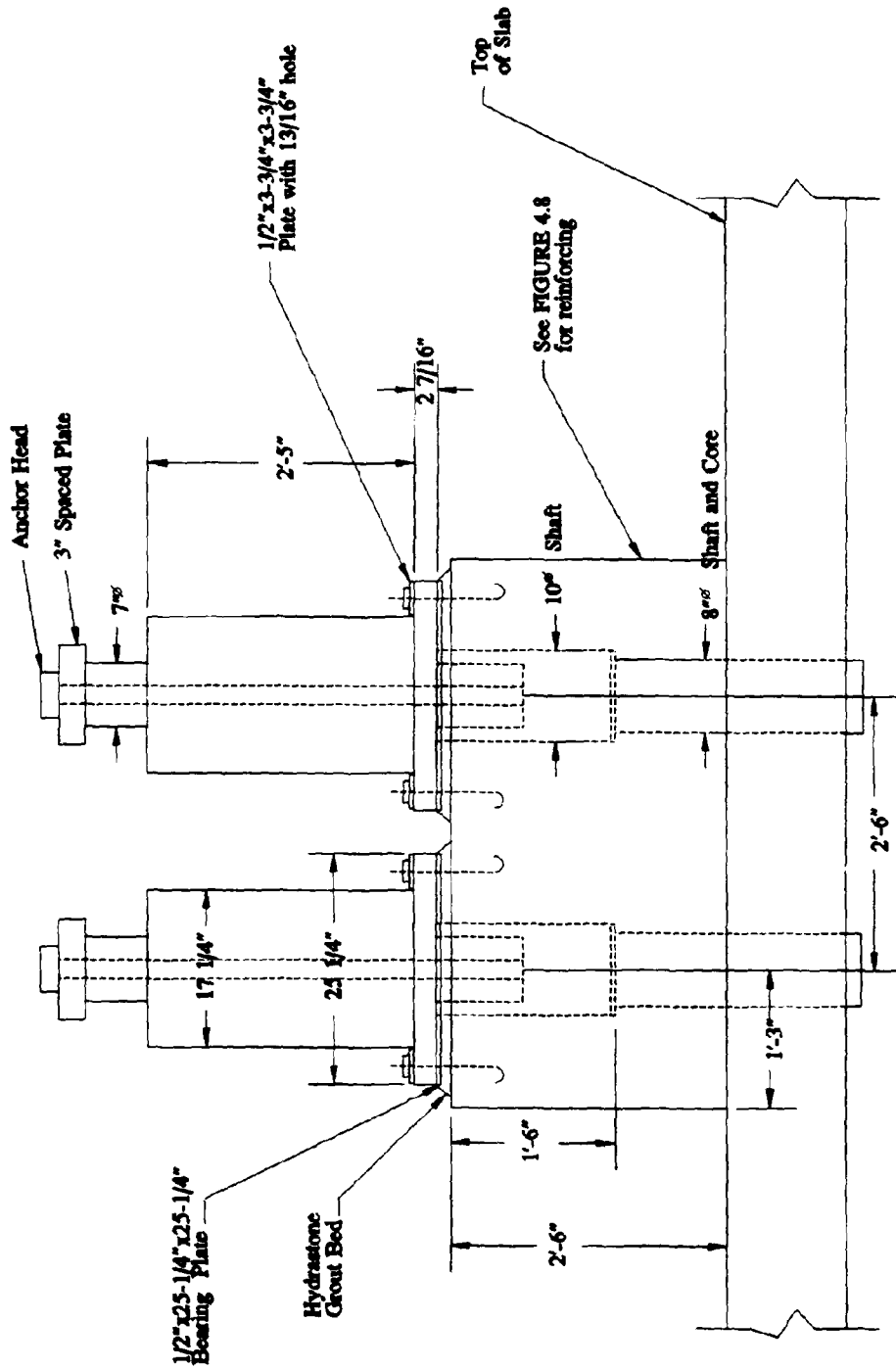


**FIGURE 4.7: DETAILS OF LOAD TRANSFER BLOCKS**

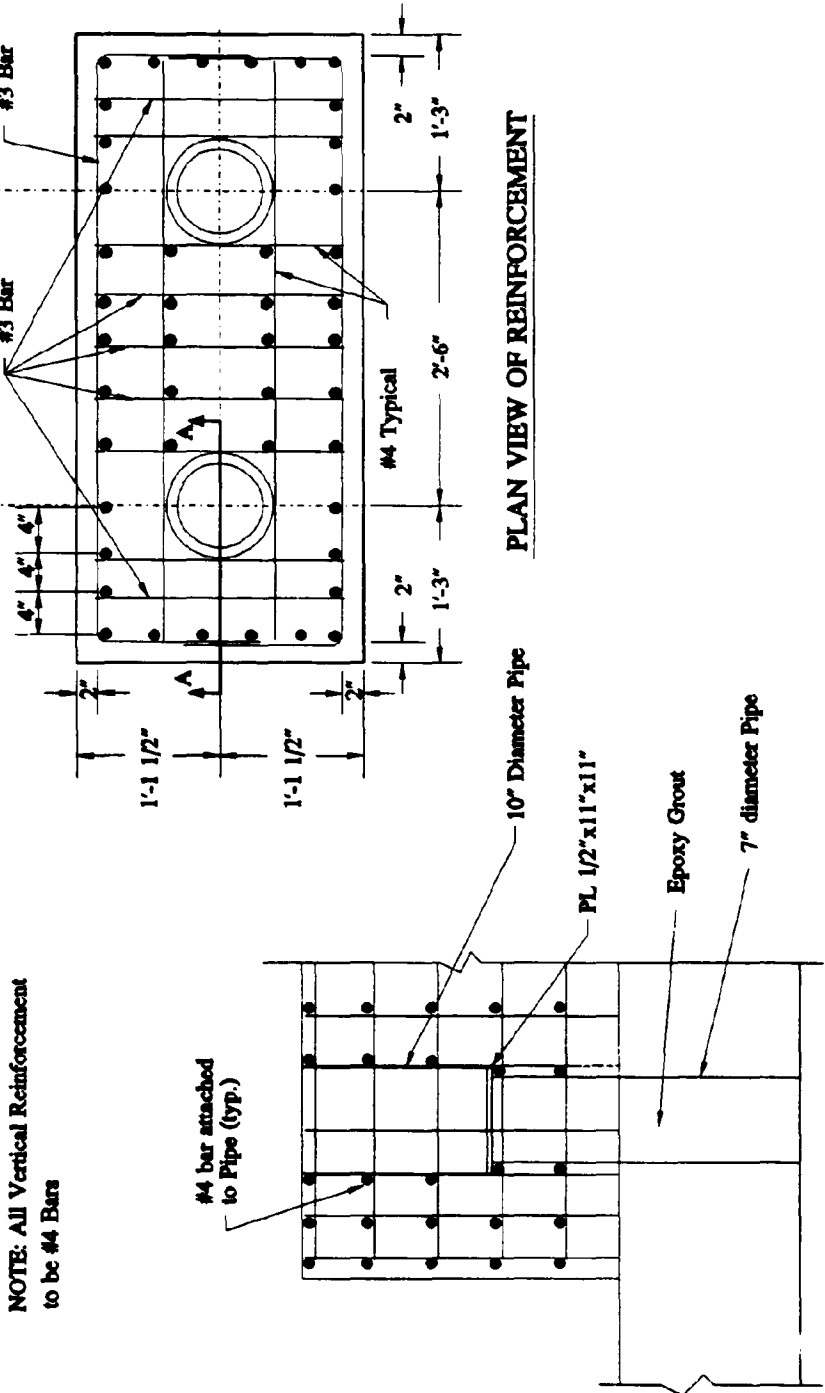
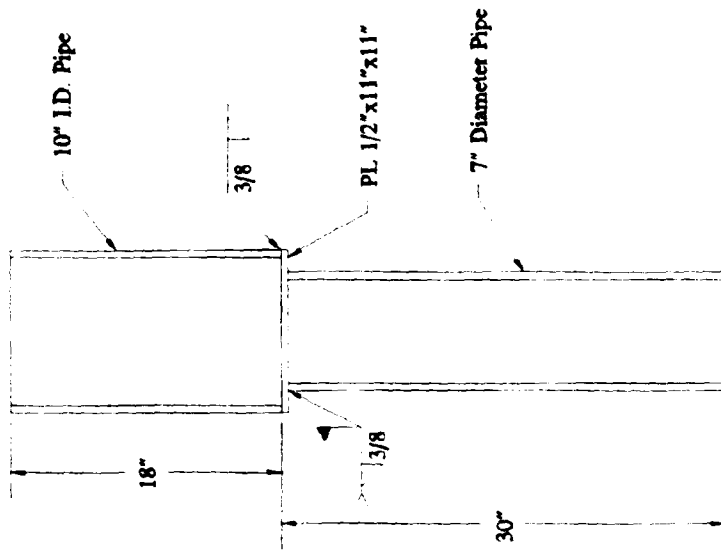


**FIGURE 4.8: REINFORCEMENT DETAILS FOR LOADING BLOCKS**



**PIPE DETAIL FOR LOADING BLOCKS**



**LOADING BLOCKS CAST ON BRIDGE**

**FIGURE 4.9: DETAILS AND PHOTO OF LOADING BLOCKS**

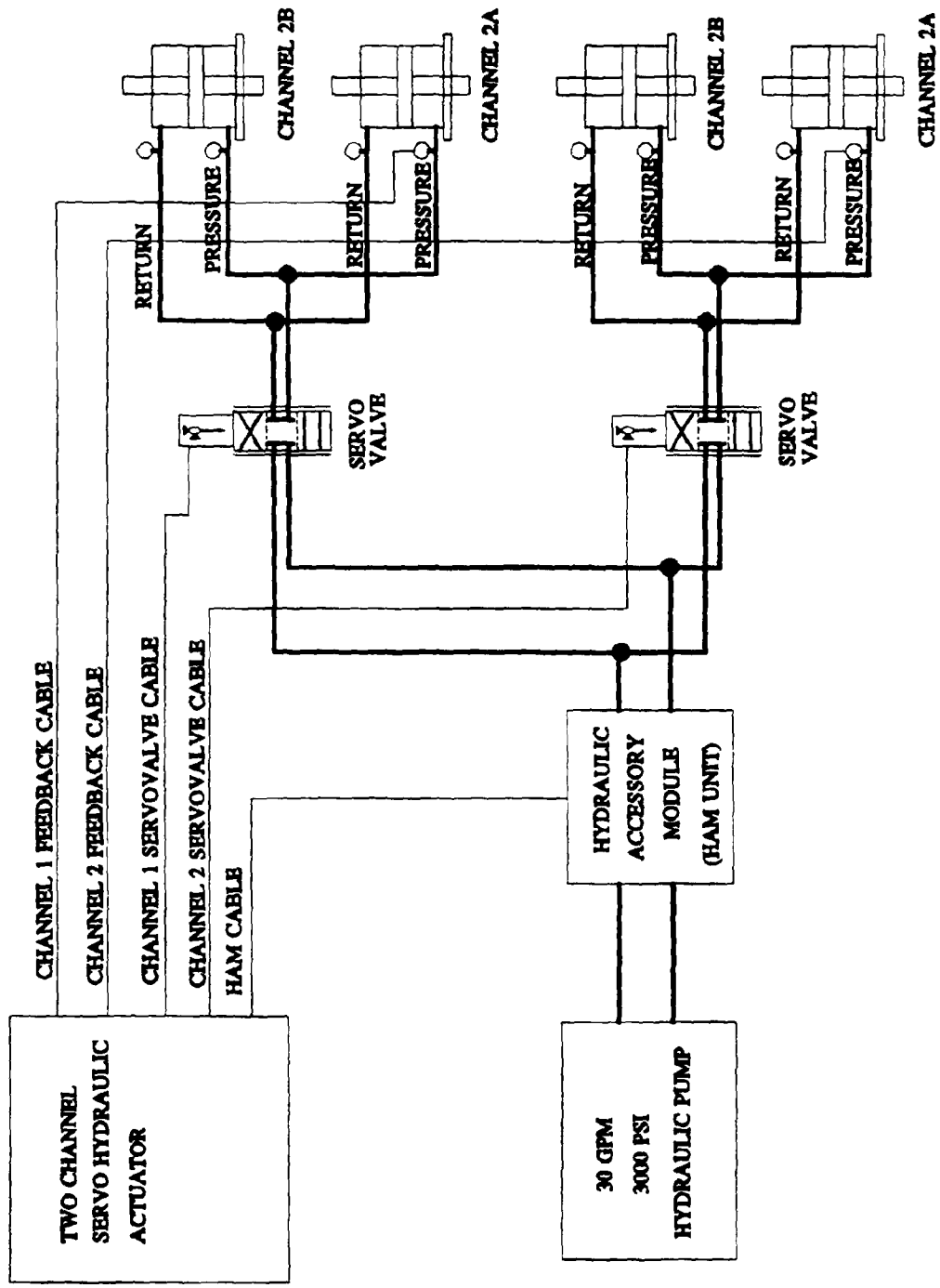


**FIGURE 4.10: SCHEMATIC OF HYDRAULIC SYSTEM**

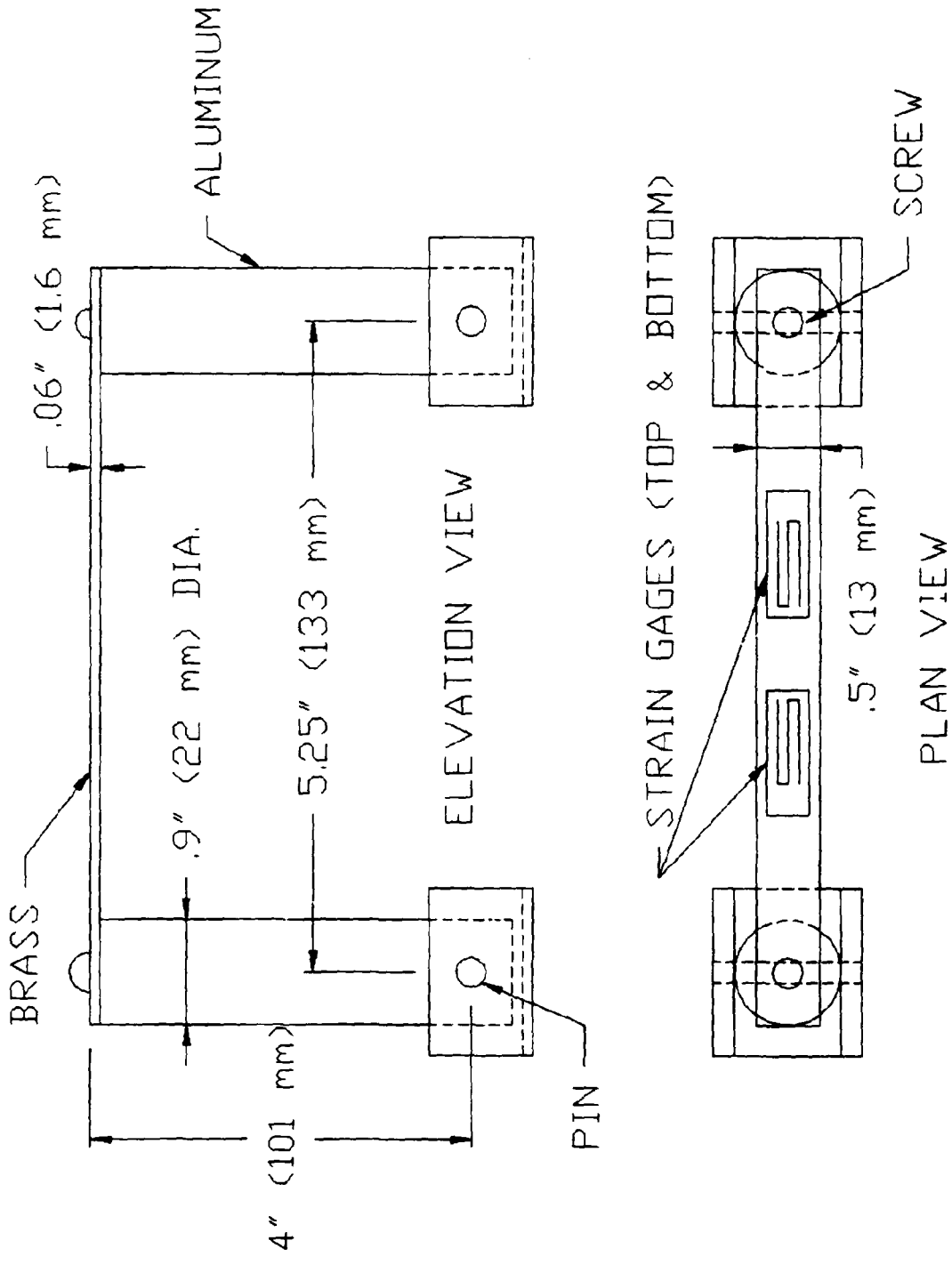
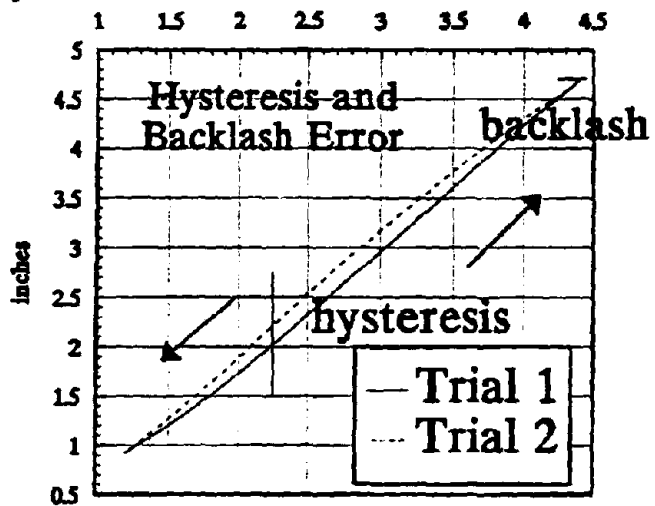
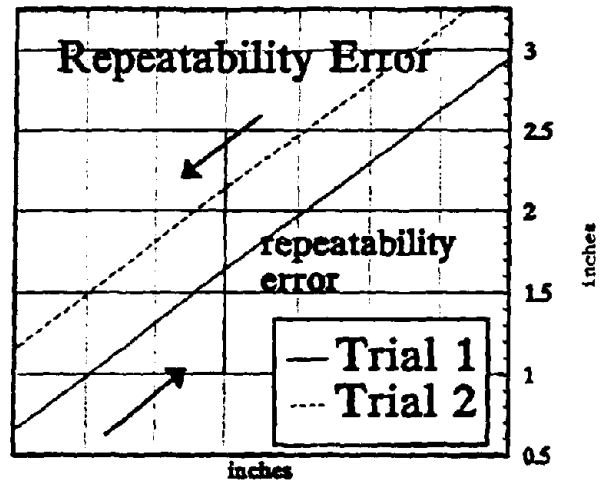
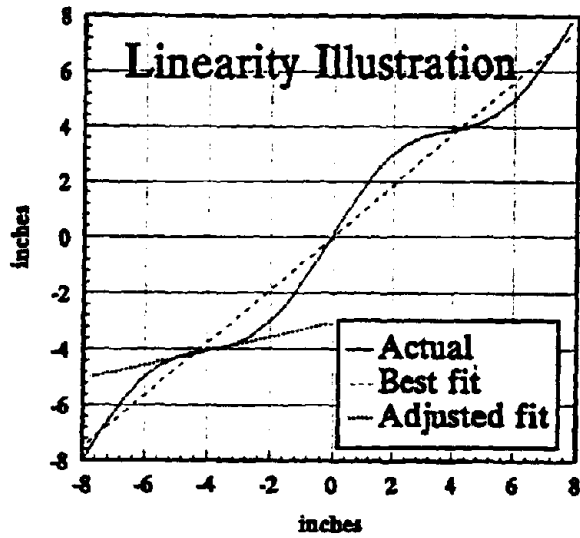


**FIGURE 4.11: CLIP GAGE**



- Linearity Illustration
- Repeatability Error
- Hysteresis and Backlash Error

**FIGURE 4.12: ILLUSTRATION OF ERRORS IN INSTRUMENTS**

### Calibration curve for typical LVDT 1" range

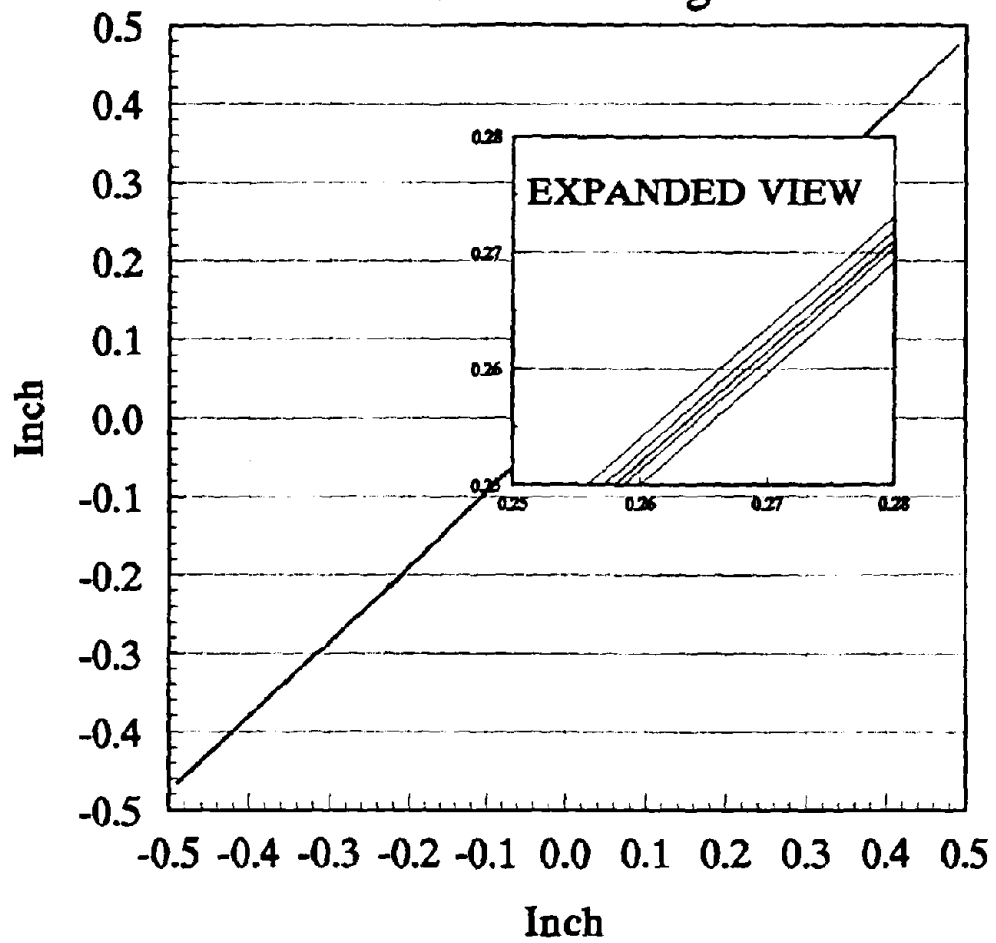


**FIGURE 4.13: DCDT CALIBRATION CURVE**

# Calibration curve for 10" Slide Pot

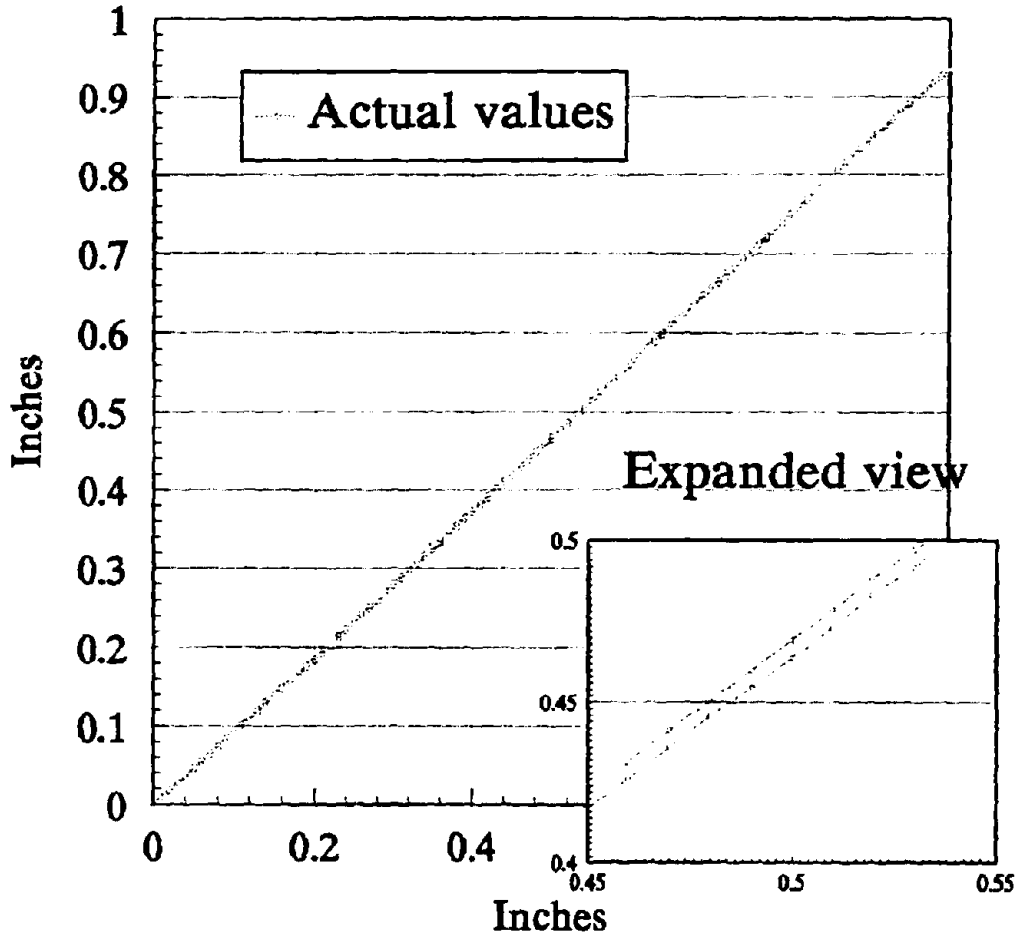
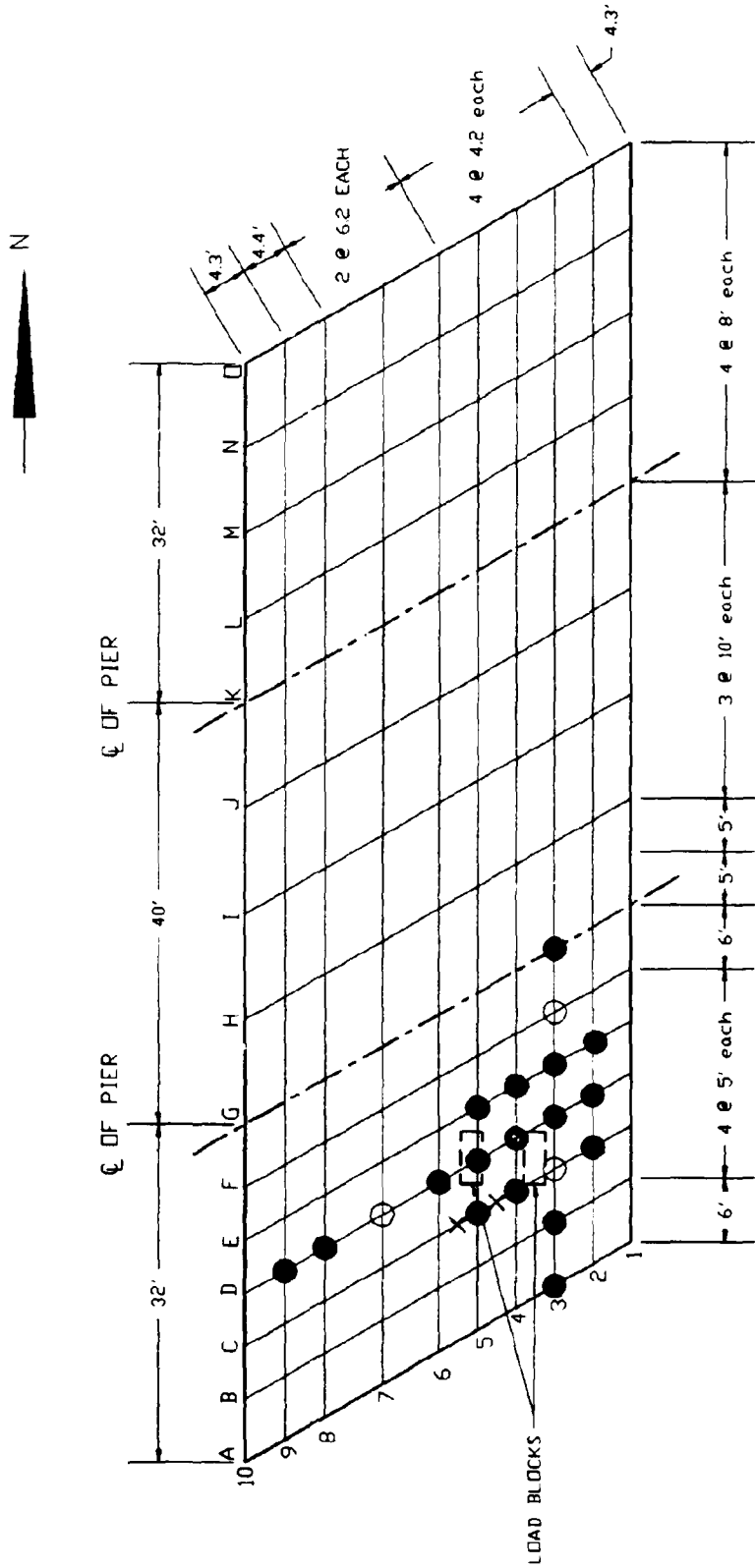


**FIGURE 4.14: SLIDE WIRE POTENTIOMETER CALIBRATION CURVE**



- Vertical Wire Pot AT C3, D4, D7, F3
- Vertical DCDT Instrument location
- X Dial Gage Near C4 & C5
- NOTE: D4 Instrumented With Both DCDT & Wire Pot

**FIGURE 4.15: TRUCK LOAD TEST INSTRUMENTATION PLAN**

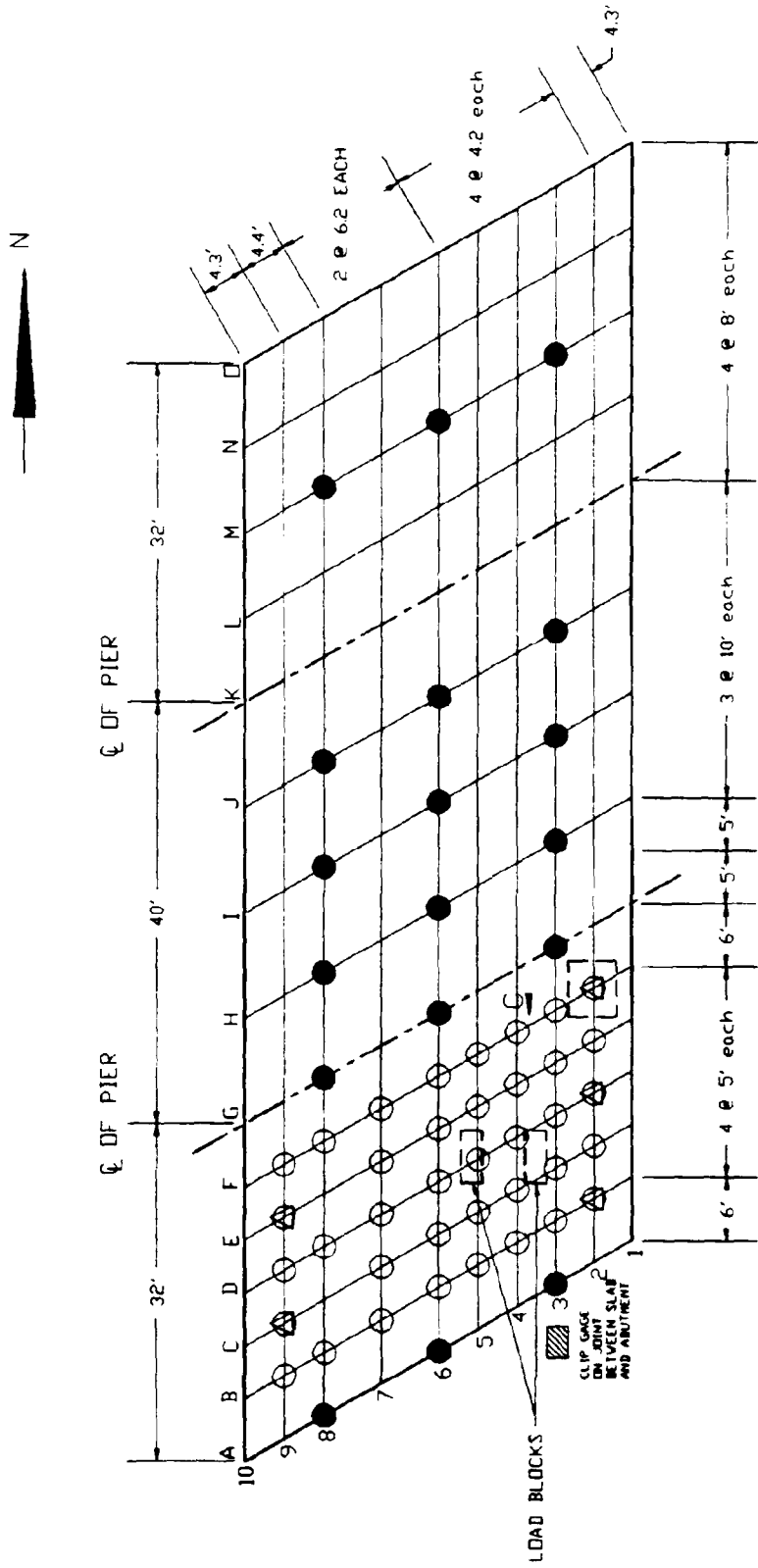
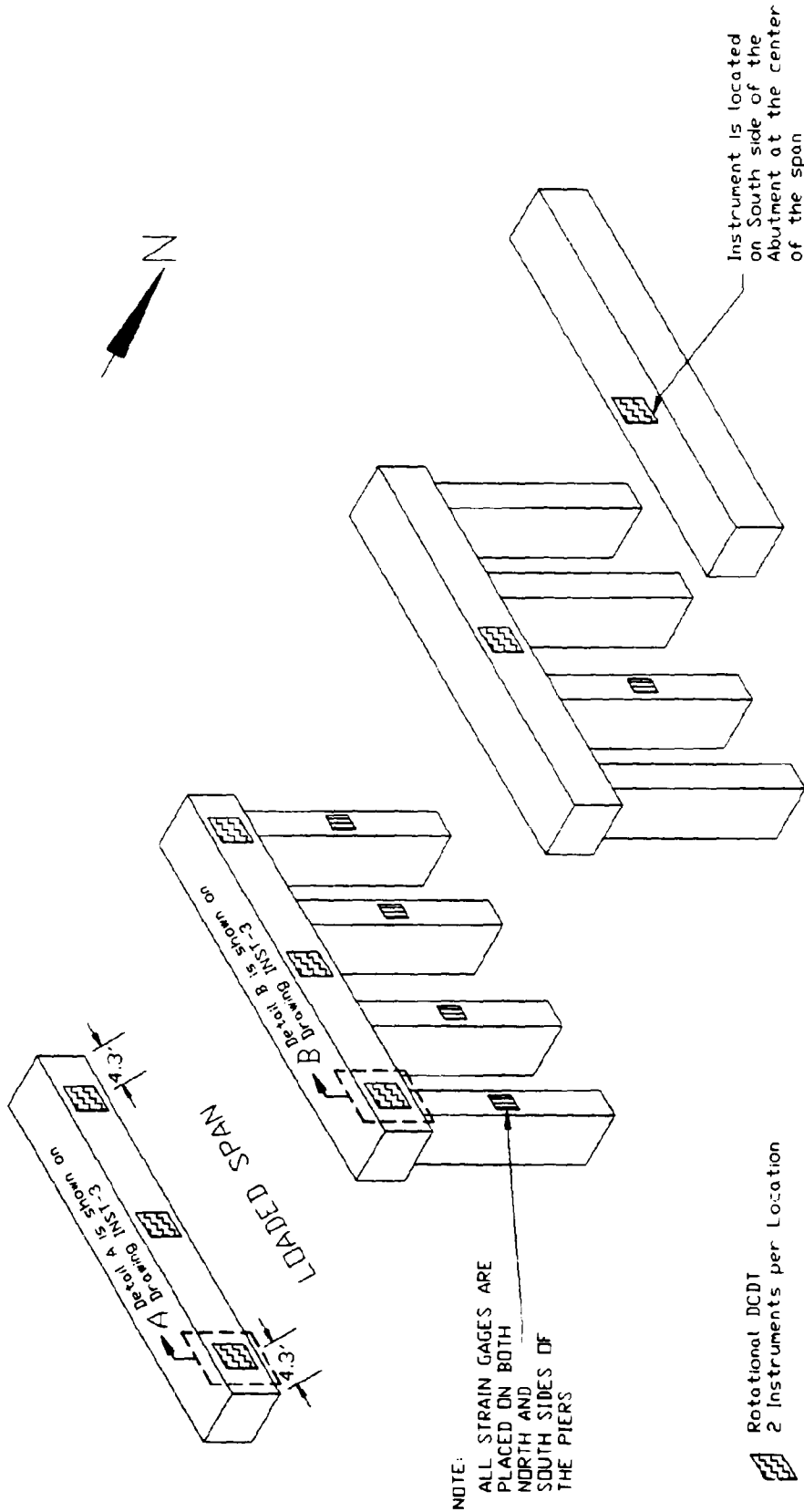
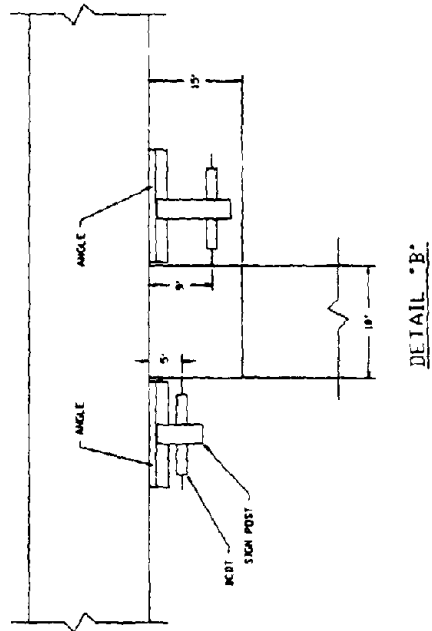


**FIGURE 4.16: DESTRUCTIVE TEST INSTRUMENTATION PLAN**

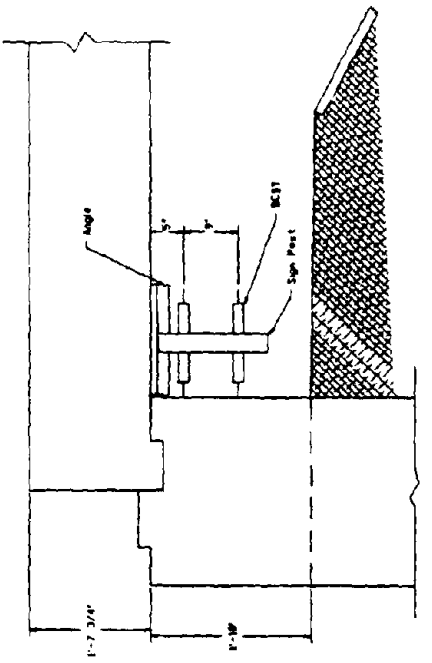


Total # of DCDT Instruments Shown=16  
 Total # of Strain Gage Instruments Shown=20

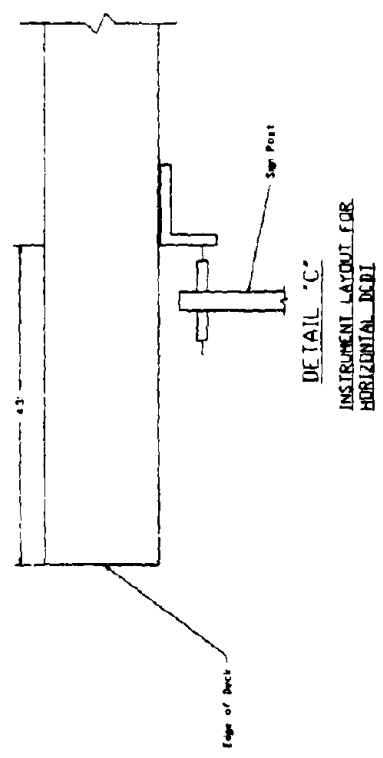
**FIGURE 4.17: DESTRUCTIVE TEST PIER INSTRUMENTATION**



DETAIL 'B'  
INSTRUMENT LAYOUT FOR PIER



DETAIL 'A'  
INSTRUMENT LAYOUT FOR ABUTMENT



DETAIL 'C'  
INSTRUMENT LAYOUT FOR  
HORIZONTAL INSTRUMENT

FIGURE 4.10. RECOMMENDED TEST INSTRUMENTATION DETAILS

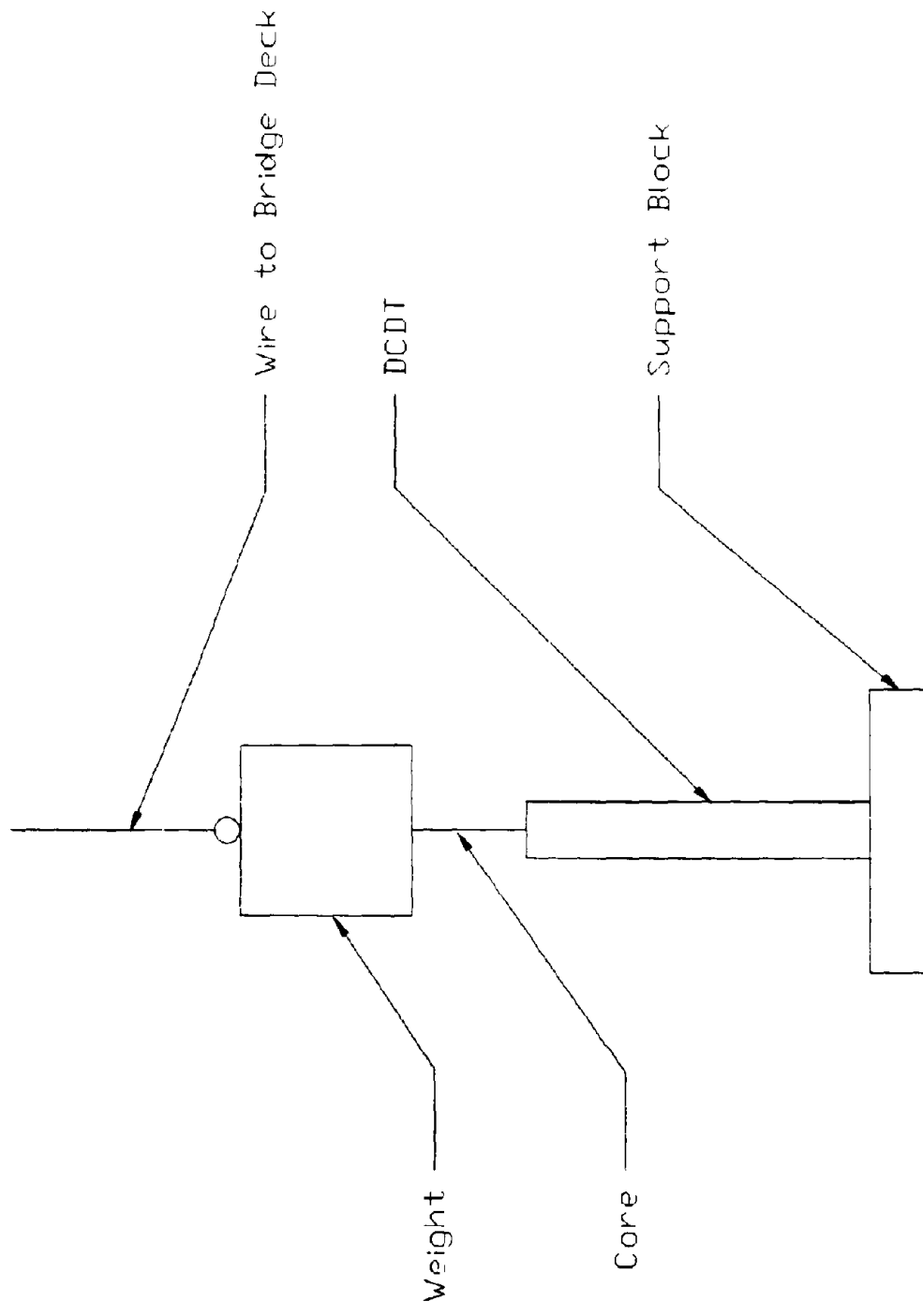
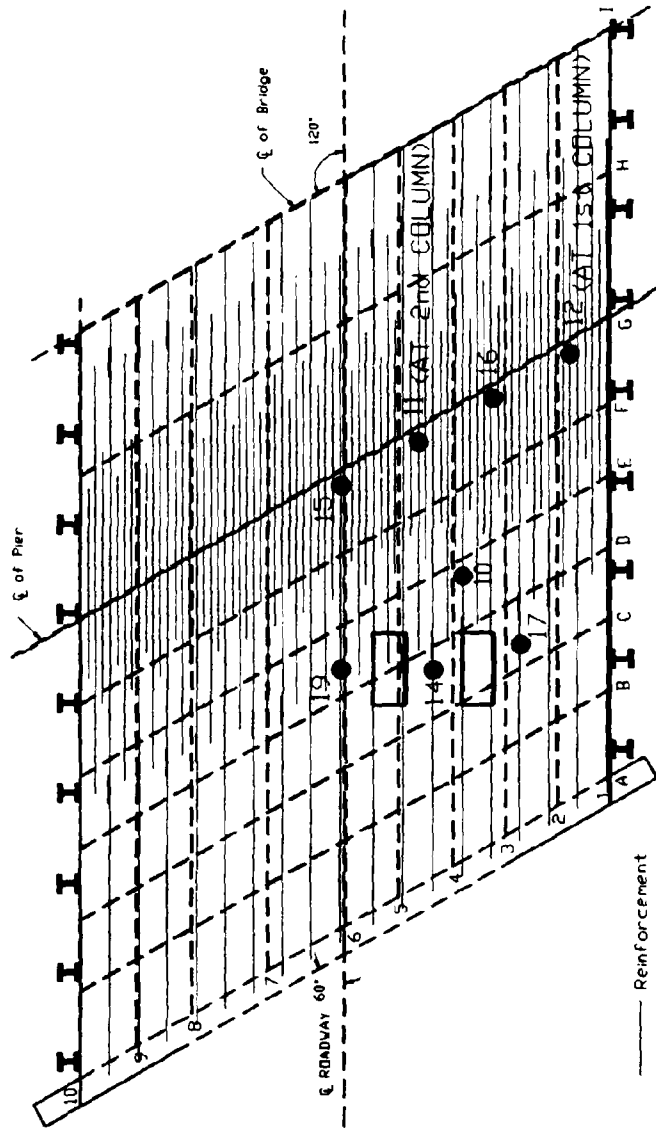


**FIGURE 4.19: DCDT AND WEIGHT APPARATUS**



- Reinforcement
- - - Instrument Grid
- ▭ Loading Block
- 

NOTE: GAGES 11, 12,  
15 AND 16 ABOVE  
FACE OF PIER CAP

REVISION 400. OVER THE ORIGINAL DRAWING

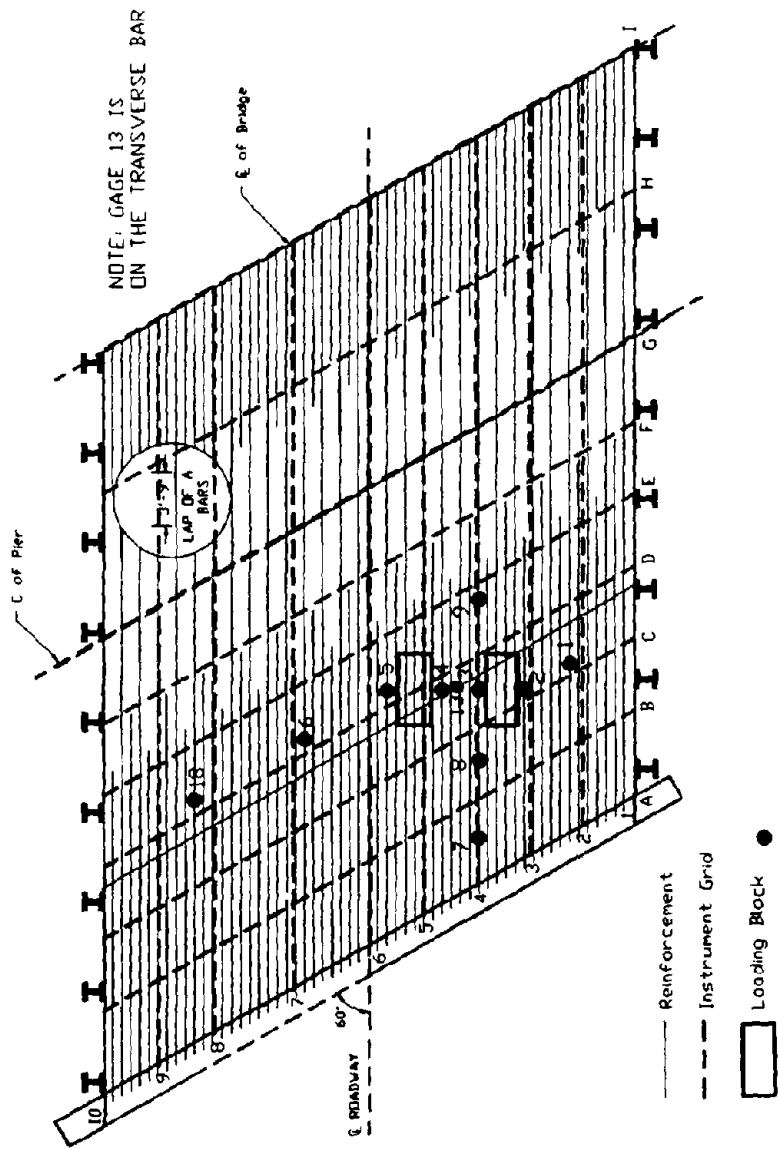


**FIGURE 4.21: STRAIN GAGE POSITIONS ON BOTTOM BARS**

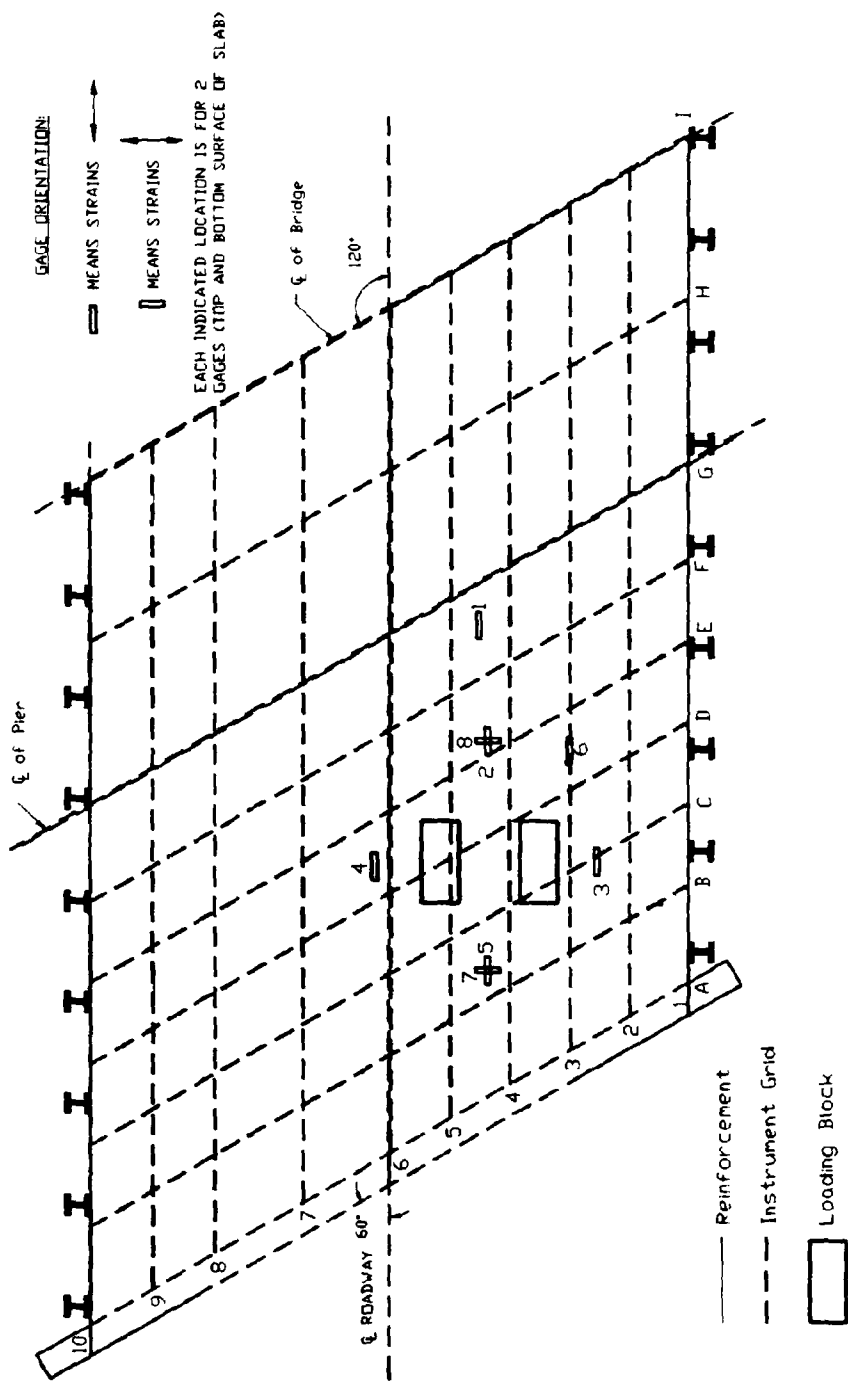


FIGURE 4.22: CONCRETE DISTORTION GAGE POSITIONS

## **CHAPTER 5: RESULTS OF DESTRUCTIVE TESTING**

This section will examine the behavior of the bridge during the destructive testing. Behavior of the skewed slab bridge, the results of the destructive testing, and the mechanics of the failure are discussed. The effects of skew played an important role in the overall bridge behavior.

### **5.1 BACKGROUND INTO BEHAVIOR OF SKEWED SLAB BRIDGES**

Skewed multi-span slab bridges have some unique behavior characteristics, most of which are not recognized in the current design and evaluation procedures. Studies have shown that the load paths of these bridges change significantly through limit states. Both experimental and Nonlinear Finite Element Analysis (NLFEA) results show that the load paths evolve as the loads are increased. Much of the observed changes in the load paths are the result of the differences between the natural behavior of the skewed bridge and the alignment of the reinforcing steel.

The first level of behavior is the linear state of the bridge which is effectively from the unloaded condition to first cracking. Throughout this stage, the concrete and steel behave homogeneously, the resulting composite material can be assumed to be linear, homogeneous and isotropic. During this phase, the skewed bridge resists loading in a manner that is consistent with the skew of the bridge, assuming the stiffness is uniform across the length of the supports. For example, the moment contours of Figure 5.1 clearly show the tendency for the contours due to dead load to follow the skew of the bridge. The bridge then tends to carry load through strips that extend perpendicularly to the abutment and piers as shown in Figure 5.2. The skewed span length of the bridge is over 4 feet shorter than the longitudinal span length, and since a structure naturally desires the path of least resistance, the skewed load path is natural.

The next level of behavior is from the point of first cracking of the slab to the point of first yield of the reinforcing steel. The load paths of the bridge evolve towards a longitudinal sense. As the bridge cracks, the structural steel more strongly affects the bridge, resulting in an increasing tendency for the load to be carried along mesh directions. Ultimately, as the load increases, the behavior of the skewed bridge begins to resemble the simplified models used in rating and design, with the load being carried by longitudinal strips. However, this behavior occurs after extensive yielding. These stages of behavior explain most of the results seen in the destructive testing, others are the result of damage or changes in the boundary conditions.

### **5.2 RESULTS OF DESTRUCTIVE TESTING**

The destructive testing was performed on two days following service-load level tests. The first day the bridge was loaded up to the equivalent of 20 rating trucks, and on the second day the bridge was loaded to the equivalent of 22 rating trucks at which point failure occurred. The actual performance of the test has some effect on the observed load displacement responses; therefore, it will be useful to review some of the loading history at this point.

The loading during the destructive testing was applied under load-control in 1/2 equivalent truck increments, or 16 kips total load per load step. Under normal conditions, the displacements were read as soon as the load stabilized (about one to two minutes) at the desired level. After

which the load would be increased to the next step. At several points, the loading was halted to mark cracks and check the instrument responses. The points at which the load was halted and the time duration are given in Table 5.1. Before loading would start again, a second reading was made, so that creep deflections at the beginning and end of the hold are recorded.

**Table 5.1 - Holds in Loading**

Hold Number	Load Equiv. Trucks	Time (min)	Notes
1	Day 1 @ 4	14	
2	Day 1 @ 6	12	
3	Day 1 @ 8	24	
4	Day 1 @ 12	36	First hold where significant creep is observed.
5	Day 1 @ 16	34	
6	Day 1 @ 20	25	Bridge was unloaded after hold.
7	Day 2 @ 20	17	First hold of second days testing.
8	Day 2 @ 22	Approx 5 min	Failure occurred and pump was shut down.

### 5.2.1 Test Monitoring and Data Reduction

During the test, the instrumentation was carefully monitored so that any sudden changes in the bridge behavior which might indicate failure would be captured. Also, the instruments were monitored for malfunction. If an instrument would have malfunctioned during the test, the bridge would have been unloaded and the instrument replaced.

During the conduct of the test, some of the instrumentation was monitored in real time. One computer on site displayed the load in each cylinder and, simultaneously, the load deflection graph for point D4 (under the loading blocks). Another on-site computer displayed the numerical output of 32 selected instruments which were slide pots and DCDTs around the loading blocks.

At the end of each day, the data from the global and critical local response instruments was processed and analyzed. This was done to look for anomalies in the instrumentation and to compare with analytical data. The data was carefully scanned to find any indication of unusual bridge behavior or the possible onset of failure mechanisms. During the test, no problems were experienced with the instruments and none of the instrument readings gave any indication that a failure was imminent. The instrument response was also carefully checked to see if any changes in the loading/unloading sequence were dictated or if any instruments were nearing the end of their range. All instrument responses seemed normal and within the range and accuracy of the instruments.

Reduction of the data was as follows. The data acquisition systems records the data in

engineering units (inch, pound, strain, etc.) and the data can be output as an ASCII file. This file can then be imported into any standard spreadsheet (Quattro Pro by Borland, Intl. was used) for further processing and plotting. Processing of data largely consisted of:

- 1) At each place where the load was held, 5 readings were taken. These readings were averaged into a single reading.
- 2) Rotations and distortions were measured by DCDTs. The data system recorded only the DCDT movement. For distortions, the DCDT movement was divided by the 6" gage length to obtain distortion (strain). Rotations are found by taking the difference between the DCDT readings and dividing by the distance between them.

### 5.2.2 Low-Level Testing

Figure 5.3 shows the load-deflection plots for point D4, directly under the load during low-level tests at the service limit state. The graphs show a slight bilinear behavior for low loads. However, the magnitude of the "kink" is below the accuracy of the instruments, so the existence of this bilinearity is questionable. All three tests follow the same line on loading. (Note: on unloading, the instruments returned to 0" (within the accuracy of the instrument), so all three curves have been started from 0" deflection)

The graph of the second and third load tests show a hysteresis. The magnitude of the hysteresis is about 0.013", which is twice the error level for the slide pot at point D4. Therefore, this hysteresis is not caused solely by the instrument but is at least partially due to energy dissipation in the structure. Both the second and third load tests follow the same unloading path and return almost to 0" (within instrument accuracy), so for all practical purposes the bridge showed no permanent deformation. It is not likely the energy dissipation in the hysteresis curve was caused by new cracking as the bridge was extensively cracked already and no new cracking was noted. It is more likely that the energy was dissipated by friction between the abutment and the slab and by the friction associated with the opening and closing of existing cracks. The low-level testing showed no new cracking and no signs of any additional distress in the bridge.

### 5.2.3 Destructive Testing

Destructive testing began the day after the low-level testing was completed (5/21/91). The bridge was loaded in 4 kips/cylinder (16 kips total load) increments to a level of 160 kips/cylinder (640 kips total load) and then unloaded in 32 kips/cylinder (128 kips total load) increments. Each time the loading was stopped, data was recorded by the data system and the bridge was checked for new cracks. All new cracking was recorded. This test finished late in the day, so testing for the day was discontinued.

On the final day of testing (5/22/92) the bridge was again loaded in 8 kips/cylinder steps up to the previous day's load and then by 4 kips/cylinder increments. However, at load of 175 kip/cylinder (720 kips total load) the bridge failed unexpectedly in shear. The shear failure is believed to have started with a diagonal crack through the slab near the pier line. This crack propagated back along the pier line to the center of the bridge and then turned toward the

abutment. This failure mechanism will be discussed in detail in later sections. The dowel action of the reinforcing bars prevented total collapse. When the bridge cracked, the prestressing cables attached to the cylinders slacked momentarily, but this slack was detected by the control system which shut down the pump, avoiding total collapse.

### 5.3 LIMIT-STATES OF BRIDGE RESPONSE

The load-displacement responses have been extensively studied to determine the limit states of the response. The definition of limit states used in the examination of the results is any change in the characteristics of a response curve that can be directly attributed to a change in the overall behavior of the bridge. Most of these limit states are not what would typically be expected, such as first cracking and yield. Instead they generally refer to changes in boundary or load path. As was mentioned, the behavior of the skewed bridge is not typical, therefore limit states outside of the typical can be determined. Also, the bridge was extensively damaged and as a result typical limit states such as first cracking have been effectively eliminated. The damage has also added some unusual limit states.

The limit states that have been determined exist at equivalent truck loads of 7, 9, 12, 17, and 22 as shown on the global response in Figure 5.4. These are loads at which the bridge is noted to have had a significant change in its characteristics. Most of the limit states show up in a very localized region of the bridge. This does not mean however that these limit states do not eventually affect the whole bridge.

**7 Truck Limit State:** Between 6 and 7 trucks, some of the instruments began to indicate nonlinearity in the measured response. Up to this point the behavior of all instruments has been fairly linear, indicating the linear service range of the bridge extended up to about 7 equivalent trucks. After this point the load deflection responses lose stiffness. This is not necessarily due to cracking, although it most likely indicates the point where existing cracks began to widen.

The most significant effect of the 7 truck limit state occurred at the abutment. The abutment encompasses a key, discussed in section 2.1, which may provide some frictional resistance. Also, there were two different details used in the abutment, one for the shoulder regions, and one for the driving lanes. Three gages were used to measure the rotations along the abutment: RT1 was located in the east shoulder region (line 2), RT2 was located directly in the center of the driving lane (line 6), and RT3 was located in the west shoulder region (line 9). At 7 trucks there is a sudden softening of the rotational response at RT2 (Figure 5.5). As shown in Figure 5.5, the other two rotation gages do not indicate any softening at this point. The response of RT1 is a typical curve, and what softening was seen can be attributed to natural bridge behavior. RT3 did not rotate enough to achieve accurate measurements.

It is theorized that up to 7 trucks, the rotational stiffness in the center portion of the bridge remained locked. As the load is increased above 7 trucks this stiffness is slowly released. It should be noted that the abutment always maintained a good amount of rotational fixity as evidenced by the larger rotations at the pier rather than at the abutment, quite contrary to what

is typically expected of a pinned connection at the abutment.

Evidence supporting rotational slip exists in the deflection profiles of several instruments near the location of the slip. First note the marked increase in deflection rate of instrument A6 (Figure 5.6) located just 6 inches from RT2. This increase can be accounted for by the increase in rotation, it is expected that an instrument that close to the point of origin would be affected strongly. Other instruments that showed a slight increase in flexibility at this point are instruments B5, B6, and B7 (Figure 5.6) which develop a fan pattern out from the probable point of origin of this occurrence.

The effects of this limit state are quite unique. The center region of the bridge was very rigid with respect to rotation at the abutment while significant rotation was allowed to occur in the shoulder regions of the abutment. This resulted in the load path being forced in the longitudinal direction during the early stages of loading. As this stiffness in the center is released, the load path would begin to move into a more natural position for a skewed bridge.

**9 Truck Limit State:** As the loads were increased above the 7 truck limit state, the bridge began to assume the more natural load path along the skew. At 9 trucks this path drifted over to the far side of the pier line which caused a sudden rotational stiffness release in the pier. This basically stems from a domino effect caused by the release in rotational stiffness at the center of the abutment.

Specifically, rotation gage RT6 (Figure 5.7), at the intersection of the pier and line 8, is where the sudden increase in rotation is noted. The other two rotation gages on the pier line do not register any appreciable change in the relative rotational stiffness at this point. However, the strain gages SG11, and SG15 begin to show increased strains at this point (Figure 5.8). SG15 is on the top reinforcement over the pier at the center line of the bridge and SG11 is also on the top reinforcement over the pier only it is located about 3 feet to the east of SG15. What is seen here is the result of a shifting load path that was brought on not by internal characteristics of the slab but by the changing boundary conditions at the abutment.

**12 Truck Limit State:** From 7 to 12 trucks the bridge was still affected by the rotational condition of the abutment. It appears that after the hold at 12 trucks the additional rotational stiffness noted at the center of the abutment was fully released. As a result, from 12 to 17 trucks the bridge finally begins to behave as would be expected for this range. That is the slab is cracking, and the load path is slowly moving towards a longitudinal path. Increased cracking is observed, as well as a decreased responses from the additional loads in the shoulder regions. This decreased influence in the shoulders is a direct result of the load paths indicated in Figure 5.2.

The first significant indications in the changed response exist in the load-deflection profiles of the instruments on the west shoulder that would be outside the load path, in the closed shoulder (Figure 5.9). All of these instruments indicate a general stiffening in their response, particularly from 12 to about 14 trucks. Instrument A8 actually begins to show uplift until about

17 trucks is reached (Figure 5.9). Instrument E9 which borders the closed corner does not show any particularly unusual response in this range, no deflections were read at C8. Outside the region no unusual effects are noted.

The shoulder on the loaded side of the bridge is effectively pulled down by the interior deflections of the bridge. Transverse profiles of lines C and F (Figure 5.10) show the results of the limit state. The point of maximum deflection changes in these profiles as the load is increased above 12 trucks, as well as an increased "kink" in the shoulder region. The change in the point of maximum deflection results from the changing load path. The increased "kink" in the shoulder results from the load being directed away from the shoulder.

As would be expected in this region of behavior, cracking is noted. Between 8 and 12 equivalent trucks, the first additional cracking was noted, and increased cracking was marked from 12 to 16 trucks (Figure 5.11). These figures reveal a developing crack pattern from coordinate A7 on the abutment to E1 on the east edge, clearly indicating the nature of the developing load path.

**17 Truck Limit States:** A change in the behavior of the bridge is noted at this load stage, however it is very difficult to grasp what is occurring. This limit state occurs very close to the failure which occurred at 22 trucks. It is felt that this corresponds to the first yield in some of the reinforcing bars that were not instrumented.

The limit state has been placed at 17 trucks largely because this is the point at which the uplift at point A8 suddenly changes and the point begins to deflect (Figure 5.9). It appears that a new limit state was developing from 17 to 21 trucks. It is speculated that as load is increased above 17 trucks some of the reinforcing began to yield, although none of the instrumented bars indicated any yielding until 20 equivalent truck loads. The bridge would have had to have survived loading past 22 trucks in order to verify the exact nature of this developing limit state. However, the available information appears to be fairly conclusive.

On the first day of testing new cracking that developed from 16 to 20 trucks was marked (Figure 5.12). The cracking marked on the first day at 20 trucks was localized to the region of the loading blocks, while during the second days test hold at 20 trucks additional cracks were mapped in the east shoulder region. If the cracks which formed between loads of 8 to 20 trucks (Figures 5.11 and 5.12) are combined, it can be seen that the new cracks form along a line roughly perpendicular to the skew. This confirms the shift of load path to a direction parallel to the skew because if the load path is acting along the skew, it is expected that flexural cracks will form perpendicular to the skew.

**22 Truck Failure State:** At 22 trucks the bridge failed suddenly. The load was held at this point for approximately 5 minutes prior to failure. It was noted that the instruments were showing considerable creep during the hold in addition to loud popping noises. A diagonal tension "shear" failure occurred along the pier from the east edge to approximately grid line 7, and then along line 7 from the pier towards the abutment. A detailed discussion of the failure

mechanisms is given in the next section. This failure was very sudden and occurred with little warning while the load was being maintained. Most likely the bridge would have taken another loading step if displacement control had been implemented. However, the nature of the failure would certainly have been the same, as the loading system would not have been able to react fast enough to control the failure mechanism. Also, the bridge likely would not be able to hold its own dead weight during the development of the failure plane. This is evidenced by the fact that the loading system lost the majority of the applied load during failure, as it simply was not fast enough to keep up with the progressing failure. A safety precaution that was built in the system turned the pressure off at failure.

## **5.4 MECHANICS OF FAILURE**

### **5.4.1 Initiation of Failure**

The first indication of the imminent failure was given by strain gage SG12 (located near point G2). This strain gage was on an exposed bar in the deteriorated shoulder region. At 16 trucks, the gage showed an increase in the rate of strain (Figure 5.13). At 20 trucks, the rate of strain began to increase significantly. During the final loading sequence, the strain gage indicated a large increase in strain when the load reached 20 trucks and the bar yielded (yield strains were experimentally determined to be 1700 microstrain). At 21 trucks, the strain dropped, perhaps indicating a slip in the bar. It is thought that this gage response shows the beginning of failure in the deteriorated shoulder area.

The adjacent strain gage, number SG 16, also shows a jump in strain starting at 16 trucks, then shows a slight hardening response near failure. This gage, which was at the edge of the deteriorated area, did not show yielding of the bar. Gages SG 11 and SG 15 (Figure 5.8) show no increase in strain after the 20 truck load level. This indicates that the load is being shifted away from this area of the bridge.

At the 20 truck load level, strain gages SG 4 and SG 13 (located between the loading blocks) showed the bottom bars to which they were attached had yielded. Strain gages attached to other bottom bars near the loading blocks showed that these bars were approaching yield. It is believed that as the bottom steel began to yield, the bar behavior began to dominate the behavior of the bridge slab. Since the bars were parallel to the traffic lanes, it appears that the load path began to shift back to a direction parallel the traffic lanes.

The second shift of the load path from parallel to the skew back to parallel with the traffic lanes may explain the final failure. When the bridge carried load along the skew (after the 7 truck limit state), the damaged shoulder area was largely excluded from the load path (Figure 5.2). With the second shift of the load path, the shoulder area near the pier would begin to take load for the first time since the 7 truck limit state. This is why there was a sudden increase in strains in strain gages SG 12 and SG 16. Both of these gages would have been out of the skewed load path but in the load path parallel to the traffic lanes. Since the shoulder area was considerably weakened by damage, it appears that this area could not resist the load which was now flowing to this area.

The final failure appears to have begun as a shear failure in the shoulder region. The failure in the deteriorated area then propagated into the sound areas of the slab as a dynamic front. On the bottom of the slab, the crack propagated along the pier line to the centerline of the bridge and then propagated along the centerline to the abutment and the failure lines were virtually straight. On the top surface the failure surface was an arc and was heavily influenced by the bar cutoffs.

#### 5.4.2 Propagation of Failure

The propagation of the failure was affected by the layout of the reinforcement. The failure otherwise is fairly typical as to what would be expected based on the nature of the failure. The only unusual circumstance in the propagation is its dynamic nature.

From the top the failure gives a different appearance than what actually occurred (Figure 5.14). This was the result of the detailing of the reinforcing steel in the top of the slab near the pier. Figure 5.15 shows the placement of the top reinforcing bars, and Figures 2.4 and 2.5 give the details of the bar cut-offs for the top reinforcement over the pier. As shown in the details of the bar cut-offs they are not cut-off uniformly. In fact the cut-offs are skewed with respect to the pier, such that the cut-offs on the west side of the bridge are shorter than on the east side. Also, three different lengths are used in this region creating three zones of bar cut-offs. The most significant of the cut-offs is those of the G and H-bars, or the shorter bars, as these contributed to the development of the visible failure plane.

Another reinforcing detail that was significant was at the bottom of the slab (Figure 2.6). Half of the bottom reinforcement was cut-off prior to reaching the abutment. The other half extended from the abutment to approximately 5 feet into the second span. This resulted in the only reinforcement along the bottom of the slab at the pier being #9 bars spaced at 15 inches. This was insufficient reinforcement to suppress the propagation of the diagonal tension failure at the bottom of the slab.

Due to the light reinforcement in the bottom regions of the slab the dynamic impact of the shear failure had little trouble propagating through the bottom half of the slab. However the #9 bars at 6 inches on center in the top of the slab was sufficient to suppress the propagation of diagonal tension plane through the top layer of the reinforcement. As a result the failure plane effectively sheared through the bottom half of the slab, and then along the bottom of the top reinforcement until the cutoffs where it was able to reach the surface (Figure 5.15). Along the longitudinal line a normal shear plane is clearly visible as the transverse reinforcement was very light.

Figure 5.16 shows the failure plane as it appeared at the edge and bottom of the bridge. It is noted that at the edge the angle of the failure plane is very shallow. In fact, due to the nature of where the top and bottom surface of the failure appeared, the entire plane initially appeared to be very shallow contrary to what would be expected from a shear type failure. However close scrutiny of the failure surface revealed that the actual shear failure plane between the upper and lower rebar meshes was approximately 45 degrees as would be expected.

There are two possible reasons for the shallow angle of shear at the edge of the bridge: 1) It is possible that the edge was not where the failure began. The initial punch through could have occurred in the damaged region, and then the shoulder was effectively ripped through to the edge. Since the concrete was made up of a series of delaminated horizontal planes it produced a very shallow angle when it ripped through; 2) Previous research (Azad, et. al, 1993) has shown that when there are existing flaws in a slab, the punching shear capacity is reduced and the most critical angle for the flaws is 20° to 30°. Flaws at these angles may reduce the punching shear capacity by as much as 50%. Since the deteriorated shoulder was damaged by freeze/thaw cycling and alkali-silica reaction, it is reasonable to assume that, although the flaws were primarily horizontal, some flaws occurred in the slab at random angles, including 20° - 30° from the horizontal. Under the increasing load, the critical flaws in the shoulder began to propagate. Once started, the cracks propagated dynamically into the sound concrete and caused the final failure.

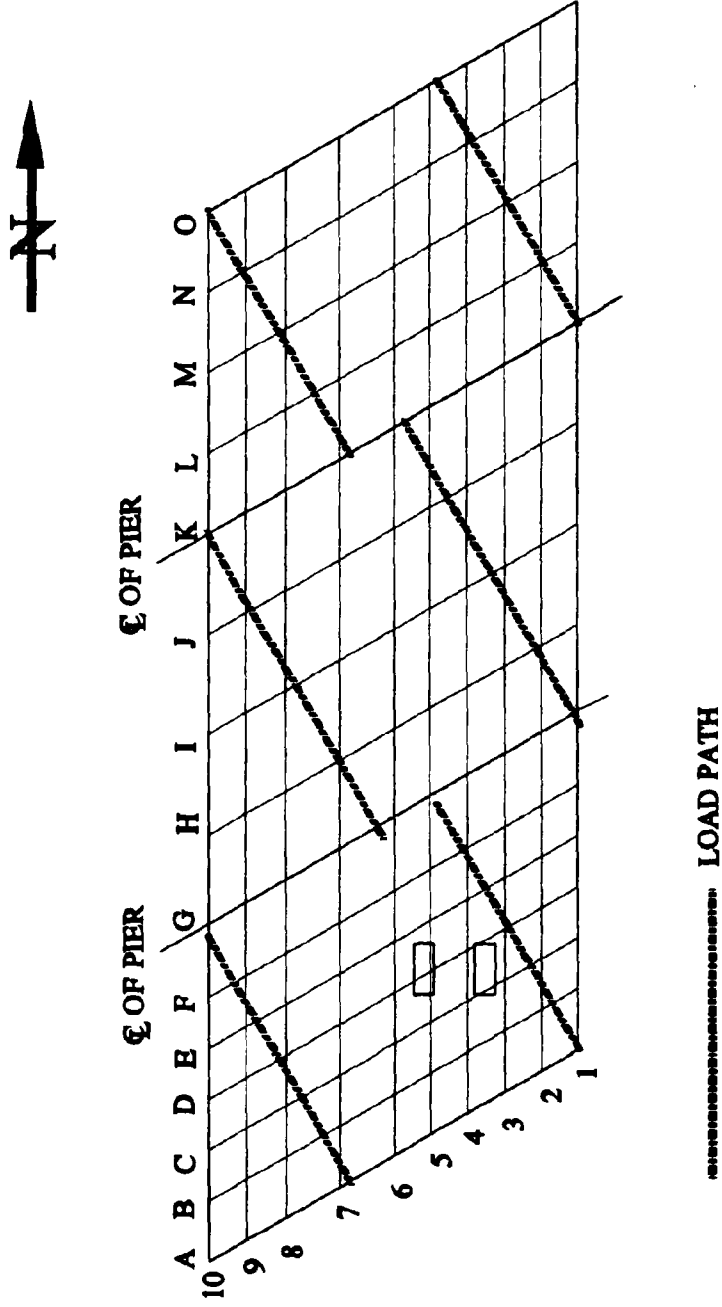
#### 5.4.3 Analysis of Failure

Figure 5.17 shows the approximate location of the failure plane, as well as shear planes based on the ACI code. The most important factor to note is that the average shear stress on the perimeter of the failure plane was less than  $1.0\sqrt{f'_c}$ . It appears that the failure was primarily a punching shear. This is a common form of failure for bridge slabs under concentrated loads (Malver, 1992; Fang, 1990). Using the formula for punching shear common to both ACI-318 and the AASHTO Standard Specifications, the punching shear capacity would be 1200 kips. The actual failure load of 720 kips is 40% less than the actual capacity. However, the previously cited research on flawed slabs indicates that the presence of flaws may reduce the punching shear capacity by as much 50%. Therefore, the marked reduction in the shear capacity is not surprising due to the tremendous damage found in the shoulder area.

The dynamic nature of the failure is also of critical importance. Had the failure been more static, the failure (fracture) front may have been arrested by reinforcing bars or aggregates, common static crack arresting mechanisms. If the failure front had been arrested, it is possible that the load may have been redistributed to the undamaged areas and the bridge may have continued to carry load until another failure mechanism formed. However, the tremendous energy release at failure drove the failure front in a dynamic fashion, through or around the arresting mechanisms into the sound areas of the bridge. Once the failure front penetrated the sound areas, it weakened these areas. The method of loading then played an important role in the failure. The bridge was tested in load control meaning that the actuators applied load in increasing load increments. When some capacity was lost due to failure of the deteriorated shoulder, the actuators continued to apply the same load. Since the total load remained constant and the shoulder could not carry any load, the load carried by the sound areas increased. The combination of the propagation of the dynamic failure front and the increasing stress in the sound areas was ultimately fatal.

It is theoretically possible that a different loading method might have resulted in a more stable failure. Had the bridge been tested using displacement control, the controller would have monitored the displacement transducer at a chosen point and tried to vary the load so that the chosen point would displace at a uniform rate. If the beginning of failure had caused an increase in the measured displacement rate at the chosen point, the controller would have reduced the load to keep the displacement rate constant. This might have resulted in a more stable failure. However, in practice, it is doubtful that using displacement control would have helped. Unless the instrument used for displacement control was near the point of failure, it would not have detected the failure in time to prevent the sudden failure from occurring. Since the point where the final failure occurred was unknown before the test, it is doubtful that a point near the final failure point would have been chosen for control. Also, the actuators needed to apply the large loads required are slow to respond due to the large amount of fluid which must be moved to apply or remove load. It is therefore doubtful that these large cylinders could have responded in time to prevent the sudden failure.





**FIGURE 5.2: TYPICAL LOAD PATHS FOR SKEWED BRIDGES**

# Load vs. Deflection at Point D4

## Low Level Testing

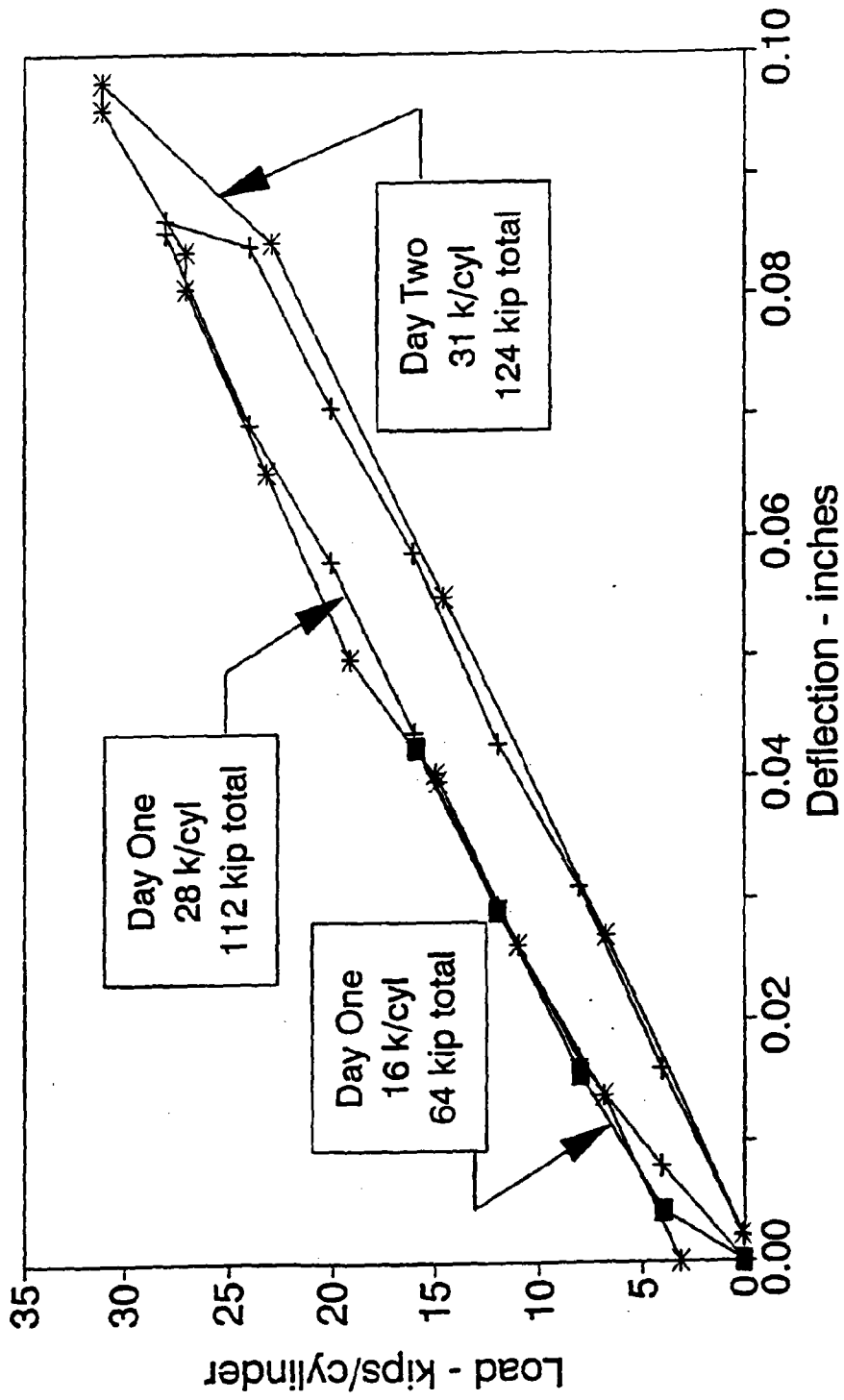
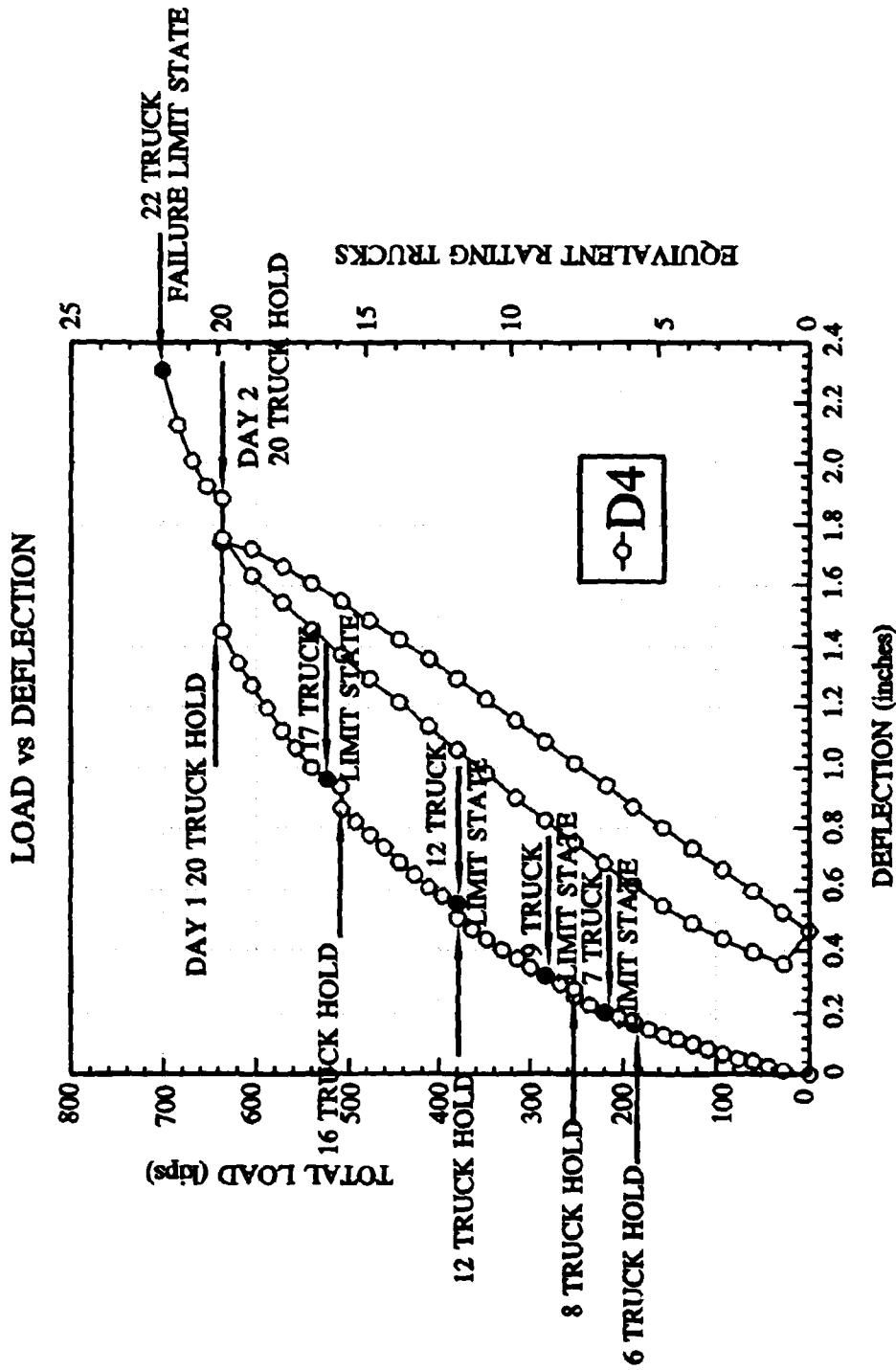
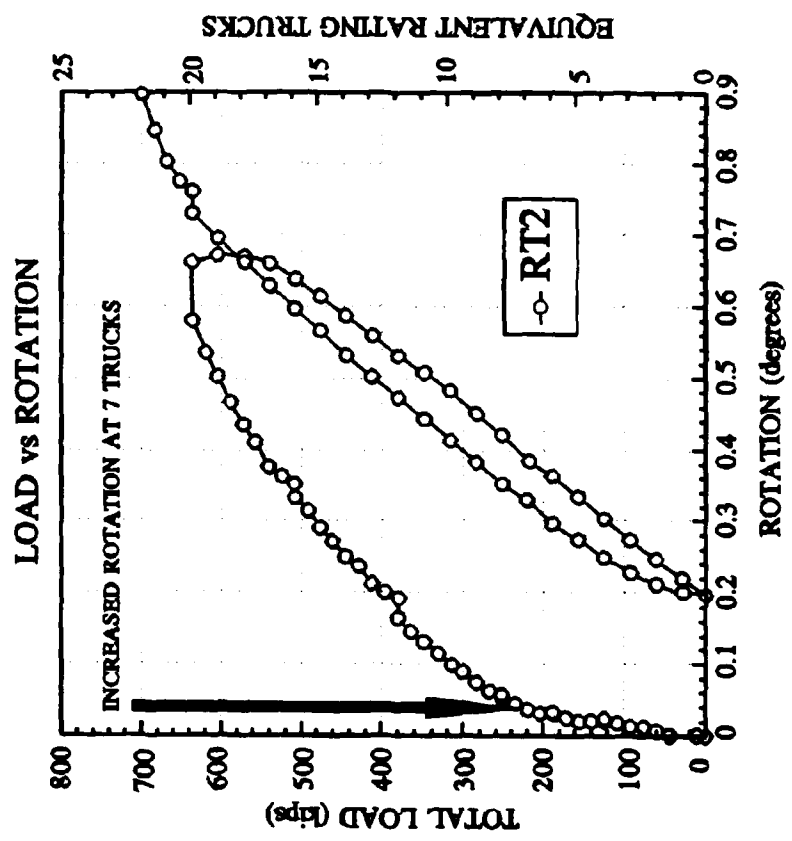
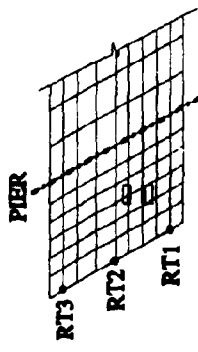
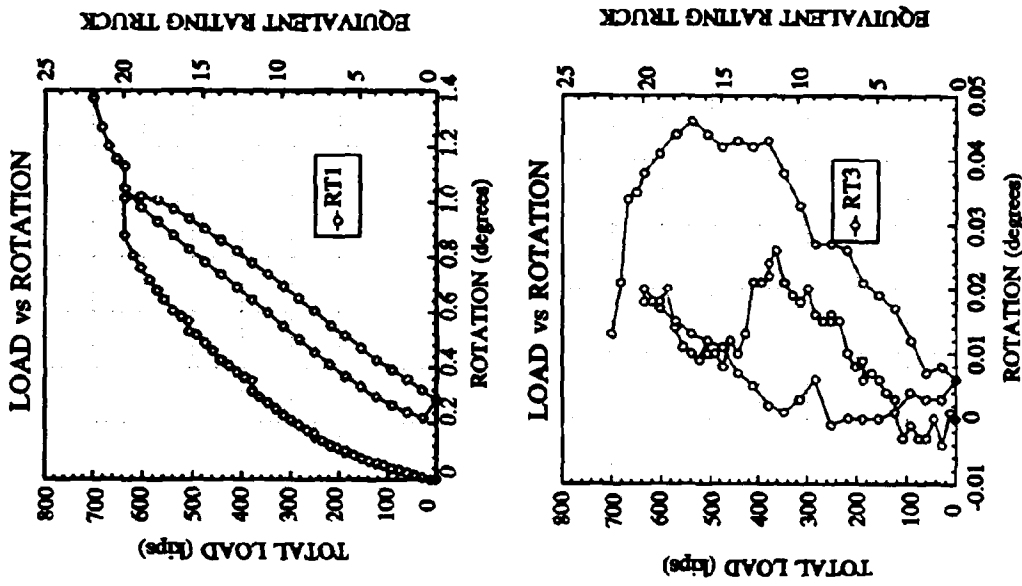


FIGURE 5.3 : DEFLECTION PROFILES SHOWING PLATEAUS AT THE HOLD



**FIGURE 5.4: CREEP IN LOAD-DEFLECTION FROM HOLDS, AND LIMIT STATES**



**FIGURE 5.5: ROTATIONAL RESPONSE AT ABUTMENT**

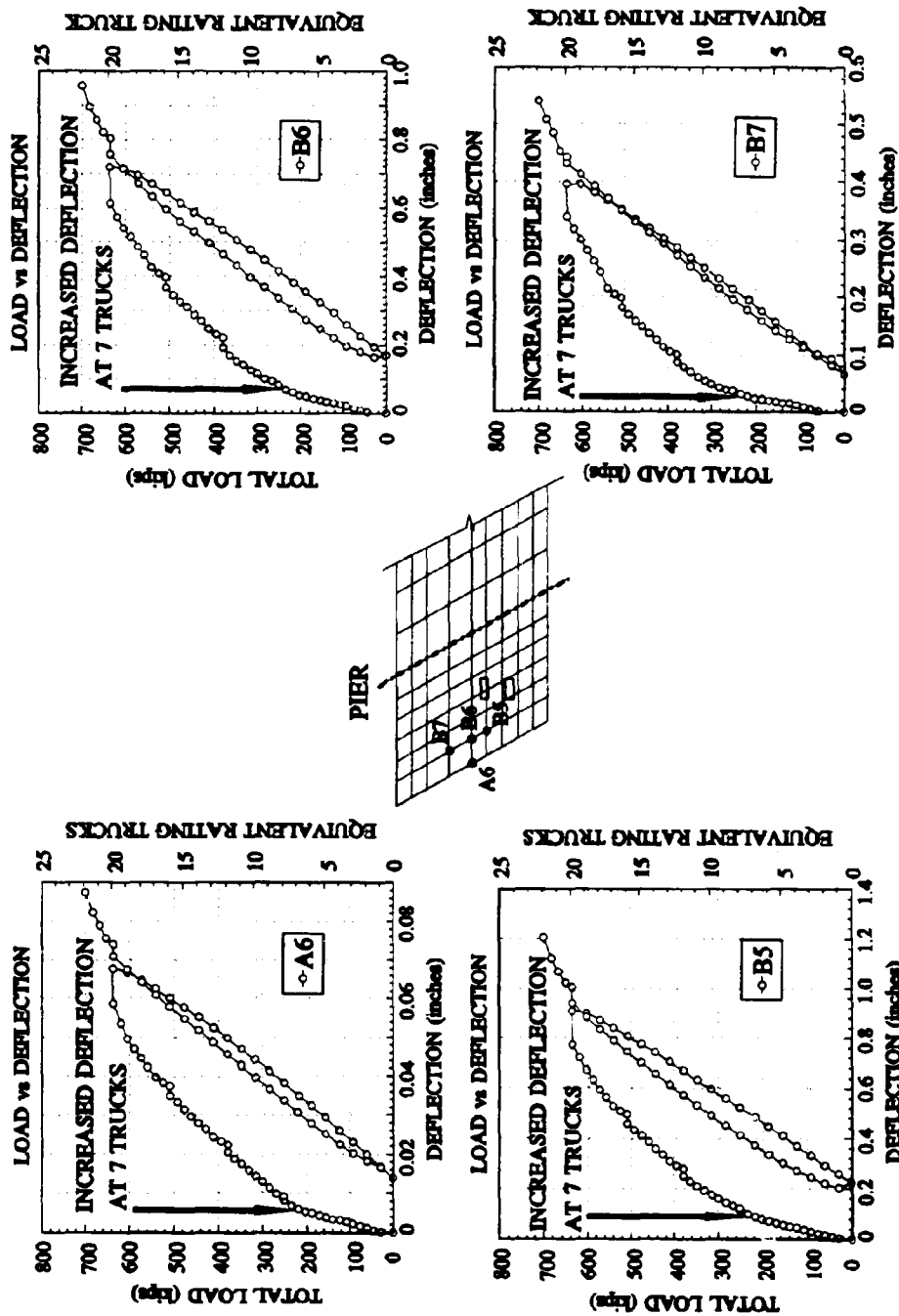
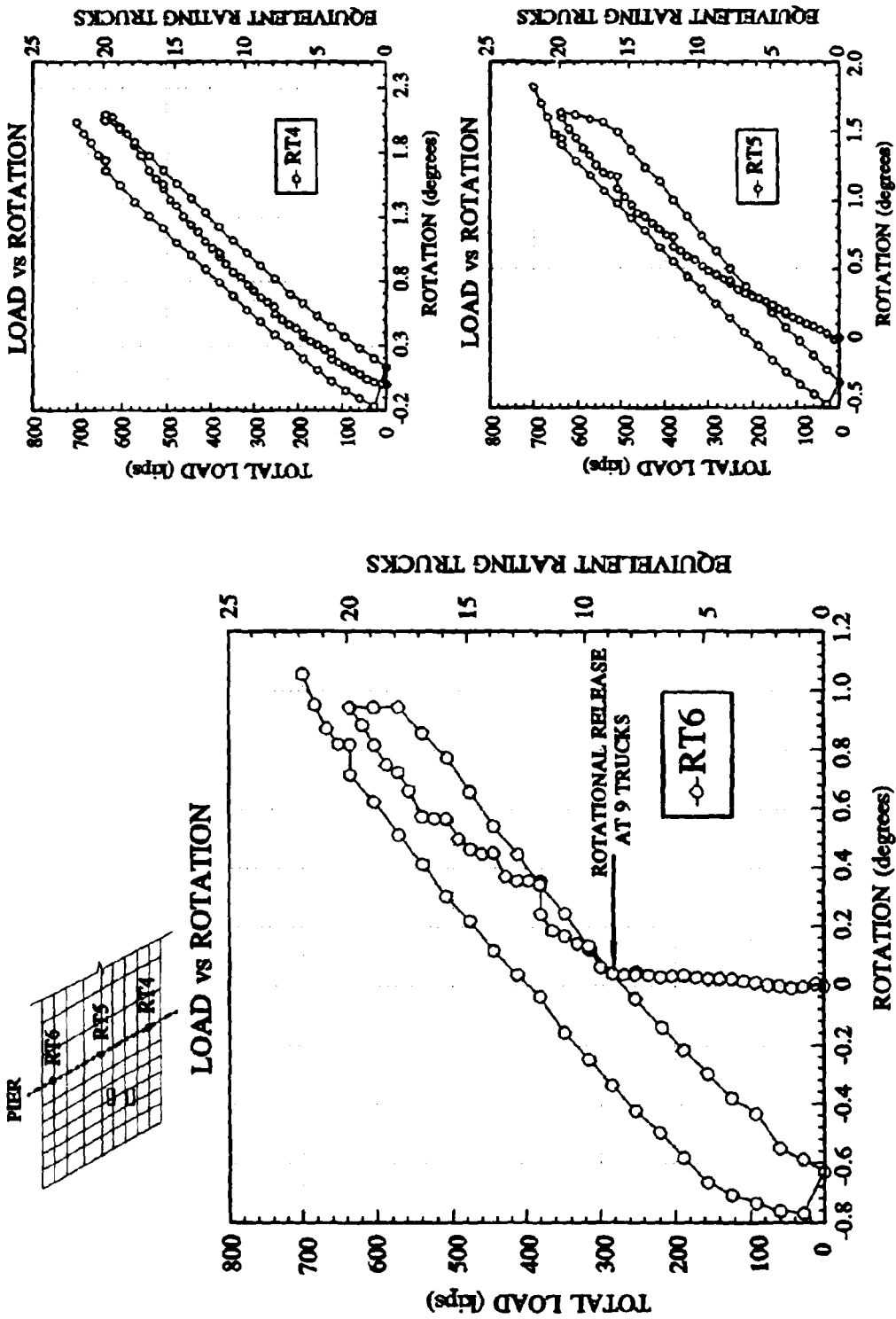


FIGURE 5.6: DEFLECTIONS NEAR ABUTMENT



**FIGURE 5.7: ROTATIONAL RESPONSE AT PIER**

SEE FIGURE 4.20 FOR LOCATIONS OF STRAIN GAGES

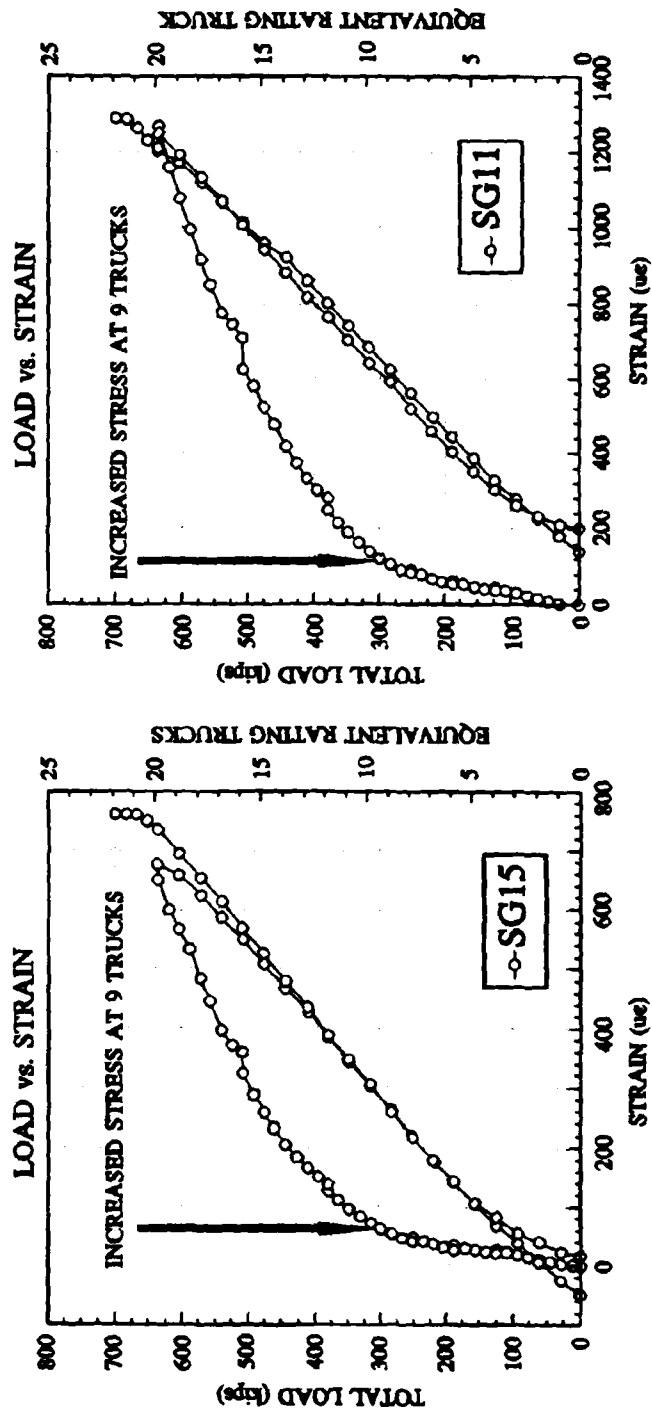


FIGURE 5.8: MEASURED STRAIN IN TOP BARS AT PIER

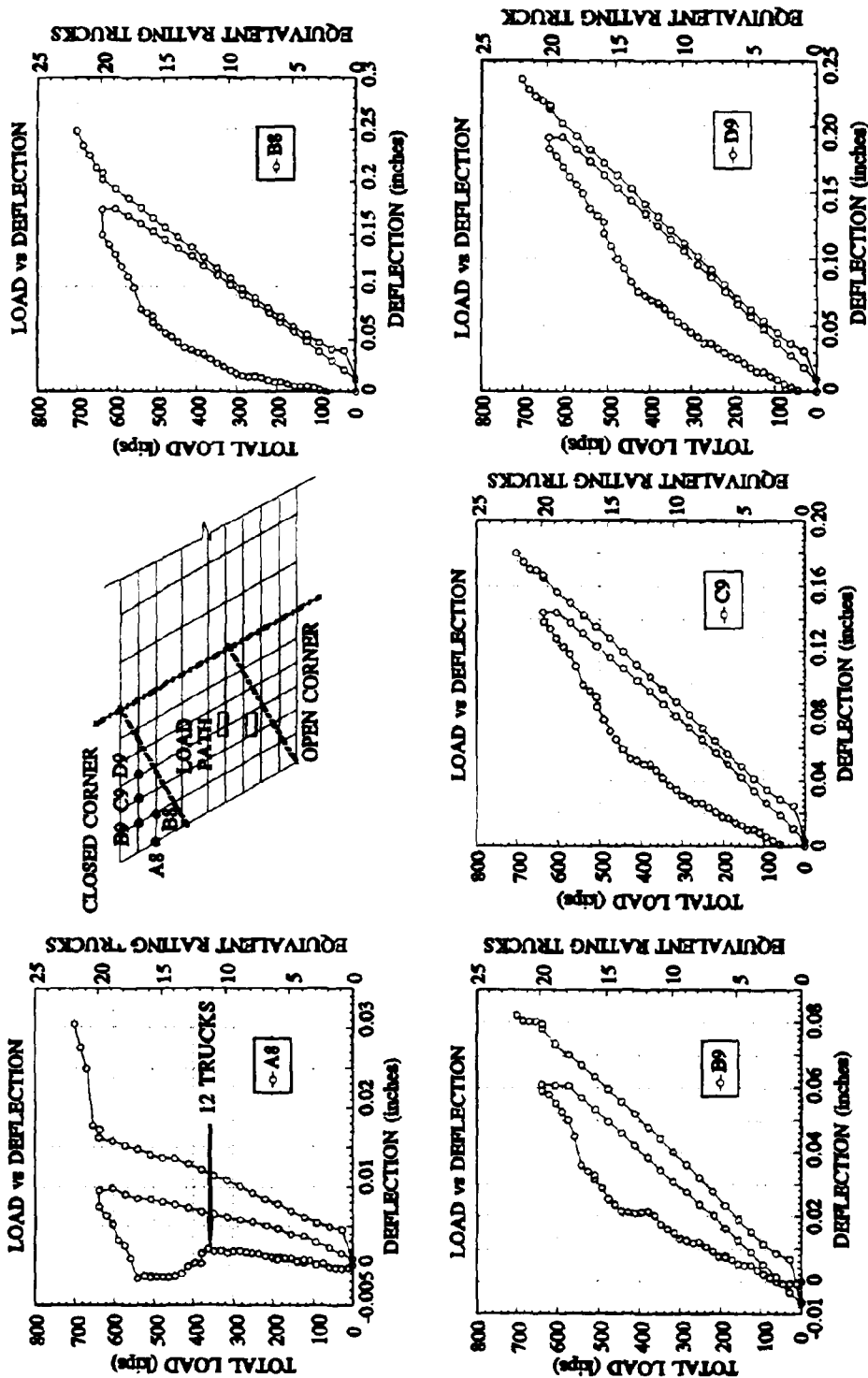
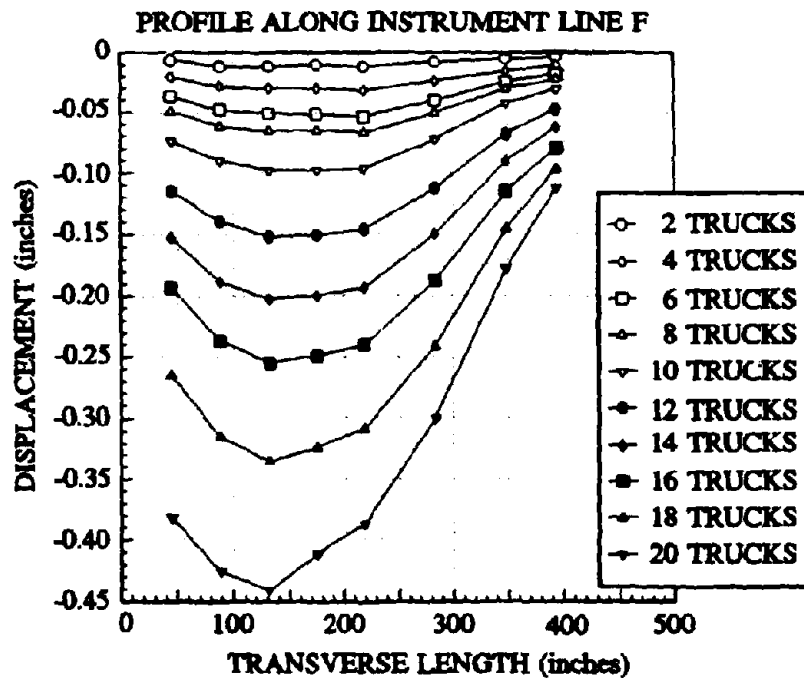
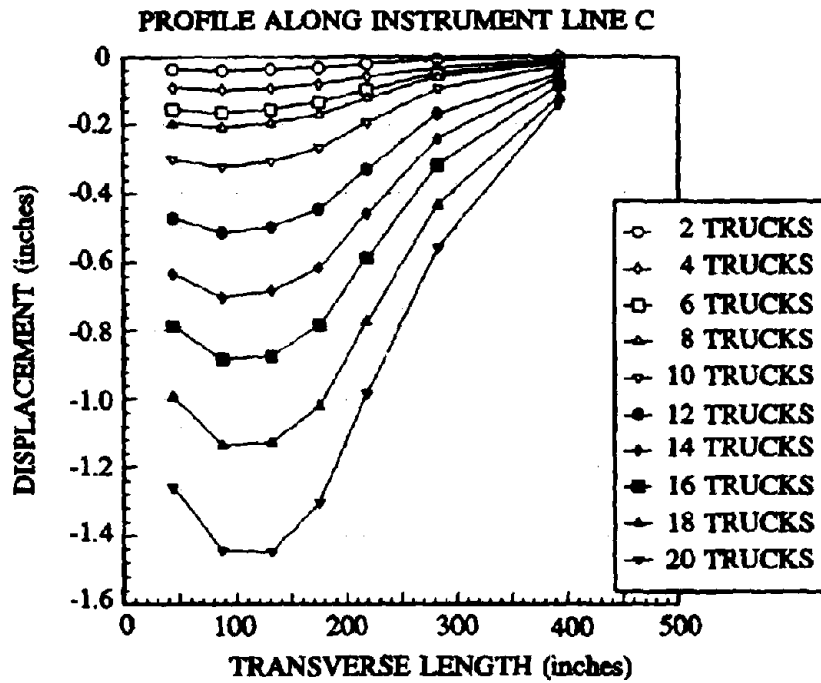
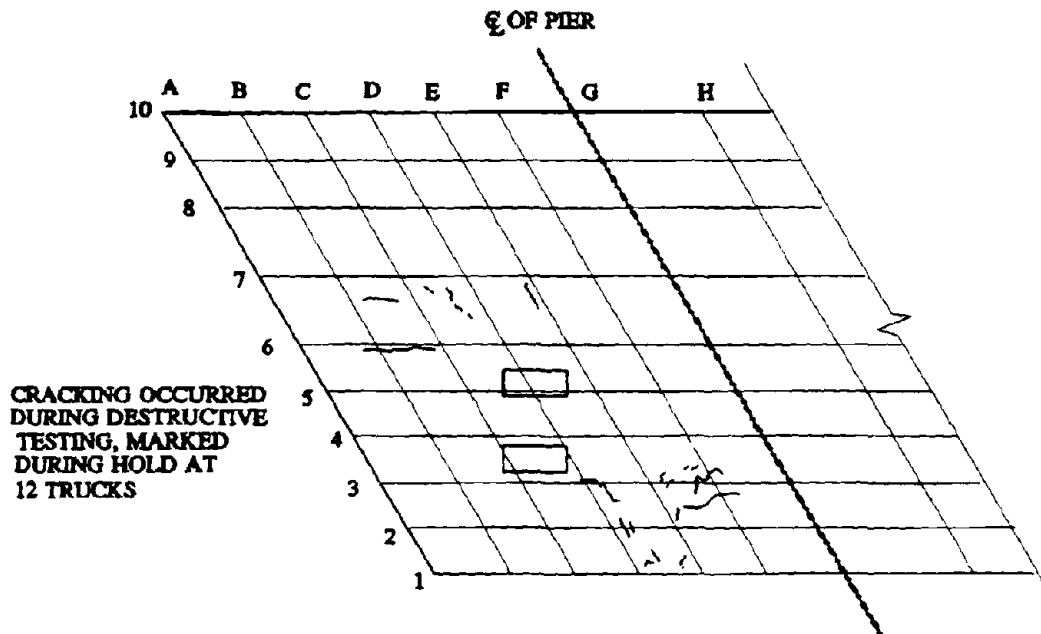


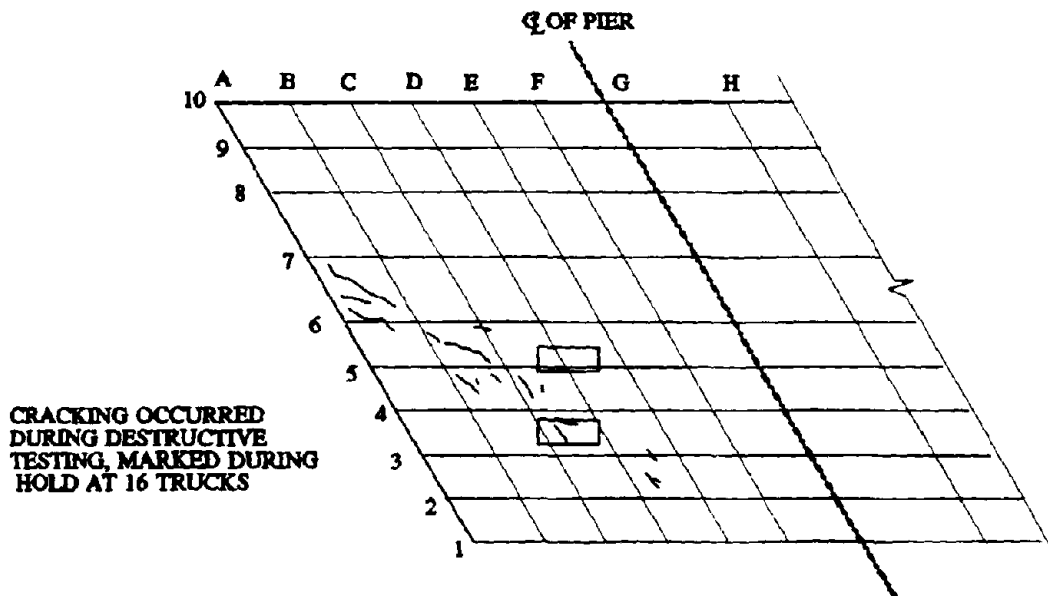
FIGURE 5.9: LOAD DEFLECTION RESPONSE IN CLOSED CORNER



**FIGURE 5.10: DEFLECTION PROFILES ALONG LINES C & F**

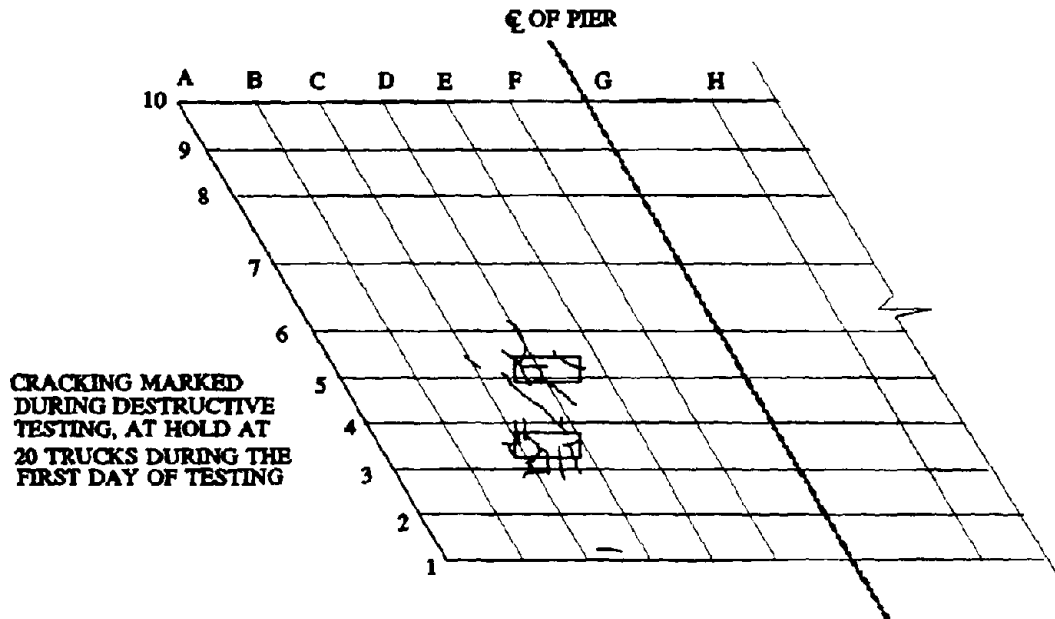


INCREMENTAL CRACKING BETWEEN 8 TO 12 TRUCK LOADS

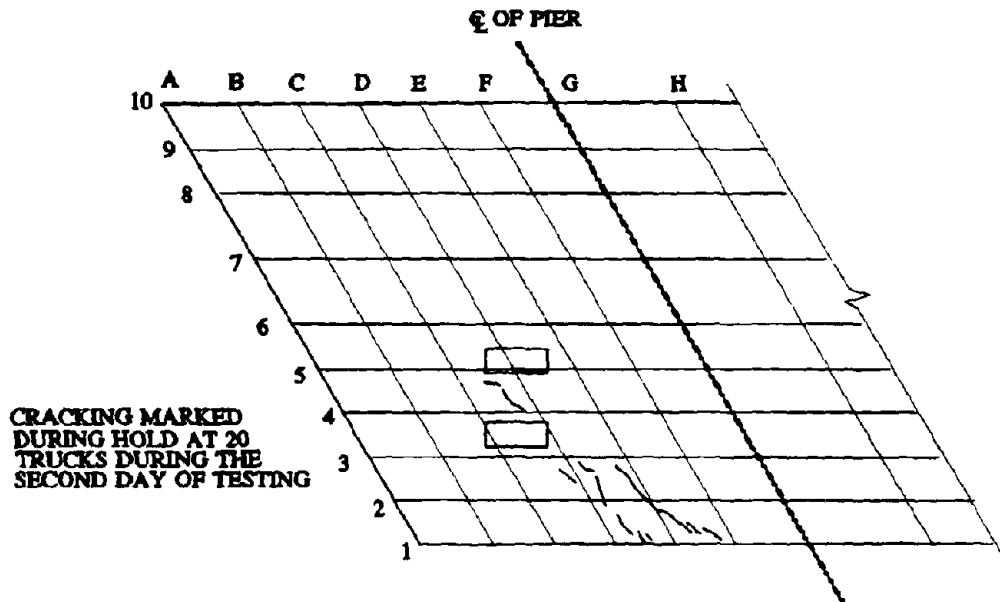


INCREMENTAL CRACKING BETWEEN 12 TO 16 TRUCK LOADS

FIGURE 5.11: INCREMENTAL CRACKING MARKED AT 12 AND 16 TRUCK LOADS

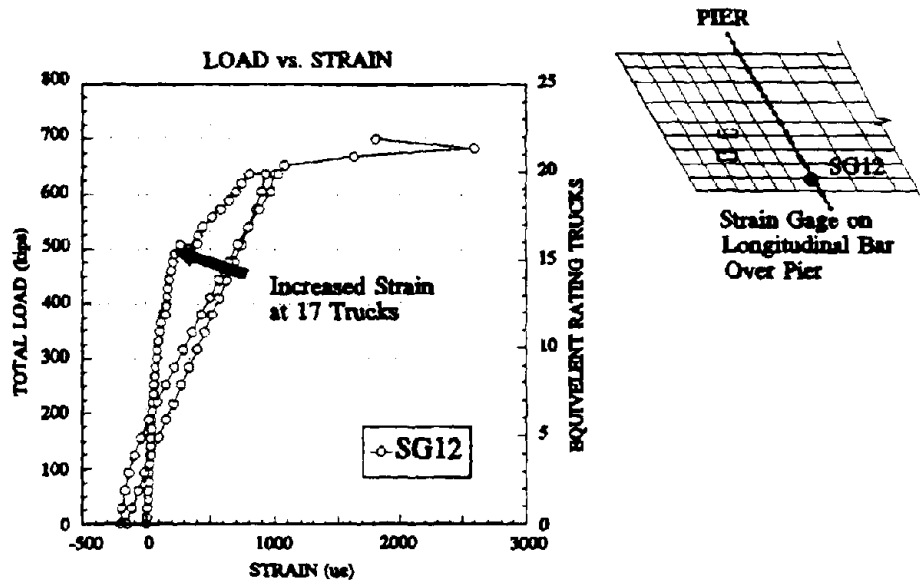


**INCREMENTAL CRACKING BETWEEN 16 TO 20 TRUCK LOADS**



**INCREMENTAL CRACKING AT 20 TRUCK LOADS DAY 2**

**FIGURE 5.12: INCREMENTAL CRACKING MARKED AT 20 TRUCKS**



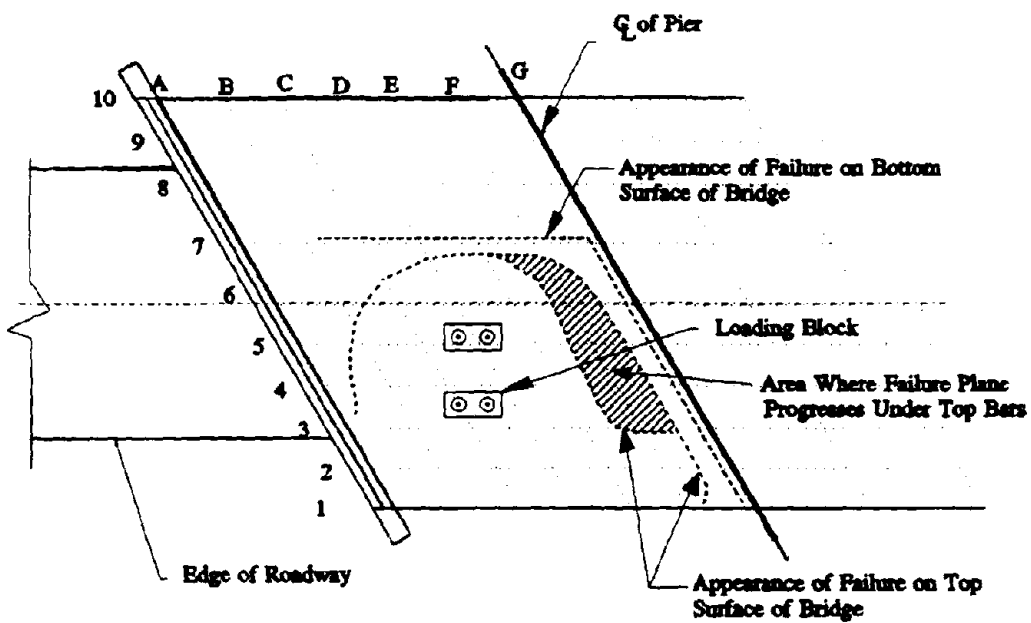
SG12 INDICATING INCREASED STRESS AT 17 TRUCKS



DIAGONAL CRACK PLANE VISIBLE ON SIDE

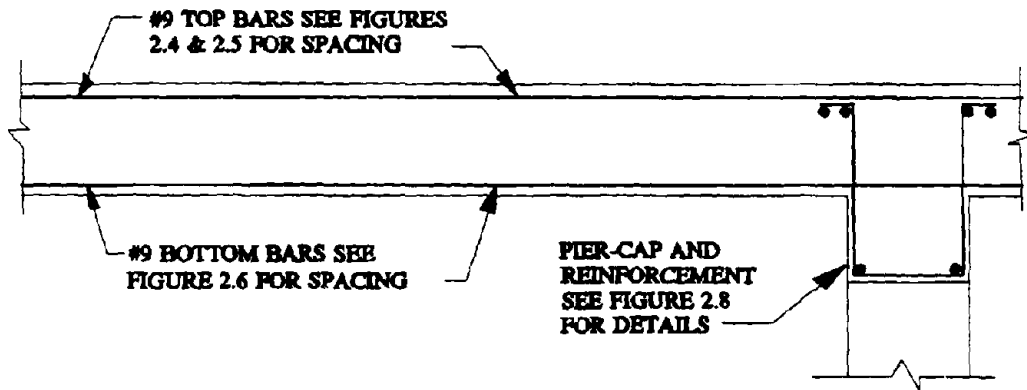
FIGURE 5.13: INITIATION OF DIAGONAL TENSION FAILURE FOLLOWING YIELDING AT CRITICAL REGION

**TOP VIEW OF FAILURE PLANE**

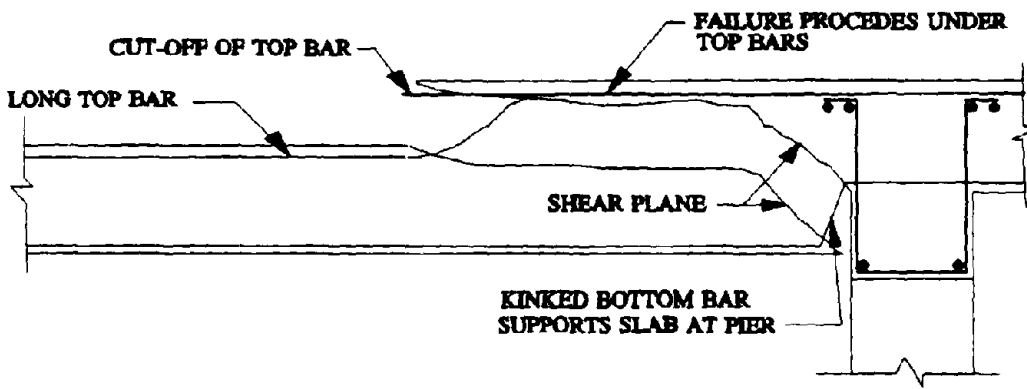


**APPEARANCE OF BOTTOM AND TOP FAILURE PLANES**

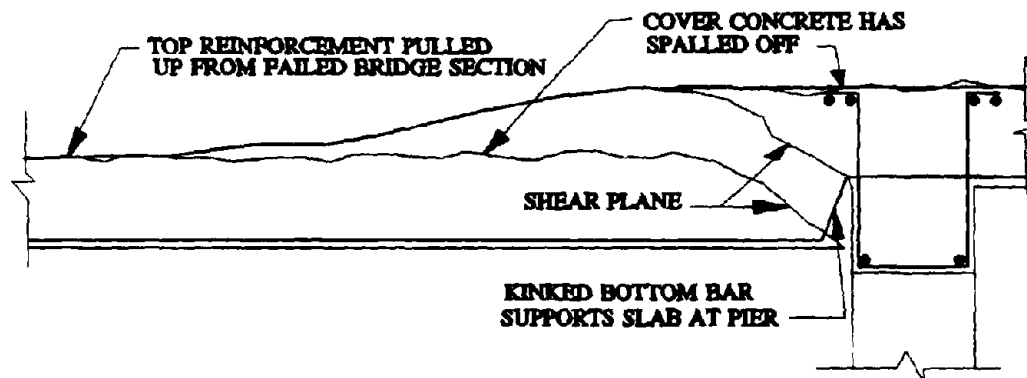
**FIGURE 5.14: FAILURE PLANE**



**UNDAMAGED TYPICAL SLAB CROSS-SECTION**



**TYPICAL DAMAGED CROSS-SECTION IN DRIVING LANES**



**TYPICAL DAMAGED CROSS-SECTION IN SHOULDER**

**FIGURE 5.15: TYPICAL CROSS-SECTIONS OF FAILURE**



SHEAR PLANE AT EDGE OF BRIDGE



BOTTOM VIEW OF SHEAR PLANE

FIGURE 5.16: FAILURE PLANE AT SIDE AND BOTTOM



## CHAPTER 6: NONDESTRUCTIVE EVALUATION STUDIES

### 6.1 INTRODUCTION

#### 6.1.1 Nondestructive Evaluation

Recently there has been considerable interest in nondestructive evaluation (NDE) of constructed facilities for detecting deterioration and damage. In 1987, a National Research Council Committee (Committee on Infrastructure Innovation, 1987) indicated that the most effective preservation strategy for the infrastructure is scheduling maintenance at the onset of deterioration. NDE techniques for detecting the onset of deterioration in structures is noted as a critical research need.

A National Cooperative Highway Research Program (NCHRP) research statement entitled "Nondestructive Load Testing and Identification for Bridge Evaluation and Rating" followed (Friedland, 1987). Following the completion of this research in 1990 (Pinjarkar et al., 1990) a continuation project was initiated in 1991 (Friedland, 1990). The NCHRP projects will lead to revisions to AASHTO's Manual of Maintenance Inspection for taking advantage of appropriate NDE methods in bridge inspection and rating.

A National Science Foundation sponsored workshop on NDE (Agbabian and Masri, 1988) was followed by other conferences (Suprenant et al., 1992) and a research initiative (NSF, 1992) by this agency. Meanwhile, a Federal Highway Administration research program focussing on NDE of bridges has been initiated with emphasis on fracture-critical bridges such as the steel-stringer type (Cooper, 1992; McGogney and Nickerson, 1992).

In spite of the attention to NDE of constructed facilities and materials, consensus definitions for related concepts and terms as well as a classification of the available NDE methods are lacking. Particularly, a quantitative health evaluation method for a complete constructed facility, i.e. a soil-foundation-structure system does not exist.

A classification of NDE methods for bridges has been offered by Pinjarkar et al. (1990). This did not include a number of powerful strategies and techniques which may be exported from other engineering disciplines such as system-identification, flexibility-monitoring (refer to Hogue et al., 1991, for definitions and literature survey), and, modal testing (refer to Raghavendrachar and Aktan, 1992, for definitions and literature survey).

#### 6.1.2 Objectives and Scope

The first objective of this section of the report is to propose a classification of NDE methodologies for constructed facilities and suggest definitions for related concepts. The second objective is to describe a quantitative NDE methodology, addressing both the global health and the local conditions of a constructed facility. The key structural index in the NDE methodology is bridge flexibility with a sufficiently fine spatial resolution. A measure of this is obtained experimentally by modal-testing. A finite-element model of the complete structure is then calibrated through system-identification. The measured flexibility is used as a baseline structural signature for diagnosing future deterioration and damage, while the

finite-element model is used for rating. In the case of first-time application to an aged facility, damage may be diagnosed by interpreting irrationalities and anomalies in the measured flexibility.

Application of the critical steps of this NDE method to the slab bridge in the context of proof-of-concept testing is described next. The test bridge was first used to demonstrate an application of the method when there is no available baseline. It was possible to diagnose extensive concrete deterioration from above an asphalt overlay. The NDE method was subsequently applied before and in the course of the destructive test program, and was able to successfully diagnose overload-induced damage while even experienced bridge engineers failed to diagnose the damage.

## **6.2 METHODS AVAILABLE FOR BRIDGE NDE**

### **6.2.1 Features Desired In a Bridge NDE Method**

While there may be multiple expectations from a bridge NDE method, a desired outcome would be quantifying the existing global and local structural conditions in terms of rational engineering indices that relate to bridge reliability. Bridge reliability has been defined as the probability that structural capacities will exceed or equal the corresponding demands during the remaining service life and given the existing condition (Imbsen et al., 1987; Moses and Verma, 1987). Presently, highway officials express and monitor bridge conditions in terms of a subjective scale based on visual inspections. NDE should transform this practice to an experiment-based objective one. This would be possible by first understanding and then quantifying the current state of structural characteristics that directly relate to structural reliability (e.g. critical global and local flexibility coefficients, localized distortions and strains, spalls, crack distribution and widths, initiation of fracture, etc.). Then these indices may be monitored intermittently or continuously by NDE tools.

The expected values of local capacities and demands are compared at the critical regions for bridge rating. Therefore, a desirable bridge NDE process should provide sufficient quantitative information about a bridge so that the critical local capacities may be confidently established based on the existing state. Finally, the NDE process should facilitate a reliable analytical characterization of a bridge for translating the dead load, traffic load and other intrinsic demands to the local demands at the critical regions.

### **6.2.2 Classification of Existing Bridge NDE Methods**

Classification of existing bridge NDE methods are presented in Figure 6.1, first classifying into system-identification vs. non-system identification approaches. Methods based on system-identification correlate experimental results with analytically simulated counterparts (Hart and Yao, 1977; Natke and Yao, 1988). Therefore, a mathematical idealization of the structure is needed for a system-identification approach. Approaches that are not based on system-identification are typically based on correlating mechanical characteristics of structures, elements or materials to a measured global or local response

empirically. System-identification approaches may be classified based on the form of the mathematical model that characterizes the structure. The "modal identification" category incorporates techniques that are based on measuring the dynamic characteristics such as frequency, damping and mode-shapes followed by a comparison of these properties to their nominal counterparts for diagnosing damage (Flesch and Kernbichler, 1988). The "numerical identification" category aims at estimating the numerical values of structural parameters such as stiffness coefficients from measured responses, and using these as a basis for diagnosing damage (Agbabian et al., 1987; Chen and Garba, 1987; Shinozuka et al., 1982). The category termed "geometric identification" aims at developing and quantifying the physical parameters of an analytical model of the structure in the geometric space, i.e. finite-element models (Ibanez, 1972; Ibrahim, 1988; Aktan et al., 1992; Hogue et al., 1991; Raghavendrachar and Aktan, 1992). Since the latter category leads to a calibrated analytical model of the structure in the geometric space, it promises all the features of a desirable NDE method as discussed earlier.

Non-system identification based NDE methods may be classified as either global or local, depending on whether a global or local index is measured. For example, the presently used visual method aims at assigning condition indices to different components of a bridge and an overall condition index for the complete bridge.

Proof-load tests aim at loading a bridge with the full level of maximum expected live load and qualitatively determining safe performance. The limitations of NDE based on visual inspection or a proof-load testing have been well established. Truck-load tests (Bakht and Jeager, 1990; Novak and Tharmabala, 1988; Shultz et al., 1992; Shahawy, 1992) have extended proof-testing by measuring bridge responses corresponding to known truck loads and taking these as a basis for NDE.

Dynamic signature analysis pertains to measuring and monitoring frequency and mode shape characteristics of a bridge for correlating to damage and deterioration (Salane et al., 1971; Mazurek and DeWolf, 1990; Hearn and Testa, 1991).

The local probing category contains techniques for measuring localized characteristics of a bridge such as member dimensions, reinforcement detailing, mechanical characteristics of the materials or defects such as scour, cracks, delamination, voids, etc. While local probes cannot lead to a definitive evaluation of the overall structural integrity, quantitative probes such as those leading to in-situ characterization of material properties or sampling and destructive testing of materials serve as an essential complement to any global NDE method (Strength Evaluation, 1991).

Most of the recent research and development efforts for NDE have focussed on qualitative local probes (Agbabian and Masri, 1988; Suprenant et al., 1992). These aim at locating defects such as voids and delamination hidden in concrete, flaws in weld or cracks and fracture in steel. Most local probes have been based on applying a nondestructive wave such as by impact, sound, heat, light, magnet, x-ray, etc. into a member and measuring the resulting output at another location of the element. Typically, changes in the characteristics

of the input to output from one location to another are empirically calibrated for detecting defects.

### **6.2.3 Proposed NDE Procedure**

The method is outlined in Table 6.1 and is based on a combination of geometric system identification and quantitative global NDE in conjunction with local NDE probes. It is designed for application to special, important and/or historic bridges in a facility-specific manner, or to a representative samples of recurring bridge types. An initial application by a specialized team would pave the way for practical intermittent monitoring by bridge engineers during routine inspections.

The initial implementation of the method leads to a comprehensive geometric system-identification as outlined on the left-hand-side column of Table 6.1. As shown on the right-hand-side column, the experimentally measured characteristics of a bridge in the course of the system-identification effort are used for reliably and quantitatively establishing the existing state of the structure. Conditions at the critical regions are quantitatively evaluated at the local level. Once a finite-element model of the subject structure is identified, this becomes a vehicle for evaluating structural reliability. The calibrated model also serves to identify the structural responses and indices that need to be monitored for evaluating reliability as discussed in the following.

## **6.3 APPLICATION OF NDE TO THE BATAVIA BRIDGE**

### **6.3.1 Overview of the Nondestructive Test Program**

A total of four modal tests were performed before, during and after the destructive tests, as shown in Figure 6.2, to provide information at several stages of damage to the bridge. In the nondestructive test part, truck load tests were conducted to measure static deflections under known loads. These truck load tests as well as the first modal test were conducted with the asphalt overlay still present. At the time of these tests, the servo-loading system had not been installed yet and the bridge was open to traffic. The second modal test was performed with the asphalt overlay removed and loading blocks and hydraulic cylinders installed but before any load was applied. The results of this test serve as a baseline for comparison with the third and fourth tests. The third modal test was done after the bridge was loaded to twenty equivalent rating truck loads by the hydraulic cylinders and released. Finally, the fourth test was conducted after the bridge was loaded to twenty-two equivalent rating truck loads and failed.

### **6.3.2 Design of the Modal Tests**

Multi-reference impact testing was chosen as the testing method, since past experience has proven this technique to be effective and reliable for structural identification of large structures (Halvorsen and Brown, 1977; Raghavendrachar and Aktan, 1992). It is a known fact that impact testing may not be as suitable as random excitation when nonlinear

GEOMETRIC SYSTEM IDENTIFICATION	DETERIORATION/DAMAGE DIAGNOSIS
<p>(A) DEVELOP A-PRIORI F.E. MODEL</p>	
<p>(B) ESTABLISH CRITICAL STRUCTURAL CHARACTERISTICS; REGIONS; PARAMETERS</p>	
<p>(C) DESIGN AND CONDUCT MODAL TEST</p>	<p>① FREQUENCIES, DAMPING UNIT-MASS SCALED MODAL VECTORS</p>
<p>(D) CALIBRATE F.E. MODAL IN THE MODAL SPACE</p>	<p>② MODAL FLEXIBILITY</p>
<p>(E) CHECK COMPLETENESS OF THE F.E. MODEL IN THE FLEXIBILITY SPACE</p>	<p>③a IF BASELINE EXISTS, EVALUATE DAMAGE BY CORRELATING MODAL FLEXIBILITY WITH BASELINE</p>
<p>(F) DESIGN AND CONDUCT ADDITIONAL EXPERIMENTS TO CAPTURE LOCAL RESPONSE MECHANISMS, USE LOCAL PROBES FOR NDE AT DAMAGED AREAS; SAMPLE AND TEST FOR MATERIAL PROPERTIES</p>	<p>③b EVALUATE ANOMALIES IN STRUCTURE BY CORRELATING MODAL AND ANALYTICAL FLEXIBILITIES        ==&gt; DIAGNOSE DAMAGE</p>
<p>(G) RIGOROUS CALIBRATION OF THE COMPLETE F.E.M. INCORPORATE LOCAL CONDITIONS</p>	<p>④ QUANTITATIVE EVALUATION OF EXISTING DAMAGE AT THE LOCAL LEVEL</p>
<p>(H) EVALUATE STRUCTURAL RELIABILITY AND DESIGN MONITORING PROGRAM</p>	

Table 6.1 - Geometric System Identification Based NDE Procedure

structures are concerned. However, due to its versatility, ease and quickness of application it is perhaps the most suitable testing method for bridges and other similar structures. Moreover, recent advances in multi-reference parameter estimation algorithms have helped to rationally linearize the bridge by utilizing the data from all the references simultaneously.

Impact tests done on a similar reinforced concrete slab highway bridge have shown that a hand-held instrumented sledgehammer is adequate in exciting the lower modes of the structure (Raghavendrachar, 1991). Of course the number of modes desired depends upon where and how the results will be used. To identify the global dynamic characteristics of the structure, the first few modes are usually adequate. To identify local response mechanisms, however, higher modes are necessary. One of the goals of this present research was to detect damage on the bridge by looking at the flexibility matrix derived from the measured modes. Since the number of modes included in the calculation of this flexibility matrix determines its accuracy to represent the real state of the structure, obtaining as many modes as possible was desired. For this purpose, the advantages of multi-reference testing was utilized to its fullest by placing twelve reference accelerometers on various locations on the bridge. One of the discerning characteristics of the test structure was its skew supports, namely, its abutments and piers. The test grid was chosen to be parallel to these supports resulting in parallelogram segments, which was also compatible with the finite element model. Two different grids were used for the four tests: the first grid was used for the first test and is shown in Figure 6.3(a), the second grid, shown in Figure 6.3(b), was used for the modal tests two through four. An attribute of both grids is that the mesh is denser in the first span (left span). Since this was the span that was loaded, a more detailed observation of this span was desired. Having a denser grid helps to capture more of the local modes of that area.

Using as many as twelve references in impact testing may seem too many. However, in the testing of large scale structures, low signal-to-noise ratio becomes important. Due to the size of the structure, exciting the higher modes became a problem consequently reducing the signal-to-noise ratio. Therefore, selecting the reference that contained the least contaminated signal from an excited mode was essential in the parameter estimation stage for obtaining accurate modal parameters. Having a large number of reference instruments increased the chances of capturing high modal amplitude response locations thereby boosting the signal level in the data.

Choosing the locations of the reference transducers is an important step in obtaining successful data in any test. In order to place the transducers, the preliminary analytical model was used. The locations were chosen by selecting the maximum amplitude locations of the analytical mode shapes.

### **6.3.3 Data Acquisition**

For measuring the response of the bridge, PCB 393C type high sensitivity seismic accelerometers were used. These instruments have a nominal sensitivity of 1 V/g, amplitude

range of  $\pm 2.5$  g (with 0.0001 g resolution) and a frequency range of 0.025 to 800 Hz (with  $\pm 5\%$  error). The accelerometers were calibrated using the gravimetric free-fall method. The GenRad 2515 data acquisition system was used to capture and store the data. The excitation was provided by a PCB 086B50 12-pound hand held impact hammer instrumented with a load cell. The hammer was calibrated using the ratio method, performed by striking a large body of known mass with the hammer and measuring the response of the mass with an accelerometer of known sensitivity. Two twelve channel PCB 483 B17 adjustable gain amplifiers were used to supply current to the hammer and accelerometers. The signals from the accelerometers were amplified ten times. Power to the data acquisition system was provided by a generator.

The frequency range of measurement was chosen to be from 0 to 64 Hz, which resulted in a fixed frequency resolution of 0.125 Hz. Preliminary analytical studies showed that a sufficient number of modes were located in this frequency range. Moreover, these modes were very closely spaced and hence needed a fine frequency resolution. Due to the nature of the data acquisition system, opting for a frequency range of 0 to 128 Hz would have decreased the frequency resolution to 0.250 Hz. In fact, this higher frequency range was explored prior to the actual test and it was observed that modes above 64 Hz were not clearly defined due to a lack of adequate excitation.

A force window on the force channel and a 10th order exponential decay window on the response channel were used. The order of the exponential window was chosen so that the response of the bridge completely decayed in the time window. The data acquisition system automatically set the anti-aliasing filters at 80 Hz. No additional filters were used during the tests. Data from each point was averaged five times for all the tests. For the first test when the bridge was still open to traffic, no vehicles were allowed on the bridge during data acquisition. The 64 Hz frequency range translated to an eight second time window for each average, so together with the autoranging hit the approximate time needed for each point was 48 seconds. The number of points hit in the first test was 97; for the latter two tests the number was 119.

Averaging is necessary to reduce the random noise error so the higher the number of impacts per station, the better the results should look. However, it was observed that increasing the number of averages beyond five did not significantly improve the data and it considerably increased the data acquisition time. Therefore, a compromise between data quality and data acquisition time was attained with the five averages.

Some of the settings of the GenRad system are given in Table 6.2. Table 6.3, on the other hand, gives an idea of the time and labor requirements for the impact tests performed on this bridge.

#### **6.3.4 Data Post-Processing**

For parameter estimation of the test data, UC-Modal, a Unix operating system based software developed by the Structural Dynamics Research Lab of the University of

Parameter	Comments
Trigger Type: 1	Data acquisition is triggered off the first channel
Trigger Level: 5	Min input force level for triggering = 5% of total range
Trigger Delay: -5	Delay of 5 time samples in data acquisition
Weighting Code: -10	Power of the exponential decay window used on the response
Ensemble Size: 5	Number of averaged data
Maximum Frequency: 64	Results in a frequency resolution of 0.125 Hz
Overlap Factor: 0	Averages were not overlapped
Reference Count: 1	Number of force channels
Response Count: 12	Number of response channels

**Table 6.2 - Data Acquisition Settings**

Job	# of People	Approximate Time
Marking/preparing the bridge	3	2-3 hours
Impact test equipment setup	3	1-2 hours
Impact testing	3	For 120 hit points: 6-8 hrs w/ light or no traffic 8-10 hrs w/ heavier traffic
Packing up	3	1 hour

**Table 6.3 - Typical Time and Labor Requirements for an Impact Test on a Highway Bridge**

Cincinnati, was used. Detailed descriptions and in-depth mathematical backgrounds of the algorithms can be found in the literature (Allemang and Brown, 1987).

Several parameter estimation algorithms were used for estimating the modes. Among these, Complex Mode Indicator Function (CMIF) (Shih et al., 1989) was used as a "pre-processor" algorithm to establish the number and location of the modes. CMIF also helped to separating the closely spaced modes easily and by indicating the number of modes present in a frequency span, assisted in determining the modal order used in the more sophisticated Polyreference Time Domain algorithm. The Polyreference Time Domain (PTD) method was then used to estimate the frequencies and damping.

The modes obtained from the testing of the bridge can be classified in four different categories:

- i) Global modes in which all three spans of the bridge move,
- ii) Local modes of the left span where the majority of the action observed takes place in the left span of the bridge,
- iii) Similar to above, local modes of the mid span,
- iv) And finally, local modes of the right span.

In order to obtain accurate modal vector estimates of the local modes, the reference that was best excited by the mode being estimated was used. As a first step however, parameter estimation was performed using all references to determine the complete set of mode shapes as best as possible. Afterwards, parameter estimation was concentrated on individual spans with the purpose of obtaining the best estimates of the modal vectors using only selected references. Global modes were captured by most of the references and in addition to that, since they were located at lower frequencies they were excited better than the higher frequency local modes. Parameter estimation in the frequency range of 3.75 Hz to 35.625 Hz was quite satisfactory. The reason for this was because all the global modes lay in this frequency span and all the modes were well defined in the FRFs. However, for the modes between 28.125 Hz and 60 Hz the curve fitting results looked poor. Also, when it came to calculating the mode shapes and looking at the modal participation factors, no single reference captured all the modes reasonably well. No single reference had enough participation in all the modes and consequently some errors in the modal vector estimation was inevitable. Therefore, the use of selective references to estimate the modal vectors was essential to obtain accurate modal estimates and hence good curve fitting. Substantial improvement was observed in the correlation between the measured and fitted FRFs when selective reference method was used, and the correlation was almost always above 90 percent. More detailed information can be found in Toksoy, 1992.

### **6.3.5 Results of the Modal Tests**

The frequencies and damping values found from the four modal tests are given in Table 6.4 and the mode shapes are given in Figures 6.4 through 6.7. From the first test, twenty modes were found. From tests two and three, nineteen modes, and from test four, fifteen

MODE #	TEST 1		TEST 2		TEST 3		TEST 4	
	f(Hz)	$\zeta$ (%)						
1	8.445	2.475	8.757	1.805	8.631	2.166	8.573	1.705
2	10.70	2.414	11.11	1.868	10.97	2.090	10.78	1.906
3	13.18	4.596	13.37	4.507	12.70	4.257	13.22	3.179
4	13.47	3.277	13.89	2.627	13.90	2.734	---	---
5	15.11	2.669	15.47	3.032	14.88	3.574	15.99	3.284
6	15.43	2.891	15.91	1.924	15.83	1.884	15.81	1.912
7	20.01	2.094	20.44	1.276	20.20	1.363	19.98	1.285
8	22.96	2.583	23.26	2.975	22.29	3.503	---	---
9	23.47	3.727	23.41	1.651	23.41	1.736	23.36	1.764
10	26.42	2.388	27.30	2.051	26.87	2.143	26.37	2.329
11	29.41	1.913	30.23	1.519	29.90	1.635	29.63	2.078
12	33.31	2.323	---	---	---	---	---	---
13	37.94	5.137	37.15	2.987	34.98	3.213	---	---
14	38.57	4.208	37.71	2.398	37.45	2.594	37.28	2.957
15	42.33	1.871	43.21	1.536	42.53	1.617	42.49	1.668
16	45.27	2.108	---	---	---	---	---	---
17	46.08	1.735	47.14	1.955	46.69	2.037	46.39	1.981
18	50.38	3.097	---	---	---	---	---	---
19	---	---	49.11	3.814	51.43	3.153	---	---
20	---	---	51.40	4.393	51.62	3.438	50.81	3.618
21	54.41	2.906	55.18	4.408	53.63	3.536	52.04	5.523
22	56.93	4.444	55.58	2.720	55.54	2.583	55.35	2.510

Table 6.4 - Frequency and Damping Values for the Four Modal Tests

modes were found. The reason for the difference in the modes captured by the first and the later two tests is due to the change in the grid and locations of the reference transducers. Furthermore, four of the modes of the first span, seen in the results of the second and third tests, were not captured in the fourth test because of the failure in the first span.

The comparison of the frequencies and damping values of the first and second tests reveals some important findings on the effect of asphalt overlay on the dynamic behavior of the bridge. As can be seen from Table 6.4, after the asphalt overlay was removed, in general, the frequencies increased 2-3 percent and the damping factors increased 24 percent on the average. It should be noted that due to the noise in the data combined with the close modal coupling of the end span modes, the frequency and especially damping estimates for these modes are not as reliable as for the global and mid span modes.

The third and fourth test results reflect the state of the bridge after different levels of controlled load was applied. The results of these tests are discussed in the following section.

### 6.3.6 Derivation of the Flexibility Coefficients From the Modal Test Results

In this section the derivation and use of the modal flexibility matrix in damage evaluation will be explained. Flexibility is a conceptual tool because the columns of the matrix themselves are identical to deflections due to a unit load at the location equal to the column index.

From here on, the term "modal flexibility" will refer to the flexibility matrix obtained from post processing of the modal test results. The term "analytical flexibility", on the other hand, will refer to the flexibility matrix obtained from the mathematical manipulation of the modal vectors obtained from the FE model. Finally, the term "exact flexibility" will refer to the inverse of the stiffness matrix developed in the FE model. The difference between analytical flexibility and exact flexibility is that analytical flexibility is derived from mass normalized modal vectors found from an eigenvalue analysis of the FEM. Analytical flexibility matrix may be calculated using any number of modes. However, as the number of modes grows larger, the analytical flexibility approaches the exact flexibility and in the limit becomes identical to the exact flexibility.

The mathematical formulation of the modal and analytical flexibility matrices is given below:

$$[F] = [\psi] [1/\omega^2] [\psi]^T$$

Where,

[F] = modal flexibility matrix,

[\psi] = unit-mass scaled modal vectors

[1/\omega<sup>2</sup>] = diagonal matrix of ascending natural frequencies.

The mathematical derivation of the flexibility matrix and the procedure for obtaining

unit-mass scaled modal vectors can be found in Raghavendrachar, 1991; and Toksoy, 1992.

In this research, the flexibility matrix of the structure is chosen as the most important damage evaluation tool. The justification for using flexibility matrix to extract information about the present state of the structure is based on the following: This matrix is a signature of the structure and since it is derived from the results of a detailed modal test, it contains information about the dynamic behavior of the structure in a form that conveniently yields itself to visual and quantitative analysis. If damage exists on the bridge, it will affect the dynamic characteristics which are measured by modal testing. Of course, these changes in the dynamic characteristics of the bridge will be reflected in the natural frequencies and damping factors. However, obtaining information about the location of the incurred damage is hardly possible from observing shifts in frequencies and damping. Flexibility on the other hand, goes one step further in reflecting the possible place of the damage or deterioration in the deflection profiles. Flexibility matrix is the transition point between the modal space defined by the modal parameters (frequencies, damping, mode shapes) and the physical space defined by deflection profiles. Figure 6.8 demonstrates the 3-D deflection pattern produced by loading the flexibility matrix obtained from the results of the second modal test.

It should be emphasized that the modal flexibility matrix is not the exact flexibility matrix of the structure since it contains the contributions of only a limited number of modes. The exact flexibility matrix would be obtained in the limit only. However, the first ten to twenty modes are usually adequate to define the overall behavior of a structure. The number of modes necessary to accurately represent the structure in terms of its flexibility is highly dependent on the structure and the location and nature of the loading. The convergence of the modal flexibility coefficients to their exact values depends on the location because at different locations on the structure, the effects of certain modes are higher than others. Whereas global modes determine only the general trend of the flexibility profiles, local modes help to define the complex shape of the deflections. Therefore, the more local modes are captured during the modal test, the better the convergence of the flexibility coefficients. The loading configuration, whether it is a point, patch or a line load, has an effect on the convergence of the flexibility coefficients because with different loading configurations, different elements in the flexibility matrix are included.

In the case of the present test, enough local modes of the bridge were captured to define the local behavior of the bridge. The convergence of the flexibility coefficients was slightly better in the middle span compared to the end spans because more local modes were captured in the middle span. Figure 6.9 shows the effect of using different number of modes in the flexibility matrix calculation. The deflection profiles were obtained from the analytical model by applying unit loads on the first and middle spans. The deflection profiles in Figure 6.9(a) show the difference between 30 modes and exact flexibility to be a maximum of 10%. The difference between 18 modes and exact flexibility is approximately 19% maximum. This indicates that there are some important local modes of the end span between mode number 18 and 30 that contribute to the flexibility. On the other hand,

Figure 6.9(b) indicates that flexibility due to 18 and 30 modes, due to the unit load on the middle span, is almost identical. Since obtaining 30 modes from such a structure is virtually impossible, the figure shows that 18 modes is about the best one can do for the flexibility convergence of the middle span. The maximum difference between 18 mode flexibility and exact flexibility is 7% which is far better than the convergence obtained in the end span.

### **6.3.7 Verification of the Modal Flexibility by Truck Load Testing**

Before the removal of the asphalt overlay and before the extent of the damage to the top of the deck was fully known, a series of truck load tests were conducted. These tests had four main goals: 1) To verify instrument performance; 2) To determine the suitability of truck load testing as a method of NDE; 3) To provide an independent verification of the modal flexibility; 4) To provide independent verification of the linear elastic finite element model. As was noted in Chapter 4, it was possible to verify the instrument performance during the truck load test. The fourth goal, to provide independent verification of the linear FE model is discussed in great detail in Chapter 8. Because most of the truck load test details are covered in Chapter 8, only a few relevant points are discussed here.

The instrumentation for the truck load test was an abbreviated form of the destructive load test instrumentation plan (see Figure 4.15). Because the deflections under truck load were expected to be small, the more accurate but shorter range DCDTs were used. These instruments were accurate to  $\pm 0.001$ ".

Combinations of one to three trucks were placed on the bridge in six different configurations (see Chapter 8, Figure 8.3 for all positions). Figures 6.12(a) and (b) show the results of two of these tests. The three lines shown in the deflection diagrams are the measured truck load deflections (truck test), the analytical deflections generated by the modal tests (modal tests) and the results of the linear finite element model (computer) which is discussed in Chapter 8. The longitudinal cross section in Figures 6.12(a) and (b) are the instruments along line "3" in Figure 4.15 and the transverse cross section refers to instrument line "D" in Figure 4.15.

When the single truck is used, the three deflection lines are similar for all three methods. Note that in this case the truck is positioned over the sound traffic lane concrete. However, when three trucks are used, thus positioning loads over the damaged shoulder regions, there is a larger difference between the three methods, especially in the transverse cross section of Figure 6.12(b). The difference between the truck test and the modal test will be discussed in the following sections. The difference between the FE model and the truck tests shows two important points: 1) The difference between the truck deflections and FE model shows that damage has made the bridge more flexible (a more complete treatment of this subject is in Chapter 8); 2) The damage is only apparent when the trucks are placed so that the damaged areas are mobilized for carrying load. Note that this second point is most important. In order to completely map damage on the bridge, a large number of truck positions are needed since damage can only be seen when the truck loads mobilize that area.

The need for a large number of different truck positions make the already cumbersome truck load testing more difficult and there is no way to assure that all possible damaged points are mobilized.

To verify the modal tests, load corresponding to the tire weight were placed on the modal analysis grid. Since the tire load rarely fell directly on a node, the tire loads were distributed to the surrounding nodes by linear approximation. Using the generated modal flexibility matrix, the predicted deflection profiles shown in Figures 6.12 a and b were generated.

The maximum difference observed between the truck load and modal test results is summarized in Table 6.5.

TRUCK LOAD CONFIGURATION	PERCENT DIFFERENCE (MAX)	
	LONGITUDINAL	TRANSVERSE
1 TRUCK	11 %	25 %
3 TRUCKS	18 %	24 %

**Table 6.5 - Comparison of the Truck Load Test Deflections With Modal Test Flexibility**

The difference in the transverse direction is greater because this cross-section corresponds to the maximum deflection values and the convergence of the flexibility coefficients for the modal test is poor in the end span especially at the maximum deflection point (see Figure 6.9). The difference between modal test and truck load test in the transverse cross-section for the case of three trucks is more or less uniform and about 25%. This is because all the flexibility coefficients along the transverse cross-section are being activated by the line loading pattern of the side-by-side trucks. Therefore, the convergence problem mentioned above holds for all the coefficients along this loaded line producing a consistent difference between the two profiles in the transverse direction.

Perhaps the most important observation from this study is: unlike the rational analytical model, the truck load and modal test deflection profiles are parallel, indicating that modal test identified the actual response pattern of the bridge due to a given loading. The immediate consequence of this observation is in the area of damage detection. Looking at the transverse deflection profile in Figure 6.10(b) reveals that whereas the analytical model shows a more stiff shoulder along the east edge of the bridge, both truck load and modal test results clearly indicate a lack of stiffness in this region. This deviation from the rational analytical behavior of the bridge indicated by both the truck load and modal test results, points to the presence of structural damage. The concept of damage detection using the results of the modal tests will be presented in detail in the following sections.

Truck load testing, which is a commonly used method in the rating of bridges, in general provides very sparse deflection information on account of being extremely hard to implement in numerous configurations on all the spans of a bridge. The above observations show the power of modal testing in predicting the actual responses of the bridge accurately and its being a potential replacement for the truck load tests. In fact, studies on other different types of highway bridges have shown that, especially for less deteriorated bridges, the results of the modal tests correlate very well with the truck load tests performed on the same bridge (Raghavendrchar and Aktan, 1992). One shortcoming of modal testing is the high level of expertise needed to perform the test and post-process its results to obtain modal parameters and consequently the modal flexibility. However, until sophisticated deflection measuring technologies such as laser holography enter the area of bridge engineering, modal testing may very well be a substitute or a complementary tool for truck load testing.

#### **6.3.8 Finite Element Modeling**

Two different finite element models were developed for damage evaluation and simulation purposes. The first one of these models was developed to represent the state of the bridge at the time of the first modal test. The second FE Model, on the other hand, was developed to model the state of the bridge at the time of the second modal test when the asphalt overlay had been removed and the loading blocks placed.

As mentioned earlier, the analytical model is developed for damage evaluation purposes as well as for the initial design of the modal test. The scope of this section will be to give a brief overview about the two analytical models, their calibration procedure and their utilization in the damage evaluation studies; more detailed information may be found in Zwick, 1992.

**The Nominal Finite Element Model:** First an a-priori model was developed. This model represented the bridge based on design dimensions, nominal material properties and simple boundary conditions. Figure 6.11 shows the mesh and the dimensions of this model; Figure 6.12 shows the abutment and pier details and gives the modeling parameters. The calibration of the nominal model was performed after obtaining the results of the first modal test. The calibration procedure was based on matching the frequencies and mode shapes of the FEM, as well as possible, with those of the modal model and hence the calibration was done in the modal space. In the process, boundary conditions and regional deck thicknesses were modified. The nominal model's parameters were calibrated by first getting the mode shapes in order, and then using a least squares approach to minimize the error between the experimental and analytical frequencies using the equation on the next page:

$$LSE = \sqrt{\sum (f_E - f_A)^2}$$

Where,

$f_E$  = experimental frequency

$f_A$  = analytical frequency at a given mode.

The least squares error (LSE) for the nominal model was calculated as 3.66 Hz. As a result of calibration, this value dropped down to 1.84 and the percentage of error for any of the first twelve modes was found to be below 5%. The abutment and pier modeling details and model parameters of the calibrated model are given in Figure 6.13. The thickness of the shell elements along the shoulders were reduced slightly to match the visible deterioration. Figures 6.14(a) through 6.14(d) show the comparison between the analytical and experimental mode shapes and frequencies. Observing the experimental end span mode shapes (e.g. modes 5,6,8,9), it is seen that most modes appear in sets of two with only one end moving significantly in each end span mode. In the corresponding analytical mode shapes however, it is seen that, rather than a single end moving, both ends exhibit motion, either in phase or out of phase with each other. This is attributed to the symmetries of the analytical model. These symmetries however do not necessarily exist in real life due to imperfections. Nevertheless, the analytical and experimental mode shapes and frequencies show a good correlation.

**Second Finite Element Model:** The second finite element model was developed to account for the changes that the bridge underwent after the first modal test. These changes were: The removal of the asphalt overlay, installation of the two loading blocks and a new modal test grid. Since the overlay was not expected to contribute to the overall stiffness of the bridge, the removal of the asphalt overlay was accounted for by decreasing the mass of the bridge. The additional mass due to the loading blocks and cylinders was incorporated into the model by smearing the mass of these blocks onto the nearby elements. The mesh chosen for the new FEM was slightly different from the previous one and it was designed to match the modal test grid at the node points. This task was achieved by subdividing the modal test mesh, thus allowing the bridge responses to be determined at the same locations from both the modal flexibility and the FEM due to any load condition. The finite element mesh for the second model is shown in Figure 6.15.

With the experience gained from the calibration of the first analytical model, it was decided to perform a more detailed calibration on the second model in the flexibility space following the modal space.

The first step in the calibration was to get the modes in order and reduce the least squares error in the frequencies, similar to the method used in the first model. After achieving a reasonable globally calibrated model, the next step was to compare flexibilities.

This was done by uniformly loading (unit load at every common point) the flexibility matrices obtained from both the analytical and modal models and comparing the deflection values of each corresponding point. The reason behind using uniform loading as opposed to any other type of loading was to utilize the information from all the columns of the flexibility matrix at the same time.

As it was mentioned earlier, the modal flexibility matrix is only an approximation to the exact flexibility matrix due to truncation. Therefore, it is best to calculate flexibility matrices of both models, analytical and modal, by including only the modal vectors common to both models. Therefore a method was developed which enabled the comparison of "corrected" modal flexibility coefficients with exact flexibility from the analytical model. Correcting the modal flexibility was achieved by finding a correction factor that would account for the missing modes and multiplying the modal flexibility by this factor. This was done by calculating the exact deflections at each node due to uniform load on the bridge and dividing them by the deflections found from the incomplete analytical flexibility matrix. In this case, 19 modes that corresponded to the modal test results were used to calculate the correction factor (CF):

$$CF(N) = \frac{D_{EXACT,N}}{D_{MODES,N}}$$

Where,

N = point number on the test grid

$D_{EXACT,N}$  = exact deflection at point N due to uniform loading of FE model;

$D_{MODES,N}$  = deflection at point N due to the uniform loading of the analytical flexibility calculated using limited number of modes.

The resultant deflections from this corrected flexibility, due to different loading patterns, served to identify the boundary conditions as well as the regional effective deck thicknesses of the bridge. The comparison of the exact analytical flexibility and corrected flexibility clearly showed that the deck thickness had to be reduced. Accordingly, the thickness was reduced from the design value of 17.25" to 16.50". It was discovered that the value of the vertical spring stiffness at the abutments and piers had a great effect on the deflection profiles. Further adjustments brought the thickness of the end spans down to 15.50". Also, a region over the east section of the north pier was found to have lost some of its structural continuity. This section was modeled with an extra row of 9 inch wide shell elements. The thickness of the elements closer to the east shoulder over the pier was reduced to simulate the loss of continuity. The notable conclusion from the local calibration of the model was that the deteriorated shoulders had little effect on the structural integrity of the bridge. In no part of the local calibration was the shoulder deck thickness needed to be reduced. The inability of the procedure to identify the deterioration along the shoulders is attributed to

the low levels of excitation in the impact testing and the stiffness retained by the shoulders in spite of deterioration. The nominal and final calibrated models are shown in Figures 6.16(a) and 6.16(b). Figures 6.17(a) through 6.17(d) compare the analytical and experimental mode shapes and frequencies.

The most important conclusion reached from local calibration is that this procedure has the ability to identify and quantify any discrepancies seen between the modal test and baseline model (modal or analytical). In other words, it may not be possible to identify the nature of damage seen in the form of a discrepancy in the deflection profiles by only visual observation. In these cases, it is worthwhile to perform a local calibration on the analytical model for the purposes of identifying the nature of the damage, quantifying and localizing it. Even though at this time local calibration is a tedious procedure which is very much dependent on experience and insight, it is a promising way of identifying the nature and amount of damage at an element level. Research is in progress to develop automated methods for locally calibrating a FE Model based on the results obtained from field tests.

#### **6.3.9 Damage Identification**

This section is divided into two parts: Identification of existing damage using the results of the first modal test and the finite element model; and identification of the loading induced damage using the results of the second and third modal tests. The first part involves using the finite element model developed for the first test as a baseline. The damage is identified by comparing the deflection profiles calculated from the flexibility matrices of both the analytical model and the modal test. In the second part, damage identification is performed by comparing the first stage modal parameters, namely, frequencies damping and mode shapes of the second and third tests as well as their flexibility matrices. Here, the second modal test serves as the baseline.

**Identifying Existing Deterioration Without a Baseline:** The nominal analytical model developed for the first test was calibrated in the modal space using the results of the first modal test to provide a suitable analytical baseline. In order to correlate comparable quantities, the modes that were common to both the modal test and FEM were selected and used in the calculation of the respective flexibility matrices. These matrices obtained from the measured and analytical modes were loaded with different load configurations and the corresponding flexibility profiles were compared. The first diagnostic load configuration was chosen to be uniform loading with 1000 lbs at each node. The resultant flexibility profiles (3-D surface and 2-D cross sections) per node are shown in Figure 6.18. Uniform loading caused all the entries in the flexibility matrix to contribute to the resulting deflection profile. In this manner it was intended to detect the locations that were damaged by observing the discrepancies in the flexibility profile. As can be seen from Figure 6.18, such discrepancies exist between the analytical model and modal test results, particularly in the form of kinks at shoulders. However, it should be emphasized that the differences seen between the two

models' flexibility profiles may not necessarily point to damage. These differences may simply originate from modeling parameters used in the calibration of the FEM or even from experimental errors. What is being sought here are unusual trends in the modal test deflection profiles that may point to the existence of possible damage or structural degradation. Naturally, a carefully controlled testing process and accurate results in the form of frequencies and modal vectors are essential for a reliable flexibility correlation procedure.

**Identifying Loading Induced Damage:** This section illustrates the capability of modal test to identify damage given that baseline information is available for the structure. The results of the second modal test, conducted prior to the controlled loading phase, constitute the baseline model. The results of the third and fourth modal tests, on the other hand, represent the damaged state of the structure. At the time the third test was conducted, the structure was visually intact and undamaged, whereas during the fourth test the structure had been severely damaged. The second and third test comparison has a special value since it is a very good demonstration of the ability of the modal test to detect critical structural damage. Before the third test was conducted, the bridge had been subjected to a load equivalent to twenty rating trucks and showed absolutely no signs of impending failure.

The studies performed on the results of the three modal tests are given below. Considering that the bridge failed after being loaded to the equivalent of twenty-two rating trucks just before the fourth test and a portion of the structure could not be tested, only the changes in the frequencies and damping of the first few modes are presented and flexibility is not investigated for the fourth test. The reader is referred to Figure 6.3 which shows the second and third modal test grids and the position of the loading blocks.

#### 6.3.10 Comparison of Frequencies, Damping and Mode Shapes

The comparison of frequencies and damping factors is given in Table 6.6. This table compares the results of tests two through four. The percent change columns represent the change in the results of the third test relative to the second test. It is observed that all the frequency shifts are less than 5%. Although the damping coefficients do indicate marked changes, the order of magnitude of possible experimental errors and processing in the measured damping coefficients is similar. Therefore neither the frequencies nor the damping coefficients can be used as sensitive indicators of damage. The mode shapes (Figures 6.5 and 6.6) are not revealing any marked changes either.

In conclusion, although a considerable number of frequencies, mode shapes and damping coefficients are available from the 2nd and 3rd tests, even such a wealth of modal data does not definitely reveal the damage which the bridge experienced after the 2nd test. Hence the use of modal flexibility as discussed in the following.

Mode #	TEST 2		TEST 3		TEST 4		T2 vs T3 Δf(%)	T2 vs T3 Δζ(%)	Mode Shape Description
	f(Hz)	ζ(%)	f(Hz)	ζ(%)	f(Hz)	ζ(%)			
1	8.757	1.805	8.631	2.166	8.573	1.705	-1.44	20.00	GLOBAL
2	11.11	1.868	10.97	2.090	10.78	1.906	-1.26	11.88	GLOBAL
3	13.37	4.507	12.70	4.257	13.22	3.179	-5.01	-5.55	GLOBAL
4	13.89	2.627	13.90	2.734	...	...	0.07	4.07	GLOBAL
5	15.47	3.032	14.88	3.574	15.99	3.284	-3.81	17.87	LOCAL LEFT
6	15.91	1.924	15.83	1.884	15.81	1.912	-0.50	-2.08	LOCAL RIGHT
7	20.44	1.276	20.20	1.363	19.98	1.285	-1.17	6.82	LOCAL MID
8	23.26	2.975	22.29	3.503	...	...	-4.17	17.75	LOCAL LEFT
9	23.41	1.651	23.41	1.736	23.36	1.764	0	5.15	LOCAL RIGHT
10	27.30	2.051	26.87	2.143	26.37	2.329	-1.58	4.49	LOCAL MID
11	30.23	1.519	29.90	1.635	29.63	2.078	-1.09	7.64	LOCAL MID
12	37.15	2.987	34.98	3.213	...	...	-5.84	7.57	LOCAL LEFT
13	37.71	2.398	37.45	2.594	37.28	2.957	-0.69	8.17	LOCAL RIGHT
14	43.21	1.536	42.53	1.617	42.49	1.668	-1.57	5.27	LOCAL MID
15	47.14	1.955	46.69	2.037	46.39	1.981	-0.95	4.19	LOCAL MID
16	49.11	3.814	51.43	3.153	...	...	4.72	-17.33	LOCAL RIGHT
17	51.40	4.393	51.62	3.438	50.81	3.618	0.43	-21.74	LOCAL LEFT
18	55.18	4.408	53.63	3.536	52.04	5.523	-2.81	-19.78	LOCAL LEFT
19	55.58	2.720	55.54	2.583	55.35	2.510	-0.07	-5.04	LOCAL RIGHT

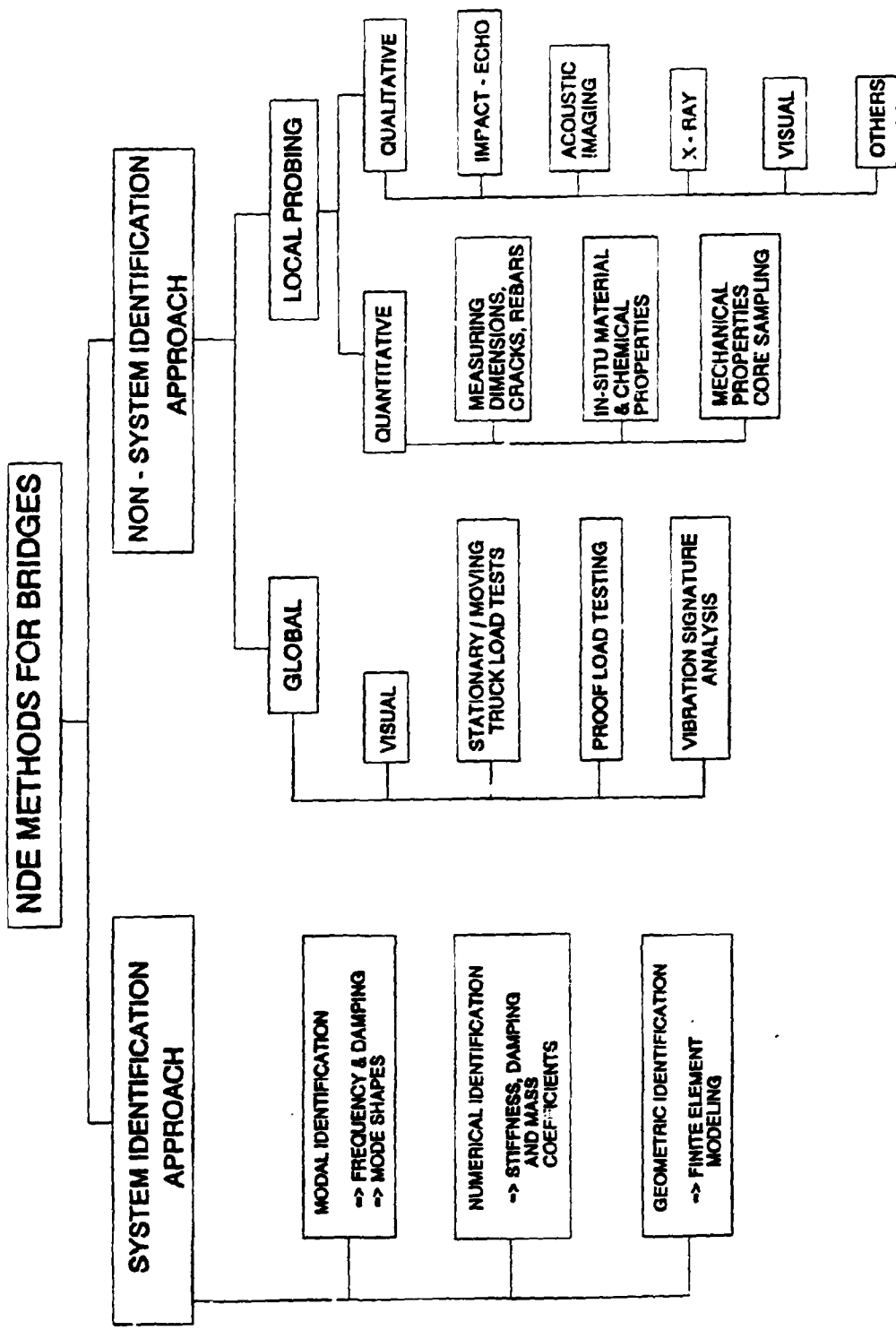
Table 6.6 - Comparison of Frequencies and Damping Values for Tests 2, 3, and 4

### 6.3.11 Comparison of Flexibility Profiles

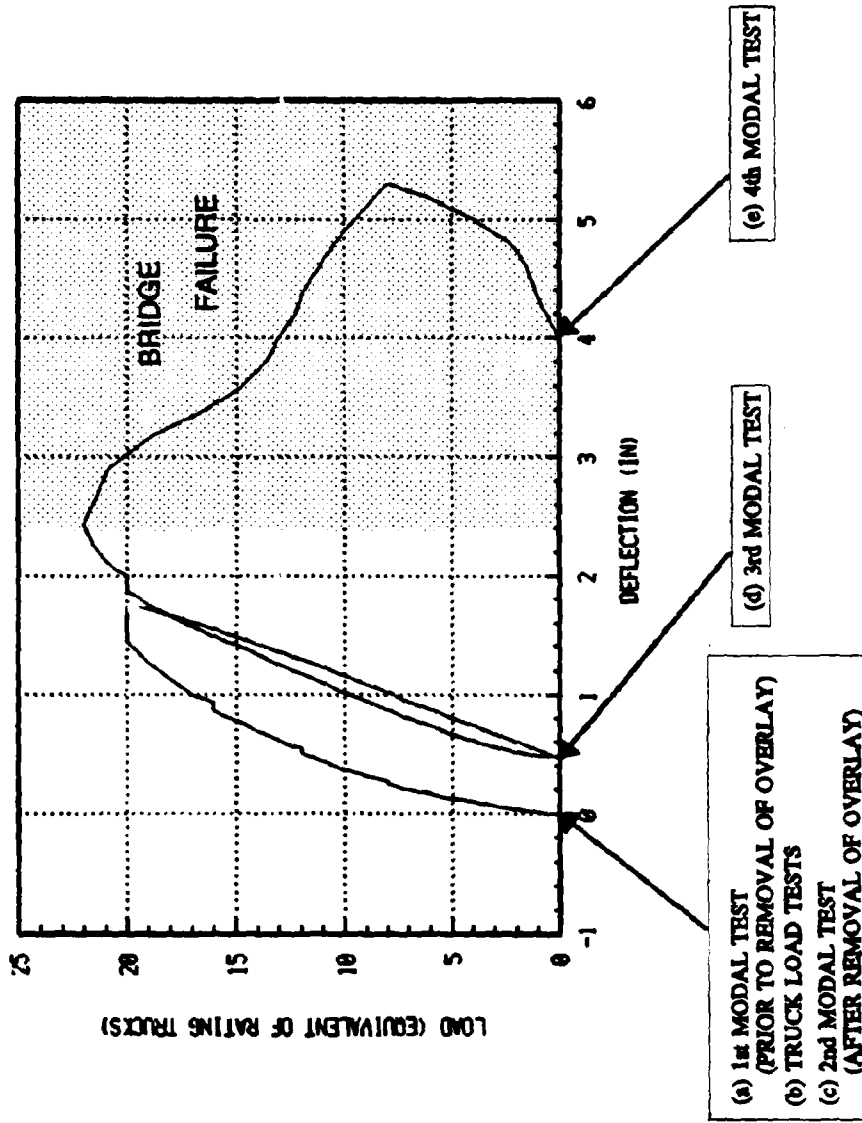
As usual, uniform loading deflection profiles were compared first (Figure 6.19). A clear discrepancy is observed between the baseline test results and the third test results. This difference is seen around the area where the loading blocks were positioned. The plot of deflections along section A-A. The plots of deflections along B-B indicates loss of stiffness due to damage on the other hand, indicates the damage is on the east side where the loading blocks were placed, compared to the west side. The location and nature of the damage was further investigated by using different line loading configurations.

Figure 6.20 shows the comparison of the flexibility profiles due to a line load on line C. The difference between the results of the two tests is apparent from the cross-section plot which shows test three deflections as much as 34 percent more when compared to test two. The same phenomenon is observed in Figures 6.21 and 6.22 which show test three deflections exceeding the baseline deflection values by as much as 30 to 40 percent when lines D and E are loaded respectively. When line F is loaded as seen in Figure 6.23, however, the difference between the two deflection profiles becomes less and takes a different shape. This is due to the diagnostic loading moving away from the maximum damage location. The preceding figures illustrate that by using this method, it is possible not only to quantify the damage but also localize it. This observation becomes clearer when Figures 6.24 and 6.25 are studied. Figure 6.24 shows the resulting deflection profiles due to a line load in the middle span. As can be seen from the figure, the difference between the two profiles drops down to 10 to 15 percent. This difference is attributed to the possible damage incurred by the pier connectivity due to the loading in the left span, which affects the continuity between the left and the middle slabs. Figure 6.25 shows the deflection profiles due to a line load on the far right span. As can be seen from the plots, there is little or no difference between the profiles of the two tests. This shows that the effects of the damage in the left span becomes diminishingly less as one moves further away from the damaged location. Using this method, different loading configurations and different cross-section plots may be studied to locally define the damaged region(s) on bridges. As an example, Figure 3.26 shows a patch load applied over the damaged region and the resulting flexibility profiles.

It may be concluded that in the presence of a baseline, modal flexibility has a remarkable capacity to diagnose damage that may not be visible. On the other hand, individual mode shapes or frequencies are not sensitive, as has been pointed out by many researchers.



**FIGURE 6.1: CLASSIFICATION OF NDE METHODS APPLICABLE TO BRIDGES**



**FIGURE 6.2: LOADING HISTORY AND STAGES AT WHICH MODEL TESTS WERE CONDUCTED**

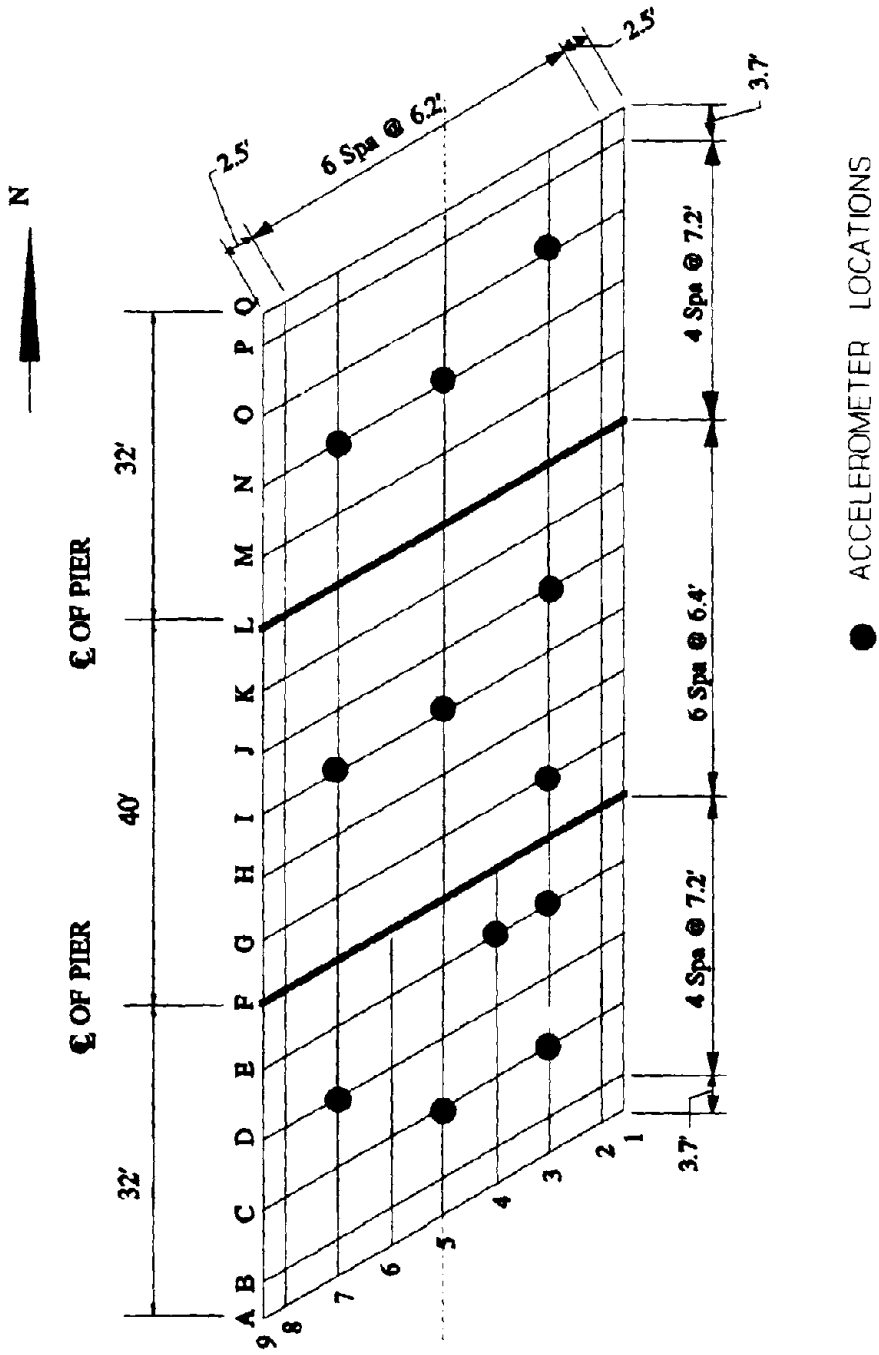
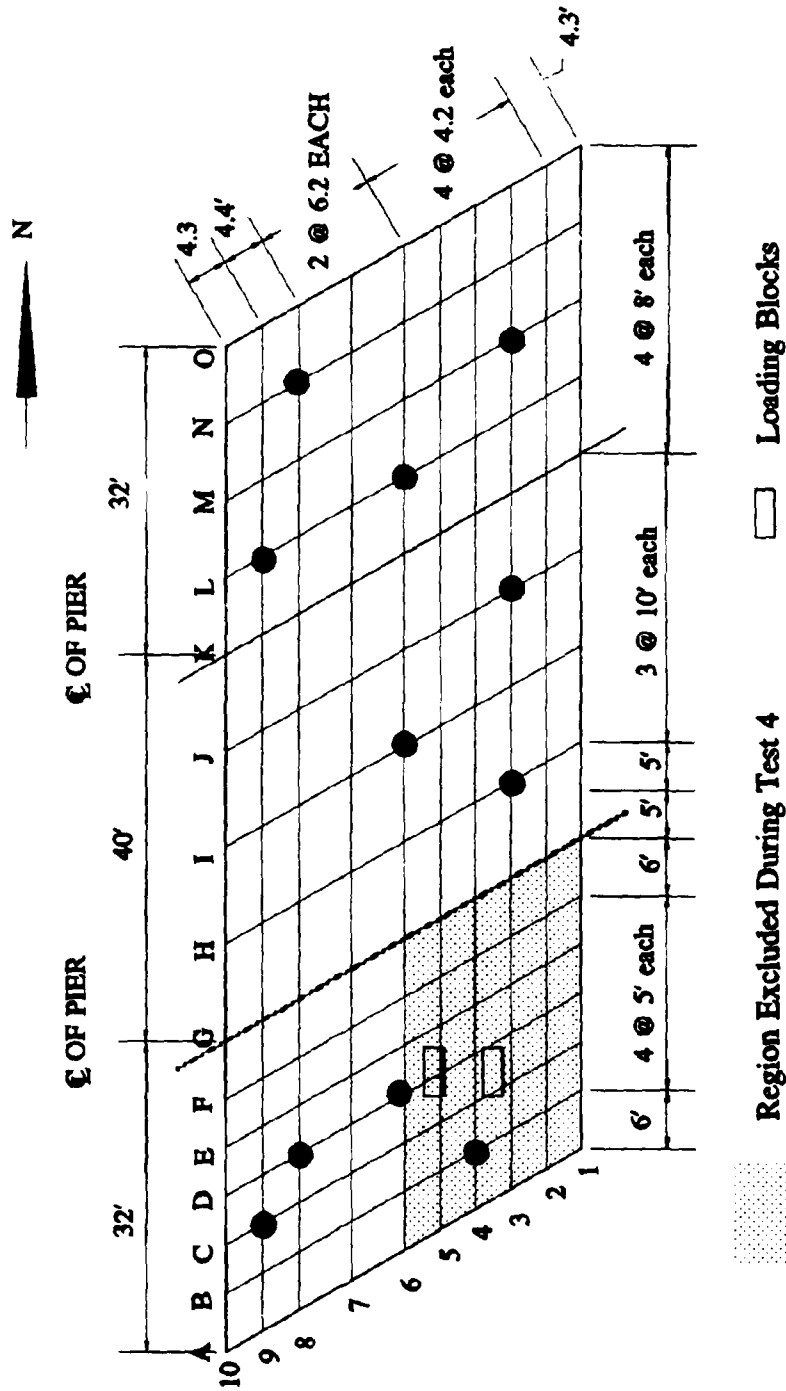


**FIGURE 6.3(a): FIRST MODAL TEST GRID**



● ACCELEROMETER LOCATIONS

FIGURE 6.3(b): SECOND, THIRD AND FOURTH MODAL TEST GRIDS

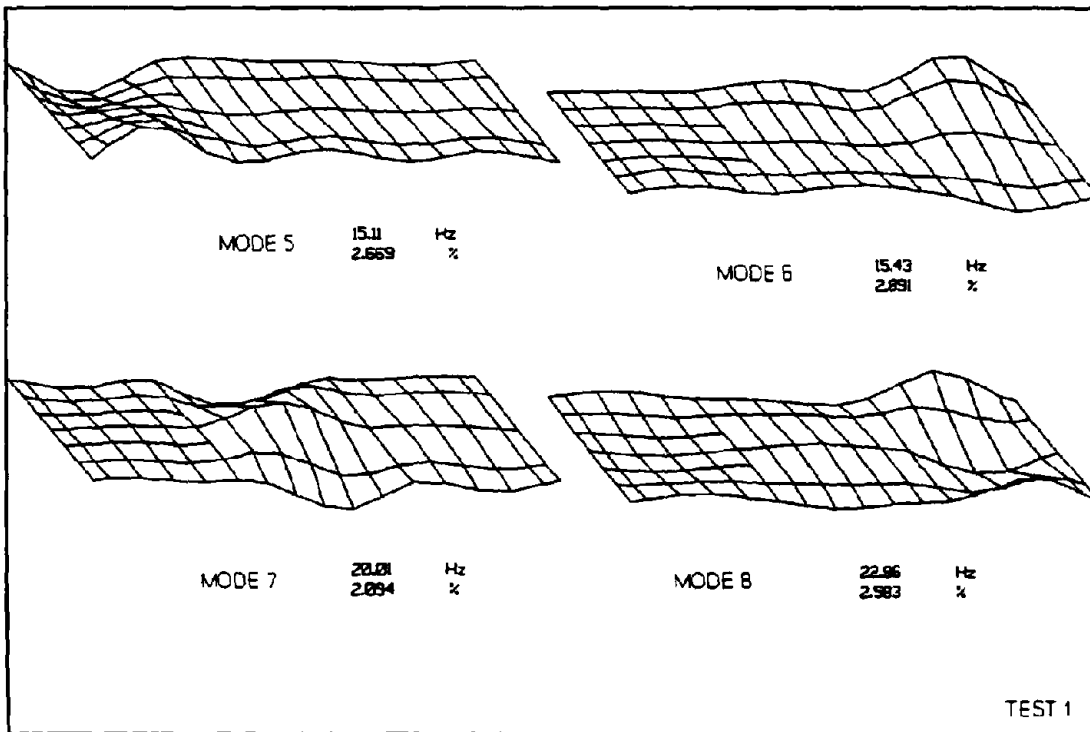
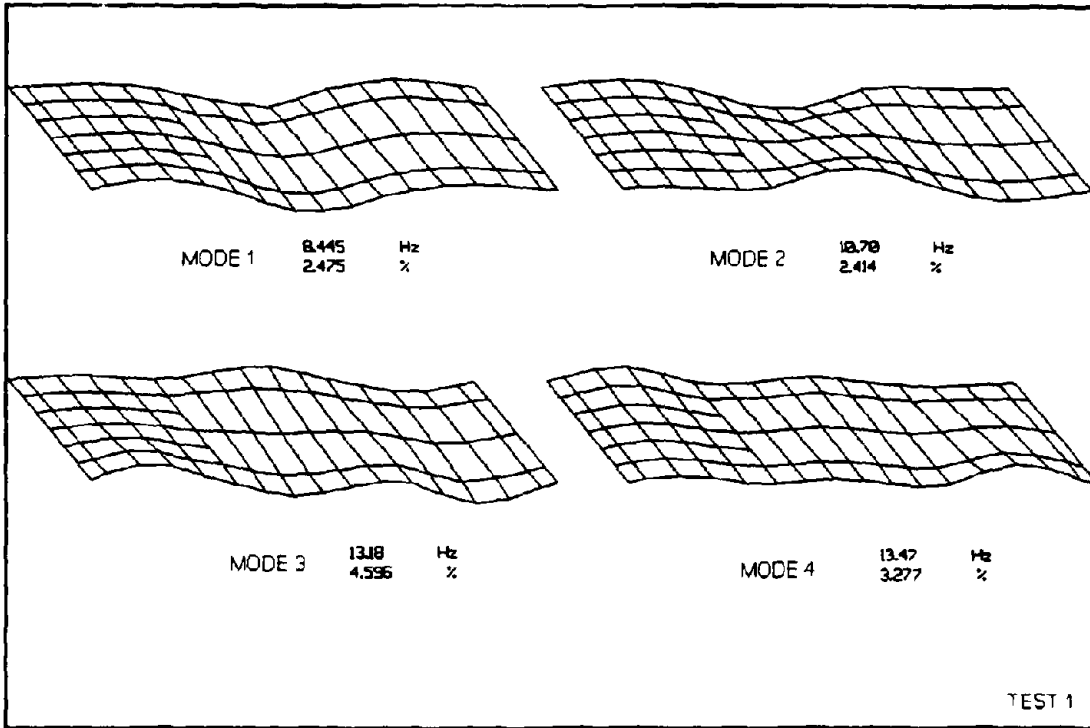


**FIGURE 6.4: MODE SHAPES FROM TEST 1**

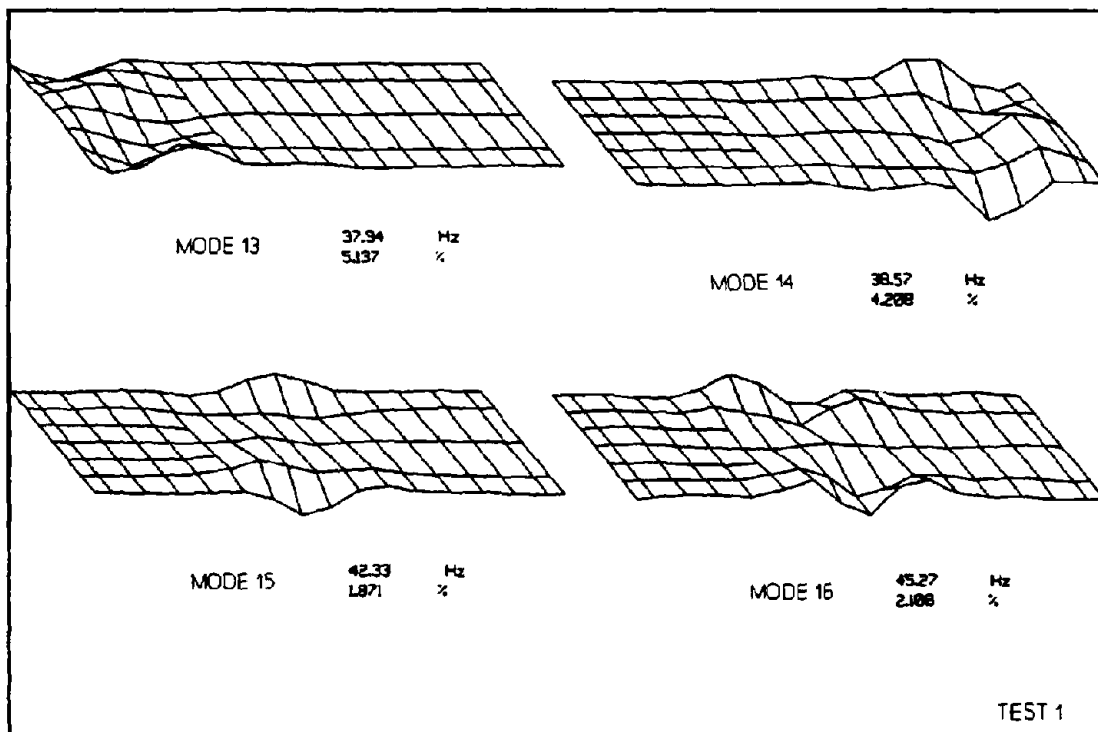
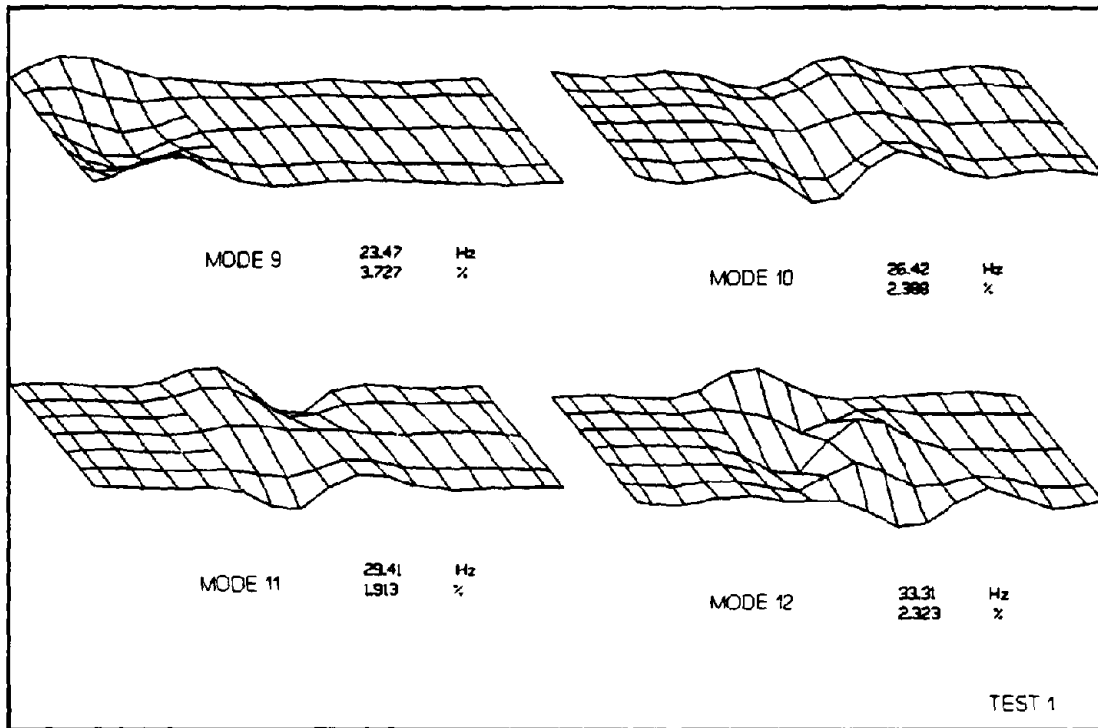


**FIGURE 6.4: MODE SHAPES FROM TEST 1 (CONTINUED)**

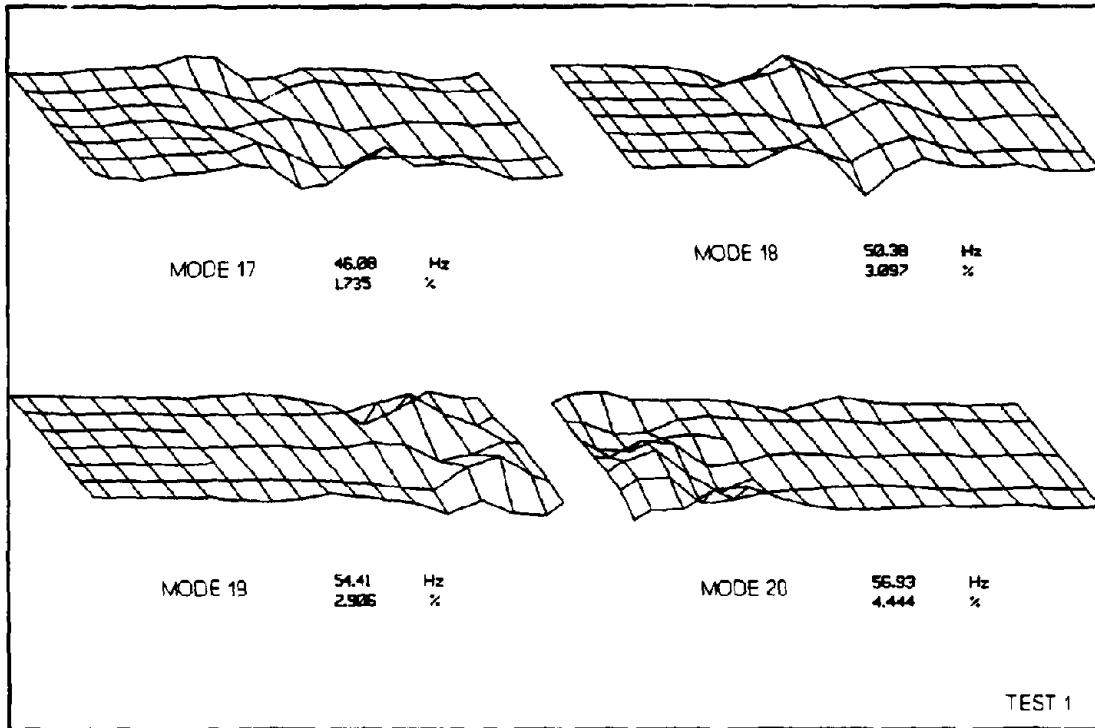


**FIGURE 6.4: MODE SHAPES FROM TEST 1 (CONTINUED)**

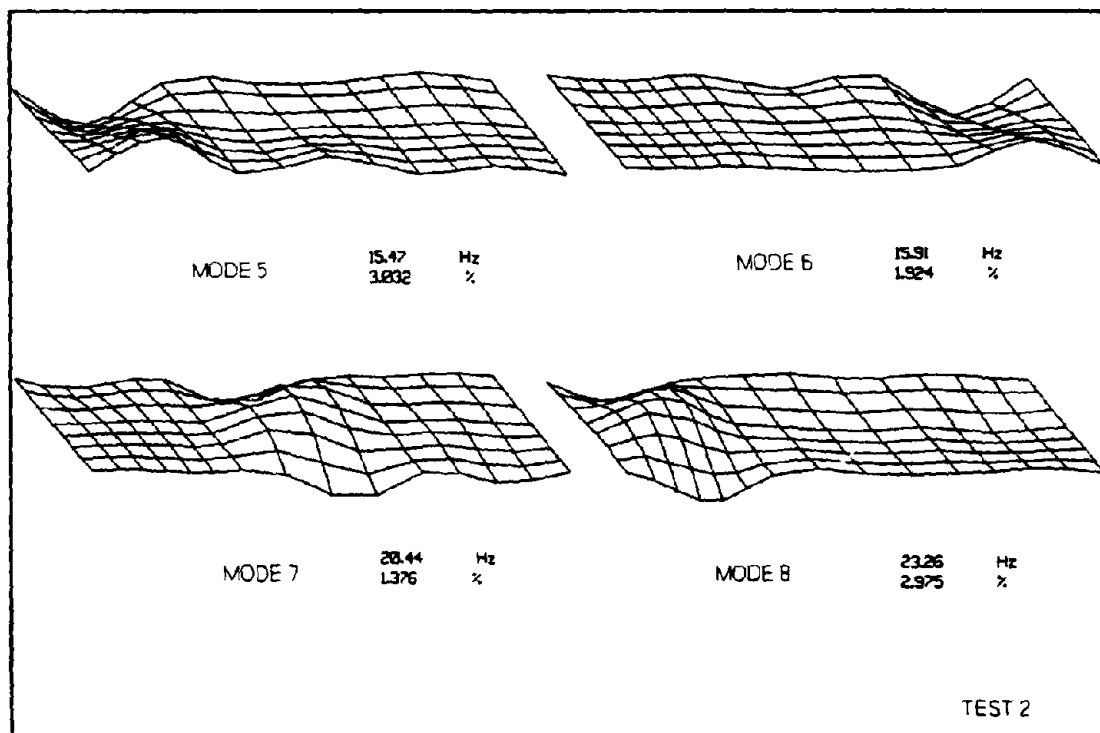
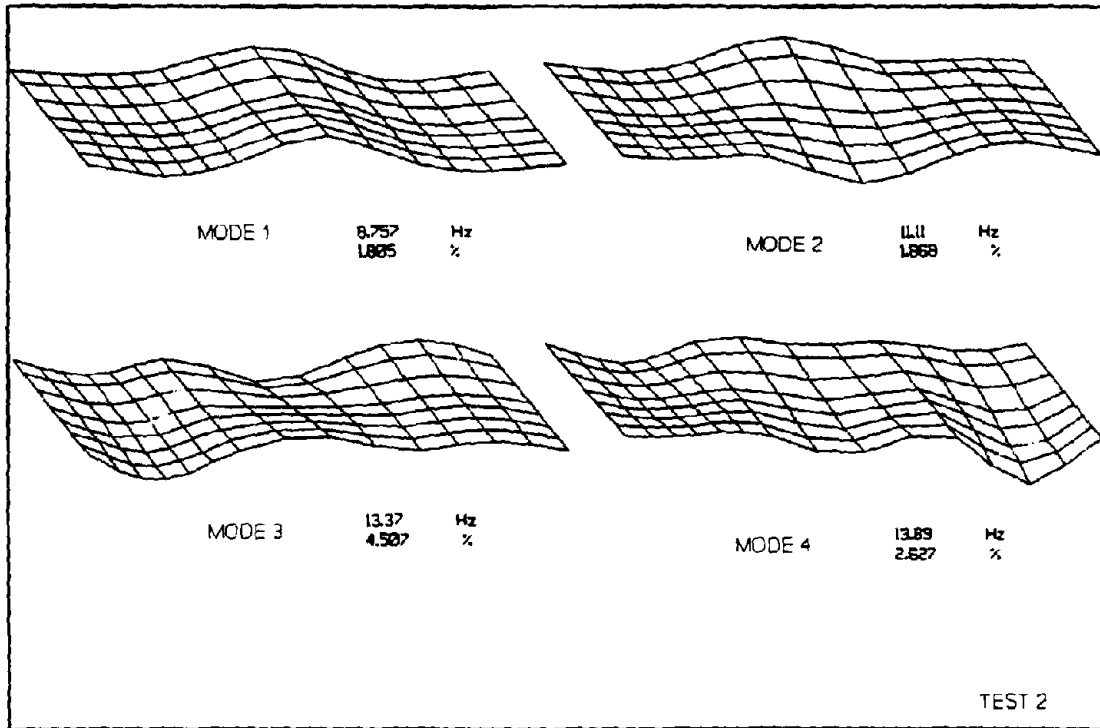


**FIGURE 6.5: MODE SHAPES FROM TEST 2**

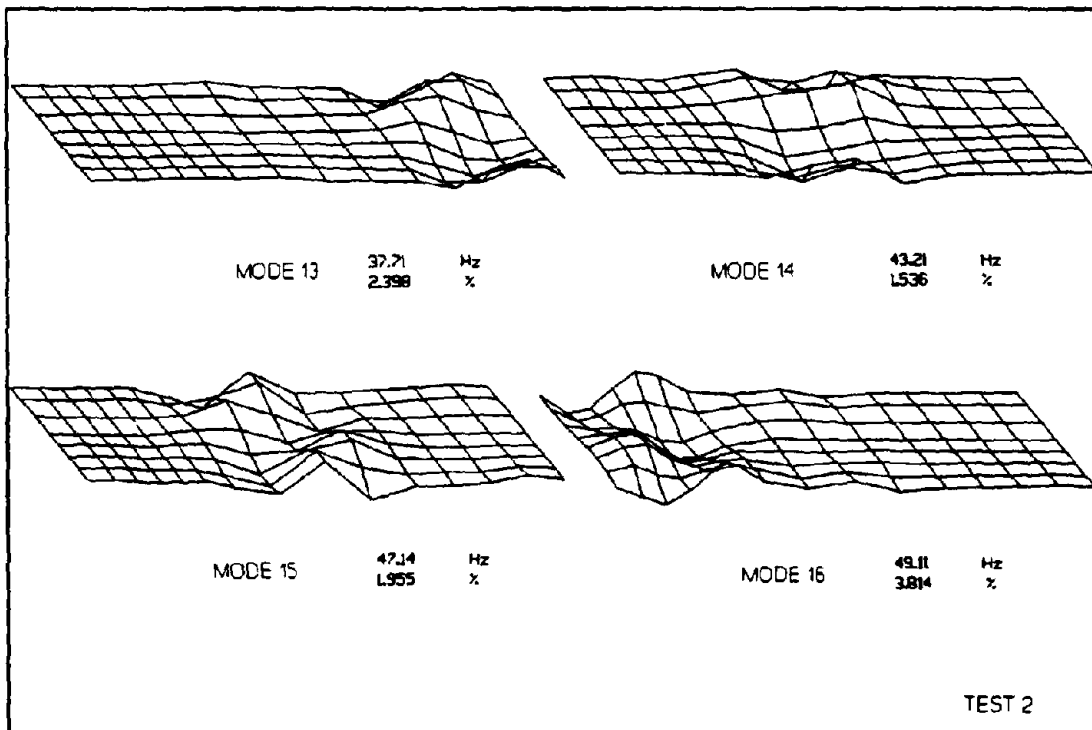
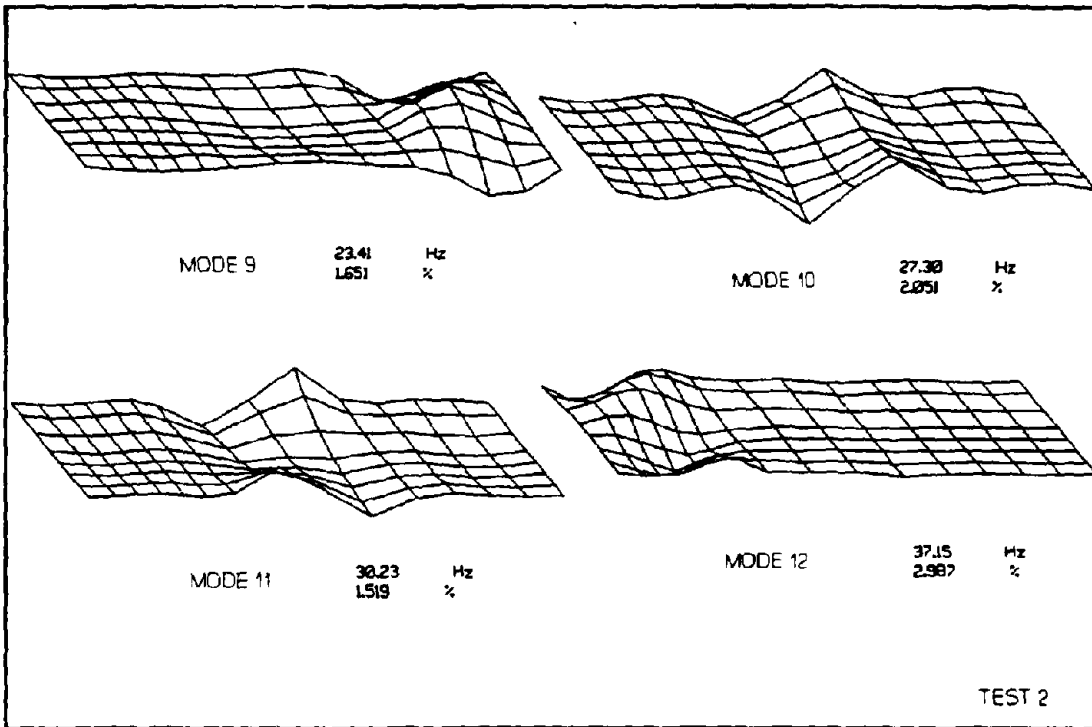


**FIGURE 6.5: MODE SHAPES FROM TEST 2 (CONTINUED)**

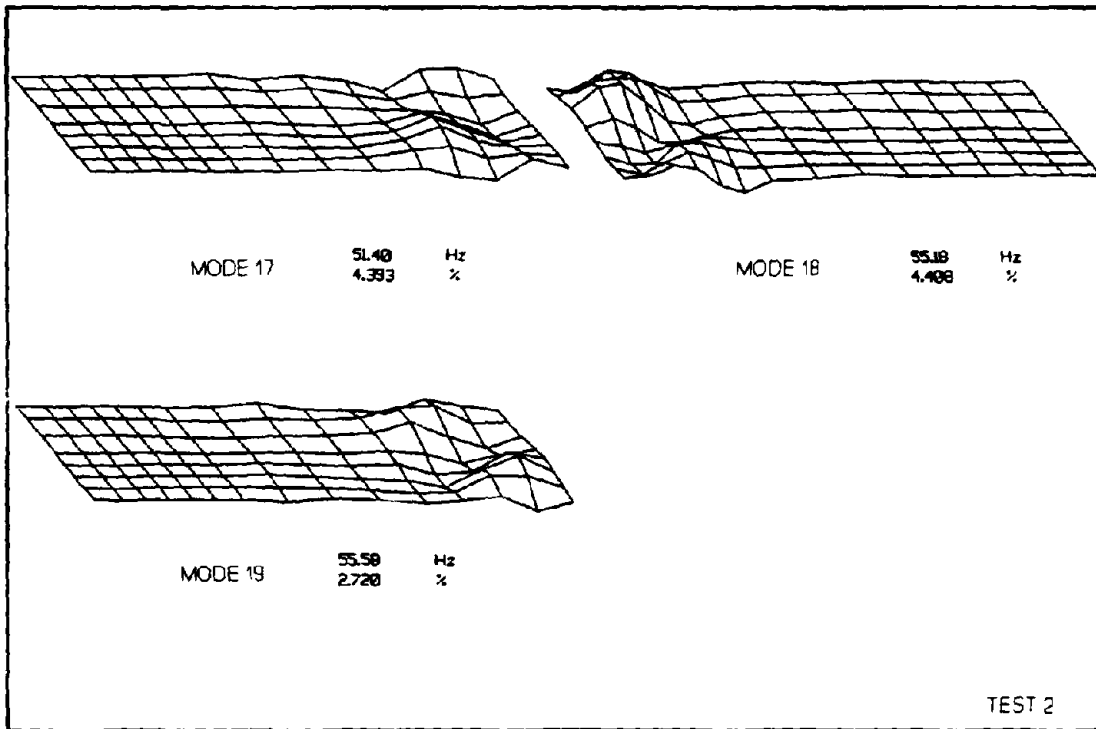


**FIGURE 6.5: MODE SHAPES FROM TEST 2 (CONTINUED)**

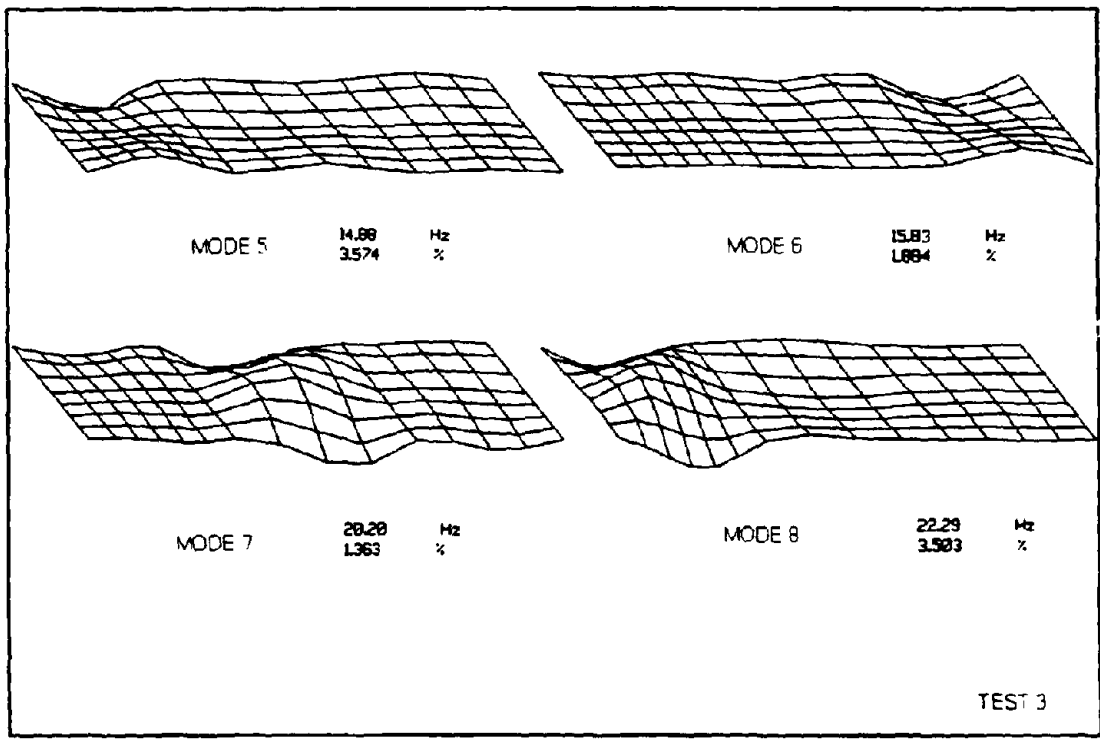
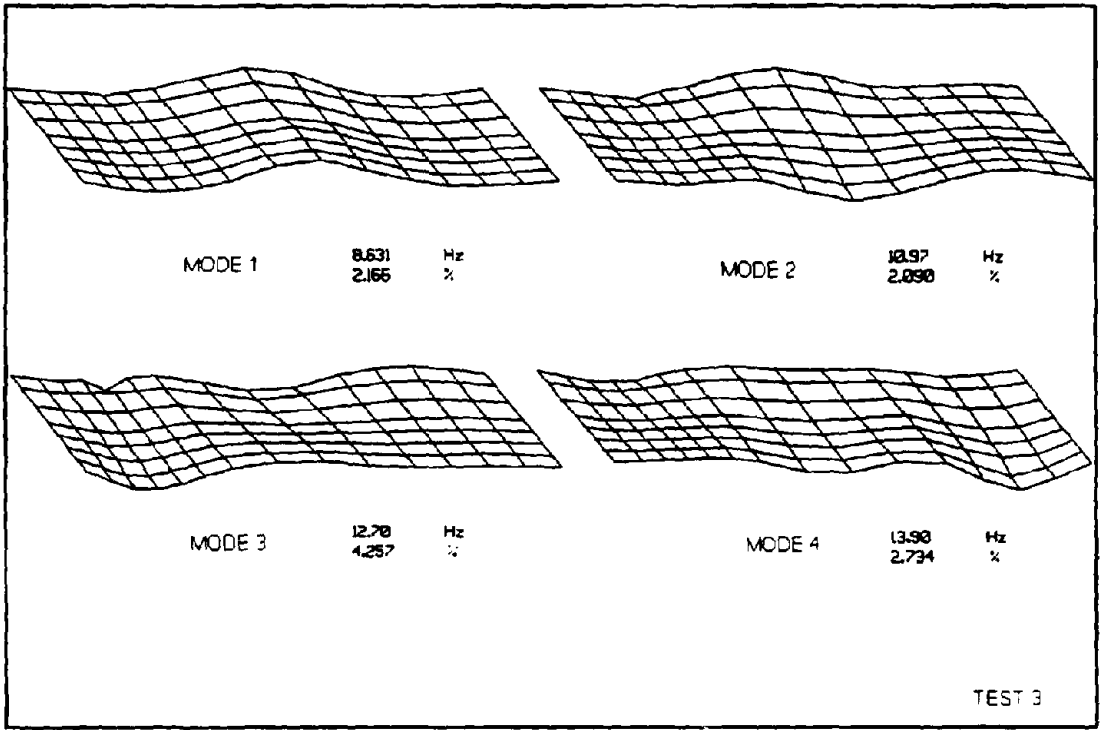


**FIGURE 6.6: MODE SHAPES FROM TEST 3**

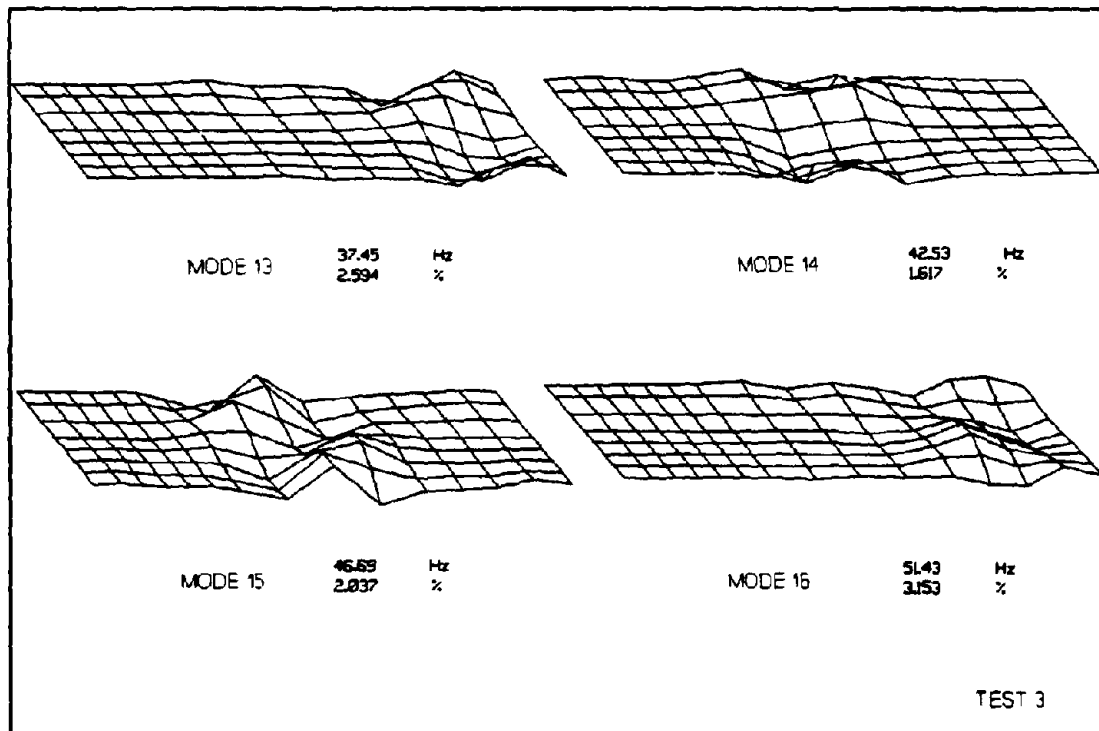
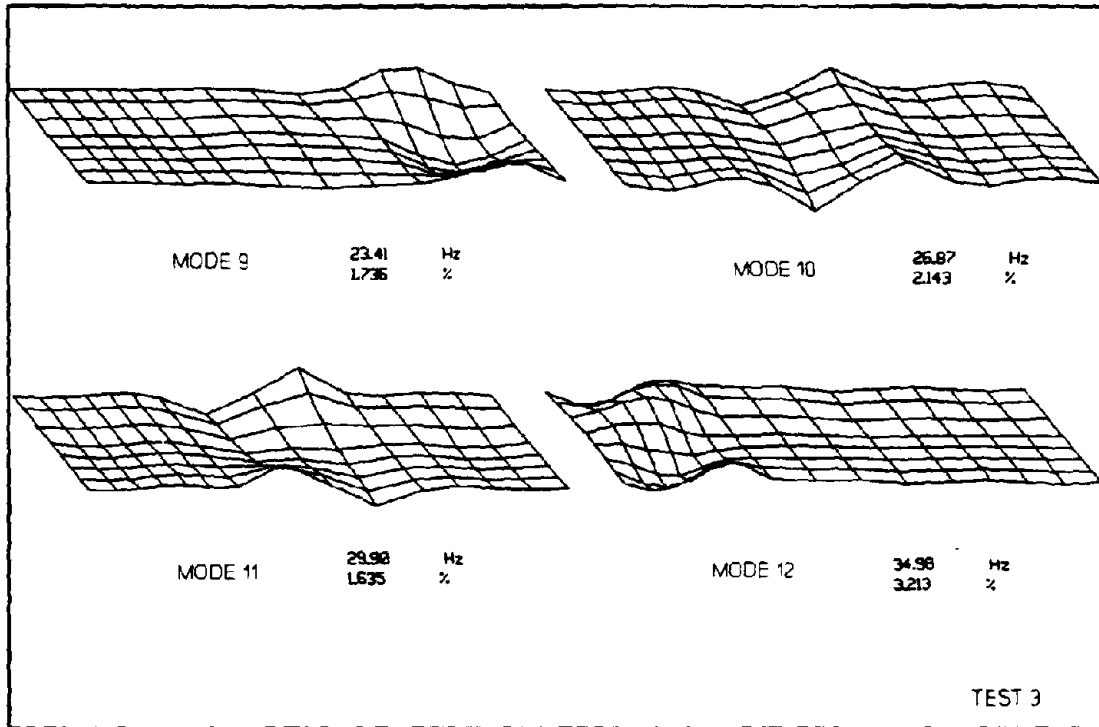


**FIGURE 6.6: MODE SHAPES FROM TEST 3 (CONTINUED)**

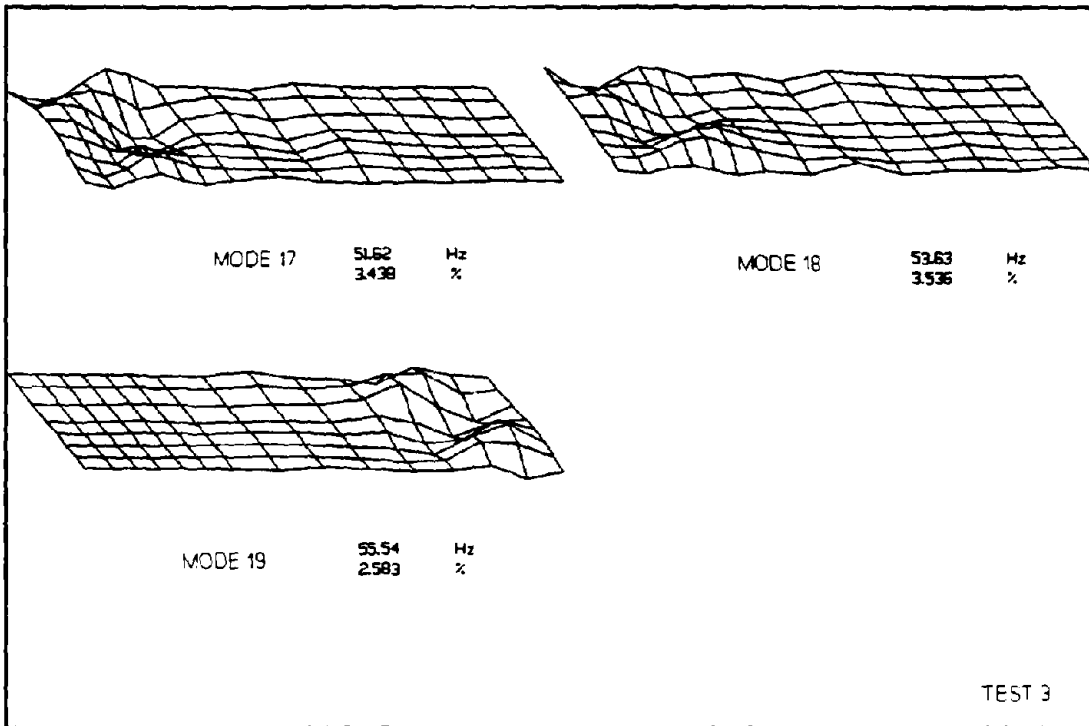


**FIGURE 6.6: MODE SHAPES FROM TEST 3 (CONTINUED)**

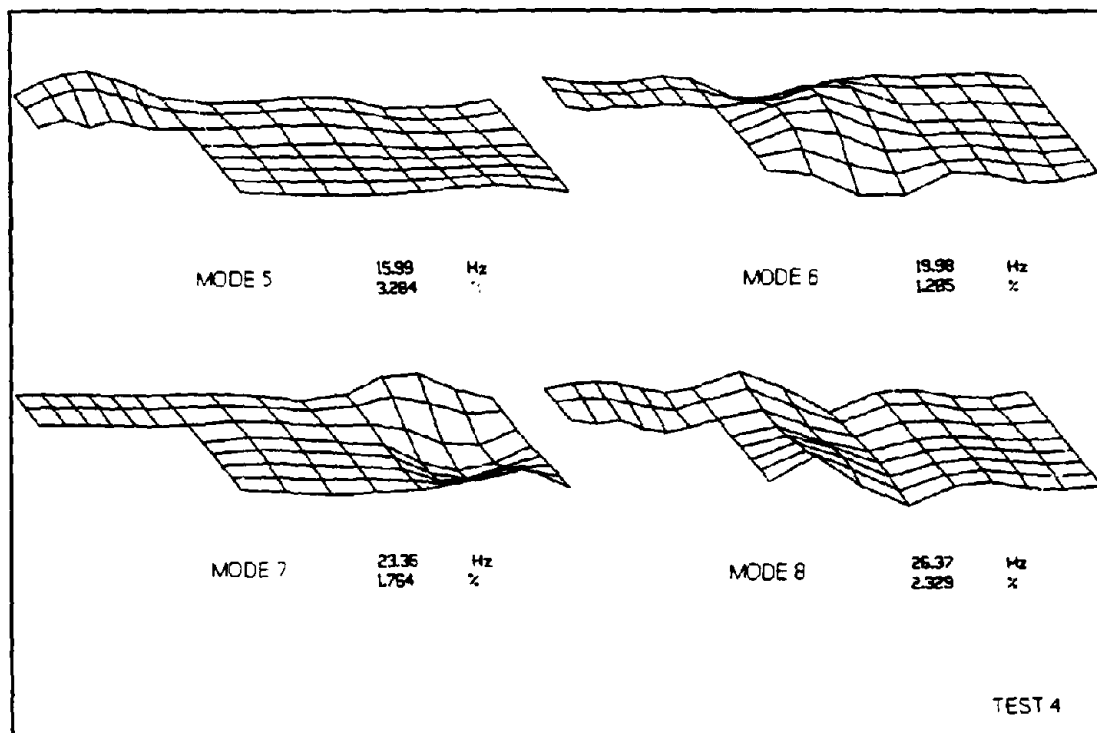
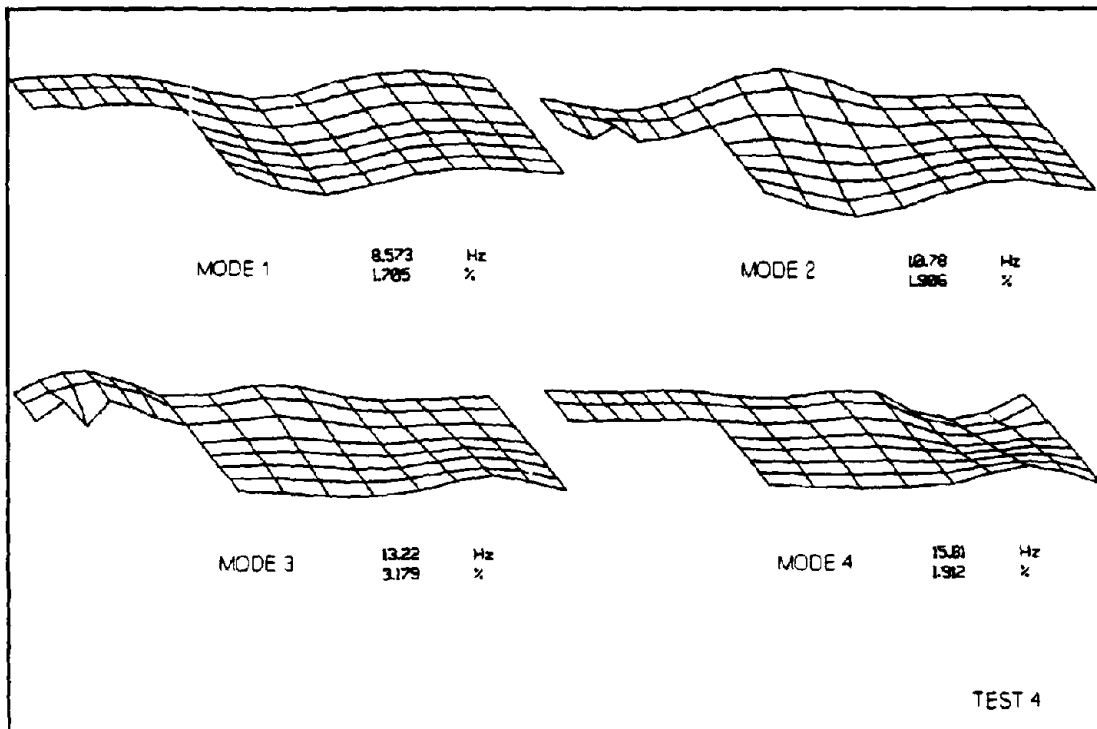


**FIGURE 6.7: MODE SHAPES FROM TEST 4**

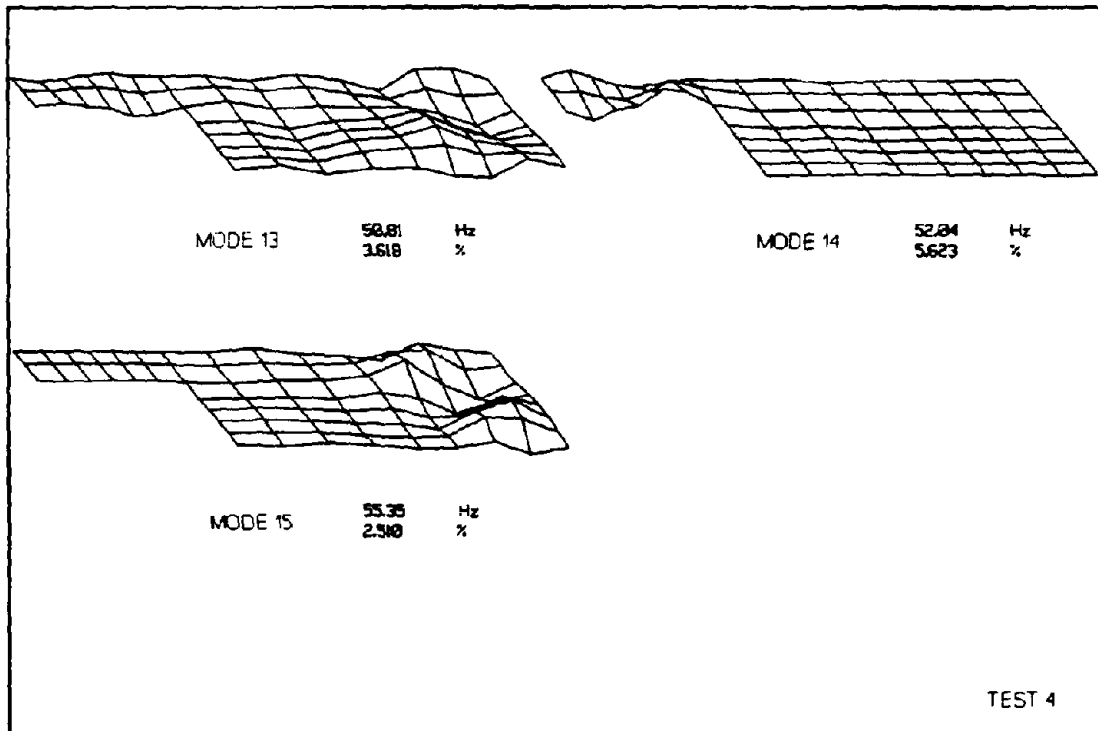
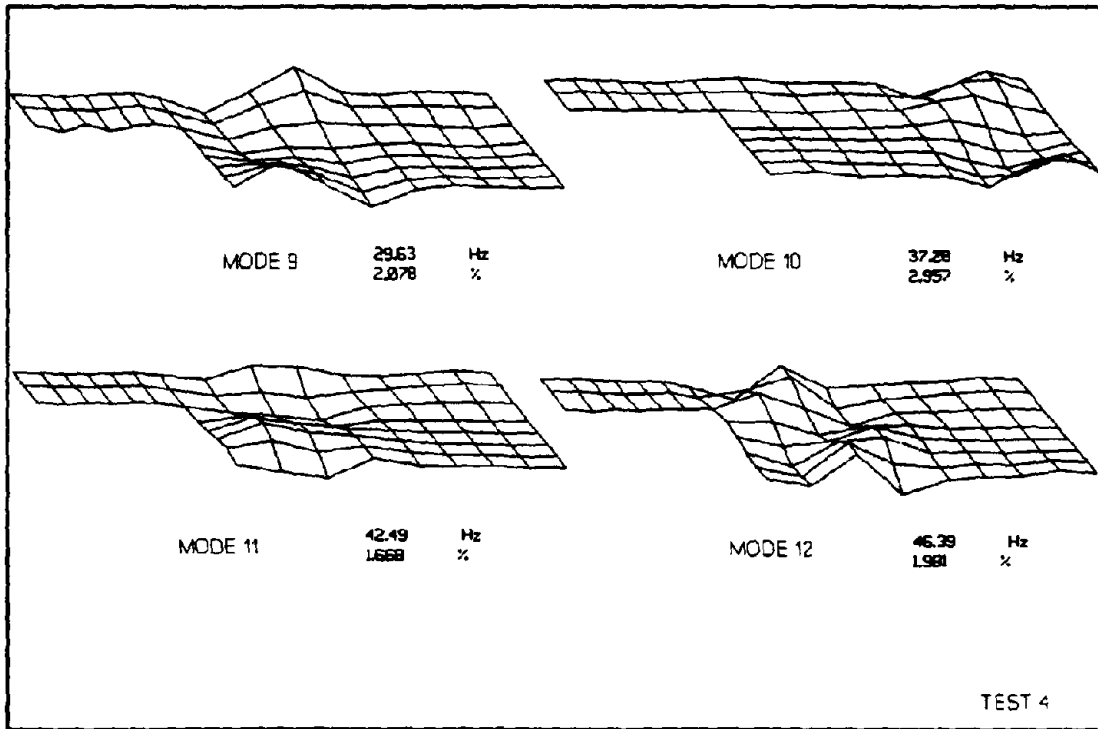


**FIGURE 6.7: MODE SHAPES FROM TEST 4 (CONTINUED)**

## FLEXIBILITY MATRIX AS A SIGNATURE OF THE STRUCTURE

$$[F] = [\psi] [1/\omega^2] [\psi]^T$$

$$\{U\} = [F] \{L\}$$

$$\{U_j\} = \begin{bmatrix} f_{1j} \\ \vdots \\ f_{Nj} \end{bmatrix} \quad \begin{bmatrix} 0 \\ \vdots \\ 1 \\ \vdots \\ 0 \end{bmatrix} \quad \begin{matrix} N \times N \\ N \times 1 \\ N \times 1 \end{matrix}$$

$[\psi]$  : mass normal modal vec.  
 $\omega$  : natural freq.  
 $\{L\}$  : load vec.  $\{U\}$  : defl. vec.

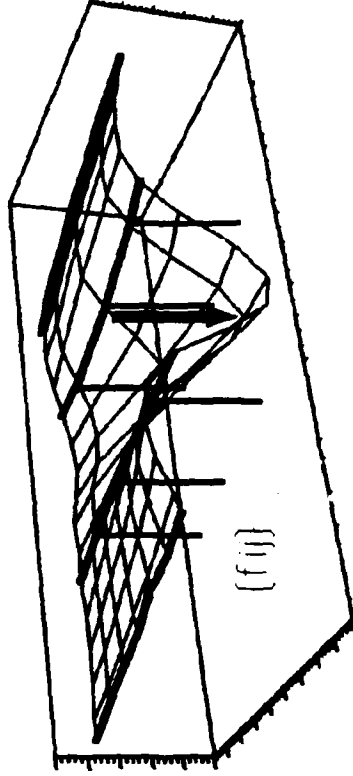


FIGURE 6.8: DEMONSTRATION OF THE USE OF FLEXIBILITY MATRIX

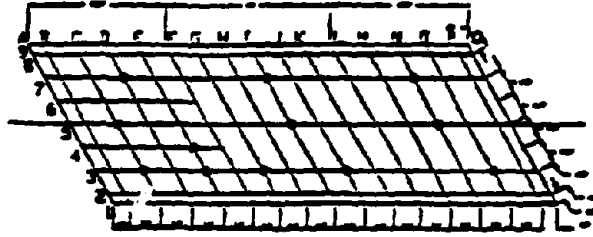
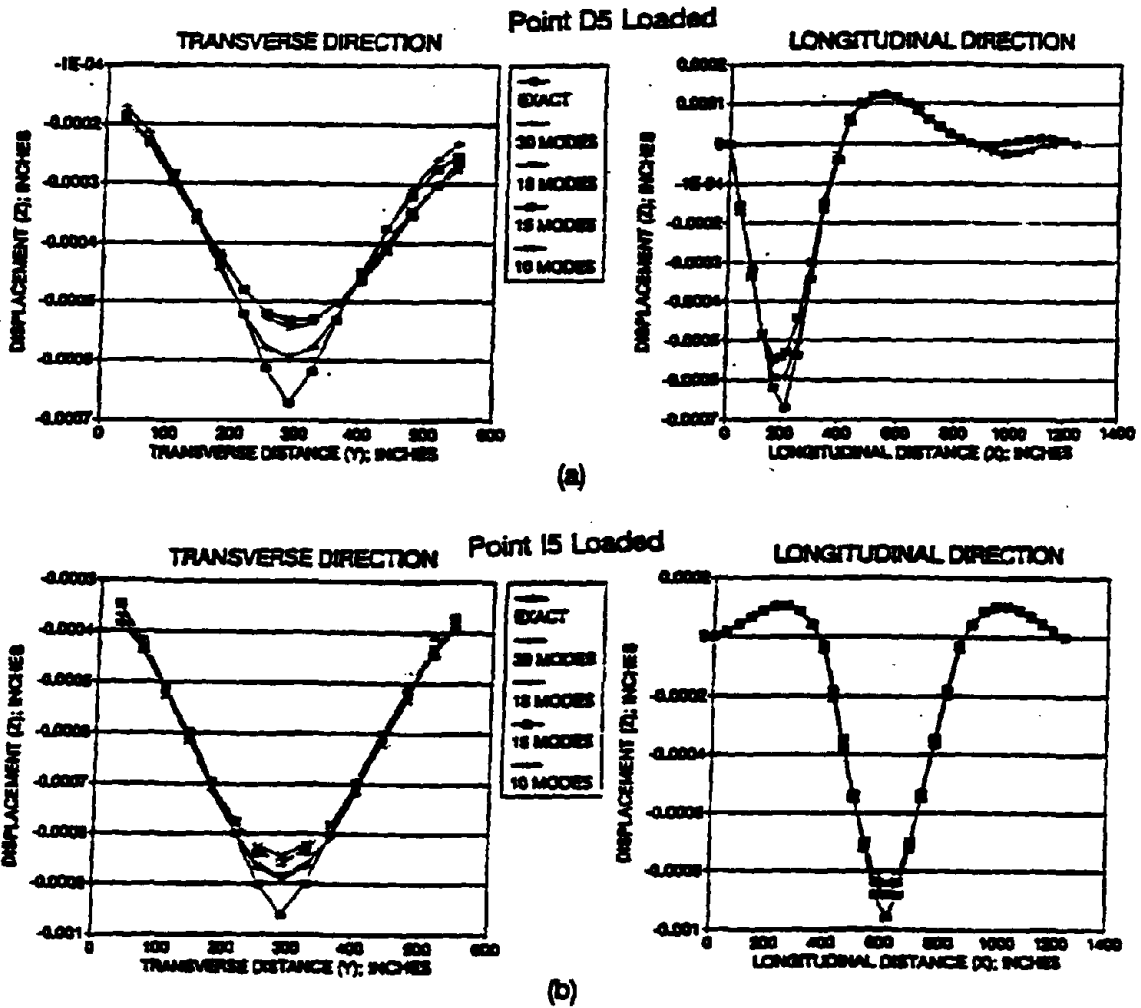
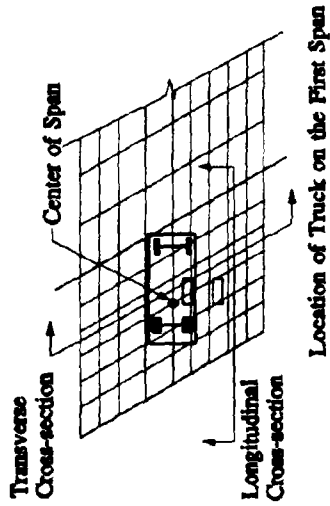


Figure 6.9: Approximate Location

Lines F and L are the Approximate Location of the Floor Lines



**FIGURE 6.9: THE EFFECT OF THE NUMBER OF MODES ON THE CONVERGENCE OF THE FLEXIBILITY COEFFICIENTS**



**TIRE WEIGHTS**

TIRE	WEIGHT
Right Rear	12,350 lbs
Right Front	4,600 lbs
Left Front	4,700 lbs
Left Rear	12,700 lbs

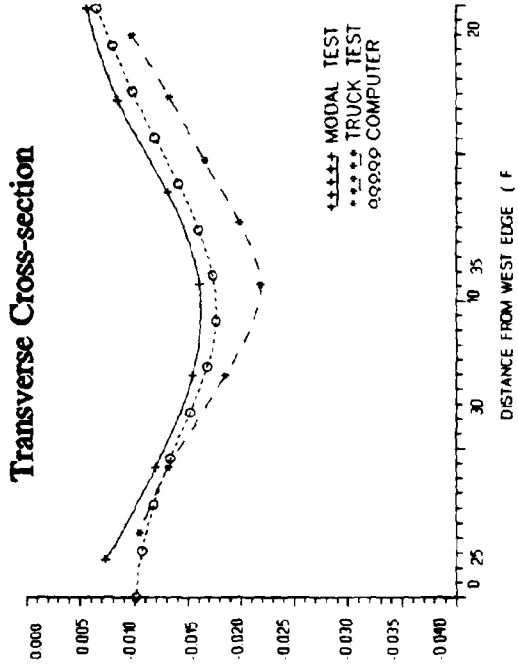
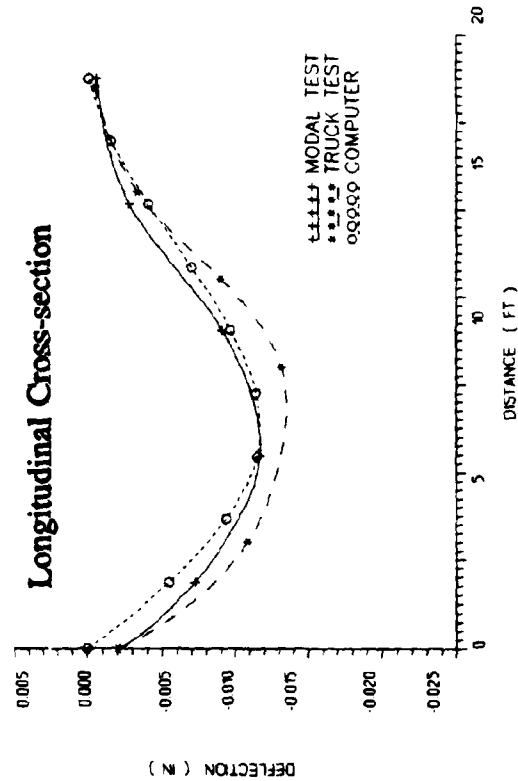
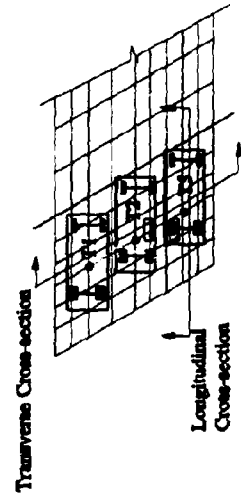


**FIGURE 6.10(a): COMPARISON OF TRUCK LOAD TEST, MODAL TEST AND F.E.M. FOR ONE TRUCK**



Location of Trucks on the First Span

TIRE WEIGHTS	TIRE	WEIGHT
	T1 Right Rear	11,950 lbs
	T1 Right Front	4,450 lbs
	T1 Left Front	4,850 lbs
	T1 Left Rear	12,300 lbs
	T2 Right Rear	10,950 lbs
	T2 Right Front	3,800 lbs
	T2 Left Front	4,000 lbs
	T2 Left Rear	10,400 lbs
	T3 Right Front	12,500 lbs
	T3 Right Rear	4,700 lbs
	T3 Left Front	4,500 lbs
	T3 Left Rear	

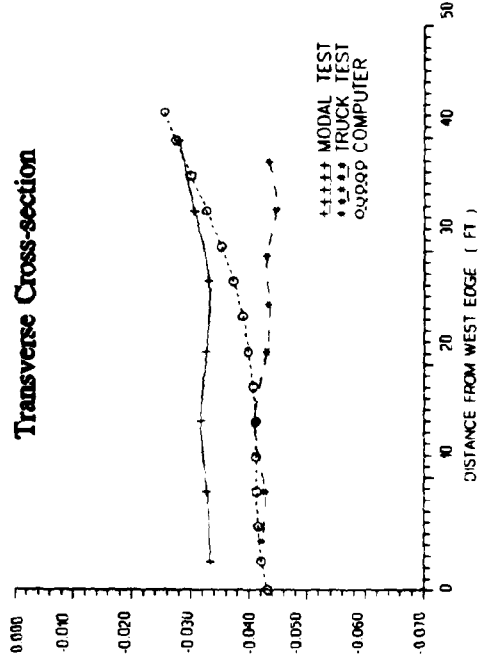
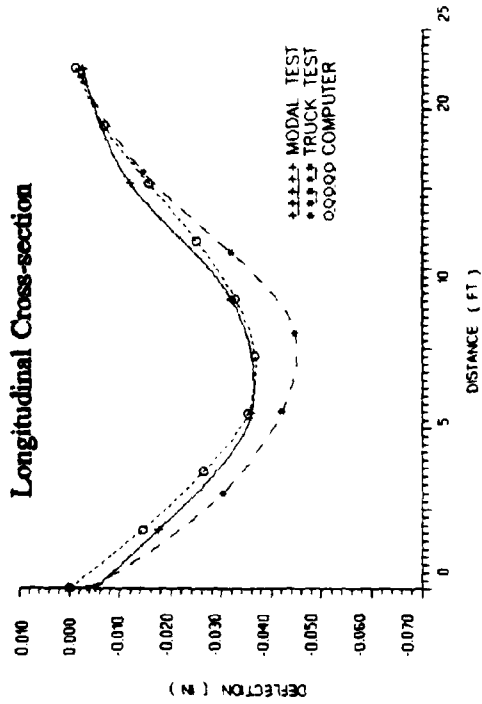
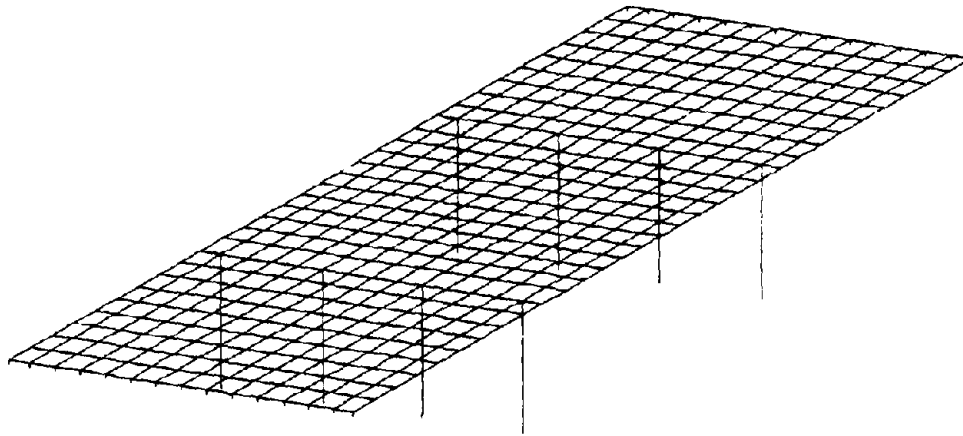
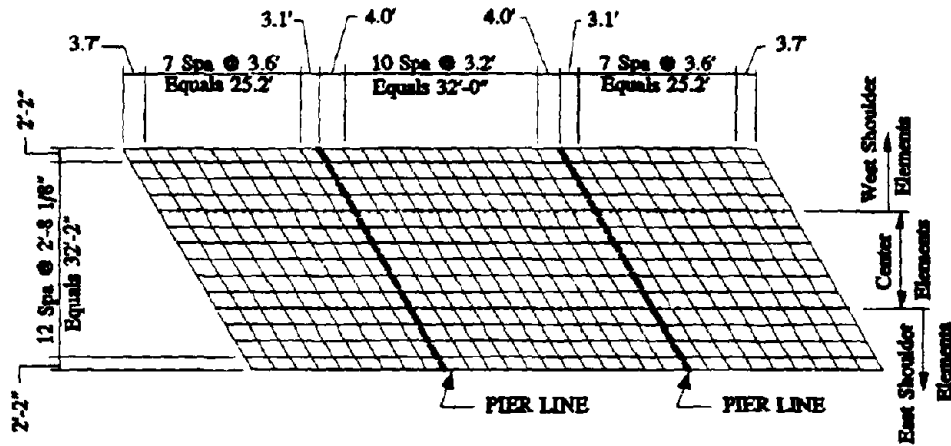


**FIGURE 6.10(b): COMPARISON OF TRUCK LOAD TEST, MODAL TEST AND F.E.M. RESULTS FOR THREE TRUCKS**

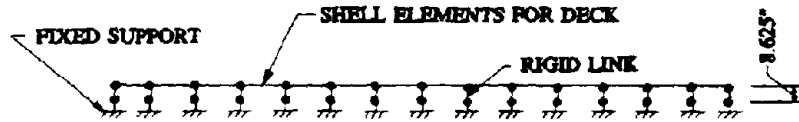


**3-D FINITE ELEMENT MODEL**

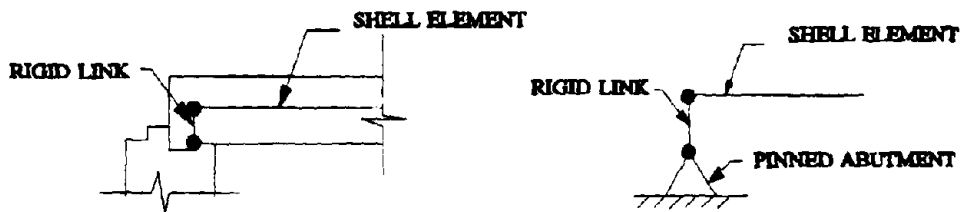


**FINITE ELEMENT MESH**

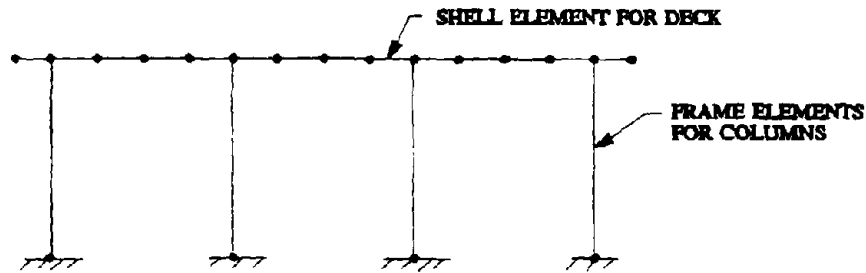
**FIGURE 6.11: FINITE ELEMENT MESH FOR 1st MODAL TEST**



**TRANSVERSE VIEW OF ABUTMENT**



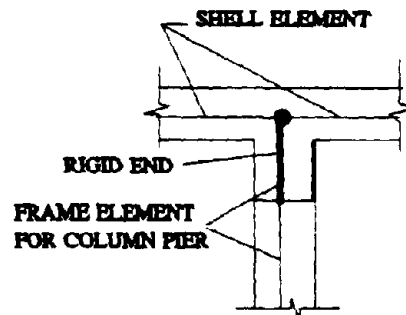
**LONGITUDINAL DETAILS OF ABUTMENT**



**TRANSVERSE VIEW OF PIER**

**MODEL PARAMETERS**

PARAMETER	VALUE
Abutment Vertical Stiffness	Fixed
Abutment Rotational Stiffness	Pinned
Pier Vertical Stiffness	Fixed
Pier Rotational Stiffness	Fixed
Deck Thickness East Shoulder	17.25 in
Deck Thickness Center	17.25 in
Deck Thickness West Shoulder	17.25 in
Abutment Horizontal Stiffness	Fixed



**DETAIL OF PIER**

**FIGURE 6.12 DETAILS OF THE FINITE ELEMENT MODEL FOR FIRST MODAL TEST**

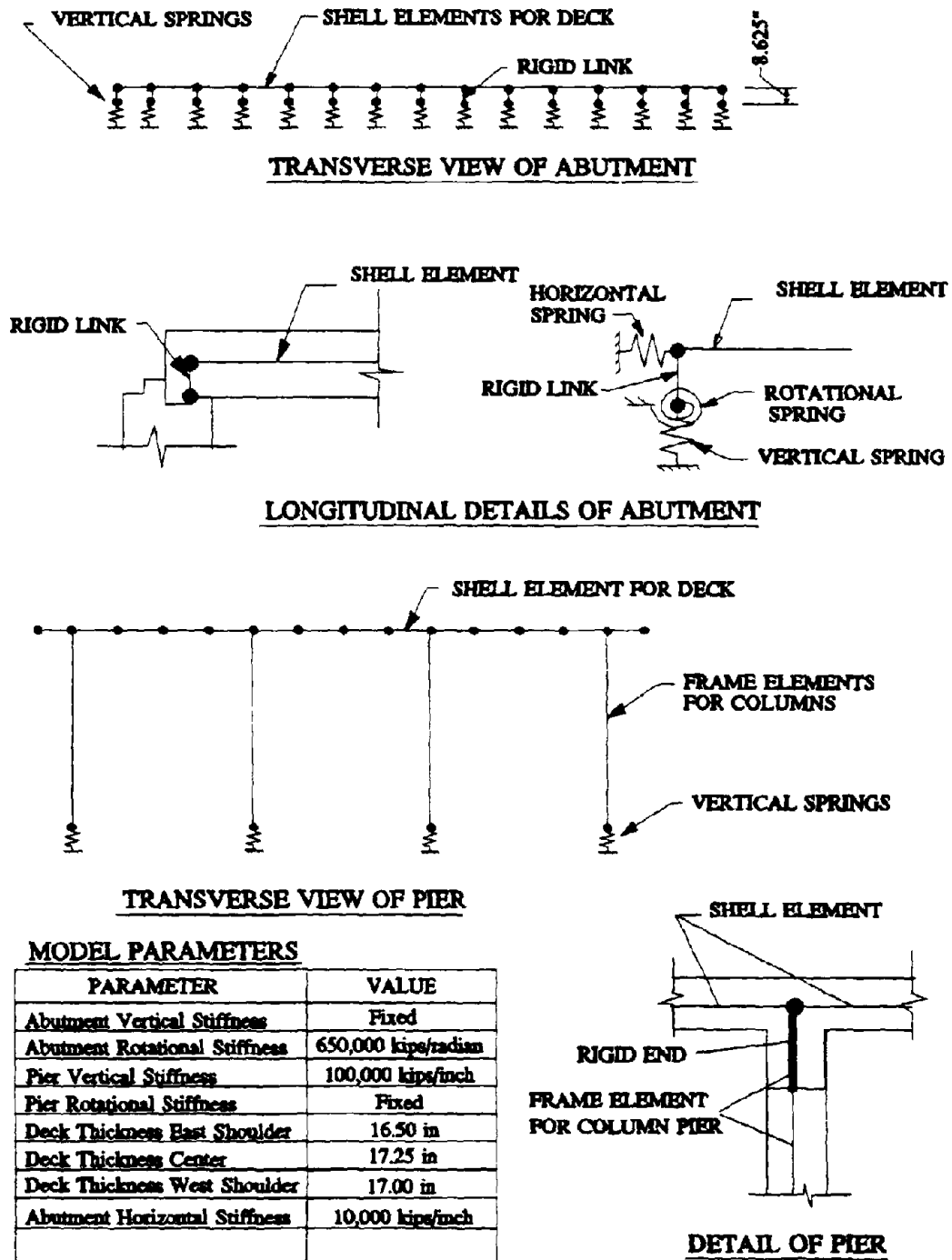


**FIGURE 6.13: CALIBRATED FINITE ELEMENT MODEL FOR FIRST MODAL TEST**

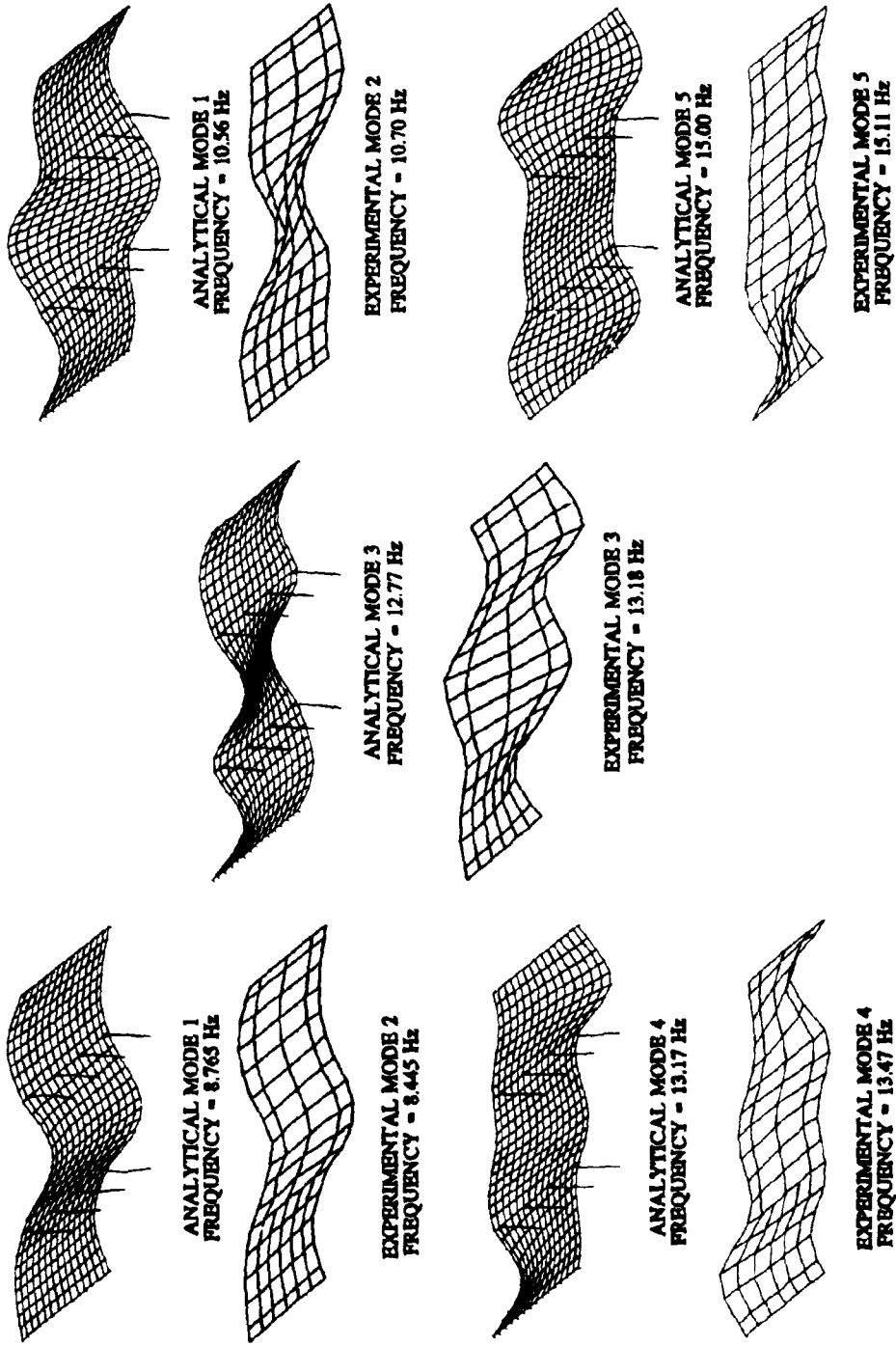


**FIGURE 6.14(a): RESULTS OF CALIBRATION OF TEST #1, MODES 1 TO 5**

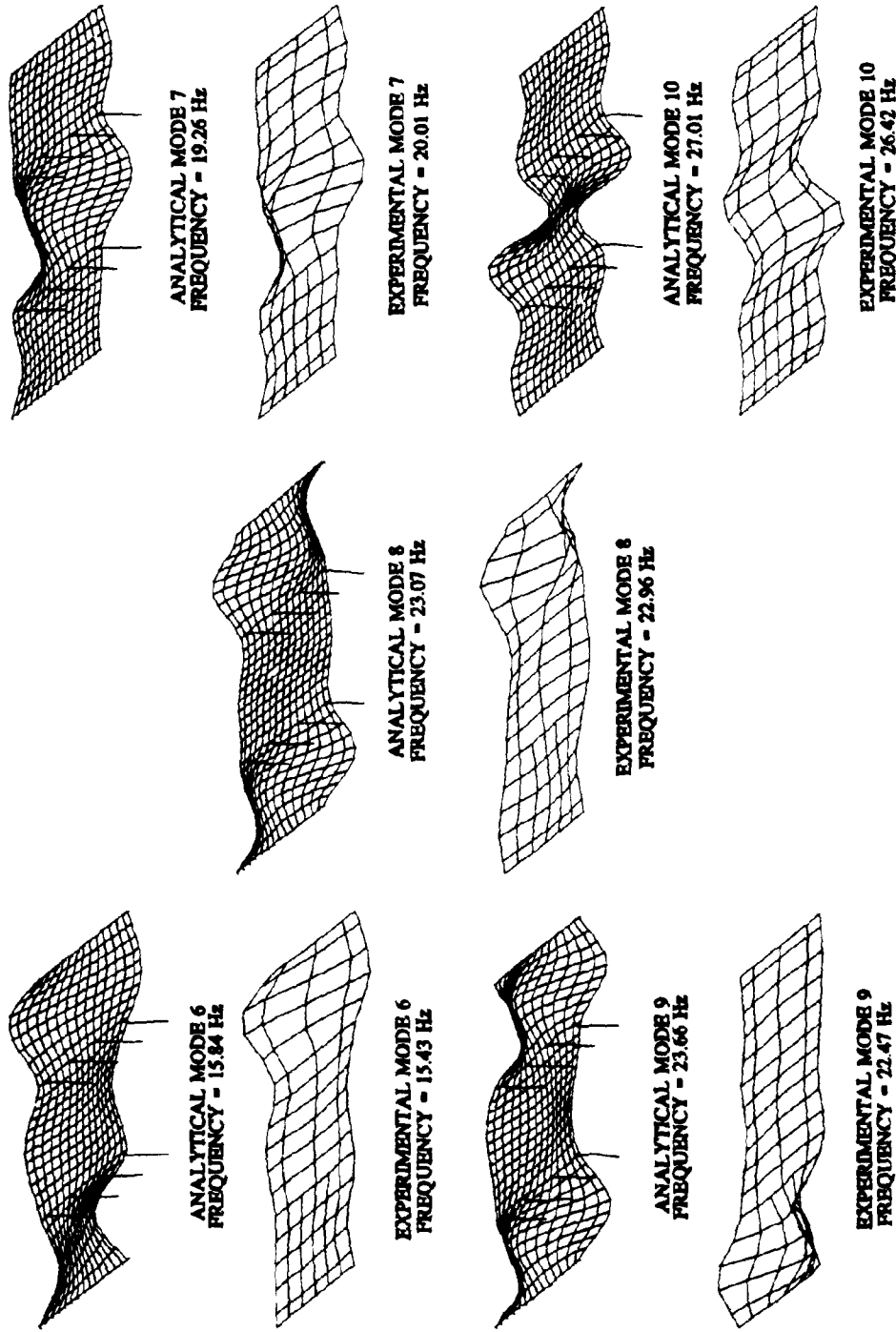


**FIGURE 6.14(b): RESULTS OF CALIBRATION OF TEST #1, MODES 6 TO 10**

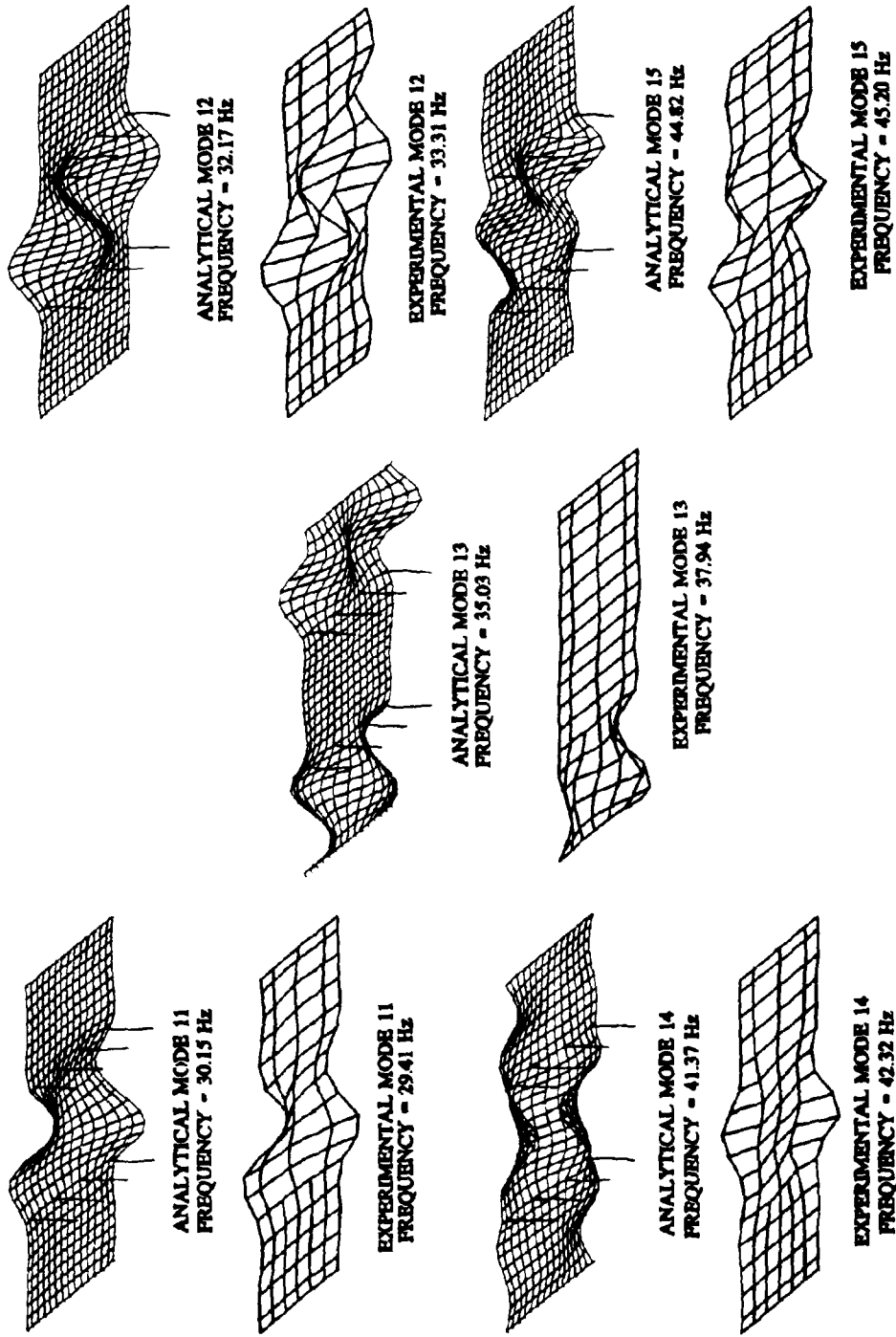


**FIGURE 6.14(c): RESULTS OF CALIBRATION OF TEST #1, MODES 11 TO 15**

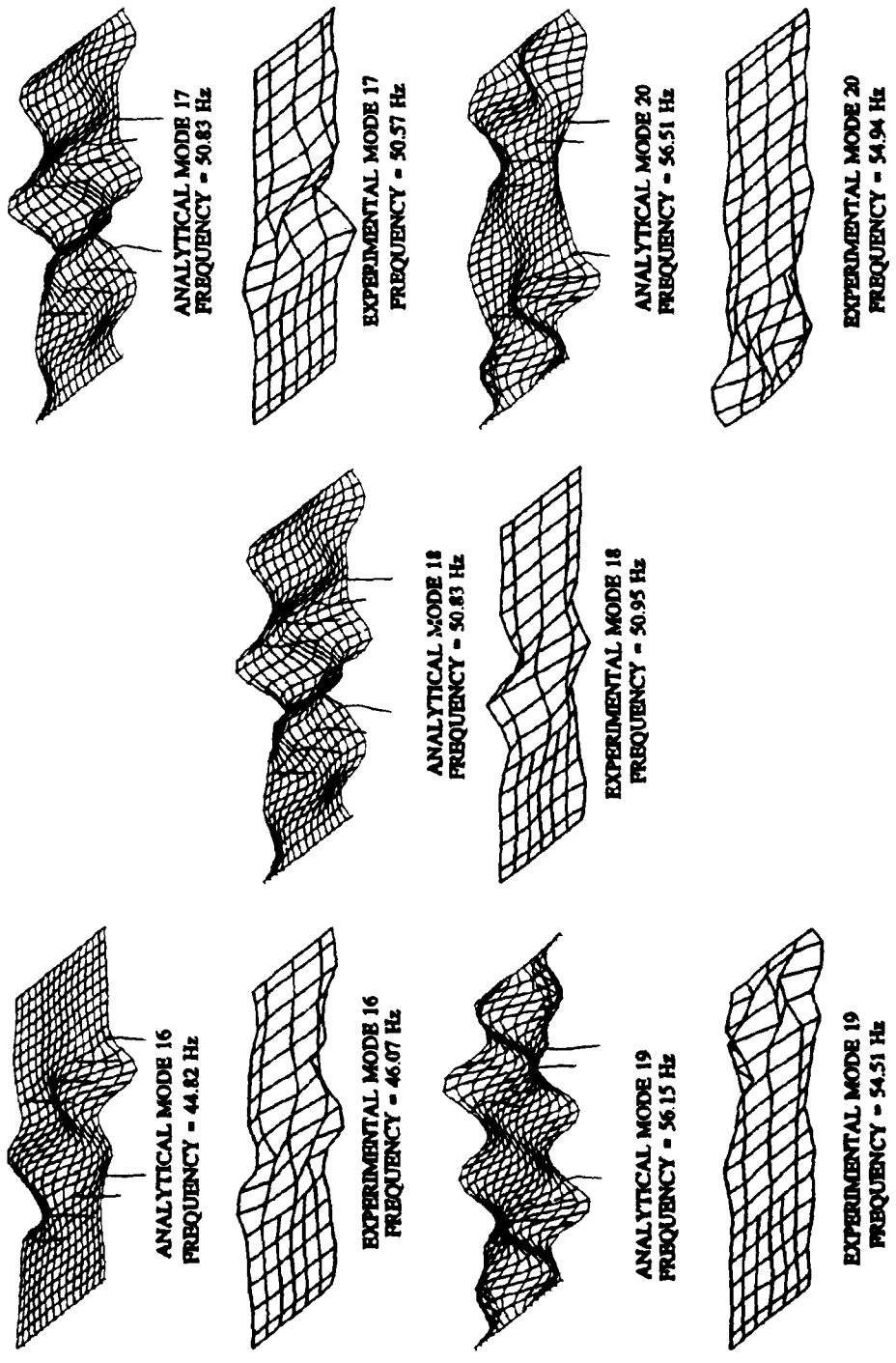
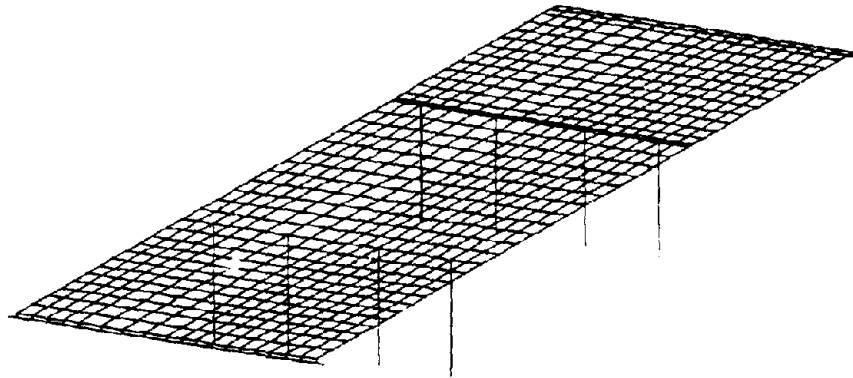


**FIGURE 6.14(d): RESULTS OF CALIBRATION OF TEST #1, MODES 16 TO 20**



**3-D FINITE ELEMENT MODEL**

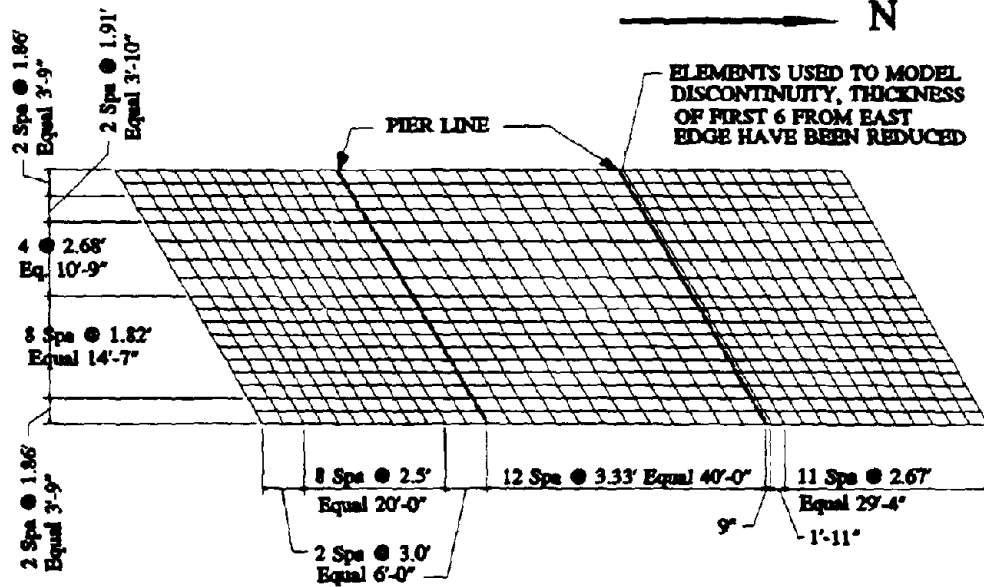


**FIGURE 6.15: FINITE ELEMENT MESH FOR 2nd MODAL TEST**

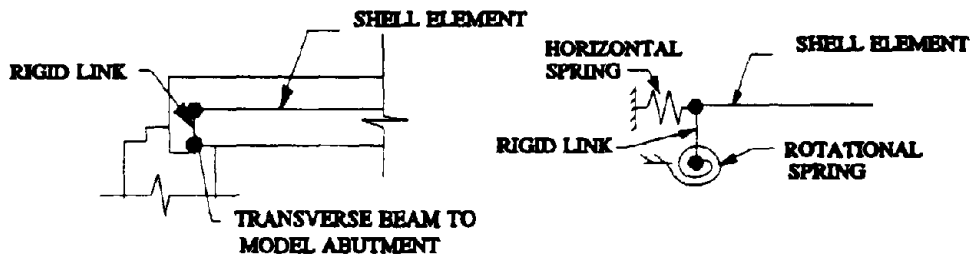
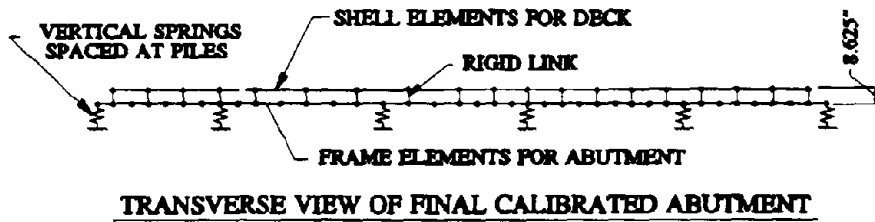
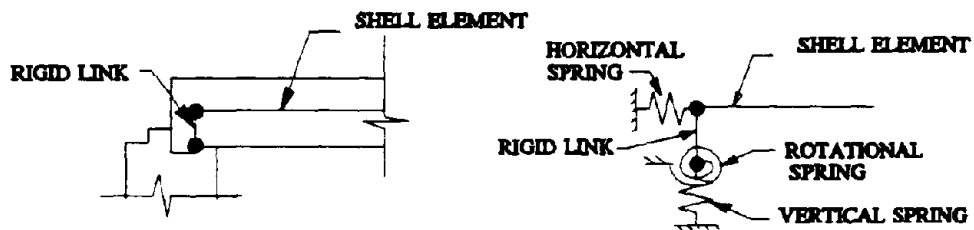
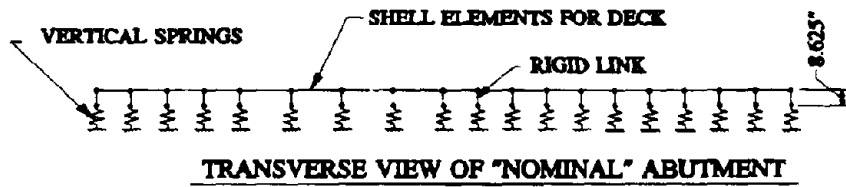
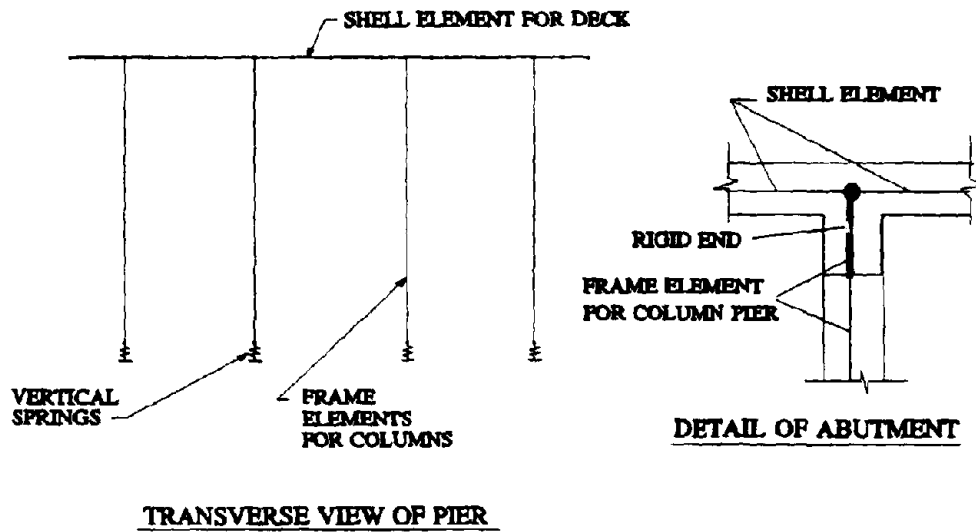


**FIGURE 6.16(a): ABUTMENT MODELING FOR 2nd MODAL TEST**



**"NOMINAL" MODEL PARAMETERS**

PARAMETER	VALUE
Abutment Vertical Stiffness	Fixed
Abutment Rotational Stiffness	650,000 kips/radian
Pier Vertical Stiffness	100,000 kips/inch
Pier Rotational Stiffness	Fixed
Deck Thickness South Span	17.25 in
Deck Thickness Center Span	17.25 in
Deck Thickness North Span	17.25 in
Abutment Horizontal Stiffness	10,000 kips/inch
Thickness of Continuity Elem.	Not Applicable

**CALIBRATED MODEL PARAMETERS**

PARAMETER	VALUE
Abutment Vertical Stiffness	8,000 kips/inch
Abutment Rotational Stiffness	4,000 kip-in/radian
Pier Vertical Stiffness	200,000 kips/inch
Pier Rotational Stiffness	Fixed
Deck Thickness East Shoulder	15.50 inches
Deck Thickness Center	16.50 inches
Deck Thickness West Shoulder	15.50 inches
Abutment Horizontal Stiffness	400,000 kips/inch
Thickness of Continuity Elem.	5.0 inches for 7 elem.

**FIGURE 6.16(b): MODEL PARAMETERS FOR 2nd MODAL TEST**

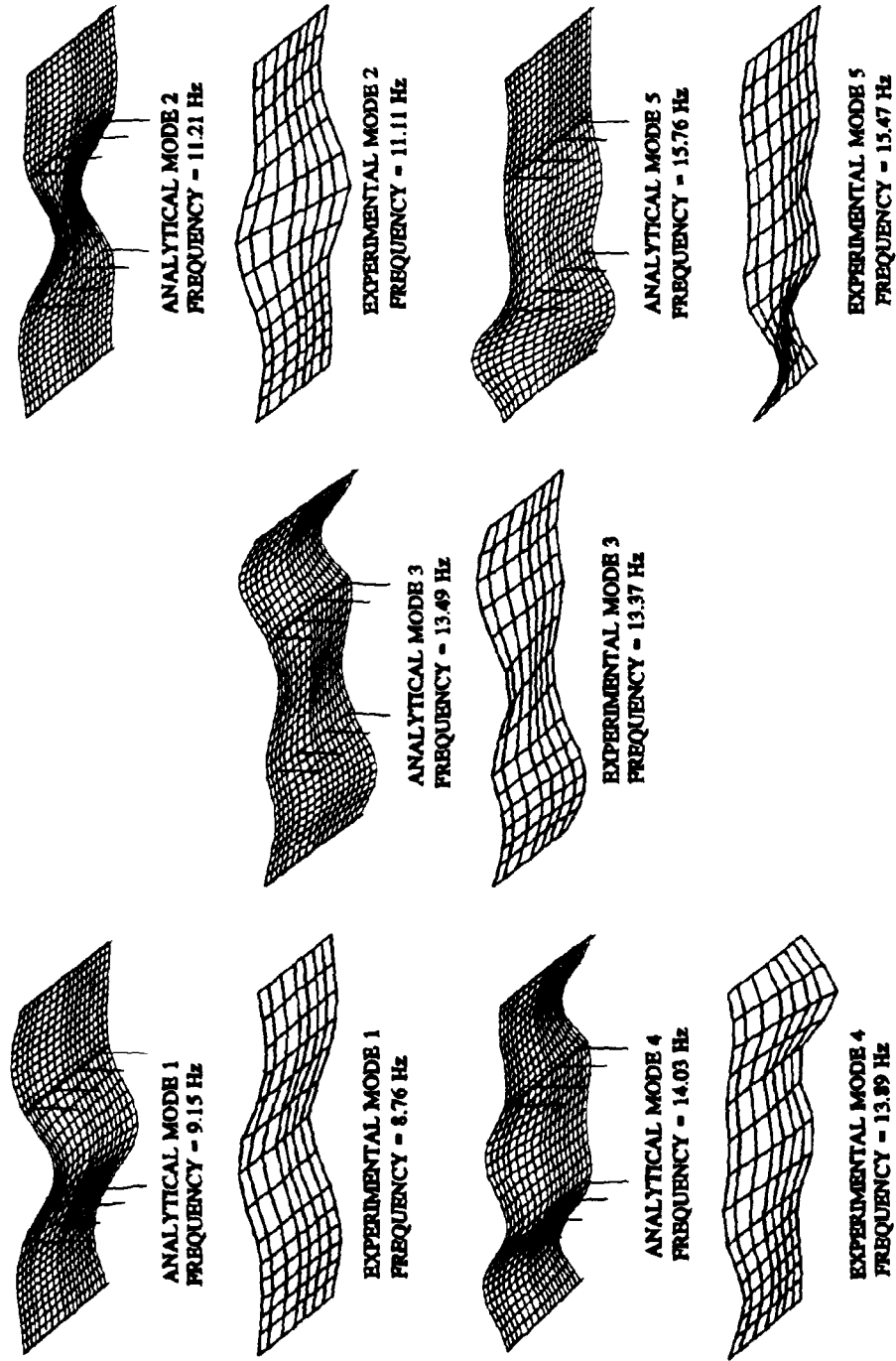


**FIGURE 6.17(a): RESULTS OF CALIBRATION OF TEST #2 MODES 1 TO 5**

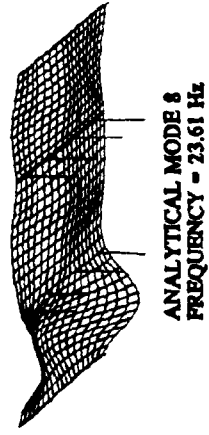
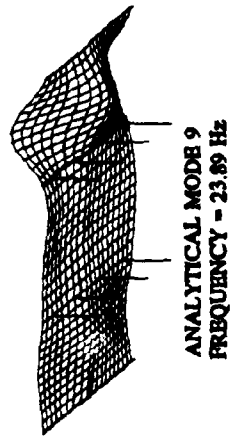
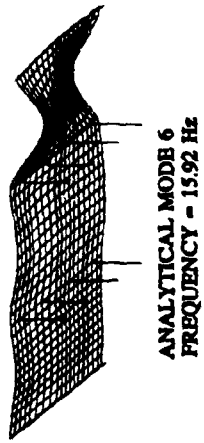


**FIGURE 6.17(b): RESULTS OF CALIBRATION OF TEST #2, MODES 6 TO 10**

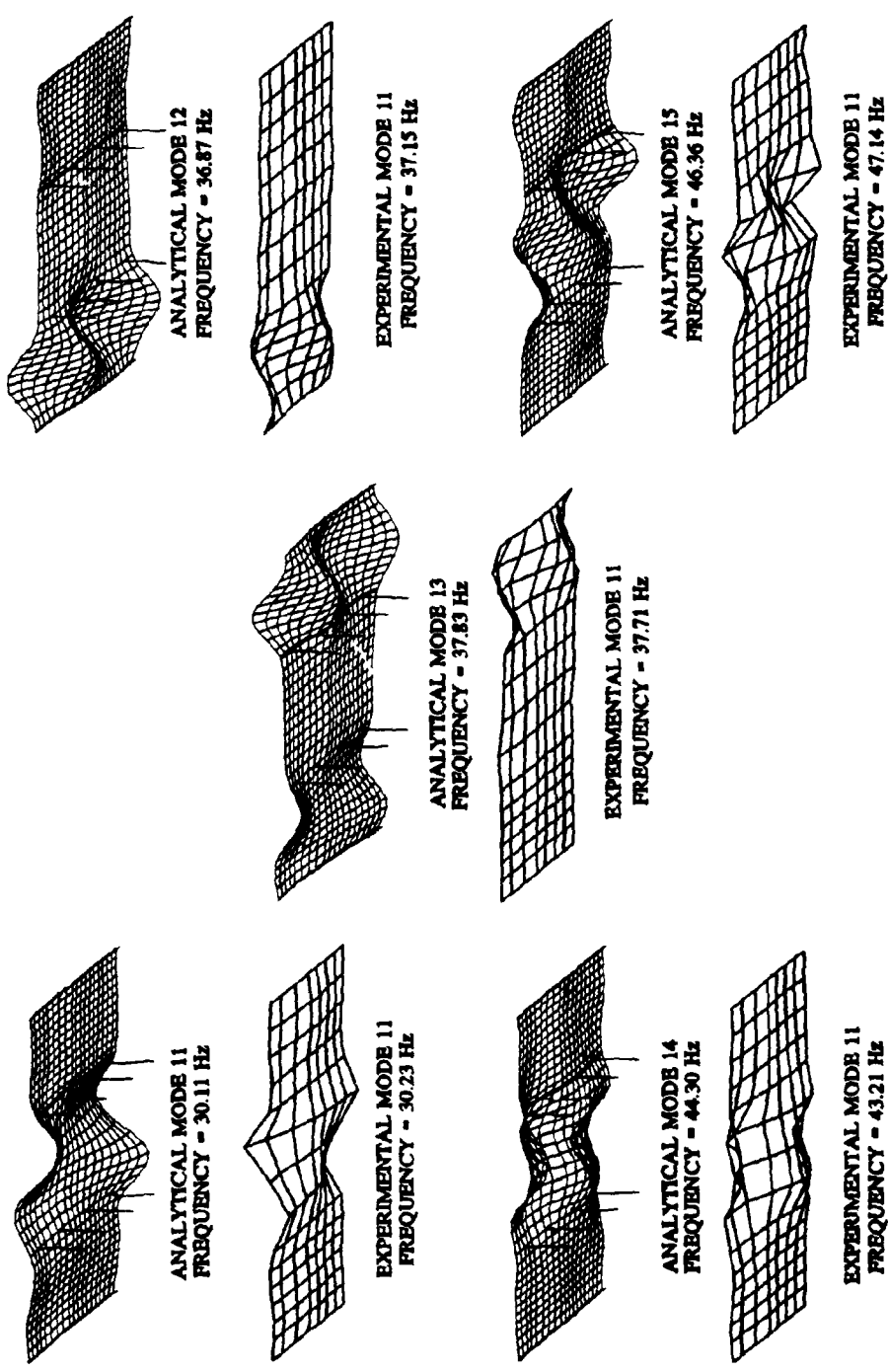


**FIGURE 6.17(c): RESULTS OF CALIBRATION OF TEST #2, MODES 11 TO 15**

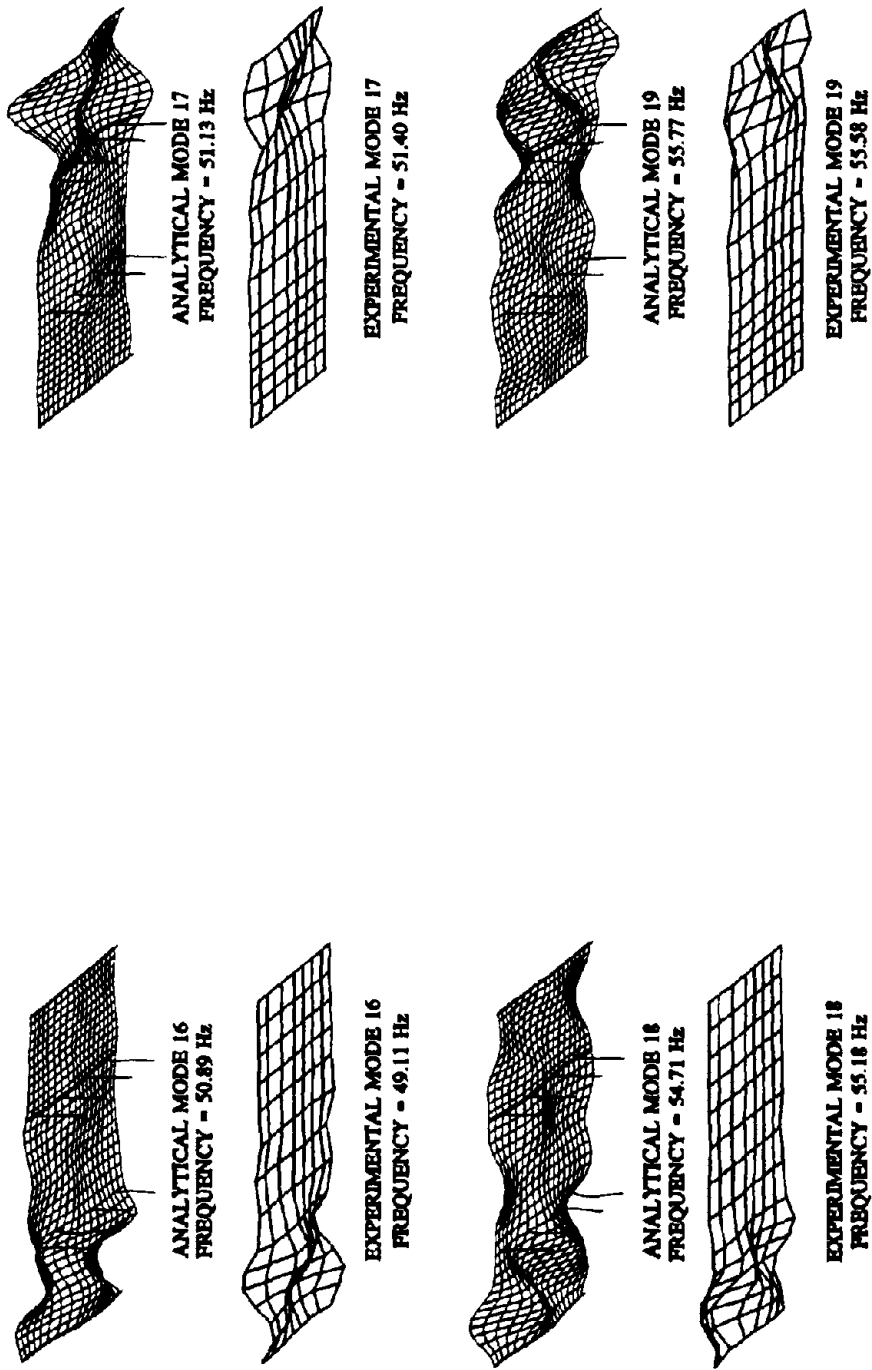


**FIGURE 6.17(d): RESULTS OF CALIBRATION OF TEST #2, MODES 16 TO 19**

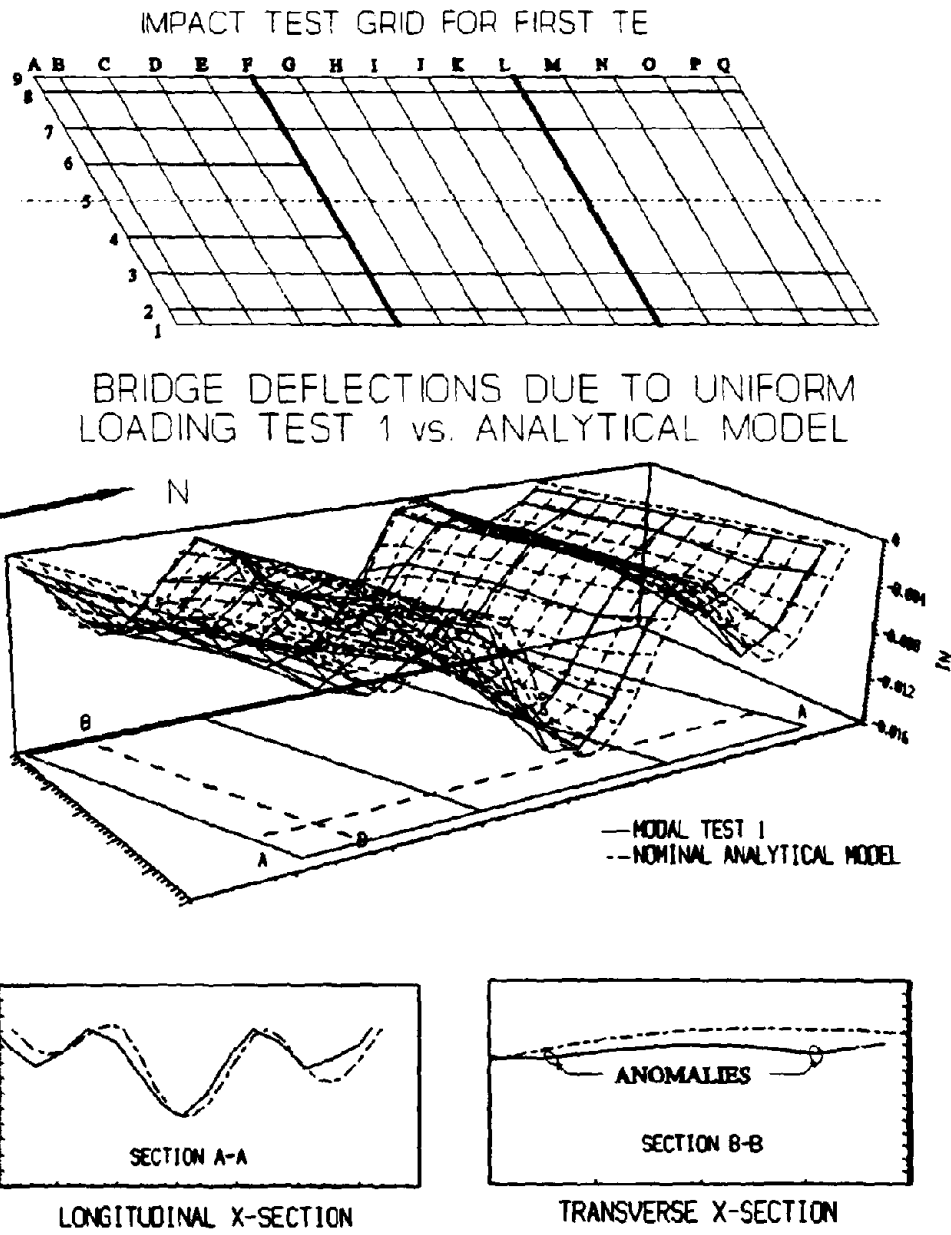


**FIGURE 6.18: 1st TEST MODAL vs ANALYTICAL FLEXIBILITY  
PROFILES - UNIFORM LOADING**

- TEST 2 --> BEFORE 20 TRUCK LOADIN  
-- TEST 3 --> AFTER 20 TRUCK LOADIN

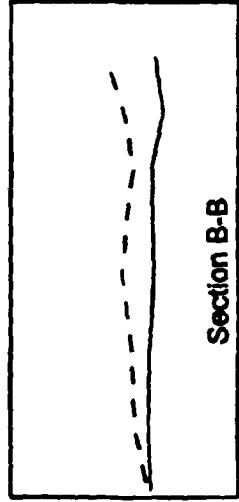
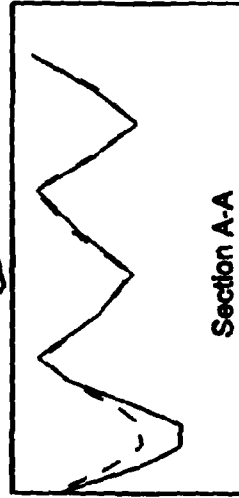
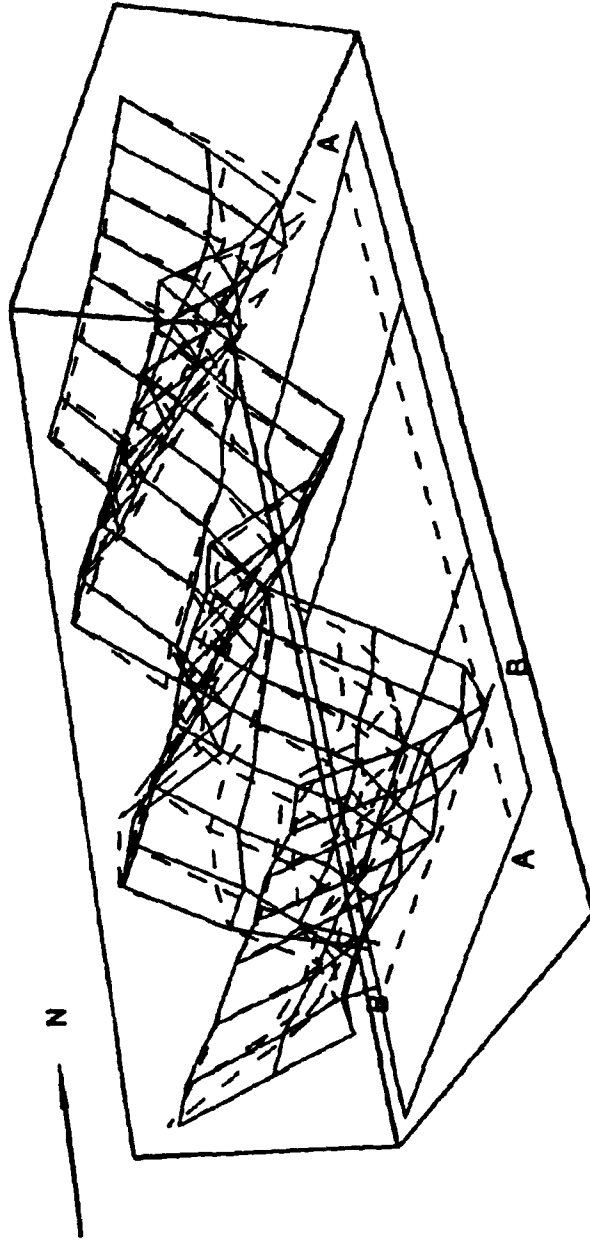
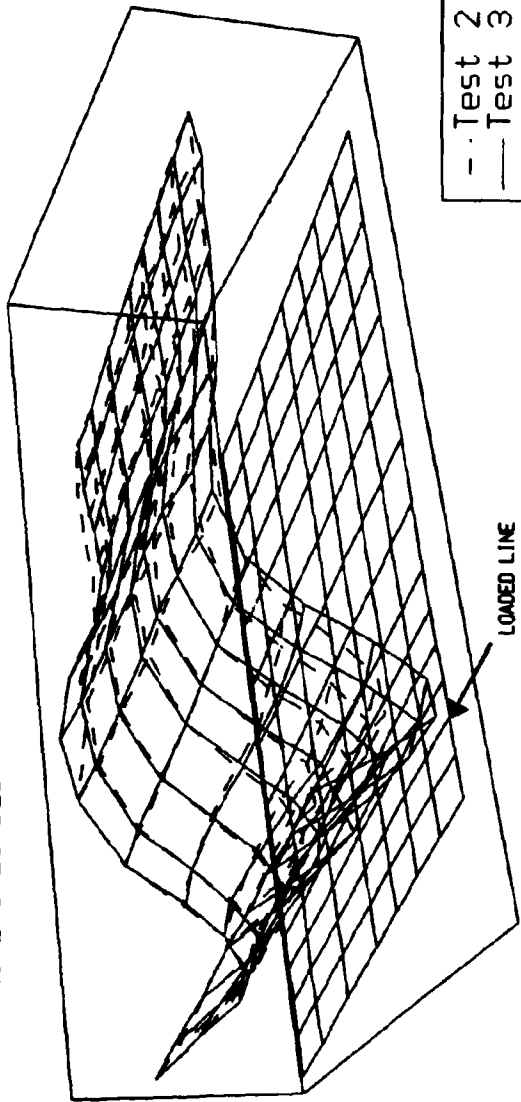


FIGURE 6.19: FLEXIBILITY COMPARISON MODAL TEST 2 vs. TEST 3 - UNIFORM LOADING

LINE C LOADED



- - Test 2  
— Test 3

CROSS-SECTION OF THE LOADED LINE

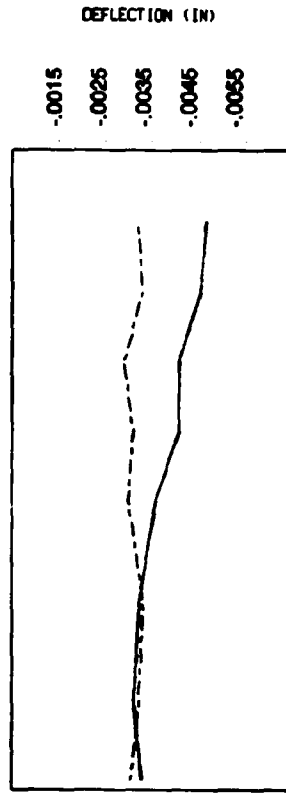
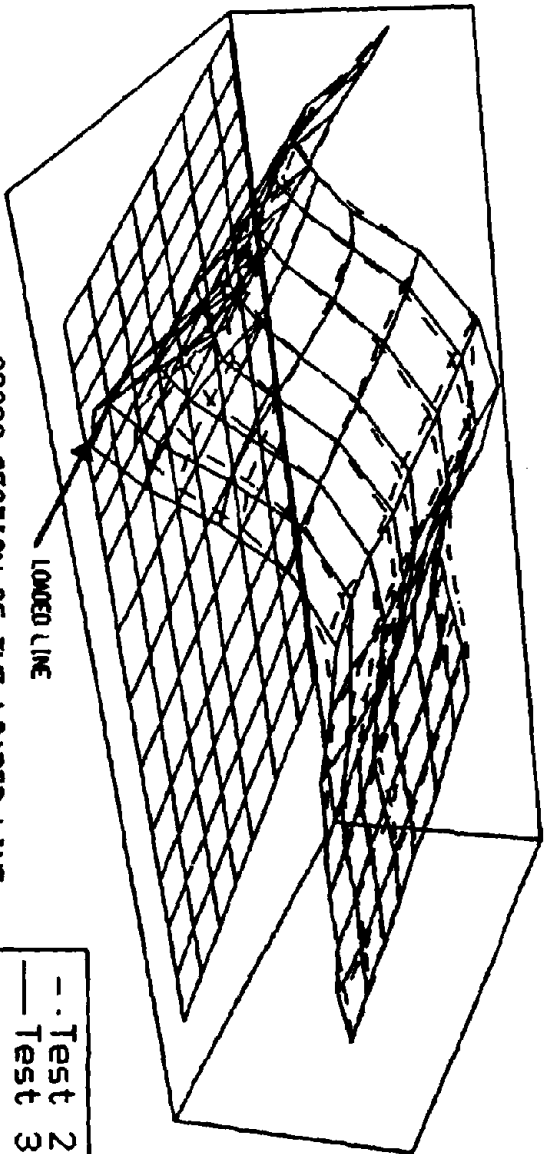
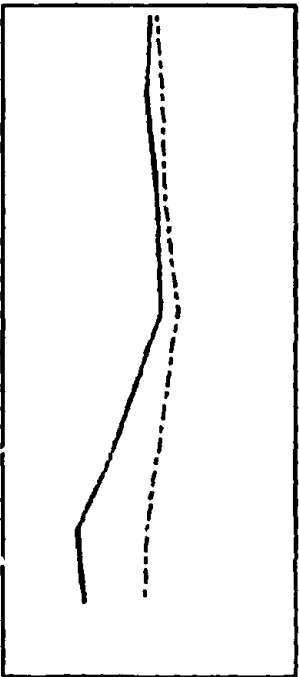


FIGURE 6.20: FLEXIBILITY COMPARISON OF MODAL TEST 2 vs TEST 3 - LINE C LOADED

LINE D LOADED



CROSS-SECTION OF THE LOADED LINE



- - Test 2  
— Test 3

FIGURE 6.21: FLEXIBILITY COMPARISON OF MODAL TEST 2 VS. TEST 3 - LINE D LOADED.

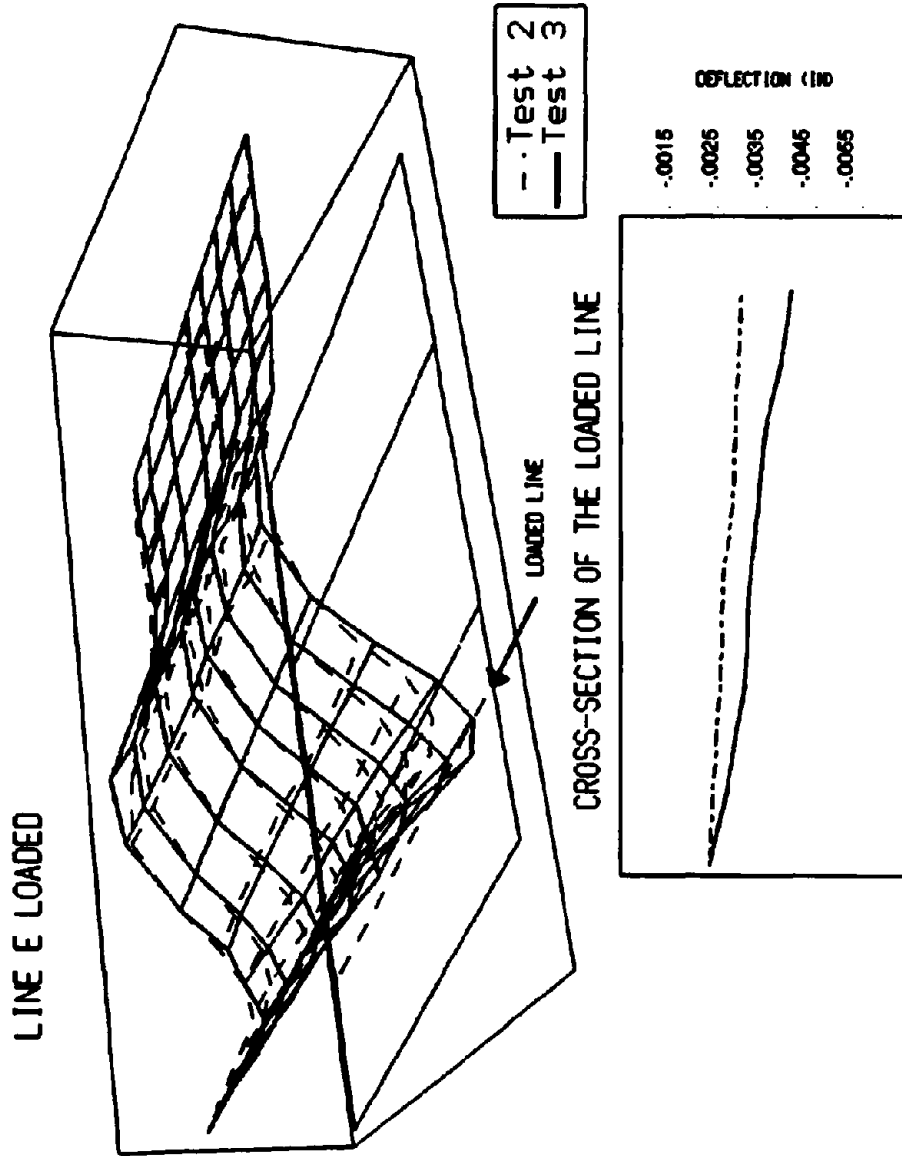


FIGURE 6.22: FLEXIBILITY COMPARISON OF MODAL TEST 2 vs. TEST 3 - LINE E LOADED

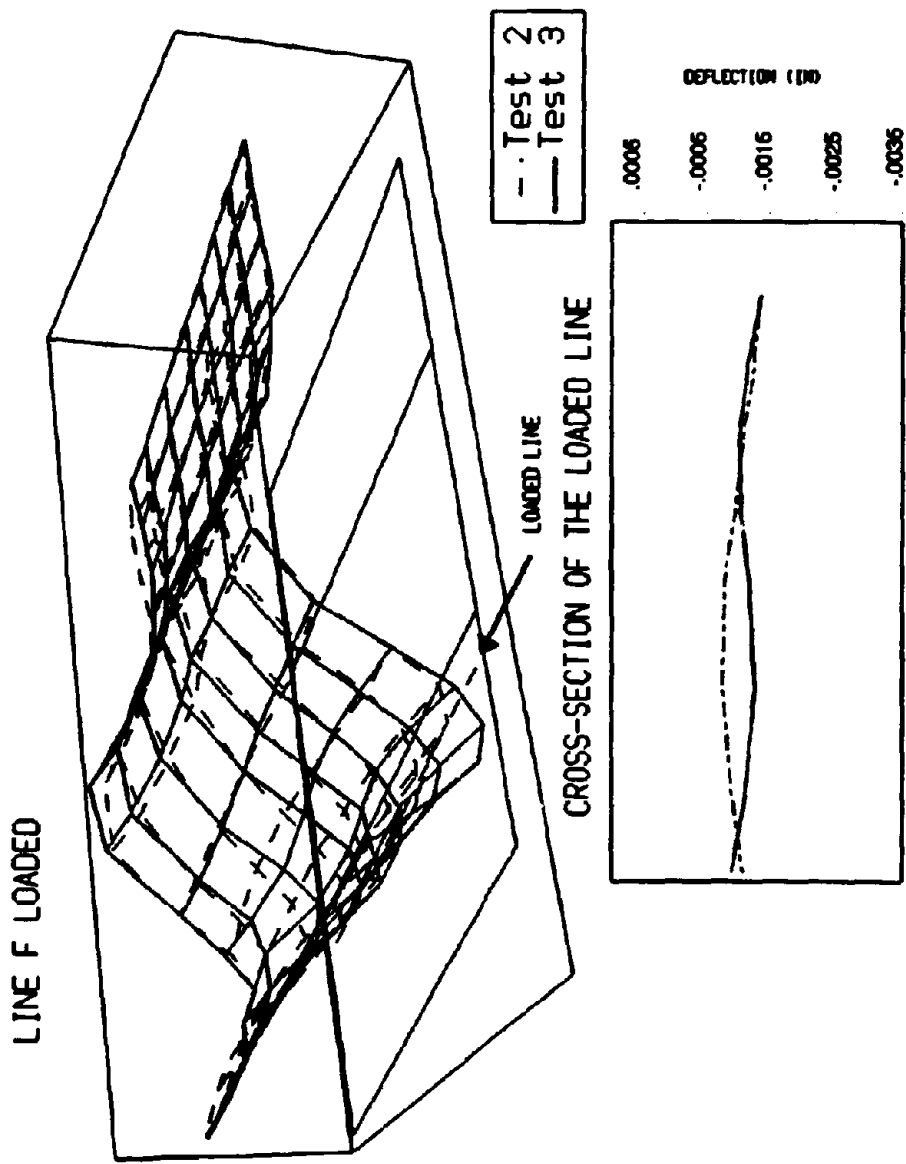


FIGURE 6.23: FLEXIBILITY COMPARISON OF MODAL TEST 2 VS. TEST 3 - LINE F LOADED

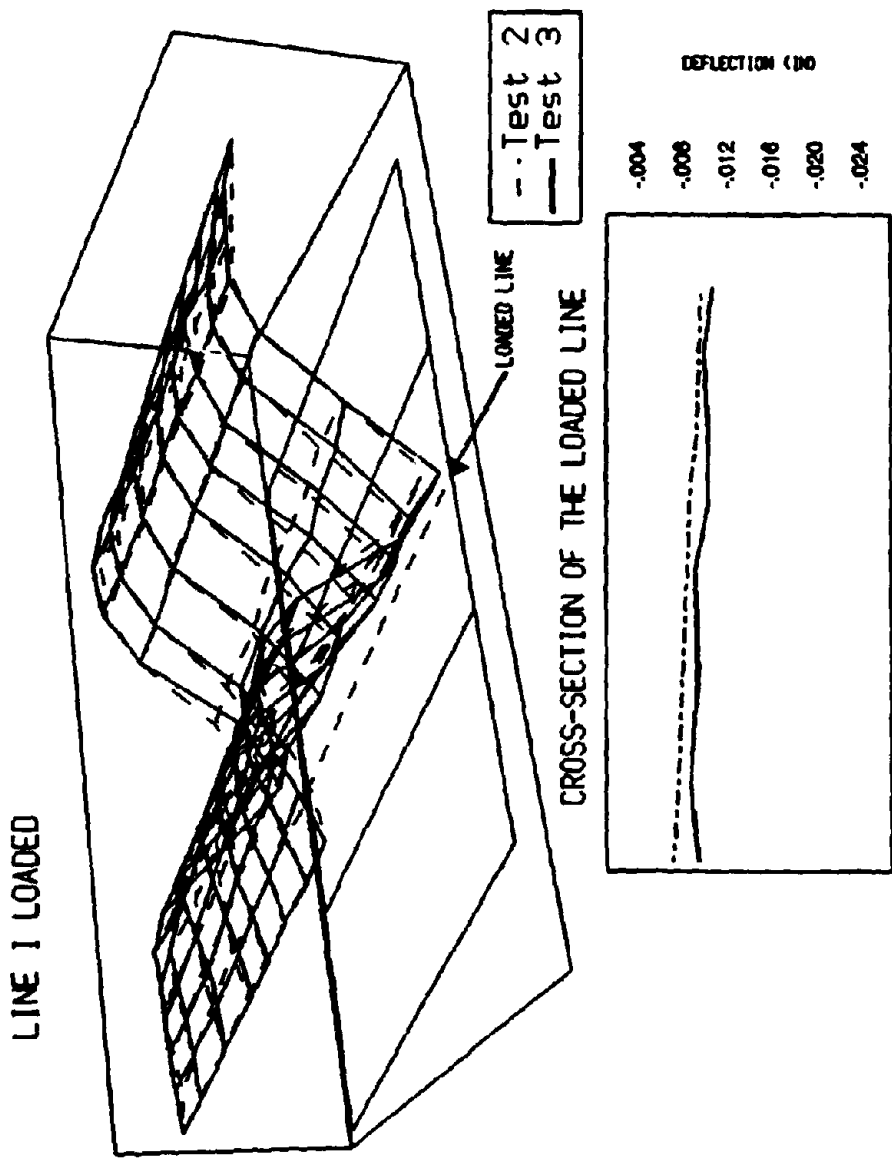


FIGURE 6.24: FLEXIBILITY COMPARISON OF MODAL TEST 2 vs. TEST 3 - LINE 1 LOADED

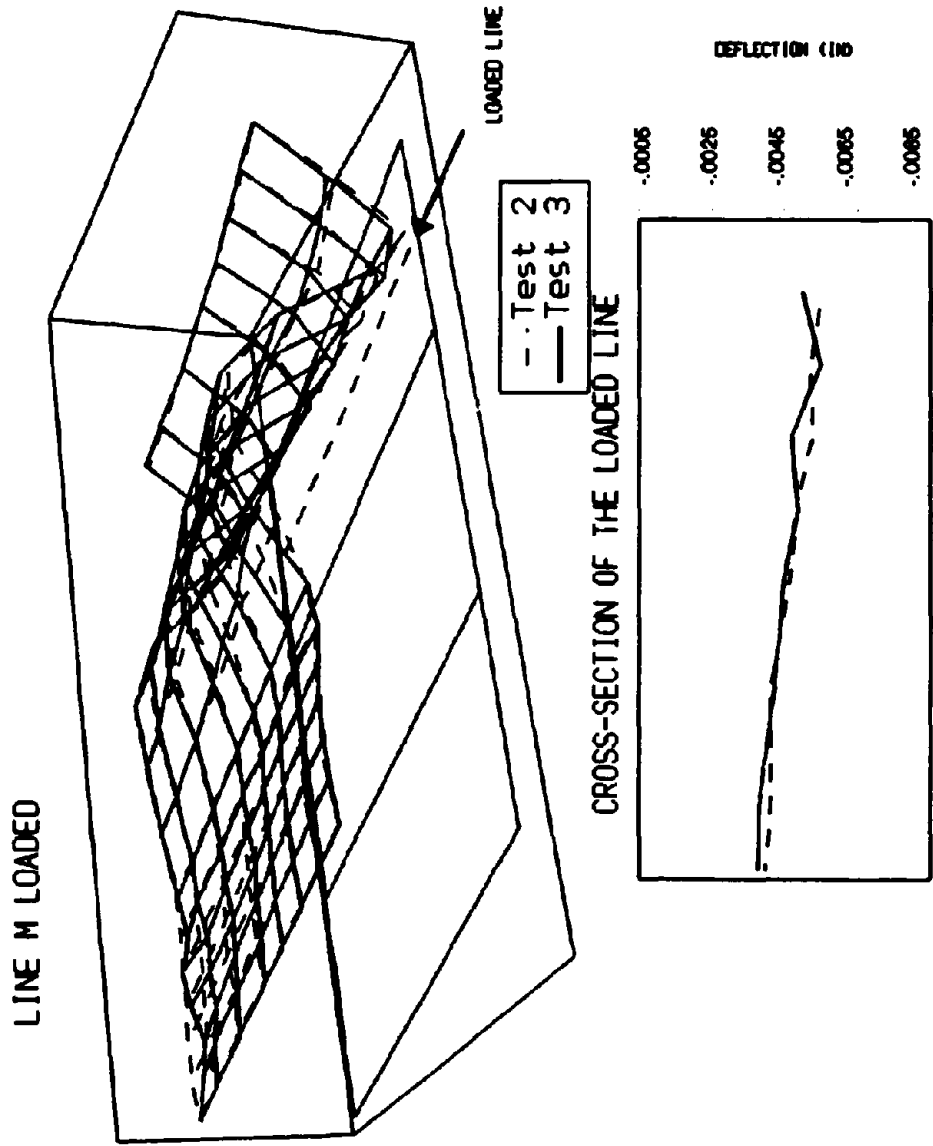
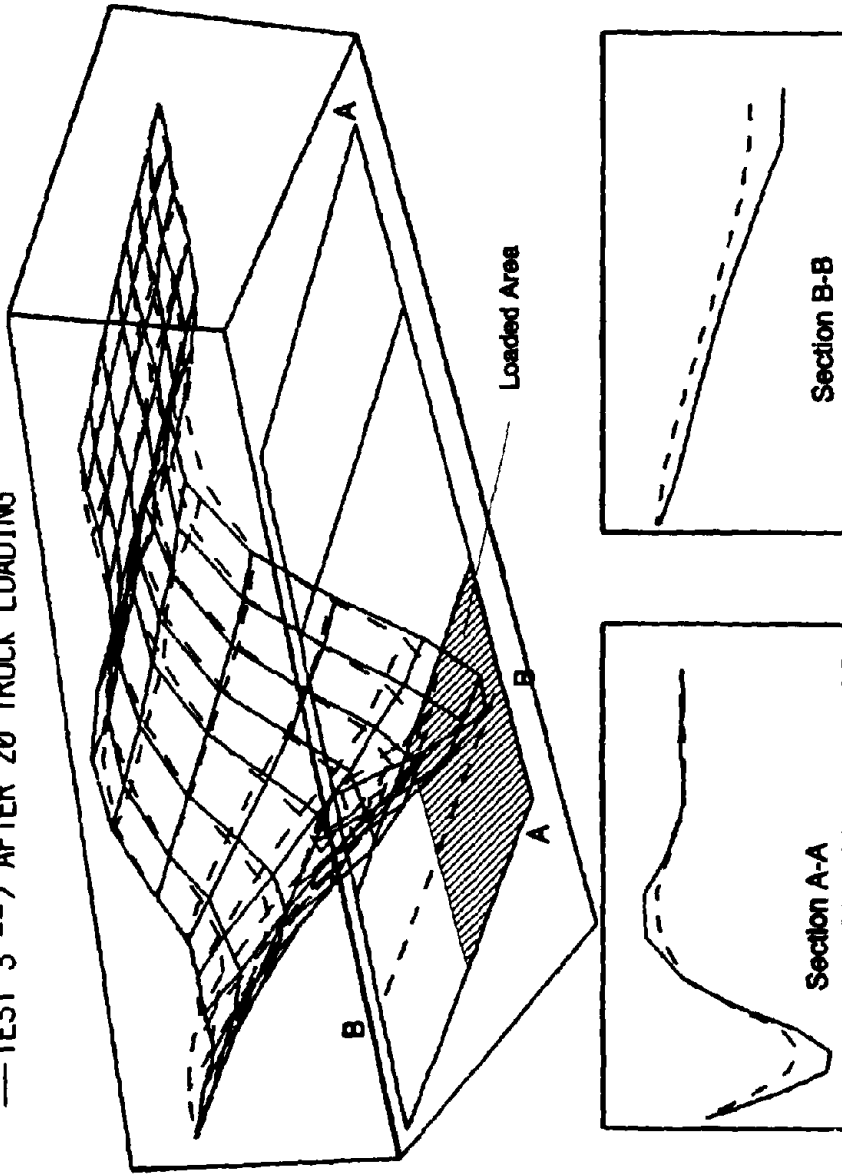


FIGURE 6.2.5: FLEXIBILITY COMPARISON OF MODAL TEST 2 vs. TEST 3 - LINE M LOADED

- TEST 2 --> BEFORE 20 TRUCK LOADING  
 — TEST 3 --> AFTER 20 TRUCK LOADING



**FIGURE 6.26: FLEXIBILITY COMPARISON PATCH LOADING IN THE DAMAGED AREA. MODAL TEST 2 vs. TEST 3**

## CHAPTER 7: BRIDGE RATING

### 7.1 INTRODUCTION

Bridge rating procedures based on different analytical modeling approaches were studied. These include a simple frame analogy in conjunction with computer software for bridge influence line analysis as well as linear finite element analysis. All of the ratings are based on either the AASHTO 1983 "Manual for Maintenance Inspection of Bridges", or the AASHTO 1989 "Guide Specifications for Strength Evaluation of Existing Steel and Concrete Bridges". The 1983 AASHTO "Standard Specifications for Highway Bridges" were applied where appropriate.

The goal of these ratings is to establish a baseline by which the different phases of the research can be correlated, as well as to study the issues in rating RC slab bridges. It is noted that a wide range of rating values can be achieved for the same bridge based on the level and complexity of analysis used in the rating process (Huria, Lee, and Aktan, 1992). In general, rating factors should increase with the complexity of the analysis, as more resistance mechanisms are incorporated in more complex models. However, to achieve the highest possible reliable rating, the bridge must be carefully inspected, material properties must be carefully identified, and care must be taken to assure the analysis would incorporate the actual bridge conditions and characteristics accurately. Also, as the complexity of the analysis increases so does the time and effort required to perform the rating.

#### 7.1.1 Specifications and Trucks

Bridge rating is typically done using the AASHTO 1983 "Manual for Maintenance Inspection of Bridges". In this method, the bridge is modeled according to the applicable AASHTO "Standard Specifications for Highway Bridges" (a sample model for a slab bridge is shown in Figure 7.1) The Standard Specifications describe how a bridge is divided into elements and how given load is to be distributed to each element of the bridge. Next, the model is loaded with the appropriate dead and live loads. Dead loads are basically the bridge self weight. The live load consists of a truck loading; either an H or HS type loading or a Type 3 loading. The 1983 Manual permits the use of equivalent lane loadings (Figure 7.2a) or a set concentrated loads which represent individual axle loads (Figure 7.2b). In general, the individual concentrated loads (Figure 7.2b) controls for short spans. The live load is then distributed to the bridge elements according to the Standard Specifications. Live loads also cause impacts loading so an impact factor for live load is determined from the 1983 AASHTO Manual. The appropriate sections (e.g. steel, concrete) of the Standard Specifications are then used to determine the resistance (capacity) of the bridge or bridge element and the bridge can be rated using the rating equation:

$$R.F. = \frac{\Phi R_n - \gamma_d \cdot D.L.}{\gamma_l \cdot L.L. + (1 + I)} \quad (\text{EQN. 7.1})$$

where R.F. is the rating factor, D.L. and L.L. are the dead and live load respectively,  $R_n$  is the nominal resistance,  $\gamma_d$  and  $\gamma_l$  are the dead and live load factors respectively,  $\phi$  is the resistance factor, and 'I' is the impact factor. Rating factors of approximately 3 are recommended while any rating factor below 1.0 indicates a structural deficiency in the bridge.

Another rating tool is the AASHTO 1989 "Guide Specifications for Strength Evaluation of Existing Steel and Concrete Bridges". This uses a method similar to the 1983 Manual with the following exceptions: 1) Only AASHTO Type 3 loadings are considered; 2) Only the discrete point load (Figure 7.2b) is used for bridges under 200 feet long (for longer bridges a new equivalent lane loading is provided); 3) The  $\phi$  factor is altered to reflect redundancy, damage/deterioration, inspection and maintenance practices; 4) The 1989 Guide allows for use of advanced analytical techniques, such as finite elements, to determine load distributions.

For concrete slab bridges, both the 1983 AASHTO Standard Specifications and the 1989 AASHTO Guidelines permit the bridge deck to be modeled as a beam with a specified effective width (E). The rating procedure requires that all lanes be loaded, but if the effective strips do not overlap, the presence of vehicles in other lanes does not affect the strip under consideration. Therefore, although the destructive test loaded only one lane, the effective strip rating model will not distinguish between the single lane load and the multiple lane load required by the AASHTO rating process.

Normally, a three span bridge like the test bridge would be modeled as a three span continuous beam with pin supports. However, the research team decided that a frame with simply supported abutments and fixed piers as shown in Figure 7.1 would be a more appropriate model. The frame idealization should provide more accurate results since the moment distribution at the pier-slab connection is better simulated by representing the piers by column elements in the analytical model.

The normal rating procedure requires the critical ratings to be based on the worst case positioning of the truck(s) as per the AASHTO requirements. However, for comparison with the destructive test, the rating factors for the pattern by which the bridge was loaded for the destructive test have also been calculated. The destructive test loading pattern was originally designed to correspond to the critical positioning of one truck placed in the northbound lane to produce maximum positive bending moment response in the south end span (see Chapter 4).

### 7.1.2 Problems in Bridge Rating

**Material Properties:** In most cases the engineer performing the rating would be restricted to the design drawings and nominal values for most of the information critical to the rating, such as the material properties. The design drawings available for this bridge did not prescribe a nominal steel strength and specified the concrete only as class "C". In the case where material strengths are not available to the engineer, the 1989 AASHTO guidelines specify the compressive concrete strength ( $f'_c$ ), and steel yield strength ( $f_y$ ). From the 1989 guidelines, for a bridge built prior to 1954, the material properties are specified as  $f_y=33,000$  psi, and  $f'_c=3,000$  psi. The guideline is vague as to whether or not provisions exist for experimentally determining the properties for

reinforced concrete. However, as part of the research, extensive material testing was performed (see Chapter 3). For the test bridge, extensive material testing produced actual average measured material properties significantly greater than those recommended by the guidelines. It would still be conservative to use values of  $f_y=43,500$  psi and  $f'_c=5,000$  psi for the experimentally determined average properties. This represents a 10% reduction in the measured steel yield strength and a reasonable value for concrete strength based on compression tests which revealed strengths as high as 8,000 psi. For comparison, all the ratings were done with both the code prescribed material properties, as well as the experimentally determined ones.

**Incorporating Damage and Deterioration:** In calculations of the section capacities for the bridge, adjustments were made for damage. Since the damage was confined largely to the top of the slab, a one inch reduction in the deck thickness was made in the positive moment regions in those areas where the deterioration of the shoulders would be most pronounced. In the negative moment regions, the damaged top would be in the tensile zone where it would have no influence since concrete on the tensile side of the neutral axis is ignored. Since the bottom surface of the concrete was in relatively good shape, it was deemed unnecessary to reduce the depth of the slab in the negative moment regions.

### 7.1.3 Analysis of Bridge for Rating

All of the analyses were performed using SAP90 version P5.31 which has the capability to apply moving loads over frame elements through its bridge module. In all of the analyses corresponding to an effective strip model, the slab is modeled as a beam with an effective width and depth as calculated as per code procedures (Figure 7.1). Figure 7.1(b) shows the typical frame model that was implemented in the analyses. The program then would move the truck along the elements that were defined as the driving lanes of the bridge to predetermined stations set in the analysis. Based on the moving truck loads the program then calculated the envelopes for moment and shear.

The resistance (capacity) was determined using the AASHTO Standard Specifications. For the effective strip model, the resistance was calculated by assuming a reinforced concrete beam of proper depth (recall that the depth was reduced in the positive moment areas to account for deterioration) and steel ratio. The width of beam is the effective width of the strip. The rating factor is calculated based on the following equation:

$$R.F. = \frac{\phi R_n - \gamma_d \cdot D.L.}{\gamma_l \cdot L.L. \cdot (1+I)} \quad (EQN. 7.1)$$

where R.F. is the rating factor, D.L. and L.L. are the dead and live load respectively,  $R_n$  is the nominal resistance,  $\gamma_d$  and  $\gamma_l$  are the dead and live load factors respectively,  $\phi$  is the resistance factor, and 'I' is the impact factor.

## 7.2 RATING BASED ON AASHTO 1983 AND HS TRUCKS

The AASHTO 1983 Specifications allow for the use of the standard H and HS trucks or the Type 3 rating trucks for rating. For this case the rating was performed using the H and HS trucks. The AASHTO 1983 specifications provide two levels of rating, operating and inventory. Inventory rating is used for rating the bridge under daily traffic patterns, whereas the operating rating is used for special permits. All of the ratings will be based on the inventory rating since none of the configurations being considered would warrant a special permit.

The effective width of the bridge (E) used to calculate the critical loads based on ratings with the AASHTO H and HS trucks is given in the AASHTO Standard Specifications for Highway Bridges. This width is required to support 1/2 of the applied loading and is calculated using the formula given in 1983 AASHTO Standard Specifications for Highway Bridges :

$$E=4+0.06*S \quad (\text{EQN 7.2})$$

where S is the clear span length. The effective width for the bridge is 5.8 feet for the end spans and 6.3 feet for the middle span. Figure 7.2 shows the loading from the standard H20-44 and HS20-44 live loading conditions, which are commonly used in designing short span bridges. The design parameters for these ratings are based on the 1983 AASHTO Standard Specifications for Highway Bridges. The resistance factors are given as  $\phi=0.9$  for bending moment, and  $\phi=0.8$  for shear. The dead load factor  $\gamma_d$  is given as 1.3, and the live load factor  $\gamma_l$  is given as 1.67. The impact factor I is given as 0.32 by the following equation:

$$I=\frac{50}{L+125} \quad (\text{EQN 7.3})$$

where L is the span length in feet. The dead load is calculated based on nominal dimensions of the bridge.

Figure 7.3 shows the analysis results for the H and HS trucks, and the rating factors based on these trucks are given in table 7.1. The critical rating comes from negative moment over the pierline; if the rating had been performed using code material properties, the critical rating would be 0.91 which indicates a slight deficiency. However, the measured material properties produce a critical rating factor of 1.61 which indicates the bridge to be in acceptable shape. The most critical factor in this rating is the material properties for the bridge, since the rating factor was increased considerably from an unacceptable level to a good level. Another interesting result of the ratings is the critical nature of the rating over the pier line. The strength of this section was calculated using its full section depth, whereas the positive moment regions had an inch reduction in its effective depth. It becomes apparent that this particular bridge was not as strong in the negative moment regions over the pier as in the positive moment regions at the midspans.

**Table 7.1 - Rating Based on the 1983 AASHTO  
Specifications: Using the AASHTO H and HS Trucks**

LOAD CONDITION	MATERIAL PROPERTIES	NOMINAL RESISTANCE	DEAD LOAD	LIVE LOAD	RATING FACTOR
MOMENT IN END SPAN (Kip-in)	CODE SPECIFIED	4,400	1,194	1,027	1.06
	MEASURED PROPERTIES	5,880	1,194	1,027	1.65
MOMENT OVER PIER (Kip-in)	CODE SPECIFIED	5,520	2,154	1,080	0.91
	MEASURED PROPERTIES	7,390	2,154	1,080	1.61
MOMENT IN MIDDLE SPAN (Kip-in)	CODE SPECIFIED	4,790	1,314	1,030	1.15
	MEASURED PROPERTIES	6,390	1,314	1,030	1.78
SHEAR AT PIERLINE (Kips)	CODE SPECIFIED	116	31.2	19.9	1.33
	MEASURED PROPERTIES	150	31.2	19.9	1.99

\* All based on load factor method and inventory rating.

### 7.3 RATING BASED ON AASHTO 1983 AND TYPE 3 RATING TRUCKS

The bridge was rated a second time, this time using type 3 rating trucks. The AASHTO code supplies three rating trucks that are based on actual truck loads and dimensions as shown in Figure 7.4. The loading from these trucks is applied to the bridge in the same manner as for the AASHTO H and HS trucks. The only difference is in the calculation of the effective width.

$$E = 0.063 \cdot S + 4.65 \qquad \text{(EQN 7.4)}$$

Based on this equation the effective widths become 6.6 feet for the end spans and 7.1 feet for the middle span. The same parameters are used for calculating the rating factor.

Once again the SAP90 bridge module was used to analyze the structure for the load cases involved with these trucks. The results from these analyses are shown in Figure 7.5, and the rating factors are given in table 7.2. For the end spans and middle span the Type 3-50 kip rating truck produced the critical loading. This is due to its ability to lump more mass into the relatively short spans than the other rating trucks. The longer Type 3S2-72 kip rating truck produced the

critical results for negative moment over the piers. The 22 foot spacing between the front and rear tandems allowed the Type 3S2 rating truck to apply significant load to both the end and the middle span at the same time producing the large negative moment over the pier.

The importance of the material properties used in the rating factors once again proved to be very important in this group of ratings. Overall, the changes between using the H and HS trucks vs. the Type 3 rating trucks was very small. The critical rating again corresponds to the negative moment over the pier line. Using the measured properties gives a very favorable rating of 1.76 where the code properties still produce a deficient rating of 0.99.

**Table 7.2 - Rating Based on the 1983 AASHTO Specifications: Using the AASHTO Type 3 Rating Trucks**

LOAD CONDITION	MATERIAL PROPERTIES	NOMINAL RESISTANCE	DEAD LOAD	LIVE LOAD	RATING FACTOR
MOMENT IN END SPANS (kip-in)	CODE SPECIFIED	5,010	1,370	1,145	1.08
	MEASURED PROPERTIES	6,690	1,370	1,145	1.67
MOMENT OVER PIER (kip-in)	CODE SPECIFIED	6,280	2,423	1,141	0.99
	MEASURED PROPERTIES	8,410	2,423	1,141	1.76
MOMENT IN MIDDLE SPAN (kip-in)	CODE SPECIFIED	5,390	1,470	1,153	1.16
	MEASURED PROPERTIES	7,200	1,470	1,153	1.80
SHEAR AT PIERLINE (kips)	CODE SPECIFIED	132	35	20.7	1.46
	MEASURED PROPERTIES	171	35	20.7	2.19

\* All based on load factor method and inventory rating.

#### 7.4 RATING BASED ON AASHTO 1989 GUIDE SPECIFICATION

The 1989 AASHTO Guide Specifications differ from the 1983 Manual by specifying values of  $\phi$ ,  $\gamma_d$ ,  $\gamma_l$ , and  $I$  to be used in rating the bridge. The guidelines also specifically called for the use of the AASHTO Type 3 rating vehicles (Fig 7.4), with the corresponding effective width calculated in the previous section. The 1989 Guide is also more specific as to the calculation of the dead load.

For rating, the dead load is calculated from nominal dimensions, and 20% is to be added to

the design thickness of any overlay. The code specifies the weights of the materials to be used in calculating the dead load. The dead load factor,  $\gamma_d$ , is specified as 1.2, and the live load factor,  $\gamma_l$ , is based on the volume of traffic and enforcement against overload. For the given bridge  $\gamma_l$  is equal to 1.3 based on a low volume roadway (ADTT, 1000) and reasonable enforcement and appropriate control of overloads. The  $\phi$  factor is based on the condition of the bridge, redundancy and frequency of inspection and maintenance. Because of the deteriorated state of the bridge  $\phi$  is taken as 0.7. The impact factor  $I$  is determined by the condition of the riding surface; based on the poor condition of the overlay,  $I$  is taken to be 0.2.

The analysis results shown in Figure 7.6 are the same as for the 1983 specifications using the Type 3 rating trucks, except the dead load has changed due to the provision of the 1989 guidelines. Table 7.3 shows the results for the ratings based on the 1989 AASHTO guidelines. Once again the critical rating values correspond to the negative moment over the middle span. However, the factors specified in the guidelines actually lead to a more conservative rating than the rating based on the 1983 manual. This reduction is largely due to the reduced resistance factor as a result of the deteriorated state of the bridge. If the bridge had been listed as being in good condition rather than as heavily deteriorated,  $\phi$  would have increased to 0.85 and the R.F. would have increased to 1.3 for code specified properties. The 1989 guidelines again show the importance of the material parameters. The trends of the ratings remained the same, with negative moment over the pier controlling.

The 1989 guidelines are judged to be a simpler procedure, which require slightly less time and effort to implement than the 1983 specifications. The guide also has specific provisions to account for damages that are not included in the 1983 AASHTO Specification. However, it lacks a quantitative means of determining the deteriorated state of the bridge. For instance, it was decided based on the very poor quality of the shoulders and loss of continuity in the north span, to rate the bridge as being heavily deteriorated. However, based on the good quality of the driving lanes and the NDE results, it could easily be justified to rate the bridge as deteriorated. This would have increased the resistance factor to 0.80 and the rating factor to 1.15, a major difference from the 0.8 rating factor given for the heavily deteriorated case.

#### **7.5 RATING BASED ON THE CALIBRATED FINITE ELEMENT MODEL**

The Batavia test bridge was also rated using the finite element model which has been calibrated to represent the characteristics of the bridge determined during the first modal test, as discussed in chapter 6. Using a finite element model to determine the load distribution is permitted by the 1989 AASHTO Guide Specifications. The application of the finite element model to rating was met with several obstacles. First, the placement of the loads from the trucks on the finite element model is complicated by the fact that SAP90's moving load provisions only work with frame elements, where as this model required shell elements. As a result the loads had to be distributed to nodes by hand for each wheel involved in each truck position. Also note that, unlike the effective strip model, it is necessary to consider both lanes loaded as required by the 1989 Guide Specifications.

**Table 7.3 - Rating Based on the 1989 AASHTO Guidelines**

LOAD CONDITION	MATERIAL PROPERTIES	NOMINAL RESISTANCE	DEAD LOAD	LIVE LOAD	RATING FACTOR
MOMENT IN END SPANS (kip-in)	CODE SPECIFIED	5,010	1,387	1,145	1.03
	MEASURED PROPERTIES	6,690	1,387	1,145	1.69
MOMENT OVER PIER (kip-in)	CODE SPECIFIED	6,280	2,476	1,141	<b>0.70</b>
	MEASURED PROPERTIES	8,410	2,476	1,141	1.24
MOMENT IN MIDDLE SPAN (kip-in)	CODE SPECIFIED	5,390	1,504	1,153	1.09
	MEASURED PROPERTIES	7,200	1,504	1,153	1.80
SHEAR AT PIERLINE (kips)	CODE SPECIFIED	132	35	20.7	1.56
	MEASURED PROPERTIES	171	35	20.7	2.41

In order to simplify the procedure as much as possible, the rating trucks which produced the maximum response, and the approximate placement of these trucks were determined from the previous ratings. Knowing which rating truck to use and approximately where the trucks should be placed to produce maximum response on the bridge cut the total effort required by over 70%. However, each analysis still required the tedious and time consuming step of placing the loads on the bridge as prescribed by the truck placement. Due to the skew nature of the bridge, the positions provided by frame models only roughly approximated the truck placements. Therefore, once the approximate positions of the trucks were established, each truck had to be moved back and forth from this position to find the exact critical load position.

The load was applied to the bridge through node forces, which posed a problem in itself, since seldom does a wheel actually end up on a node. To account for this, one of the wheels on the truck was placed in a position in its lane directly over a joint. The position of the remaining

wheels was then calculated based on the position of the first wheel. The load from the individual wheels was then distributed to the surrounding nodes by linear interpolation. This method allowed the truck to be moved forward in increments of the width of one element with minimal recalculating for the positions of the wheels.

The previous rating analyses clearly show that for critical moment in the end span, the Type 3-50 kip rating truck should be placed at approximately 40% of span. For negative moment over the piers, the Type 3S2-72 kip rating truck should be placed so the tandem axles straddle the pier. For the positive moment in the midspan, the Type 3-50 kip rating trucks should be placed at approximately mid-span. Based on these approximate conditions, the analyses were set up so that the trucks would move through ranges guaranteeing maximum response. By making each individual truck placement a separate load case, it was possible to combine the load cases from each lane in such a manner as to cover all the possible truck positions. Figure 7.7 gives the placement of the trucks that produced the maximum responses in each specific area of the bridge. The dead load moment response for the test bridge is given in Figure 7.8, and is standard for all loading configurations. Figure 7.9 gives the live load moment response for the loading configuration producing maximum moment in the end span. Figure 7.10 shows live load moment contours for responses over the pier, and Figure 7.11 gives the live load moment contours for the middle span. Table 7.4 summarizes the resulting rating factors.

Interpretation of the finite element results requires some expertise. Consider Figure 7.8 which shows the moment contours due to dead load. Initial inspection would indicate that the highest moment over the piers is -32.5 k-in/in. However, this is would be an incorrect assessment. This high moment occurs over the columns in the area where the slab is supported by the column cap. The correct moment for assessing the slab is the moment at the face of the support, as required by the code and good engineering judgement. In Figure 7.8, the pier is shown. Note that contour of 19.5 k-in/in runs almost along the pier line. In a few places, the contour line for 25 k-in/in (not marked) crossed the face of the support, but this is in only a few localized areas and considering only such localizations would be incorrect. Inspection of these results shows that a moment of 21 k-in/in is a reasonable value for the moment at the face of the support. Similar arguments can be made assessing the other moment values.

Also note that the maximum dead and live load moments do not always occurs at the same point. However, they are in all cases in close proximity and the resulting rating factor is influenced very slightly. The coarse movement used in positioning the trucks is not conservative, and this assumption provides the additional conservation to alleviate this problem.

The finite element program outputs moments in kip-ft/inch of width and provides only load distribution, not resistance. The resistance was calculated by assuming a 1" wide beam with proper depth and steel ratio. This 1" wide beam provided a resistance in units consistent with the FE program output. The actual resistance was calculated using the AASHTO Standard Specifications. Shear was not considered in the finite element ratings due to post processing limitations of the software.

Table 7.4 summarizes the rating using the finite element model (note, Table 7.4 shows the

factored dead and live load moments). The rating factors are now greatly improved over the AASHTO methods because the finite element model is capable of providing a much more realistic load distribution by considering the actual geometry of the bridge and interaction between the adjoining "strips" used in the AASHTO method. The critical rating factor also shifts to the moment at the middle of the midspan, but the rating factors of the moment in the middle span and the moment over the piers are now so close, that practically speaking both places have the same rating.

**Table 7.4 - Rating Based on the 1989 AASHTO Guidelines: Using Calibrated Finite Element Model**

LOAD CONDITION	MATERIAL PROPERTIES	NOMINAL RESISTANCE	FACTORED DEAD LOAD	FACTORED LIVE LOAD	RATING FACTOR
MOMENT IN END SPANS (Kips in/in)	CODE SPECIFIED	63.3	16.5	14.7	1.89
	MEASURED PROPERTIES	84.5	16.5	14.7	2.90
MOMENT OVER PIER (Kips in/in)	CODE SPECIFIED	79.3	25.2	15.6	1.62
	MEASURED PROPERTIES	106.2	25.2	15.6	2.62
MOMENT IN MIDDLE SPAN (Kips in/in)	CODE SPECIFIED	63.3	18.8	16.5	1.55
	MEASURED PROPERTIES	84.5	18.8	16.5	2.45

#### 7.6 RATING BASED ON DESTRUCTIVE TEST LOADING POSITION

In order to correlate the bridge ratings with the results of the destructive test, the bridge had to be rated one additional time using the loading configuration from the destructive test. As indicated in chapter 4, the loading system is based on the standard HS20-44 truck positioned in the northbound lane to provide maximum moment in the south span (Figure 7.12). The loads applied during the test were equivalent to the tandem rear axle of a HS20-44 truck. The loading system ignored the influence of the front axle since it was over the pier.

Due to the nature of the loading that this system develops, it is more appropriate to perform the analysis based on the methods of the 1989 guidelines. Thus, the rating was carried out using the parameters established in the 1989 guidelines for effective width, live load factor, dead load factor, and resistance factor. However for this case the impact factor is left to zero since it is impossible for the loading system to produce a significant impact during the loading sequence.

Two procedures were used to rate the bridge for this loading case; the first is the simple frame analogy used in the original ratings based on the 1989 code. The second procedure uses the finite element model developed from the second modal test. This modal test serves as the baseline for the destructive testing, therefore it seemed more reasonable to use the model resulting from the 2nd modal test for the ratings based on the destructive test. This modal test does not incorporate the overlay which was removed prior to testing.

Figure 7.13 shows the results for the analysis based on the frame concept. Table 7.5 give the rating factors based on these analyses. The factored results given in the table indicate a rating factor of 2.3 for the destructive test based on the measured material properties. Removing all of the safety factors the rating would increase to 5.23, which according to the theory applied in the ratings should produce yielding in the reinforcement. Therefore, according to the procedures of the 1989 AASHTO Guidelines the steel in the slab should begin to yield at just above 5 equivalent rating trucks load. As it turns out the bridge was still exhibiting linear behavior at 5 trucks and no yielding of the steel was noted until 20 equivalent truck loads. This demonstrates the problems centered around the simplifying assumptions used in the procedures outlined in the

**Table 7.5 - Rating Factors Based on Destructive Test Loading**

RATING PARAMETER	MATERIAL PROPERTIES	R.N.	D.L.	L.L.	R.F. 1989 GUIDE
POSITIVE MOMENT IN END SPAN (kip-in)	CODE SPECIFIED	5,010	1,370	1,017	1.41
	MEASURED PROPERTIES	6,690	1,370	1,017	2.30
NEGATIVE MOMENT OVER PIER (kip-in)	CODE SPECIFIED	6,280	2,423	667	1.72
	MEASURED PROPERTIES	8,410	2,423	667	3.44
SHEAR AT PIER (kips)	CODE SPECIFIED	132	35	8.14	4.62
	MEASURED PROPERTIES	177	35	8.14	7.74

1989 Guidelines.

The finite element model used to rate the bridge was based the model developed from the second modal test. This model is calibrated to characterize the bridge just prior the destructive testing. Figure 7.14(a) gives the moment contours of this model under dead load. Note the effects on the discontinuity over the north pier on the east shoulder. The moment contours of the analysis for the destructive test loading are given in Figure 7.14(b). In this case, the

maximum dead load moment and live load are not near the same point therefore it was necessary to sum the responses at every node due to the dead load and the live load to find the node with the maximum response. The largest total response was noted at node #124 as shown in Figure 7.14(b). Up to this case the moments from the dead and live loads produced their maximum response at approximately the same location, so it was reasonable to ignore the difference.

The moment due to live load at node 124 is 8.04 kips/in/in width, and the moment due to dead load is 7.08 kips/in/in. With a nominal capacity of 84.5 kips/in/in based on the measured material properties, this produces a rating factor of 4.85. Without safety factors, the rating factor is increased to 9.63, or approximately 10 equivalent truck loads. This would indicate that the steel should have yielded at 10 equivalent truck loads during the destructive test which doubles the 5 equivalent trucks predicted by the simple frame analogy. However this is still only about one half of the load at which yield actually occurred during the destructive test.

#### 7.7 COMPARISON OF RATING PROCEDURES

Overall, the rating seemed to be more influenced by the material properties that are used for the rating than the procedure used in rating the bridge. No matter what technique was implemented, the material properties specified in the code produced excessively conservative results. On the other hand when the real material properties of the bridge were used, in every case the bridge produced ratings usually well above 1. It is therefore, very important for the purpose of ratings to use as accurate material properties as possible.

The method of analysis was also critical. The simple frame analysis based on the AASHTO Standard Specifications is extremely conservative since it does not account for additional load carrying mechanisms such as slab action (interaction between adjacent beam strips) or the actual geometry of the bridge. Using the frame, the bridge was rated as deficient when the code specified material properties were used. However, when a linear finite element program was used a more reasonable load distribution was obtained since this model considers geometry and additional load carrying mechanisms. Even using the conservative code specified material properties, the finite element model rated the bridge as satisfactory, a conclusion borne out by the destructive test.

However, both the frame and the linear finite element model were still far from perfect in assessing the bridge. In the destructive test, 19 rebars were strain gaged and not one was noted to have yielded prior to the applied load of 20 equivalent trucks. However, using the models corresponding to the destructive test loading, the frame analogy predicted this effect would occur at 5 equivalent truck loads, while the finite element model predicted it would occur at 10 equivalent truck loads. Part of the problem is that both the finite element model and the strip model are linear and that the non-linear behaviors are ignored. Advanced techniques such as nonlinear finite element analysis would produce even more accurate results (Hurja, Lee, and Aktan, 1992). A nonlinear finite element analysis of this bridge is presented in the following chapter.

The finite element model represents a model that is very conservative, since prior to the

application of any of the loading, impact or resistance factors a safety factor of two is already applied (noted from the fact that actual yield occurred at 20 trucks and the model predicted 10). When all of the factors are added in, it ultimately ends up providing a safety factor of 4 for this bridge under the destructive test load conditions. Similar safety factors would probably be obtained for other loading conditions. The frame representation had a factor of safety of 4 before the factors were added in, again based on comparing the predicted yield point from the model against the actual test. As a result, once the dead load, live load and impact factors are added in, the bridge has a total safety factor of about 8.5.

Whereas bridge failure is very undesirable, a rating factor of 2.3 (frame model, midspan moment, destructive test loading) seems to be excessively conservative since the bridge actually failed at 20 trucks. A more reasonable factor would be the 4.85 given through the FE rating. Therefore, using advanced analytical tools, such as finite element analysis, seems very useful, as it removes a great deal of the excessive conservatism present in other procedures. However, the engineer performing the ratings must be aware of the probable accuracy of the analysis so that correct moments and shears are used in the rating and so that the safety factor does not become unreasonably small.

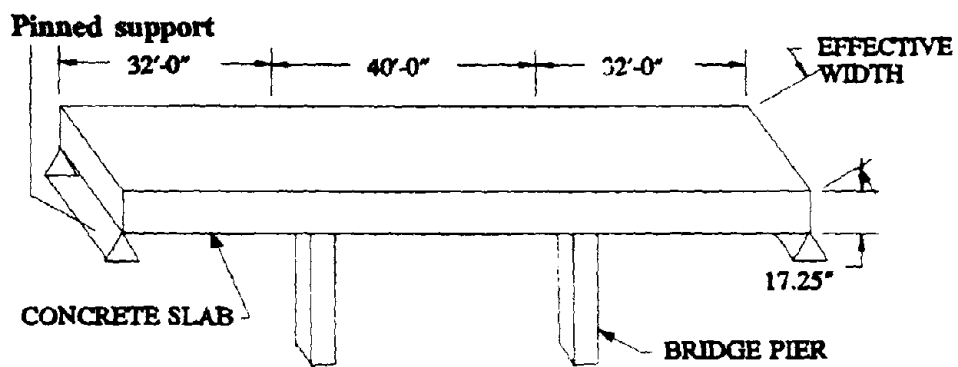


**FIG 7.1a: BRIDGE MODEL USED IN RATING**

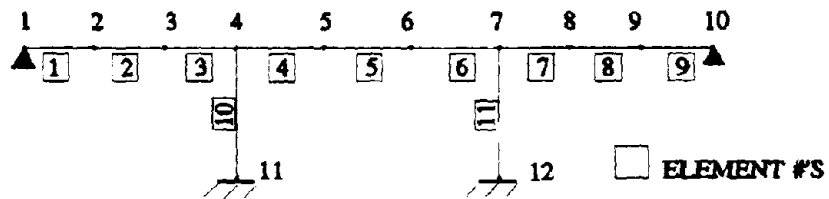
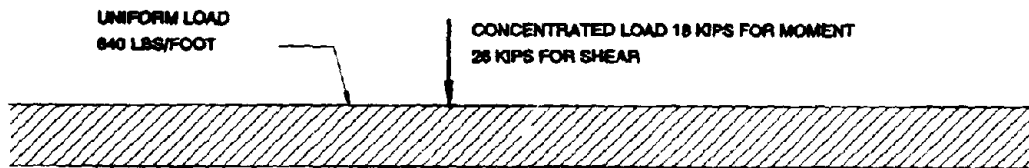


**FIG 7.1b: ANALYTICAL MODEL FOR RATINGS**

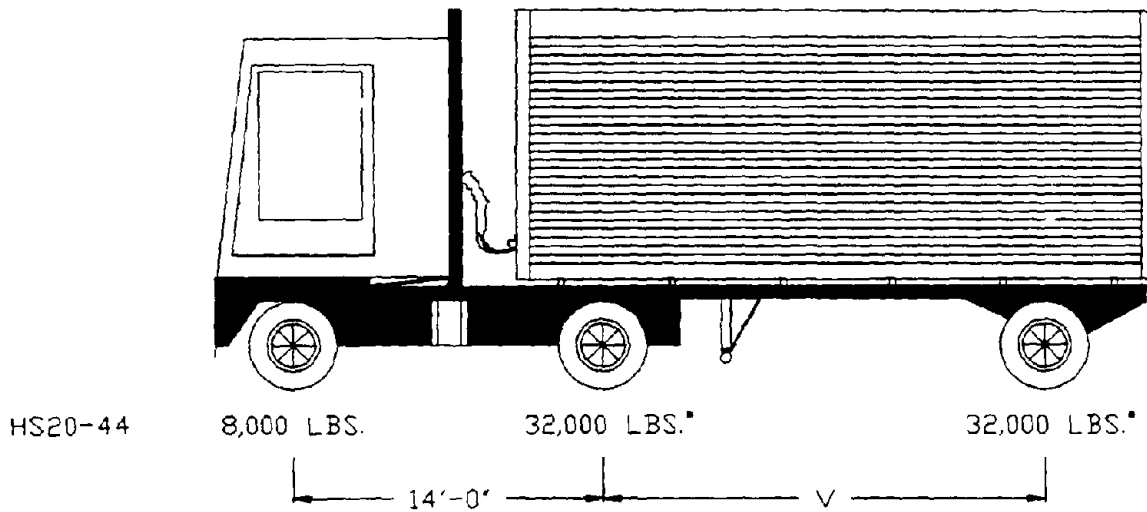
**FIGURE 7.1: SIMPLE FRAME CONCEPT & ANALYTICAL MODEL**

NOTE: FOR POSITIVE MOMENT USE ONE CONCENTRATED LOAD  
 FOR NEGATIVE MOMENT USE TWO CONCENTRATED LOADS  
 ONE ON EITHER SIDE OF THE PIER



**H20-44 AND HS20-44 LOADINGS**

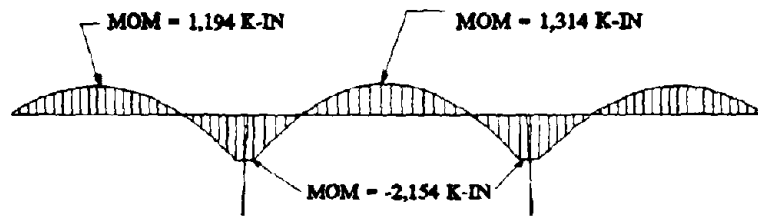
**FIGURE 7.2a: H AND HS LOADING**



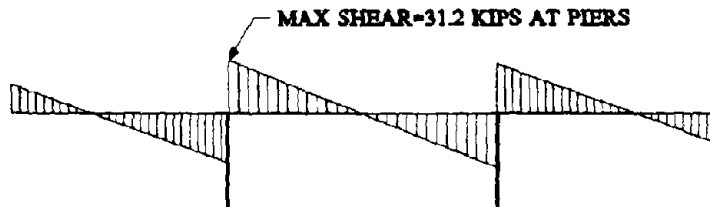
V = VARIABLE SPACING - 14 FEET TO 30 FEET INCLUSIVE. SPACING TO BE USED IS THAT WHICH PRODUCES MAXIMUM STRESSES.

**FIGURE 7.2b: H AND HS TRUCK**

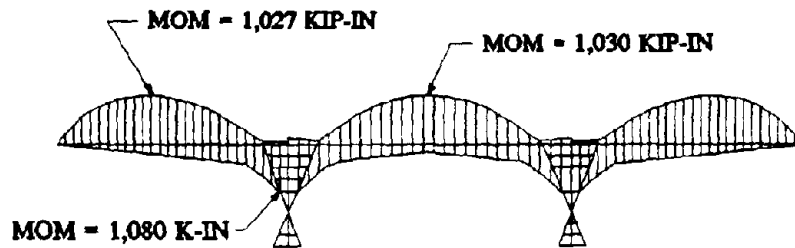
**FIGURE 7.2: H AND HS LOADING TRUCKS**



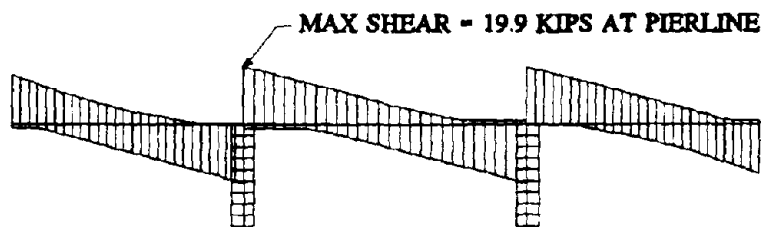
MOMENTS DUE TO DEAD LOAD



SHEARS DUE TO DEAD LOAD

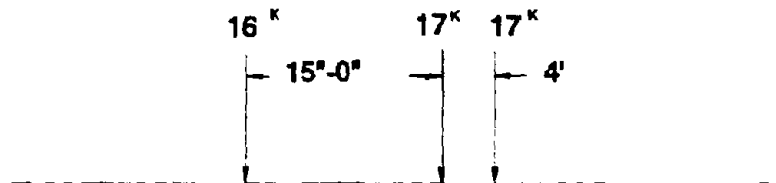


MOMENT DUE TO LIVE LOAD

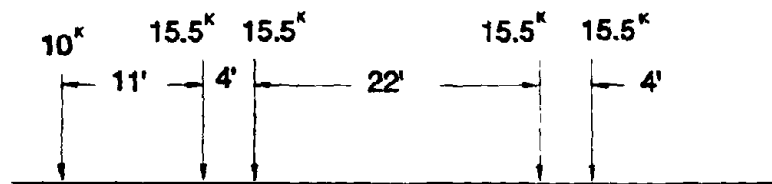


SHEAR DUE TO LIVE LOAD

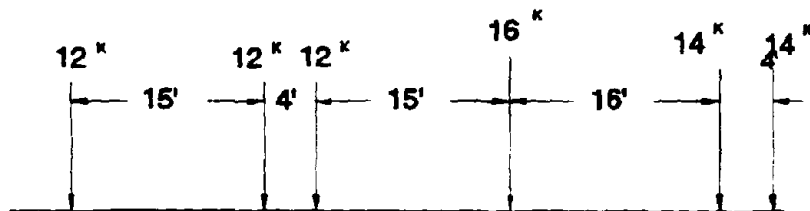
FIGURE 7.3: RESPONSE UNDER H & HS TRUCKS



TYPE 3 UNIT WEIGHT = 50 KIPS

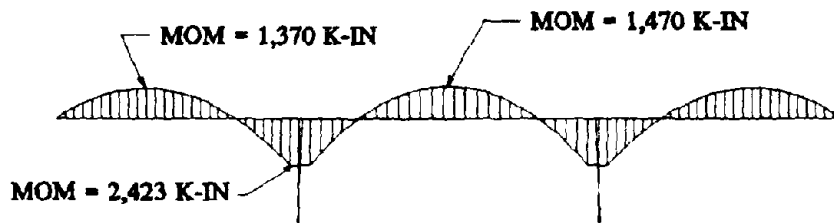


TYPE 3S2 UNIT WEIGHT = 72 KIPS

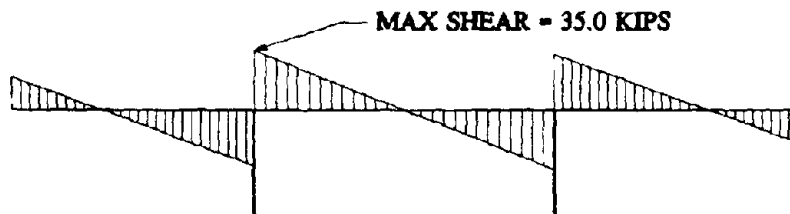


TYPE 3-3 UNIT WEIGHT = 80 KIPS

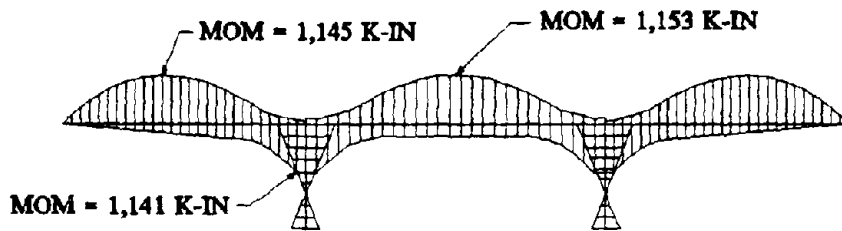
**FIGURE 7.4: LOADING PATTERNS OF TYPE 3 RATING TRUCK**



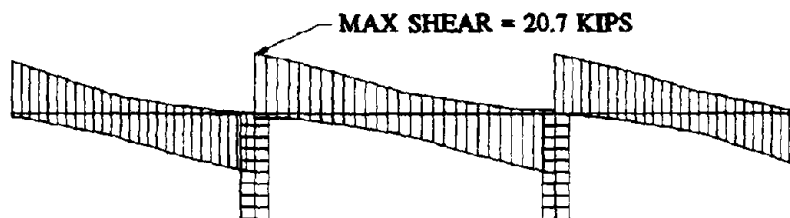
MOMENTS DUE TO DEAD LOAD



SHEARS DUE TO DEAD LOAD

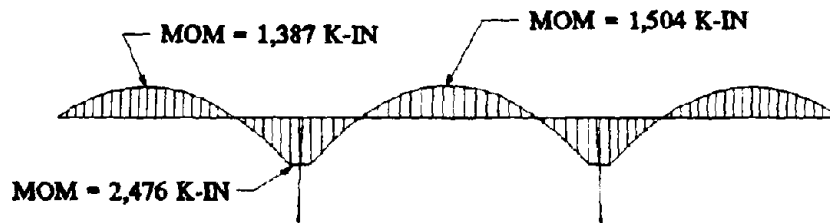


MOMENTS DUE TO LIVE LOAD

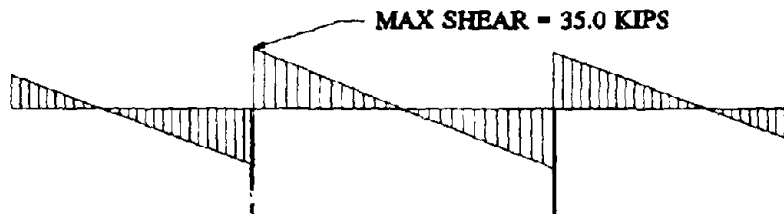


SHEARS DUE TO LIVE LOAD

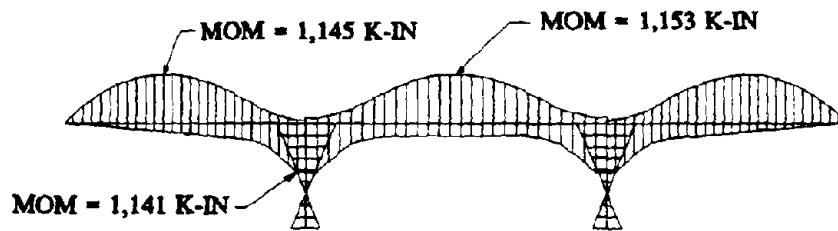
FIGURE 7.5: RESPONSE UNDER TYPE 3 RATING VEHICLES



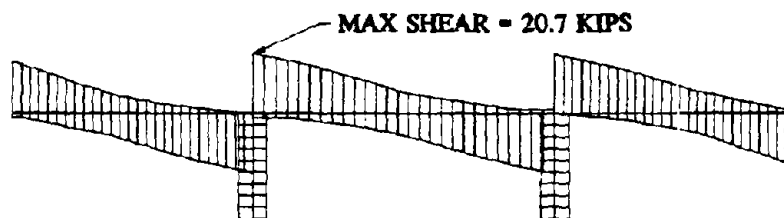
MOMENTS DUE TO DEAD LOAD



SHEARS DUE TO DEAD LOAD

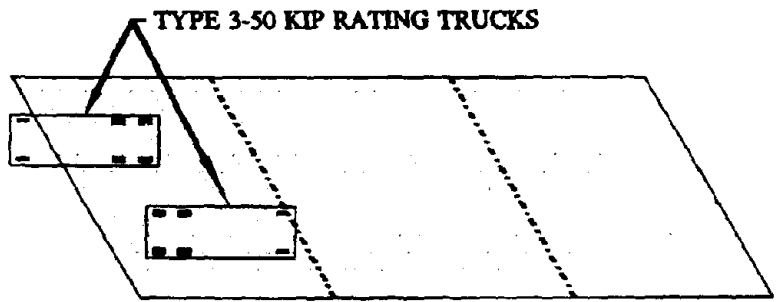


MOMENTS DUE TO LIVE LOAD

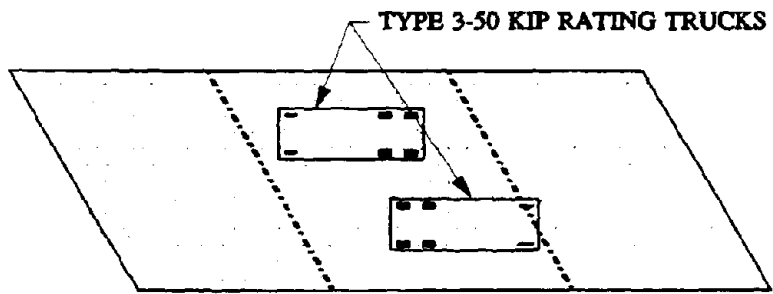


SHEARS DUE TO LIVE LOAD

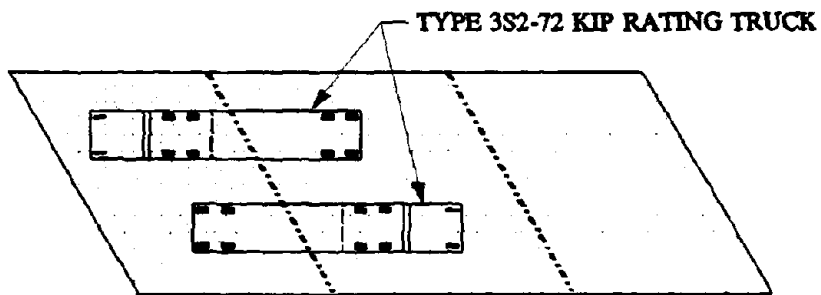
FIGURE 7.6: RESPONSE UNDER TYPE 3 RATING VEHICLE



PLACEMENT OF TRUCKS TO DEVELOP MAXIMUM MOMENT IN END SPAN



PLACEMENT OF TRUCKS TO DEVELOP MAXIMUM MOMENT IN MIDDLE SPAN



PLACEMENT OF TRUCKS TO DEVELOP MAXIMUM MOMENT OVER PIER

FIGURE 7.7: PLACEMENT OF RATING TRUCKS

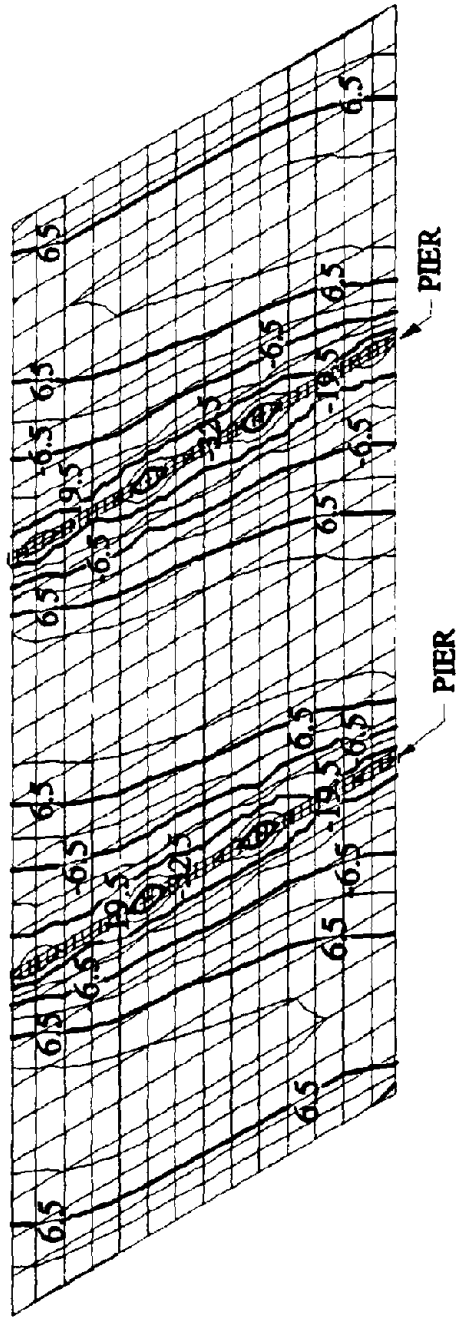
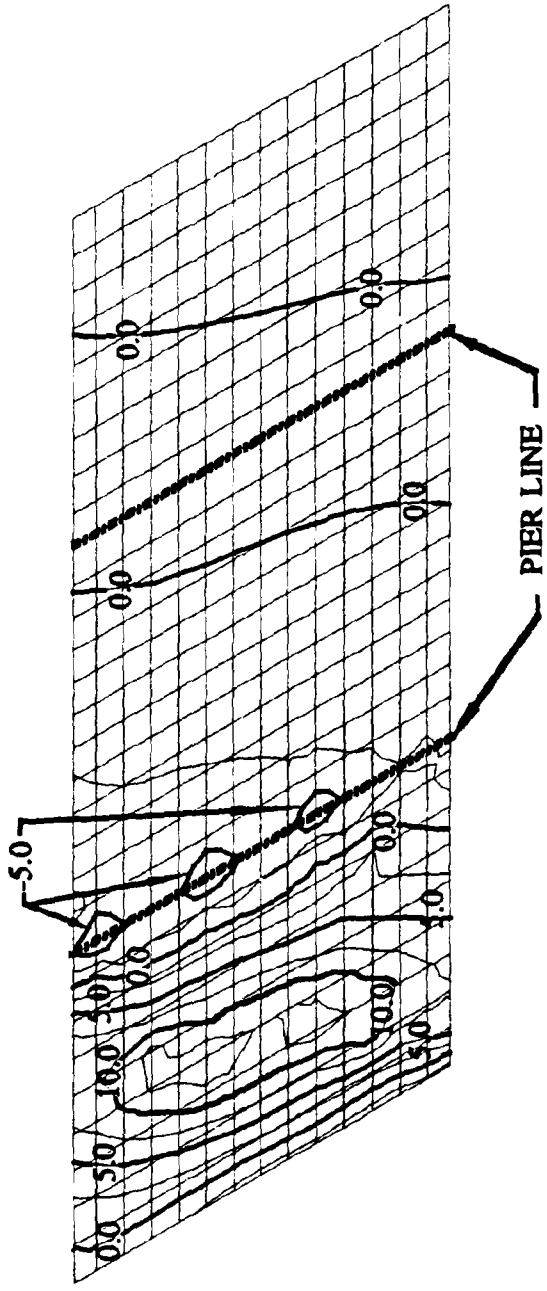


**FIGURE 7.8: MOMENT CONTOURS DUE TO DEAD LOAD**



NOTE: TRUCK LOADING AS PER FIGURE 4.5.1  
 TO DEVELOP MAXIMUM MOMENT IN END SPAN

**FIGURE 7.9: MAXIMUM MOMENT CONTOURS DUE TO LOADING IN END SPAN**

NOTE: LOADING AS SHOWN IN FIGURE 4.5.1  
TO DEVELOP MAXIMUM MOMENT OVER PIER

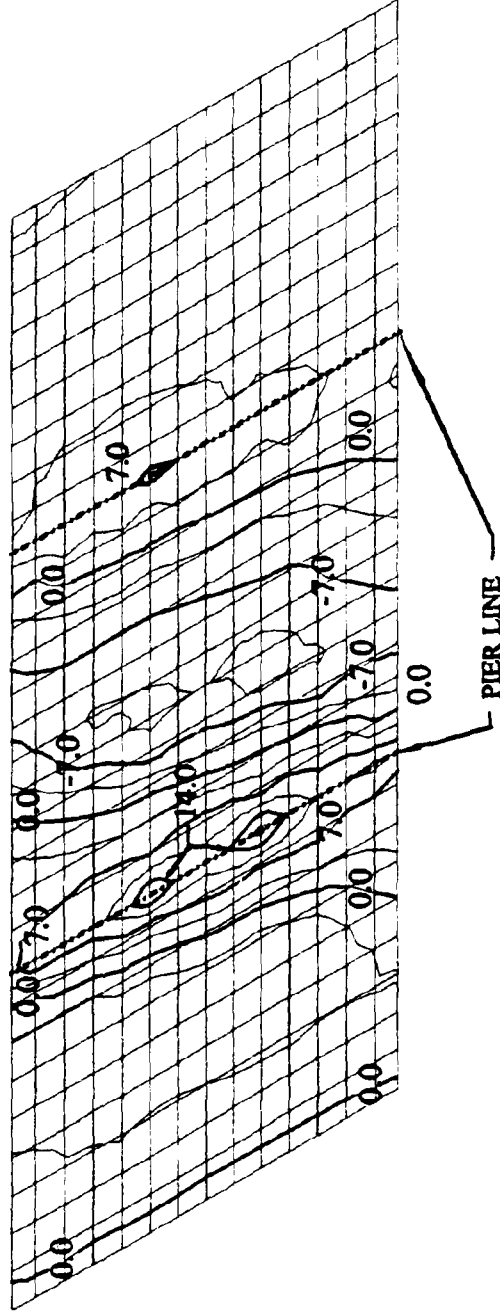


**FIGURE 7.10: MAXIMUM MOMENT CONTOURS DUE TO LOADING OVER PIER**

NOTE: TRUCKS PLACE AS IN FIGURE 4.5.1  
TO DEVELOP MAXIMUM MOMENT IN MIDDLE SPAN

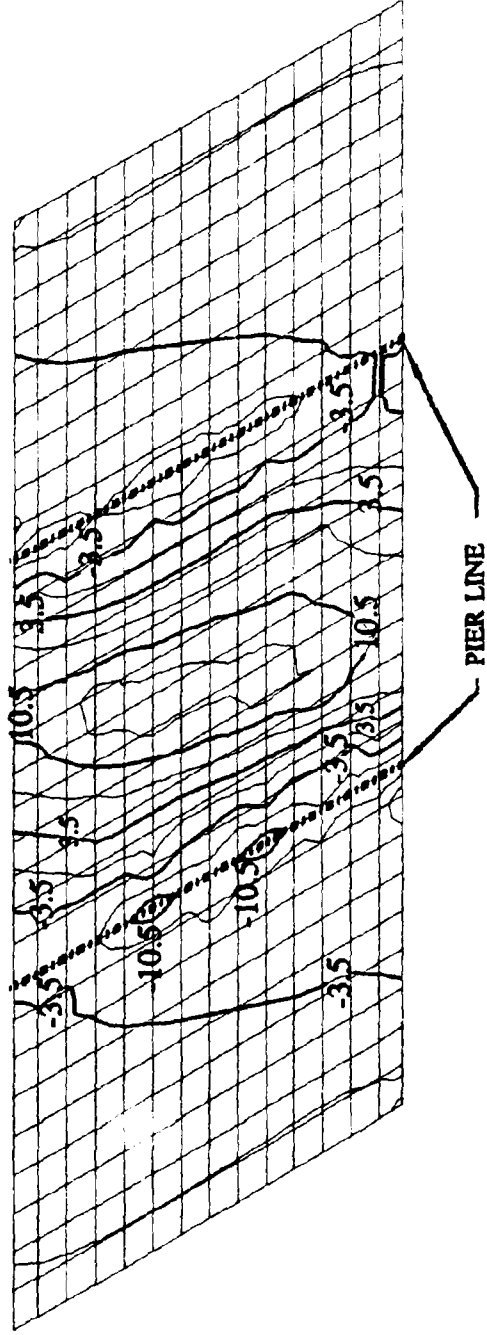
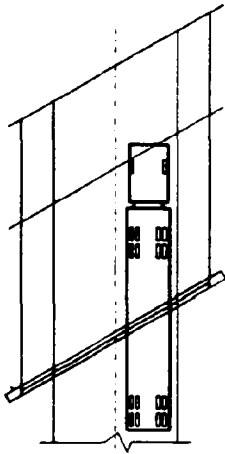
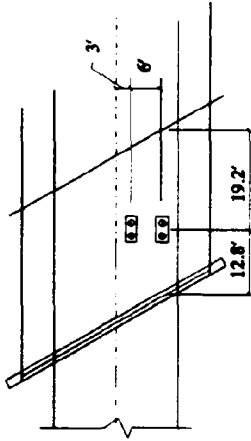


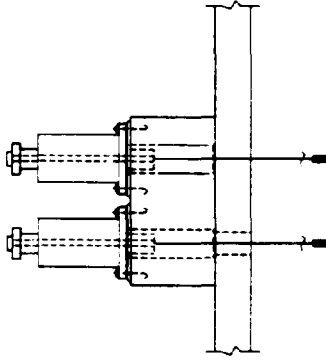
**FIGURE 7.11: MAXIMUM MOMENT CONTOURS DUE TO LOADING IN MIDDLE SPAN**



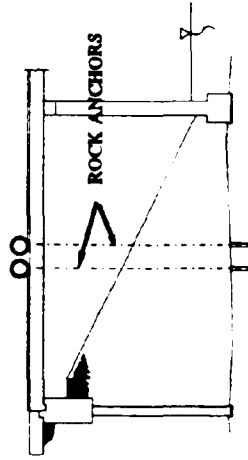
A) LOADING IS DESIGNED TO SIMULATE AN HS20-44 TRUCK ENTERING THE BRIDGE



B) LOADING BLOCKS ARE PLACED AS THE TANDEM AXLE WOULD TO DEVELOPE MAXIMUM MOMENT IN THE END SPAN

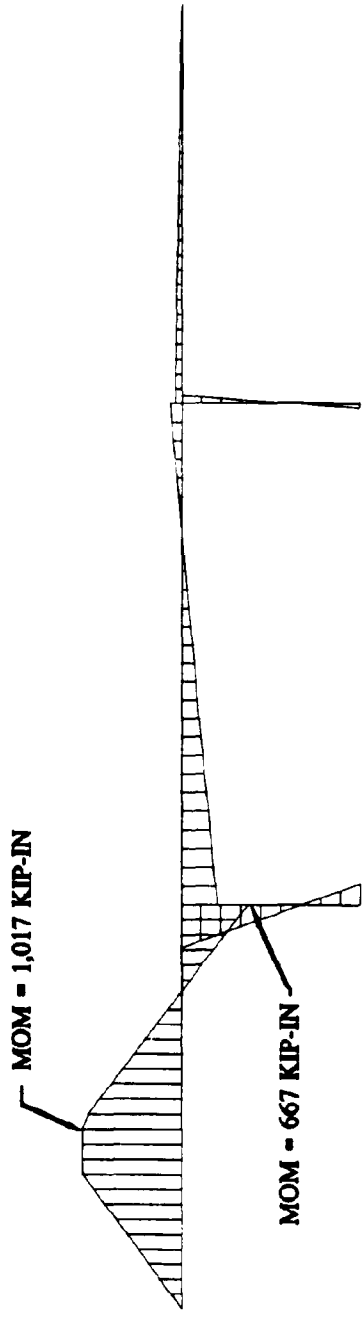


C) HYDRAULIC ACTUATORS ARE PLACED ON THE LOADING BLOCKS TO SUPPLY THE LOAD

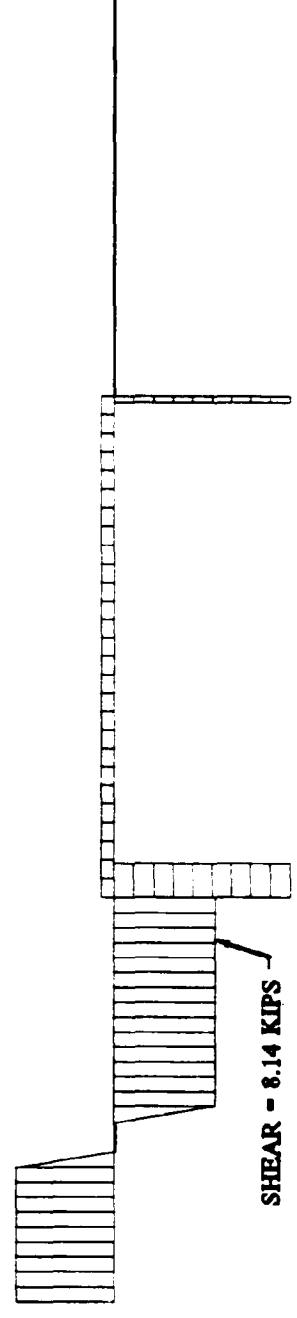


D) ROCK ANCHORS ARE USED TO TIE OF THE TOP OF THE ACTUATORS TO DEVELOPE THE FORCE.

**FIGURE 7.12: LOADING SCHEME USED IN DESTRUCTIVE TESTING**



MOMENT DUE TO 1 EQUIVALENT TRUCK FROM DESTRUCTIVE TESTING



SHEARS DUE TO 1 EQUIVALENT TRUCK FROM DESTRUCTIVE TESTING

**FIGURE 7.13: RESPONSE OF SIMPLE FRAME MODEL TO DESTRUCTIVE TEST LOADING**

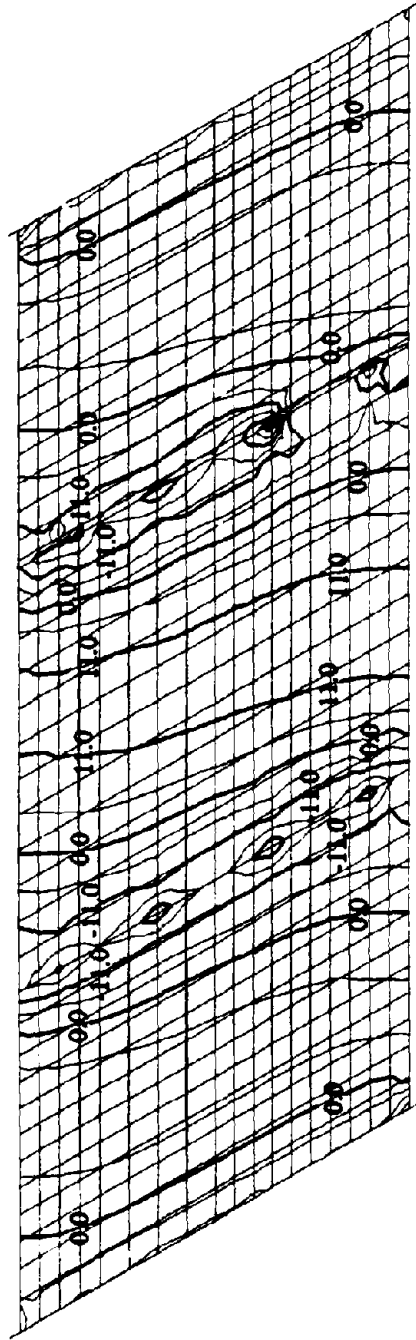


**FIGURE 7.14(a): DEAD LOAD MOMENT CONTOURS FOR 2nd TEST MODEL**

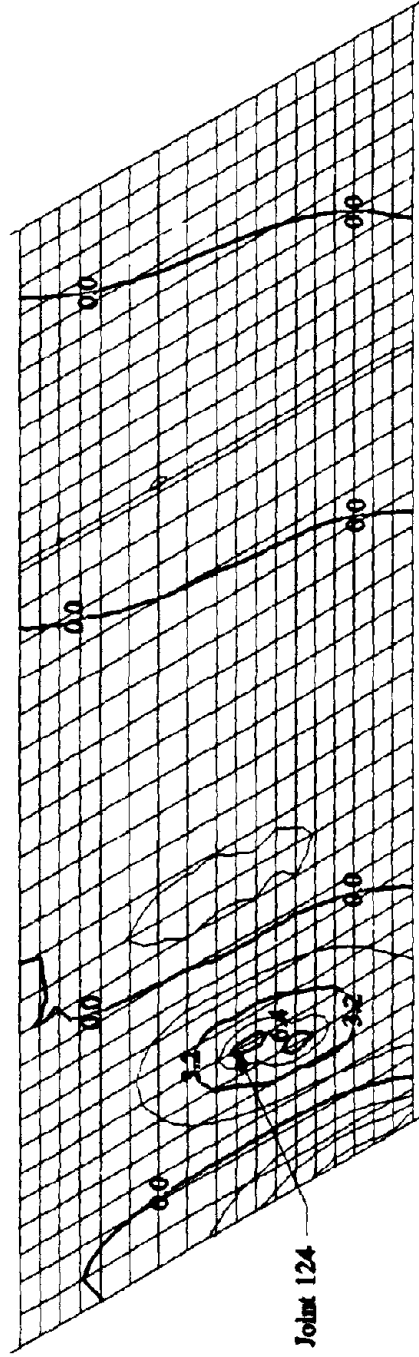
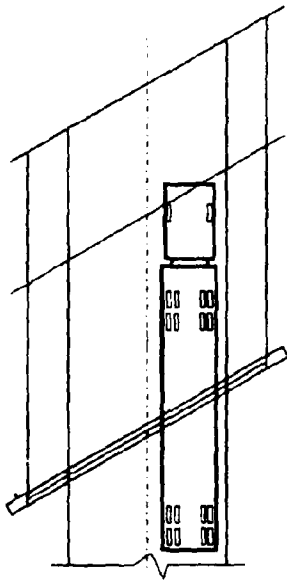
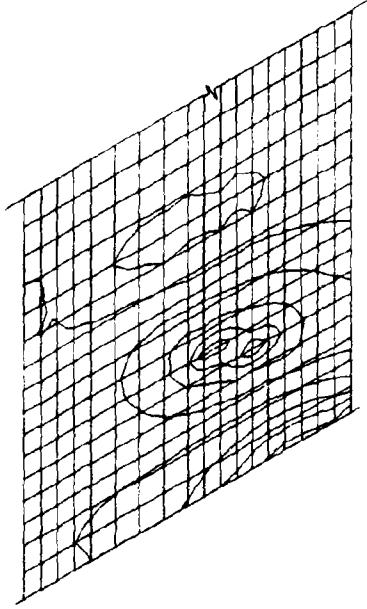


**FIGURE 7.14(b): LIVE LOAD MOMENT CONTOURS FOR DESTRUCTIVE TEST LOADING**



LOADING IS DESIGNED TO SIMULATE AN HS20-44 TRUCK ENTERING THE BRIDGE



MOMENT CONTOURS DUE TO SIMULATED LOADING

RATING FACTORS BASED ON DESTRUCTIVE TEST LOADING

	$\phi$	$\gamma_d$	$\gamma_l$	I	R.F.
AASHTO 1983 SPECIFICATIONS	0.9	1.3	1.67	0.32	1.89
AASHTO 1989 GUIDELINES	0.7	1.2	1.3	0.2	1.92
AASHTO 1989 w/ FEM MODEL	0.7	1.2	1.3	0.2	4.04
AASHTO 1989 w/ TEST RESULTS	0.7	1.2	1.3	0.2	9.87

FIGURE 7.15: COMPARISON OF RATING FACTORS

## **CHAPTER 8: LINEAR AND NONLINEAR FINITE ELEMENT ANALYSES**

### **8.1 INTRODUCTION**

Motivated by the need to better understand seismic behavior of reinforced concrete frames, nonlinear analysis of such structures has gone through significant improvements in the past three decades, and correspondingly many analysis codes have been developed (e.g., NONSAP, DRAIN-2D, ANSR). These codes were largely "calibrated" based on observations made on simple elements and/or structural systems. Nevertheless, in the realm of inelastic response of simple but complete reinforced concrete frame structures, severe shortcomings have been observed. Examples abound where seemingly reasonable modeling assumptions regarding formulation of hysteresis behavior, element behavior in the inelastic range, kinematic interaction between various elements, and material interaction between different orthogonal phenomena (among others) have provided inadequate response correlation (e.g., Betero et al., 1984; Charney and Betero, 1982; Aktan and Nelson, 1988; Shahrooz and Moehle, 1987). Through continued efforts to overcome these difficulties, techniques for proper nonlinear analysis of complete reinforced concrete frame structures appear to be well established now.

Nonlinear finite element analysis (NLFEA) has evolved rather similarly. However, most efforts in NLFEA are still focused on simulating response of individual elements. Applications of NLFEA to complete structures have been limited to design of special structures (e.g., van Mier, 1987; Muller, 1985; Milford and Schnobrich, 1984) or to analytical studies of large structures (e.g., Huria et al., 1991; Meschke et al., 1991). Only recently have there been some attempts to utilize NLFEA for correlation of experimental data from tests on complete structures, e.g. correlation studies of data from tests conducted on a containment vessel (Iding et al., 1992) and simulation of response of the reinforced concrete frame-wall model in the US-Japan cooperative study (Chesi and Schnobrich, 1991). As a result, reliability of NLFEA for complete structures has not been fully explored. Continued correlation studies of complete structures are needed to calibrate nonlinear finite element analysis, verify that NLFEA can be used as a reliable tool, and if NLFEA is to become of practical use.

The reported research provided a rare opportunity to evaluate the reliability of NLFEA in conjunction with system identification to assess strength and stiffness characteristics of aged reinforced concrete bridges. In addition, it became possible to address some of the engineering aspects of modeling of complete, aged structures; and to gauge the effectiveness of NLFEA for predicting response of complete structures at various limit states.

Following is a report on the analyses that were conducted as part of the research. It begins with the predictive analyses conducted prior to any other testing on the bridge, and concludes with the post test correlation studies using the results of all the testing conducted.

### **8.2 PRELIMINARY ANALYSES**

Prior to the destructive testing phase of the research program, a number of analyses

were conducted. These analyses were conducted primarily for establishing the expected strength and stiffness, which were necessary for design of the loading setup and instrumentation (see Chapter 4).

The level of complexity in performing the predictive analyses ranged from simple yield line analysis to nonlinear finite element analysis. Considering the time constraints, it was decided not to incorporate the observed visual damage, most notably on the sides of the bridge. The nonlinear analyses were aided by system identification, and were conducted in the context of establishing probable upper-bounds of response. Attempts were made to limit typical wide variations of predicted response. For example, experimentally-generated material properties were used, and results from nondestructive modal tests were utilized to "calibrate" support conditions.

#### **8.2.1 Yield Line Analysis**

Simple yield line analyses were carried out in reference to the loaded span. The boundary conditions were assumed to be (a) simple supports at both the abutment and pier cap and (b) fixed at the abutment and simple support at the pier cap. Due to uncertainties in material properties at the time when the yield line analyses were performed, the concrete compressive strength was assumed to range between 3,000 to 7,000 psi, the steel yield stress was taken as 40,000 psi and 50,000 psi to conform with the grade of reinforcing bars in use at the time of the construction of the test bridge. Strain hardening in the reinforcing bars was approximated by setting the available ultimate moment strength equal to 1.25 times the nominal strength computed per ACI (ACI, 1989).

The loading blocks were simulated by using two concentrated loads located six feet apart and perpendicular to the center line of the bridge. Because the deflections under the blocks during the destructive tests were expected to be different, two kinematics were selected. In one case, the deflections under both blocks were assumed to be equal, and in the other case the deflection under the block closer to the edge was arbitrarily assumed to be 25 percent larger than the deflection under the other block. Four yield-line patterns (see Figure 8.1) were identified after a number of case studies. The ultimate load was found to range between 348 kips and 632 kips. Using the measured material properties, the yield line analyses were repeated. The upper- and lower-bound estimates of the ultimate load range between 446 kips and 636 kips. The yield line analyses appear to have correlated well with the ultimate load resisted by the bridge (720 kips) rather closely.

#### **8.2.2 Linear Finite Element Analysis**

The linear finite element analyses were performed to ensure that the elastic behavior of the bridge could be computed reliably before attempting to simulate the behavior in the nonlinear range. The bridge was modeled by using SAP90 (Habibullah and Wilson, 1989) as shown in Figure 8.2. The bridge deck was modeled by using a three-dimensional isotropic shell element which includes plate bending and membrane actions. A number of mesh

sensitivity studies were conducted before arriving at the illustrated mesh layout. Three-dimensional frame elements were used to model the piers and pier caps. Figure 8.2 illustrates the connection between the frame elements and shell elements. The shear keys at the abutments Figures 2.9 and 2.10 were assumed to provide sufficient horizontal restraint for the slab. Hence, the slab at the abutments was assumed to be hinged. To simulate the rotational stiffness at the abutments which was observed during the modal tests, linear rotational springs were used. Based on the modal-test results, appropriate spring stiffness constants were identified such that the measured and computed modal characteristics of the bridge match closely.

The elastic modulus was defined as 5,000,000 psi and Poisson's ratio was set equal to 0.25. The stiffness of the frame elements was calculated based on gross-section properties. These analyses were conducted before finding that the deck had experienced damage over approximately a six-foot width on each shoulder. Hence, the nominal slab thickness (17.25 in.) was assumed in the analyses.

In order to verify the analytical model and the rotational stiffness constants at the boundaries, an attempt was made to correlate the vertical deflections measured during the truck load tests. During the third and fourth load cases (Figure 8.3), the instrument at C3 malfunctioned, and the corresponding experimental data are not shown. As seen from Figure 8.4, the analytical and experimental longitudinal deflection profiles are generally similar, except at point F3 (refer to Figure 8.3 for the location of this point) during the first, second, third, and fifth tests. A similar observation can be made for the deflections in the transverse direction. Nevertheless, for the fifth and sixth tests, where two or three trucks had been positioned symmetrically as shown in Figure 8.3, the experimental measurements indicate a symmetrical deflection profile, whereas the analytically-generated deflection profiles do not follow the same trend. To further understand this difference, a simple case study was conducted.

A simply-supported skewed panel was loaded symmetrically (Figure 8.5), and the resulting deflection profile was found to be symmetrical (Figure 8.6). This observation is expected as the stiffness of the two supports are identical, and the two load points are positioned equally from the supports. However, when an identical panel is added (Figure 8.7) the deflection profile is no longer symmetrical; see Figure 8.8. This trend could be explained in reference to Figure 8.9, in which the slab has been discretized into parallel strips. These strips may be viewed as beams supported at points along AB, CF, DE, and free edges AFE or BCD. Representative "beam strips" with approximate boundary conditions are depicted in Figure 8.9. It is apparent that the strips perpendicular to side AFE are more flexible than those corresponding to side BCD; hence, points closer to side AFE will deflect more. These observations are valid as long as the slab stiffness is uniformly distributed. The symmetrical nature of the measured deflection profiles during the destructive tests suggest that the damage changed the slab stiffness unevenly.

In general, the computed deflections are smaller than the measured values, particularly

at locations close to the edges where most of the damage was present. This observation is expected as the existing damage and cracking were not incorporated in the analyses. Small deviations from the experimental data at other locations are also attributed to ignoring the observed damage in the analytical model. However, the differences were deemed negligible for the initial predictive analyses.

### 8.2.3 Nonlinear Finite Element Testing

**Modeling:** The nonlinear analyses were conducted using a microcomputer-based software named 3DSCAS (Lee et al., 1991). The architecture and numerical algorithms of the program are based on ANSR-III (Ougourlian and Powell, 1982), and it includes several linear and nonlinear elements. The particular elements used in this study were a 5-spring R.C. beam-column element (Ghusn and Saïidi, 1986), a linear spring (Huria et al., 1991), and a R.C. 9-node degenerated isoparametric shell element (Milford and Schnobrich, 1984). The shell element is based on layering concept, by which up to 10 layers of concrete and up to 4 layers of steel bars can be simulated. Different properties can be assigned to each concrete or steel layer.

To preserve the continuity between adjacent spans, it was decided to model the entire slab-pier-abutment system. For this purpose, 102 R.C. shell elements (located at the mid-depth of the physical slab) were used to model the bridge deck, as shown in Figure 8.10. Additional refinement of the mesh size and layout was not carried out as mesh sensitivity studies did not indicate significant improvements beyond the illustrated mesh. The piers and pier caps were modeled by using 32, 5-spring R.C. beam-column (frame) elements. The connections between piers, pier caps, and bridge deck were modeled as shown in Figure 8.10, which is similar to the model used for linear finite element analyses conducted by SAP90 (Figure 8.2). The two loading concrete blocks were simulated by several concentrated loads acting on the nodes covered by the blocks (refer to Figure 8.10).

Considering that the deck was connected to the abutments by shear keys, the horizontal movement of the bridge deck at the abutments was restrained in the analytical model. Rotational springs were used to simulate the rotational restraint observed during the modal tests. The rotational stiffness at the abutments was taken equal to that used in the linear finite element analyses.

The concrete and steel constitutive relationships are shown in Figure 8.11. The material properties were obtained based on ASTM standard tests of several steel coupons and concrete cores taken from the bridge. The critical values are summarized in Figure 8.11. The tensile behavior of the concrete before and after cracking was considered. Based on split cylinder tests, the tensile strength was taken as 650 psi. The post-cracking participation of the concrete was assumed to diminish at a strain corresponding to 10 times the cracking strain, i.e.  $k = e_c / e_{cr} = 10$ , where  $e_c$  is the strain at which tensile strength diminishes, and  $e_{cr}$  is cracking strain. This model is referred to as model A. This value is within the range expected for typical reinforced concrete slabs with no or little confinement (Gilbert and

Warner, 1978). A higher participation of concrete beyond cracking was also considered to obtain an upper-bound estimate of strength and stiffness to ensure that the actuators would have adequate stroke and capacity. For this purpose, the concrete was assumed to provide tensile resistance until a strain of 20 times the cracking strain ( $k=20$ ). This model is referred to as model B. The values of Poisson's ratio and shear retention factor are predefined in 3DSCAS as 0.2 and 0.25, respectively. Other values could not be specified, but variations in modeling of local responses (e.g., transfer of shear stress across cracks, or Poisson's ratio) produce little difference in *the global* behavior of slabs, as will be discussed later in this chapter. Hence, these values are sufficiently accurate.

The concrete failure envelope was based on the envelope proposed by Kupfer and Gerstle (1973). This envelope is shown in Figure 8.12. Depending on the ratio of maximum principal stress to minimum principal stress ( $\alpha_2$ ), the following four different failures may occur (Darwin and Pecknold, 1974).

(1) Bi-axial compression

$1 > \alpha_2 > 0$ , Failure: yielding and crushing of concrete

$$\sigma_{2c} = \frac{1 + 3.65\alpha_2}{(1 + \alpha_2)^2} f_c$$

$$\sigma_{1c} = \alpha_2 \sigma_{2c}$$

$$e_{2c} = e_{cx} (1 - \nu \alpha_2) (3p_2 - 2)$$

$$e_{1c} = e_{cx} (1 - \nu \alpha_1) (-1.6p_1^3 + 2.25p_1^2 + 0.35p_1)$$

(2) Bi-axial Tension Compression

$0 > \alpha_2 > -0.17$ , Failure: yielding and crushing of concrete

$$\sigma_{2c} = \frac{1 + 3.28\alpha_2}{(1 + \alpha_2)^2} f_c$$

$$\sigma_{1r} = \alpha_2 \sigma_{2c}$$

$$e_{2c} = e_{cx} (1 - \nu \alpha_2) (4.42 - 8.38p_2 + 7.54p_2^2 - 2.58p_2^3)$$

$$e_{1r} = \frac{\sigma_{1r} (1 - \nu \alpha_1)}{E_c}$$

(3) Bi-axial Tension Compression

$-0.17 > \alpha_2 > \infty$ , Failure: cracking in tension

$$\sigma_{2c} = -0.65f_c$$

$$\sigma_{1t} = f_t$$

$$e_{2c} = e_{c1}(1 - \nu \alpha_2)(4.42 - 8.38p_2 + 7.54p_2^2 - 2.58p_2^3)$$

$$e_{1t} = \frac{\sigma_{1t}(1 - \nu \alpha_1)}{E_o}$$

(4) Biaxial Tension

$\infty > \alpha_2 > 1$ , Failure: cracking in tension

$$\sigma_{it} = f_t$$

$$e_{it} = \frac{\sigma_{it}(1 - \nu \alpha_j)}{E_o}$$

where,

$\sigma_{ic}$  = Maximum biaxial compressive stress in the  $i^{\text{th}}$  principal direction

$\sigma_{it}$  = Maximum bi-axial tensile stress in the  $i^{\text{th}}$  principal direction

$e_{ic}$  = Strain corresponding to  $\sigma_{ic}$

$e_{it}$  = Strain corresponding to  $\sigma_{it}$

$\alpha_i$  = Stress ratio ( $\sigma_j / \sigma_i$ )

$i, j$  = 1 or 2

$E_o$  = Initial tangent modulus of elasticity under uni-axial stress

$\nu$  = Poisson's ratio

$p_i$  = ( $\sigma_i / f_c$ )

The longitudinal and transverse deck reinforcement was simulated with four layers of steel. The steel was assumed to be smeared, defined by the direction of reinforcing bars and reinforcement ratio at each integral point. The slab was divided into eight concrete layers each having identical material properties. An orthogonal smeared crack model was utilized, and the directions of cracks were allowed to rotate. Potential dowel action of reinforcing bars across cracks could not be modeled. Perfect bond between reinforcing bars and concrete, and between various concrete layers is assumed in the shell element.

**Verification:** Prior to conducting the nonlinear finite element analyses, the model as well as the program 3DSCAS were verified in the elastic as well as inelastic range. The response of the test bridge under 40 kips was evaluated by using the programs SAP90 and 3DSCAS using the models shown in Figures 8.2 and 8.10. Based on previous analyses, this level of

load is not expected to cause cracking. The material properties, boundary conditions, and rotational spring stiffness constants were kept identical between the two programs. As the shell element incorporated in SAP90 is intended for isotropic members, the steel ratios at the Gauss points in 3DSCAS were set equal to zero such that both programs would result in similar slab flexural stiffness.

From Figure 8.13, it is apparent that the resulting deflection profiles in the transverse and longitudinal directions are rather close. With the exception of the region near the abutment, the moment contours in the longitudinal direction are also similar, refer to Figures 8.14 and 8.15. The difference in the moments along the abutments is mainly due to the differences in the stress resultants for the shell elements in the two programs, as shown in Figure 8.16. It is evident that the shell element in SAP90 does not consider the out-of-plane deformations. This effect would not be important if the twisting moment ( $M_{12}$ ) is not large relative to the flexural moment ( $M_{22}$ ). Considering that near the abutments the twisting and flexural moments are comparable (Figures 8.14 and 8.17), lack of simulation of the out-of-plane deformations would significantly affect the moments, and hence the results from the two programs are different along the abutments.

As a further verification, the response of a reinforced concrete cantilever beam under a concentrated load at the tip (Figure 8.18) was computed by nonlinear finite element analysis and simple beam theory. The average moment-curvature response (determined from the Gauss points closer to the fixed support) was compared with that obtained by conventional layering concepts for moment-curvature analysis (Wallace, 1992). The concrete and steel constitutive relationships were approximately identical in both approaches. The cracking and yield moments are rather close as seen from Figure 8.19. The small discrepancies are mainly due to the formulation differences, i.e. one is based on plate theory and the other is based on simple beam theory, and shear deformations were not considered in the simple analysis; and the differences between the constitutive relationships used for the nonlinear finite element analysis and for the simple moment-curvature analysis.

**Results:** A Newton-Raphson iteration scheme with automatic stiffness updates every 5 iterations was used. The predicted overall load-deflection curves of the bridge at Point A (Figure 8.10) are illustrated in Figure 8.20. A larger participation of concrete beyond the initial cracking ( $k=20$ ) resulted in slightly larger strength and stiffness. The ultimate load-carrying capacity of the bridge was estimated to range between 1730 kips to 1835 kips, with a corresponding vertical deflection of 3.7 in. at Point A. The first yielding of the reinforcing bars was computed to occur at 1120 kips. This load is considerably larger than its experimental counterpart (650 kips).

On the same graph, the experimental load-deflection is also plotted. Beyond 160 kips a distinct difference between the analytical and experimental overall stiffness is observed. The vertical deflection of the deck at Point A prior to failure (2.7 in.) was approximately four times larger than the computed deflection at a load corresponding to the measured

ultimate load. The total load on the bridge at collapse corresponded to approximately 40 percent of the predicted strength. Therefore, the stiffness and strength were clearly overestimated. The lower and upper bounds of strength as computed by yield line analysis (446 kips and 636 kips) are closer to the measured strength. An explanation for this observation will be provided in section 8.3.4.

### 8.3 PARAMETRIC STUDIES

Lower computed stiffness and strength may be attributed to the existing damage which was not accounted in the predictive analyses. Of equal importance are assumptions regarding geometric modeling and material properties. The modal tests were useful in identifying the initial support conditions at the abutments. It is questionable whether the initial boundary stiffness would remain valid under large loads causing significant inelastic action. For example, the abutment stiffness was observed to change significantly as the testing progressed (see chapter 5).

A number of analyses were conducted to determine the potential sensitivity of the computed responses to assumptions regarding various critical parameters. The parameters were the concrete material properties and constitutive relationships, modeling of support stiffness at the abutments, and simulation of slab-pier cap connection. A majority of these analyses was conducted by a nonlinear finite element analysis package named POLO-FINITE (Lopez et al., 1987). This program, which was used for the post-test correlation studies, will be described in detail later in this chapter.

#### 8.3.1 Concrete Material Characteristics

**Poisson's Ratio and Shear Retention Factor:** Shear retention factor is a number specified to reflect reduction of shear force transfer across cracks. This factor is typically taken as 0.25. Three analyses were conducted by varying the values of Poisson's ratio ( $\nu$ ) from 0.15 to 0.2 while selecting 0.25 or 0.4 for shear retention factor ( $\beta$ ). The resulting load-deflection at point A (refer to Figure 8.10 for the location of this point) is plotted in Figure 8.21. It is clear that the results are not affected by these two parameters. For all the subsequent analyses, Poisson's ratio was taken as 0.2 and shear retention factor was set to 0.25.

**Tensile Strength and Post-cracking Behavior:** Various models have been proposed to assess post-cracking behavior of reinforced concrete structures. These models account for the concrete stiffness between cracks, i.e. tension stiffening. Three models were considered: (1) a bilinear function (Gilbert and Warner, 1978), (2) the model proposed by Vecchio-Collins (1986), and (3) the model developed at the University of Tokyo (Okamura et al., 1985). These models are illustrated in Figure 8.22. For the same concrete tensile strength, it is possible to control the amount of tensile resistance in the concrete after cracking, refer to Figure 8.23. For example, by setting parameter  $c$  in the model from the University of Tokyo equal to 0.2, this model and the Vecchio-Collins' model are rather close.

The effects of selecting different post-cracking models were investigated by computing the load-deflection response of a panel with two simply-supported ends and two free edges, as shown in Figure 8.24. The central deflection of this panel under a concentrated load was computed by using POLO-FINITE. The observed differences (Figure 8.24) are relatively small, yet more significant than the effects of Poisson's ratio or shear retention factor. It should be noted that Vecchio-Collins' model was calibrated based on tests on heavily confined panels. In addition, the model developed at the University of Tokyo indicates some residual tensile strength even for very large concrete tensile strains. This behavior does not appear to be appropriate for a reinforced concrete slab with little or no confinement, and particularly if it is damaged. Therefore, in all the subsequent analyses it was decided to use the bilinear model in which the tensile strength drops to zero at some specified strain.

Using the test bridge, the effects of varying two other parameters related to tensile behavior of concrete were studied. These parameters were the magnitude of tensile strength and the strain at which the tensile strength drops to zero. The bridge was modeled identically to the model used in the preliminary analyses (Figure 8.10) with Poisson's ratio and shear retention factor taken as 0.2 and 0.25, respectively. Three different analyses were conducted by varying the tensile strength and the ultimate concrete strain at which tensile stress drops to zero ( $\epsilon_u$ ). The resulting load-deflection curves at point A (this location is shown in Figure 8.10) are presented in Figure 8.25. The results indicate that the response is somewhat sensitive to the assumed tensile behavior of concrete. Furthermore, the response exhibits a more flexible behavior when the tensile strength is reduced.

### 8.3.2 Support Stiffness at Abutments

The shear keys at the slab-deck connection are expected to provide some degree of horizontal restraint. As a result, in all the previous analyses the slab was assumed to be hinged at the abutments. However, the experimental results suggest some level of horizontal movement at the top of the bridge deck along the abutment (see Chapter 5). Such horizontal flexibility is expected to reduce the stiffness and the level of membrane force in the slab which significantly affect the overall behavior.

Two analyses were conducted to study the effects of horizontal restraint. The geometric model, concrete material properties and constitutive relationships were kept identical to those discussed in the aforementioned sections. In one analysis, the horizontal movement of the slab was restrained by using hinges at the abutments, and in the second analysis the slab-abutment connection was simulated as rollers. A drastic difference in the load-deflection response at point A (Figure 8.10) can be seen from Figure 8.26. The computed ultimate load drops by 50 percent when rollers are used, and the stiffness is also reduced. The reduction is attributed to reducing the membrane force which can be developed in the slab if it is restrained horizontally, see Figure 8.27. It is clear that at the same level of total load on the bridge, the membrane force is reduced by as much as 2.5 times when the

horizontal restraint at the abutments is relaxed. The effects of the horizontal support condition at the abutments are considerably more significant than the other parameters studied so far. The influence of rotational stiffness at the abutments will be discussed later in Sections 8.4.1 and 8.4.2.

### **8.3.3 Geometric Modeling of Slab-Pier Cap Connection**

In all the previous models, the pier caps and piers were modeled as frame elements which were connected to the nodes of the shell elements (Figure 8.28). A rigid end zone (28" long) equal to pier cap thickness and half slab thickness was specified at the top of each frame element representing the piers. This model is referred to as pier model 1. A second model (pier model 2) was considered in which the geometric characteristics were identical to pier model 1, except amplifying the torsional stiffness of the horizontal frame element along the width of the slab connecting the shell nodes to the vertical frame elements. The torsional stiffness was increased by a factor of 10 over the value obtained from the cross-sectional dimensions of the pier caps. In the third model (pier model 3), the horizontal frame element was replaced by a thicker shell element as shown in Figure 8.28.

Based on the experimental results and observations, the piers or pier caps did not experience any inelastic action. As a result, elastic analyses were conducted to study the influence of various techniques for modeling the slab-pier connection. For this purpose, the response of the bridge for load case 3 of the truck load tests (which was more critical than the other cases, see Figure 8.3) was computed by using pier models 1, 2, and 3. The deflection profiles are obviously not affected by the technique used to model the slab-pier connection, as evidenced from Figure 8.29. In all the subsequent analyses, model 1 was used as it is a simple model yet it does not adversely affect the response.

### **8.3.4 Summary**

The response of the test bridge was found to be sensitive to the tensile characteristics of concrete, and more significantly to the assumed horizontal boundary conditions at the abutments. This finding is in accord with other observations that membrane force could double flexural strengths of reinforced concrete slabs (Park and Gamble, 1980). The level of membrane force depends on whether the boundary conditions are restrained horizontally to develop such force. The changes in horizontal restraint affect the response more appreciably when the concrete tensile strength is smaller (Shahrooz et al., 1992). A better estimate of the measured strength by the yield line analyses may be attributed to the fact that the effects of membrane force were not considered.

The previous observations might imply that the large discrepancies between the preliminary computed results and the experimental strength and stiffness could be remedied by releasing the horizontal restraint at the abutments. However, this solution is in conflict with the presence of the shear keys at the abutments. Such shear keys are expected to provide some degree of restraint against horizontal movement.

It is believed that this paradox is due to idealizations of geometry in simulating the connection between the bridge deck to the abutments. At the abutments, the rotational springs, hinges, or rollers were attached to the nodes of the shell elements (representing the slab) located at the mid-depth of the bridge deck. Even if the bridge deck is restrained horizontally by the shear keys at the abutment level, the rotation of the bridge deck could result in an apparent horizontal movement at the mid-depth as illustrated in Figure 8.30. This "rocking" motion of the slab was observed experimentally. Near failure the rotation at the south abutment was measured to be as large as  $1.4^\circ$ . Hence, when the horizontal restraint at the abutments is relaxed, a better correlation of the measured response is possible because the movement of the bridge deck at its mid-depth is indirectly taken into account. It should be noted that this approach is overly simplistic, and does not consider the kinematics shown in Figure 8.30.

An attempt was made to model the expected kinematics at the abutments more reasonably. The model consists of rigid links attaching the shell elements which represent the bridge deck to hinges simulating the shear keys at each abutments, as illustrated in Figure 8.31. The rotational springs are placed at the hinges. This model was utilized in the correlation studies explained in the following sections.

#### **8.4 POST-TEST CORRELATION STUDIES**

As described in detail in Chapter 3, the condition survey of the bottom surface of the slab revealed light deterioration, comprising of small cracks and minor spalling. The top surface had experienced significant deterioration. Approximately 3 in. of the concrete had either deteriorated severely or spalled off completely along both shoulders over a 6 ft. to 8 ft. width. Several of the rusted top reinforcing bars had been exposed on the shoulders. Furthermore, the concrete quality and strength were much poorer on the shoulders than the driving lanes.

The damage was simulated by reducing thickness around the shoulders. Considering the uncertainties regarding local variations of concrete properties, it was decided to use identical material properties for the entire slab. First, the results from the truck load tests were correlated. With the same calibrated geometric model, the response of the test bridge during the destructive test was correlated.

##### **8.4.1 Simulation of Results from Truck Load Tests**

Using SAP90 (Habibullah and Wilson, 1989), the bridge was modeled as shown in Figure 8.32. The slab thickness was reduced at the shoulders according approximately to the field measurements. The thickness along the eastern (zone A) and western (zone C) shoulders was reduced by 3 in. and 1 in., respectively (see Figure 8.32). The nominal thickness (17.25 in.) was used for the driving lanes (zone B). The abutment-slab connection was modeled as described previously (Figure 8.31), and the stiffness of the rotational springs along the abutments was selected based on the modal test results. The total spring stiffness in the x

and y directions along the abutment were 43,740 k-in/rad. and 75,760 k-in/rad., respectively. The slab-pier cap was modeled similar to the preliminary model described in Section 8.3.3. The measured value of modulus of elasticity (approximately 5,000,000 psi) was used, and Poisson's ratio was taken as 0.20.

The resulting deflection profiles in the longitudinal and transverse directions are plotted in Figure 8.33. It is clear that the experimental results are correlated very closely. Hence, the effects of damage were apparently simulated properly.

Some of the rotational stiffness observed during the modal tests is taken into account by the improved model of the slab-abutment connection. To verify this observation, the rotational springs were completely removed from the hinges located at the level of shear keys (Figure 8.31). The resulting model is labelled model 2. As seen from Figure 8.33, the deflection profiles did not change noticeably. Hence, these rotational springs could be eliminated for the elastic analyses.

#### 8.4.2 Correlation of Results from Destructive Test

**Modeling:** The correlation studies were conducted by using a general-purpose program for linear and nonlinear finite element analysis program called POLO-FINITE (Lopez et al., 1987). This program was installed on a 400-series Apollo workstation. It has several element types and material models. In contrast to 3DSCAS, the elements and material models are independent of each other and can be combined. Several different material models can be used in conjunction with one element. The particular elements selected from the element library were a 3-D frame element with a linear material model, a spring element with a nonlinear material model for which several segments with identical tensile and compressive properties can be specified, and a 9-node isoparametric shell element with a nonlinear material model. The shell element is identical to that implemented in 3DSCAS, but the material model is different. One of the major differences is the concrete failure criterion. A four-parameter failure surface defined by a triaxial stress function has been incorporated (Hsieh, Ting, and Chen, 1982). This function is as follows, and it is shown in Figure 8.34.

$$F(I_1, J_2, \sigma_1) = A \frac{J_2}{f_c} + B \sqrt{J_2} + C \sigma_1 + D I_1 - f_c = 0$$

where

$I_1$  = the first stress invariant =  $\sigma_1 + \sigma_2 + \sigma_3$ ;

$J_2$  = the second deviatoric stress invariant =  
 $[(\sigma_1 - \sigma_2)^2 + (\sigma_2 - \sigma_3)^2 + (\sigma_3 - \sigma_1)^2]/6$ ; and

$\sigma_1, \sigma_2,$  and  $\sigma_3$  are the three principal stresses.

Based on the experimental data from Kupfer, Hilsdorf, Rusch (1969), the values of A, B,

C, and D can be shown to be 2.0108, 0.9714, 9.1412, and 0.2312, respectively (Gallegos-Cazares and Schnobrich, 1988). These values were used herein. Depending on the loading conditions, three modes of failure are defined by a crushing coefficient  $\alpha$ :

- (1) Pure cracking,  $\alpha < 1$
- (2) Pure crushing,  $\alpha > (1 + \nu)/(1 - 2\nu)$
- (3) Mixed mode,  $1 \leq \alpha \leq (1 + \nu)/(1 - 2\nu)$

where

$\nu$  is Poisson's ratio,

$$\alpha = \frac{I_1}{2\sqrt{3}J_2 \cos\theta},$$

$\theta$  is an angle in the deviatoric plane, which is defined as:

$$\theta = \cos^{-1}\left(\frac{\sqrt{3}\sigma_1 - \frac{1}{\sqrt{3}}I_1}{2\sqrt{2}}\right)$$

The angle  $\theta$  ranges between  $-60^\circ$  and  $60^\circ$ .

The geometric model including slab-pier connection and simulation of damage is identical to that used for the linear finite element analyses. The mesh sizes are different as the shell element coded in SAP90 is a 4-node element, whereas the element in POLO-FINITE is a 9-node element. The mesh layout is illustrated in Figure 8.35. A number of models were used to represent the slab-abutment connection. These models will be discussed in the following subsection. The material properties are identical to those used in the preliminary nonlinear analyses, with the exception of the tensile stress-strain relationships of the concrete. The tensile strength was taken as 300 psi, and a bilinear model was used to simulate tension stiffening behavior of the concrete, as discussed in Section 8.3.1. The strain at which the tensile stress drops to zero was taken as 10 times the cracking strain. The stiffness of the rotational springs was kept identical to that used in the linear analyses. The reinforcing bars were assumed to be smeared, defined by the direction of reinforcing bars and reinforcement ratio at each Gauss point. Eight concrete layers and four steel layers (top and bottom bars in each direction) were used as part of modeling of the bridge deck. An orthogonal smeared cracked model was utilized, and the directions of cracks were allowed to rotate.

**Results:** A restart option in POLO-FINITE was used such that the convergence of the results can be checked intermittently, and modify the nonlinear solution parameters can be modified as necessary. A Newton-Raphson solution method with stiffness updates every five

iterations was implemented. The stiffness matrix was updated automatically at the beginning of each load step. Prior to cracking, the total load on the bridge was increased at intervals ranging between 40 kips to 64 kips. After cracking, the load increments were approximately doubled. As the failure load was reached, the load increments were reduced back to those used prior to cracking. Finally, near failure the loads were increased automatically by the program. That is, if no convergence could be reached within the specified number of iterations and tolerances, the load step was reduced to one-quarter of the previous value.

In model 1, the slab-abutment connection was similar to that for the linear finite element analyses (Figure 8.31). The resulting load-deflection at point A (the location of this point is shown in Figure 8.10) is compared with the experimental result in Figure 8.36. A rather good correlation of the experimental strength and stiffness is observed for loads as large as about 500 kips. Nevertheless, beyond this point the computed and experimental results deviate significantly. This deviation may also be seen from the computed deflection profiles along grid lines D and 4 (refer to Figure 8.3) which are compared with the experimental results in Figure 8.37. This difference is more pronounced beyond 512 kips. The measured and computed rotations along the south abutment are compared in Figure 8.38. It is clear that this model has failed to match the measured response. For example, the computed slab rotation at ROT1 (the location is shown in Figure 8.35) decreases beyond about 400 kips while the experimental data indicate a continuously increasing trend with larger loads. The correlation is somewhat better for location ROT2 (the location is shown in Figure 8.35), but beyond about 250 kips the experimental data show a rapid increase in rotation while the computed rotation increases at a much slower rate.

To increase the rotation along the abutment, a reduction of the rotational stiffness at the abutments appears to be a plausible solution. Nevertheless, a complete removal of the rotational springs (model 2) did not appreciably change the load-deflection, deflection profiles, and rotation at the south abutment (refer to Figures 8.36, 8.37 and 8.38). This behavior, which was also observed in the elastic range, suggests that the large differences are not due to the magnitude or distribution of the rotational springs along the abutments.

**Refined Modeling:** As mentioned previously, the level of membrane force is expected to notably influence the overall behavior of the slab. The experimental data indicate that the horizontal restraint at the south abutment was reduced during the destructive test, altering the level of membrane force which can be developed in the slab. To simulate this behavior, a refined model was constructed by using horizontal springs attached to rollers at locations corresponding to the shear keys (Figure 8.39). Considering the insignificance of the rotational stiffness along the abutment, the rotational springs were removed. The experimentally-obtained rotations along the abutment shown in Figure 8.38 appear to indicate three limit states with progressively reduced stiffness. This behavior was simulated by using a trilinear load-deflection response for the horizontal springs as shown in Figure 8.39. Due to inadequate experimental data, a trial and error procedure had to be followed

to define the characteristics of the trilinear horizontal springs.

Under small loads, the shear keys are expected to provide horizontal restraint. Hence, the slope of the first segment at each horizontal spring was arbitrarily set to a large value. The last segmental slope of this nonlinear spring is automatically pre-defined as zero by the program. The slope of second segment and two break points were obtained by following procedures: (i) *Define the location of the first break point*- An analysis was performed by assigning the deflection at the first break point of each horizontal spring as a very large value (i.e. 1 inch). The computed deflection profiles at each load step was then plotted. By comparing these displacement profiles with the experimental data, the maximum total load up to which a good correlation was still possible could be established. The spring force corresponding to this load step was used to establish the deflection at the first break point for each spring. The procedure is shown schematically in Figure 8.40. This procedure would result in different break point displacements for each horizontal spring. (ii) *Define the slope of the second segment*- By giving different values to the second slope, the deflection profiles were computed. This procedure was repeated until an optimal slope leading to a good correlation of deflection profiles was found. (iii) *Define the second break point*- In order to avoid numerical instability problems, the load at the second break point of each spring was selected such that this load could not be reached when the bridge had developed its ultimate load.

The final stiffnesses of horizontal springs, and the break points are summarized in Figure 8.41. To match the measured global and local responses, four types of springs were identified (Type A, B, C, D shown in Figure 8.41). It is clear that the spring constants near the east shoulder are considerably smaller than the corresponding values near the west shoulder. This observation corresponds to the level of damage which was more extensive near the east shoulder, and also because of the differences in finite element mesh sizes in the east and west shoulders. It should be also noted that the springs attached to the "internal" nodes (e.g. nodal no. 2, 4, 6, etc.) are expectedly larger than those attached to "external" nodes (e.g. nodal no. 5, 7, 9, etc.). Considering the trial and error nature of identifying the characteristics of the horizontal springs, the slopes and break points indicated in Figure 8.41 are not unique solutions.

In this refined model, the gross cross-sectional properties of the cross-hatched region shown in Figure 8.30 were used to define the properties of the rigid links connecting the hinges to the shell nodes. The cross-hatched region is composed of the portion of the slab within the length of the shear key, slab thickness, and width of the slab. The nonlinear solution strategy is identical to that discussed previously, but the load steps were changed. The load steps were equivalent to 4, 8, 12, 16, and 20 trucks (each weighing 32 kips).

The resulting load-deflection at point A (refer to Figure 8.10 for the location of point A) and the slab rotations at ROT1 and ROT2 (the locations are shown in Figure 8.35) correlate very well with the experimental data, as illustrated in Figure 8.42. Furthermore,

a reasonable match of the deflection profiles is clear from Figure 8.43. Using the calibrated model, it was also possible to match very reasonably the locations and load at which the first yielding in the reinforcing bars were detected. The experimental results suggest that the bars at locations 4, 8, 13 (refer to Figure 8.44) yielded when the total load on the bridge was approximately 650 kips. The first yield was computed to be at locations shown in Figure 8.44 corresponding to a total load equal to 640 kips.

It is noted that the test bridge failed when the total load reached 704 kips, and the strain gage readings indicated that the slab reinforcing bars had just yielded at a few locations when the bridge failed. These readings reinforce the observed failure mode that the bridge failed predominately in shear. The flexural capacity of the slab had not been developed at failure. The analytical model does not account for inelastic shear response. Therefore, the computed ultimate load (800 kips) was larger than the experimental result (704 kips). Shear stress contours at 800 kips (i.e., the computed ultimate load) indicate larger magnitudes along lines AA and BB, refer to Figure 8.45. It is expected that shear failure would be initiated along these two lines, which approximately coincide with the observed failure pattern (Figure 5.17).

Positive-Moment Yield Line ———

Negative-Moment Yield Line - - - - -

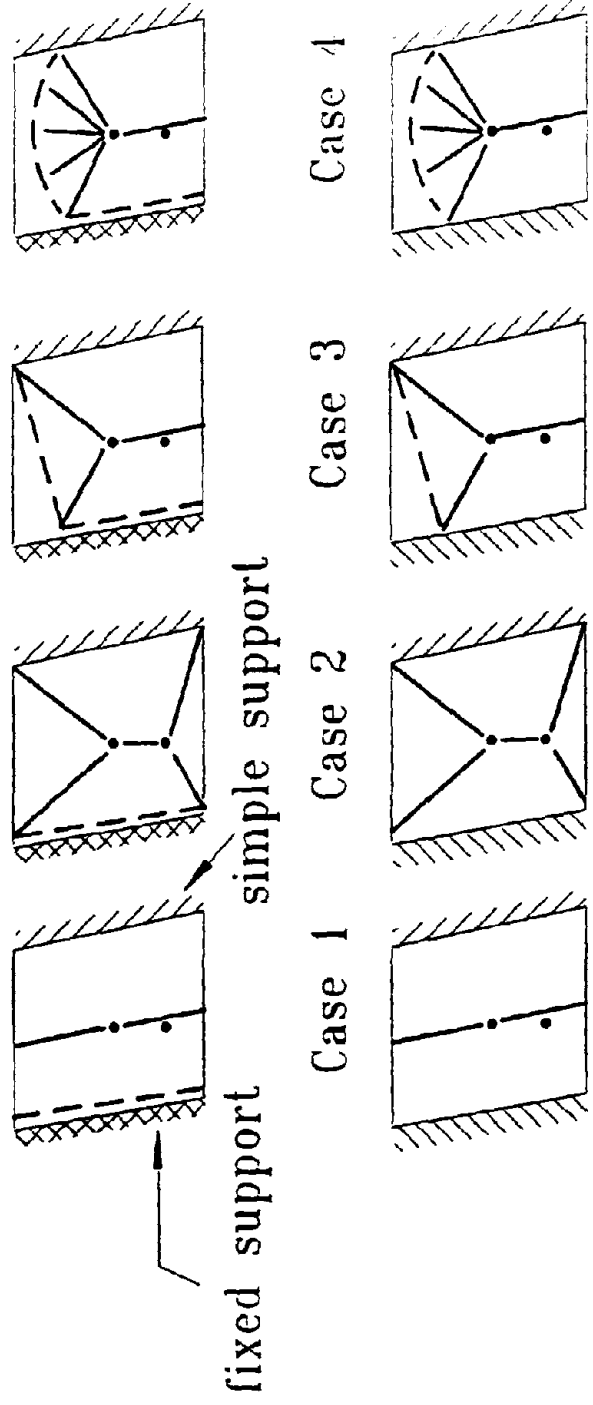


**FIGURE 8.1: YIELD LINE PATTERNS**

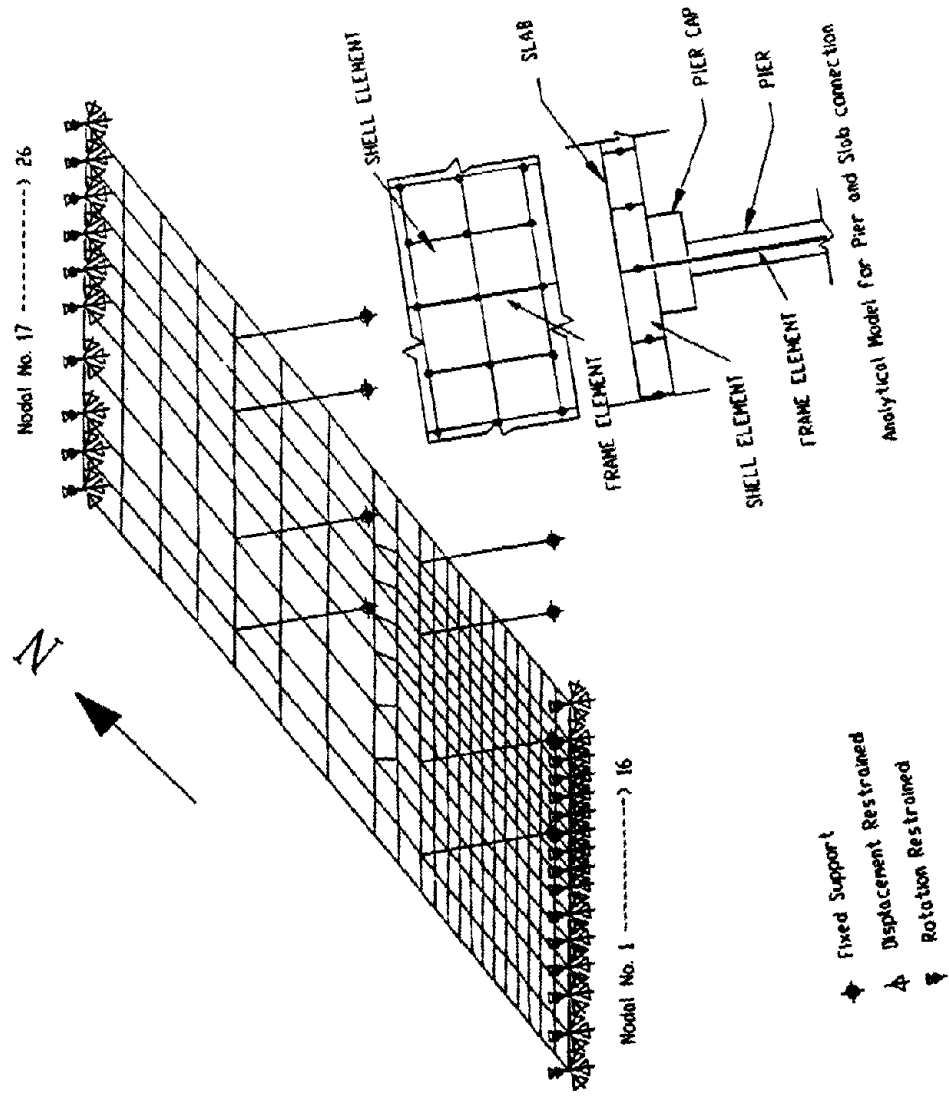
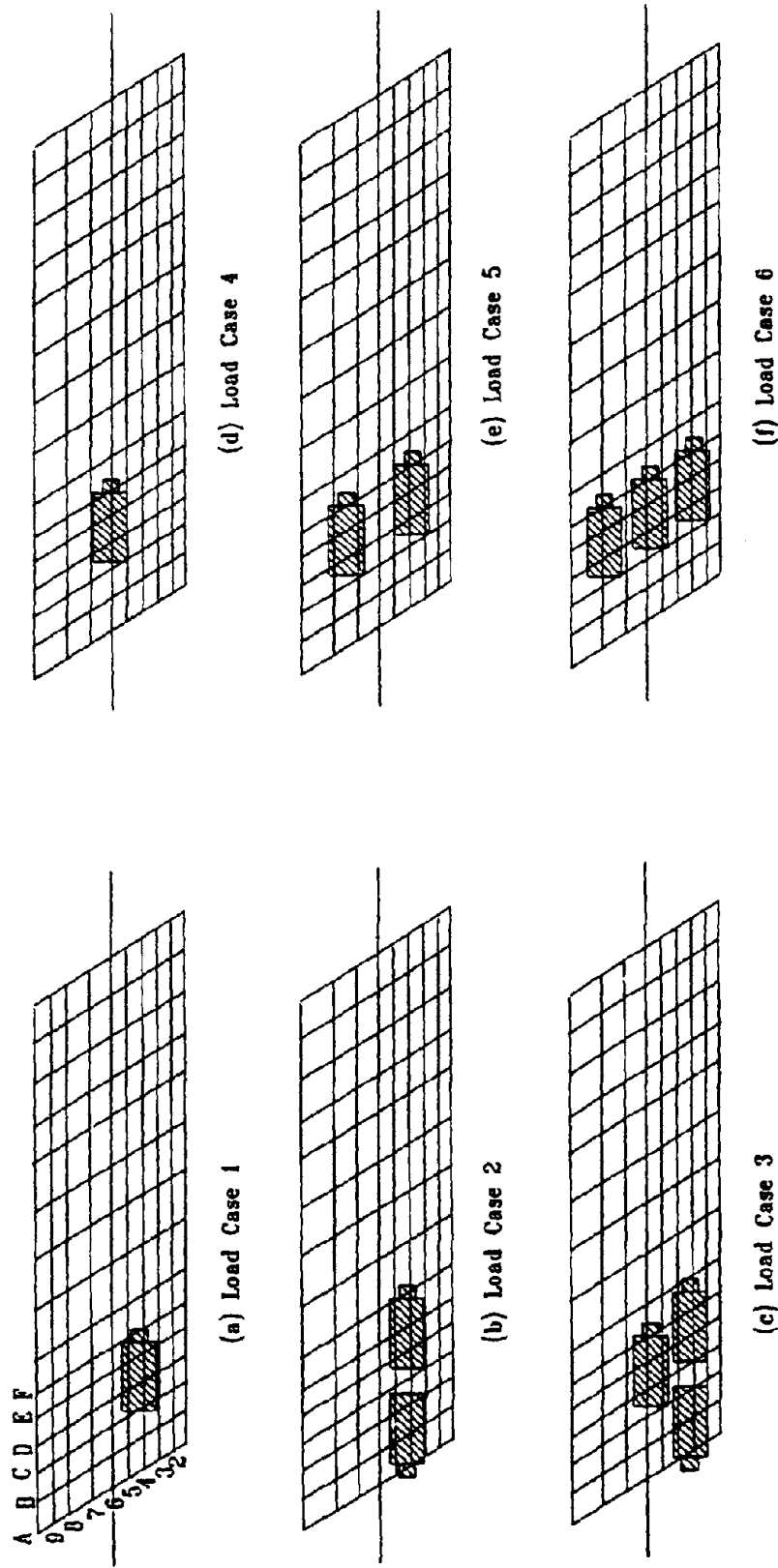
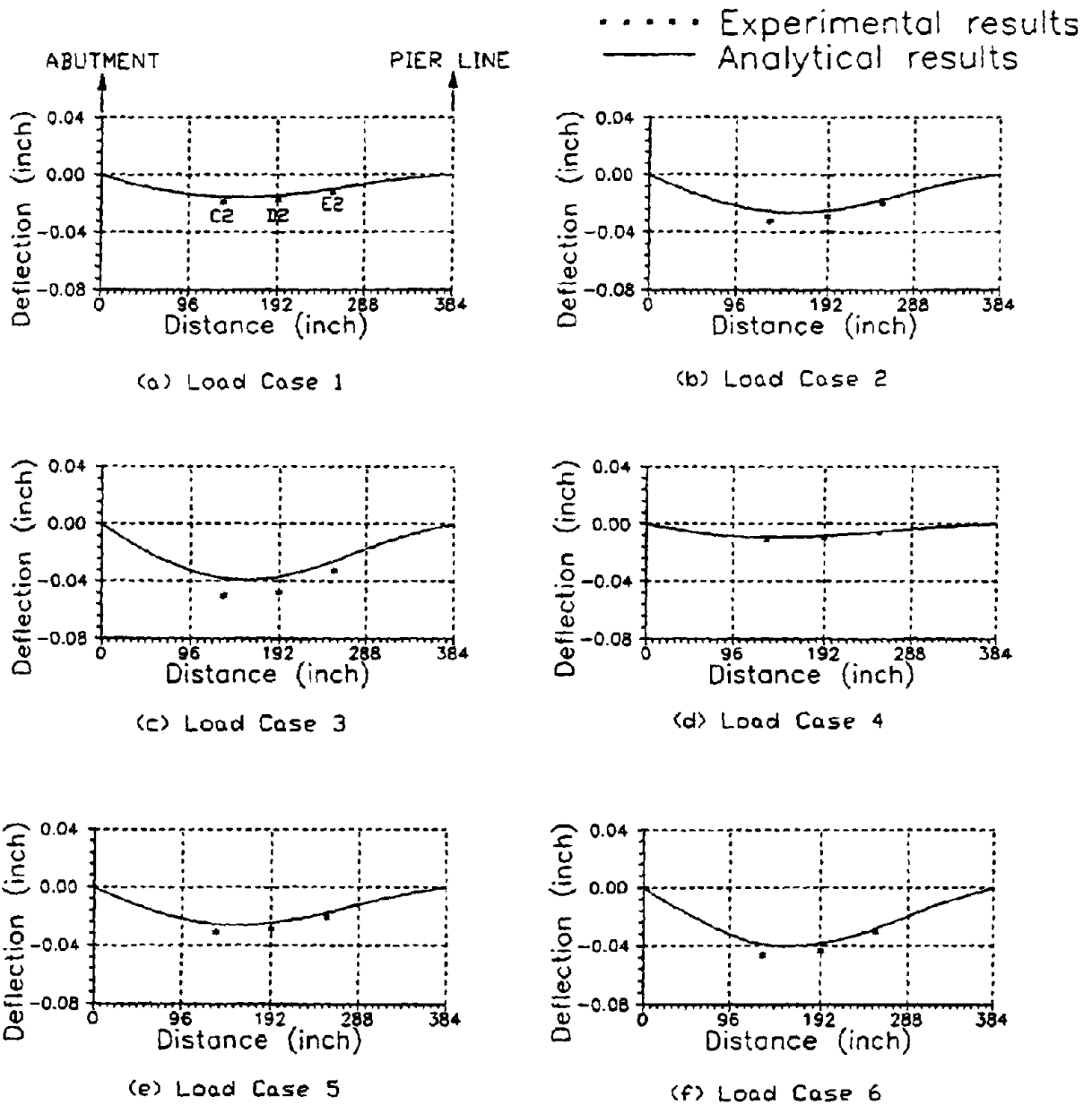


FIGURE 8.2: ELASTIC FINITE ELEMENT MODEL



**FIGURE 2.3: TRUCK LOAD TEST CONFIGURATIONS**



**FIGURE 8.4(a): COMPARISON OF DEFLECTION PROFILES  
ALONG INSTRUMENTATION LINE 2**

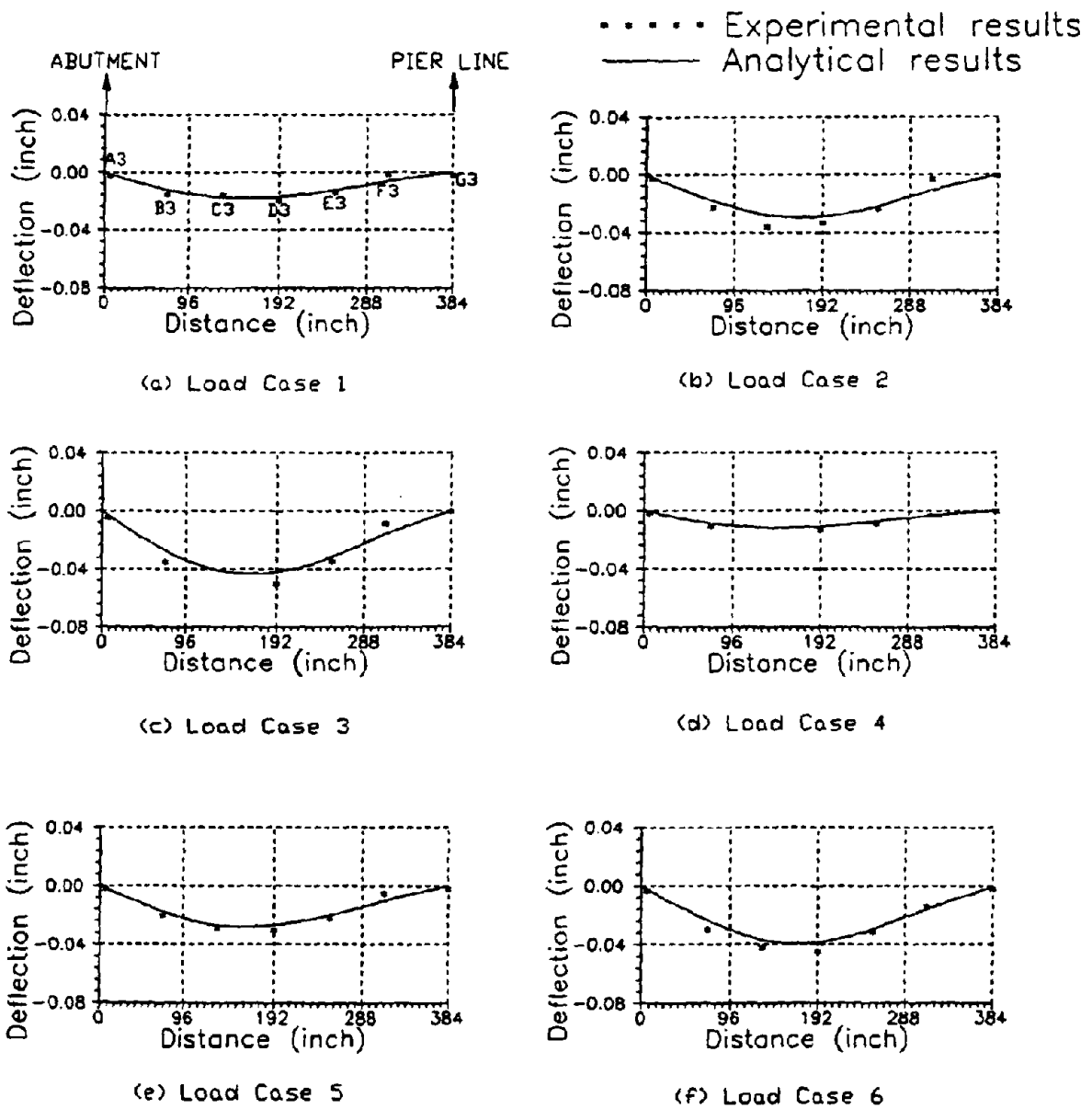


**FIGURE 8.4(b): COMPARISON OF DEFLECTION PROFILES  
ALONG INSTRUMENTATION LINE 3**

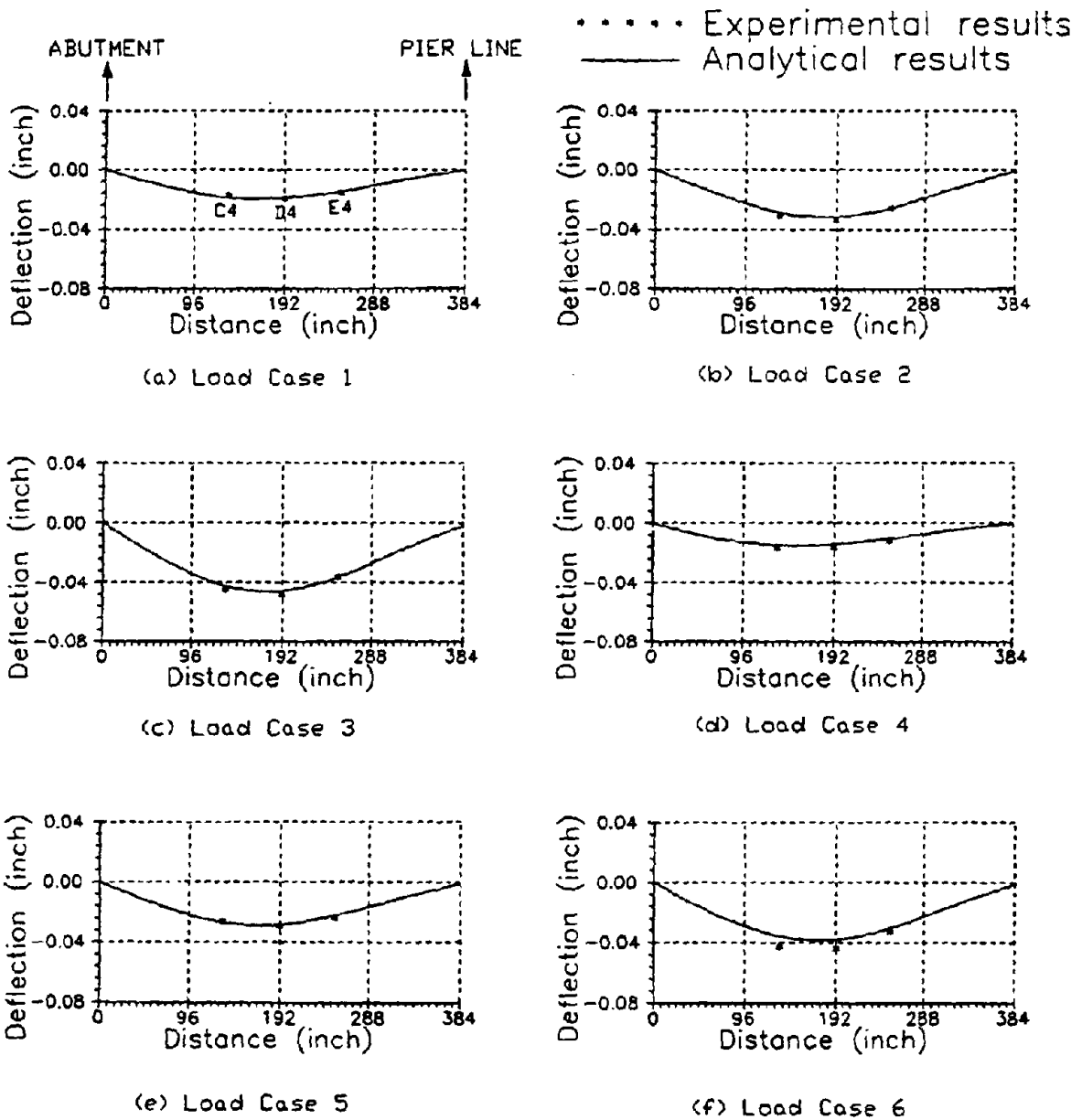


**FIGURE 8.4(c): COMPARISON OF DEFLECTION PROFILES  
 ALONG INSTRUMENTATION LINE 4**

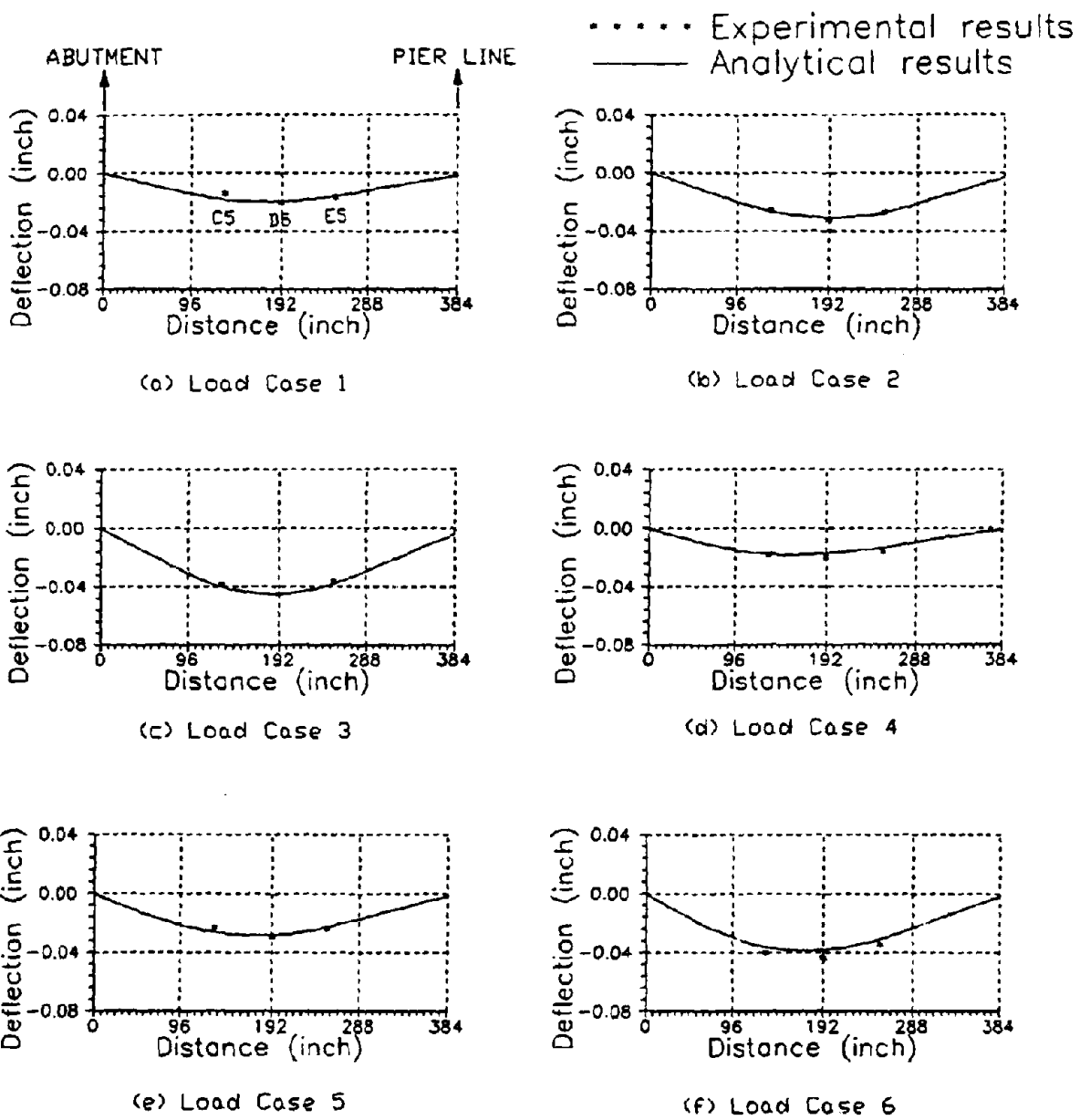


**FIGURE 84(d): COMPARISON OF DEFLECTION PROFILES  
 ALONG INSTRUMENTATION LINE 5**

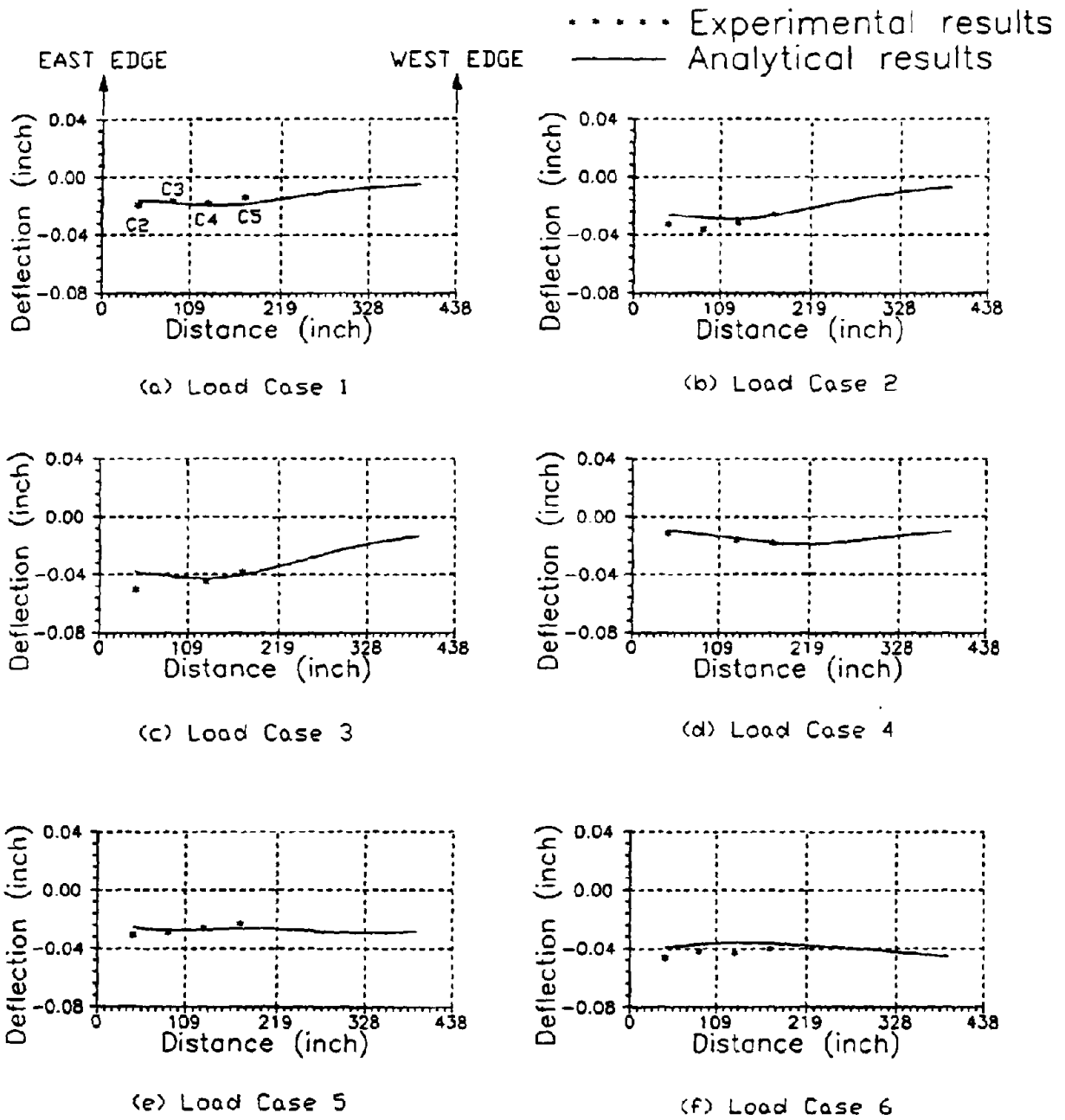


**FIGURE 8.4(e): COMPARISON OF DEFLECTION PROFILES  
ALONG INSTRUMENTATION LINE C**

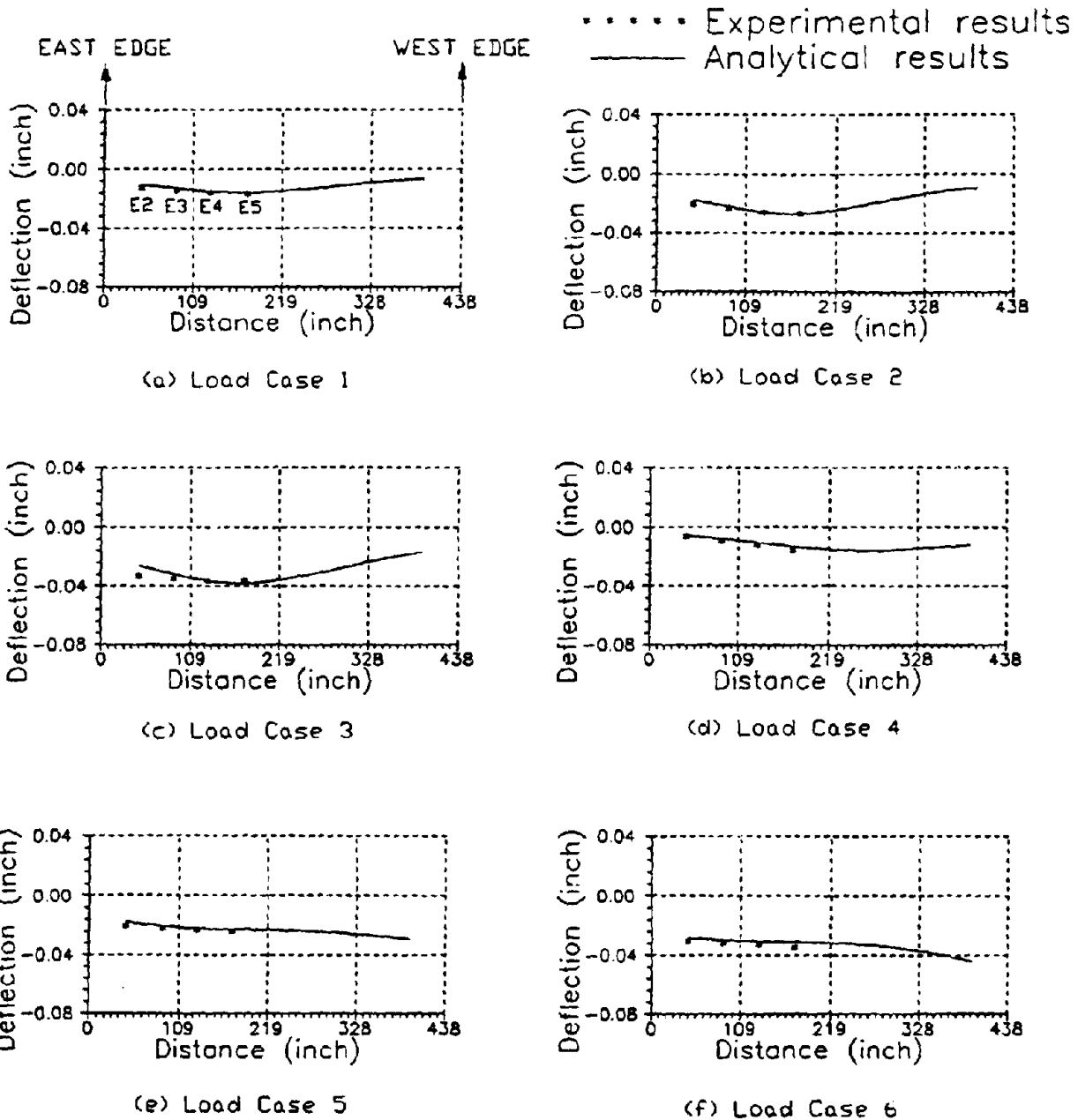


**FIGURE 8.4(g): COMPARISON OF DEFLECTION PROFILES  
ALONG INSTRUMENTATION LINE E**

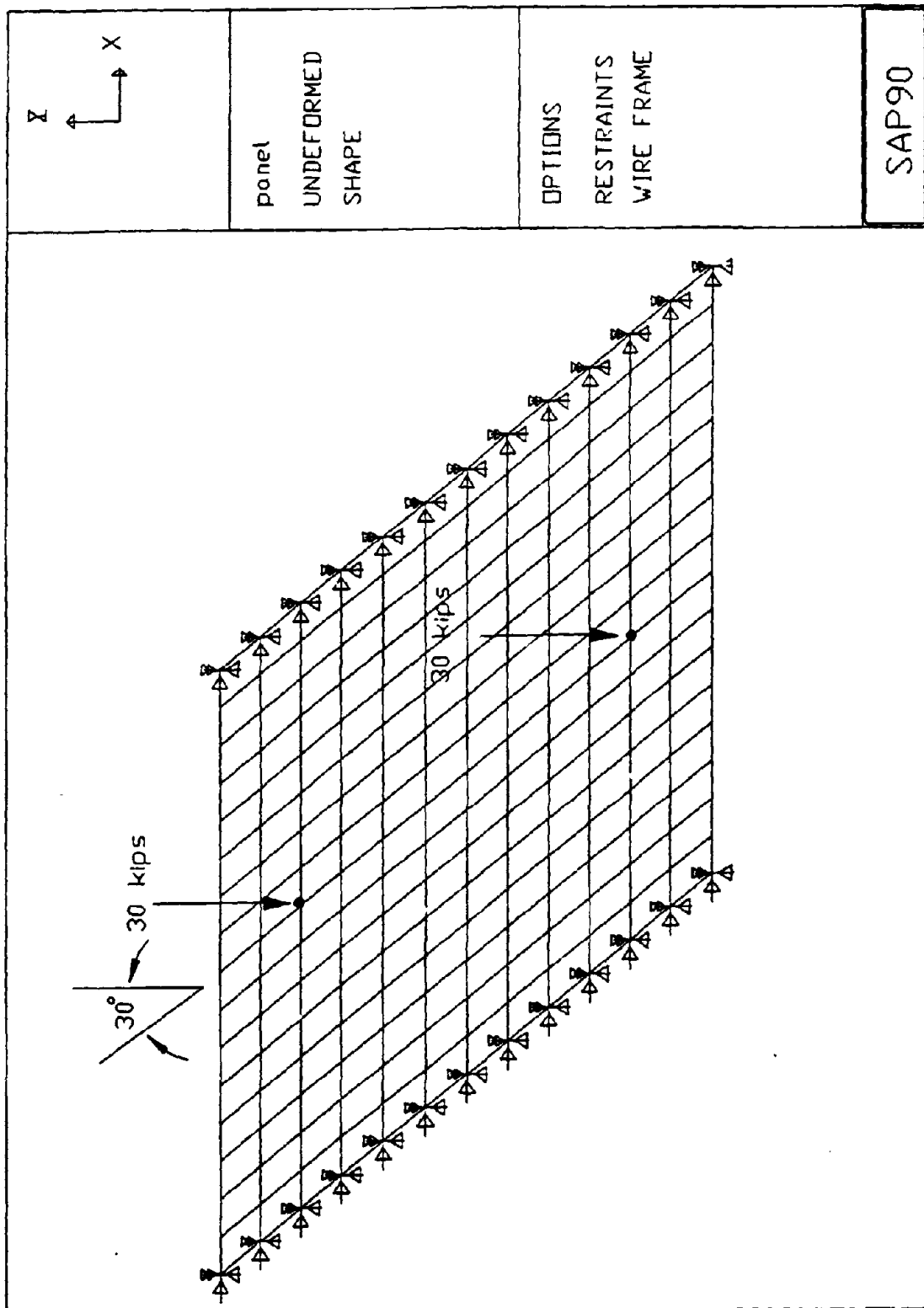


FIGURE 8.8: ANALYTICAL MODEL FOR A SINGLE SKEWED PANEL

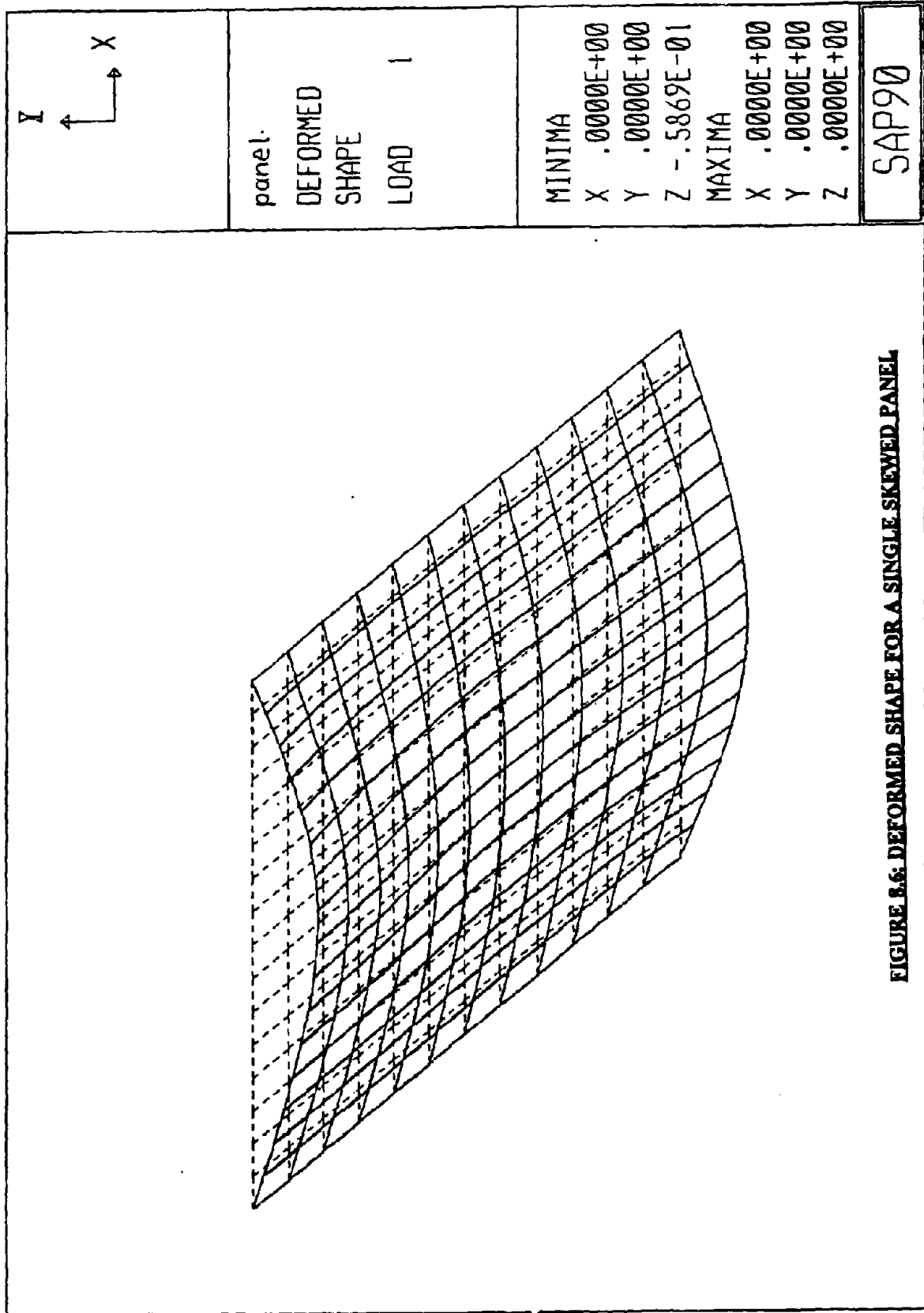


FIGURE B.6: DEFORMED SHAPE FOR A SINGLE SKEWED PANEL

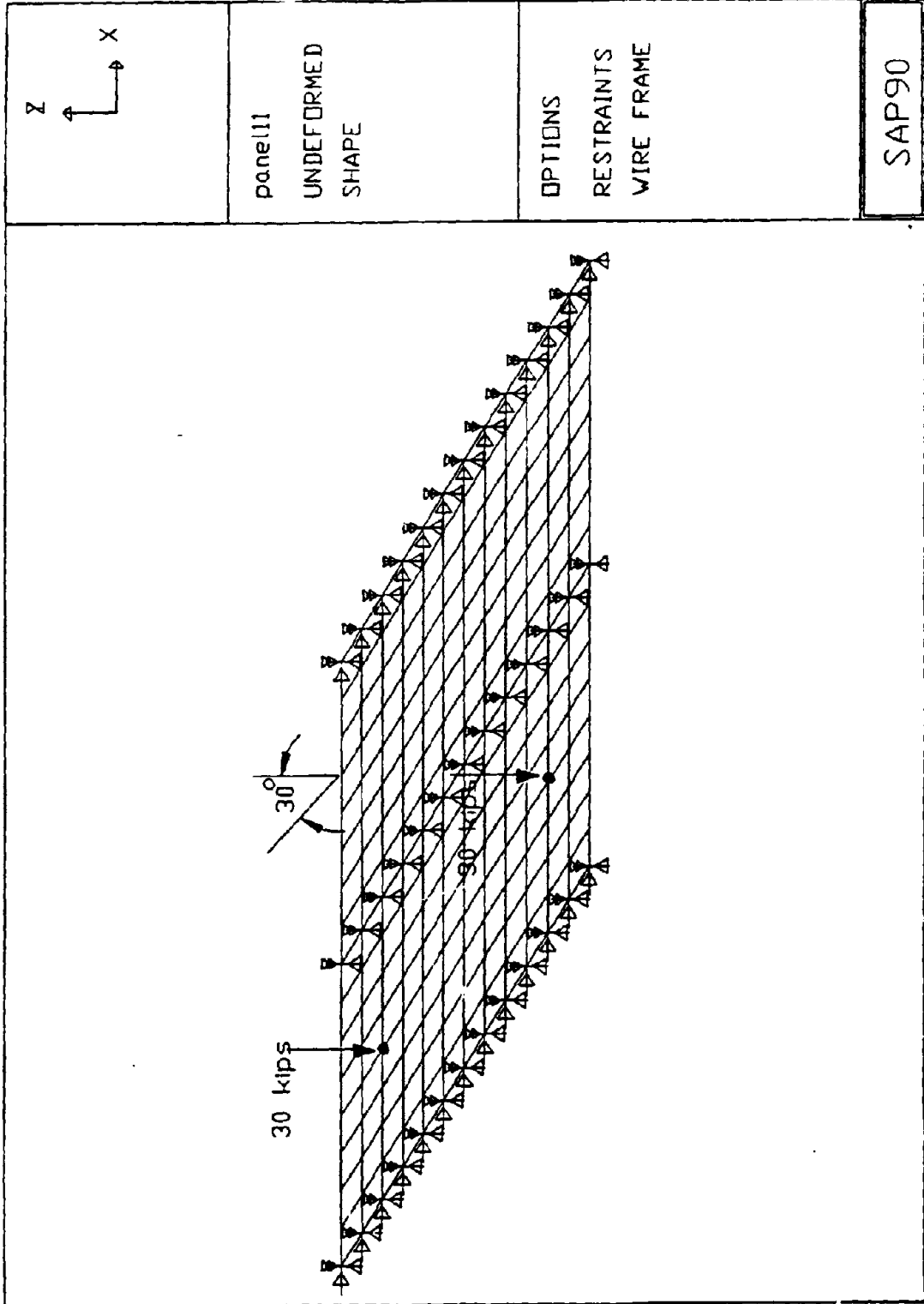


FIGURE 8.7: ANALYTICAL MODEL FOR A 2-SPAN SKEWED PANEL

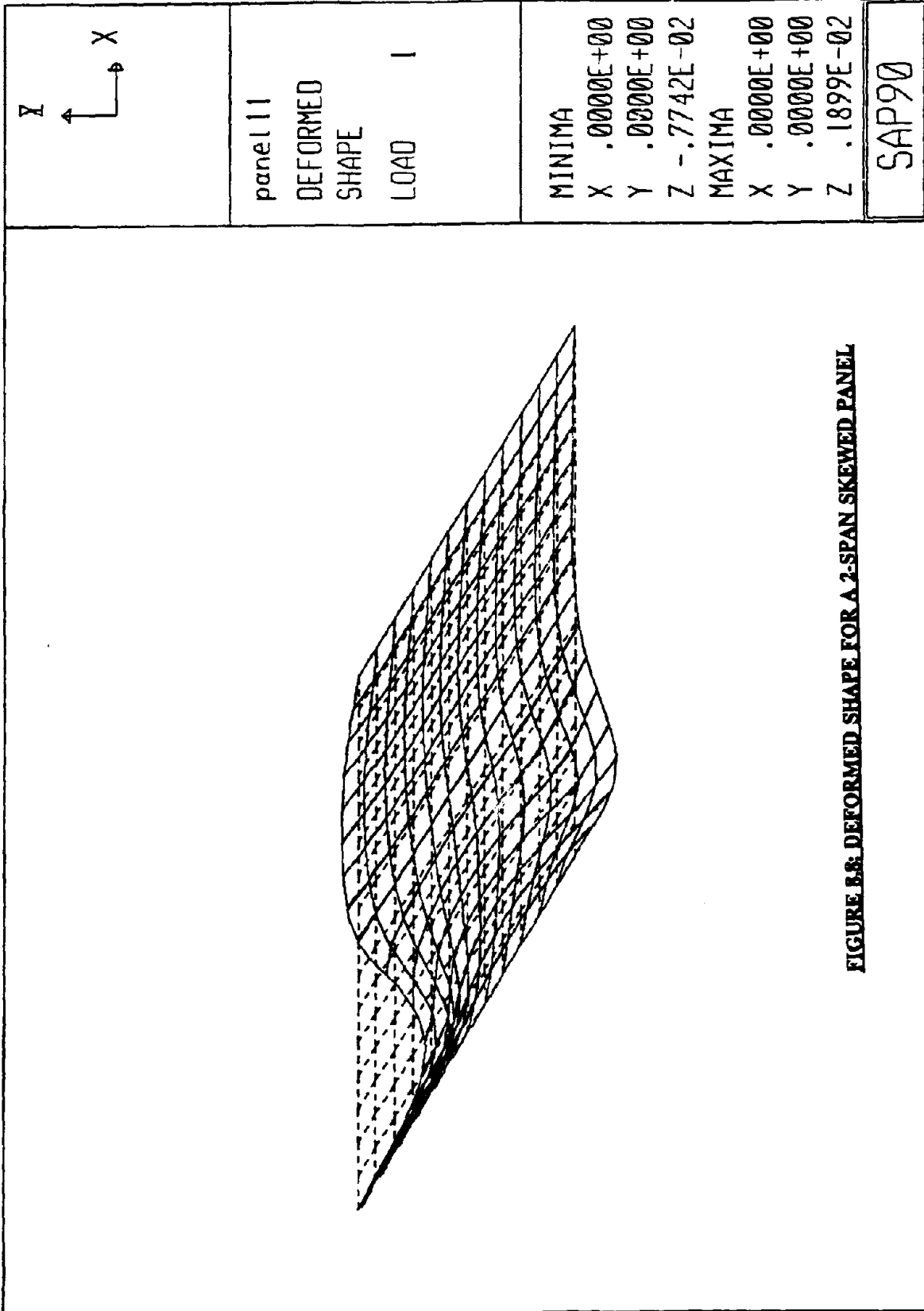
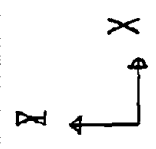


FIGURE B.8. DEFORMED SHAPE FOR A 2-SPAN SKEWED PANEL



panel 11  
 DEFORMED  
 SHAPE  
 LOAD 1

MINIMA  
 X .0000E+00  
 Y .0000E+00  
 Z -.7742E-02  
 MAXIMA  
 X .0000E+00  
 Y .0000E+00  
 Z .1899E-02

SAP90

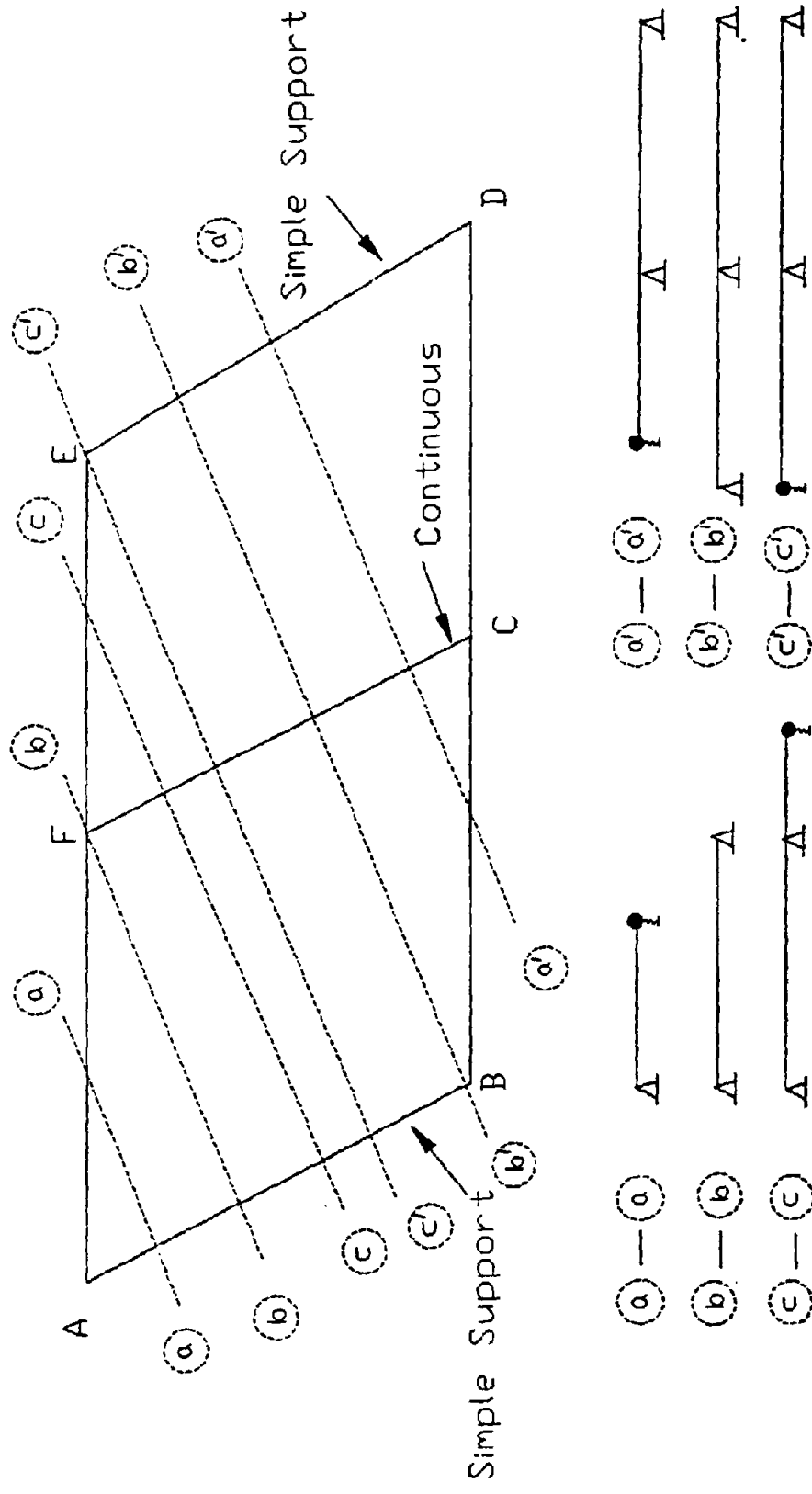
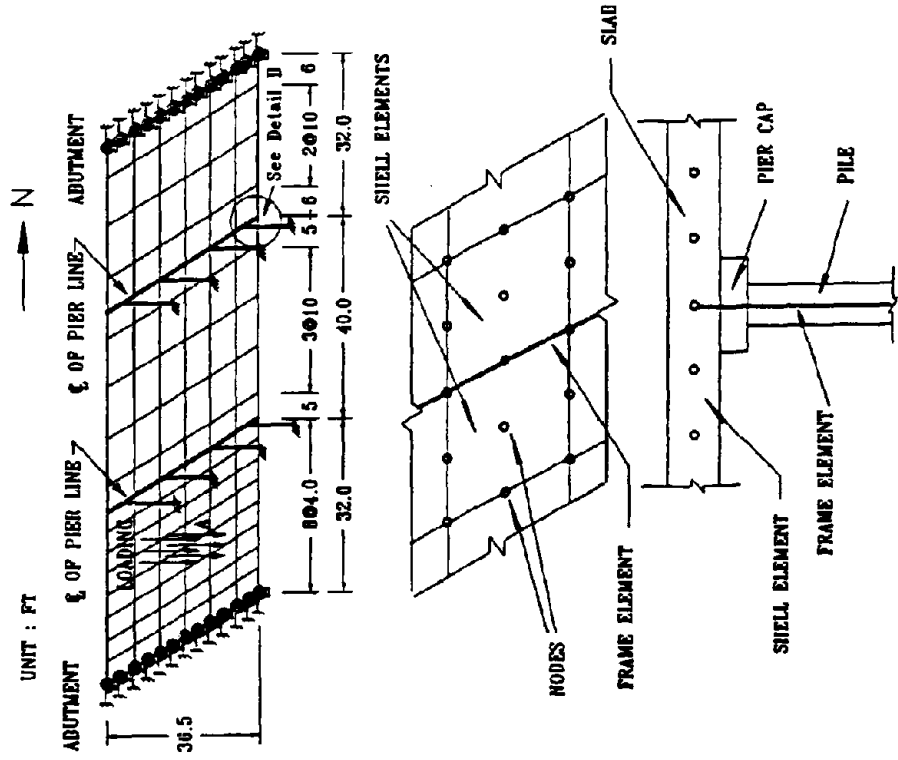
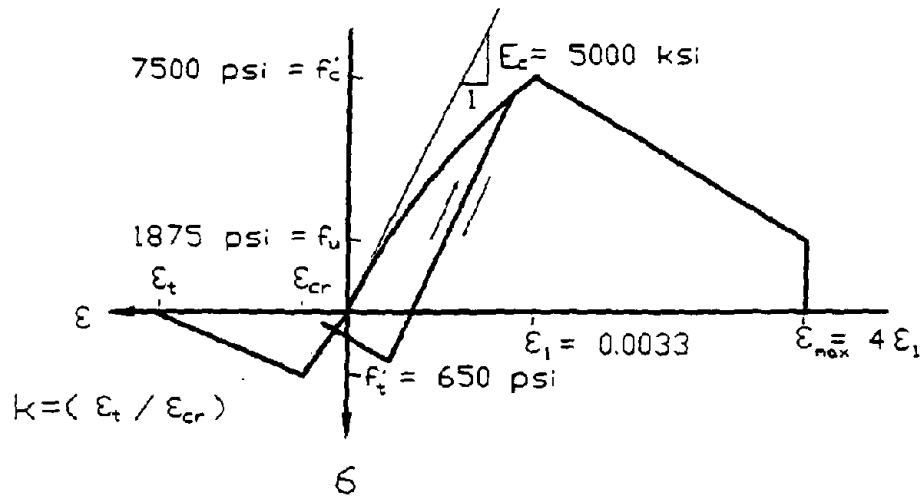


**FIGURE 8.9: ILLUSTRATION OF SLAB BEHAVIOR BY BEAM STRIPS**

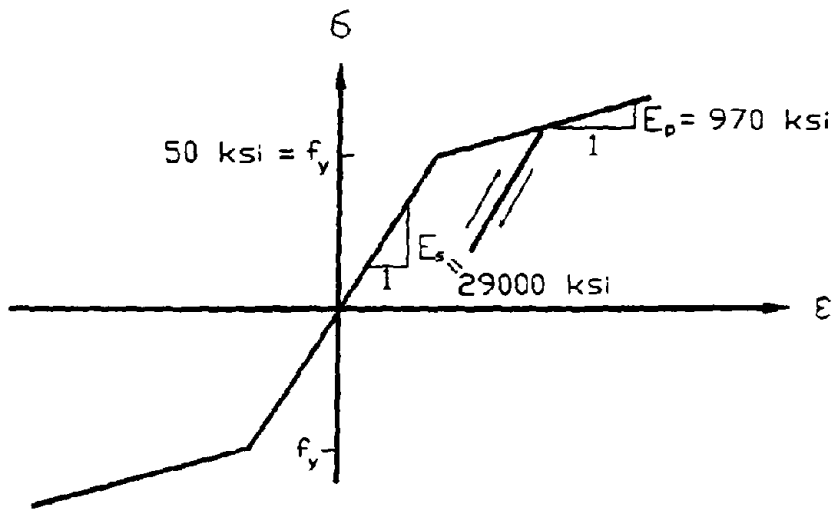


Detail B : ANALYTICAL MODEL FOR PIER AND SLAB CONNECTION

FIGURE 8.10: NONLINEAR FINITE ELEMENT MODEL (3DSCAS)



Material Model for Concrete



Material Model for Steel

**FIGURE 8.11: MATERIAL MODELS**

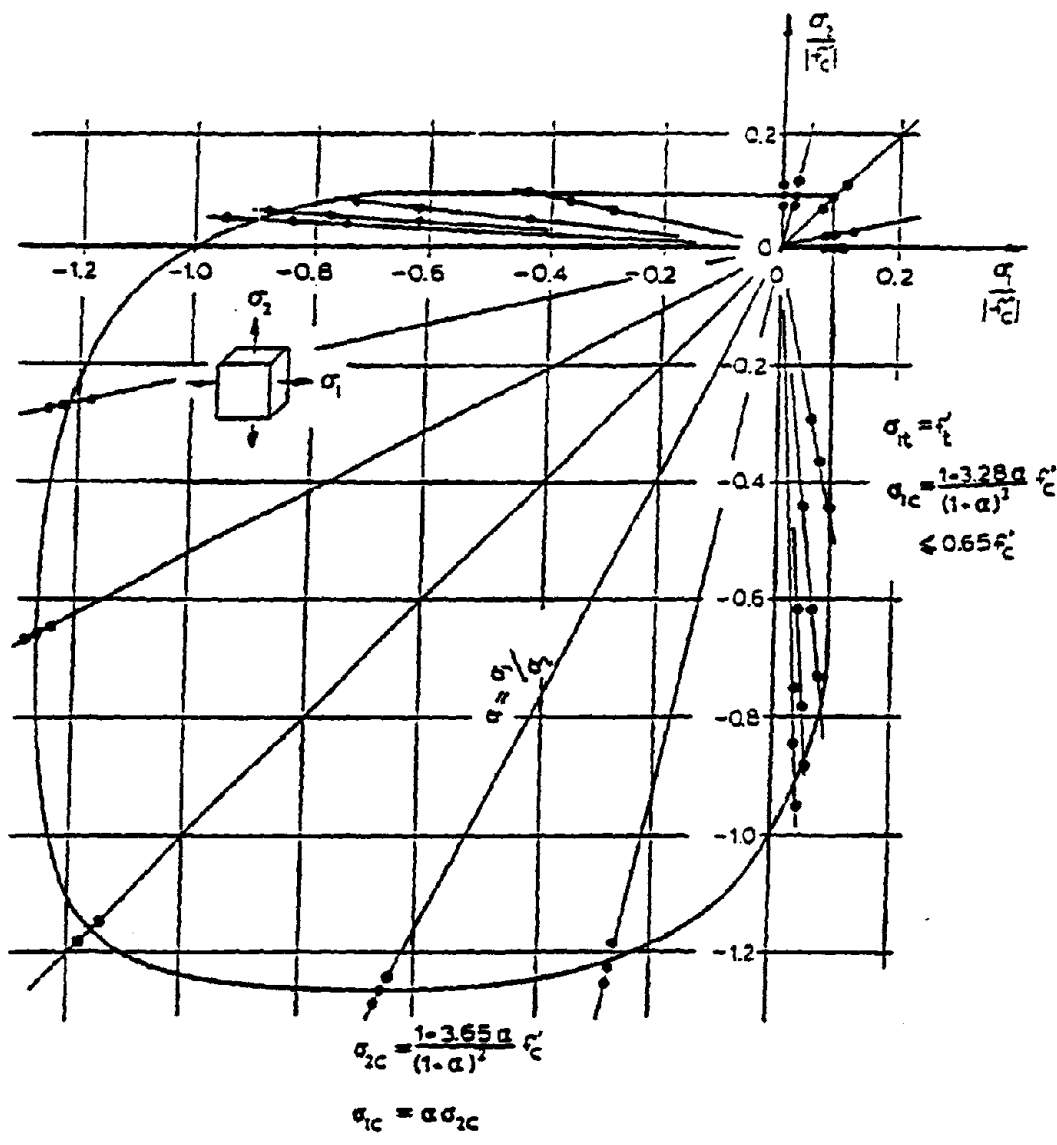
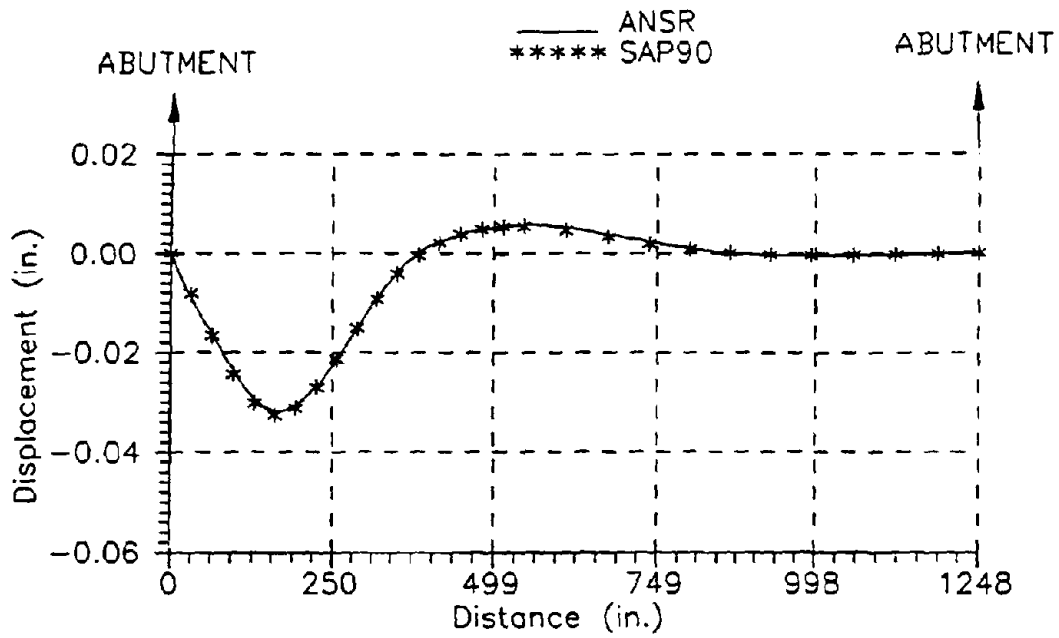
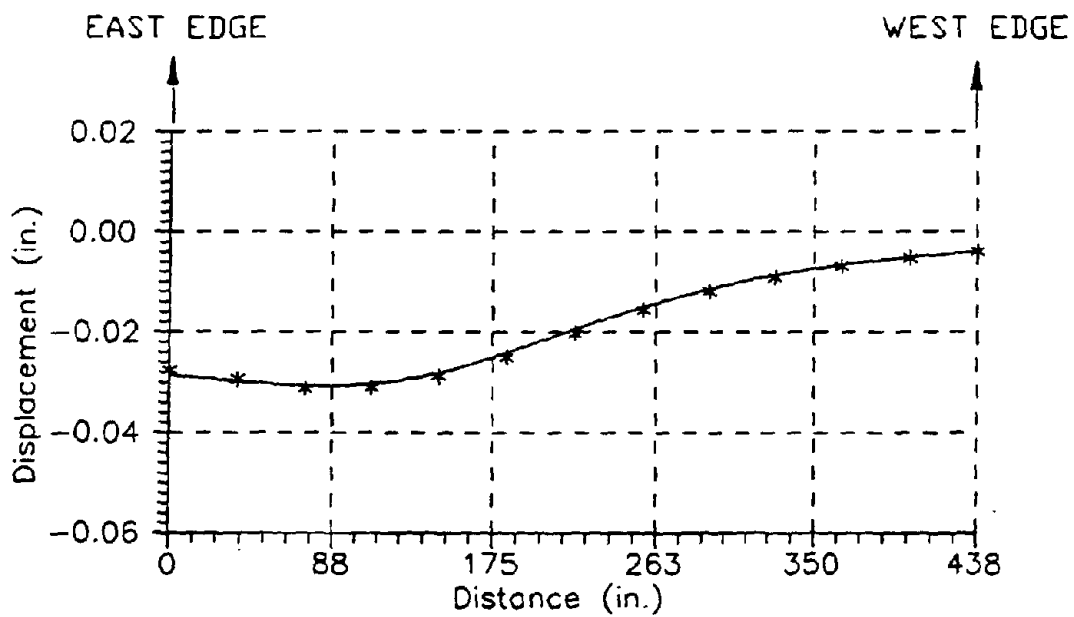


**FIGURE 8.12: BIAxIAL FAILURE ENVELOPE (KUPFER & GERSTLE)**

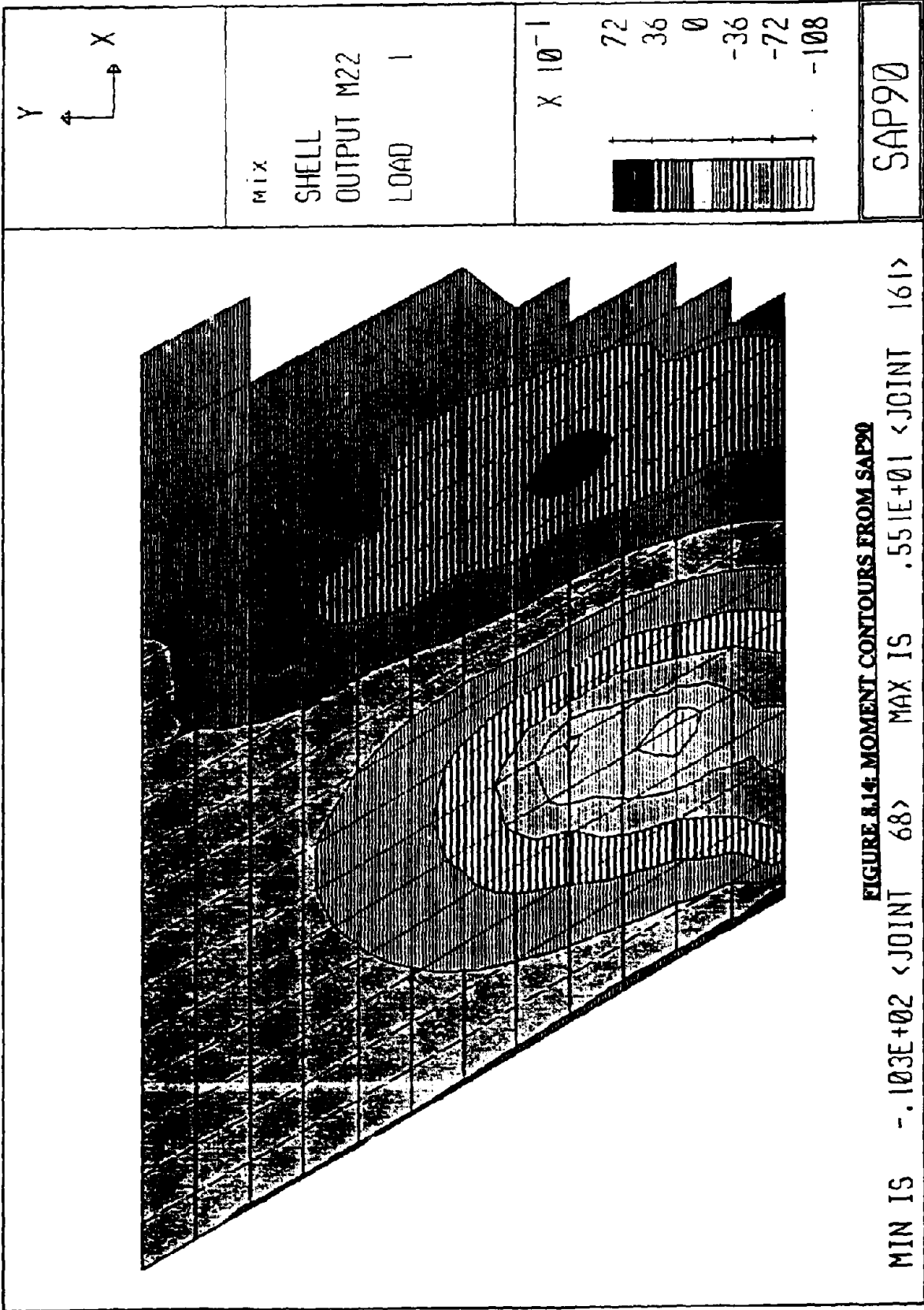


(a) Longitudinal Direction



(b) Transverse Direction

**FIGURE 8.13: DEFLECTION PROFILES**



MIN IS - .103E+02 <JOINT 68> MAX IS .551E+01 <JOINT 161>  
**FIGURE 8.14: MOMENT CONTOURS FROM SAP90**

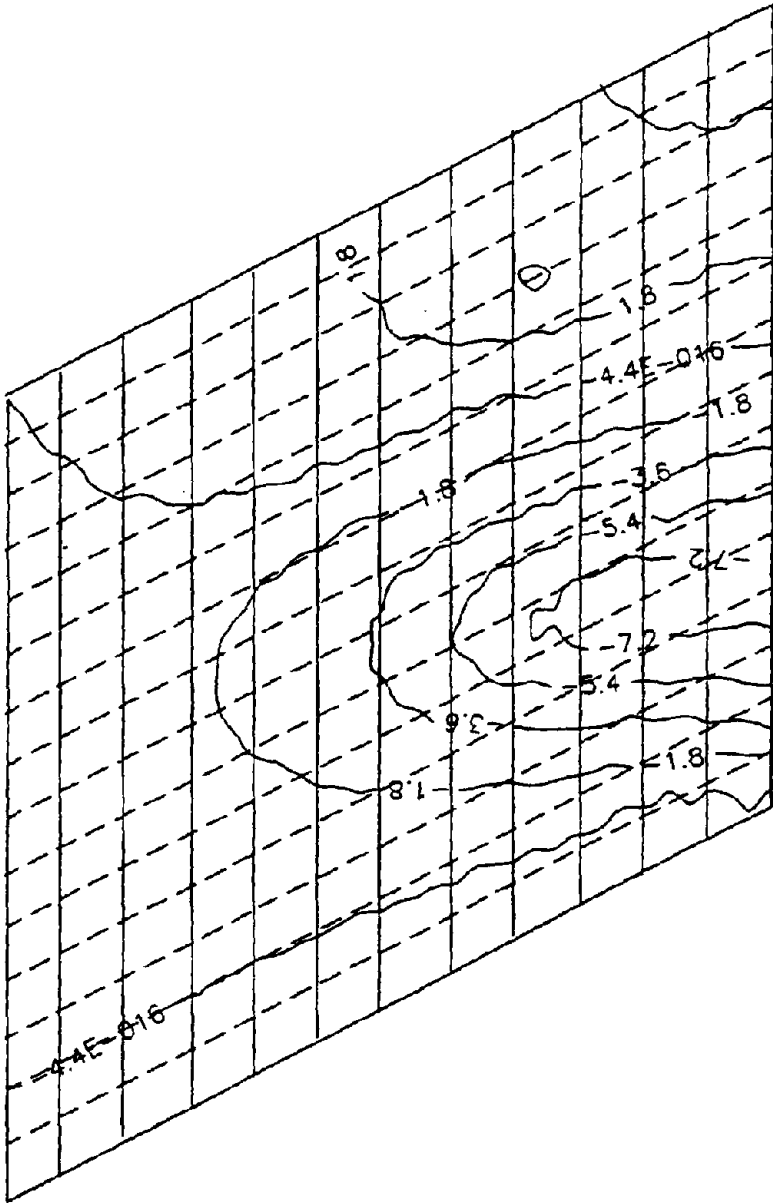
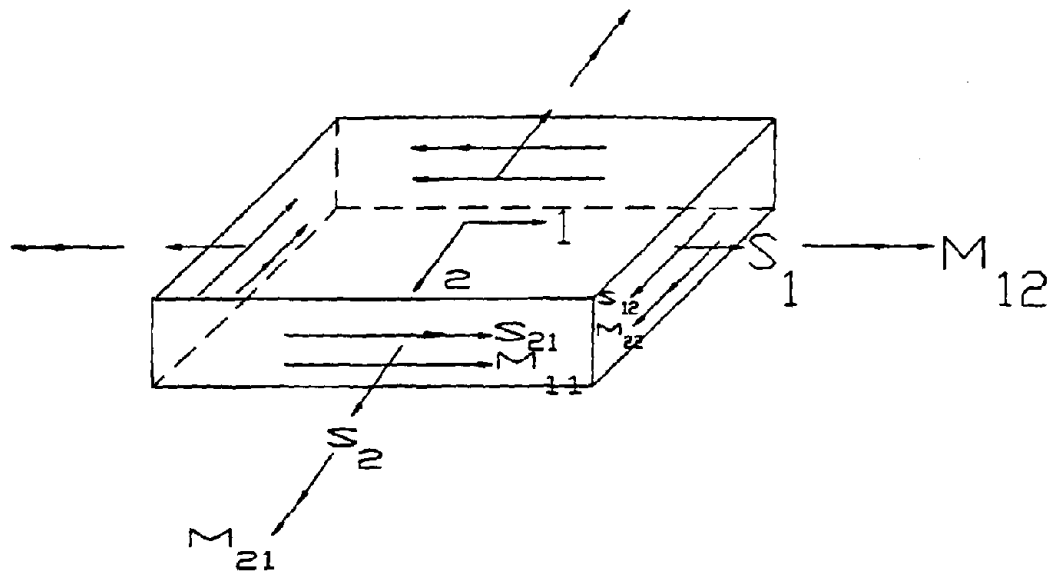
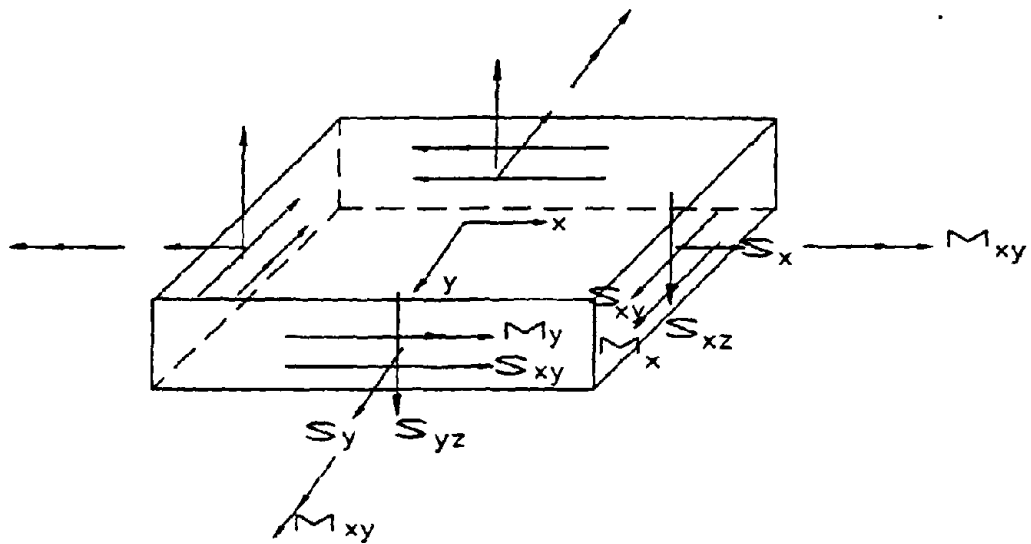


FIGURE 8.15: MOMENT CONTOURS FROM 3DSCAS

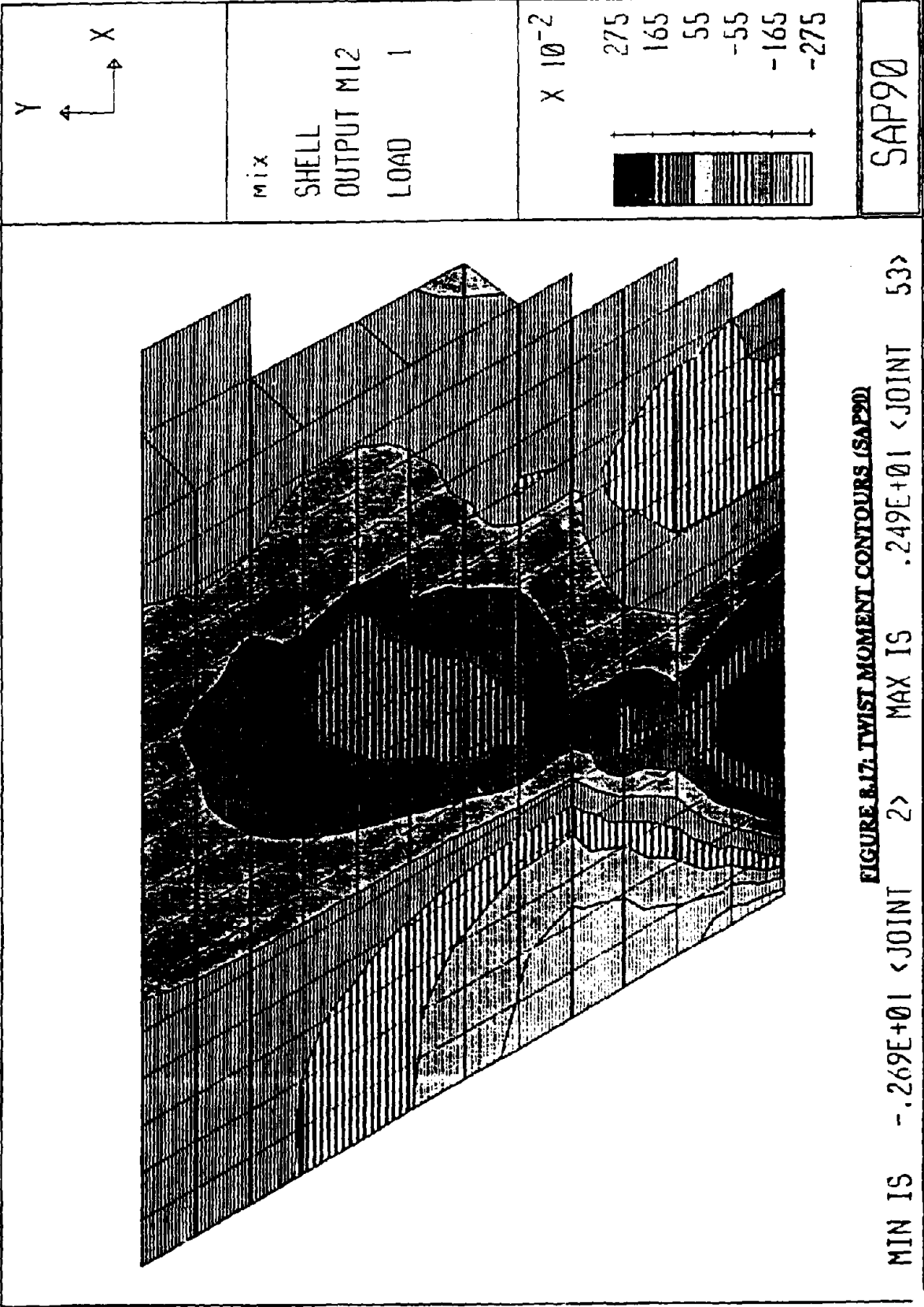


(A) SAP 90



(B) 3DSCAS

**FIGURE 8.16: STRESS RESULTANTS**



MIN IS -.269E+01 <JOINT 2> MAX IS .249E+01 <JOINT 53>  
 FIGURE B.17: TWIST MOMENT CONTOURS (SAP90)

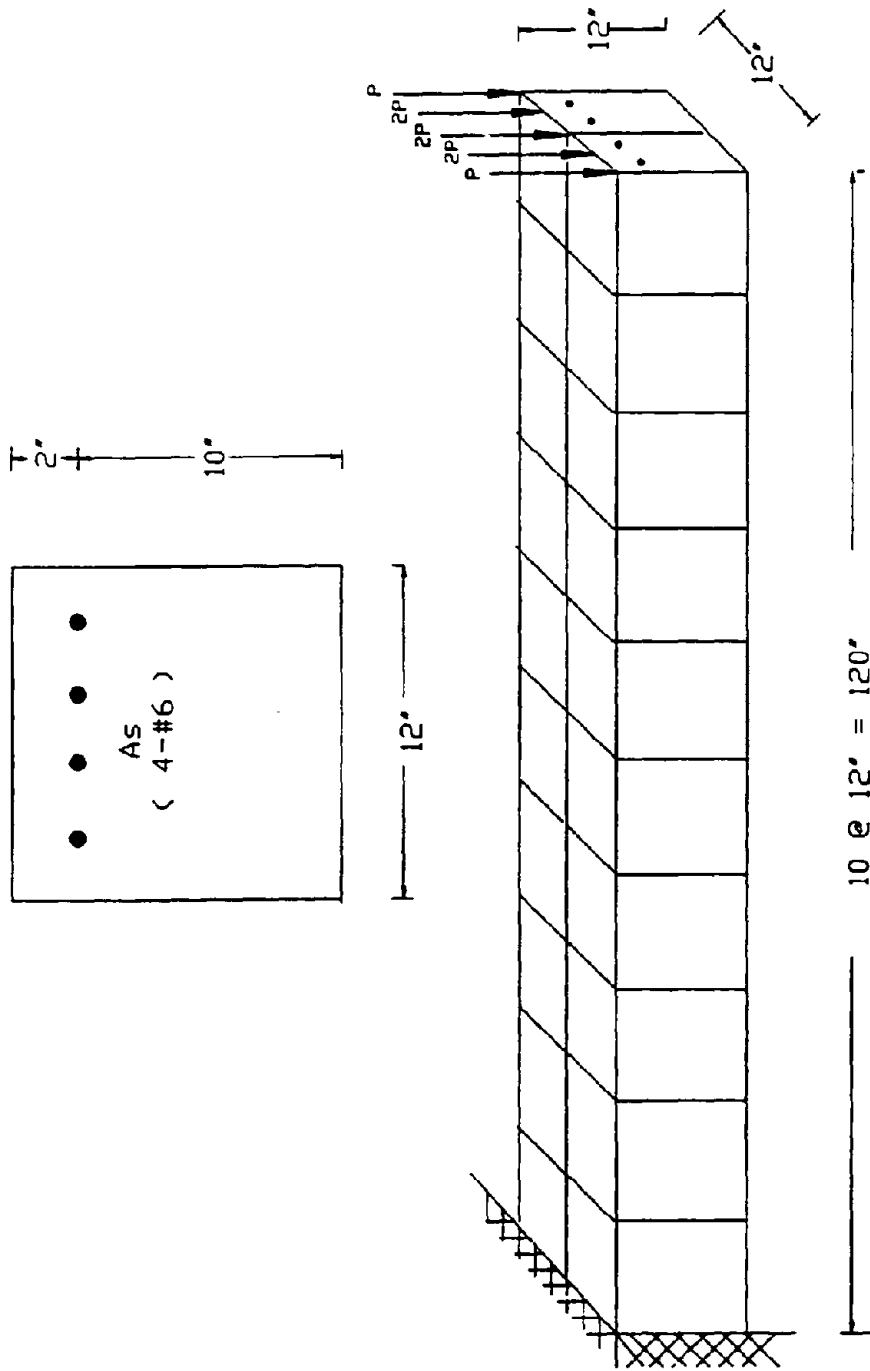


**FIGURE B.18: FINITE ELEMENT MODEL OF CANTILEVERED BEAM**

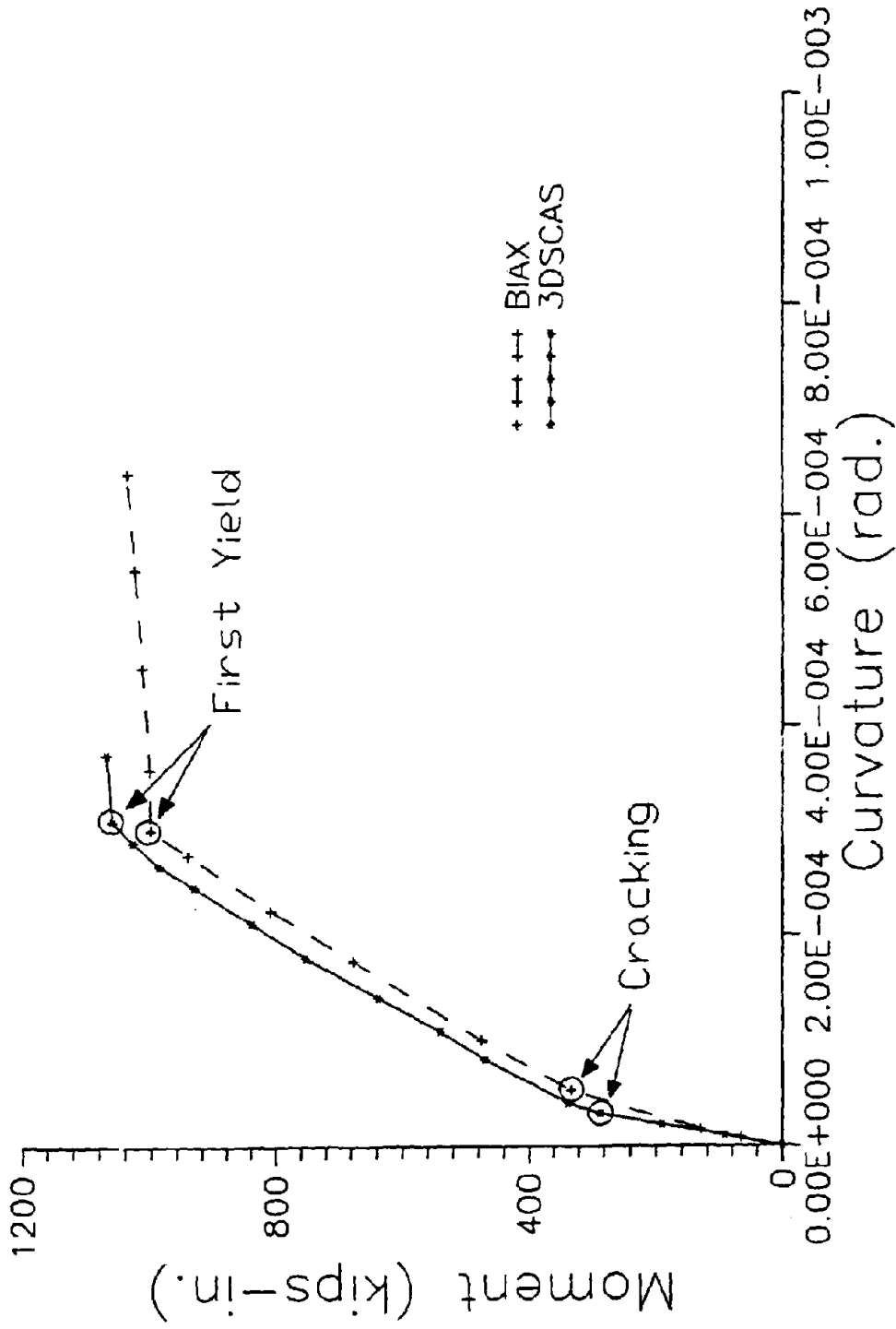
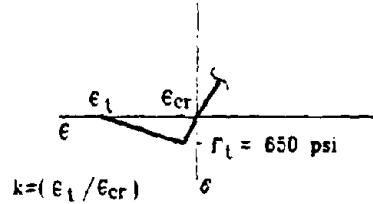
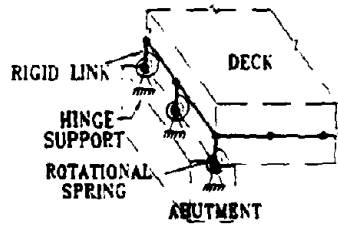


**FIGURE 8.19: MOMENT-CURVATURE RESPONSE**



SLAB AND ABUTMENT CONNECTION MODELS

TENSION STIFFENING MODEL FOR CONCRETE

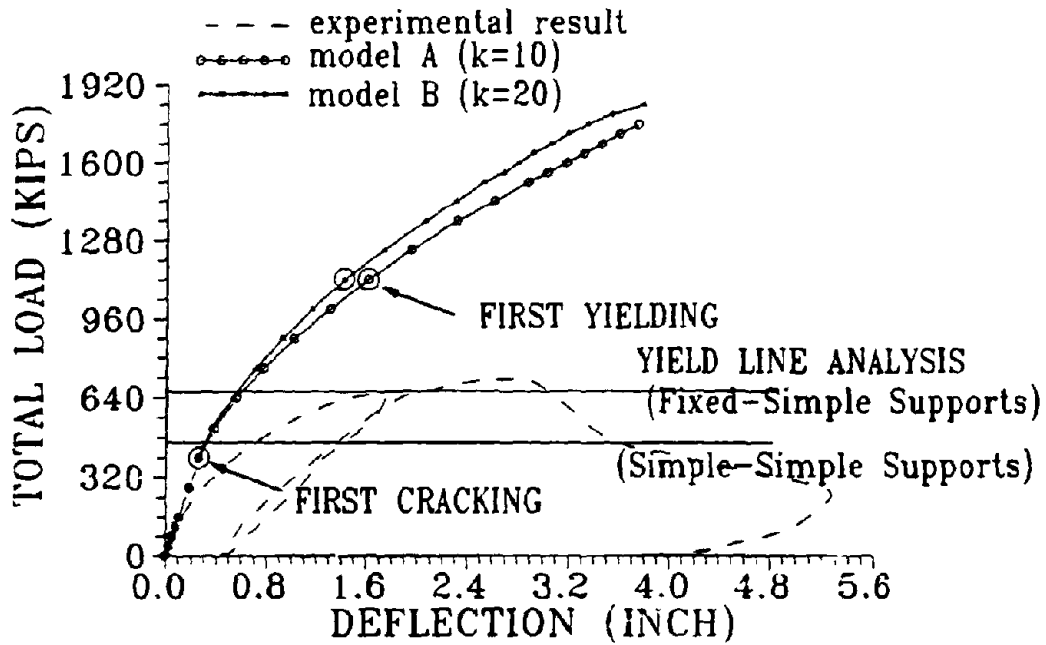
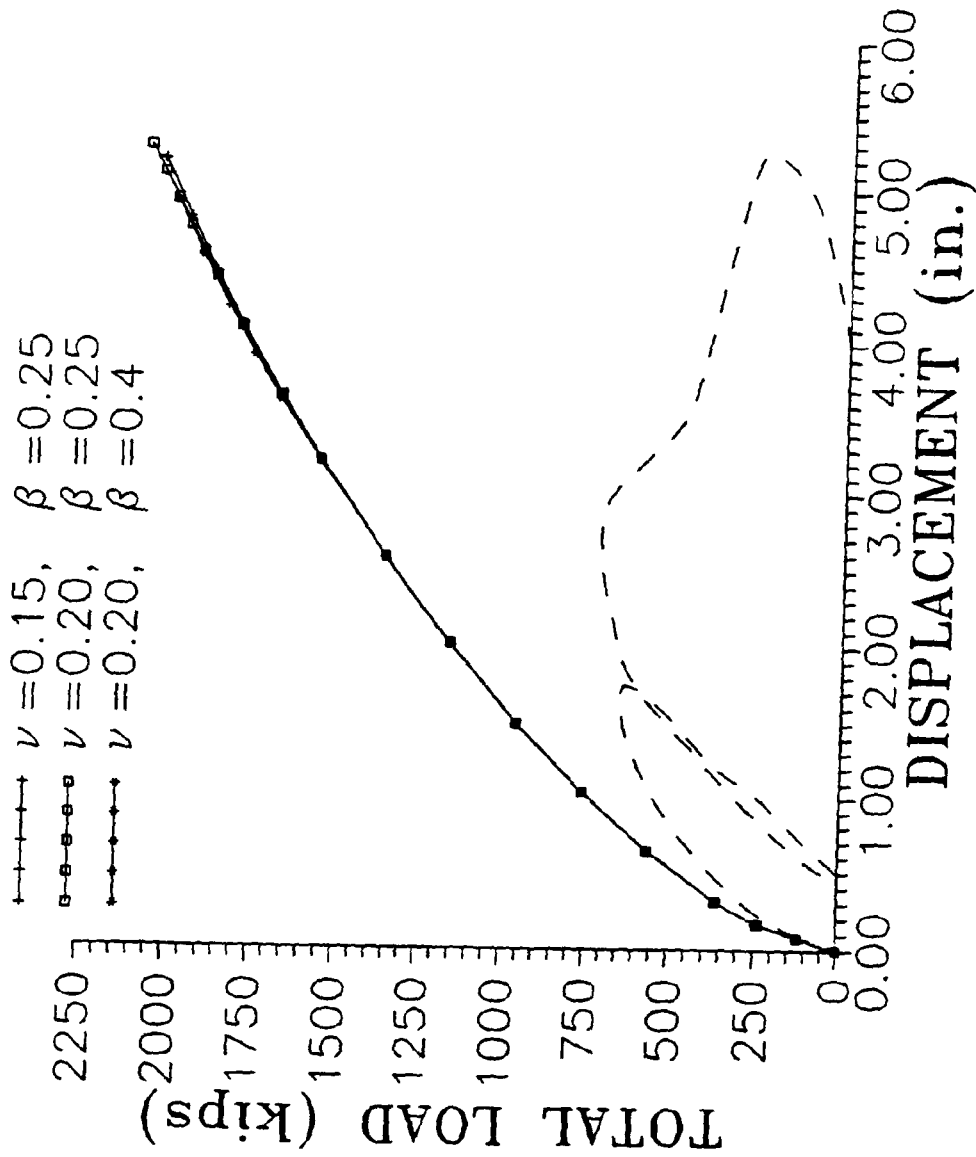
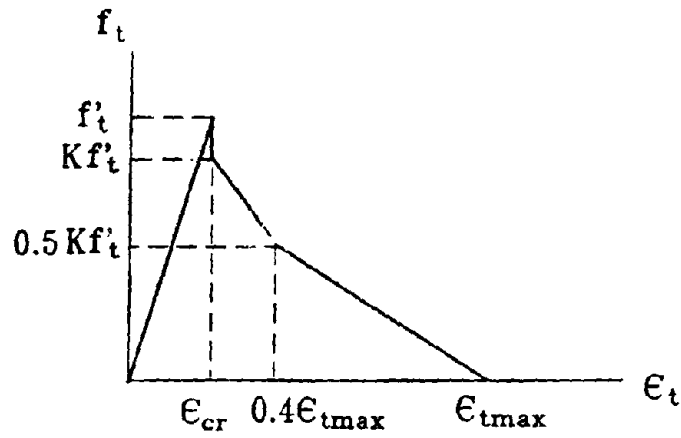


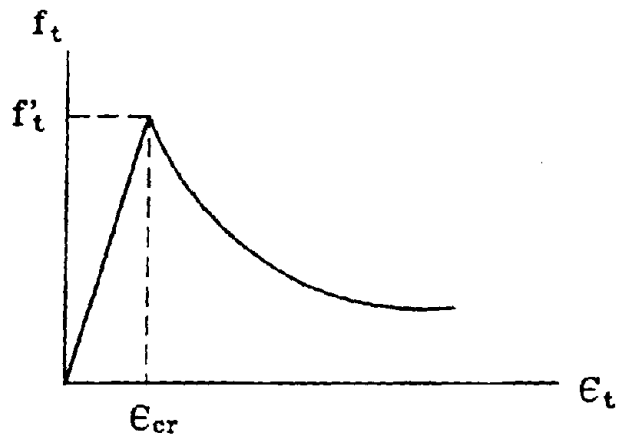
FIGURE 8.20: COMPARISON OF LOAD-DEFLECTION CURVES



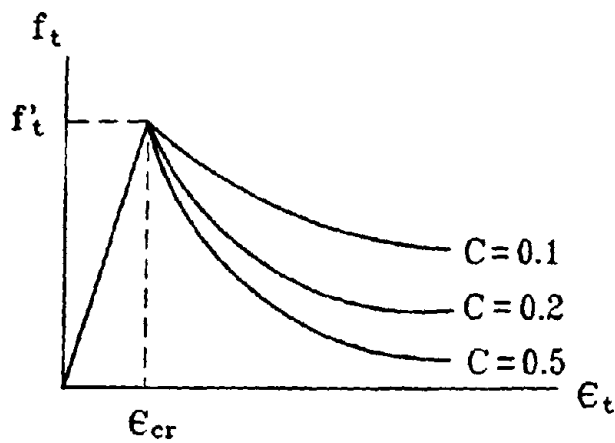
**FIGURE B.21: EFFECTS OF POISSON'S RATIO (ν) AND SHEAR RETENTION FACTOR (β)**



(A) Bilinear Model



(B) Vecchio-Collins Model



(C) Model from University of Tokyo

**FIGURE 8.22: TENSION STIFFENING MODELS**

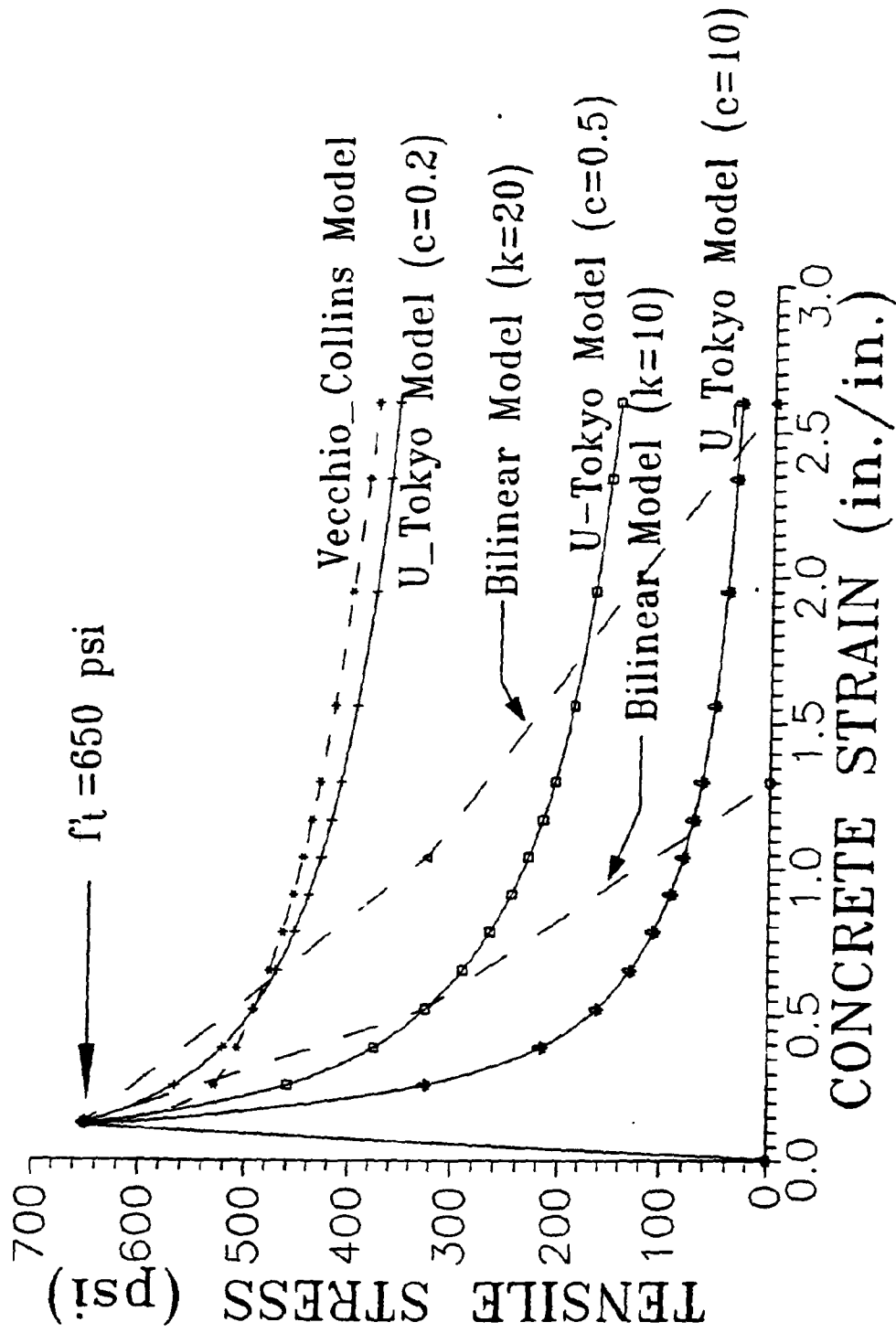


**FIGURE 8.23: STRESS-STRAIN RELATIONSHIP FROM DIFFERENT TENSION STIFFENING MODELS**

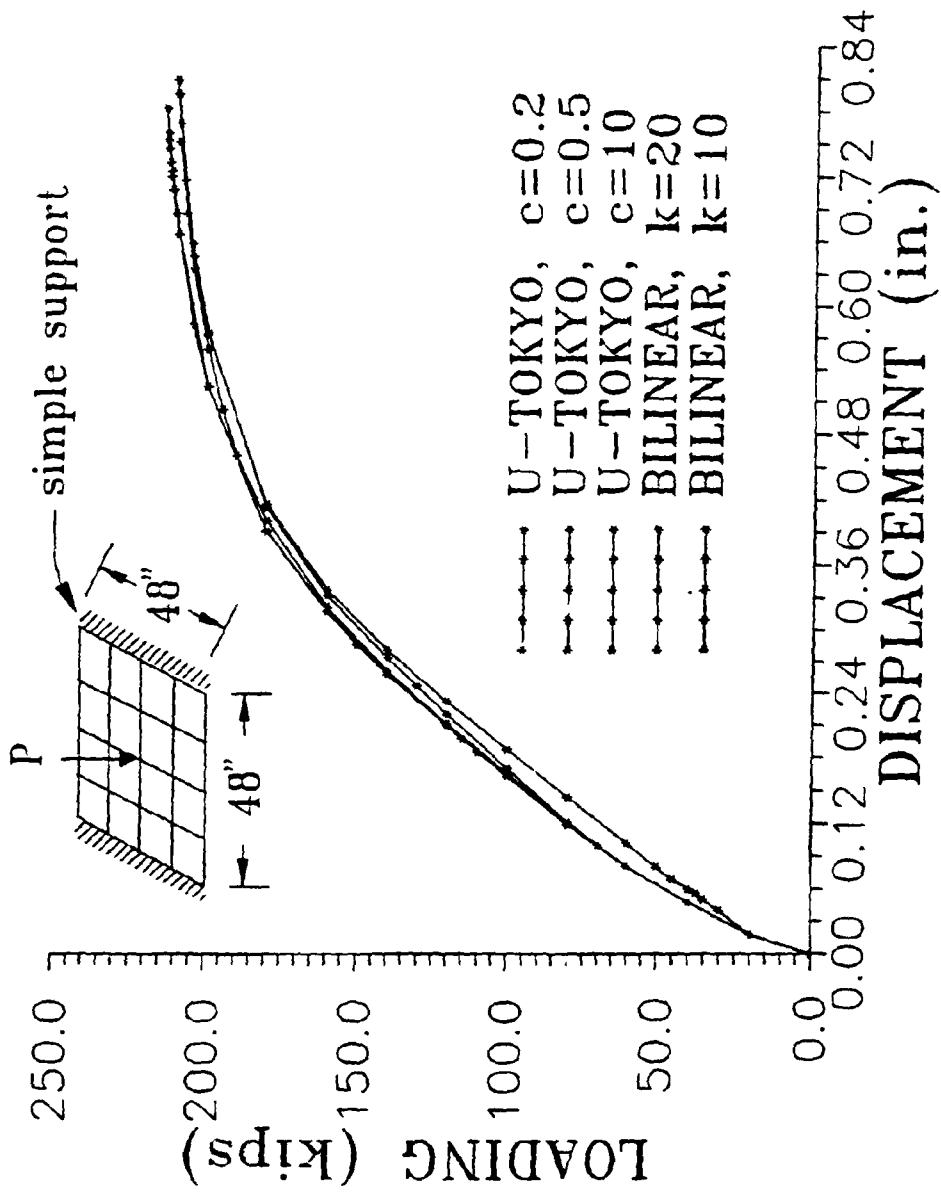
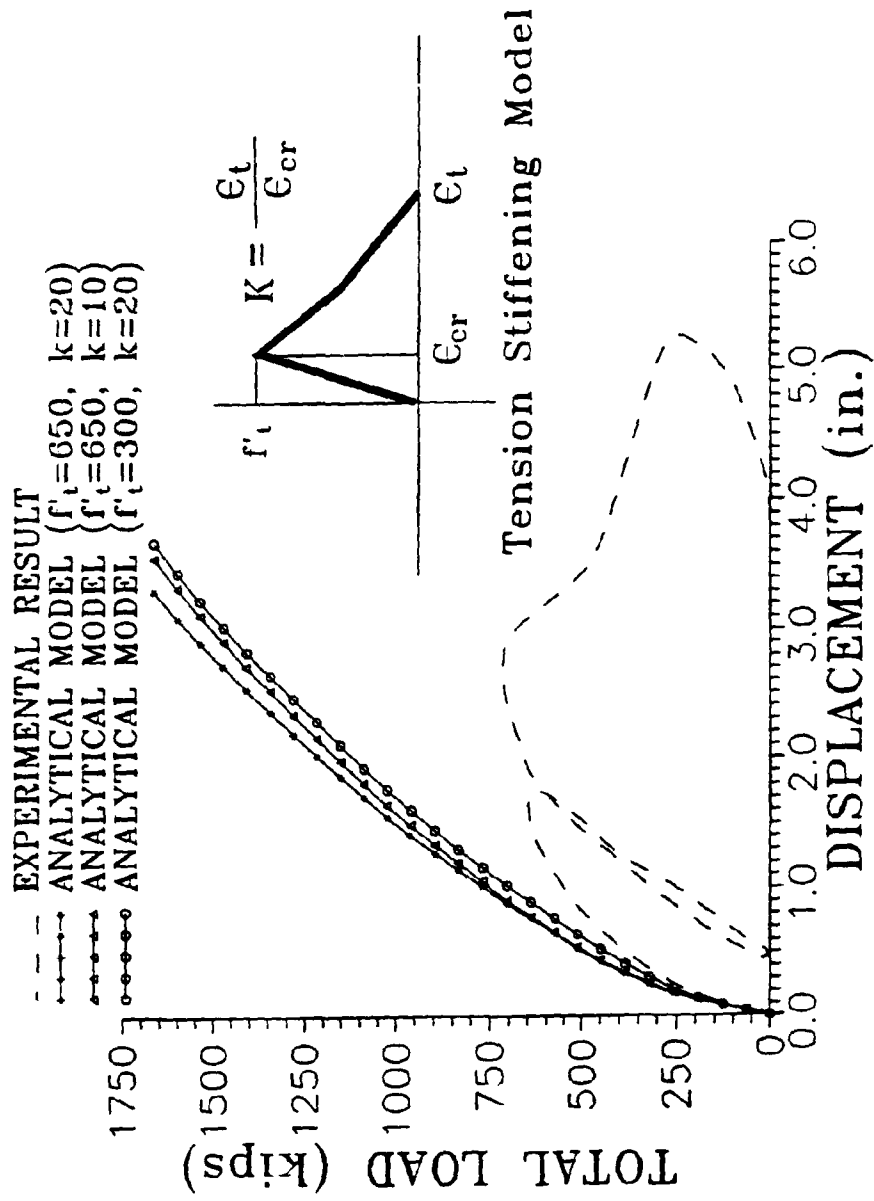
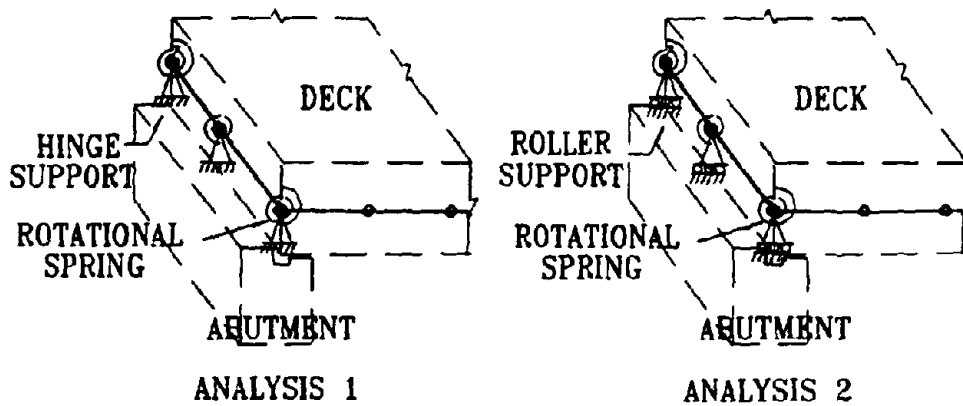


FIGURE 8.24: EFFECTS OF USING DIFFERENT TENSION STIFFENING MODELS



**FIGURE 8.25: EFFECTS OF TENSILE CHARACTERISTICS OF CONCRETE**



SLAB AND ABUTMENT CONNECTION MODELS

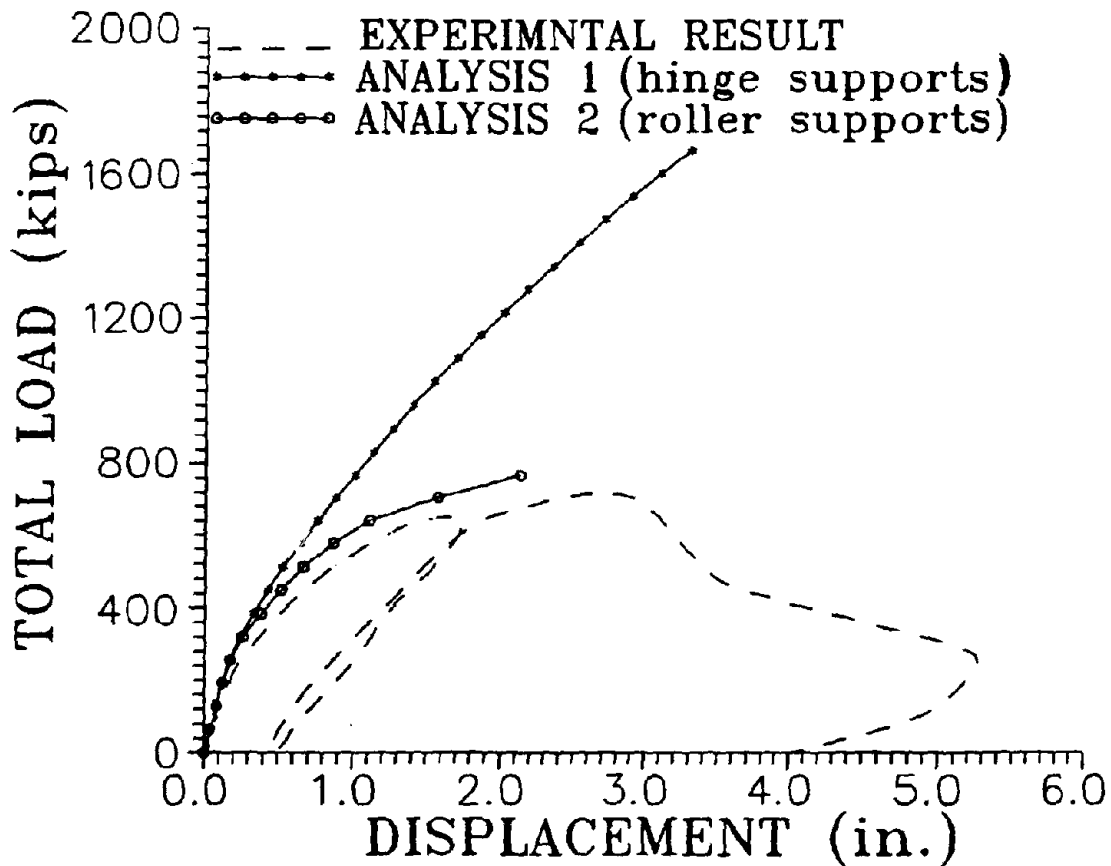
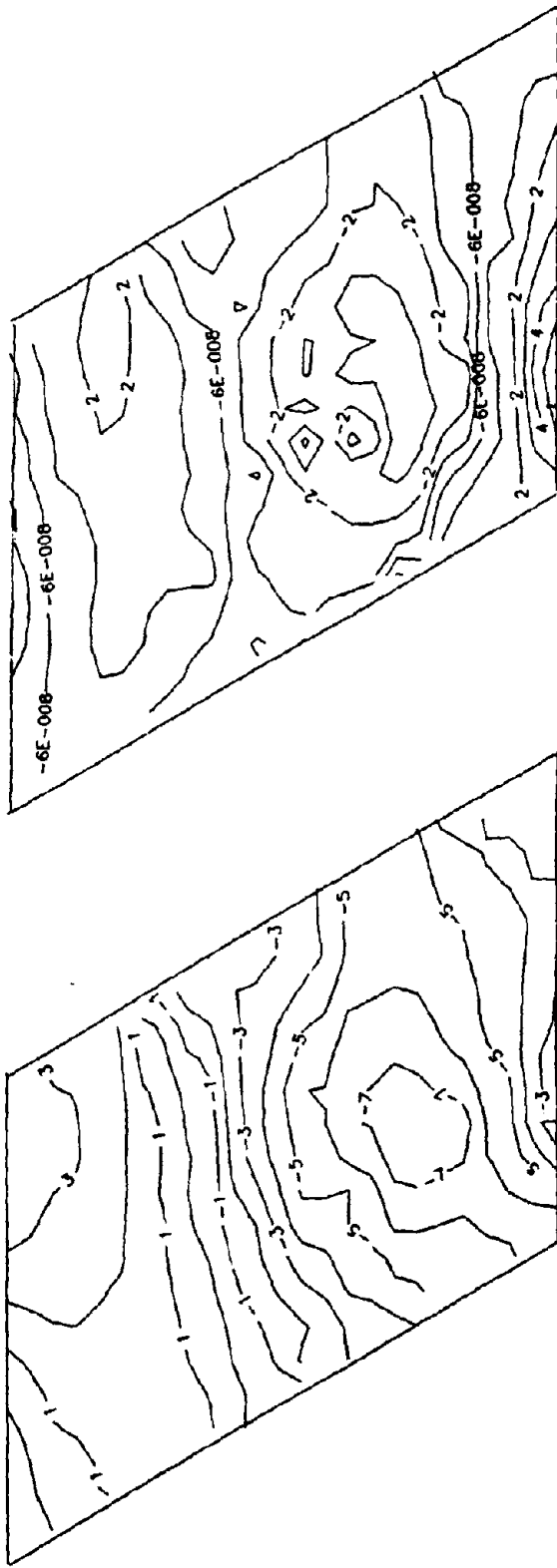


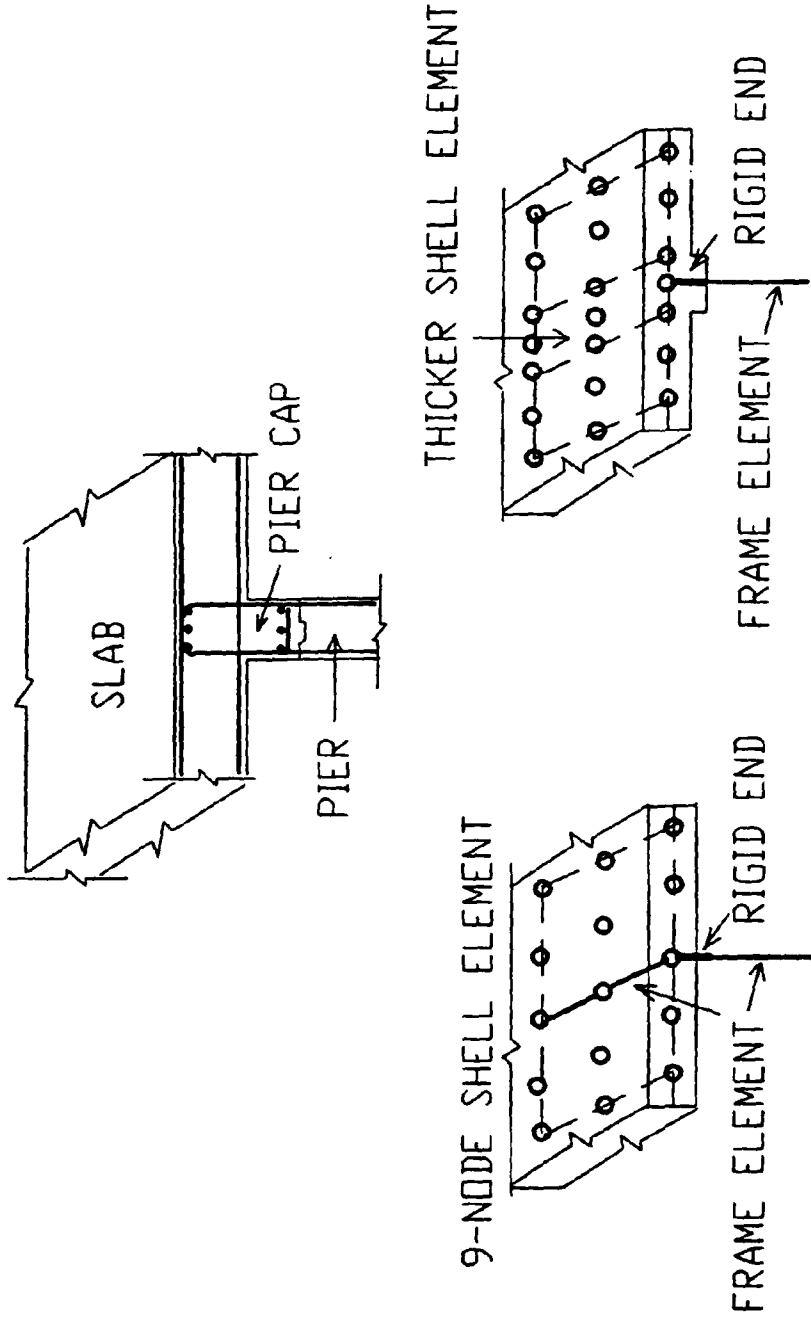
**FIGURE 8.26: SENSITIVITY OF LOAD-DEFLECTION RESPONSE TO HORIZONTAL BOUNDARY CONDITIONS**



(a) Model 1 (hinge support)

(b) Model 2 (roller support)

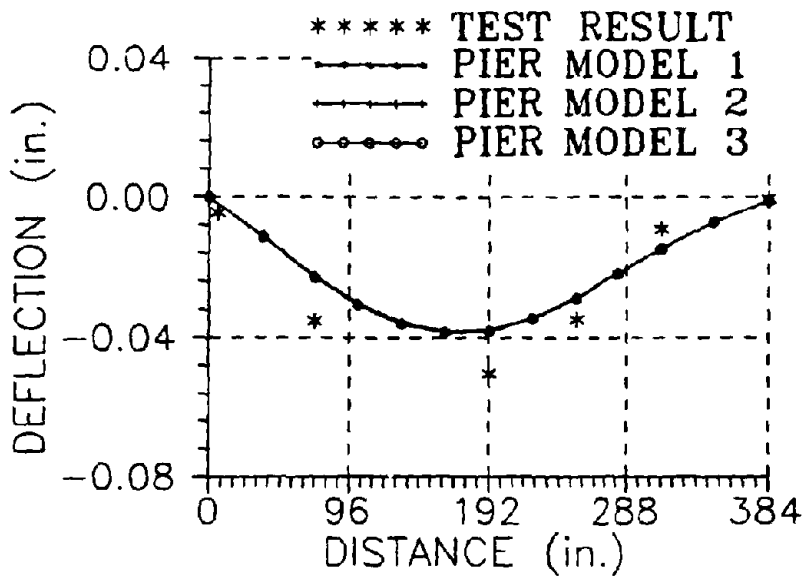
**FIGURE 8.27: MEMBRANE FORCE CONTOURS**



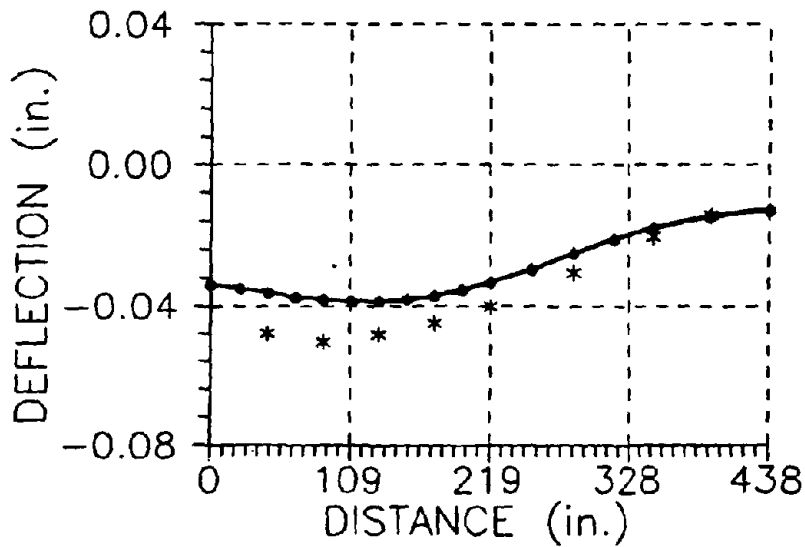
PIER MODEL 3

PIER MODEL 1 & 2

FIGURE 8.28: ANALYTICAL MODEL OF SLAB-PIER CAP CONNECTION



(a) PROFILE ALONG LINE 3



(B) PROFILE ALONG LINE D

**FIGURE 8.29: DEFLECTION PROFILES FOR DIFFERENT SLAB-PIER CAP MODELS**

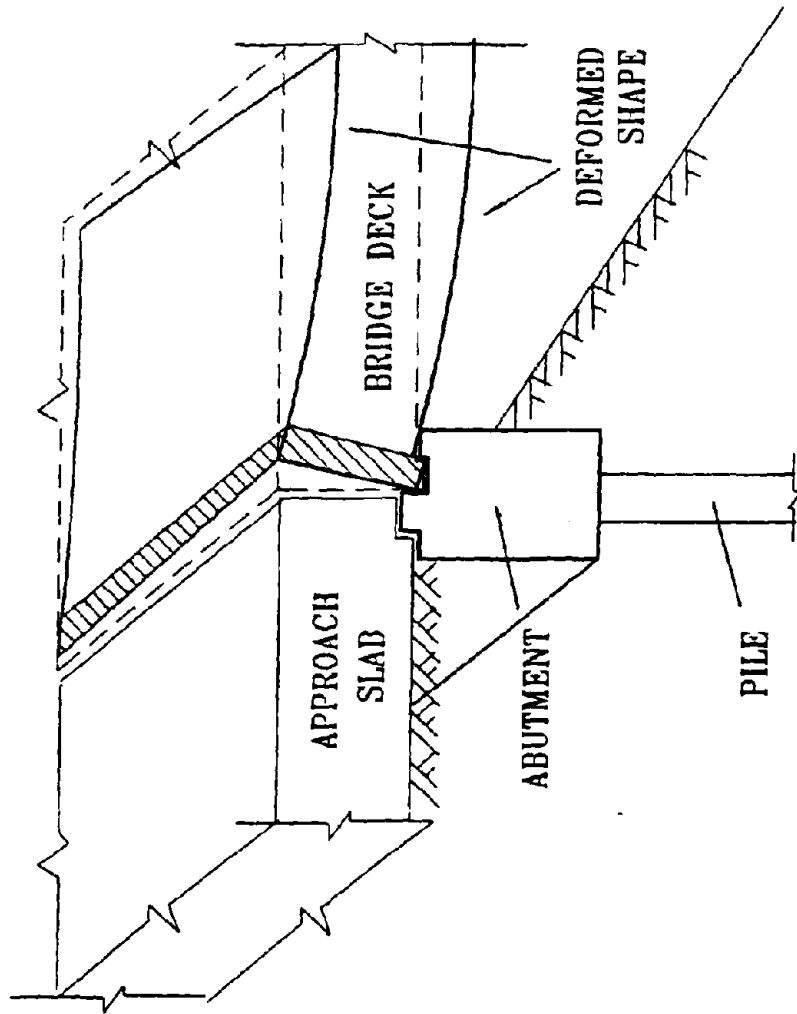


**FIGURE 8.20 OBSERVED BEHAVIOR OF BRIDGE DECK AT ABUTMENT**

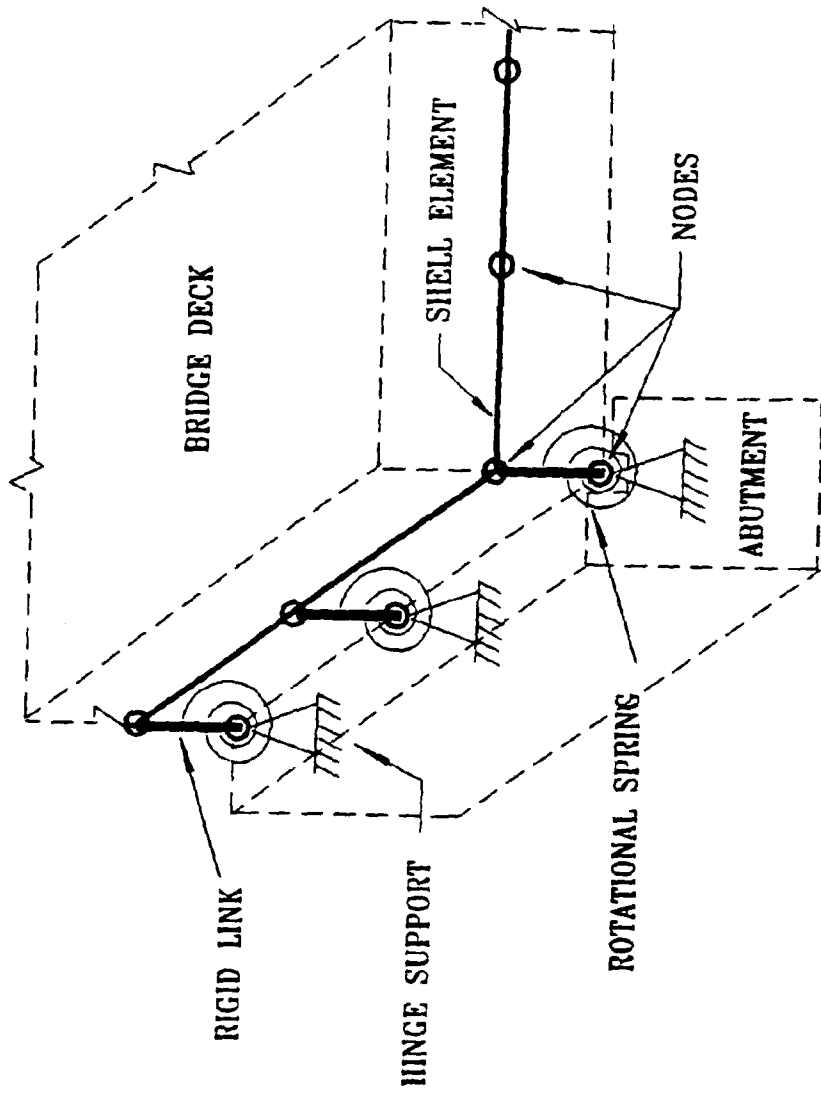


**FIGURE 8-31: ANALYTICAL MODEL OF SLAB-ABUTMENT CONNECTION**

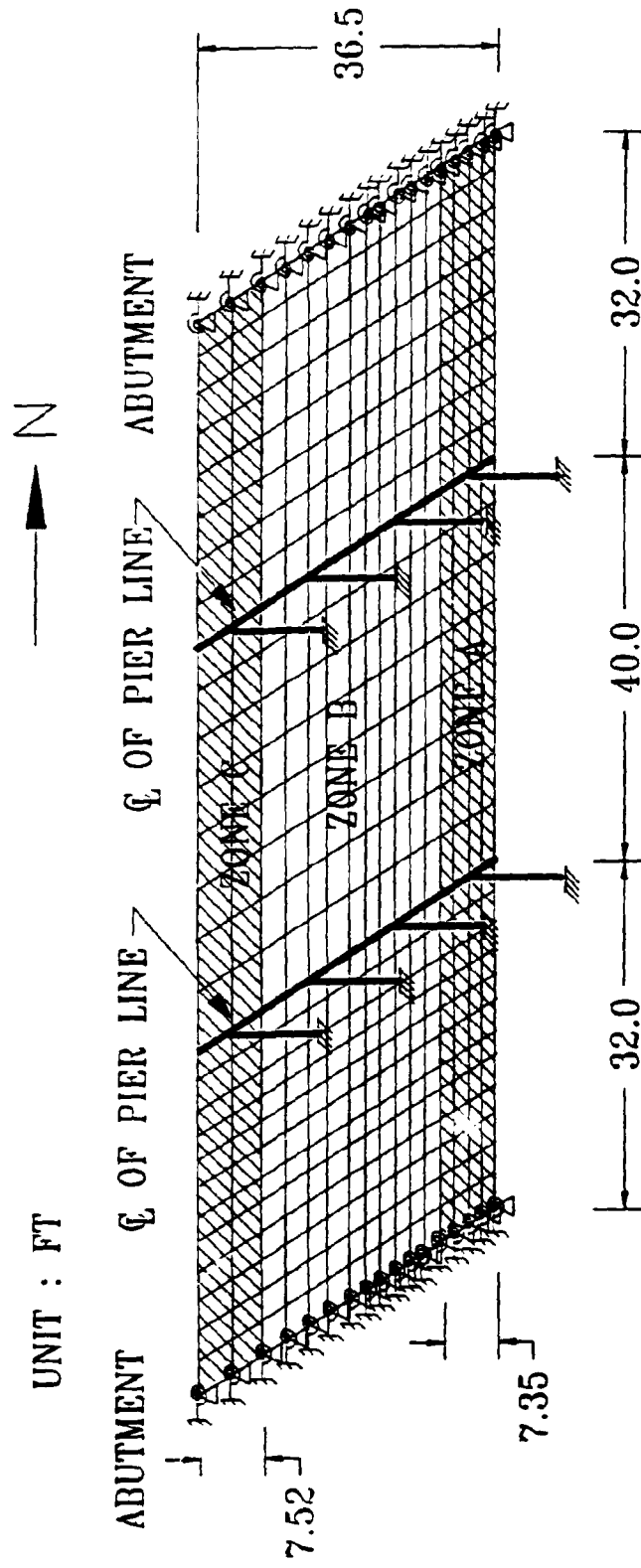


**FIGURE B.32. SIMULATION OF DAMAGE**

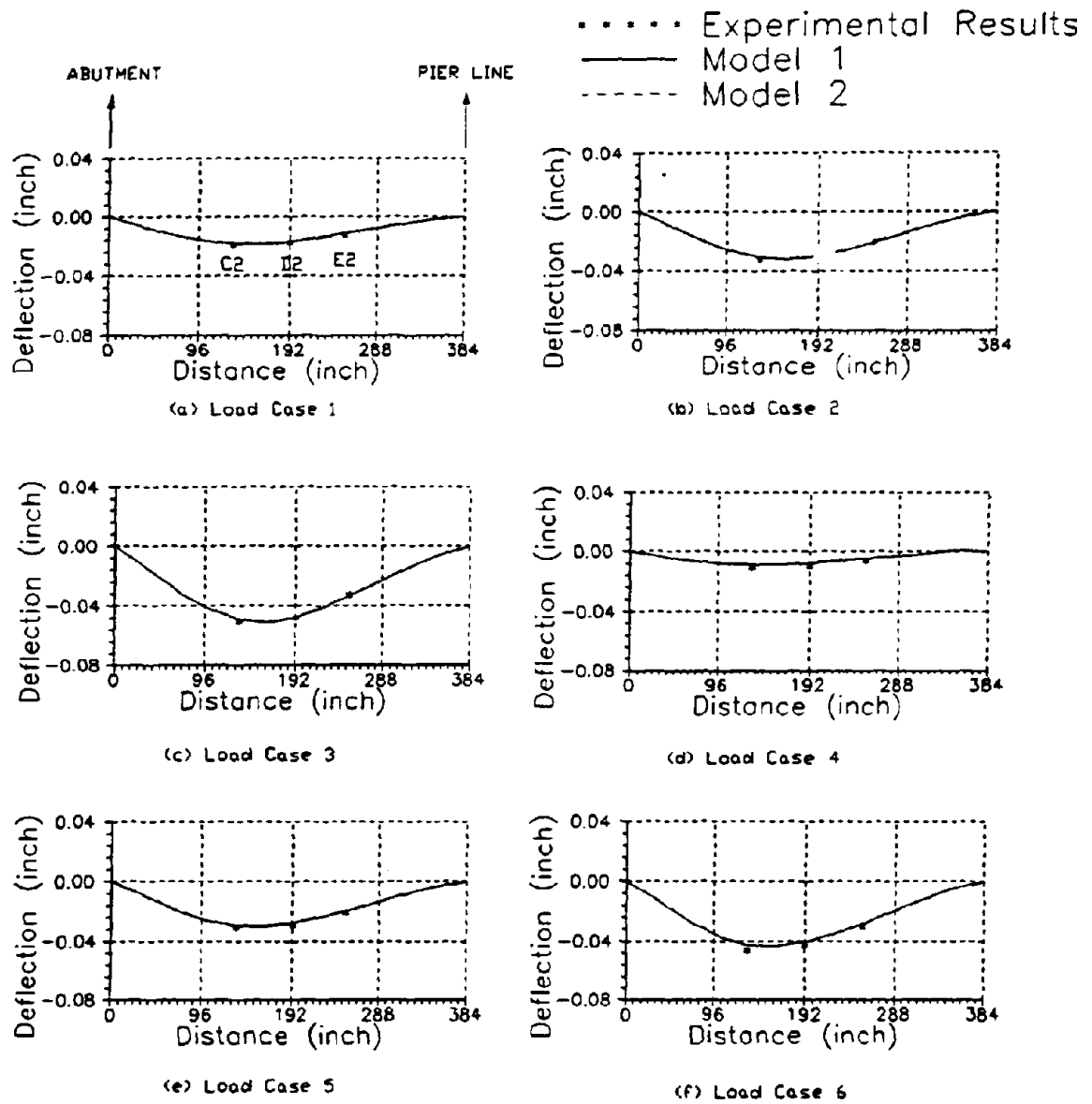


**FIGURE 8.33(a): CORRELATION OF DEFLECTION PROFILES UNDER TRUCK LOAD TESTS (LINE 2)**

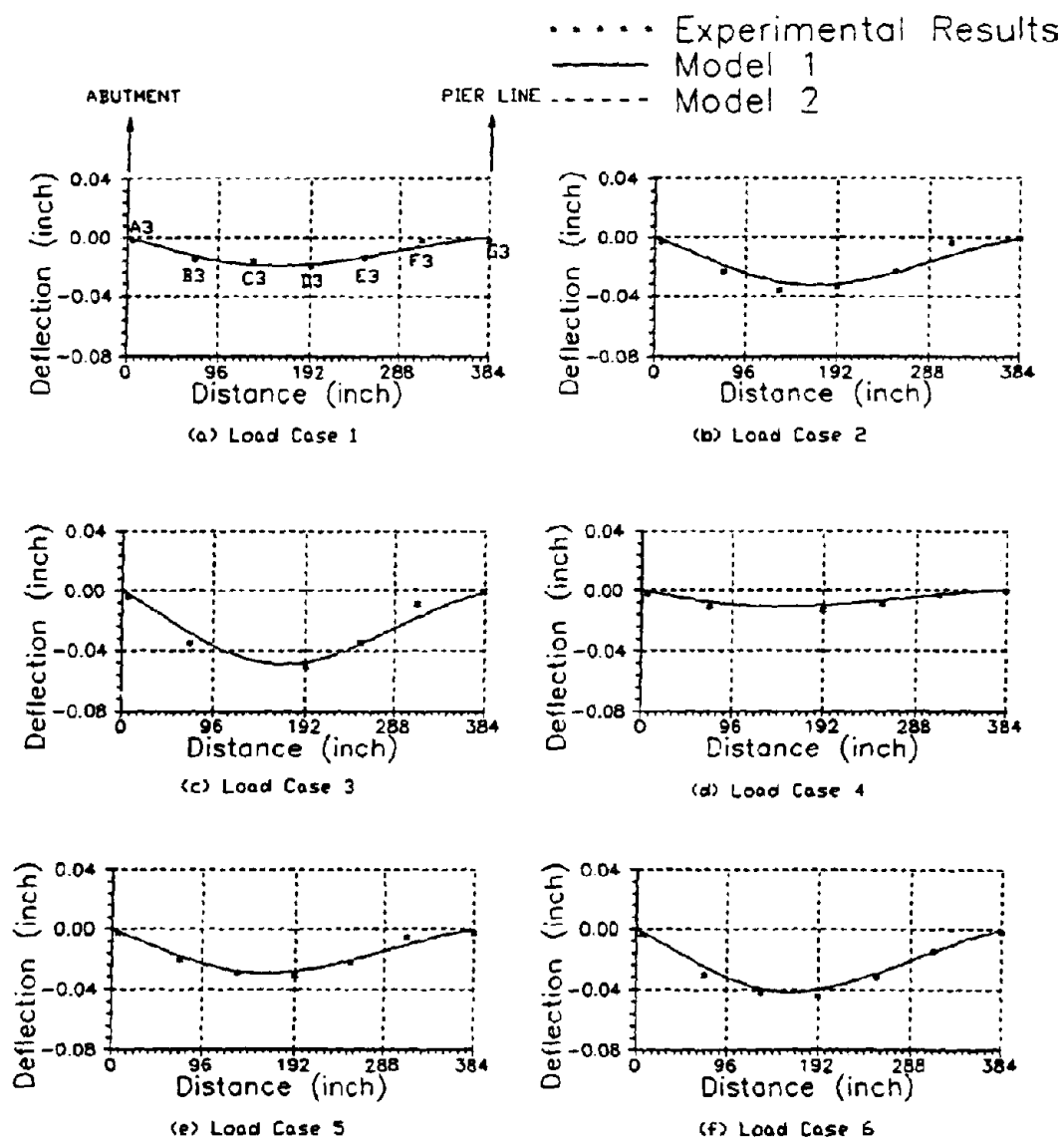


**FIGURE 8.33(b): CORRELATION OF DEFLECTION PROFILES  
UNDER TRUCK LOAD TESTS (LINE 3)**

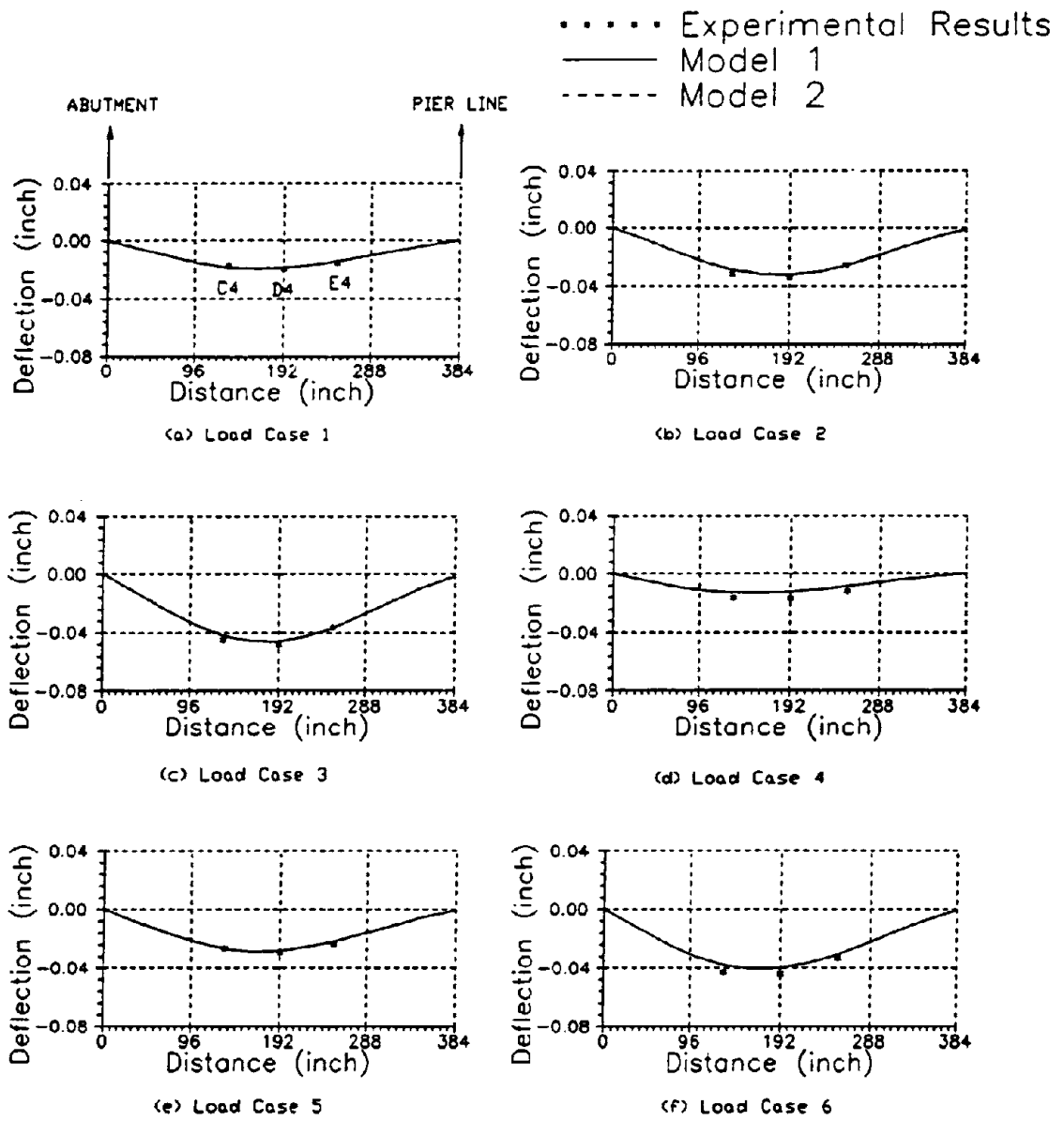


**FIGURE 8.33(c): CORRELATION OF DEFLECTION PROFILES UNDER TRUCK LOAD TESTS (LINE 4)**

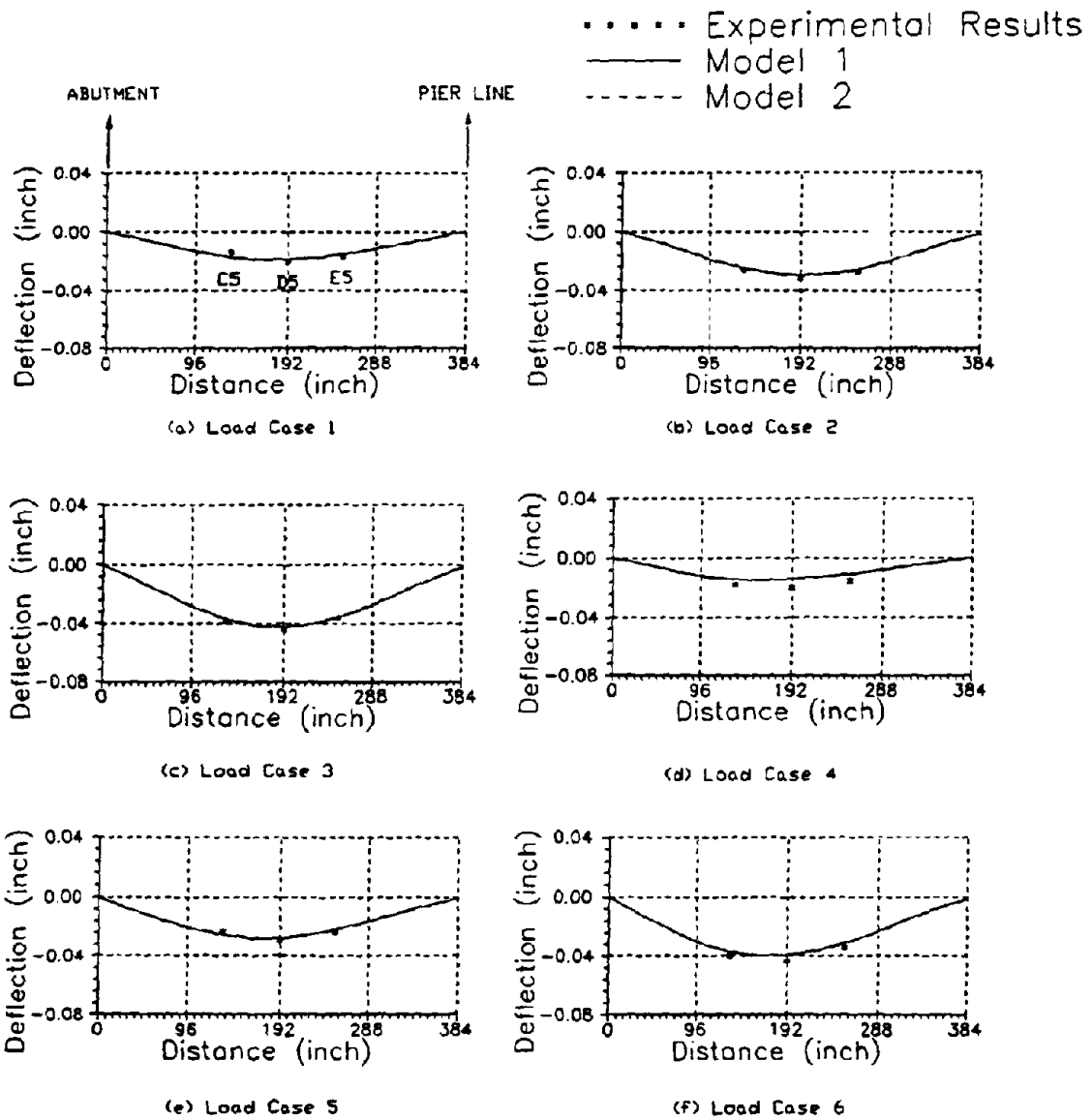


**FIGURE 8.33(d): CORRELATION OF DEFLECTION PROFILES UNDER TRUCK LOAD TESTS (LINE 5)**

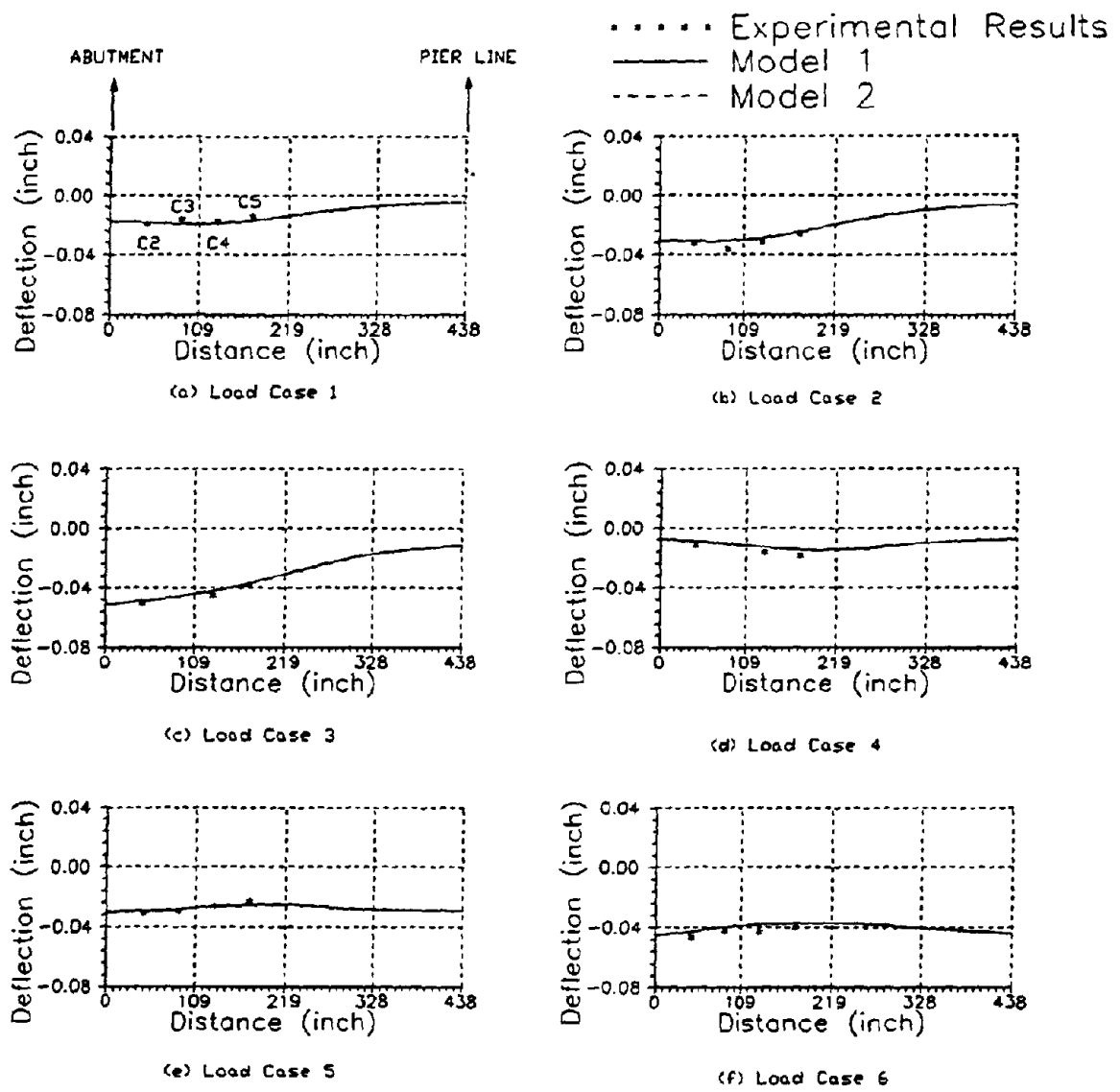


**FIGURE 8.33(e): CORRELATION OF DEFLECTION PROFILES UNDER TRUCK LOAD TESTS (LINE C)**

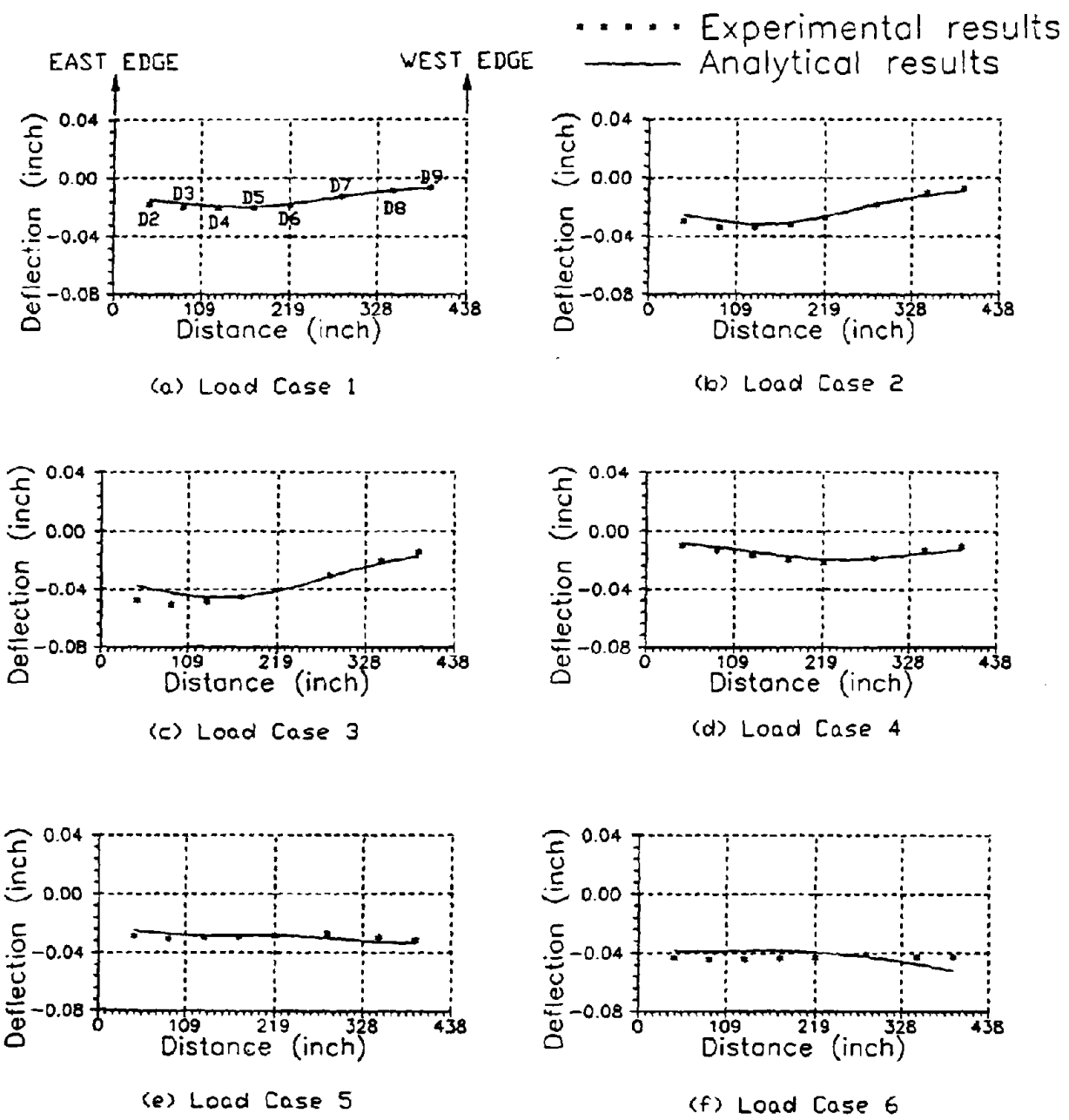


**FIGURE 84(f): COMPARISON OF DEFLECTION PROFILES  
ALONG INSTRUMENTATION LINE D**

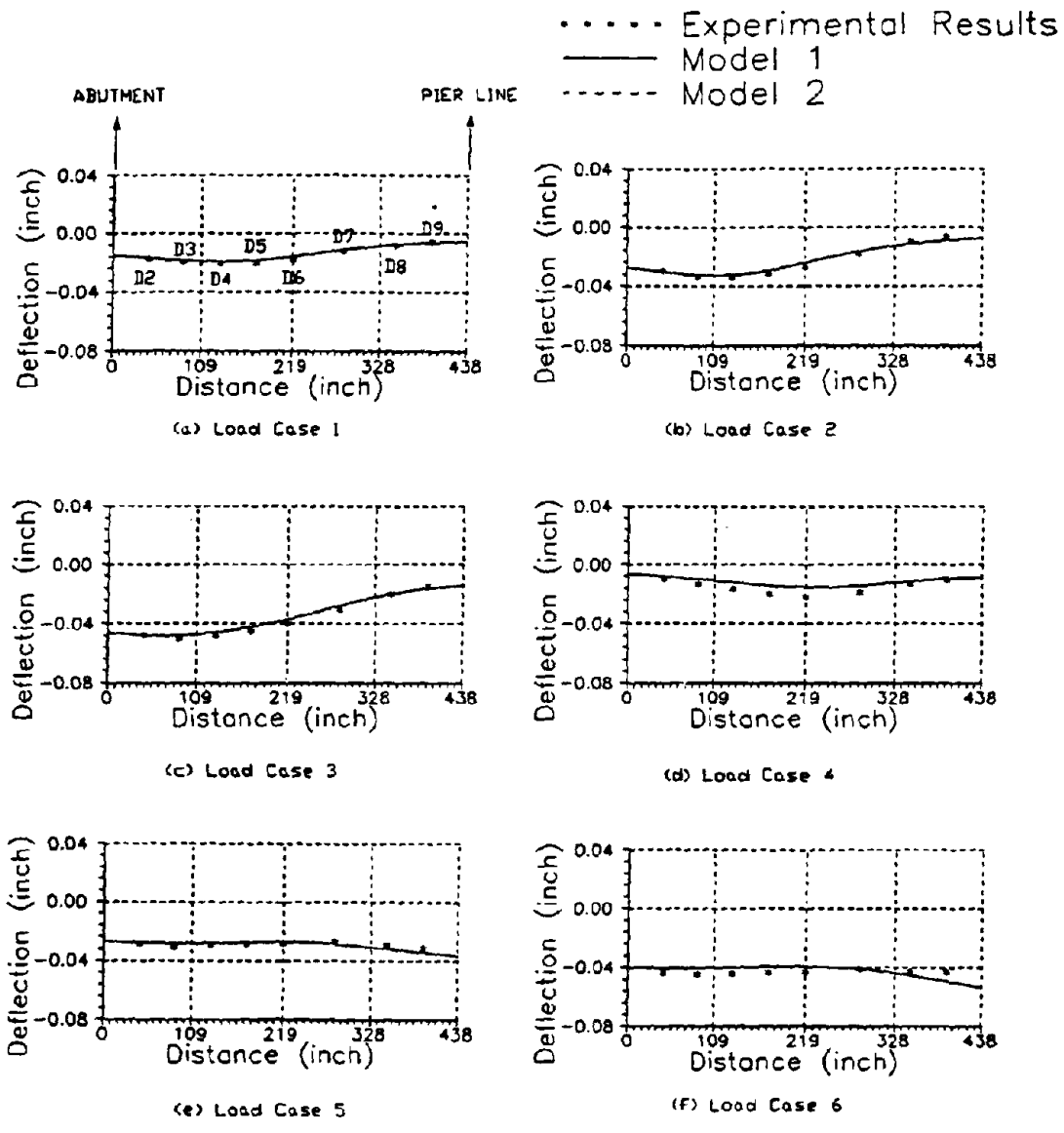


**FIGURE 8.33(D): CORRELATION OF DEFLECTION PROFILES UNDER TRUCK LOAD TESTS (LINE D)**

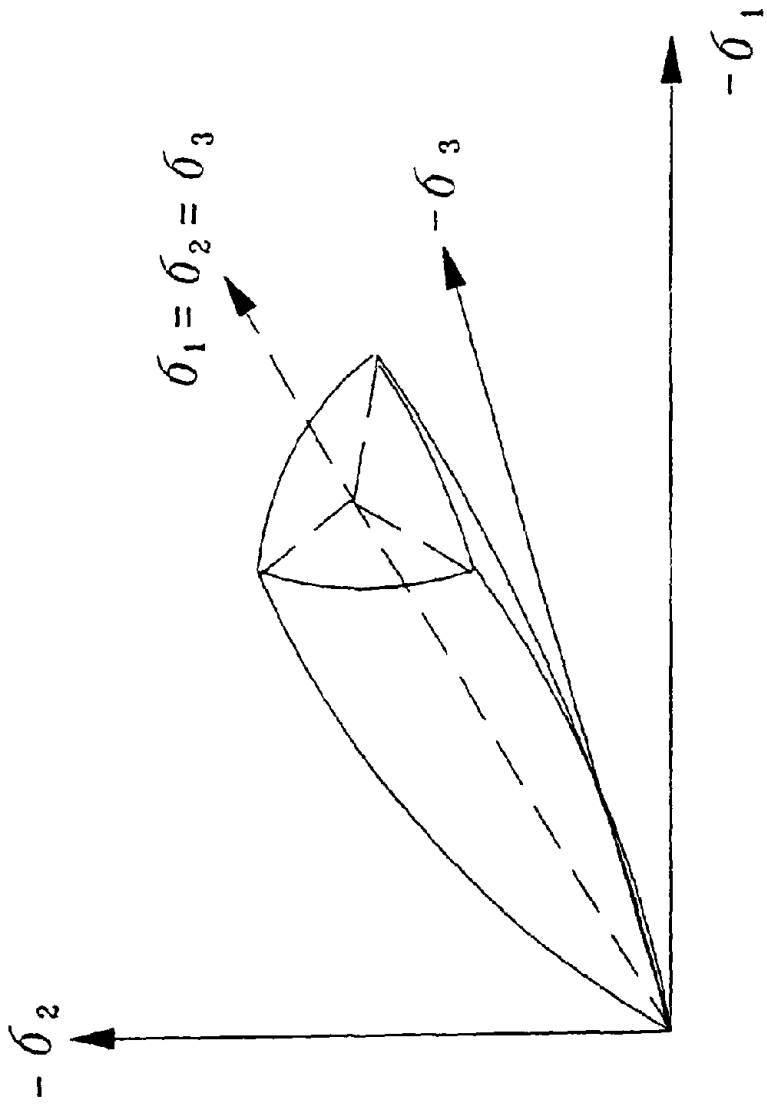


**FIGURE 8.14: FAILURE SURFACE PROPOSED BY HSEIN, TING AND CHEN**

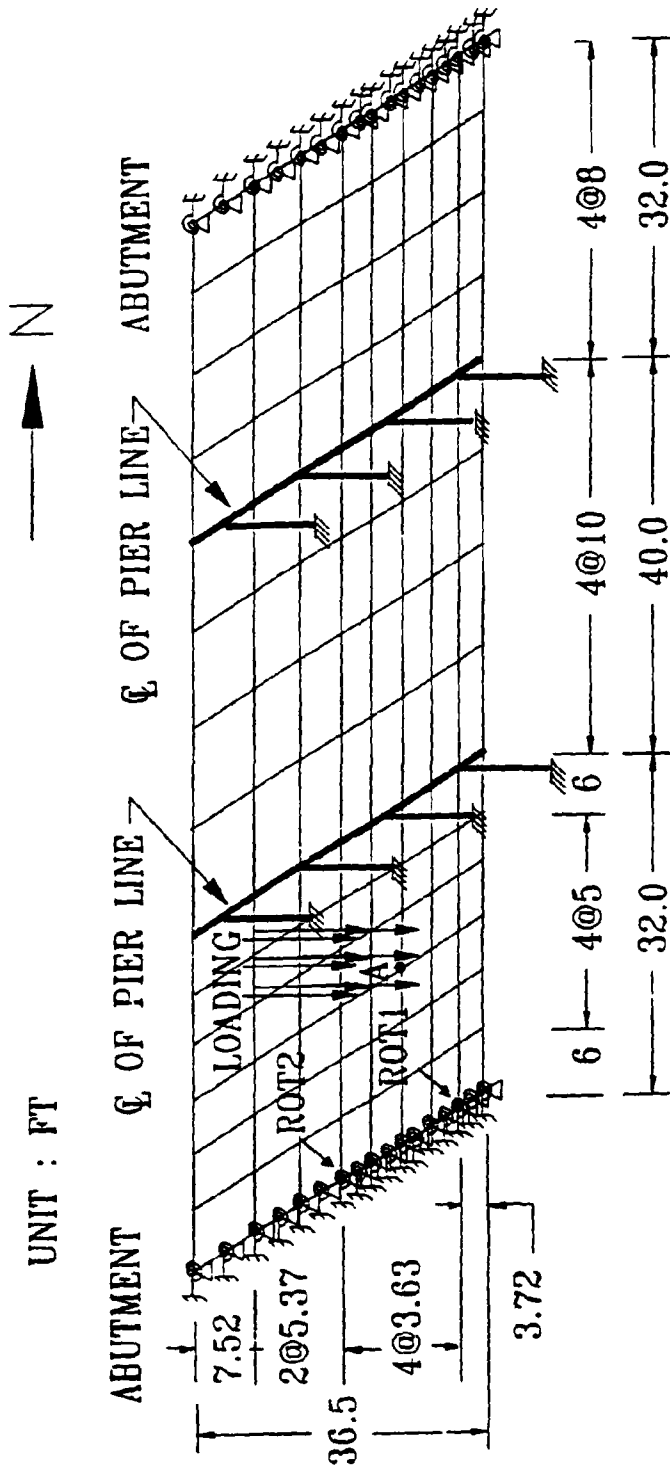


**FIGURE 8.35: FINAL FINITE ELEMENT MESH FOR NONLINEAR ANALYSES**

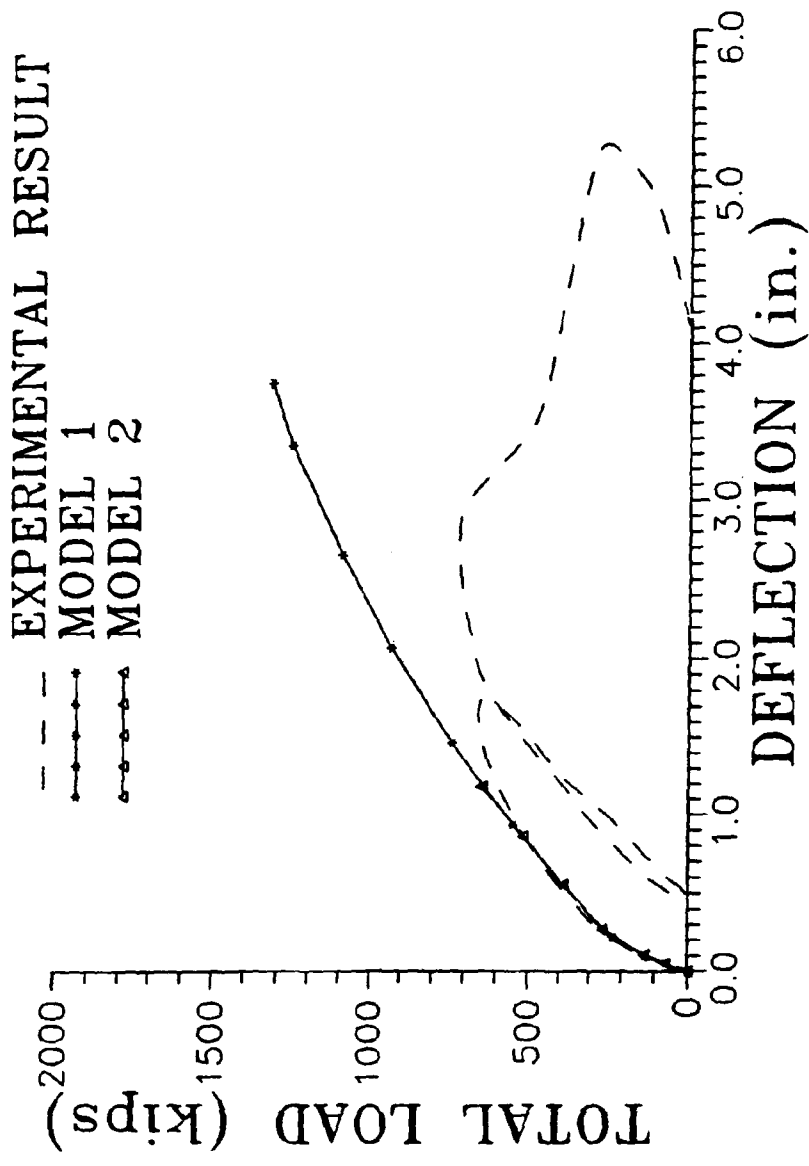


**FIGURE 8.36: COMPARISON OF COMPUTED LOAD-DEFLECTION CURVES WITH EXPERIMENTAL RESULTS**

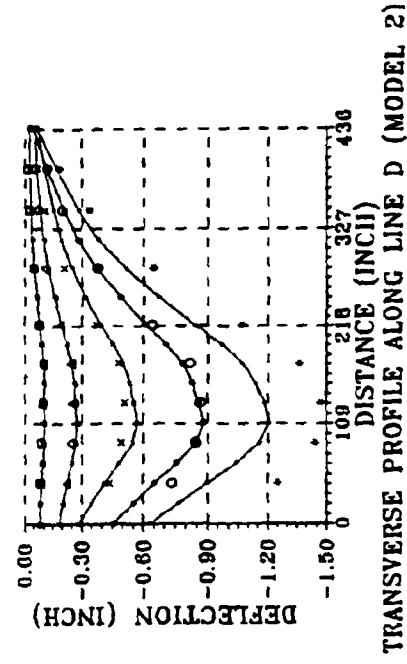
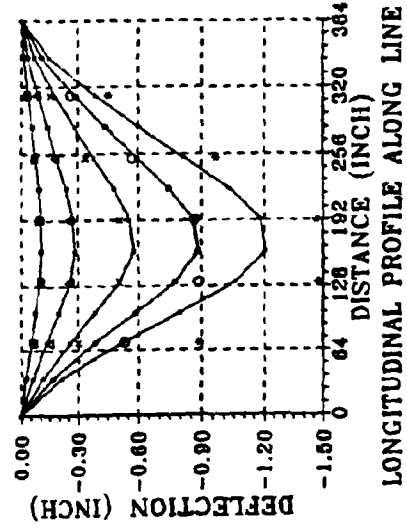
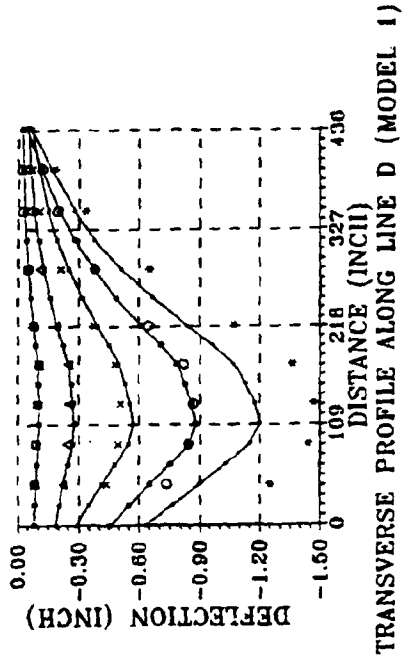
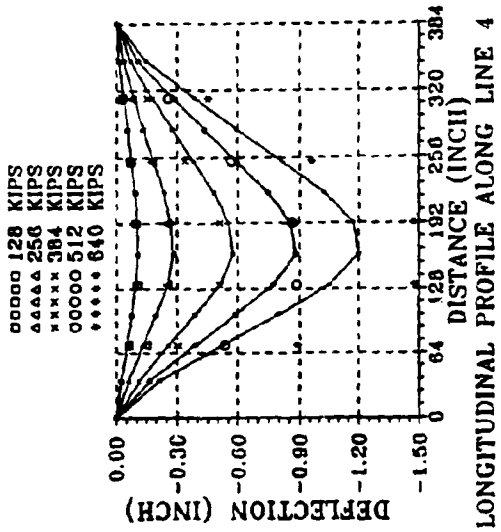


**FIGURE 8.17: CORRELATION OF COMPUTED LOAD-DEFLECTION CURVES WITH**

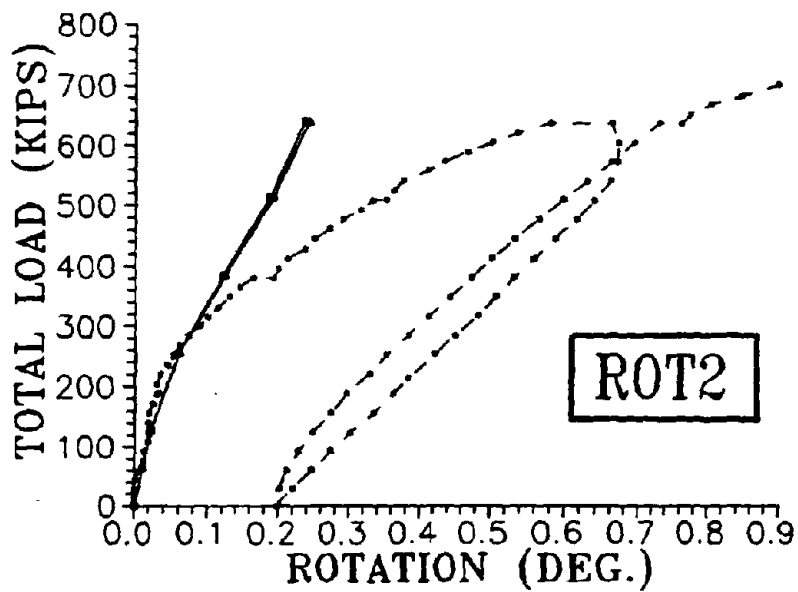
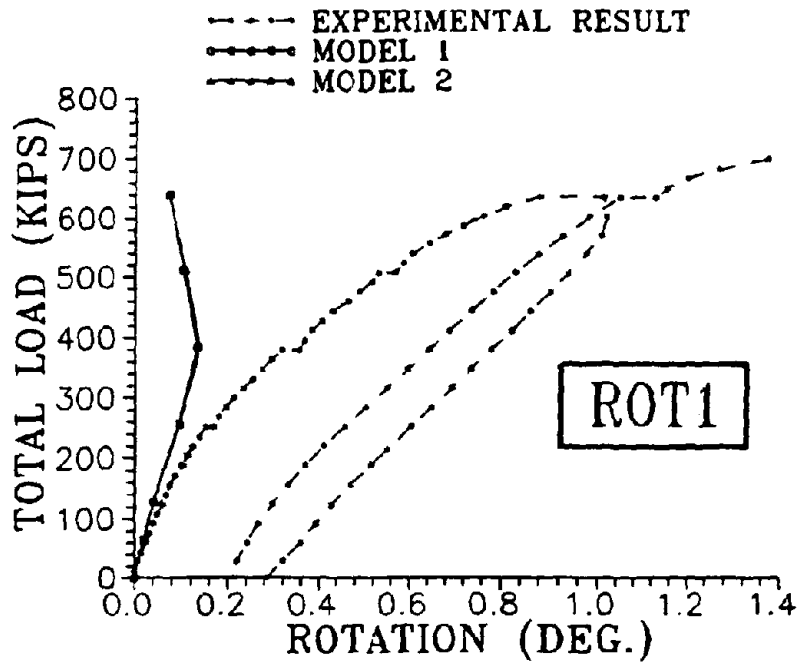
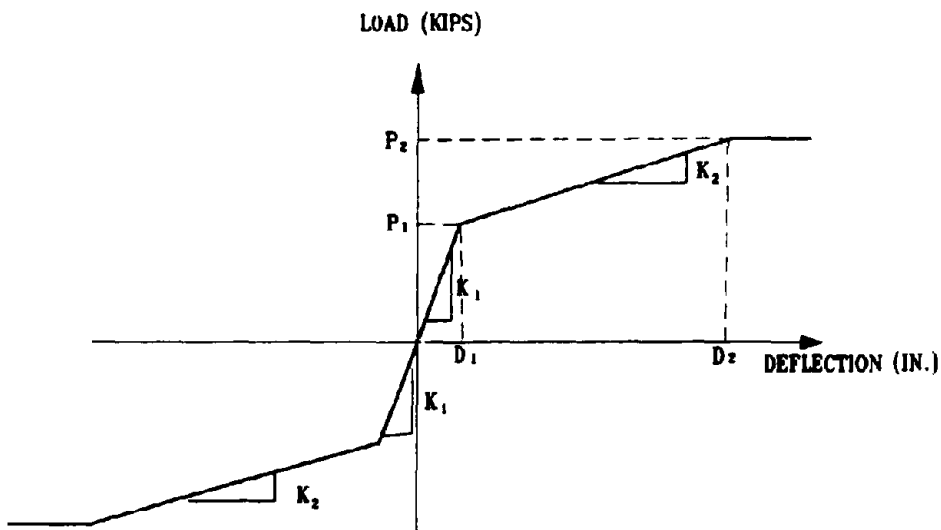
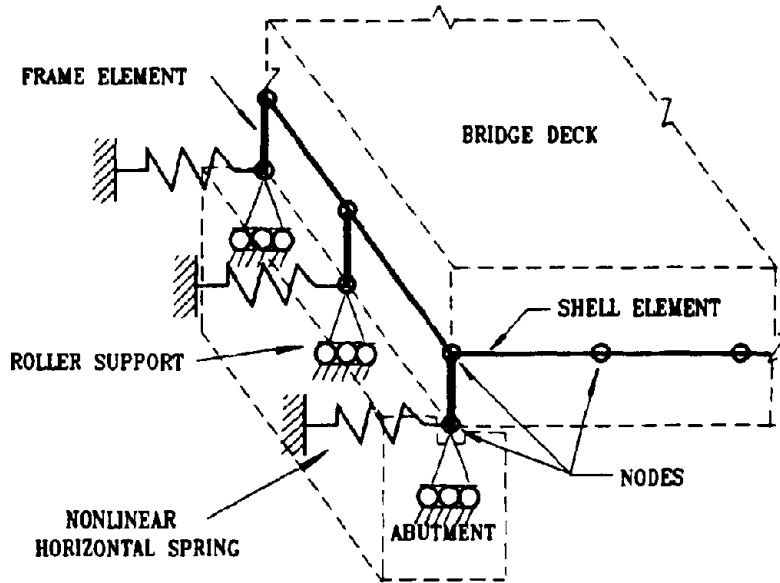
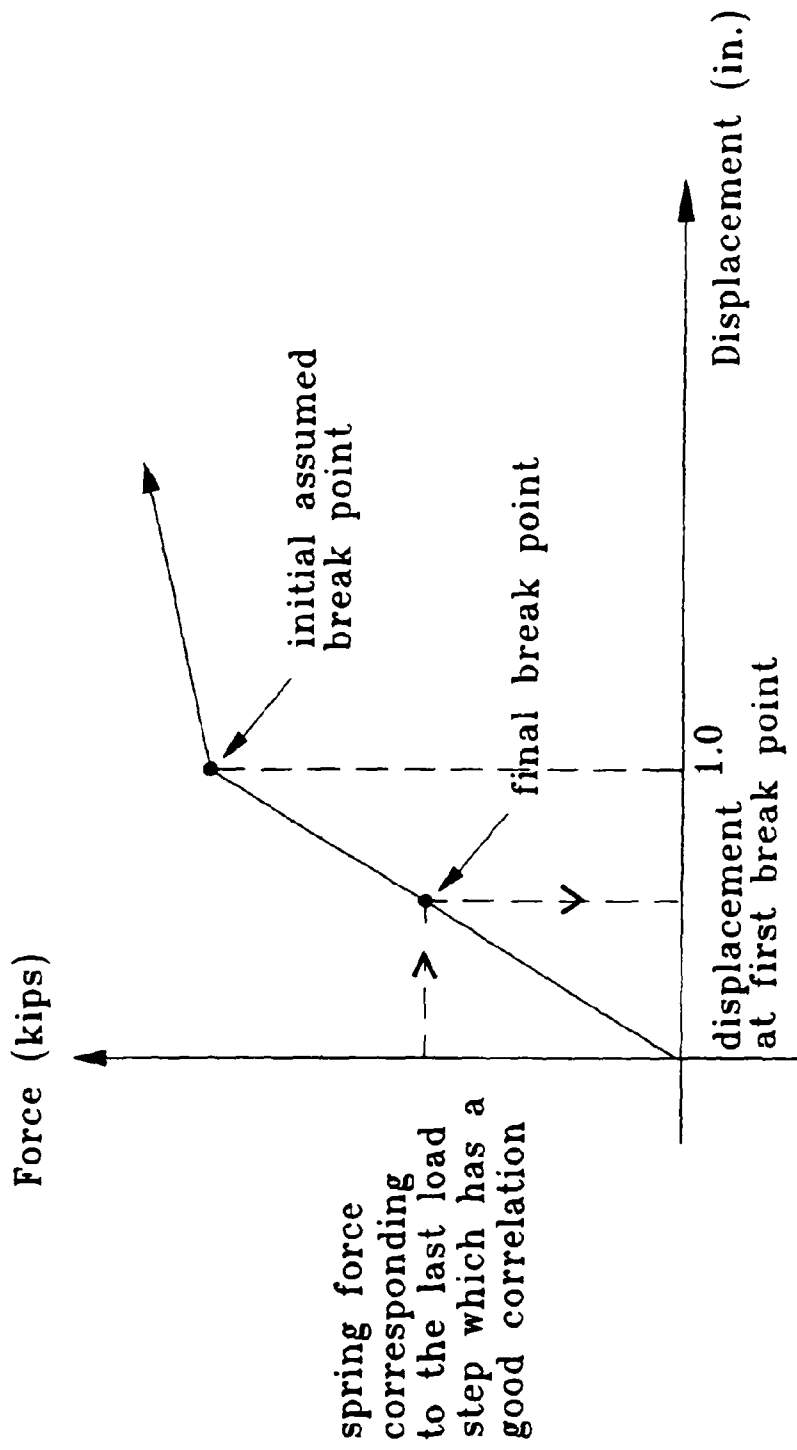


**FIGURE 8.38: MEASURED AND COMPUTED LOAD-DEFLECTION RESPONSE AT SOUTH ABUTMENT**



MATERIAL MODEL FOR NONLINEAR SPRING

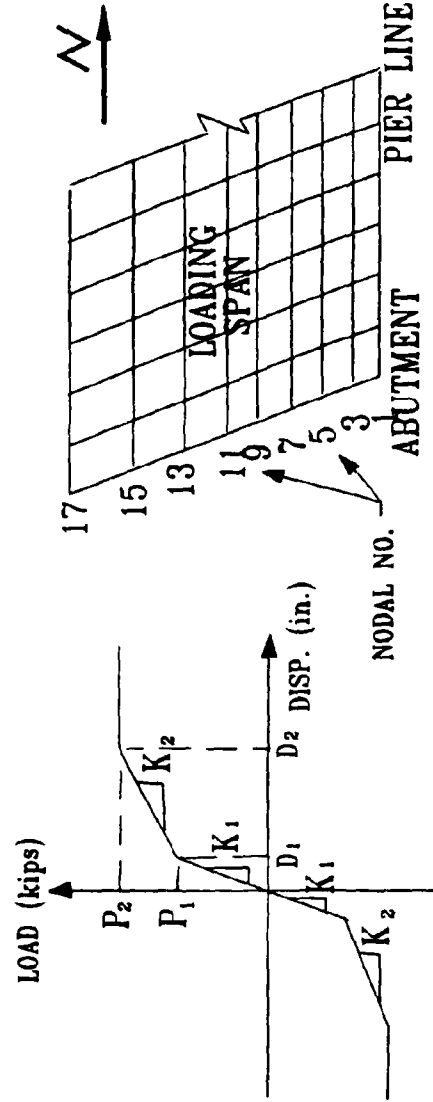
**FIGURE 8.39: REFINED ANALYTICAL MODEL OF SLAB-ABUTMENT CONNECTION**



**FIGURE 8.40: ILLUSTRATION OF THE TECHNIQUE TO DETERMINE THE SLOPES AND BREAK-POINTS OF TRILINEAR HORIZONTAL SPRINGS**

**FIGURE 8.41: CHARACTERISTICS OF HORIZONTAL SPRINGS**

TYPE	$(\frac{P_1}{D_1})$	$(\frac{P_2}{D_2})$	$K_1$	$K_2$	NODAL NO.
A	(44.0) 0.008	(95.0) 0.15	5500	359	1
B	(130.0) 0.0134	(250) 0.5013	9702	246	2,4,6,8,12,
C	(80) 0.0133	(160) 0.367	6015	226	3,5,7,8,10,11,17
D	(150) 0.0005	(435) 0.01	30000	30000	13,14,15,16



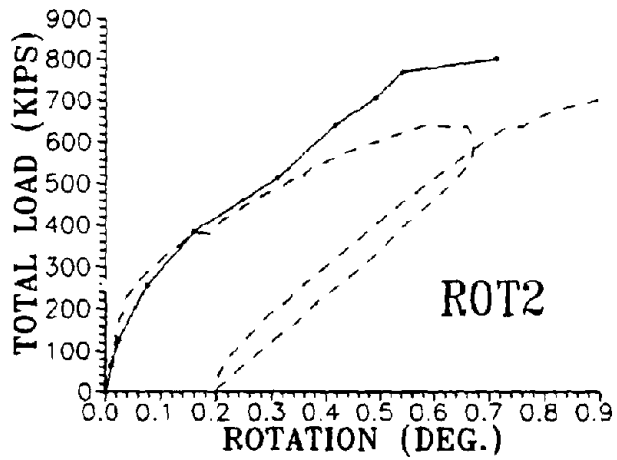
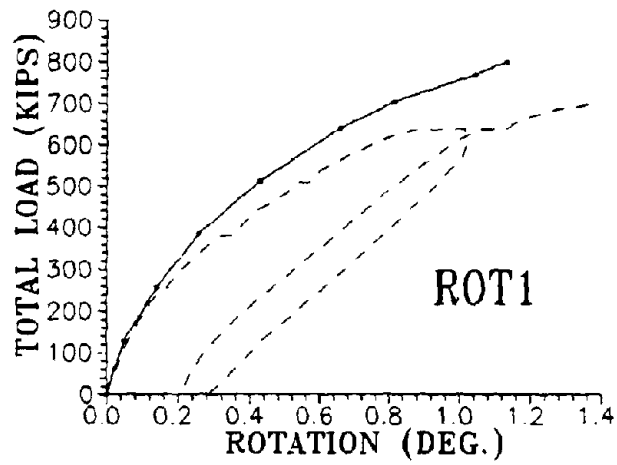
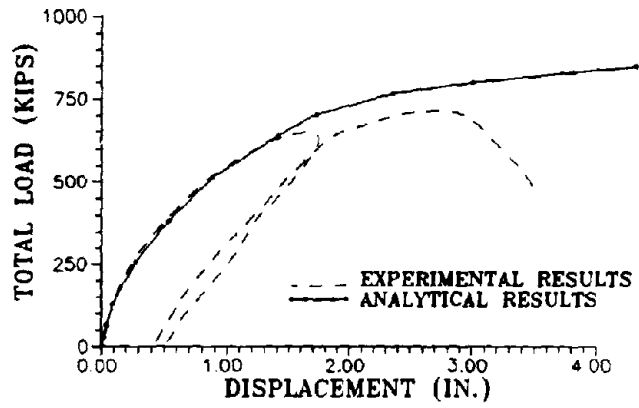


**FIGURE 8.42: COMPARISON OF COMPUTED LOAD-DEFLECTION AND LOAD-ROTATION CURVES WITH EXPERIMENTAL RESULTS**

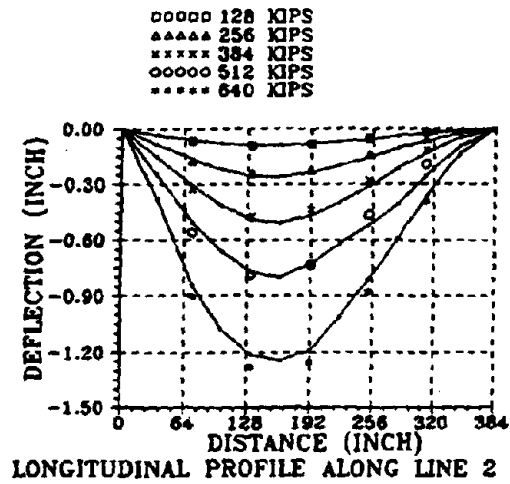
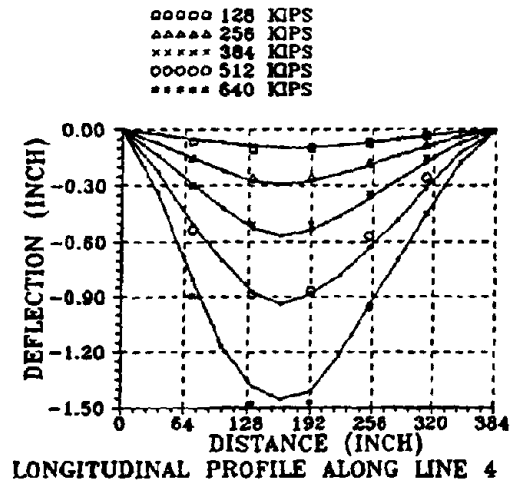
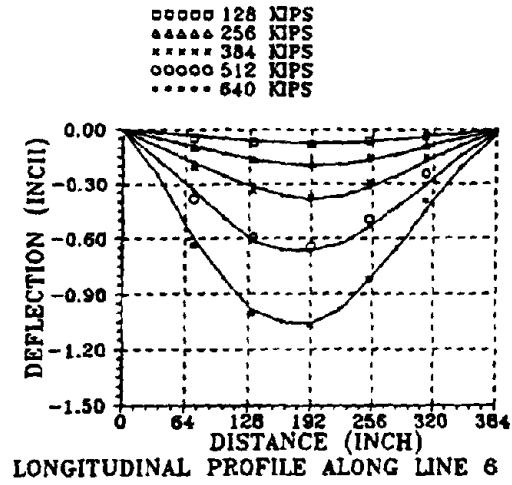


**FIGURE 8.43(a): COMPARISON OF DEFLECTION PROFILES FROM REFINED MODEL**

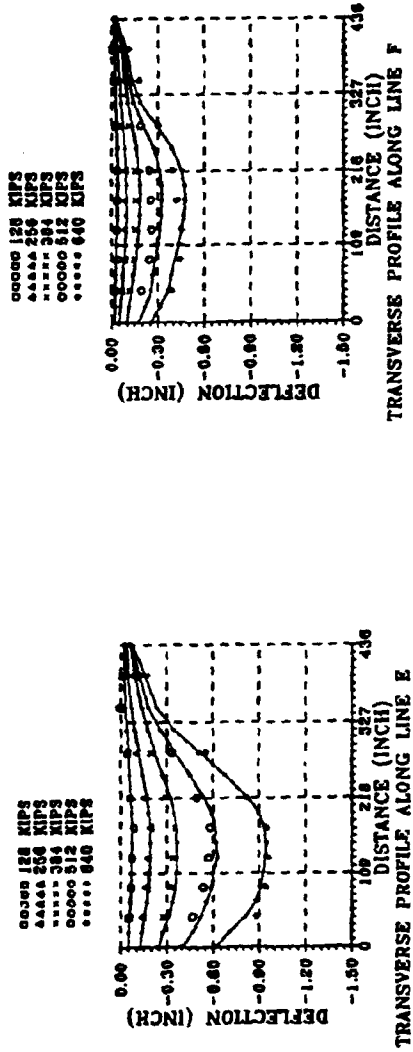
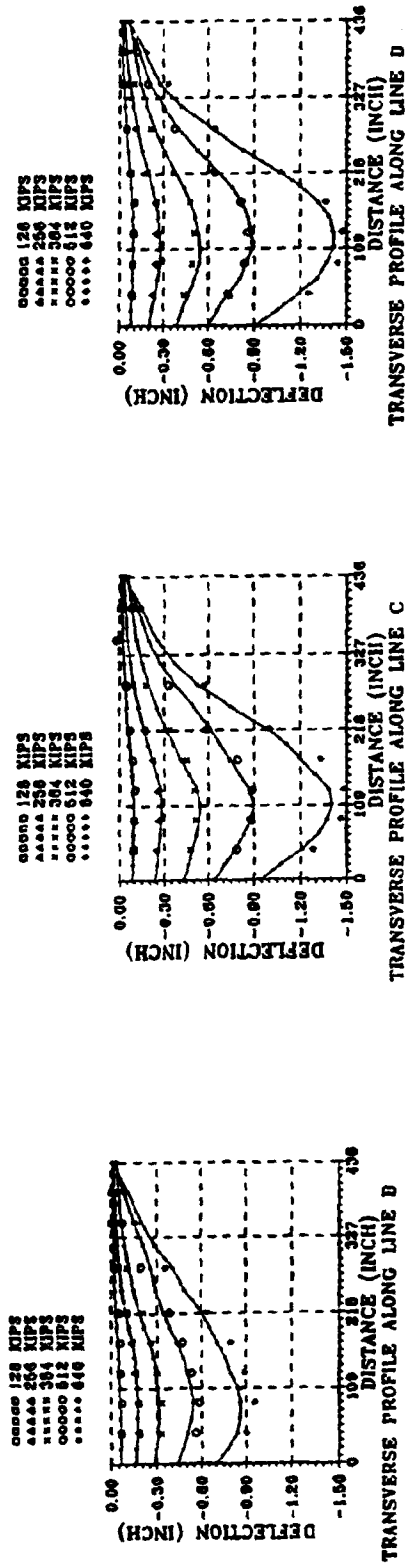


**FIGURE 8.43(b): COMPARISON OF DEFLECTION PROFILES FROM REFINED MODEL**

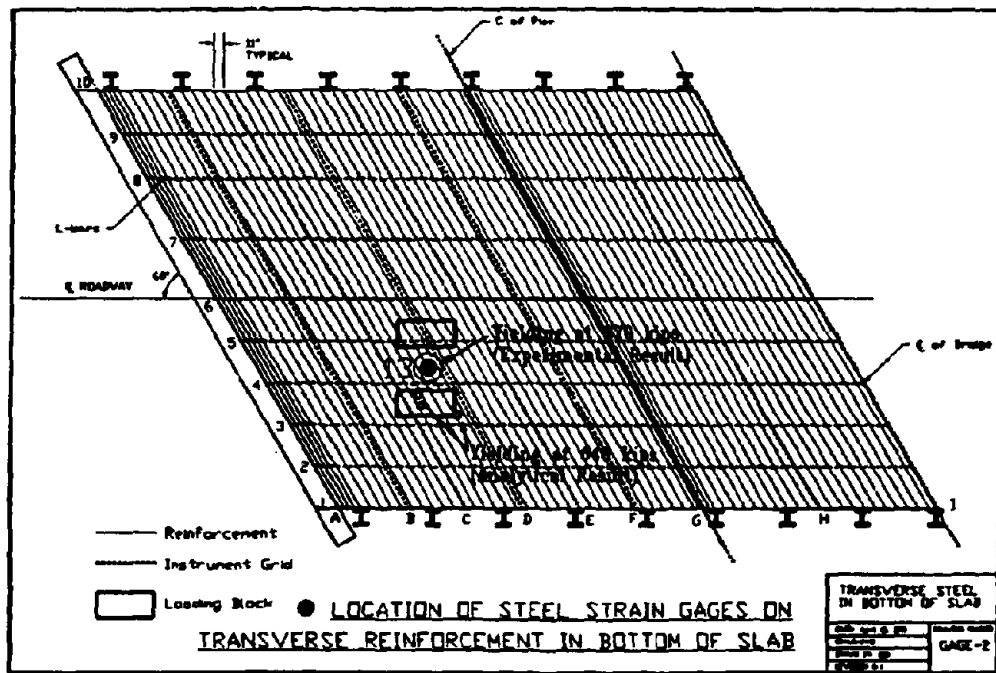
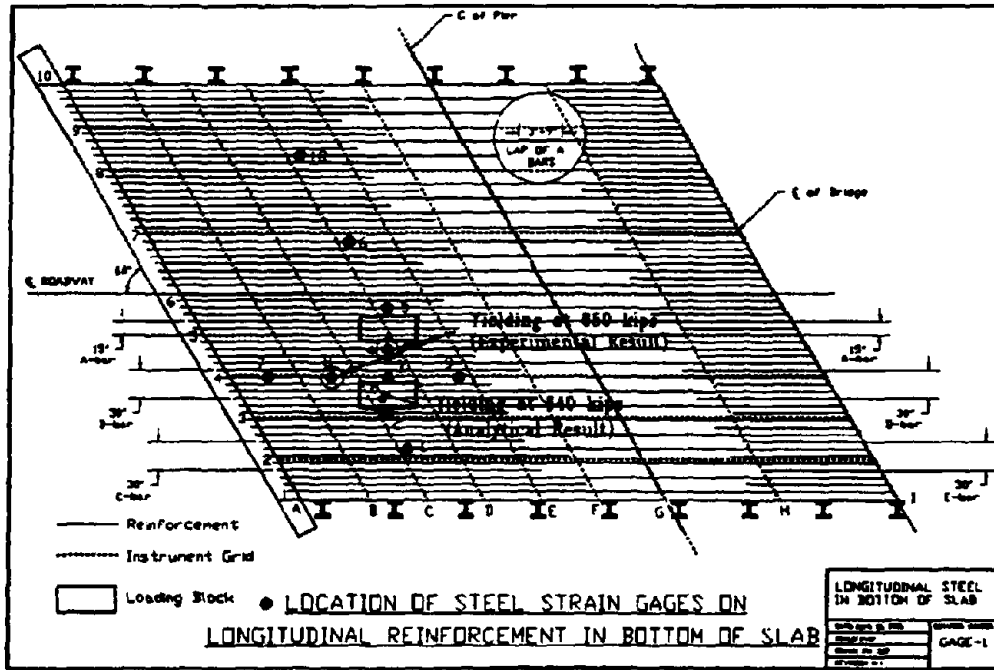
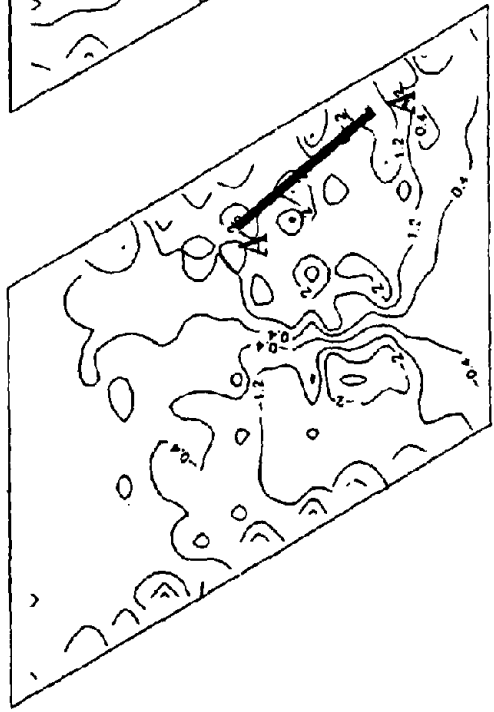
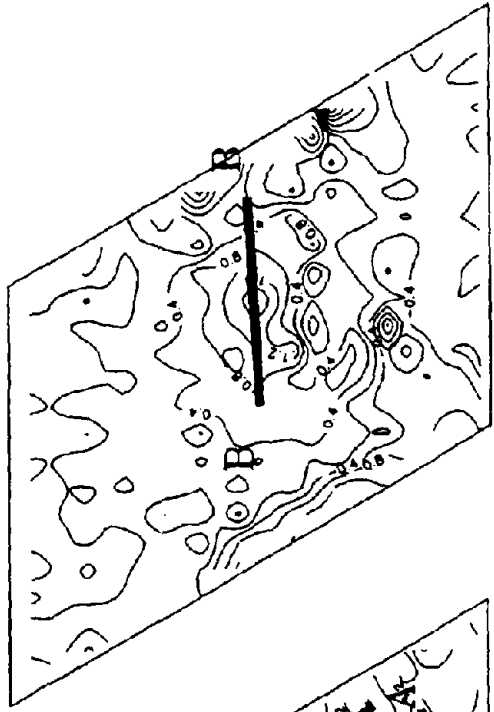


FIGURE 8.44: COMPARISON OF REBAR YIELD LOCATIONS



X-DIRECTION



Y-DIRECTION

**FIGURE 8.45: OUT-OF-PLANE SHEAR FORCE CONTOURS IN THE LOADING SPAN**

**(THIS PAGE INTENTIONALLY LEFT BLANK)**

## CHAPTER 9: CONCLUSIONS

### 9.1 GENERAL CONCLUSIONS

This project began with three basic goals: 1) To test a highly redundant structure, a slab bridge, to failure in an effort to better understand the capacity and behavior of such a structure; 2) To use various methods of nondestructive evaluation to assess the bridge condition. Specifically, material sampling, modal testing and truck load testing were used; 3) To examine the various methods of analyzing and rating the bridge to assess accuracy and usability. All three goals were accomplished.

The test bridge was a three span concrete slab bridge. This structure had abutments and piers skewed at a 30° angle. The bottom of the slab, the piers and the abutments were in reasonably good condition. The edges of the slab and the shoulder area on the top of the slab were severely deteriorated, often with reinforcing bars exposed. The driving lane area on the top of the slab was still sound. Petrographic and other forms of material analysis indicated that the deterioration of the concrete was due to poor quality aggregate which was susceptible to freeze/thaw cracking and alkali-silica reaction and a lack of proper air entrainment in the paste. Tests on the reinforcing bar revealed that the rebar retained its basic yield and ultimate strength, but that the loss of area due to corrosion was as much as 35%.

In spite of the severe deterioration, the bridge still held over 720,000 pounds before failing. This was equivalent to 22 HS-20 trucks. Final failure appears to have occurred when the shear capacity of the deteriorated shoulder was exceeded. A shear crack propagated from this shoulder in an arc around the points to the abutment. The failure surface was heavily influenced by the rebar layout and followed the cut off bar ends.

The bridge behavior was highly influenced by geometric conditions and the load carrying mechanism varied during the test. Originally, the bridge carried the load parallel to the traffic lanes. At a load of about 225,000 pounds, there was an abrupt change in the stiffness at the abutment. After this change, the bridge slowly redistributed the load to a path perpendicular to the skew, the more natural load path (as shown by linear finite element analysis). This change in load path was not sudden, but gradual. As a result, most of the limit states identified were associated with changes in the load path. Limit states dealing with cracking of the concrete were reached late in the loading cycle and yield of the rebar had just begun at failure.

The basic conclusion from the destructive test was that the slab bridge had far more capacity than had been anticipated and, in fact, it highly improbable that the final failure load could have even been placed on the bridge by traffic. This bridge could have been repaired and its service life extended had the true capacity been known beforehand. However, the brittle shear failure is of concern and more research into the capacity of deteriorated concrete is indicated.

Nondestructive testing proved to be a useful, although sometimes cumbersome, method of detecting damage in the bridge. Originally, the bridge deck was covered with an asphalt

overlay which prevented the research team from evaluating the bridge deck condition. Coring revealed that the shoulder region was deteriorated, but the extent of deterioration could not be determined without taking an inordinate number of cores.

Since the bridge can be modeled as linear under service loads, comparisons between the truck load tests and a linear FE model provided useful information. Damage to the shoulder and edge regions was detected as these regions were more flexible than the model predicted. However, the major drawback to the truck load testing was that it is only useful when the load is of sufficient magnitude and properly positioned to activate the damaged area. As a result, a large number of different truck positions would be needed for a complete test.

Modal testing showed a great deal of promise for nondestructive testing due to its ability to provide a modal flexibility matrix. This matrix can be used in conjunction with finite element analysis to detect damage in the entire structure. Initial tests were able to detect damage to the shoulder areas and in the northwest corner of the north span even through the asphalt overlay, but without an available baseline test, the results were largely qualitative. However, when the initial test was used as a baseline for the destructive test, modal analysis was able to accurately detect the severe damage to the slab well before it was visible or detectable by other means.

The bridge was rated in order to provide insight into the current rating system. Rating was performed under the 1983 and 1989 AASHTO Guidelines and by finite element analysis. In all cases, the rating was governed by the negative moment capacity over the piers. The rating was heavily influenced by the choice of material properties. Using the assumed values given in the AASHTO guidelines, the bridge was found to be deficient under both AASHTO rating methods ( $RF < 1$ ). The bridge was found acceptable under both AASHTO methods when actual material properties were used. When a linear finite element program was used (SAP 90), the rating factor increased, but not substantially.

When performing a rating, safety factors are included. Theoretically, if the safety factors are removed the result should be the bridge capacity. After removing the safety factors, the 1989 AASHTO Guidelines predicted yield at 5 equivalent trucks while the finite element program predicted yield at 10 equivalent trucks. Evidence from the destructive test indicated that yield was detected at 20 equivalent trucks (although uninstrumented bars may have yielded at 17 equivalent trucks); a much higher level than predicted by the rating process. This confirms that the current process does not fully utilize the capacity of slab bridges and even finite element analysis may considerably underrate their actual resources of strength.

Nonlinear and linear finite element analyses indicate the importance of the tensile behavior of concrete and more significantly membrane force, particularly in the inelastic range. Due to the significance of membrane force, which is influenced directly by the support conditions at the abutments, a careful modeling of slab-abutment connection is a prerequisite for detailed evaluation of slab bridges. Such models must simulate the expected

kinematics at the abutments, and be able to "regulate" the level of membrane force developed in the slab at different limit states. Only after careful calibration of slab-abutment model was it possible to correlate the measured global, regional, and local responses. Simulation of existing damage in deteriorated bridges is also an important component of comprehensive analysis. Considering uncertainties regarding local variations of material properties, simple techniques such as reducing the effective slab depth of the deteriorated regions appears to be adequate. More refined damage models are needed.

The sensitivity of analytical responses points to the fact that the "actual" ultimate strength and stiffness characteristics of slab bridges cannot yet be established through nonlinear finite element analysis (NLFEA). For design of new bridges or upgrade of existing structures, upper and lower bounds of behavior need to be determined by parametric studies conducted by NLFEA.

## **9.2 SPECIFIC CONCLUSIONS FROM EACH CHAPTER**

### **9.2.1 Chapter 1 Conclusions**

Research has shown that the capacities of highly redundant structures, such as reinforced concrete slab bridges, are not well understood. Other research, or perhaps more correctly lack of research, has indicated that the capacities of deteriorated structures are not well understood due to difficulties in detecting and assessing the severity of damage and how local damage affects structural capacity. This research was designed to completely study a deteriorated slab bridge through a combination of nondestructive testing, destructive testing and analytical modeling and rating. It is hoped that this research will provide insight into the behavior of deteriorated slab bridges and provide some rational basis for future decisions about their repair or replacement.

### **9.2.2 Chapter 2 Conclusions**

Core tests indicated that the bridge deck concrete had strengths between 7180 and 8180 psi with an average strength of 7660 psi. Samples of the reinforcing bar were machined into standard ASTM tensile specimens and it was found that the reinforcing bar was grade 40 with an average yield strength of 49,000 psi and an average ultimate strength of 98,000 psi.

### **9.2.3 Chapter 3 Conclusions**

All three bridge spans showed about the same level of deterioration on the shoulders and edges of the deck. The cores showed that horizontal cracking and fragmentation occurred up to 4 feet to 6 feet from the east and west edges of the deck (to the edge of the roadway lanes). There were also signs of deterioration in the west lane of the north span as cores in this area came out fragmented.

A petrographic analysis was performed of core samples and samples removed after destructive testing. It was confirmed that cyclic freezing ("D" cracking) of the aggregate had damaged the shoulder concrete and alkali silica reaction (ASR) had also formed in these

areas. Ettringite formation and leaching of soluble compounds had also occurred.

The most probable cause of deterioration of the bridge deck is that water, snow, and deicing salts were brushed to the sides of the deck by plows and traffic. Some of it laid on the shoulders while the rest washed over the edge of the deck. The drainage of the bridge was very poor and salt laden water and snow was probably retained on the deck. The water that melted over the edge of the deck may have seeped in between the asphalt and concrete deck due to a poor seal and water and melted salt that had soaked through the asphalt layer was caught between the two layers. This would have saturated the concrete. The asphalt layer may have done more harm than good by trapping water and salt and allowing it to saturate the side areas of the deck. Once saturated, the large aggregates "D" cracked under freeze/thaw cycles and caused horizontal cracking in the deck. After horizontal cracks due to "D" cracking had occurred, the water and salt that drained off the edge of the deck penetrated the cracks and provided an environment for ASR.

"D" cracking had occurred before ASR set in, because cracking had first occurred at the rebar level, which is characteristic of "D" cracking and not ASR. ASR cracking occurs between the rebar levels in good concrete because the rebars put compressive stresses in the concrete at the rebar levels as the concrete expands. The "D" cracking began the first time an aggregate was saturated and the temperature dropped below 0°C, which was probably the first winter during the life of the bridge.

ASR had also caused a considerable amount of damage, but it took longer for the alkalis and silica to react and reach a damaging stage. ASR and "D" cracking worked together in the later stages of deterioration. The ASR cracking had followed the path of the existing "D" cracking because this was the path least resistance. It was hard to distinguish between cracking due to ASR and "D" cracking, and more research is needed to determine the type of cracking caused by the two mechanisms in bridge decks.

The top layer of concrete on the east and west shoulders of the deck was spalled. The rebars on the east shoulder of the deck were severely corroded due to rusting while those on the west shoulder were not rusted, so that the expansion of the rebars due to rusting did not cause the concrete to spall on the west side. The rusted bars on the east shoulder might have contributed to the spalling of the top layer of concrete, but this is not certain since it is not known when the corrosion occurred. Corrosion of the east shoulder steel may have occurred after the top layer of concrete spalled.

Many of the reinforcing bars on the east shoulder of the deck were severely corroded. However, testing showed that the internal strength parameters, yield and ultimate stress, were not affected by rust on the reinforcing bars. The rusted rebar was 95% effective in carrying loads, once the cross sectional areas were adjusted for area lost due to corrosion. For the calculation of the load carrying capacity of a deteriorated bar, the areas along the length of the bar would need to be measured very carefully after cleaning all loose rust and the capacity could be estimated using  $0.95 \cdot A_{\text{measured}} \cdot f_y$  as a safe load capacity for corroded steel bars.

When compared to unrusted bars, it was found that the rusted bars had lost a considerable amount of cross sectional area. Some of the bars had lost up to 34% of their original area, while most had lost 5%-21%.

#### **9.2.4 Chapter 4 Conclusions**

When planning the instrumentation for tests, it is necessary to consider the quantities being measured, the probable value of those quantities and conditions under which the quantities will be measured. For the destructive test, a combination of field measurements, analytical studies and careful assessment of field conditions all played vital roles in the final instrument selection. Four instruments were selected:  $\pm 1"$  range DCDTs, 10" range slide wire potentiometers, bondable strain gages and clip gages.

Careful calibration can uncover better accuracy in many instruments. It is also necessary to calibrate instruments with actual cabling and data acquisition system which will be used since the cables and data acquisition system may affect the instrument performance. The slide wire potentiometers and DCDTs were carefully calibrated and four separate types of error were identified and evaluated. The types of error were linearity, repeatability, hysteresis (including backlash) and drift. The accuracy of the instrument was found by combining the numerical values of the errors. The careful calibration also identified the dominant error. In the case of the DCDTs the dominant error is linearity for which compensation is possible. After minimizing the linearity error in the DCDTs, accuracy was increased by four to ten times (depending on the range used) over the manufacturer's stated values. Accuracy of slide wire potentiometers was increased by a factor of two.

Finally, it is important to note that laboratory calibration is not, in itself, sufficient. The actual field conditions can affect the behavior of the instrument. It is vital to check the performance of the instrument in the field prior to any testing.

#### **9.2.5 Chapter 5 Conclusions**

Destructive load testing can reveal a wealth of information about structural condition and projected performance. The results of visual inspections, non destructive tests and destructive load testing can be combined to provide the necessary information for modeling structures. However, in order to obtain reliable information from either service (design) load testing or destructive testing, great care must be taken in the design of the test and the instrumentation. Measurements of load and deflection can be useful, especially in detecting loss of stiffness due to damage. However, to fully understand the complete behavior of a bridge (or any structure), it is also necessary to measure boundary rotations, boundary movements, material strains and local deformations.

The bridge displayed limit states 224,000 pounds (7 equivalent HS-20 trucks), 384,000 pounds (12 trucks) and 544,000 pounds (17 trucks) before failing at 720,000 pounds (22 trucks). The first two limit states have been associated with changes in the boundary conditions. Initially, the bridge carried the load parallel to the traffic lanes even though it

is more natural for a skew bridge to carry loads perpendicular to the skew. At the first limit state, there was an abrupt change in the stiffness at the abutment. After the first limit state, the bridge began to slowly change the load carrying mechanism to the more natural skew mechanism. The second limit state (384,000 pounds or 12 trucks) seems to mark the end of this transition. It is of interest that the first two limit states are associated with geometrical considerations rather than the usual material considerations (i.e. yield or cracking).

The third limit state (544,000 pounds or 17 trucks) seems to be associated with material behavior. This limit state was marked with additional cracking and it is suspected that some of the uninstrumented reinforcing bars may have begun to yield.

The bridge carried a total of 720 kips before failure. This was equivalent to 22 HS-20 trucks. However, the failure was in shear, not flexure. It is believed that the final failure surface began as a crack in the deteriorated shoulder region. The final failure surface was an approximate arc which followed the ends of the cut off negative steel bars on the top of the slab. The shear failure was a surprise since the shear capacity, as predicted by the ACI code, was much higher than the failure load. This leads to concern over possible nonductile failure and the inability of current methods to predict the behavior of damaged concrete.

The severe deterioration along the shoulder area did not appear to seriously affect the service load bridge performance, although loss of stiffness in the damaged region was clearly detectable. This deterioration appeared only to affect the ultimate strength of the bridge. Since the ultimate strength at failure was many times the probable maximum traffic load, it is possible that the bridge could have served for many more years if the bars had been cleaned and the area resurfaced although the effect of repairing the damaged shoulders on the ultimate load capacity is uncertain.

## **9.2.6 Chapter 6 Conclusions**

### **9.2.6.1 Regarding the Modal Test Procedure**

System identification by experimental methods is crucial in determining the true characteristics of any structure. The governing characteristics of the structure are expressed as system parameters in an input-output relation. Whether the system parameters are to be used in a structural identification scheme for evaluating the performance of the structure or for the purposes of designing a control system, accurate determination of these parameters is very important. In structural dynamics these parameters are natural frequencies, damping values and modal vectors.

As an experimental tool for structural identification of highway bridges, modal testing, and especially impact testing, performs very well. As a result of an extensive impact test on a medium size slab bridge, the first twenty natural frequencies, damping values and modal vectors may be determined. Compared to other forms of excitation (sine sweep, random, etc.) which require a large exciter, impact testing has demands lesser hardware and manpower needs. Furthermore, since impact testing may be performed without the need

to completely close a bridge to traffic, it is a feasible experimental method for existing highway bridges during use.

**Data Acquisition:** Several critical observations pertaining to the impact testing of large civil structures and especially bridges are listed below:

i) A preliminary finite element model of the bridge aids in the design of the impact test in terms of selecting the grid and positioning of the accelerometers as well as the estimated locations of the modes

ii) Geometrically similar structures have similar mode shapes. Therefore, by forming a database from all the tests performed on different bridges, it is possible to choose an appropriate test grid and locations for the reference transducers. Locating the reference instruments on maximum amplitude positions in the mode shapes greatly helps to capture the modes and improves the signal-to-noise ratio in the measured frequency response functions.

iii) A simple single reference test performed prior to the actual impact test helps to select the frequency range of interest.

iv) A good rule of the thumb to improve signal-to-noise ratio is to use a high number of averages. In the tests conducted on this bridge five averages per point were used. It is felt that if more averages had been taken, the data would have been cleaner and easier to manipulate. However, in selecting the number of averages for a certain test, factors such as the size of the structure, magnitude of the input force and most importantly time constraints must be taken into account.

v) To better excite the higher modes of the structure it is recommended that a force level higher than the one used here, be employed. Development of an automated, powerful impact hammer specially designed for highway bridges would help to reduce signal processing problems by delivering consistent impacts and a higher signal-to-noise ratio.

vi) All other data acquisition settings such as exponential window decay rate, trigger delay time and amplification are naturally dependent on the structure being tested and should be adjusted prior to the actual test to give the best frequency response functions.

vii) Another important consideration specific to bridge testing is fixing of the transducers on the structure. In general hot glue performs very well. However, if regions of the bridge where transducers or hit points are located have deteriorated and concrete is loose, then these locations should be cleaned or scraped until sound concrete is reached. Locating transducers or hitting on loose aggregate causes inaccurate measurements and frequent overloads.

**Data Reduction:** Due to the noisy nature of the data and reciprocity problems, performing parameter estimation on bridge impact test data can be tedious. In the case of this bridge, parameter estimation of the modes between twelve and nineteen was troublesome. The problem stemmed not only from the noise in the data but also from the closely coupled

nature of the modes. At times separating the modes became quite a challenge. Complex Mode Indicator Function (CMIF) parameter estimation algorithm performed well in locating the modes. Therefore, CMIF was used as a first step algorithm before the more sophisticated Polyreference Time Domain (PTD) method was used to estimate the frequencies and damping. For estimating the modal vectors, Polyreference Frequency Domain (PFD) method was used. With PFD, it was possible to incorporate the effects of the modes outside the frequency range (residual terms).

After performing parameter estimation on the data, it was seen that the modes of the structure were grouped in two categories: global modes and local modes. Although the global modes were captured by almost all of the references, the local modes of the three spans were captured mainly by the references located on each respective span. When estimating the local mode of a span, it was observed that the contribution of the transducers located on other spans was negligible. Therefore, in order to eliminate the possible distorting effects of the other references, only the transducers located on one span were used to estimate the modes of that span. This procedure, called selective reference method, produced better curve fitting and more accurate frequency and damping estimation.

#### **9.2.6.2 Regarding the Use of Modal Testing as a Nondestructive Evaluation Tool**

This study has shown that impact testing and subsequent post processing of its results can be used as a health monitoring tool for many of the existing highway bridges. Provided that a modal baseline exists, modal testing is a far better solution to detecting structural changes than many of the historically used nondestructive methods on bridges. Commonly used methods for rating bridges such as static and moving truck load tests and proof load testing are cumbersome and do not provide comprehensive quantitative results about the present state of the test specimen. On the other hand, localized damage detection procedures such as core sampling, acoustic imaging, impact echo techniques and visual inspection do not provide any information about the global state-of-health of the bridge. When used in conjunction with the proposed methodology, however, they may become increasingly useful for localized evaluation.

The results of the two impact tests done before and after twenty equivalent rating truck loads demonstrate the ability of the modal test to predict and quantify the damage the bridge had sustained. Changes in the frequencies and damping values hinted at the presence of damage. However, no changes in the mode shapes were observed. Such changes can only be observed in the high local modes which may be captured by highly advanced modal filtering methods. The development of such special data processing methods is a future research topic.

The most striking observation was made possible by the use of the flexibility profile method. When the flexibility matrix obtained from the results of the modal test was loaded with different loading configurations, the resulting deflection profiles clearly revealed the location of damage.

In the absence of a baseline modal model, using a calibrated finite element model as a baseline was attempted. The flexibility profiles of this analytical model are compared to the ones obtained from the first modal test to identify discrepancies and anomalies. This study was qualitative in nature and showed promise to identify gross structural damage or degradation.

Dynamic monitoring of critical highway bridges is seen as a feasible alternative to present inspection methods. A monitoring program may be divided into two parts:

- i) modal testing and finite element modeling to form a baseline model on existing critical bridges (new or already in use) and,
- ii) periodic monitoring of the bridges. This can be in the form of acquiring operational data and monitoring possible shifts in the natural frequencies. When changes in the frequencies are recorded, a modal test and subsequent studies may be performed to fully diagnose the problem.

Such a bridge monitoring program could lead to "smart" vibration monitoring systems being placed on critical bridges in the future. It should be emphasized that the process of modal testing and subsequent analyses requires extensive expertise and is not yet in the realm of standard bridge engineering practice. However, until more sophisticated, commercially available deflection measuring methods such as laser holography are developed for civil structures, obtaining the flexibility matrix and subsequently the 3-D deflection profiles from the results of a modal test appear to be a promising tool in the health monitoring process of critical bridges.

#### 9.2.7 Chapter 7 Conclusions

Bridge rating software presently used by highway engineers generally conducts analyses with over-idealized analytical models. Several programs have been more recently developed that can aid the engineers in bridge design and rating (ref. SAP90 Bridge Module). However, even these packages lack the capability of more advanced finite elements such as shell elements. Hopefully, improved packages will be available soon. At present, the time requirements needed to rate a bridge using FEM is considerably more than would be practical in most cases.

Overall, based on these ratings, the bridge has been proven worthy and capable of continuing operations as normal. The worst rating factors were based on the code material properties and would warrant the posting and eventual replacement of the bridge. However, when the measured material properties were used, the bridge passed all rating easily and would only appear to be in need of repair.

These ratings are all based on a RC slab bridge and findings here should not be carried over to other bridge types. Also, the skew nature of the bridge creates special conditions. Therefore, care should be taken in any attempt to use the findings here on any other type of bridge, or a non-skewed slab bridges.

### 9.2.8 Chapter 8 Conclusions

Through linear and nonlinear finite element analyses it was possible to make some important observations regarding modeling of reinforced concrete slab bridges. It became apparent that the tensile behavior of concrete and more significantly membrane force in the slab greatly influence the response, particularly in the inelastic range. The level of membrane force which can be developed is directly influenced by support conditions at abutments. For cases where supports are restrained horizontally, which will result in large membrane force, strength and stiffness are magnified appreciably. Other parameters such as shear retention factor, Poisson's ratio, or modeling of slab-pier cap are not apparently important.

Considering the significance of support conditions, a proper modeling of the slab-abutment connection emerges as one of the most important modeling steps. A successful model must simulate the expected kinematics, i.e. allow "rocking" of slab while restraining horizontal movement at shear keys. Only after developing such comprehensive model was it possible to replicate reasonably both the measured local and global responses of the test bridge. Other simple methods such as complete removal of horizontal restraints at the abutments may lead into acceptable correlations, but these techniques do not account for the deformation kinematics at abutments.

Simulation of damage is a prerequisite for comprehensive modeling of deteriorated structures. For the test bridge, a simple method involving reduction of slab thickness in the regions where damage had occurred was found to be sufficient. Considering uncertainties regarding local variations of material properties even in new structures, models where concrete properties (most notably compressive and tensile strengths, and modulus of elasticity) are varied locally appear somewhat questionable.

Simple yield line analyses gave very close estimates of the measured strength. Response of the test bridge and mode of failure, however, suggest a significant influence of shear. Only a limited number of bars was at or beyond yield at failure. Hence, the close match between the total load resisted by the bridge and that predicted by yield line analyses appears to be coincidental.

The nonlinear finite element analysis was found to be reliable only after careful modeling of material properties, simulation of boundary conditions, and geometric modeling of the entire slab-pier system. If experimental data are not available to calibrate the model, the upper and lower bounds of the ultimate strength and stiffness characteristics should be established by parametric studies.

## **References**

- AASHTO (1983). "Manual for maintenance inspection of bridges," Washington, D.C.
- AASHTO (1989). "Specifications for strength evaluation of existing steel and concrete bridges." Washington, D.C.
- AASHTO (1983). "Standard specifications for highway bridges." Washington, D.C.
- ACI (1989). "Building code requirements for reinforced concrete." ACI 318-89, Detroit, Michigan.
- Agbabian, M. S. and Masri, S. F., Eds., (1988). Proceedings of the international workshop on nondestructive evaluation for performance of civil structures. University of Southern California.
- Agbabian, M. S., Masri, S. F. et al. (1987). "A system identification approach to the detection of changes in structural parameters." Proceedings of the Workshop on Structural Safety Evaluation Based on System Identification Approaches, Lambrecht/Pfalz, Germany.
- Aktan, A. E. et al. (1992). "Bridge nondestructive evaluation by structural identification; 1) description of methodology, 2) applications." Proceedings, Third NSF Workshop on Bridge Engineering Research in Progress, Department of AMES, University of California at San Diego, San Diego, California.
- Aktan, A. E. and Nelson, C. E. (1988). "Problems in predicting seismic responses of reinforced concrete buildings." Journal of Structural Engineering, ASCE, September.
- Aktan, A. E. and Raghavendrachar, M. (1990). "Nondestructive testing and identification for bridge rating: pilot project." Research Report 90-1, Department of Civil and Environmental Engineering, University of Cincinnati, Cincinnati, Ohio.
- Allemang, R. J. and Brown, D. L. (1987). "Experimental modal analysis and dynamic component synthesis." Technical Report AFWAL-TR-87-3062, SDRL, University of Cincinnati, Cincinnati, Ohio.
- ASTM C114. (1988). "Standard test methods for chemical analysis of hydraulic cement." Vol. 4.01, Philadelphia, Pennsylvania, 94.
- ASTM C295-85. (1988). "Standard practice for petrographic examination of aggregates for concrete." Vol. 4.02, Philadelphia, Pennsylvania, 410-422.
- ASTM C642-82. (1988). "Standard test method for specific gravity, absorption, and voids in hardened concrete." Vol. 4.02, Philadelphia, Pennsylvania, 310-311.
- ASTM C856-83. (1988). "Standard practice for petrographic examination of hardened concrete." Vol. 4.02, Philadelphia, Pennsylvania, 410-422.
- Bakht, B. and Jeager, L. G. (1990). "Bridge testing - a surprise every time." Journal of Structural Engineering, ASCE, 116(5).
- Betero, V. V. et al. (1984). "Earthquake simulator tests and associated analytical and correlation studies of a 1/5 scale model." Special Publication, SP-84, Earthquake Effects on Reinforced Concrete Structures, American Concrete Institute, Detroit, Michigan.
- Browne, R. D. and Domone, P. L. (1975). Proceedings, conference on underwater construction technology. University College, Cardiff.
- Burdette, E. G. and Goodpasture, D. W. (1988). "Correlation of bridge load capacity estimates with test data." NCHRP Report #306, Transportation Research Board, National Research Council, Washington D.C.
- Charney, F. A. and Betero, V. V. (1982). "An evaluation of the design and analytical seismic response of a seven-story reinforced concrete frame-wall structure." Report No. UCB/EERC-82/08, Earthquake Engineering Research Center, University of California at Berkeley, Berkeley, California.
- Chen, J-C. and Garba, J. A. (1987). "Structural damage assessment using a system identification technique." Proceedings of the Workshop on Structural Safety Evaluation

- Based on System Identification Approaches, Lambrecht/Pfalz, Germany.
- Chesi, C. and Schnobrich, W. C. (1991). "Three-dimensional effects in lateral behavior of frame-wall systems." J. Struct. Div., ASCE, 117(2), 391-409.
- Coggins, F. B. and French, C. W. (1990). "Chloride ion distribution in twenty-year old prestressed bridge girders." ACI Materials Journal, 87(5), 479-488.
- Committee on Infrastructure Innovation of the National Research Council. (1987). Infrastructure for the 21st century.
- Cooper, J. M., Chief, Structures Division, Office of Research, Development and Technology, FHWA, (1992). "Keynote address." 9th International Bridge Conference, Pittsburgh, Pennsylvania.
- Darwin, D. and Pecknold, D. A. (1974). "Inelastic model for cyclic biaxial loading for reinforced concrete." Civil Engineering Studies, SRS 409, University of Illinois at Urbana, Urbana, Illinois.
- Fang, I. et. al. (1990), "Load Capacity of Isotropically Reinforced, Cast in Place and Precast Panel Bridge Decks," PCI Journal, July-Aug., 1990.
- Flesch, R. G. and Kernbichler, K. (1988). "Bridge inspection by dynamic tests." Proceedings, Structural Safety Evaluation Based on System Identification Approaches, Eds. Natke, H. G. and Yao, J. T. P., Lambrecht/Pfalz, Germany.
- Friedland, I. M. (1987). "Nondestructive testing and identification for bridge evaluation and rating." NCHRP Project Statements 12-28(13) and 12-28(13)A, Transportation Research Board, Washington, D.C.
- Friedland, I. M. (1990). "Nondestructive testing and identification for bridge evaluation and rating." NCHRP Project Statements 12-28(13) and 12-28(13)A, Transportation Research Board, Washington, D.C.
- Gallegos-Cazares, S. and Schnobrich, W. C. (1988). "Effects of creep and shrinkage on the behavior of reinforced concrete gable and roof hyperbolic-paraboloids." Civil Engineering Series, SRS No. 543, University of Illinois at Urbana, Urbana, Illinois.
- Ghush, G. E. and Saidi, M. (1986). "A simple hysteresis element for biaxial bending R.C. columns and implementation in NEABS-86." Report No. CCEER86-1, Center for Civil Engineering Earthquake Research, University of Nevada-Reno, Reno, Nevada.
- Gilbert R. I. and Warner, R. F. (1978). "Tension stiffening in reinforced concrete slabs." J. Struct. Div., ASCE, 104(12), 1885-1900.
- Habibullah, A. and Wilson, E. L. (1989). "SAP90 user's manual." Computers and Structures Inc., Berkeley, California.
- Hadipriono, F. C. (1985). "Analysis of events in recent structural failures." Journal of Structural Engineering, ASCE, 111(7), 1468-1481.
- Halvorsen, W. G. and Brown, D. L. (1977). "Impulse technique for structural frequency response testing." Sound and Vibration, November.
- Hart, G. C. and Yao, J. T. P. (1977). "System identification in structural dynamics." Journal of the Engineering Mechanics Division, ASCE, 103(EM6).
- Hearn, G. and Testa, R. B. (1991). "Modal analysis for damage detection in structures." Journal of Structural Engineering, ASCE, 117(10).
- Hogue, T. D., Aktan, A. E., and Hoyos, A. (1991). "Localized identification of constructed facilities." Journal of Structural Engineering, ASCE, 117(1).
- Hsieh, S., Ting, E., and Chen, W. F. (1982). "A plastic fracture model for concrete." International Journal of Solids and Structures, 18(3), 181-197.
- Huber, F. (1991). "Update: bridge scour." Civil Engineering, ASCE, September, New York, New York.
- Huria, V., Lee, K-L and Aktan, A. E. (1993a), "Nonlinear Finite Element Analysis of RC Slab Bridge," Journal of Structural Engineering, ASCE, Vol 119, No. 1, January, 1993, pp. 88-

- Huria, V., Lee, K-L and Aktan, A. E. (1993b), "Integrated Inspection and Rating of RC Slab Bridges," Submitted as a Technical Note, Journal of Structural Engineering, ASCE, March, 1993.
- Ibanez, P., (1972). "Identification of dynamic structural models from experimental data." Engineering Report, UCLA-ENG-7225, UCLA, Los Angeles, California.
- Ibrahim, S. R. (1988). "Correlation of analysis and test in modeling of structures: assessment and review." Proceedings, Structural Safety Evaluation Based on System Identification Approaches, Eds. Natke, H.G. and Yao, J.T.P., Lambrecht/Pfalz, Germany.
- Iding, R. H. et al. (1992). "Specific applications of finite element analysis to concrete structures." Proceedings, 10th Structures Congress, San Antonio, Texas, 955-958.
- Imbsen, R. A., Lui, W. D., Schamber, R. A., and Nutt, R. V. (1987). "Strength evaluation of existing reinforced concrete bridges." NCHRP Report #292, Transportation Research Board.
- Kress, V. (1991). "Laboratory studies of several concrete specimens for the university of Cincinnati." WJE No. 918473.
- Kupfer, H. and Gerstle, K. N. (1973). "Behavior of concrete under biaxial stresses." J. Eng. Mech. Div., ASCE, 99(4), 852-866.
- Kupfer, H., Hilsdorf, H. K., and Rusch, H. (1969). "Behavior of concrete under biaxial stress." ACI Journal, 66(8), 656-666.
- Lee, K-L., Chuntavan, C., Huria, V., and Aktan, A. E. (1991). "Computer program for three-dimensional static collapse analysis of structures-(3DSCAS), Version II." Report No. 091, Department of Civil and Environmental Engineering, University of Cincinnati, Cincinnati, Ohio.
- Locke, C. E. (1986). "Corrosion of steel in portland cement concrete: fundamental studies." Corrosion Effect of Stray Currents and the Techniques for Evaluating Corrosion of Rebars in Concrete, ASTM STP-906, Ed. Chaker, V., American Society for Testing and Materials, Philadelphia, Pennsylvania, 5-14.
- Lopez, L. A., Dodds, R. H., Rehak, D. R., and Schmidt, R. J. (1987). "POLO-FINITE: a structural mechanics system for linear and nonlinear, static and dynamic analysis." Civil Engineering Systems Laboratory, University of Illinois at Urbana, Urbana, Illinois; Department of Civil Engineering, University of Kansas, Lawrence, Kansas; Department of Civil Engineering, Carnegie-Mellon University, Pittsburgh, Pennsylvania; and Department of Civil Engineering, University of Wyoming, Laramie, Wyoming.
- Malvar, L. (1992), "Punching Shear Failure of a Reinforced Concrete Pier Deck Model," ACI Structural Journal, Vol. 89, No. 5, Sept.-Oct. 1992, pp. 569-576.
- Maslehuddin, M. et al. (1990). "Effect of rusting of reinforcing steel on its mechanical properties and bond with concrete." ACI Materials Journal, Sept.-Oct., 496-502.
- Mazurek, D. F. and DeWolf, J. T. (1990). "Experimental study of bridge monitoring technique." Journal of the Structural Engineering, ASCE, 116(9).
- McGogney, C. H. and Nickerson, R. L. (1992). "Nondestructive evaluation: the seat belt for bridge safety." 9th International Bridge Conference, Pittsburgh, Pennsylvania.
- Meschke, G. et al. (1991). "Finite element analyses of cracked cooling tower shell." J. Struct. Div., ASCE, 117(9), 2620-2639.
- Milford, R. V. and Schnobrich, W. C. (1984). "Nonlinear behavior of reinforced concrete cooling towers." Civil Engineering Studies, Structural Research Series, No. 514, University of Illinois at Urbana, Urbana, Illinois.
- Miller, R., Krouskop, B., Minkarah, I., and Bodocsi, A. (1992). "Chloride penetration and the effect on porosity in a pavement." Transportation Research Record, 1392, August, 1993.
- Mindess, S. and Young, J. F. (1981). Concrete. Prentice-Hall, Inc., Englewood Cliffs, New

Jersey.

- Moses, F. and Verma, D., (1987). "Load capacity evaluation of existing bridges." NCHRP Report #301, Transportation Research Board.
- Muller, T. K. (1985). "Concrete tanks subjected to fire load," Graduate Thesis, Part II, Delft University of Technology, Delft, Netherlands (in Dutch).
- Natke, H. G. and Yao, J. T. P., Eds., (1988). Proceedings of the workshop on structural safety evaluation based on system identification approaches. Lambrecht/Pfalz, Germany.
- Novak, A. S. and Tharmabala, T. (1988). "Bridge reliability evaluation using load tests." Journal of Structural Engineering, ASCE, 114(10).
- NSF (1992). "Quantitative nondestructive evaluation for construction facilities."
- Okamura H., Maekawa K., and Sivasubramaniyam, S. (1985). "Verification of modeling for reinforced concrete finite element." Finite Element Analysis of Reinforced Concrete Structures. Eds. Meyer C. and Okamura H., ASCE, 528-543.
- Ougourlian, C. V. and Powell, G. H. (1982). "ANSR-III, general purpose computer program for nonlinear structural analysis." Computer and Structures, 15(4), 365-377.
- Park, R. and Gamble, W. L. (1980). Reinforced concrete slabs. Wiley-Interscience, New York, New York.
- Pinjarkar, S. G., Guedelhoefer, O. C., Smith, B. J., and Kritzler, R. W. (1990). "Nondestructive load testing for bridge evaluation and rating." Final report for NCHRP, Transportation Research Board.
- Raghavendrachar, M. (1991). "Global and local structural identification of a RC bridge by impact testing," thesis presented to the University of Cincinnati, Cincinnati, Ohio, in partial fulfillment of the requirements for the degree of Doctor of Philosophy.
- Raghavendrachar, M. and Aktan, A. E. (1992). "Flexibility by multireference impact testing for bridge diagnostics." Journal of Structural Engineering, ASCE, 118(8).
- Salane, H. J., Baldwin, J. W., and Duffield, R. C. (1971). "Dynamics approach for monitoring bridge deterioration." Transportation Research Record No. 832, Transportation Research Board, Washington, D.C.
- Schulz, J. X., Goble, G. G., and O'Fallon (1992). "Static testing of highway bridges." Transportation Research Board Paper 920204, to be published in the Transportation Research Record.
- "Section 4500 Cl-Chloride, D. potentiometric method" Standard Methods for the Examination of Water and Wastewater, 17th ed., Port City Press, Baltimore, Maryland, (4-67) and (4-72).
- Shahawy, M. A. (1992). "Strength evaluation and load testing of existing bridges." Transportation Research Board Paper 920245, to be published in the Transportation Research Record.
- Shahrooz, B. M. et al. (1992). "Nonlinear finite element analysis of a reinforced concrete R.C. bridge." ASCE Structural Journal, to be published February, 1994.
- Shahrooz, B. M. and Moehle, J. P. (1987). "Experimental study of seismic response of R.C. setback buildings." Report No. UCB/EERC-87/16, Earthquake Engineering Research Center, University of California at Berkeley, Berkeley, California.
- Shih, C. Y., Tsuei, Y. G., Allemang, R. J., and Brown, D. L. (1989). "Complex mode invention function and its application to spatial domain parameter estimation." Proc., Seventh International Modal Analysis Conference, Las Vegas, Nevada.
- Shimozuka, M., Yun, C. B., and Imai, H. (1982). "Identification of linear structural dynamic systems." Journal of Engineering Mechanics Division, ASCE, 106(6).
- Slater, J. E. (1983). "Corrosion of metals in association with concrete." ASTM STP-818, 1-18.
- Stark, D. (1991). "Handbook for identification of Alkali-Silica reactivity in highway structures." SHRP-C/FR-91-101, Strategic Highway Research Program, National Research

- Council, Washington, D.C., 1-49.
- "Strength evaluation of existing concrete buildings." (1991). ACI 437R-91, American Concrete Institute, Detroit, Michigan.
- Suprenant, B. A., Noland, J. L., and Schuller, M. P. (1992). Proceedings, nondestructive evaluation of civil structures and materials. University of Colorado, Boulder, Colorado.
- Toksoy, T. (1992). "Nondestructive evaluation of a reinforced concrete highway bridge based on modal analysis," thesis presented to the Department of Mechanical, Industrial, and Nuclear Engineering, University of Cincinnati, Cincinnati, Ohio, in partial fulfillment of the requirements for the degree of Master of Science.
- van Mier, J. G. M. (1987). "Examples of nonlinear analysis of reinforced concrete structures with DIANA." HERON, 32(3).
- Vecchio F. J. and Collins M. P. (1986). "The modified compression-field theory for reinforced concrete elements subjected to shear." ACI Struct. J., 83(2), 219-231.
- Wallace, J. W. (1992). "BIAX: Revision 1, a computer program for the analysis of reinforced concrete and reinforced masonry sections." Report CU/CEE-92/4, Department of Civil Engineering, Clarkson University, Potsdam, New York.
- Wilkins, N. J. M. and Sharp, J. V. (1990). "Localized corrosion of reinforcement in marine concrete." 3rd International Symposium on Corrosion of Reinforcement in Concrete Construction, Society of Chemical Industry, United Kingdom, 3-17.
- Zwick, M., Toksoy, T., and Aktan, A. E. (1992). "Nondestructive evaluation and destructive testing of a highway bridge." Paper # IBC 92-8, International Bridge Conference, Pittsburgh, Pennsylvania.